

# IUTAM Symposium on Reynolds Number Scaling in Turbulent Flow

# FLUID MECHANICS AND ITS APPLICATIONS

## Volume 74

---

*Series Editor:* R. MOREAU

*MADYLAM*

*Ecole Nationale Supérieure d'Hydraulique de Grenoble*

*Boîte Postale 95*

*38402 Saint Martin d'Hères Cedex, France*

### *Aims and Scope of the Series*

The purpose of this series is to focus on subjects in which fluid mechanics plays a fundamental role.

As well as the more traditional applications of aeronautics, hydraulics, heat and mass transfer etc., books will be published dealing with topics which are currently in a state of rapid development, such as turbulence, suspensions and multiphase fluids, super and hypersonic flows and numerical modelling techniques.

It is a widely held view that it is the interdisciplinary subjects that will receive intense scientific attention, bringing them to the forefront of technological advancement. Fluids have the ability to transport matter and its properties as well as transmit force, therefore fluid mechanics is a subject that is particularly open to cross fertilisation with other sciences and disciplines of engineering. The subject of fluid mechanics will be highly relevant in domains such as chemical, metallurgical, biological and ecological engineering. This series is particularly open to such new multidisciplinary domains.

The median level of presentation is the first year graduate student. Some texts are monographs defining the current state of a field; others are accessible to final year undergraduates; but essentially the emphasis is on readability and clarity.

*For a list of related mechanics titles, see final pages.*

# IUTAM Symposium on Reynolds Number Scaling in Turbulent Flow

Proceedings of the IUTAM Symposium  
held in Princeton, NJ, U.S.A.,  
11–13 September 2002

Edited by

ALEXANDER J. SMITS

*Princeton University,  
Princeton, U.S.A.*

**SPRINGER-SCIENCE+BUSINESS MEDIA, B.V.**

A C.I.P. Catalogue record for this book is available from the Library of Congress.

---

ISBN 978-94-010-3763-1      ISBN 978-94-007-0997-3 (eBook)

DOI 10.1007/978-94-007-0997-3

---

*Printed on acid-free paper*

All Rights Reserved

© 2004 Springer Science+Business Media Dordrecht

Originally published by Kluwer Academic Publishers in 2004

Softcover reprint of the hardcover 1st edition 2004

No part of this work may be reproduced, stored in a retrieval system, or transmitted in any form or by any means, electronic, mechanical, photocopying, microfilming, recording or otherwise, without written permission from the Publisher, with the exception of any material supplied specifically for the purpose of being entered and executed on a computer system, for exclusive use by the purchaser of the work.

# CONTENTS

<b>Preface</b>	xi
T. Tatsumi <i>Opening Address IUTAM and Turbulence</i>	1
<b>1. TURBULENT WALL-BOUNDED FLOWS (I)</b>	
M. H. Buschmann, M. Gad-el-Hak <i>Reynolds-number-dependent scaling law for turbulent boundary layers</i>	5
K. Knobloch, H.-H. Fernholz <i>Statistics, correlations, and scaling in a canonical, incompressible turbulent boundary layer with <math>Re_{\delta 2} \leq 1.15 \times 10^5</math></i>	11
I. Marusic, G. J. Kunkel <i>Turbulence intensity similarity laws for turbulent boundary layers</i>	17
K. Iwamoto, Y. Suzuki, N. Kasagi <i>Nonlinear interaction of coherent structures in wall turbulence at low-to-moderate Reynolds numbers</i>	23
M. Hayakawa <i>Empirical assessment on the mean flow similarity of flat-plate turbulent boundary layers</i>	29
O. Kitoh, K. Nakabayashi <i>Similarity law of turbulence intensity distribution for channel flows</i>	33
<b>2. ATMOSPHERIC FLOWS</b>	
B. L. Sawford, M. S. Borgas, P. K. Yeung <i>Lagrangian modelling of turbulent diffusion in the atmosphere -- recent developments</i>	37

J. C. Klewicki, M. Metzger <i>Studies of high Reynolds number turbulence in the atmospheric surface layer over the salt playa of western Utah</i>	45
U. Högström, J. C. R. Hunt, A.-S. Smedman <i>A top-down theory for the neutral atmospheric surface layer compared with experiments</i>	53
M. Oberlack, S. Guenther <i>New scaling laws of shear-free turbulent diffusion and diffusion-waves</i>	59
S. C. Morris, J. F. Foss <i>The non self similar scaling of vorticity in a shear layer</i>	65
S. M. de Bruyn Kops, J. J. Riley, K. B. Winters <i>Reynolds and Froude number scaling in stably-stratified flows</i>	71
J. F. Foss, S. C. Morris <i>The non-universality of the large wave number vorticity field at <math>R_\lambda = 850</math></i>	77
M. Metzger, J. Klewicki, P. Priyadarshana <i>Reynolds number dependencies in boundary layer axial stress and scalar variance transport</i>	83
A.-S. Smedman, U. Högström, J. C. R. Hunt <i>Effects of shear sheltering in atmospheric surface layer flow</i>	89
<b>3. SUPERFLUID HELIUM MINISYMPOSIUM</b>	
R. J. Donnelly <i>Background on superfluid turbulence</i>	93
W. J. Vinen <i>Superfluid turbulence: experiments, physical principles, and outstanding problems</i>	101
C. F. Beranghi <i>Numerical simulations of vortex reconnections in superfluid turbulence</i>	109
<b>4. TURBULENT WALL-BOUNDED FLOWS (II)</b>	
P. A. Priyadarshana, J. C. Klewicki <i>Reynolds number scaling of wall layer velocity-vorticity products</i>	117

M. Tsubokura, T. Tamura <i>Scaling of the large-scale motions in fully developed turbulent channel flow</i>	123
F. Durst, E. S. Zanoun, H. Nagib <i>The mean velocity profile of two-dimensional fully-developed turbulent plane-channel flows</i>	129
S. Jung, B. D. Storey, J. Aubert, H. L. Swinney <i>Non-extensive model for turbulent flow in a rapidly rotating annulus</i>	137
S. C. Ling, H. P. Pao <i>A unified theory for the origin of turbulence and its subsequent evolution</i>	141
K. Bobba, J. C. Doyle, M. Gharib <i>A Reynolds number independent model for turbulence in Couette Flow</i>	145
P. Hancock <i>Scaling of the near-wall layer beneath reattaching separated flow</i>	151

## 5. HOMOGENEOUS AND ISOTROPIC FLOWS (I)

Y. Kaneda, T. Ishihara, M. Yokokawa, K. Itakura, A. Uno <i>High resolution Direct Numerical Simulation of turbulence: spectra of fourth order velocity moments</i>	155
P. K. Yeung, S. Xu, M. S. Borgas, B. L. Sawford <i>Scaling of multi-particle Lagrangian statistics in Direct Numerical Simulations</i>	163
R. D. Moser, P. Zandonade <i>Development of high Reynolds number optimal LES models</i>	169
Y. Tsuji <i>Similarity scaling and statistics of pressure fluctuation in turbulence</i>	175
T. Nakano, T. Gotoh <i>Convection, pressure and dissipation in three-dimensional turbulence</i>	181
N. Rimbert, O. Séro-Guillaume <i>Dependence of Levy statistics with Reynolds number</i>	187
L. Castillo, X. Wang <i>The asymptotic profiles in forced convection turbulent boundary layers</i>	191

R. B. Cal, L. Castillo <i>Scaling turbulent boundary layer with suction or blowing</i>	195
<b>6. HOMOGENEOUS AND ISOTROPIC FLOWS (II)</b>	
L. Biferale, I. Daumont, A. Lanotte, F. Toschi <i>Homogeneous anisotropic turbulence</i>	201
L. J. Jiang, S. S. Shy, T. S. Yang, J. H. Lee <i>Four-dimensional measurements of the structure of dissipative scales in an aqueous near-isotropic turbulence</i>	207
E. Villermaux <i>Mixing: randomness, space dimension, and Reynolds number</i>	215
W. K. George, H. Wang <i>The spectral transfer in isotropic turbulence</i>	223
B. R. Pearson, P. Å. Krogstad, G. R. Johnson <i>Re dependence of the Kolmogorov constant and scaling</i>	229
H. Miura <i>Suppression of vortical motions in compressible isotropic turbulence</i>	237
J. Lewalle <i>On the regularity of solutions to the Navier-Stokes equations</i>	241
J. Cleve, M. Greiner <i>News about the intermittency exponent</i>	245
T. S. Yang, S. S. Shy <i>A gas-phase near-isotropic turbulence and its wavelet analysis for studying fine-scale intermittency</i>	249
B. Eckhardt, A. Jachens, J. Schumacher <i>Asymmetric time correlations in turbulent shear flows</i>	253
<b>7. TURBULENT WALL-BOUNDED FLOWS (II)</b>	
A. V. Johansson, B. Lindgren, J. M. Österlund <i>Experimental tests of mean velocity distribution laws derived by Lie group symmetry methods in turbulent boundary layers</i>	257
B. J. McKeon, J. F. Morrison, W. Jiang, J. Li, A. J. Smits <i>Revised log-law constants for fully-developed turbulent pipe flow</i>	265

<b>CONTENTS</b>	<i>ix</i>
M. B. Jones, N. Nishizawa, M. S. Chong, I. Marusic <i>Scaling of the turbulent boundary layer at high Reynolds numbers</i>	271
R. Abstiens, W. Schröder, W. Limberg <i>Hot-wire measurements of two point correlations in the flat plate boundary layer at high Reynolds numbers</i>	279
M. Wosnik, T. G. Johansson <i>On the experimental sorting of competing theories for wall-bounded turbulent flows</i>	285
Y. Nagano, T. Houra <i>Scaling of near-wall structures in turbulent boundary layers subjected to adverse pressure gradient</i>	291
S. Mochizuki, T. Kameda, H. Osaka <i>An experimental study of a self-preserving boundary layer with a power-law variation of free-stream velocity</i>	297
T. Buffin-Bélanger, A. G. Roy <i>On the use of Reynolds number to scale the effect of obstacles on a depth-limited flow in a gravel-bed river</i>	301
W. H. Brewer <i>Investigating Reynolds scaling of tip-leakage vortex flow via numerical simulations</i>	305
V. J. Kaku, M. C. Boufadel, A. D. Venosa <i>Evaluation of mixing energy in laboratory flasks</i>	311
J. Park, C. Henoch, K. S. Breuer <i>Drag reduction in turbulent flows using Lorentz force actuation</i>	315
<b>List of Participants</b>	319
<b>Author Index</b>	323

## PREFACE

This volume presents selected papers from the IUTAM Symposium on Reynolds Number Scaling in Turbulent Flow, convened in Princeton, NJ, USA, September 11-13, 2002.

The behavior of turbulence at high Reynolds number is interesting from a fundamental point of view, in that most theories of turbulence make very specific predictions in the limit of infinite Reynolds number. From a more practical point of view, there exist many applications that involve turbulent flow where the Reynolds numbers are extremely large. For example, large vehicles such as submarines and commercial transports operate at Reynolds numbers based on length of the order of  $10^9$ , and industrial pipe flows cover a very wide range of Reynolds numbers up to  $10^7$ . Many very important applications of high Reynolds number flow pertain to atmospheric and other geophysical flows where extremely high Reynolds numbers are the rule rather than the exception, and the understanding of climate changes and the prediction of destructive weather effects hinges to some extent on our appreciation of high-Reynolds number turbulence behavior.

The important effects of Reynolds number on turbulence has received a great deal of recent attention. The objective of the Symposium was to bring together many of the world's experts in this area to appraise the new experimental results, discuss new scaling laws and turbulence models, and to enhance our mutual understanding of turbulence.

Papers were presented in the following areas: similarity scaling, high Reynolds number asymptotics, isotropic and homogeneous turbulence, simulation and modeling of high Reynolds number flows, control of high Reynolds number flows, and applications of Reynolds number scaling.

The Symposium provided a stimulating forum for scientists from a wide variety of backgrounds, and produced many useful interactions. Although the Symposium started on a somber note (the opening day was the first anniversary of the September 11, 2001 terrorist attacks in the US), there was

a friendly and relaxed atmosphere throughout the proceedings which helped to stimulate intense and productive exchanges.

The Symposium Co-Chairs were A. J. Smits (Princeton University), H.-H. Fernholz (TU, Berlin), and K. Sreenivasan (U. Maryland).

The Scientific Committee consisted of P. Bandyopadhyay (USA), D. M. Bushnell (USA), H. Fernholz (Germany), W. K. George (USA), J. Hunt (UK), N. Kasagi (Japan), Y. Nagano (Japan), F. T. M Nieuwstadt (The Netherlands), I. Procaccia (Israel), A. J. Smits (USA), R. M. C. So (Hong Kong), K. R. Sreenivasan (USA), C. Wark (USA) , and T. Tatsumi (Japan).

Countries represented and number of participants: Australia (3), Canada (2), England (6), France (2), Germany (8), Israel (1), Italy (1), Japan (18), Netherlands (2), Spain (2), Sweden (8), Taiwan (2), USA (34).

The organizers extend their thanks to the International Union of Theoretical and Applied Mechanics, Kluwer Academic Publishers, and Princeton University for sponsorship of this IUTAM Symposium.

*Alexander J. Smits  
Editor*

# IUTAM AND TURBULENCE

## *Symposium Opening Address*

Tomomasa Tatsumi

Kyoto University (Emeritus)  
26-6 Chikuzen-dai, Momoyama,  
Kyoto 612-8032, Japan

Professor Smits, Ladies and Gentlemen! Just now we have had our moment of silent remembrance on the tragic events which took place in New York and Washington just one year ago. First of all, let me express my deepest grief to the victims and their relatives and profound sympathy to all people concerned.

Now, it is my great honor and pleasure to give an Opening Address in this IUTAM Symposium on “*Reynolds Number Scaling in Turbulence*” on behalf of the IUTAM.

### 1. IUTAM and ICAM

As you know, the present symposium is one of the IUTAM Symposia sponsored by the *IUTAM* or the *International Union of Theoretical and Applied Mechanics*. The IUTAM was founded in 1947 shortly after the end of the World War II as an international scientific union under the *ICSU* or the *International Council of Scientific Unions* in the United Nations. Thus, the IUTAM has a good tradition of more than half a century.

It should be noted, however, that the IUTAM has a great prehistory as the *ICAM* or the *International Congress of Applied Mechanics*. The first Congress of the ICAM was held in 1924 at Delft, the Netherlands, under the joint chairmanship of Theodore von Kármán, Tullio Levi-Civita and J.M. Burgers [1]. The naming of the “Applied Mechanics” actually dates back to this Congress organized by these young scientists at that time.

As is well known, the first quarter of the 20th Century is marked by two revolutionary developments in Physics, *Relativity Theory* by Albert Einstein and *Quantum Theory* by Max Planck. These theories actually opened a new *Era of Physics and Mechanics*.

Similar innovations took place in Fluid Mechanics during this period, *Turbulence* by Osborn Reynolds, *Shock Wave* by G.I. Taylor and *Boundary Layer* by Ludwig Prandtl. Thanks to these innovations, all unphysical singularities associated with Hydrodynamics of an inviscid fluid have been replaced by physical realities such as turbulent flows, supersonic flows including shock waves and inviscid flows with boundary layers, all governed by the Navier-Stokes equations of a viscous fluid.

The idea of these young scientists was to establish such new fields as *Applied Mechanics*, independent from their mother disciplines like Mathematics, Physics and Engineering. Their idea was widely supported by scientist of many countries and the Delft Congress really opened a series of international congresses on *Applied Mechanics*, that is the *ICAM*, which have been held mostly every four years in various cities in the world.

Among them, I would like to note the 5th ICAM which was held in 1938 at Cambridge, Massachusetts, first in USA. This Congress was attended by a number of eminent scientists in *Applied Mechanics*, as we notice in its group-photo several great names such as Ludwig Prantdl, G.I. Taylor, T. von Kármán, Sydney Goldstein, Norbert Wiener, W. Tollmien, H. Schlichting and many others. Its Proceedings published by McGraw Hill Publishers contained valuable contributions by these participants and actually marked the Golden Age of *Applied Mechanics*.

## 2. “TAM” OR “Theoretical And Applied Mechanics”

After an interruption by the World War II, the ICAM was reopened by the IUTAM, under the new title, the *ICTAM* or the *International Congress of Theoretical and Applied Mechanics*.

The first of the new series was held as the 6th ICTAM in 1946 at Paris, France, and the last one in the 20th Century was held as the 19th ICTAM in 1996 at Kyoto, Japan. Then, the first one in this Millennium was held as the 20th ICTAM in 2000 at Chicago, which is actually the third Congress in USA, the second-being the 12th Congress held in 1968 at Stanford.

The Chicago ICTAM was a very successful one attended by 1430 participants from 51 countries. On this occasion, I would like to note a nice feature of this Congress that it was accompanied with many well-organized programs arranged by the Congress President, Hassan Aref, for increasing the general publicity of the Congress and its subject, “TAM” or “Theoretical and Applied Mechanics”. His wish was warmly supported by the Governor

of Illinois who declared to call the first day of the Chicago ICTAM as the "TAM Day" in Illinois [2]. Recently, I have heard from Hassan that another "TAM Day" was announced in Virginia and now he feels "a certain momentum building!"

The publicity is not a minor problem for the "TAM", since it exerts a considerable influence on the attraction of this research field to the younger generation. During eighty years since the first ICAM, the progress in the "TAM" is really enormous. Such a rapid progress sometimes causes a false impression of the "TAM" that most of significant problems in this field have already been solved and there remain only numerical exercises.

I know that most of you do not admit such a view, but this is a rather popular superstition in the public, against which we have to fight. The "TAM Day" is an useful means for that, but I think it must be accompanied with more direct attacks. That is to give a strong counter-evidence against the superstition in the public and I think that is an honorable task of the IUTAM Congresses and Symposia, including our Symposium on "*Reynolds Number Scaling in Turbulence*".

### 3. "TAM" and Turbulence

As briefly mentioned above, *Fluid Mechanics* has achieved great progress during the last century by dealing with real fluids associated with compressibility and viscosity. In the latter half of the century, the progress has been largely promoted by invention of novel concepts such as *Local Equilibrium of Turbulence* by Kolmogorov, *Soliton* by Zabusky and Kruskal, *Chaos* by Lorenz and *Fractal* by Mandelbrot. Also, an enormous contribution of the progress in high-speed numerical computation and high-technological experimental measurement should be noted. Thus the 20th Century may be considered as the *Era of Real Fluid* compared with the 19th Century and before as the *Era of Ideal Fluid*.

An obvious exception from this classification may be *Turbulence*. It is needless to say that *Turbulence* research has achieved enormous progress so far, particularly during the latter half of the last century. Nevertheless, there still remain a number of theoretical issues to be settled before *Turbulence* problem, even in its simplest aspects, can be said to be completely solved.

On the other hand, the demand for the compact and reliable information of *Turbulence* is increasingly urgent as the realm of *Fluid Mechanics* is rapidly expanding from classical aeronautical and marine engineering to modern physics at very-low and very-high temperatures, high-speed combustion and chemical-reaction engineering, new-energy and environmental problem, earth and geophysical science, planetary and astrophysical science, biological and medical science, and so on. Thus, it

may be said that the future problems of the “TAM” are substantially identified with those of *Turbulence* research.

The basic concept of the present Symposium, “*Reynolds number scaling of turbulent flow*”, is directly related with the solution of the *Turbulence* problem. It is well known that the great success in physical and biological sciences in the last century is largely the result of the *scale-separation* of physical phenomena into human- and molecular sizes and the *reduction* of a physical law from *macro-* to *microscopic* descriptions.

In the early days of turbulence research, the *scale-separation* was employed in the form of the *mixing length* which is analogous to the *mean-free-path* of the molecular theory of gas [3]. This analogy, however, turned out to be unsatisfactory because the *scale-separation* is not sufficient between the large- and small-scale motions of turbulence.

The true *scale-separation* has first been introduced to turbulence by Kolmogorov who proposed to assume the statistical independence of small-scale motion of turbulence from large-scale motion in the limit of *vanishing viscosity* or *infinite Reynolds numbers* [4]. Now it is well known that Kolmogorov's hypothesis is well satisfied in various turbulent flows at very large Reynolds numbers.

Thus, it is very interesting to observe that *Reynolds Number Scaling* is chosen as the main subject of this Symposium and various turbulent phenomena at *high Reynolds numbers* such as turbulence in Helium II and the earth atmosphere are being dealt with.

Now, we are looking forward to learning the foremost frontier works of *Turbulence* research from this Symposium in the beginning of the Millennium.

## REFERENCES

- [1] Battimelli, G (1988) The early international congresses of applied mechanics, in S. Juhasz (ed.) *IUTAM-A Short History*, Springer Verlag, pp.9-13.
- [2] Aref, H. & Phillips, J.W. (eds.) (2001) *Mechanics for a New Millennium*. Kluwer Academic Publishers, pp. xvii-xviii.
- [3] Goldstein. S. (1938) *Modern Developments in Fluid Dynamics*, I, II. Clarendon Press, Oxford; (1965) Dover Publications, pp. I 203-214, II 331-358.
- [4] Kolmogorov, A.N. (1941) The local structure of turbulence in incompressible viscous fluid for very large Reynolds numbers. Dokl. Akad. Nauk. SSSR, **30**, 301-305.

# REYNOLDS-NUMBER-DEPENDENT SCALING LAW FOR TURBULENT BOUNDARY LAYERS

Matthias H. Buschmann

*Institut für Strömungsmechanik*

*Technische Universität Dresden*

*Dresden, Germany*

[hanno@ism.mw.tu-dresden.de](mailto:hanno@ism.mw.tu-dresden.de)

Mohamed Gad-el-Hak

*Department of Mechanical Engineering*

*Virginia Commonwealth University, USA*

[gadelhak@vcu.edu](mailto:gadelhak@vcu.edu)

**Abstract** Based on an extension of the two-layer approach a compact function for the mean velocity profile of a turbulent boundary layer is presented. The profile shows an explicit dependence on the Kármán number. It is applied successfully to profiles over a large Reynolds number range.

**Keywords:** turbulent boundary layer, mean velocity profile, asymptotic analysis

## Introduction and motivation

During the past few years, there has been considerable controversy concerning the validity of the universal logarithmic law of turbulent boundary layers. Alternative Reynolds-number-dependent power laws (George & Castillo 1997, Barenblatt et al. 2000, Afzal 2001) have been advanced. New ideas result also from Lie-group analysis (Oberlack 2001) which considers linear, algebraic, logarithmic and exponential laws for the mean velocity of stationary parallel turbulent shear flows.

If the classical logarithmic law with Reynolds number independent parameters is actually fallible several problems would occur for flow modelers including experimentalists. One consequence would be that since practically all turbulence models are calibrated to reproduce the law of the wall, failure of this relation virtually guarantees that Reynolds-averaged turbulence models would fail, too. Another example is the ex-

perimental determination of the wall skin friction. Many of the currently applied techniques like Clauser-plot and Preston-tube method are based on the classical logarithmic law. This situation automatically provided the motivation for our investigation.

We start with an *analysis* of recently proposed models for the mean flow profile of a canonical turbulent boundary layer. This type of flow is understood as a fully-developed turbulent boundary layer which is free of effects of three-dimensionality, compressibility, pressure gradient, curvature, roughness, freestream turbulence, etc.. On the basis of these results we apply an extended two-layer model for the *synthesis* of a generalized mean velocity profile. Different experimental data sets are used to carry out a *validation* of this relation.

## 1. Data analysis

Several diagnosis functions (see e.g. Österlund et al. 2000) were suggested to check if a logarithmic or a power law is valid in the overlap region. For the analysis presented here the so-called fractional difference *FD* is used. The fractional difference method was first applied by Zagaglola et al. 1997 to evaluate the original superpipe data. This measure is the related difference between the experimental and a theoretical value of  $u^+$  at the same  $y^+$ -position. The fractional difference should not be confused with the experimental error.

$$FD\% = 100 \times \left[ 1 - \frac{u_{theor}^+}{u_{exp}^+} \right] \quad (1)$$

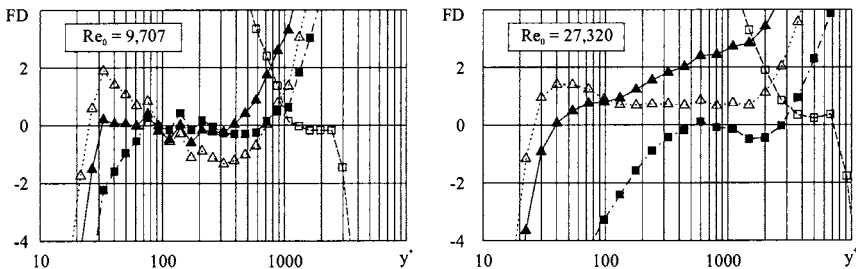


Figure 1. Examples of fractional difference plots (data from Österlund 1999)  $\blacktriangle$  : log. law with  $\kappa = 0.41$ ,  $C = 5.0$ ;  $\triangle$  : log. law with  $\kappa = 0.38$ ,  $C = 4.1$  (Österlund et al. 2000);  $\blacksquare$  : inner and  $\square$  : outer power law (Barenblatt et al. 2000)

More than 100 mean velocity profiles in a range of momentum-thickness Reynolds numbers  $Re_\theta$  of 500–27,320 were analyzed using the fractional

difference method (for details see Buschman & Gad-el-Hak 2002b). The main results are as follows

- Neither the logarithmic law nor the power law is valid across the entire "overlap" region. There is no distinct outer power law region in the wake zone of the profile.
- Nevertheless the classical logarithmic law is still a good "workhorse" for engineering applications having high Reynolds number.
- However, a high Reynolds number dependence persists until the Reynolds number reaches infinity. Therefore, the classical two-layer approach should be extended to higher-order terms which take into account this dependence.

## 2. Extension of the two-layer approach

Traditionally the canonical turbulent boundary layer is split into an inner and outer region. While in the inner zone friction is of importance the outer zone is dominated by inertia. Both zones are described using series expansions. Due to the limited space available here the following is restricted to the inner zone (see also Buschmann & Gad-el-Hak, 2002a).

The asymptotic expansion for the inner layer reads

$$u^+ \sim u_1^+(y^+) + \gamma_2(\delta^+) u_2^+(y^+) + \gamma_3(\delta^+) u_3^+(y^+) + \dots \quad (2)$$

Here  $u^+$  and  $y^+$  denote the usual nondimensional velocity  $u/u_\tau$  and the wall-normal coordinate  $y u_\tau / \nu$ , respectively. The similarity variable  $\delta^+$  is called Kármán number. It represents the ratio of characteristic length scales of the outer (scaling with the boundary layer thickness  $\delta$ ) and inner zone (scaling with  $\nu / u_\tau$ ).

Asymptotic matching can now be applied to obtain the mean velocity profile in the overlap zone. Before finding the higher-order terms concerning  $\delta^+$ , one has to find the higher order  $y^+$ -terms of  $u_1^+$  first. Based on a consideration of the governing equations of the mean motion of fully-developed pipe and channel flows, Afzal (1976) introduced a special gauge function  $\gamma_i(\delta^+)$  and developed a certain scheme to derive these higher order terms. We generalize this procedure to obtain the generalized inner law.

$$\begin{aligned} u^+ = & A_1 \ln(y^+) + C_1 + \sum_{i=1}^m \frac{E_{1,i}}{y^{+i}} + \\ & \sum_{j=2}^n \epsilon^{j-1} \left( A_j \ln(y^+) + C_j + \sum_{i=1}^{j-1} B_{j,i} y^{+i} + \sum_{i=1}^m \frac{E_{j,i}}{y^{+i}} \right) \end{aligned} \quad (3)$$

Here  $A_j$ ,  $C_j$ ,  $B_{j,i}$  and  $E_{j,i}$  denote parameters and  $\epsilon$  stands for  $1/\delta^+$ . To simplify the generalized inner law the following identities, were  $x$  can be any variable, are applied.

$$\exp(x) = \sum_{n=0}^{\infty} \frac{x^n}{n!} \quad \text{and} \quad \ln(1+x) = \sum_{n=1}^{\infty} (-1)^{n+1} \frac{x^n}{n} \quad (4)$$

Rearranging and rewritting (3) using (4), the generalized inner law is obtained as

$$u^+ = \sum_{j=1}^{\infty} \epsilon^{j-1} (A_j \ln(y^+ + D_j) + G_{1,j} \exp(-G_{2,j} \eta)) \quad (5)$$

Again  $A_j$ ,  $D_j$ ,  $G_{1,j}$  and  $G_{2,j}$  denote parameters which have to be determined from experiments and  $\eta$  is  $y/\delta$ .

For  $\delta^+ \rightarrow \infty$  and  $\eta \rightarrow 0$  the exponential term of (5) becomes unity.

$$u_{\infty}^+ = A_1 \ln(y^+ + D_1) + G_{1,1} \quad \text{with} \quad A_1 = 1/\kappa_1 \quad (6)$$

The resulting relation is identical with the logarithmic law derived by Oberlack (2001) based on first principles applying Lie-group analysis. Due to  $D_1$  the mean velocity profile will not show a straight line in the semilogarithmic plot. This theoretical finding was confirmed by Lindgren et al. (2002) who analyzed experimental data. The additional exponential terms in (6) partly represent the usual wake region of the profile.

For simplicity let us assume that  $D_j = D_1$  and  $G_{2,j} = G_2$ . Equation (5) can than be rewritten as

$$u^+ = \sum_{j=1}^{\infty} \epsilon^{j-1} A_j * \ln(y^+ + D_1) + \sum_{j=1}^{\infty} \epsilon^{j-1} G_{1,j} * \exp(-G_2 \eta) \quad (7)$$

The sum terms are equivalents for the Kármán constant  $\kappa$  and the additive constant  $B$ , respectively. These usually constant parameters of the classical logarithmic law are now functions depending on the Kármán number. To determine the parameters of (7) we make use of the data set by Österlund 1999 (see fig. 2).

For large Kármán numbers  $\kappa$  approaches a value of 0.394 and  $G_1$  converges to 4.125. Both values are close to  $\kappa = 0.38$  and  $B = 4.1$  proposed by Österlund et al. 2000. A similar small  $\kappa$ -value of 0.372 was derived by Yakhot & Orszag 1986 applying renormalization-group analysis. Exemplarily, the generalized logarithmic law is applied to the profiles from fig. 1 and five profiles from Osaka et al. (1998) (fig. 3). Note that all of these profiles have  $Re_\theta$  larger than 2,000 so that low Reynolds-number effects can be excluded.

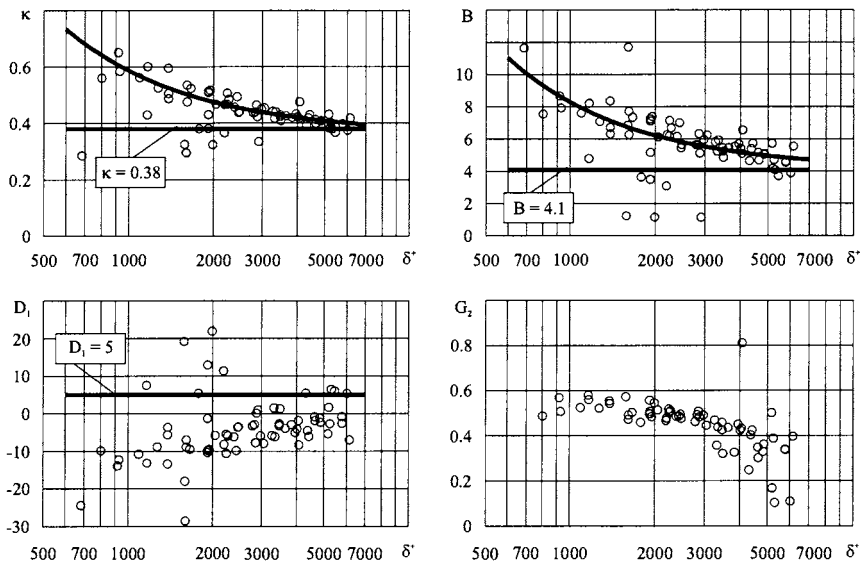


Figure 2. Parameters of generalized logarithmic law derived from data by Österlund 1999, full lines in the diagrams for  $\kappa$  and  $B$  show curve fits according to equ. (7)

### 3. Conclusion

With the presented profiles, compact functions are found for the description of the mean velocity profile of a canonical turbulent boundary layer. These functions represent a blending of two results which were derived based on first principles applying Lie-group analysis. The conclusion from that finding is that the extension of the classical method of asymptotic matching used here is in agreement with first principles of fluid mechanics. A comparison with experimental data shows that the generalized law can be applied successfully.

### References

- Afzal, N. (2001). *Power law and log law velocity profiles in fully developed turbulent boundary layer flow: equivalent relations at large Reynolds numbers*. Acta Mechanica, Vol. 151, Nos. 3 & 4, 2001, pp. 195–216.
- Afzal, N. (1976). *Millikan's argument at moderately large Reynolds number*. Phys. Fluids 19, pp. 600–602.
- Barenblatt, G. I., Chorin, A. J., Prostokishin, V. M. (2000). *Analysis of experimental investigations of self-similar intermediate structures in zero-pressure boundary layers at large Reynolds number*. Report No. PAM-777, Center for Pure and Applied Mathematics, University of California at Berkeley

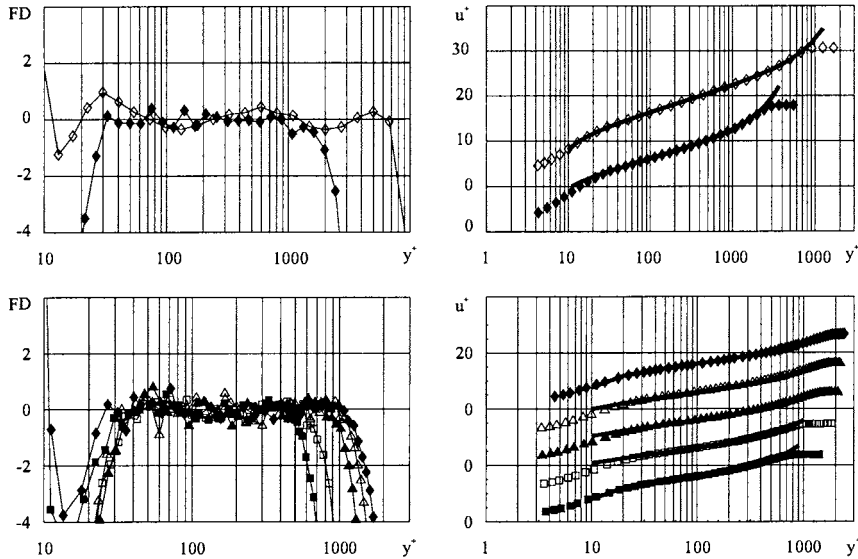


Figure 3. Fractional difference and mean velocity profiles on top :  $\blacklozenge$  ( $Re_\theta = 9,707$ ),  $\lozenge$  ( $Re_\theta = 27,320$ ) Österlund 1999 below :  $\blacksquare$  ( $Re_\theta = 2,100$ ),  $\square$  ( $Re_\theta = 2,990$ ),  $\blacktriangle$  ( $Re_\theta = 4,430$ ),  $\triangle$  ( $Re_\theta = 5,230$ ),  $\blacklozenge$  ( $Re_\theta = 6,040$ ) Osaka et al. (1998)

- Buschmann, M. H. & Gad-el-Hak., M. (2002a) *The Generalized Logarithmic Law and Its Consequences*. to appear AIAA-Journal, 2002
- Buschmann, M. H. & Gad-el-Hak., M. (2002b) *The debate concerning the mean-velocity profile of a turbulent boundary layer*. to appear AIAA-Journal, 2002
- George, W. K. & Castillo, L. (1997). *Zero-pressure-gradient turbulent boundary layer*. Appl. Mech. Rev., 50 (12), 689–729.
- Lindgren, B., Österlund, J. M., Johansson, A. V. (2002). *Evaluation of scaling laws derived from Lie-group symmetry methods in turbulent boundary layers*. AIAA 2002-1103, Reno, NV.
- Oberlack, M. (2001). *A unified approach for symmetries in plane parallel turbulent shear flows*. J. Fluid Mech., 427, pp. 299–328.
- Osaka, H., Kameda, T., Mochizuki, S. (1998). *Re-examination of the Reynolds number effect on the mean flow quantities in a smooth wall turbulent boundary layer*. JSME Int. J., Vol. 41, pp. 123–129.
- Österlund, J. M., Johansson, A. V., Nagib, H. M., Hites, M. H. (2000). *A note on the overlap region in turbulent boundary layers*. Phys. Fluids, Vol. 12, pp. 1–4.
- Österlund, J. M. (1999). *Experimental studies of zero-pressure gradient turbulent boundary-layer flow*. Ph.D. thesis, Royal Institute of Technology, Stockholm.
- Yakhot, V., Orszag, S. A. (1986). *Renormalization-group analysis of turbulence*. Phys. Rev. Letters, Vol. 57, pp. 1722–1724.
- Zagarola, M. V., Perry, A. E., Smits, A. J. (1997). *Log laws or power laws : The scaling in the overlap region*. Phys. Fluids, Vol. 9, pp. 2092–2100.

# STATISTICS, CORRELATIONS, AND SCALING IN A TURBULENT BOUNDARY LAYER AT $Re_{\delta_2} \leq 1.15 \times 10^5$

K. Knobloch and H.-H. Fernholz

*Hermann-Föttinger-Institut für Strömungsmechanik*

*Technische Universität Berlin*

*Straße des 17. Juni 135, 10623 Berlin, Germany*

*knobloch@pi.tu-berlin.de*

**Abstract** A canonical turbulent boundary layer at Reynolds numbers up to  $1.15 \times 10^5$  (based on momentum thickness  $\delta_2$ ) has been investigated experimentally. Hot-wire measurements and PIV images yield information about mean velocity profiles and turbulence quantities of all three velocity components. Various scalings were tested for the new data set. Special emphasis was put on correlation functions in wall-normal direction. This investigation extends earlier work by Fernholz et al., 1995.

**Keywords:** canonical turbulent boundary layer, experiment, wall-normal correlations, scaling

## Introduction

Although there are many investigations of the canonical boundary layer at low and medium Reynolds numbers ( $Re_{\delta_2} \leq 20000$ ), it is not clear how far scaling laws can be extended to a high Reynolds number range which is more realistic for practical applications such as airplanes or ship hulls. Towards infinite Reynolds numbers asymptotic behaviour of the scaling should hold.

Besides mean-velocity and Reynolds-stress profiles a further goal of this experiment was to determine various correlation functions inside the turbulent boundary layer in wall-normal direction. Based on these data, scaling laws will be addressed for boundary layers at Reynolds numbers (based on momentum thickness and free-stream velocity) between  $4 \times 10^4$  and  $1.15 \times 10^5$ .

## 1. Experimental facility and measuring techniques

The experiments were performed in the Large Low-Speed Facility of the German-Dutch windtunnel (DNW-LLF) using measuring equipment of the boundary layer group at the Hermann-Föttinger-Institut. The  $8 \times 6\text{m}^2$  test section of the LLF was used which had sufficient length to generate thick boundary layers. In the empty test section of this facility, the streamwise pressure gradient is smaller than 0.05% of the dynamic pressure per meter and the freestream turbulence level is below 0.1% (Hucho, 1998). The test runs had freestream velocities of approximately 40, 60, and 80m/s.

In order to make as much use of the tunnel as possible, measurements were carried out in parallel at two locations in the test section by the group from TU Berlin and at a third location by colleagues from RWTH Aachen. Our first measuring station was located on a  $15 \times 8\text{m}^2$  smooth flat plate (roughness  $1.2\mu\text{m}$ ) about 13.5m from the elliptical shaped leading edge (figure 1). The boundary layer was tripped by means of 2 rows of embossing tape (capital letter "V") to fix transitions along the span.

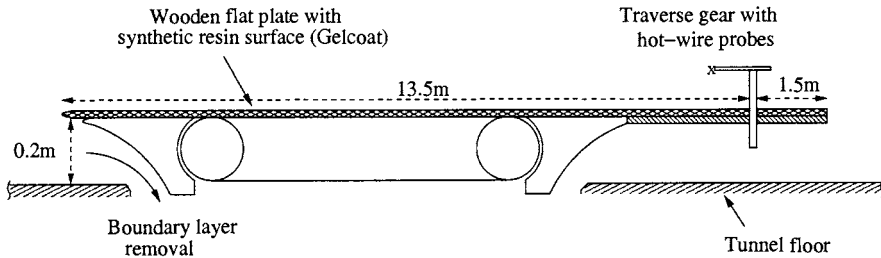


Figure 1. Flat plate configuration (not drawn to scale !) with defined origin of the boundary layer

A second measuring station was on the tunnel side wall which was covered by a 3m wide smooth surface extending over the whole upstream length of the test section. Here the wall roughness was  $5\mu\text{m}$  in comparison with a viscous length scale ( $l^* = \nu/u_\tau$ ) of  $6.5\mu\text{m}$  at 80m/s. Only this test site could be used for the runs at the highest velocity.

For the hot-wire measurements standard normal-wire (NWP) and triple-wire (TWP) miniature probes were used which were calibrated in situ. Design and properties of the TWP were described by Bruns and Dengel, 1998.

The traverse gear could move two probes independent of each other in the wall-normal direction in order to obtain space correlations of the three velocity components  $u'$ ,  $v'$  and  $w'$ . Time series of – in most cases – 40 seconds were recorded at a frequency of 125 kHz.

At the flat plate measuring station additional measurements with PIV were carried out in a plane set up by the streamwise and wall-normal direction. The 2-component measurements covered the full height of the boundary layer and the 3-component measurements only the inner layer. Since the data evaluation is still in progress results will be shown in a subsequent paper.

## 2. Results

### 2.1 Mean velocity profiles

Mean velocity profiles were obtained on the flat plate and the tunnel side wall. They are plotted in inner-law scaling in figure 2 and in various outer scalings in figures 3 and 4. The profiles collapse in inner scaling on a straight line in the log-law region extending over at least two decades of  $y^+$ . They lie slightly below the logarithmic law formed by the constants  $\kappa = 0.40$  and  $C = 5.1$ . Skin friction could not be measured easily and was therefore calculated using the semi-empirical relationship of Fernholz, 1971. As for the scaling in outer variables, there appears

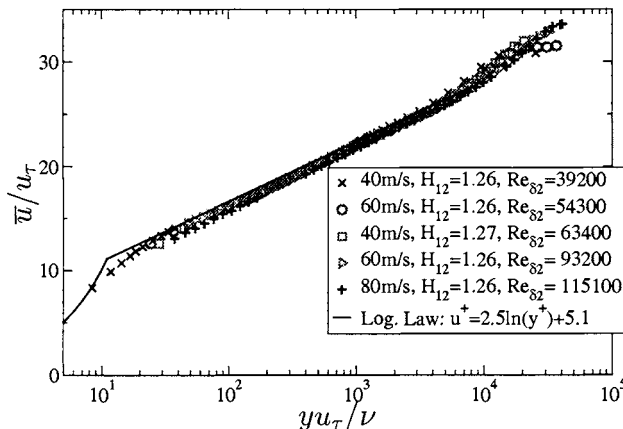


Figure 2. Mean velocity profiles (measured with NWP) in inner scaling.

to be little difference between the scalings of Rotta, 1962  $(u_\delta - \bar{u})/u_\tau$  against  $y/\Delta$ , George and Castillo, 1997  $(u_\delta - \bar{u})/u_\delta$  against  $y/\delta_{99}$ , and Smits and Marusic, 1999  $(u_\delta - \bar{u})/(u_\delta \delta^*/\delta)$  against  $y/\delta_{99}$ , where  $\delta^*$  is the displacement thickness and  $\Delta$  the Rotta-Clauser-length.

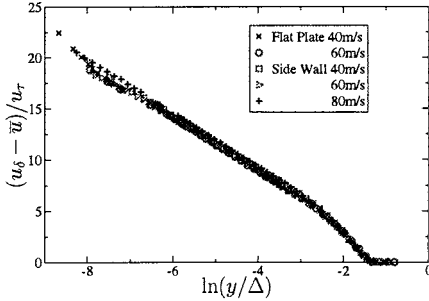


Figure 3. Mean velocity profiles in outer scaling proposed by Rotta ( $\Delta$  denotes the Rotta-Clauser length).

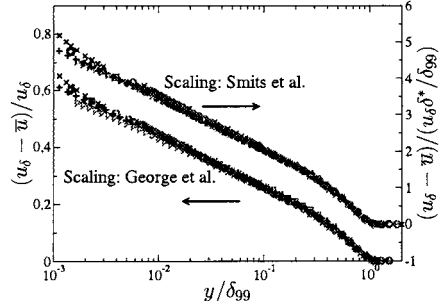


Figure 4. Mean velocity profiles in outer scaling using  $u_\delta$ ,  $\delta^*$ , and  $\delta$ . For symbols see figure 2.

## 2.2 Turbulence Quantities

Reynolds normal stresses and shear stresses were measured by hot-wire anemometry and are shown in figures 5 – 8. Figure 5 shows the Reynolds normal-stress component  $\overline{u'^2}$  made dimensionless by the friction velocity  $u_\tau$ . Due to the very small viscous length scales at these high Reynolds numbers, the near wall peak ( $y_{max}^+ \approx 14$ ) could not be reached. The level of the  $\overline{u'^2}$ -profiles rises with increasing  $Re_{\delta_2}$  following the trend observed before (e.g. Fernholz and Finley, 1996). The data collapse if plotted against  $y/\Delta$  (figure 6), showing no dependence on Reynolds number. Agreement between the data measured by the two different probe types is good.

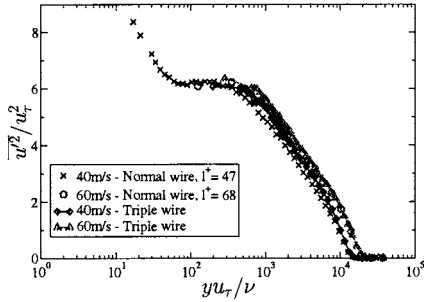


Figure 5. Reynolds normal-stress component  $\overline{u'^2}$  in inner scaling. Flat plate.

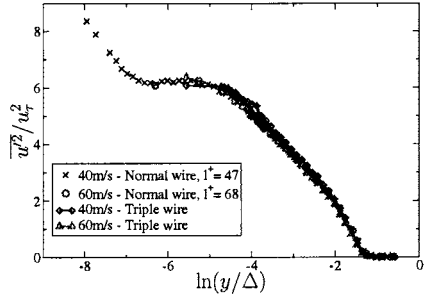


Figure 6. Reynolds normal-stress component  $\overline{u'^2}$  in outer scaling. Flat plate.

The Reynolds normal-stress component  $\overline{v'^2}$  and the shear stress  $\overline{u'v'}$  (figures 7,8) show a distinct region of almost constant values in the inner part of the boundary layer. A value above unity for  $\overline{u'v'}/u_\tau^2$  – for which

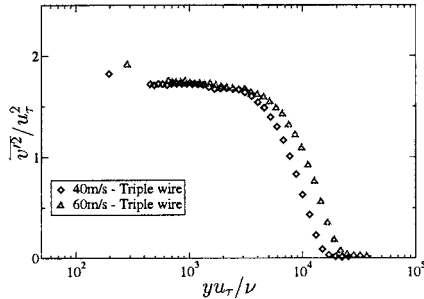


Figure 7. Reynolds normal-stress component  $\overline{v'^2}$  in inner scaling. Flat plate.

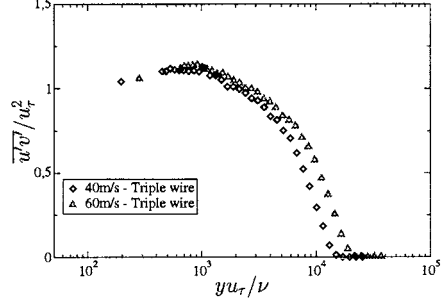


Figure 8. Reynolds shear stress  $\overline{u'v'}$  in inner scaling. Flat plate.

we have no explanation yet – was also observed for instance by Fernholz et al., 1995.

### 2.3 Correlations

Figure 9 shows examples of the 2-point velocity correlation functions for the three components  $u'$ ,  $v'$ , and  $w'$  at two fixed positions normal to the wall. The correlation coefficients for the fixed probe close to the wall

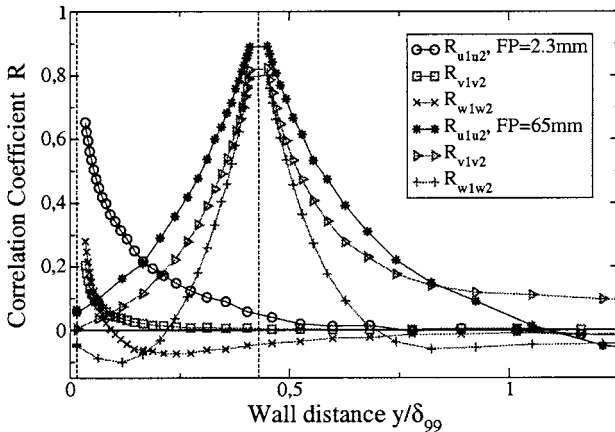


Figure 9. Correlation coefficient for two different fixed points (marked by the dashed line). Flat plate, 40m/s,  $Re_{\delta_2} = 39200$ .

are smaller than further out in the boundary layer and all correlations approach zero with the spanwise-component ( $R_{w1w2}$ ) from the negative side.  $R_{u1u2}$  crosses zero somewhere at the “edge” of the boundary layer while  $R_{v1v2}$  seems not to approach zero within a reasonable distance for

the fixed probe at 65mm. This behaviour of the correlation functions agrees qualitatively with the measurements of Grant, 1958 which were made, however, at much lower Reynolds numbers. No difference was found between our normal-wire and triple-wire measurements.

### 3. Conclusions

Profiles of the mean velocity, of Reynolds stresses, and correlation functions measured in a turbulent boundary layer at high Reynolds numbers were presented. The mean velocity profiles follow the “classical log law” for the inner part and either of the three outer laws using the scaling of Rotta, Smits, and George. Despite spatial resolution problems very close to the wall, the profiles of the velocity fluctuations agree qualitatively with earlier investigations (Fernholz and Finley, 1996) and the 2-point-correlations with these of Grant, 1958.

### Acknowledgments

The financial support of the Deutsche Forschungsgemeinschaft (DFG) is gratefully acknowledged.

### References

- Brunns, J. M. and Dengel, P. (1998). A miniature triple hot-wire probe for wall bounded flows. *Exp. in Fluids*, 24(6):479–488.
- Fernholz, H.-H. (1971). Ein halbempirisches Gesetz für die Wandreibung in kompressiblen turbulenten Grenzschichten bei isothermer und adiabater Wand. *Z. Angew. Math. Mech.*, 51:T146–T147.
- Fernholz, H.-H., Krause, E., Nockemann, M., and Schober, M. (1995). Comparative measurements in the canonical boundary layer at  $Re_{\delta_2} \leq 6 \times 10^4$  on the wall of the German-Dutch windtunnel. *Phys. Fluids*, 7(6):1275–1281.
- Fernholz, H.-H. and Finley, P. J. (1996). The incompressible zero-pressure-gradient turbulent boundary layer: an assessment of the data. *Prog. Aerospace Sci.*, 32:245–311.
- George, W. K. and Castillo, L. (1997). Zero-pressure-gradient turbulent boundary layer. *Appl. Mech. Rev.*, 50(12):689–729.
- Grant, H. L. (1958). The large eddies of turbulent motion. *J. Fluid Mech.*, 4:149–190.
- Hucho, W.-H. (1998). Vehicle Aerodynamics in the German-Dutch Wind Tunnel. DNW brochure: Automotive Testing Facility.
- Rotta, J. C. (1962). Turbulent boundary layers in incompressible flow. *Prog. Aerospace Sci.*, 2:1–219.
- Smits, A. J. and Marusic, I. (1999). High Reynolds Number Flows: A Challenge for Experiment and Simulation. *AIAA Paper 99-3530*. 30th AIAA Fluid Dynamics Conference.

# TURBULENCE INTENSITY SIMILARITY LAWS FOR TURBULENT BOUNDARY LAYERS

Ivan Marusic

Gary J. Kunkel

*Department of Aerospace Engineering and Mechanics*

*University of Minnesota*

*Minneapolis, MN 55455*

*marusic@umn.edu, kunkel@aem.umn.edu*

**Abstract** Turbulence intensity similarity laws, which are based on the attached eddy hypothesis, are tested with new high Reynolds number data obtained in the atmospheric surface layer. The existing formulation for the streamwise component was until now restricted to the log region and above. A new extended version is proposed that applies across the entire boundary layer for smooth wall flows and explains why the near-wall mixed scaling proposed by DeGraaff and Eaton, 2000 appears to be successful.

**Keywords:** Turbulence intensity similarity, atmospheric surface layer, high Reynolds number, attached eddy hypothesis

## Introduction

Data obtained in the surface layer of the atmospheric boundary layer are used to analyze turbulence intensity similarity laws. Historically, the streamwise turbulence intensity is believed to be independent of Reynolds number when scaled with inner-flow variables (the friction velocity,  $U_\tau$ , and the kinematic viscosity) in the entire wall region (viscous sublayer, buffer layer and logarithmic layer) of the turbulent boundary layer. This view is supported by Mochizuki and Nieuwstadt, 1996 and is also used in many computational turbulence models. Recently DeGraaff and Eaton, 2000 have suggested a new mixed scaling that incorporates both  $U_1$  (freestream velocity) and  $U_\tau$  and have shown experimental results that support this scaling in the inner-wall region (sublayer and buffer layer). Metzger et al., 2001 have verified this scaling using experimental data from the laboratory and the atmosphere.

Marusic et al., 1997 (referred to here on as MUP) proposed a similarity formulation that is valid in the entire region above the buffer layer

and that is dependent on Reynolds number. Their formulation is based on the scaling arguments of the power spectral densities and is consistent with Townsend's attached eddy hypothesis. It was found to accurately describe the turbulence intensity over a large range of Reynolds numbers ( $Re_\tau \leq 10^4$ ), however, it was not compared to experimental data obtained at very high Reynolds numbers. To further test the formulations at high Reynolds numbers several experiments have been conducted at the SLTEST (Surface Layer Turbulence and Environmental Science Test) facility located on the western Utah salt flats. The MUP formulation is then extended to apply across the entire boundary layer for smooth wall flow. The extended formulation is compared with laboratory and atmospheric data and is consistent with the suggested mixed scaling of DeGraaff and Eaton, 2000.

## 1. Experimental Method

A detailed description of the SLTEST site and a discussion of the advantages of the site are found in Klewicki et al., 1998. For the data given here the surface roughness was estimated at approximately 10 mm and the effect of the roughness can be seen in the offset in the mean velocity profiles (not shown). However, by Townsend's Reynolds-number-similarity hypothesis this does not effect the turbulence intensities in the outer region of the flow where our measurements are taken. Also, the stability parameter,  $z/L$ , where  $z$  is the wall normal distance and  $L$  is the Obukhov length, at the highest wall normal position, 2 m, was positive and less than 0.03. Pahlow et al., 2001 show that the normalized standard deviation of the streamwise velocity component is constant with respect to the stability parameter for positive values of  $z/L < 0.1$ . Therefore, any slight buoyancy effects that might exist are assumed to be negligible. Turbulence intensity profiles are obtained using arrays of cross-wire anemometers that are calibrated at the beginning and end of each run.

## 2. Results and Discussion

Figure 1 shows the streamwise turbulence intensities from several wall normal positions from two data sets obtained in the atmospheric boundary layer ( $Re_\tau = O(10^6)$ ). For the data shown the boundary layer thickness was estimated as 200 m for both data sets (solid symbols). For comparison, data from DeGraaff and Eaton, 2000 are also shown (open symbols). The similarity formulation of MUP,

$$\frac{\langle u^2 \rangle}{U_\tau^2} = B_1 - A_1 \ln\left[\frac{z}{\delta}\right] - V_g[z^+, \frac{z}{\delta}] - W_g[\frac{z}{\delta}], \quad (1)$$

for the corresponding Reynolds numbers are shown along with the formulations if the boundary layer thickness was  $\pm 50\%$  of the estimated value. Here  $u$  is the streamwise fluctuating velocity component,  $\delta$  is the boundary layer thickness, and  $\langle \rangle$  represents a long time average. The similarity formulations of Högström et al., 2002 are also shown. The MUP formulation appears to describe the data at high Reynolds numbers well. The wall-normal turbulence intensities and the corresponding similarity formulations (Hafez, 1991)

$$\frac{\langle u^2 \rangle}{U_\tau^2} = A_3 - B_3 \frac{z}{\delta} - V[z^+], \quad (2)$$

are shown in figure 2. Strictly the formulations are only valid for  $z^+ > 100$  and  $z/\delta < 0.15$ , however, they have been extended across the entire layer (dashed portions).

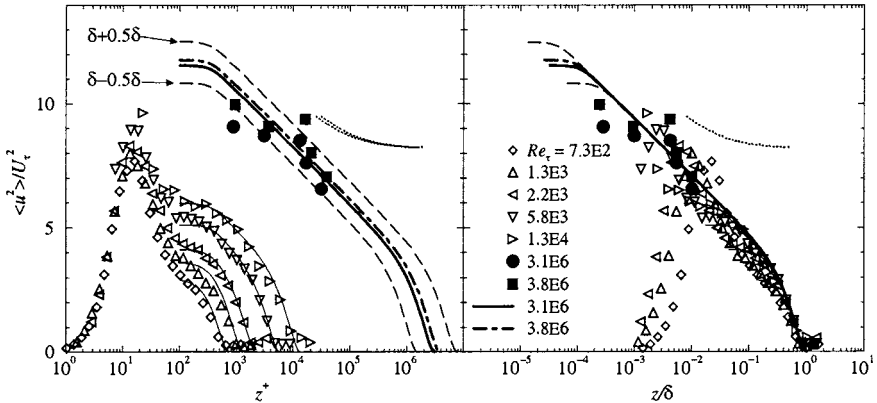


Figure 1. Streamwise turbulence intensities. Solid and dot-dashed lines are the MUP similarity formulation and the dotted lines are the Högström et al., 2002 formulation.

Figure 3 shows the streamwise, wall-normal, and co-spectra with inner-flow scaling. The spectra are consistent with most of the expected spectral scaling laws described in Marusic and Perry, 1995 and with the incomplete similarity hypothesis described by Morrison et al., 2002. For instance, a considerably shorter  $-1$  law is obtained for  $\Phi_{11}$  than would be expected by complete similarity (Perry et al., 1986).

### 3. Extended Formulation

While the MUP formulation appears to describe the high Reynolds number data well, it is only applicable in the log region and above. To extend this formulation for smooth walls a blending of scaling regions is

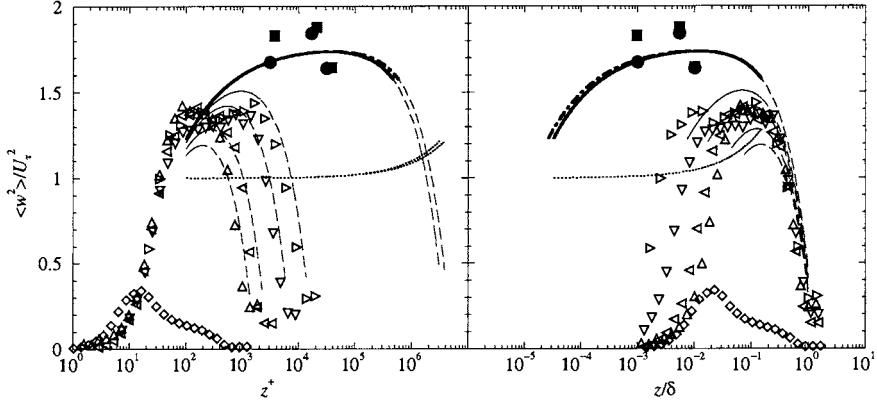


Figure 2. Wall-normal turbulence intensities. Solid and dot-dashed lines are the Hafez, 1991 similarity formulation, other symbols as in figure 1.

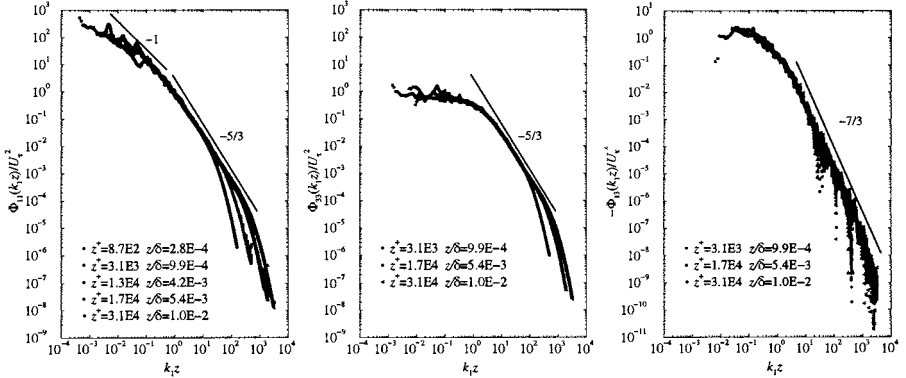


Figure 3. Streamwise, wall-normal and co-spectra with inner-flow scaling in the logarithmic region of the atmospheric surface layer.

considered. The outer part of the boundary layer,  $z^+ > 150$ , is described by the existing MUP formulation (Eq. 1) that is valid for smooth and rough wall boundary layers. The inner part of the layer  $z^+ < 30$  is described by

$$\frac{\langle u^2 \rangle}{U_\tau^2} = f_1[z^+] f_T[z^+, Re_\tau], \quad (3)$$

where

$$f_1[z^+] = \frac{0.16(z^+)^2}{(1 + a_1(z^+)^2)^{1/2} (1 + (a_2 z^+)^{2a_3})^{1/2}} \quad (4)$$

is an empirical curve fit of moderate Reynolds number data valid only for smooth wall boundary layers. Here  $f_T$  is a simple scaling function that

is linear in  $\ln z^+$  with a slope proportional to the increase (or decrease) in Reynolds number from the original logarithmic curve fit. These two regions are then blended with a cubic fit between  $30 < z^+ < 150$ . Here  $a_1 = 0.008$ ,  $a_2 = 0.115$ , and  $a_3 = 1.6$ .

The extended formulation with laboratory and atmospheric data can be seen in figure 4a. The extended formulation fits the laboratory data well and suggests that the peak in the turbulence intensity does increase with increasing Reynolds number when scaled with inner-flow variables. The peak in the turbulence intensity, scaled with the friction velocity, as a function of Reynolds number is shown in figure 4b. The functional form that results from the extended similarity formulation is very similar to the empirical curve fit given by Metzger et al., 2001.

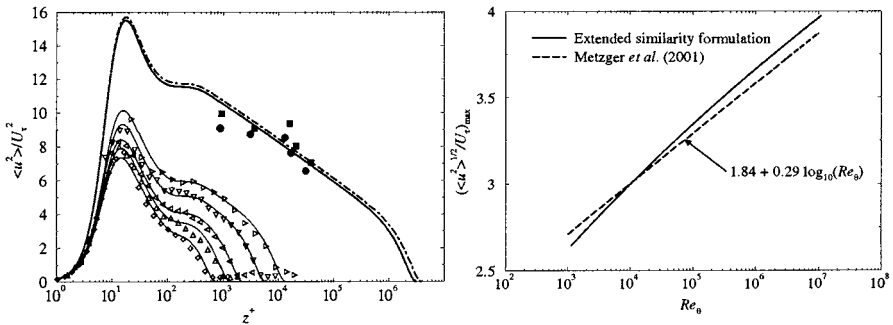


Figure 4a. Extended similarity formulations. Symbols in figure 1.

Figure 4b. Peak in streamwise turbulence intensity.

Figure 5 shows the extended formulation, laboratory data and atmospheric data with mixed scaling. The extended formulation seems to explain the results of DeGraaff and Eaton, 2000 and why mixed scaling appears to work well.

#### 4. Conclusion

An extended similarity formulation has been developed to describe the streamwise turbulence intensity across an entire smooth wall zero pressure gradient turbulent boundary layer. The extended formulation has been compared to moderate and high Reynolds number data obtained in the laboratory and atmospheric boundary layer respectively. The extended formulation is seen to describe the data well and is consistent with the mixed scaling suggested by DeGraaff and Eaton, 2000.

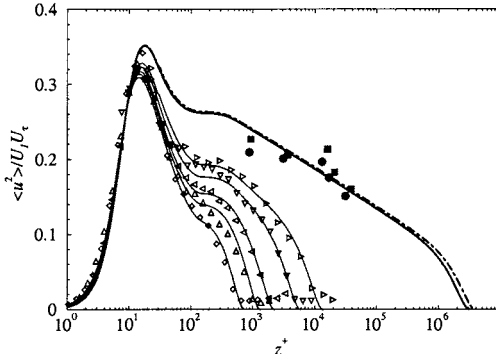


Figure 5. Extended similarity formulations. Symbols in figure 1.

## References

- DeGraaff, D. B. and Eaton, J. K. (2000). Reynolds-number scaling of the flat-plate turbulent boundary layer. *J. Fluid Mech.*, 422:319–346.
- Hafez, S. H. M. (1991). *The structure of accelerated turbulent boundary layers*. PhD thesis, University of Melbourne, Australia.
- Högström, U., Hunt, J. C. R., and Smedman, A. (2002). Theory and measurements for turbulence spectra and variances in the atmospheric neutral surface layer. *Boundary-Layer Meteorology*, 103:101–124.
- Klewicki, J. C., Foss, J. F., and Wallace, J. M. (1998). High Reynolds number [ $R_\theta = O(10^6)$ ] boundary layer turbulence in the atmospheric surface layer above Western Utah's salt flats. In Donnelly, R. J. and Sreenivasan, K. R., editors, *Flow at Ultra-High Reynolds and Rayleigh Numbers*, pages 450–466. Springer.
- Marusic, I. and Perry, A. E. (1995). A wall-wake model for the turbulence structure of boundary layers. Part 2. Further experimental support. *J. Fluid Mech.*, 298:389–407.
- Marusic, I., Uddin, A. K. M., and Perry, A. E. (1997). Similarity law for the streamwise turbulence intensity in zero-pressure-gradient turbulent boundary layers. *Phys. Fluids*, 9(12):3718–3726.
- Metzger, M. M., Klewicki, J. C., Bradshaw, K. L., and Sadr, R. (2001). Scaling the near-wall axial turbulent stress in the zero pressure gradient boundary layer. *Phys. Fluids*, 13(6):1819–1821.
- Mochizuki, S. and Nieuwstadt, F. T. M. (1996). Reynolds-number-dependence of the maximum in the streamwise velocity fluctuations in wall turbulence. *Exp. Fluids*, 21:218–226.
- Morrison, J. F., Jiang, W., McKeon, B. J., and Smits, A. J. (2002). Reynolds number dependence of streamwise velocity spectra in turbulent pipe flow. *Physical Review Letters*, 88(21):214501–1 – 4.
- Pahlöw, M., Parlange, M. B., and Porté-Agel, F. (2001). On Monin-Obukhov similarity in the stable atmospheric boundary layer. *Boundary-Layer Meteorology*, 99:225–248.
- Perry, A. E., Henbest, S. M., and Chong, M. S. (1986). A theoretical and experimental study of wall turbulence. *J. Fluid Mech.*, 165:163–199.

# NONLINEAR INTERACTION OF COHERENT STRUCTURES IN WALL TURBULENCE AT LOW-TO-MODERATE REYNOLDS NUMBERS

Kaoru Iwamoto, Yuji Suzuki, and Nobuhide Kasagi

*Department of Mechanical Engineering, The University of Tokyo,*

*Hongo, Bunkyo-ku, Tokyo, 113-8656 Japan*

*iwamoto@tthlab.t.u-tokyo.ac.jp*

**Abstract** Direct numerical simulation of turbulent channel flow at  $Re_\tau = 110 \sim 650$  is made in order to examine the nonlinear interaction of coherent structures in wall turbulence through the Karhunen-Loëve decomposition of turbulent fluctuations. When  $Re_\tau = 110$ , the nonlinear interaction acts as sink for the turbulence energy of vortical structures at  $y^+ \sim 20$ , which correspond to the near-wall streamwise vortices. The energy is transferred toward/away from  $y^+ \sim 20$ . On the other hand, when the Reynolds number increases, the streamwise vortices gains energy through the nonlinear interaction from the vortical structures at  $20 < y^+ < 100$ . It is also found that direct interaction between inner ( $y^+ < 100$ ) and outer ( $y^+ > 100$ ) layers has minor effect on near-wall dynamics even at  $Re_\tau = 650$ .

**Keywords:** Nonlinear interaction, Karhunen-Loëve decomposition, coherent structure, direct numerical simulation, turbulent channel flow.

## 1. Introduction

In the last few decades, transport mechanism of wall turbulence has been examined in detail. It is found through direct numerical simulation (DNS) of low-Reynolds-number wall turbulence that near-wall streamwise vortices play a dominant role in the turbulence energy production, wall shear stress and wall heat flux [1, 2]. However, dynamics of coherent structures at higher Reynolds numbers still remains unclear, since various Reynolds number effects on turbulence statistics and coherent structures are observed [3, 4].

The purpose of the present work is to examine the Reynolds number effect on dynamics of coherent structures through Karhunen-Loëve (KL) decomposition of wall turbulence at low-to-moderate Reynolds numbers.

## 2. Numerical Method

A pseudo-spectral method [5] is employed for the present DNS of turbulent channel flow. The Reynolds number  $Re_\tau$  based on the wall friction velocity  $u_\tau$ , the channel half-width  $\delta$  and kinematic viscosity  $\nu$  is chosen as 110, 300, and 650. Although it is not shown here, turbulence statistics of the present computation for plane channel flow are in good agreement with the DNS data of Moser et al.[3], and are available on the web page at <http://www.thtlab.t.u-tokyo.ac.jp>. Hereafter,  $u$ ,  $v$ , and  $w$  denote the velocity components in the  $x$ -,  $y$ -, and  $z$ -directions, respectively. Superscript (+) represents quantities non-dimensionalized with  $u_\tau$  and  $\nu$ . In the present study, KL decomposition [6] is employed, and the fluctuating velocity field is decomposed into a sum of eigenfunctions  $\psi_i$  of the two-point correlation tensor  $\kappa_{ij}$  as:

$$\int_0^{2\delta} \kappa_{ij}(y, y', m, n) \psi_j(y', m, n) dy' = \lambda(m, n) \psi_i(y, m, n), i, j = 1 - 3, \quad (1)$$

where  $m$  and  $n$  respectively denote wavenumbers in the  $x$ - and  $z$ -directions, while  $\lambda$  denotes the eigenvalue. Using the quantum number  $q$  to specify an eigenfunction for a wave number index pair, the triplet  $k = (m, n, q)$  completely specifies an eigenfunction [7].

## 3. Nonlinear Interactions between Coherent Structures

In order to investigate the dynamics of coherent structures in detail, wall elevation of each KL mode is characterized with the center of the vortices  $y_v$ , which is defined by the global minimum of the second invariant of the deformation tensor  $Q^+$  [8]. Then, the KL modes are divided into subgroups depending on the location of the center of the vortices  $y_v$ . The  $n$ -th subgroup  $u_i^{<n>}$  is composed of linear superposition of the KL modes, of which  $y_v$  exists in between  $y_{n-1}$  and  $y_n$ :

$$u_i^{<n>}(x, y, z, t) = \sum_{y_{n-1} < y_v < y_n} a^k(t) \phi_i^k(x, y, z), \quad (2)$$

where  $\phi_i$  is the eigenfunction in physical space, and  $y_i^+ = 5 \cdot 1.5^{i-1} (i \geq 1, y_0^+ = 0)$  for all the Reynolds numbers. Hence, the number of subgroups are 9, 11, and 13 for  $Re_\tau = 110, 300$ , and 650, respectively. Because of the linear superposition of the KL modes, each subgroup as a whole satisfies the incompressibility, the no-slip boundary condition and the orthogonality. Hereafter, quantities of the subgroup  $u^{<n>}$  is plotted at  $y_s = 0.5(y_{n-1} + y_n)$  in all figures.

Figure 1 shows an instantaneous flow field for  $Re_\tau = 110$ , in which both the near-wall vortical structures and the subgroup of  $y_s^+ = 21$  are represented. Both of them are visualized with 3-D contours of the second invariant of the deformation tensor  $Q^+ (= u_{i,j}^+ u_{j,i}^+) = -0.02$ . It is found that vortical structures associated with the subgroup of  $y_s^+ = 21$  have the wall elevation  $y^+ \sim 21$  and correspond to the leg vortices in the instantaneous flow field. Thus, the subgroup having vortex center at  $y_s^+$  mainly represents the instantaneous vortical structures around  $y^+ = y_s^+$ .

### 3.1 Contribution of KL subgroups to Reynolds shear stress

The Reynolds shear stress can be written using the KL subgroups as

$$\overline{-u'v'} = \sum_n \overline{-u^{<n>} v^{<n>}} + \sum_m \sum_{n(\neq m)} \overline{-u^{<m>} v^{<n>}}, \quad (3)$$

where the first term of RHS corresponds to the correlation between the same KL subgroup, while the second term is that between different subgroups. It is found that the latter is less than 1% of the former and is negligible.

Figure 2 shows the contribution of typical KL subgroups to the Reynolds shear stress for  $Re_\tau = 110$ . The peak location of each subgroup is  $y^+ \approx y_s^+$ . Thus, each KL subgroup has large contribution to the Reynolds stress near its vortex center. The subgroup of  $y_s^+ = 21$  dominates close to the wall ( $y^+ < 20$ ), and the contribution of the subgroups of  $y_s^+ > 47$  is negligibly small. On the other hand, when  $Re_\tau = 650$  (Figure 3), not only the near-wall subgroups but also the subgroups away from the wall ( $y_s^+ \leq 107$ ) have finite contribution to the Reynolds stress in the near-wall region.

### 3.2 Nonlinear interactions between KL subgroups

The energy balance equation of  $u_i^{<n>}$  is derived as

$$\begin{aligned} 0 &= \sum_m \overline{-u_i^{<n>} \cdot u_j^{<m>} \cdot U_{i,j}^+} - \sum_m \overline{u_{i,j}^{<n>} \cdot u_{i,j}^{<m>}} \\ &\quad + \sum_{m(\neq n)} \overline{-u_i^{<n>} \cdot u_j^+ \cdot u_{i,j}^{<m>}}, \end{aligned} \quad (4)$$

where the three terms of RHS respectively correspond to the production, dissipation and nonlinear interaction between subgroups (NL). The over bar in Eq. (4) denotes the space-time average.

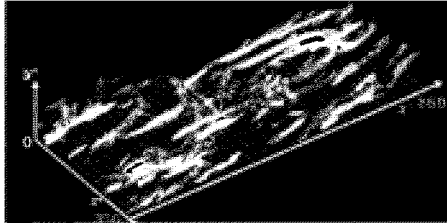


Figure 1. Near-wall coherent structures for  $Re_\tau = 110$  (translucent gray, the second invariant of the deformation tensor ( $Q^+ < -0.02$ ); white, the second invariant of the deformation tensor of the subgroup of  $y_s^+ = 21$  ( $Q^+ < -0.02$ )).

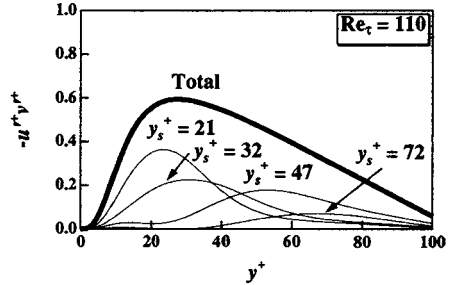


Figure 2. Contribution of KL subgroup to the Reynolds shear stress at  $Re_\tau = 110$ .

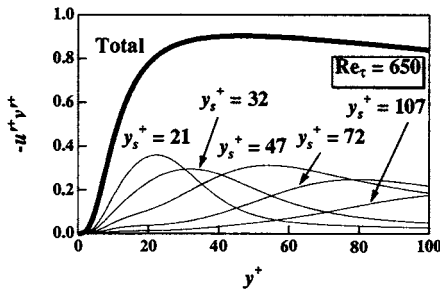


Figure 3. Contribution of KL subgroup to the Reynolds shear stress at  $Re_\tau = 650$ .

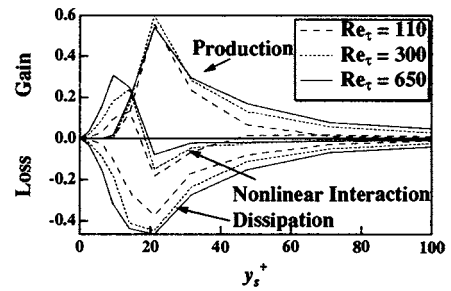


Figure 4. Energy budget of KL subgroup.

Figure 4 shows the three terms of Eq. (4) of each KL subgroup. For  $Re_\tau = 110$ , the subgroups below  $y_s^+ = 10$  have no production, and they gained energy from other subgroups through NL. The subgroup of  $y_s^+ = 21$ , which corresponds to the streamwise vortices, has the largest production. About one third of the energy produced is transferred to the other subgroups through NL, and the rest is lost through dissipation. All the terms become smaller with increasing  $y_s$ , but the absolute value of NL is always larger than 10% of that of the production term at each subgroup. Therefore, NL plays an important role in the energy budget. Note that NL is only negative at  $17 < y_s^+ < 45$ , which shows similar trend with the turbulent diffusion of the total turbulent kinetic energy. It is also noted that the production and dissipation terms (the first two terms of Eq. (4)) have finite value only when  $m = n$  (not shown).

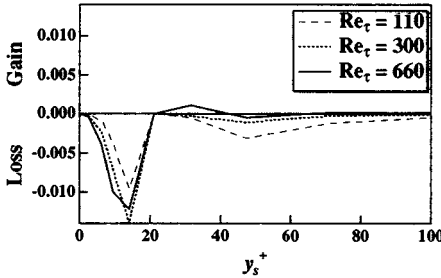


Figure 5. Nonlinear interaction term of the subgroup of  $y_s^+ = 21$ .

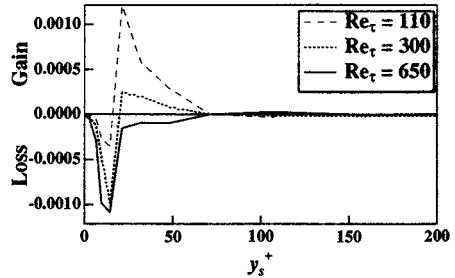


Figure 6. Nonlinear interaction term of the subgroup of  $y_s^+ = 72$ .

When the Reynolds number increases, the subgroups below  $y_s^+ = 10$  gain larger energy from the other subgroups through NL. Production of the subgroups of  $y_s^+ = 21$  remains unchanged, while NL energy transfer to the other subgroups is decreased. For  $y_s^+ > 45$ , NL becomes negative, which implies that the vortices away from the wall transfer their energy to the other subgroups through NL.

Figure 5 shows the nonlinear interaction term  $\overline{-u_i^{+<n>} \cdot u_j^+ \cdot u_{i,j}^{+<m>}$  of the subgroup of  $n = 5$  ( $y_s^+ = 21$ ), which corresponds to the near-wall streamwise vortices. For  $Re_\tau = 110$ , the energy is transferred not only to the near-wall subgroups but also to the subgroups away from the wall. When the Reynolds number increases, the negative peak at  $y_s^+ \sim 45$  disappears, and the net nonlinear interaction term only acts as inward energy transfer.

Figure 6 shows the nonlinear interaction term of the subgroup of  $n = 8$  ( $y_s^+ = 72$ ). For  $Re_\tau = 110$ , the subgroup gains the energy from the subgroups of  $14 < y_s^+ < 72$ , and loses the energy to the subgroups of  $y_s^+ < 14$ . For  $Re_\tau = 650$ , on the other hand, the energy gain at  $14 < y_s^+ < 72$  disappears and the subgroup loses the energy to the subgroups of  $y_s^+ < 72$ . Therefore, the outward energy transfer becomes smaller, and the inward energy transfer becomes larger with increasing the Reynolds number. We also found that there is almost no direct interaction between the subgroup of  $y_s^+ = 72$  and outer ( $y_s^+ > 100$ ) layers even at  $Re_\tau = 650$ .

Previous studies have shown that the near-wall structures are self-sustained through regeneration mechanisms [9]. Recently, Jimenez & Pinelli [10] claim that the damping of velocity fluctuations at  $y^+ < 60$  results in laminarization, whilst the near-wall turbulence remains mostly unchanged when all the velocity fluctuations at  $y^+ > 60$  are filtered out.

The present findings with the KL decomposition demonstrate quantitatively that the near-wall turbulence mechanism depends only on the structures near the wall, say around  $y^+ < 100$ , even at  $Re_\tau = 650$ .

## 4. Conclusions

Direct numerical simulation of turbulent channel flow was made in order to examine quantitatively the effect of Reynolds number on the nonlinear interaction between coherent structures. When  $Re_\tau = 110$ , most of the turbulence energy is generated in the Karhunen-Loëve modes corresponding to the near-wall streamwise vortices and redistributed toward/away from the wall. Thus, the streamwise vortices play a dominant role in the dynamics of wall turbulence. When the Reynolds number is increased, the nonlinear interaction among the inner layer structures ( $y^+ < 100$ ) becomes larger, and it acts as the energy transfer toward the wall. Moreover, the production term of the vortical structures at  $20 < y^+ < 100$  is increased. Therefore, not only the streamwise vortices but also the vortices at  $20 < y^+ < 100$  have large contribution to the near-wall turbulent dynamics. The direct interaction between the inner ( $y^+ < 100$ ) and outer ( $y^+ > 100$ ) layers remains inactive even at  $Re_\tau = 650$ .

## References

- [1] Robinson, S. K., 1991. Coherent motions in the turbulent boundary layer. *Annu. Rev. Fluid Mech.* 23, 601-639.
- [2] Kasagi, N., Sumitani, Y., Suzuki, Y., and Iida, O., 1995. Kinematics of the quasi-coherent vortical structure in near-wall turbulence. *Int. J. Heat & Fluid Flow* 16, 2-10.
- [3] Moser, R. D., Kim, J., and Mansour, N. N., 1999. Direct numerical simulation of turbulent channel flow up to  $Re_\tau = 590$ . *Phys. Fluids* 11, 4, 943-945.
- [4] Adrian, R. J., Meinhart, C. D., and Tomkins, C. D., 2000. Vortex organization in the outer region of the turbulent boundary layer. *J. Fluid Mech.* 422, 1-54.
- [5] Kim, J., Moin, P., and Moser, R., 1987. Turbulence statistics in fully developed channel flow at low Reynolds number. *J. Fluid Mech.* 177, 133-166.
- [6] Lumley, J. L., 1970. Stochastic tools in turbulence. Academic.
- [7] Webber, G. A., Handler, R. A., and Sirovich, L., 1997. The Karhunen-Loëve decomposition of minimal channel flow. *Phys. Fluids* 9, 1054-1066.
- [8] Iwamoto, K., Suzuki, Y., and Kasagi, N., 2002. Reynolds number effect on wall turbulence: toward effective feedback control. *Int. J. Heat & Fluid flow* 23, 678-589.
- [9] Hamilton, J. M., Kim, J., and Waleffe F., 1995. Regeneration mechanisms of near-wall turbulence structures. *J. Fluid Mech.* 287, 317-348.
- [10] Jimenez, J., and Pinelli, A., 1999. The autonomous cycle of near-wall turbulence. *J. Fluid Mech.* 389, 335-359.

# **EMPIRICAL ASSESSMENT ON THE MEAN FLOW SIMILARITY OF FLAT-PLATE TURBULENT BOUNDARY LAYERS**

Michio Hayakawa

Graduate School of Engineering, Hokkaido University, N13 W8, Sapporo 060-8628, Japan

**Abstract:** Existing experimental data on the zero-pressure-gradient turbulent boundary layer are analyzed with the aim to assess the Reynolds number similarity of the mean flow. It is shown that the velocity profile in the intermediate region is logarithmic rather than algebraic. The wall-normal range and the minimum Reynolds number for the logarithmic profile to exist are virtually consistent with those proposed by Österlund *et al.*(2000). An alternative power law with an additive constant is shown to hold over a significant portion of the outer layer where the velocity-defect scales with the free-stream velocity multiplied by the ratio of displacement thickness to boundary layer thickness.

**Key words:** Turbulent boundary layer, Mean flow scaling, Reynolds number similarity.

## **1. INTRODUCTION**

In the past decade or so, Reynolds number effects in wall-bounded turbulent shear flows have received renewed interest of many investigators, not only from a fundamental point of view but also from a standpoint of practical applications, specifically concerning with the utility of drag reduction devices in high Reynolds number regimes. In spite of considerable efforts by many researchers, however, even the mean-flow scaling of canonical flows, such as a circular pipe flow and a flat-plate boundary layer, remains an issue of controversy. Typically, conflicting conclusions have been drawn among different research groups by processing a same set of experimental data.

The present work focuses on the mean-flow similarity of zero-pressure-gradient turbulent boundary layers and analyses existing experimental data

without subjective preference to any theory and empirical laws.

## 2. DATA SOURCES AND ANALYSIS

Experimental data sets used in the present analysis are listed in Table 1. The Reynolds number  $Re$  is based on free-stream velocity  $U_e$  and momentum thickness, and the boundary layer thickness  $\delta$  is defined as the wall-normal distance  $y$  at which the local mean velocity  $U$  is equal to  $0.99U_e$ . The velocity gradient  $dU/dy$  is calculated with using the second-order central difference method. As the  $dU/dy$  distributions often exhibit discontinuity, the method of weighted least squares is applied to the initially determined  $dU/dy$ .

Table 1. List of experimental data sources.

#	Investigators	Reference	Symbols	$Re$ range
①	Purtell <i>et al.</i>	[1]	▽	700 ~ 5,100
②	Osaka <i>et al.</i>	[2]	□	800 ~ 6,100
③	DeGraaff & Eaton	[3]	◇	1,400 ~ 30,900
④	Österlund <i>et al.</i>	[4]	○ ⊙	2,500 ~ 27,300
⑤	Smith & Walker	[5]	×	3,800 ~ 48,300
⑥	Fernholz <i>et al.</i>	[6]	△	20,800 ~ 60,800
⑦	Winter & Gaudet	[7]	+	25,500 ~ 213,200

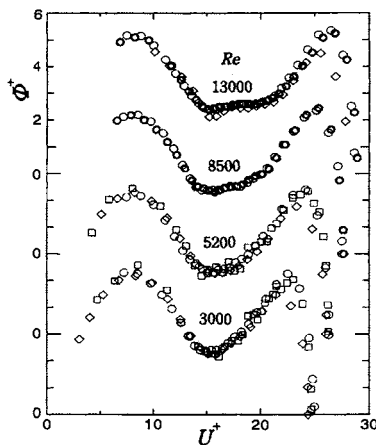
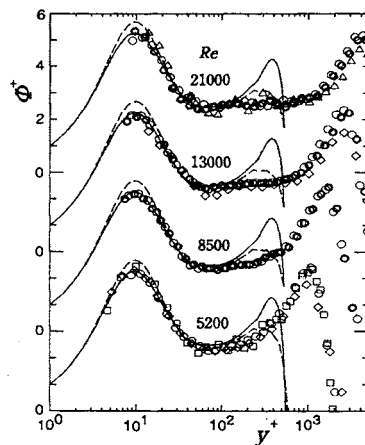
## 3. RESULTS

### 3.1 Intermediate region

In order to examine whether the flow in the intermediate(or “overlap”) region fits a logarithmic relation or a power law, a diagnostic function  $\Phi^+ = y^+(dU^+/dy^+)$  is employed here;  $\Phi^+$  must be constant for the log law and be directly proportional to  $U^+$  for the power law.

In Fig.1, data plots of  $\Phi^+$  versus  $U^+$  are shown for several  $Re$  values. The  $\Phi^+$  distributions have two peaks; one is always located in  $U^+=7\sim 9$ , and the other in  $U^+>20$  such as the  $U^+$  value increases with increasing  $Re$ . In addition,  $\Phi^+$  exhibits a local minimum at  $U^+\approx 15$ . For  $Re<5000$ , there is no distinct region where  $\Phi^+$  is constant. As  $Re$  exceeds about 6000, a plateau appears. The  $U^+$  range of the plateau increases with increasing  $Re$ . The value of  $1/\Phi^+$  (i.e., the Karman constant) in that range is in 0.37~0.39. Note that  $\Phi^+$  is nearly linear to  $U^+$  in the region between the plateau and the second peak; the slope is close to 0.5. This will be discussed later in Sec.3.2.

Figure 2 shows the variation of  $\Phi^+$  against  $y^+$ , in which the DNS results ( $Re\approx 1500$ ) of a boundary layer([9], solid lines) and a channel flow ([10], broken lines) are included for reference. The  $\Phi^+$  distribution has a shallow hollow in  $50 < y^+ < 100$  irrespective of  $Re$  values and a nearly constant region

Figure 1.  $\Phi^+$  versus  $U^+$ .Figure 2.  $\Phi^+$  versus  $y^+$ .

beyond  $y^+ = (150 \sim 200)$  when  $Re > 6000$ . That is, the log law holds in the region away from the outer edge ( $y^+ = 30 \sim 50$ ) of the buffer layer. It may be important to note that even for  $Re > 10^4$ , the  $\Phi^+$  variation in  $y^+ < 100$  is in a good agreement with that of the DNS results at much lower  $Re$ -numbers.

These results on the  $Re$ -number and wall-normal ranges for the log law to be applicable are virtually consistent with those of Österlund *et al.*[4].

### 3.2 Outer region

While the friction velocity has been customarily used in the scaling of velocity-defect profiles, a simple consideration leads to an alternative scaling.

Suppose that velocity-defect profiles are expressed by a Reynolds-number independent form, as  $(U_e - U)/u_D = F(y/\delta)$ . Here,  $u_D$  is a certain velocity scale to be determined. Then, the similarity requirement that the integration of  $F$  with respect to  $y/\delta$  should be constant, yields  $U_e \delta^*/u_D \delta = \text{const.}$ ; here,  $\delta^*$  is displacement thickness. Hence the proper velocity scale is given by  $u_D = U_e \delta^*/\delta$  without loss of generality, provided that the length scale is chosen as  $\delta$ . This velocity scale has been proposed also by Zagarola & Smits[10] who inferred it from their experimental result of a circular pipe flow.

Figure 3 shows velocity-defect profiles (for  $Re > 2500$ ) based on the above scaling and demonstrates that the present representation works fairly well over a wide range of  $Re$ -number. In fact, the collapse of data was better than the conventional scaling based on the friction velocity. It may be noteworthy that the better data collapse was observed even in the log region, suggesting a possibility that the log law would scale with the outer-layer variables.

Finally, the mean velocity in  $0.2 < y/\delta < 0.6$  is approximately proportional

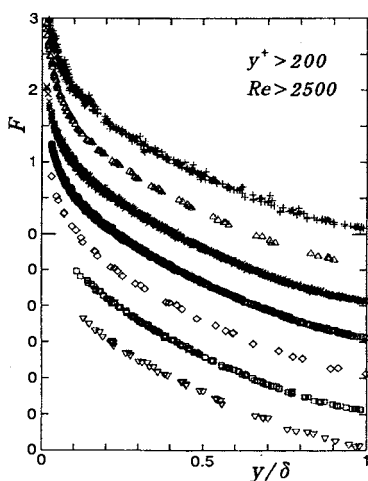


Figure 3. Velocity-defect profiles.

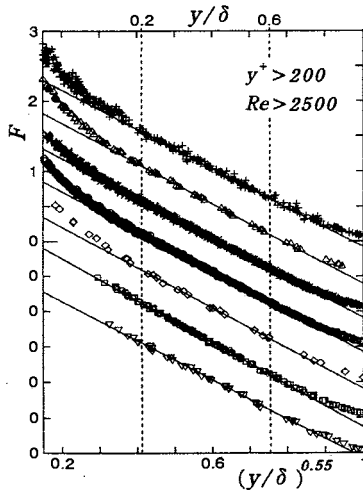


Figure 4. Power-law representation.

to a half power of  $y$ , as shown in Fig.4 where  $F$  is plotted against  $(y/\delta)^{0.55}$ . This new power law is thus expressed by  $(U_e - U)/u_D = -C_1 (y/\delta)^{0.55} + C_2$ . Although  $C_1$  and  $C_2$ , are somewhat different for different data sets, each data set appears self-consistent without any clear dependency on  $Re$ -number.

## ACKNOWLEDGEMENTS

The author would like to thank Professors J.K.Eaton, H.H.Fernholz, H.Osaka, J.M.Österlund, A.J.Smits and their coworkers for kindly making their experimental data available to him, and also to Professors W.K.George and Y.Kobashi for their invaluable comments to this study.

## REFERENCES

- [1] Purtell,L.P., Klebanoff,P.S. and Buckley,F.T., 1981, *Phys.Fluids* **24**, 802-811.
- [2] Osaka,H., Kameda,T. and Mochizuki,S., 1998, *JSME Int'l J.* **41**, 123-129.
- [3] DeGraaff,D.B. and Eaton,J.K., 2000, *J.Fluid Mech.* **422**, 319-346.
- [4] Österlund,J.M. et al., 2000, *Phys.Fluids* **12**, 1-4.
- [5] Smith,D.W. and Walker,J.H., 1959, NACA TR, R-26.
- [6] Fernholz,H.-H. et al. 1995, *Phys.Fluids* **7**, 1275-1281.
- [7] Winter,K.G. and Gaudet,L., 1973, Aeronautical Research Council R&M 3712.
- [8] Spalart,P.R., 1988, *J.Fluid Mech.* **187**, 61-98.
- [9] Moser,R.D., Kim,J. and Mansour,R., 1999, *Phys.Fluids* **11**, 943-945.
- [10] Zagarola,M.V. and Smits,A.J., 1998, *J.Fluid Mech.* **373**, 33-79.

# **SIMILARITY LAW OF TURBULENCE INTENSITY DISTRIBUTION FOR CHANNEL FLOWS**

Osami Kitoh and Koichi Nakabayashi

*Nagoya Institute of Technology, Gokishocho Showaku, Nagoya 466-8555, Japan and Aichi University of Technology, Nishisakocho, Gamagori 443-0047, Japan*

**Abstract:** A leading parameter for the turbulence intensity profile in a channel flow is shown to be shear stress gradient  $\mu$  rather than Reynolds number  $Re_*$ . Similarity laws such as the linear, plateau and half power law are developed. The universal wall law is realized in Couette flow with  $Re_* \geq 100$ . The flow regime diagram is given to show the global parameter dependency.

**Key words:** Couette flow, Poiseuille flow, Turbulence intensity, Shear stress gradient

## **1. Introduction**

Although many works concerning turbulence intensity distribution in channel have been reported, few discuss the effect of shear stress gradient [1]. The main objectives of this study in addressing this issue are : (1) To derive the similarity laws of the turbulence intensity profile of channel flows for the various limiting conditions and compare them with the existing experimental data of Poiseuille, Couette and Couette-Poiseuille flows reported so far. (2) To draw the flow regime diagram of the channel flow based on the turbulence intensity profiles and on the similarity laws in order to see the global parameter dependency of the flows.

## **2. Similarity laws and flow regime diagram**

First, we develop the similarity laws of turbulence intensity  $u$  (root mean square value of the streamwise component) for Couette-Poiseuille flow using dimensional analysis.  $u$  can be expressed as

$$u = f(y, v, u_*, \alpha, h) \quad (1)$$

where  $y$ ,  $u_*$ ,  $\alpha$  and  $h$  are the wall distance, friction velocity ( $=(\tau_w/\rho)^{1/2}$ ), shear stress gradient ( $=1/\rho \cdot d\tau/dy$ ) and channel half height, respectively. The non-dimensional form of Eq. (1) taking  $u^+$  and  $v^+$  as basic variables is

$$u^+ = u/u_* = f(y/\delta_v, \delta_s/\delta_v, h/\delta_v) = f(y^+, \mu, Re_*) \quad (2)$$

where  $\delta_v = v/u_*$  is a viscous length scale,  $\delta_s = (u_*)^2/\alpha$  is a shear stress gradient length scale and  $\mu = \delta_s/\delta_v$  is a shear stress gradient parameter. Equation 2 shows that the distribution of  $u^+$  can be considered on the parameter plane of  $\mu$ - $Re_*$ . Poiseuille flows are on a line of  $Re_* = -\mu$ , whereas Couette flows are realized at  $|\mu| \rightarrow \infty$ . Various similarity laws of  $u^+$  distribution are expected for limiting value of  $y^+$ ,  $\mu$  and/or  $Re_*$ .

In the case of  $|\mu| \rightarrow \infty$ , i.e. Couette flow,  $\mu$ -dependence disappears from Eq. (2) and it takes

$$u^+ = f(y^+, Re_*) \quad (3)$$

Figure 1 shows the experimental results of Couette flow [2].  $Re_*$  has a small effect only in the range of  $10 \leq y^+ \leq 70$  when  $Re_*$  is smaller than about 100. This  $Re_*$ -dependency may be caused by the change of the turbulence structure itself and/or the penetration of the wall layer from the other side. When  $Re_* \geq 100$ , there appears to be no Reynolds number effect at all, and the universal wall law of the turbulence intensity can be obtained as

$$u^+ = f(y^+) = f(y/\delta_v) \quad (4)$$

For very small  $y^+$  this relation reduces to the linear relation

$$u^+ = A_0 y^+ \quad (5)$$

Because of no viscous effect at large  $y^+$ ,  $f(y^+)$  should be constant there. So we have a plateau region that can be expressed as

$$u^+ = A_1 = \text{const.} \quad (6)$$

From the experimental results,  $A_0 = 0.3 \sim 0.33$  and  $A_1 = 1.9 \sim 2.1$  (for  $y^+ \geq 100$ ).

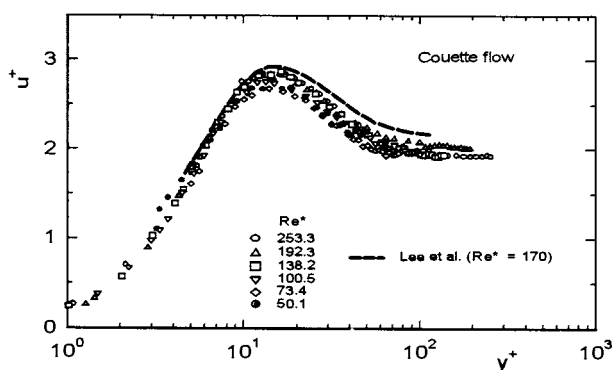


Fig. 1 Turbulence intensity distribution for Couette flow

As  $\mu$  approaches zero while keeping  $Re_*$  large, the shear stress gradient has an appreciable effect on  $u^+$ , and Eq. (2) for the wall region becomes

$$u^+ = f(y^+, \mu) \quad (7)$$

Shear stress distribution in a channel can generally be expressed as

$$\tau^+ = \tau / \tau_w = 1 + y^+ / \mu . \quad (8)$$

In the region of  $y^+ / \mu \gg 1$ , that is  $y > K_s \delta_s$  ( $K_s$ : constant around 2~3),  $\tau_w$  is no more important, so  $u^*$  does not appear in the functional form of Eq. (7). Thus we obtain the following half power law for  $u^+$ .

$$u^+ = A_{1/2} (y^+ / \mu)^{1/2} \quad (\mu > 0) \quad (9)$$

Since it is difficult to perform the experiment of low  $\mu$  at high  $Re_*$ , only the data at rather low  $Re_*$  are available now [3] which are plotted as  $u^+ \mu^{1/2}$  versus  $(y^+)^{1/2}$  in Fig. 2. Even these data are in marginal condition for half power law they collapse on a line. The universal constant  $A_{1/2}$  is about 2.4.

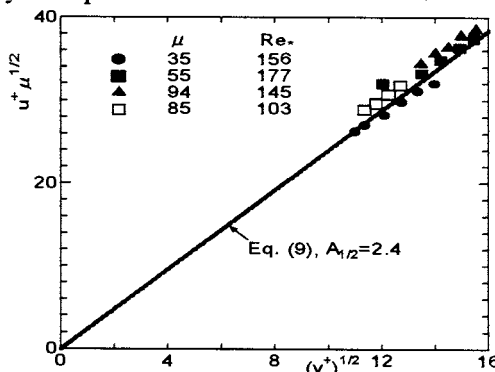


Fig. 2 Half power law

Figure 3 shows  $u^+$ -profile for Poiseuille flow [4] which varies largely with  $Re_*$  unlike Couette flow. Because of the relation of  $Re_* = -\mu$ , change of  $Re_*$  means the change of  $Re_*$  itself and  $\mu$ . It has been reported that  $\mu$  is a dominant cause of the profile change [3]. At high  $Re_*$  the profile is similar to Couette flow as expected because  $|\mu| (= Re_*)$  is large. It is only beyond  $Re_* = 1500$  that the plateau region seems to appear. In the core region there is a position ( $y^+ = Re_*$ ) of  $\tau_w = 0$  where no turbulent kinetic energy production occurs and around which low turbulence intensity prevails.

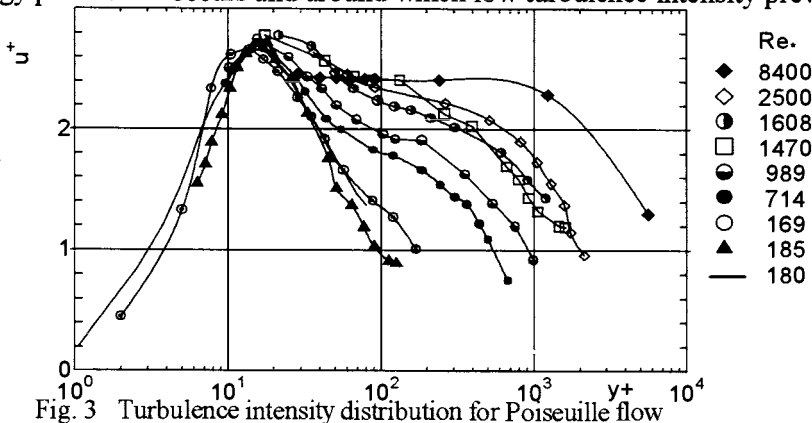


Fig. 3 Turbulence intensity distribution for Poiseuille flow

In the limiting conditions we can obtain simple similarity laws as shown above. However, a transitional condition from one similarity law to another appears. The flow regime diagram shows the overall picture of the ranges of the similarity law and the transitional area. Figure 4 shows a diagram for Poiseuille flow in the  $y^+$ - $Re_*$  plane as for example, where a parameter  $\mu$  is included in  $Re_*$ , because of  $Re_* = -\mu$ . In the figure, open circles show the lower boundary of the  $Re_*$ -affected region. Hatching shows the estimated boundaries between different similarity laws.

Figure 5 is a diagram of  $\mu$  effect in the wall region estimated from Couette-Poiseuille flow data [3]. Lack of data for high  $Re_*$  prevents us from drawing definite boundaries. The half power law is only for  $\mu > 0$ . There is some difference in the boundary of the  $\mu$  affected region between positive and negative  $\mu$ .

### 3. Conclusions

For the turbulence intensity profile in the wall region, a leading parameter is  $\mu$ , while  $Re_*$  has a secondary effect. The large difference in  $u^+$  profile between Couette and Poiseuille flows exists due to the  $\mu$  effect in the latter flow. As  $Re_*$  increases, the Poiseuille flow profile approaches that of Couette flow in the wall region. The half power law is developed for small  $\mu$  ( $> 0$ ).

### References

- [1] M. M. M. El Telbany & A. J. Reynolds, J. Fluid Mech., Vol. 111 (1981), 283-318.
- [2] K. Nakabayashi, O. Kitoh & F. Nishimura, Proc. 11th Symp. TSF Grenoble, (1997), 11: 10-15.
- [3] K. Nakabayashi, O. Kitoh & Y. Katou, Proc. 2nd Symp. TSFP Stockholm, (2001), 49-54.
- [4] O. Kitoh & K. Nakabayashi, Trans JSME (B), Vol. 59, No. 564 (1998), 2443-2449.

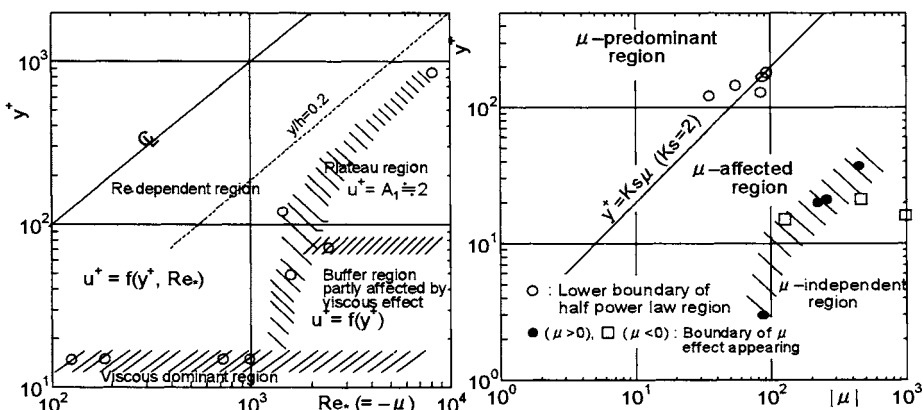


Fig. 4 Flow regime diagram for P flow

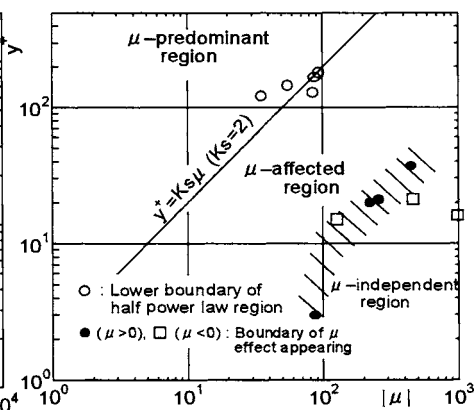


Fig. 5 Flow regime diagram for CP flow

# LAGRANGIAN MODELLING OF TURBULENT DIFFUSION IN THE ATMOSPHERE - RECENT DEVELOPMENTS

B.L. SAWFORD<sup>1</sup>, M.S. BORGAS<sup>1</sup> and P.K. YEUNG<sup>2</sup>

<sup>1</sup>*CSIRO Atmospheric Research, PMBI Aspendale, VIC 3195, Australia;* <sup>2</sup>*School of Aerospace Engineering, Georgia Institute of Technology, Atlanta, GA 30332, USA*

**Abstract:** Lagrangian methods have been used to describe turbulent diffusion since G.I. Taylor's classic work and are now well established at a practical level in applications in the atmosphere. Nevertheless there remain fundamental issues associated with the development of Lagrangian models for turbulent transport and diffusion and in our recent work we have attempted to address some of these issues using direct numerical simulations. Although this is a powerful approach, it necessarily involves consideration of finite Reynolds number effects that are generally ignored in the atmosphere. Here we give a brief overview of some of this recent work underpinning Lagrangian modelling of turbulent dispersion in the atmosphere.

**Key words:** Reynolds number dependence, turbulent mixing, concentration statistics, acceleration statistics

## 1. INTRODUCTION

Turbulent mixing of trace materials is central to many processes in the atmosphere, and understanding and treatment at different levels is needed for different applications.

At the most basic level, the mixing and dilution of air pollution from large industrial sources or the spread of pests and diseases within crop canopies (and of the sprays applied to control them) require knowledge of the mean concentration at a point. Similarly, the inverse problem of determining the source "footprint" associated with a measurement of the concentration flux is a one-point mean field problem.

However, more complex aspects of the scalar field are also important. For example, human response to odorous pollutants is determined by short-term peaks in concentration, not by the mean. Similarly, chemical reactions in the atmosphere (as in other turbulent flows) depend on the covariance of the reactant concentrations, not the product of the means. These are still 1-point problems, but require understanding and treatment of fluctuations about the mean, which are often large because of the local nature of the sources.

Finally, some problems require a treatment of the full space-time structure of the scalar field. Examples are the way in which animals find mates or food sources by tracking a chemical plume back to its source, or in military and civil defence applications, finding the location of explosive or other dangerous materials.

Here we give a brief overview of some of the recent work underpinning Lagrangian modelling of these aspects of turbulent dispersion in the atmosphere.

## 2. LAGRANGIAN DESCRIPTION

The Lagrangian formalism provides an essentially exact connection between concentration statistics and the displacement statistics of marked fluid particles that conserve the concentration of a scalar quantity along the trajectory of the particle through the fluid. Thus for example, the  $n$ th-order  $n$ -point concentration moment is given in terms of the  $n$ -point displacement probability density function (pdf)  $P$  and the source distribution  $S$  by

$$\overline{c(\mathbf{x}_1, t_1) \dots c(\mathbf{x}_n, t_n)} = \int_{-\infty}^{t_1} \int_{-\infty}^{t_2} \dots \int_{-\infty}^{t_n} \int_V P(\mathbf{x}_1, t_1; \dots; \mathbf{x}_n, t_n; \mathbf{x}'_1, t'_1; \dots; \mathbf{x}'_n, t'_n) \times S(\mathbf{x}'_1, t'_1) \dots S(\mathbf{x}'_n, t'_n) d\mathbf{x}'_1 dt'_1 \dots d\mathbf{x}'_n dt'_n \quad (1)$$

All of the modelling is associated with developing a realistic representation of the displacement statistics. The standard approach is to assume that the Lagrangian velocity can be modelled as a continuous Markov process; i.e. as a generalised Langevin equation (Thomson, 1987).

## 3. MODELLING THE MEAN FIELD

In order to calculate the mean concentration we write down a stochastic differential equation for the trajectory of a single particle (Thomson, 1987)

$$d\mathbf{u}_i = a_i(\mathbf{u}, \mathbf{x}, t) dt + \sqrt{C_0 \varepsilon} d\xi_i(t) \quad (2)$$

where  $\mathbf{u}$  is the Lagrangian velocity,  $\varepsilon$  is the rate of dissipation of turbulence kinetic energy and  $d\xi$  is the incremental Wiener process.

Information about the turbulence is imposed by matching to Kolmogorov's similarity theory at small scales and by requiring that the model be consistent with specified Eulerian velocity statistics at the energy containing scales. Thus the Lagrangian structure function constant  $C_0$  is a parameter (which controls the Lagrangian time scale) in the modelling and the constraint imposed by the Eulerian velocity statistics represents a closure for the mean acceleration conditioned on the velocity  $\langle A_i; \mathbf{u} \rangle$  (Sawford & Yeung, 2000). One of the issues we address here is the value taken by  $C_0$  in the limit of large Reynolds number and its effective value at finite Reynolds number.

$C_0$  is defined in the inertial sub-range as the Lagrangian velocity structure function divided by the dissipation rate and the lag  $\tau$

$$C_0 = \frac{1}{3} \overline{(u_i(t+\tau) - u_i(t))^2} / \varepsilon \tau \quad (3)$$

In principle a plot of this quantity as a function of lag would show a plateau of height  $C_0$  in the inertial sub-range. In practice we find at the low Reynolds numbers of direct numerical simulations (DNS) that there is a peak rather than a plateau and the height of the peak increases with Reynolds number, asymptoting to a value of  $C_0 \sim 6.5$  (Sawford & Yeung, 2001). Modelling of laboratory dispersion data imply a lower effective value of about 3 (Borgas and Sawford, 1996), which is roughly consistent with the DNS at comparable Reynolds number. However, models applied in the atmosphere at much larger Reynolds numbers also use a value of  $C_0 \sim 3$ , which is in conflict with the asymptotic value from DNS. This issue remains unresolved.

### 3.1 Modelling the acceleration: Re effects

The effect of Reynolds number can be represented explicitly by modelling the velocity and acceleration as a joint Markov process, thus introducing the Kolmogorov time scale as an extra time scale (Sawford, 1991). In this case, in order to constrain the drift term we need to specify the Eulerian joint acceleration-velocity pdf, or equivalently, since we know the velocity pdf, the pdf for the acceleration conditioned on a specified velocity. Thus modelling the acceleration explicitly focuses attention on the

acceleration variance and on conditional statistics such as the conditional mean acceleration,  $\langle A_i; u \rangle$ , and the conditional covariance of the acceleration  $\langle A_i A_j; u \rangle$ , which we are again able to study using DNS results.

### 3.2 Acceleration variance

In Kolmogorov scaling, the acceleration variance is

$$a_0 = \frac{1}{3} \left\langle A_i^2 \right\rangle / \left( \left\langle \varepsilon \right\rangle^{3/2} \nu^{-1/2} \right) \quad (4)$$

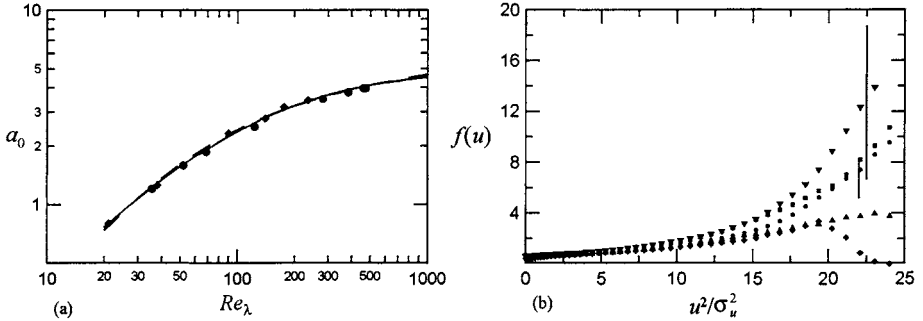


*Figure 1.* (a) The acceleration variance in Kolmogorov scaling as a function of Taylor scale Reynolds number. DNS data: Gotoh and Fukayama (2001) ( $\bullet$ ), Vedula and Yeung (1999) ( $\blacklozenge$ ). Theory:  $5/(1+110/Re_\lambda)$  (—),  $1.9 Re_\lambda^{0.135}/(1+85/Re_\lambda^{1.135})$  (—). (b) The longitudinal conditional variance function versus the square of the magnitude of the velocity normalized by the component velocity variance. Symbols are for DNS results at  $Re = 38$  ( $\blacklozenge$ ),  $Re = 90$  (—),  $Re = 140$  ( $\bullet$ ),  $Re = 235$  ( $\blacksquare$ ),  $Re = 420$  ( $\blacktriangledown$ ). The vertical lines are representative of 95% confidence intervals on the data for large  $u$  at  $Re = 140$  (short line) and  $Re = 420$  (long line).

The DNS results in Figure 1(a) show that  $a_0$  is a function of Reynolds number, and the question is what is the behaviour at large Reynolds number? From a purely empirical point of view these data are inconclusive at presently accessible Reynolds numbers,  $Re < 500$ . We can fit a form consistent with Kolmogorov's similarity theory and Batchelor's calculation of the mean square pressure gradient (the solid line in Figure 1) and we can also fit a form consistent with the refined similarity hypothesis using a multifractal representation of the intermittency (the dashed line, which is almost indistinguishable from the solid line in the figure). On theoretical grounds, the latter is favoured, but the data at this stage do not distinguish between the two. These differences are not critical for our modelling, because direct effects of Reynolds number are more important, and so for simplicity we use the Kolmogorov form.

### 3.3 Conditional acceleration covariance

The acceleration covariance conditioned on the velocity is a second order tensor function of a vector, so in isotropic turbulence is fully specified by two functions: a longitudinal function  $f(u)$  in which the acceleration is parallel to the velocity vector, and a transverse function  $g(u)$  in which it is perpendicular to the velocity vector

$$\langle A_i A_j; \mathbf{u} \rangle = \sigma_A^2 (f - g) \frac{\mathbf{u}_i \mathbf{u}_j}{\mathbf{u}^2} + \sigma_A^2 g \delta_{ij} \quad (5)$$

where we have written the unconditional acceleration variance as  $\sigma_A^2$ .

Figure 1(b) shows data for the longitudinal function at various values of  $Re_\lambda$  from 38 to 420 as a function of the velocity. Note the normalisation by the corresponding variances, which removes most of the dependence on  $Re$  at small velocities. At large velocities there may still be some dependence on Reynolds number, although the sampling uncertainty indicated by the vertical solid lines is large. The most striking feature is the magnitude of the conditional variance at large  $u$ .

We have some speculative ideas suggesting a  $u^6$  behaviour at large velocities (Sawford et al., 2002) and there is some support for this power law in data for the unconditional acceleration pdf. If we assume a Gaussian form for the conditional acceleration pdf, with a power law variance at large velocity, and a Gaussian velocity pdf, then we can show that the tails of the acceleration pdf have a stretched exponential form. The  $u^6$  behaviour in the conditional covariance, corresponds to a power of a half in the stretched exponential, close to the value of 0.41 observed in laboratory data (La Porta et al., 2001). However, the magnitude of the pdf in the tails is much too low when calculated like this, so non-Gaussian effects in the conditional acceleration pdf must also be important.

## 4. MODELLING FLUCTUATIONS

### 4.1 Pair trajectories

In order to study the second level of problems outlined in the Introduction, that is concentration fluctuations at a point, we need to model the joint motion along a pair of trajectories. Formally this can be done in terms of Markov models as outlined above (Thomson, 1990, Borgas and Sawford, 1994) and although there has been much work, the full pair

problem still awaits a fully satisfactory treatment. Progress has been made recently using quasi-1D models (Kurbanmuradov and Sabelfeld, 1995; Borgas and Yeung, 1998) for the magnitude of the separation  $\Delta$  of the particle pair and the velocity component  $u_\Delta$  parallel to the separation vector. The corresponding SDE is then

$$\begin{aligned} du &= a(u, \cdot, t)dt + \sqrt{2C_0\varepsilon}d\xi(t) \\ d &= u dt \end{aligned} \quad (6)$$

If we assume also that the drift term is quadratic in velocity, then we can tie the model down by specifying just the first four moments of the pdf for the Eulerian velocity difference at two points. DNS results (Borgas & Yeung, 1998; 2002) show that this quadratic form model is reasonable. Using this simple model, and data on the Eulerian velocity moments, Borgas & Yeung (2002) have calculated the Lagrangian statistics of the relative dispersion and compared them with DNS results.

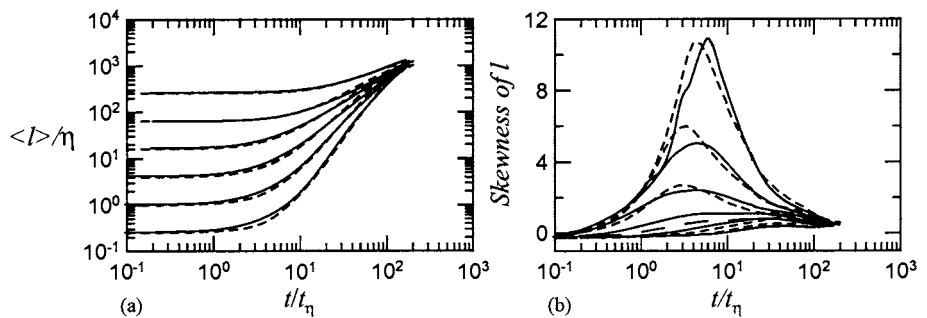


Figure 2. Comparison of stochastic model (--) and DNS results (—) for (a) the rms separation of a pair of particles and (b) the skewness of the separation, as functions of time using Kolmogorov scaling. The initial separations are (from bottom to top)  $l_0/\eta = 1/4, 1, 4, 16, 64, 256$  and  $Re_\lambda = 230$ .

Figure 2(a) shows that the relative dispersion at these Reynolds numbers does not have an inertial sub-range corresponding to Richardson's  $t^3$ -law of relative dispersion, and in fact the modelling shows that apparent manifestations of Richardson's law in low Reynolds number laboratory and DNS results is spurious (Borgas & Yeung, 2002). Figure 2(b) shows that these models are capable of reproducing the highly non-Gaussian Lagrangian relative velocity statistics observed in DNS, a very stringent test.

## 4.2 Higher order moments

These results give us some confidence in modelling pair trajectories (and hence from (1) the second moment of the concentration field), but it is clear that we cannot keep going along explicitly modelling 3-point, 4-point, 5-point and so on, trajectories. Fortunately there is a suggestion from DNS studies of the dispersion of three and four particles that most of the non-Gaussian effects are incorporated in the scale or size of the cluster and that the shape is closer to Gaussian (Borgas, 1998; Pumir et al., 1999; Yeung et al., 2002). Borgas (1998) has built a model for the  $n$ -point displacement pdf on this basis, incorporating non-Gaussian separation statistics and Gaussian shape statistics. This model can be used to calculate the full concentration pdfs for point and line sources which are in excellent agreement with experimental data in grid turbulence.

## 5. MODELLING THE SPATIAL STRUCTURE

Finally we touch on the most difficult problem, that of representing the spatial structure of the scalar field as encapsulated in the structure functions

$$\langle (c(\mathbf{r}) - c(0))^p \rangle \sim r^{\zeta_p} \quad (7)$$

There is much interest in these statistics because they show scaling deviating from Kolmogorov-Obukhov-Corrsin (KOC) similarity theory (so-called anomalous scaling). Borgas and Sawford (2002) show that the  $n$ -point displacement pdf gives an extreme form of anomalous scaling behaviour in which the exponents of 2-point scalar structure functions of all orders are equal.

## 6. CONCLUSIONS

We have briefly reviewed some of the recent more fundamental work underpinning Lagrangian modelling of various aspects of turbulent dispersion in the atmosphere. This work relies heavily on DNS results and in order to make the link through to atmospheric scales we have discussed the asymptotic behaviour at large Reynolds number of quantities like the Lagrangian velocity structure function constant  $C_0$ , the acceleration variance, and acceleration statistics conditioned on the velocity. We have also briefly

outlined new modelling of relative dispersion at low Reynolds numbers and indicated how this can be extended to modelling the  $n$ -point displacement pdf, the one point scalar concentration pdf and scalar structure functions.

## REFERENCES

- Borgas, M.S., 1998. Meandering plume models in turbulent flows, *Proceedings 13<sup>th</sup> Australasian Fluid Mechanics Conference*, Monash University, Australia, pp. 139-42.
- Borgas M.S. and B.L. Sawford, 1994. A family of stochastic models for two-particle dispersion in isotropic homogeneous stationary turbulence, *J. Fluid Mech.* **279**, 69-99
- Borgas M.S. and B.L. Sawford, 1996. Molecular diffusion and viscous effects on concentration statistics in grid turbulence, *J. Fluid Mech.* **324**, 25-54
- Borgas, M.S. and B.L. Sawford, 2002. Simple Lagrangian models for anomalous high Reynolds number scaling of scalar structure functions, *Proceedings IUTAM Symposium on Reynolds Number Scaling in Turbulent Flow*, Kluwer, Dordrecht, (this volume).
- Borgas M.S. and P.K. Yeung, 1998. Conditional fluid-particle accelerations in turbulence, *Theoret. Comput. Fluid Dyn.* **11**, 69-93
- Borgas M.S. and P.K. Yeung, 2002. Relative dispersion in isotropic turbulence: Part 2. A new stochastic model with Reynolds number dependence, *J. Fluid Mech.*, (Submitted).
- Gotoh, T. and D. Fukayama, 2001. Pressure spectrum in homogeneous turbulence, *Phys. Rev. Lett.*, **86**, 3775-8.
- Kurbanmuradov O A and K.K. Sabelfeld, 1995. Stochastic Lagrangian models of relative dispersion of a pair of fluid particles in turbulent flows, *Monte Carlo Methods Appl.* **1**, 101-36
- La Porta, A., G.A. Voth, A.M. Crawford, J. Alexander and E. Bodenschatz, 2001. Fluid particle accelerations in fully developed turbulence, *Nature*, **409**, 1017-19.
- Pumir, A., B.I. Shraiman, and M. Chertkov, 2000. Geometry of Lagrangian dispersion in turbulence, *Phys. Rev. Lett.*, **85**, 5324-27.
- Sawford B L., 1991. Reynolds number effects in Lagrangian stochastic models of turbulent dispersion, *Phys. Fluids* **A3**, 1577-86
- Sawford, B. L. and P.K. Yeung, 2000. Eulerian acceleration statistics as a discriminator between Lagrangian stochastic models in uniform shear flow, *Phys. Fluids*, **12**, 2033-45.
- Sawford, B.L. and P.K. Yeung, 2001. Lagrangian statistics in uniform shear flow: DNS and Lagrangian stochastic models, *Phys. Fluids*, **13**, 2627-34.
- Sawford, B.L., P.K. Yeung, M.S. Borgas, P. Vedula, A. La Porta and E. Bodenschatz, 2002. Acceleration variance and conditional variance statistics in turbulence, *Phys. Fluids*, (Submitted).
- Thomson D.J., 1987. Criteria for the selection of stochastic models of particle trajectories in turbulent flows, *J. Fluid Mech.* **180**, 529-56
- Thomson D.J., 1990. A stochastic model for the motion of particle pairs in isotropic high-Reynolds-number turbulence, and its application to the problem of concentration variance. *J. Fluid Mech.* **210**, 113-53
- Vedula, P. and P.K. Yeung, 1999. Similarity scaling of acceleration and pressure statistics in numerical simulations of isotropic turbulence, *Phys. Fluids*, **11**, 1208-20.
- Yeung, P.K., Shuyi Xu, M.S. Borgas and B.L. Sawford, 2002. Scaling of multi-particle Lagrangian statistics in Direct Numerical Simulations, *Proceedings IUTAM Symposium on Reynolds Number Scaling in Turbulent Flow*, Kluwer, Dordrecht, (this volume).

# **STUDIES OF HIGH REYNOLDS NUMBER TURBULENCE IN THE ATMOSPHERIC SURFACE LAYER OVER THE SALT PLAYA OF WESTERN UTAH**

J.C. Klewicki\* and M.M. Metzger

*Physical Fluid Dynamics Laboratory*

*Department of Mechanical Engineering*

*University of Utah*

*Salt Lake City, Utah 84112*

## **Abstract**

The Surface Layer Turbulence and Environmental Science Test facility resides on the salt playa of Utah's west desert. A major intended use of this facility is to take advantage of the low speeds and large length scales of the atmospheric surface layer over extremely homogeneous terrain for the purpose of probing the detailed structure of high Reynolds number turbulence, and, in particular, boundary layer turbulence. The physical attributes of the site and the dedicated infrastructure and instrumentation at the facility are described. A particularly significant issue relates to the conditions under which the flow is near neutral stratification. Wall shear stress, mean velocity and Monin-Obukhov stability parameter measurements are used to explore this issue. A discussion is provided of some of the studies that have employed the facility. Potential future studies are identified.

## **1. Introduction**

Owing to its relevance regarding a number of scientific and engineering applications, over the past decade the high Reynolds number turbulent boundary layer has been the subject of increasingly intense study. Experimental access to the detailed nature of high Reynolds number boundary layer turbulence (and/or high Reynolds number turbulence

---

\*corresponding author: klewicki@eng.utah.edu

in general), however, presents a formidable challenge. A primary reason for this is that for flows that achieve a high Reynolds number (say  $R_\theta = U_\infty \theta / \nu$ , where  $U_\infty$  is the free stream velocity,  $\theta$  the momentum deficit thickness and  $\nu$  the kinematic viscosity) primarily through increasing  $U_\infty$  and/or decreasing  $\nu$ , the dynamics of the smallest eddies are driven to such small lengths and high frequencies that they are generally well beyond the capabilities of existing sensors. In this regard, there are clear advantages to achieving the high  $R_\theta$  condition by producing a low speed boundary layer having a very large  $\theta$ . With this as a primary interest, the Surface Layer Turbulence and Environmental Science Test (SLTEST) facility has been developed in the Great Salt Lake Desert of western Utah. The purpose of this paper is to provide an overview of the SLTEST facility, a summary of some of its flow characteristics and a brief discussion of results that, to date, have been derived from experiments at the SLTEST site.

## 2. SLTEST Site Attributes

The SLTEST site is located near the southern end of the Great Salt Lake Desert ( $113^\circ 16'W$ ,  $40^\circ 8.5'N$ ) on the U.S. Army Dugway Proving Ground. A topographical map of this region of Utah is shown in Fig. 1. In this figure the view is from the south, and extends about 60km north of the SLTEST site. The Great Salt Lake Desert encompasses the remnants of the ancient Lake Bonneville. Its surface consists of an extremely flat salt playa. For example, over the 100km fetch north of the SLTEST site, the overall surface elevation variation is less than 20m. Under typical summer conditions (i.e., clear skies and a high pressure synoptic weather pattern), the flow at the site during evening transition is from north to south.

During the late spring, the naturally high water table associated with the salt playa recedes. This leaves stable ground approximately 1m thick that has a very smooth surface composed of a thin, dust free crust. Longer wavelength vertical undulations in this crust typically range from 2mm to 4mm. For these “smooth wall” conditions, sparse crust imperfections, constituting the actual surface roughness, are generally less than 1mm. As the summer proceeds, however, the surface typically dries and cracks and its roughness increases. Aerodynamic roughness lengths have been measured to vary between 0.3mm and 3.0mm. Under low wind conditions and/or a recently wetted surface, direct measurements (Klewicki et al., 1995) indicate the existence of a measurable viscous sublayer.

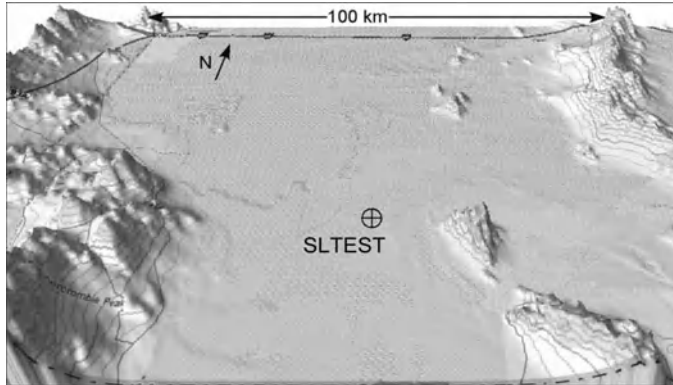


Figure 1. Topographical map of Utah's west desert/SLTEST site.

### 3. Thermal Stratification Effects

An important use of the atmospheric surface layer (ASL) flow at the SLTEST site is the study of high Reynolds number, shear generated, boundary layer turbulence. It is thus often desirable to make measurements that are as devoid of thermal stratification effects as possible. For this reason, most of the high resolution turbulence measurements at the site have been acquired during the time period in the late afternoon and early evening when the ASL flow passes through neutral thermal stability. During this time, tower-based sonic anemometry, sodar and balloon based observations have been used to quantify the characteristics of the ASL. A relevant issue in this regard is whether, and to what degree, the flow properties in the ASL are coupled to the mechanical shear at the surface.

Monin-Obukhov length based stability parameter,  $\zeta = z/L$ ,  $L = -u_\tau^3/(\kappa(g/\Theta_v)\bar{v}\theta_v)$ , measurements have been acquired at about 2m from the surface using sonic anemometry. During the same time period, direct measurements of the surface shear stress,  $\tau_{wall}$ , and the kinematic Reynolds stress,  $\bar{uw}$  were acquired. (Note that in the present coordinate system  $u$  is the along-wind velocity fluctuation and  $w$  is the vertical velocity fluctuation.) These measurements were then used to provide two independent measures of the friction velocity,  $u_\tau$ . Data from the drag plate (Sadr and Klewicki, 2000) allow utilization of the fundamental definition,  $u_\tau = \sqrt{\tau_{wall}/\rho}$ , and the Reynolds stress data employ the common estimate that the turbulent flux of momentum near the surface is transmitted to the surface shear stress,  $u_\tau = \sqrt{-\bar{uw}}$ . Under the negligible influence of thermal stratification effects (i.e., purely shear driven turbulence), these two measures of  $u_\tau$  should be the same. Typical re-

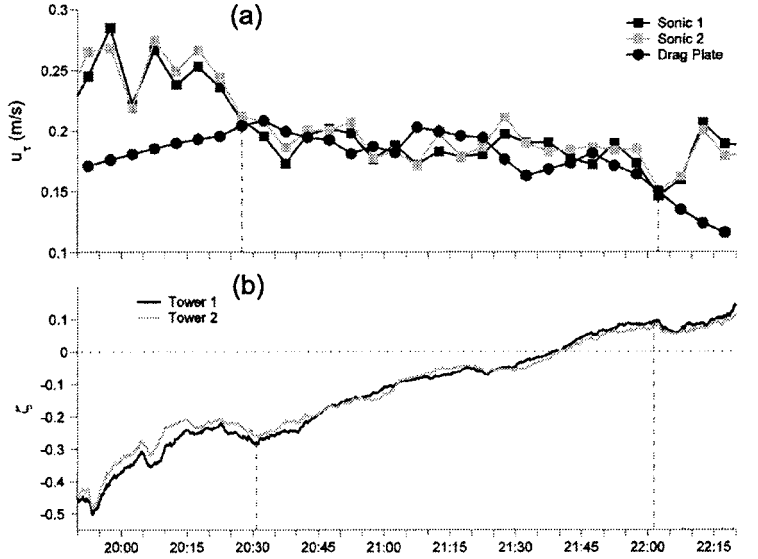


Figure 2. Evening transition measurements of (a) friction velocity and (b)  $\zeta = z/L$ , where  $L$  is the Monin-Obukhov length.

sults of simultaneously acquired  $\zeta$  and  $u_\tau$  measurements taken before, during and after evening transition are shown in Fig. 2. Comparison of the sonic-based and drag plate-based  $u_\tau$  measurements indicates a period in which the turbulent shear stress measured above the surface correlates strongly with the actual surface shear stress. Reference to the time series of  $\zeta$  indicates that during the time in which there is good agreement between the sonic anemometer and drag plate data,  $\zeta$  exhibits a nearly linear temporal behavior. Examination of a number of plots such as those shown in Fig. 2 appears to indicate that a good measure of near-neutral conditions is when  $\zeta$  is displaying this linear dependence. In this regard, it is interesting to note that this behavior occurs during a time period that nominally, but not always, brackets sunset. More extensive measurements, especially for  $\zeta$  values derived from a greater range of  $z$  locations, are needed to further characterize this behavior.

Another indication that there is a significant period during evening transition in which the SLTEST site ASL is near neutral stability may be found in mean velocity measurements. That is, numerous experiments (e.g., see Garratt, 1992) have shown that the mean profile exhibits well established deviations from logarithmic behavior when influenced by thermal stratification. In this regard, Figs. 3(a) and (b) show mean pro-

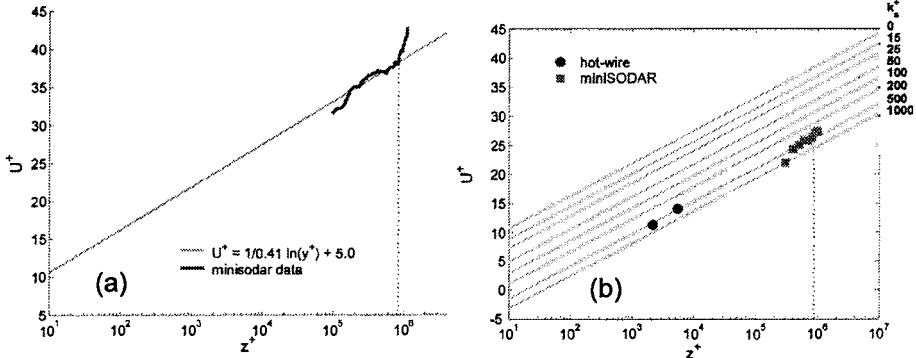


Figure 3. Inner normalized SLTEST site mean velocity profiles, (a) smooth wall and (b) rough wall.

file data taken during evening transition for both smooth and rough wall conditions respectively. The sodar data in Fig. 3(a) indicate that the inner normalized mean profile (using  $u_\tau$  as derived from the drag plate) closely follows the established smooth wall logarithmic line as derived from laboratory data up to  $z^+ = zu_\tau/\nu \cong 8.7 \times 10^6$ . Similarly, the results in Fig. 3 (b) indicate that the simultaneously acquired hot-wire and sodar data exhibit the same downward shift associated with the presence of a rough surface (in this case  $k^+ \cong 500$ ). Taken together, the results of Figs. 3 provide rather strong evidence that during the evening transition period (i.e., when  $\zeta$  displays a linear dependence on time) the flow across the ASL is mechanically coupled to the state of stress at the surface. Operationally, the position above the surface at which the mean profile deviates from a logarithmic line is taken to be the analogue of a laboratory boundary thickness,  $\delta$ . At greater distances from the surface there exists the “mixed layer” portion of the planetary boundary layer. By definition, the mixed layer is largely decoupled from the surface condition. During evening transition, the ASL thickness at the SLTEST site is typically about 100m. As indicated in Fig. 3 (a) this corresponds to  $\delta^+ \cong 1 \times 10^6$  or equivalently  $R_\theta \cong 5 \times 10^6$ .

#### 4. Previous, On-going and Future Studies

An attractive feature of the boundary layer flow at the SLTEST site is that, owing to the low flow speeds and large boundary layer thickness, standard hot-wires have very good spatial and temporal resolution. For example, under typical conditions an  $l = 1\text{mm}$  scale sensor will have a normalized scale,  $l^+ = lu_\tau/\nu$ , of less than ten. This sensor resolution is very good even at low Reynolds number, and is unique at high Reynolds

number. Because of the ability to attain very high resolution measurements, the infrastructure at the SLTEST facility has been put in place to largely accommodate the use of instrumentation and sensors typical of laboratory studies. This infrastructure includes dedicated on-site power, air-conditioned trailers and a near-surface measurement platform that provides for the convenient calibration and rapid deployment of hot-wire sensors. All together, this infrastructure has been established to facilitate detailed near-surface turbulence measurements by multiple users. Owing to these attributes and consistent with intent of the facility, researchers from 9 universities have thus far conducted experiments at the SLTEST facility. In what follows, some of the previous, on-going and planned future studies at the SLTEST site are discussed.

Over the past 40 years, flow visualization studies have proven highly useful in educating boundary layer physics. Many flow visualization techniques, however, become difficult to use at high speed, and thus are generally limited to low Reynolds number flows. In this regard, the SLTEST flow has a distinct advantage because it is both at low speed and very high Reynolds number. An early flow visualization study at the SLTEST site was conducted to investigate the properties of the viscous sublayer at  $R_\theta = O(10^6)$  (Klewicki et al., 1995). The results of this study confirmed the existence of sublayer streaks at high Reynolds number, and revealed that the inner normalized streak spacing is invariant with  $R_\theta$ . More recently, vertical light sheet flow visualization studies at the SLTEST site have provided evidence for hairpin vortex packets at high  $R_\theta$  (Hommema and Adrian, 2000).

The decreasing spatial resolution of sensors with increasing  $R_\theta$  has plagued the ability of experimental measurements to properly resolve the fine scale properties of turbulence at high  $R_\theta$ , and thus properly characterize  $R_\theta$  dependencies. As previously mentioned, however, measurements at the SLTEST site are of unusually high resolution, even when compared to low Reynolds number studies. A number of measurements of turbulent velocity and scalar fluctuations have been made at the SLTEST site, (e.g., Metzger and Klewicki, 2001; Marusic and Kunkel, 2002; Aivalis et al., 2002). For example, through the use of existing high resolution, low  $R_\theta$  data and high  $R_\theta$  data from the SLTEST site Metzger et al., 2001 were able to show that the peak inner normalized axial intensity exhibits a logarithmic dependence on  $R_\theta$ . On-going studies of the turbulent intensities in the logarithmic layer exhibit similar behaviors. For example, the data of Klewicki et al., 2000 show that the log layer axial intensities exhibit a significant increase at high  $R_\theta$ , and that roughness has only a very small (if any) effect on this statistic. These

results also compare favorably with the similarity analysis predictions of Marusic et al., 1997.

The high spatial resolution afforded at the SLTEST site also allows for the accurate measurement of velocity and scalar gradient fluctuations (Folz, 1997; Metzger et al., 2002; Priyadarshana and Klewicki, 2002). Such measurements are particularly relevant to the study of turbulent transport and stress gradient generation mechanisms, as well as the characterization of turbulent vorticity field (Klewicki et al., 1994; Klewicki et al., 2000; Foss et al., 2002).

Finally, though many of the measurements at the SLTEST facility have focused on near neutral conditions, the site also offers opportunities to explore the effects of thermal stratification. In this regard, balloon-based studies have explored the behavior of the vertical temperature distribution during evening transition (Fernando et al., 2001). Furthermore, an extensive set of measurements covering a range of stability conditions from an array of 16 sonic anemometers have recently been acquired (Higgins et al., 2002). It is also worth noting that the flatness and horizontal homogeneity of the salt playa is particularly attractive for the study of stably stratified flows. This is because these flows are particularly sensitive to sloping terrain, and thus studies at the SLTEST site are largely devoid of such effects.

## 5. Summary

Although the SLTEST facility is not a wind tunnel, the emerging data indicate that, at times, the flow at the site provides a natural analogue sufficient to educe many properties of high Reynolds number turbulence. On-going efforts to characterize the flow at the SLTEST site, and thus the degree to which it behaves like a large wind tunnel, will continue. Overall, the intent of the SLTEST site is to provide a resource that serves both the engineering and atmospheric science communities.

## 6. Acknowledgements

The SLTEST facility was developed through an NSF-OSTI grant with major contributions from Utah State University, University of Utah and the U.S. Army Dugway Proving Ground. Portions of the present work were supported by the NSF and ONR, grant monitors M. Plesniak and R. Joslin respectively. The authors would also like to thank researchers from other universities who have, to date, utilized the SLTEST facility. These include, R. Adrian, J. Fernando, J. Foss, I. Marusic, E. Malek, C. Meneveau, S. Morris, A. Naguib, M. Parlange, F. Porte-Agel, K. Sreenivasan and J. Wallace.

## References

- Aivalis, K., Sreenivasan, K., Klewicki, J., and Biltoft, C. (2002). Temperature structure functions for air flow over a moderately-heated ground. *Phys. Fluids*, 14:2439.
- Fernando, H., Lee, S., Anderson, J., Princevac, M., Pardyjak, E., and Grossman-Clarke, S. (2001). Urban fluid mechanics: Air circulation and contaminant dispersion in cities. *Env. Fluid Mech.*, 1:107.
- Folz, A. (1997). *An experimental study of the near-surface turbulence in the atmospheric boundary layer*. Ph.D. dissertation, University of Maryland.
- Foss, J., Maher, M., Prevost, R., and Morris, S. (2002). Velocity-vorticity correlations in the high Re boundary layer at the SLTEST site-Utah. In *Proc. 47th American Physical Society, Division of Fluid Dynamics Meeting*. American Physical Society.
- Garratt, J. (1992). *The atmospheric boundary layer*. Cambridge University Press.
- Higgins, C., Kleissl, J., Kumar, V., Tvaroha, A., Meneveau, C., Parlange, M., and Klewicki, J. (2002). SGS-2002: Field experimental study of subfilter stress and flux statistics in the atmospheric surface layer over smooth terrain. In *Proc. 47th American Physical Society, Division of Fluid Dynamics Meeting*. American Physical Society.
- Hommema, S. and Adrian, R. (2000). Structure of wall eddies at very large Reynolds number - A large scale PIV study. *Bull. Am. Phys. Soc.*, 45:132.
- Klewicki, J., Metzger, M., Kelner, E., and Thurlow, E. (1995). Viscous sublayer flow visualizations at  $R_\theta \cong 1500000$ . *Phys. Fluids*, 7:857.
- Klewicki, J., Murray, J., and Falco, R. (1994). Vortical motion contributions to stress transport in turbulent boundary layers. *Phys. Fluids*, 6:277.
- Klewicki, J., Priyadarshana, P., Sadr, R., and Metzger, M. (2000). Axial turbulent stress transport in high and low Reynolds number boundary layers. *Bull. Am. Phys. Soc.*, 45:36.
- Marusic, I. and Kunkel, G. (2002). Turbulence intensity similarity laws for high Reynolds number boundary layers. In *Proc. IUTAM Symposium on Reynolds Number Scaling in Turbulent Flow*. Princeton University.
- Marusic, I., Uddin, A., and Perry, A. (1997). Similarity law for the streamwise turbulence intensity in zero pressure-gradient turbulent boundary layers. *Phys. Fluids*, 9:3718.
- Metzger, M. and Klewicki, J. (2001). A comparative study of wall region structure in high and low Reynolds number turbulent boundary layers. *Phys. Fluids*, 13:692.
- Metzger, M., Klewicki, J., Bradshaw, K., and Sadr, R. (2001). Scaling the near-wall axial turbulent stress in the zero pressure gradient boundary layer. *Phys. Fluids*, 13:1819.
- Metzger, M., Klewicki, J., and Priyadarshana, P. (2002). Reynolds number dependences in the behavior of boundary layer axial stress and scalar variance transport. In *Proc. IUTAM Symposium on Reynolds Number Scaling in Turbulent Flow*. Princeton University.
- Priyadarshana, P. and Klewicki, J. (2002). Reynolds number scaling of wall layer velocity-vorticity products. In *Proc. IUTAM Symposium on Reynolds Number Scaling in Turbulent Flow*. Princeton University.
- Sadr, R. and Klewicki, J. (2000). Surface shear stress measurement system for boundary layer flow over a salt playa. *Meas. Sci. Technol.*, 11:1403.

# A top-down theory for the neutral atmospheric surface layer compared with measurements

Ulf Högström<sup>1</sup>, J.C.R. Hunt<sup>2,3</sup> and Ann-Sofi Smedman<sup>1</sup>

<sup>1</sup>*Uppsala University, Department of Earth Sciences, Meteorology, Villavägen 16, SE-752 36 Uppsala, Sweden;* <sup>2</sup>*Department of Space, Climate Physics and Geological Sciences, University College, Gower Street, London WC1, U.K.;* <sup>3</sup>*J.M. Burgers Centre, Delft Univ. of Technology*

**Abstract:** A new theory for very high Reynolds number turbulent boundary layers predicts that detached eddies formed in the lower parts of the boundary layer but above the top of the surface layer play a fundamental role for the dynamics of this boundary layer. Eddies impinging onto the surface result in strongly distorted elongated eddies in the lower one third of the surface layer. This paper demonstrates that the theory gives predictions in good agreement with atmospheric near-neutral surface layer data.

**Key words:** Top-down process, impinging eddies, turbulence

## 1. INTRODUCTION

According to Hunt and Morrison (2000), in the case of very high turbulent Reynolds number,  $Re_\tau = u_e L_e / \nu > 10^4$ , where  $u_e$  is a typical turbulence velocity scale of order the friction velocity,  $u_*$ ,  $L_e$  an eddy length scale above the surface layer and  $\nu$  kinematic viscosity, the momentum exchange process in a boundary layer is governed by detached eddies being formed in the shear above the surface layer – an essentially inviscid mechanism that amplifies the turbulence as seen in studies of homogeneous shear flow. These eddies impinge onto the wall, where they become strongly distorted and elongated in the strong shear. This scraping along the wall of the large high Reynolds number eddies creates smaller scale, sloping eddies which help keep the vertical gradient of Reynolds stress negative.

As shown in detail in Högström et al. (2002), predictions based on Rapid Distortion Theory calculations have been successfully tested against extensive atmospheric measurements from several sites during near neutral conditions. The present contribution stresses certain findings from that study and carries the analysis a step forward.

## 2. PREDICTIONS FOR THE VERTICAL VELOCITY COMPONENT

When eddies of finite size approach the surface from above, blocking at the surface creates a potential flow component that modifies the vertical velocity, which results in the following expression:  $\sigma_w^2 / u_*^2 = 1 + (z / L_e)^{2/3}$ . The length scale  $L_e$  is assumed to be  $\sim$  the depth of the surface layer,  $h_s$ . If  $h_s$  is defined as the height where the momentum flux  $\tau(z)$  has been reduced compared to its value at the surface,  $\tau(0)$  by a certain small amount, of the order 5 or 10 percent, it follows from the equation of motion that, provided the mean flow is horizontally homogeneous and stationary,  $h_s = \text{const.} \cdot h$ , where  $h \approx 0.2u_* / f_c$ , where  $f_c$  is the Coriolis parameter. In the analysis of near-neutral data from ten surface layer experiments (Högström et al., 2002) the assumption was therefore made that  $L_e \sim u_* / f_c$ . As explained in detail in Högström et al. (2002), the data, which represented a range of measuring heights from 1.6 m to 32 m and sites with widely varying roughness, were well represented in the mean by the above relations for  $\sigma_w^2 / u_*^2$  and for  $L_e$ , with a proportionality constant of  $10^{-2}$ , which is of the expected order.

Thus if the momentum transport mechanism is dominated by eddies of size  $L_e = 10^2 u_* / f_c \sim O(10 \text{ m})$ , these would be expected to show up in an analysis of coherent structures in the neutral atmospheric surface layer, which was indeed found by Högström and Bergström (1996). Using a method by Tiederman (1989), which also worked well for the atmospheric data, they found that more than 90% of the total momentum flux occurs within the identified structures, and that 70-80% of the flux is caused by the conditional mean component flux  $u_c w_c$ . The mean duration of bursts and sweeps,  $\delta T$  was found to be independent of wind speed and equal to 4 to 5 seconds, so that  $L = U\delta T = \text{const. } u_* / f_c$ , and the constant is about  $10^{-2}$ .

The blocking process acting on detached eddies is quite scale-selective. Thus Hunt (1984) has derived an expression for the case of shear-free

boundary layer flows, which after application of Taylor's hypothesis for 'frozen' turbulence, and further pre-multiplication by frequency  $n$  and division by  $u_*^2$ , results in:

$$\frac{nS_w(n)}{u_*^2} = \frac{\alpha_3}{(2\pi\kappa)^{2/3}} \varphi_\varepsilon^{2/3} f^{2/3} \quad (1),$$

where  $\alpha_3$  is the transverse Kolmogoroff constant = 0.67,  $\kappa$  is the von Karman constant = 0.40, and  $\varphi_\varepsilon = \varepsilon k z / u_*^3$ , the non-dimensional dissipation rate, found by Högström (1990, 1992) to be 1.24 during neutral conditions;  $f$  is the non-dimensional frequency,  $nz/\bar{u}$ ,  $\bar{u}$  being the mean wind speed at height  $z$ . Inserting numerical values for the parameters in Eq (1) gives the value 9 for the factor of proportionality. In Figure 1 this prediction is compared with an extensive set of atmospheric, near-neutral measurements from two sites and three heights each. It is clear that the two mean spectra collapse onto the low-frequency asymptote predicted by Eq. (1).

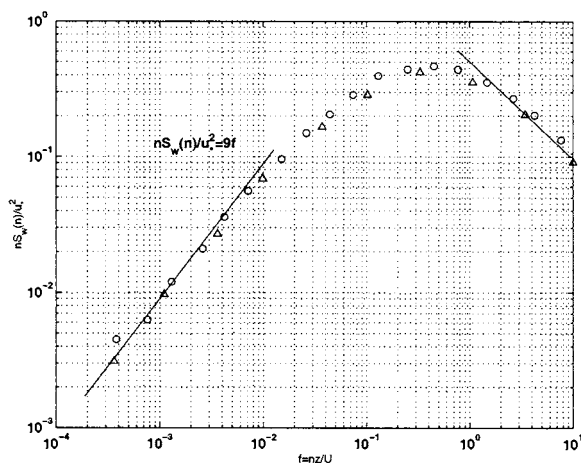


*Figure 1.* Mean normalized neutral velocity spectra against normalized frequency from two sites and three heights each. Also included is the prediction for low frequencies

### 3. LONGITUDINAL SPECTRA

In Högström et al (2002) it was noted that the normalized longitudinal spectrum pre-multiplied by frequency obtained during neutral conditions close enough (see below) to the surface could be sub-divided into three frequency ranges. Figure 2 is a typical example.  $nS_u(n)/u_*^2$  is plotted

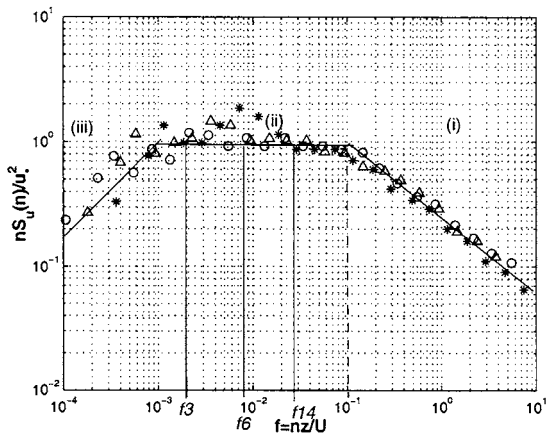
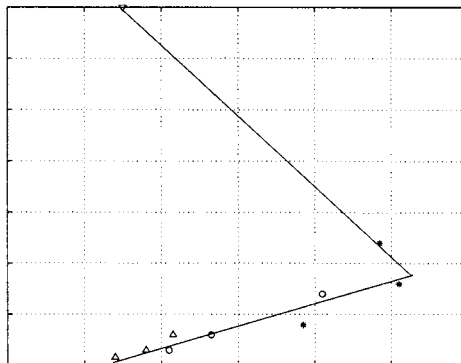


Figure 2. Example (30min mean) of normalized longitudinal spectrum plotted against normalized frequency. Data from Lövsta (Högström, 1990). Symbols: circles, 3m; triangles, 6m; stars, 14m

against normalized frequency  $f$  for three heights, see figure legend. Range (i) is the inertial subrange, where the three spectra collapse. In range (ii)  $nS_u(n)/u_*^2$  is constant and close to unity. This is the self-similar range of Perry et al. (1986). Its extension in normalized frequency, denoted by  $f(z)$ , is seen to vary considerably with height: At 3m (circles in Figure 2) the range extends from  $f(3) \approx 1.5 \cdot 10^{-3}$  to  $10^{-1}$ ; at 6m from  $f(6) \approx 8 \cdot 10^{-3}$  to  $10^{-1}$ ; at 14m from  $f(14) \approx 3 \cdot 10^{-2}$  to  $10^{-1}$ . Range (iii) contains the largest boundary-layer-scale eddies, and the prediction is (Perry et al., 1986, Hunt and Carlotti, 2001):  $nS_u(n) = \Lambda_s n / \bar{u}$ , where  $\Lambda_s$  is of order the boundary layer height,  $h$ . Since  $h \sim u_* / f_c$ ,  $\Lambda_s = A u_* / f_c$ . At the extrapolated intersection between range (ii) and (iii),  $nS_u(n)/u_*^2 \approx 1$ , so that it is possible to obtain an expression for  $A$ , see Högström et al. (2000), Eq. (15).

Note that Eq. (6) does not give curves that collapse in the representation of Figure 2.

In Figure 3 have been plotted mean values of  $A$  derived from measurements at four sites with widely different roughness length,  $z_0$ . Data taken from heights below about 20m are well represented by



*Figure 3.* Parameter  $A$  as a function of height. Triangles with flat side down are mean values for three heights at site 'Laban's mills'; circles from site Lövsta; stars from Östergarnsholm; triangle with flat side up from Sprogøe (Mann, 1994)

a straight line,  $A$  increasing with height. This corresponds to  $\Lambda_s$  increasing from being close to the (nominal) height of the boundary layer near the surface to three times that value around 15 – 20m. For greater heights,  $\Lambda_s$  decreases rapidly with height.

#### 4. DISCUSSION AND CONCLUSIONS

It has been demonstrated that predictions from the new theory for very high Reynolds number turbulence, which predicts detached eddies impinging onto the wall, where each generates its own turbulence field, is of decisive importance for the boundary-layer dynamics and agrees well with atmospheric measurements from several sites during near-neutral conditions. It was demonstrated that the non-dimensional variance of vertical velocity increases by about a factor of two from the bottom to the top of the surface layer. The detached eddies were shown to have a scale of 10 – 15m. The momentum transport by these eddies was demonstrated to be quite effective and well organized.

Predictions for the blocking effect on the vertical velocity spectrum were shown to agree quite well with measured data.

Longitudinal spectra in the lowest c. 15 m were shown to contain a self-similar range, where the non-dimensional spectrum is constant and close to unity. The high-frequency limit of this range corresponds to about  $k_{1z} = 0.1$ , as also found by Katul and Chou (1998). The low-frequency limit is, however, strongly variable with height. Thus, at 1.6m the extension of the self-similar range is almost two decades, decreasing gradually to zero at 15 – 20m height. The largest boundary-layer scale,  $\Lambda_s$  is shown to increase from  $h$  near the ground to  $3h$  at 15 – 20m, decreasing rapidly for greater heights.

Acknowledgement. We gratefully acknowledge important contributions by our collaborators J. Morrison, P. Carlotti and R.P. Hoxey and the seminal ideas of the late A.E. Perry.

## References

- Högström, U.: 1990, Analysis of turbulence structure in the surface layer with a modified similarity theory formulation for neutral conditions. *J. Atm. Sci.*, **47**, 1949-1972.
- Högström, U.: 1992, Further evidence of inactive turbulence in the near-neutral atmospheric surface layer, in *Proceedings of 10th Symposium of Turbulence and Diffusion*, 29 Sept.-2 Oct., 1992, Portland, Or., pp. 188-191.
- Högström, U. and Bergström, H.: 1996, Organized turbulence structures in the near-neutral surface layer. *J. Atm. Sci.*, **53**, 2452-2464.
- Högström, U., J.C.R. Hunt and A. Smedman: 2002, Theory and measurements for turbulence spectra and variances in the atmospheric neutral surface layer. *Boundary-Layer Meteorol.*, **103**, 101-124.
- Hunt, J.C.R.: 1984, Turbulence structure in thermal convection and shear-free boundary-layers. *J. Fluid Mech.*, **138**, 161-184.
- Hunt, J.C.R. and P. Carlotti: 2001, Statistical structure of the high Reynolds number turbulent boundary layer, *Flow, Turbulence, Combustion*, **66**, 453-475.
- Hunt, J.C.R. and J.F. Morrison: 2000, Eddy structure in turbulent boundary layers, *Euro J. Mech.B – Fluids* **19**, 673-694.
- Katul, G. and C.-R. Chu: 1998, A theoretical and experimental investigation of energy-containing scales in the dynamic sublayer of boundary-layer flows, *Boundary-Layer Meteorol.*, **86**, 279-312.
- Mann, J.: 1994, The spatial structure of neutral atmospheric surface-layer turbulence. *J. Fluid Mech.*, **273**, 141-168.
- Perry, A.E., S. Henbest and M.S. Chong: 1986, A theoretical and experimental study of wall turbulence. *J. Fluid Mech.*, **165**, 163-199.
- Smedman, A., U. Högström, H. Bergström, A. Rutgerson, K.K. Kahma and H. Pettersson: 1999, A case study of air-sea interaction during swell conditions. *J. Geophys. Res.*, **104**, 25,833-25,851.
- Tiederman, W.G.: 1989, Eulerian detection of turbulent bursts. *Near Wall Turbulence. Proc. Z. Zoriac Conf. 1988*, S.J.Kline and N.H. Afgan, Eds., Hemisphere, 874-887.

# NEW SCALING LAWS OF SHEAR-FREE TURBULENT DIFFUSION AND DIFFUSION-WAVES

Martin Oberlack

Silke Guenther

*Hydromechanics and Hydraulics Group, Darmstadt University of Technology,*

*Petersenstraße 13, 64287 Darmstadt, Germany*

*oberlack@hyhy.tu-darmstadt.de, guenther@hyhy.tu-darmstadt.de*

**Abstract** We consider the problem of turbulence generation at a vibrating grid in the  $x_2$ - $x_3$  plane. Turbulence diffuses in the  $x_1$  direction. Analyzing the multi-point correlation equation using Lie-group analysis we find three different solutions (scaling laws): classical diffusion-like solution (heat equation like), decelerating diffusion-wave solution and finite domain diffusion due to rotation. All solution have been obtained using Lie-group (symmetry) methods. It is shown that models based on Reynolds averaging are only capable to model either the diffusion-like solution or the decelerating diffusion-wave solution. The latter solution is only admitted under certain algebraic constraints on the model constants. Turbulent diffusion on a finite domain induced by rotation is not admitted by any of the classical models.

**Keywords:** Vibrating grid turbulence, similarity solutions, multi-point correlation equation, Lie group analysis, symmetries

## 1. Introduction

We reconsider the problem of shear-free turbulent diffusion with no production due to a mean-velocity gradient. Turbulence is generated at the plane  $x_1 = 0$  and diffuses in the direction  $x_1 > 0$ . Turbulence is homogeneous in the  $x_2$ - $x_3$  plane. This problem was first considered by Lele (1985) raising the question whether a turbulent diffusion-wave exists by analyzing the  $k$ - $\varepsilon$  model. In the following we show, based on the infinite sequence of multi-point correlation equations, that a variety of invariant solutions (scaling laws, see e.g. Oberlack 2001) of the diffusion problem exist employing Lie-group analysis (see e.g. Bluman & Kumei 1989).

## 2. Symmetries and invariant solutions of the correlation equation

For the subsequent analysis we employ the multi-point correlation equation which is believed to properly model the statistical quantities of turbulence at all scales. Since the multi-point equations of different tensor order have similar structure, in the following we solely present the two-point correlation equation. It is important to note that all results to be presented below are fully consistent with all higher order correlation functions up to an arbitrary order.

We adopt the two-point correlation equations in a form derived from a singular asymptotic expansion in Oberlack (2000). Therein it was proven that similar to the laminar boundary layer equations we may separate the correlation equations into an inner and outer equation corresponding to small- and large-scale turbulence. The inner equations cover the inertial range and the dissipation range. The outer equations include all large scales down to inertial range. The inertial range is the matching region.

Since we are primarily interested in large-scale quantities such as the Reynolds-stress tensor or the integral length-scale we adopt the large-scale two-point correlation equation which for the present flow case reduces to

$$\begin{aligned} \frac{\partial R_{ij}}{\partial t} + \delta_{i1} \frac{\partial \overline{p' u'_j}}{\partial x_1} - \frac{\partial \overline{p' u'_j}}{\partial r_i} + \frac{\partial \overline{u'_i p'}}{\partial r_j} + \frac{\partial R_{(i1)j}}{\partial x_1} \\ - \frac{\partial}{\partial r_k} [R_{(ik)j} - R_{i(jk)}] + 2 \Omega_k [e_{kli} R_{lj} + e_{klj} R_{il}] = 0, \end{aligned} \quad (1)$$

extended by the kinematic conditions for the correlation functions derived from the continuity equation (see e.g. Rotta 1972)

$$\begin{aligned} \delta_{i1} \frac{\partial R_{1j}}{\partial x_1} - \frac{\partial R_{ij}}{\partial r_i} = 0, \quad \frac{\partial R_{ij}}{\partial r_j} = 0, \quad \frac{\partial \overline{u'_1 p'}}{\partial x_1} - \frac{\partial \overline{u'_j p'}}{\partial r_j} = 0, \\ \frac{\partial \overline{p' u'_i}}{\partial r_i} = 0, \quad \delta_{i1} \frac{\partial R_{1(jk)}}{\partial x_1} - \frac{\partial R_{i(jk)}}{\partial r_i} = 0, \quad \frac{\partial R_{(ik)j}}{\partial r_j} = 0. \end{aligned} \quad (2)$$

$R_{ij}$ ,  $\overline{p' u'_i}$ ,  $\overline{u'_j p'}$ ,  $R_{i(jk)}$ ,  $R_{(ik)j}$  are respectively the two-point velocity correlation, the two two-point pressure-velocity correlations and the two two-point triple-velocity correlations. The integral length-scale is defined as

$$\ell_t = \frac{1}{K} \int_{V_r} R_{kk} dr, \quad (3)$$

where  $K$  is the turbulent kinetic energy.

For a non-rotating frame ( $\Omega = 0$ ) the equations (1) and (2) admit the following classical symmetries

$$\bar{T}_{sx} : t^* = t , \quad x_1^* = e^{a_1} x_1 , \quad \mathbf{r}^* = e^{a_1} \mathbf{r} , \quad \mathbf{R}^* = e^{2a_1} \mathbf{R} , \quad \dots \quad (4)$$

$$\bar{T}_{st} : t^* = e^{a_2} t , \quad x_1^* = x_1 , \quad \mathbf{r}^* = \mathbf{r} , \quad \mathbf{R}^* = e^{-2a_2} \mathbf{R} , \quad \dots \quad (5)$$

$$\bar{T}_x : t^* = t , \quad x_1^* = x_1 + a_3 , \quad \mathbf{r}^* = \mathbf{r} , \quad \mathbf{R}^* = \mathbf{R} , \quad \dots \quad (6)$$

$$\bar{T}_t : t^* = t + a_4 , \quad x_1^* = x_1 , \quad \mathbf{r}^* = \mathbf{r} , \quad \mathbf{R}^* = \mathbf{R} , \quad \dots \quad (7)$$

which respectively correspond to scaling of space, scaling of time, translation in space and translation in time. Dots denote the remaining correlation functions which have been omitted due to lack of space.

From a given set of symmetries we know from basic group theory that also any combination of them is a symmetry. Hence we may combine all of the latter symmetries and rewrite the resulting symmetry in infinitesimal form. Invoking the condition of an invariant solution (in turbulence called scaling law) we obtain (see e.g. Bluman and Kumei 1989)

$$\frac{dx_1}{a_1 x_1 + a_3} = \frac{dt}{a_2 t + a_4} = \frac{dr_{[k]}}{a_1 r_{[k]}} = \frac{dR_{[ij]}}{2(a_1 - a_2) R_{[ij]}} = \dots , \quad (8)$$

where indices in brackets indicate no summation. Depending on the scaling group parameter  $a_1$  and  $a_2$  we distinguish three different cases. In the following we employ the abbreviation  $m = \frac{a_1}{a_2} - 1$ .

### Turbulent diffusion with spatially growing integral length-scale ( $a_1 \neq 0$ , $a_2 \neq 0$ )

Integration of (8) leads to a set of invariants which are taken as the new independent and dependent variables

$$\begin{aligned} \tilde{x}_1 &= \frac{x_1 + x_o}{(t + t_o)^{1/(m+1)}} , \quad \tilde{\mathbf{r}} = \frac{\mathbf{r}}{x_1 + x_o} , \\ R_{ij}(x_1, t, \mathbf{r}) &= (x_1 + x_o)^{-2m} \tilde{R}_{ij}(\tilde{x}_1, \tilde{\mathbf{r}}) , \quad \dots \end{aligned} \quad (9)$$

where here and in the following subsections  $x_o$  and  $t_o$  are combinations of the  $a_i$ . The key achievement is that the variables (9) lead to a similarity reduction of (1)/(2). A similar reduction in the following two subsections are due to the new variables (11) and (13). From (3) and by invoking the one-point limit in (9) we obtain

$$\begin{aligned} \overline{u'_i u'_j}(x_1, t) &= (x_1 + x_o)^{-2m} \widetilde{\overline{u_i u_j}}(\tilde{x}_1) \text{ and} \\ \ell_t(x_1, t) &= (x_1 + x_o) \widetilde{\ell_t}(\tilde{x}_1). \end{aligned} \quad (10)$$

$\ell_t$  is linearly growing with  $x_1$  independent of  $m$ . From experiments we usually have  $m = 0.43 \dots 0.75$  such that  $\overline{u'_i u'_j}$  decreases algebraically with the distance from the turbulence source at  $x_1 = 0$ .  $\tilde{x}_1$  is a diffusion type of similarity variable such as for the heat equation. For the steady problem i.e.  $t \rightarrow \infty$  we can show that  $\widetilde{\overline{u_i u_j}}$  and  $\ell_t$  become constants.

### Turbulent diffusion at constant integral length-scale ( $a_1 = 0$ , $a_2 \neq 0$ )

Since from the invariant surface condition (8) we can derive invariant solutions for arbitrary  $a_i$  we may also impose certain symmetry breaking constraints. For the present case we impose  $a_1 = 0$ , which according to (4), corresponds to the symmetry breaking of scaling of space or in other words  $a_1 = 0$  amounts to a constant integral length-scale.

Under this constraint and similar to (9) we obtain from (8)

$$\tilde{x}_1 = x_1 - x_o \ln(t + t_o), \tilde{\mathbf{r}} = \mathbf{r}, R_{ij}(x_1, t, \mathbf{r}) = e^{-2\frac{x_1}{x_o}} \tilde{R}_{ij}(\tilde{x}_1, \tilde{\mathbf{r}}), \dots \quad (11)$$

The corresponding one-point quantities read

$$\overline{u'_i u'_j}(x_1, t) = e^{-2\frac{x_1}{x_o}} \widetilde{\overline{u_i u_j}}(\tilde{x}_1) \quad \text{and} \quad \ell_t(x_1, t) = \tilde{\ell}_t(\tilde{x}_1). \quad (12)$$

Equation (12) implies two important results. Due to the symmetry breaking, e.g. imposed by periodic boundary conditions in the  $x_2$ - $x_3$ -plane, a diffusion-wave is induced with decreasing amplitude in  $x_1$ -direction and decreasing wave speed proportional to  $1/t$  as may be taken from (11). Second, the spatial decay behavior has changed from an algebraic to an exponential behavior and the integral length-scale becomes constant in space for  $t \rightarrow \infty$ .

### Turbulent diffusion in a constantly rotating frame ( $a_1 \neq 0$ , $a_2 = 0$ )

In contrast to the previous case we now consider the symmetry breaking of scaling of time  $a_2 = 0$  imposed by an external time scale due to frame rotation ( $\tau = 1/|\Omega|$ ). In this case we find from (8)

$$\begin{aligned} \tilde{x}_1 &= (x_1 + x_o)e^{-\frac{t}{t_o}}, \quad \tilde{\mathbf{r}} = \frac{\mathbf{r}}{x_1 + x_o}, \\ R_{ij}(x_1, t, \mathbf{r}) &= (x_1 + x_o)^2 \tilde{R}_{ij}(\tilde{x}_1, \tilde{\mathbf{r}}), \quad \dots \end{aligned} \quad (13)$$

The one-point quantities are similar to (10) with  $m = -1$  and  $\tilde{x}_1$  has to be taken from (13).

The surprising result for this case is that even for  $t \rightarrow \infty$  the turbulent diffusion only influences a finite domain due to the quadratic behavior of the large-scale turbulence quantities.

### 3. Model implications

Classical two-equation models such as the  $k$ - $\varepsilon$  and Reynolds-stress transport models were investigated. If only one-dimensional and time-dependent diffusion is considered we find that for the generic case of no symmetry breaking the value of  $m$  in subsection 2 which determines the spatial decay and the temporal behavior in (9)/(10), is determined by the quadratic

$$(12\sigma_K - 6c_{\varepsilon_2}\sigma_\varepsilon)m^2 + 7\sigma_K m + \sigma_K = 0 \quad (14)$$

and a quartic equation

$$\begin{aligned} & (456c_\varepsilon c_1 c_s c_{\varepsilon_2} - 144c_1^2 c_\varepsilon^2 + 144c_1 c_\varepsilon^2 - 336c_\varepsilon c_s c_{\varepsilon_2} - 216c_s^2 c_{\varepsilon_2}^2)m^4 \\ & + (168c_1 c_\varepsilon^2 - 168c_1^2 c_\varepsilon^2 - 196c_\varepsilon c_s c_{\varepsilon_2} + 266c_\varepsilon c_1 c_s c_{\varepsilon_2})m^3 \\ & + (73c_1 c_\varepsilon^2 - 28c_\varepsilon c_s c_{\varepsilon_2} - 73c_1^2 c_\varepsilon^2 + 38c_\varepsilon c_1 c_s c_{\varepsilon_2})m^2 \\ & + (14c_1 c_\varepsilon^2 - 14c_1^2 c_\varepsilon^2)m - c_1^2 c_\varepsilon^2 + c_1 c_\varepsilon^2 = 0 \end{aligned} \quad (15)$$

derived from the classical  $k$ - $\varepsilon$  and the Launder-Reece-Rodi model (LRR) (Launder *et al.* 1975) respectively. From (14) and (15) and the standard model constants we respectively obtain the solutions for  $m$ :  $m_1 = -0.14$ ,  $m_2 = 2.49$  and  $m_1 = -0.76$ ,  $m_2 = -0.18$ ,  $m_3 = -0.13$ ,  $m_4 = 2.17$ .

Since any of the values for  $m$  represent a solution of the corresponding model equations multiple solutions are admitted. This property of Reynolds averaged models is known to be important under certain conditions. In Durbin & Pettersson Reif (2001) it is shown that multiple solutions and the corresponding bifurcation of homogeneous shear flows are an important property which in fact models true physics.

The second case in subsection 2 where the symmetry breaking of scaling of space is imposed, i.e. when a constant integral length-scale is considered, the solution (11)/(12) is only admitted if the model constants are modified. E.g. in case of the  $k$ - $\varepsilon$  model constants need to obey the equation

$$\sigma_k = C_{\varepsilon_2}\sigma_\varepsilon. \quad (16)$$

The corresponding polynomial equations from the LRR model is given by

$$\begin{aligned} & (3c_1^2 c_\varepsilon^2 - 12c_1 c_\varepsilon^2 - 8c_1 c_\varepsilon c_s c_{\varepsilon_2} + 112c_s c_\varepsilon c_{\varepsilon_2} - 144c_s^2 c_{\varepsilon_2}^2) * \\ & (9c_1^2 c_\varepsilon^2 - 12c_1 c_\varepsilon^2 - 104c_1 c_\varepsilon c_s c_{\varepsilon_2} + 112c_s c_\varepsilon c_{\varepsilon_2} + 144c_s^2 c_{\varepsilon_2}^2) = 0. \end{aligned} \quad (17)$$

It is important to note that for a given set of model constants only one solution type is admissible, either the algebraic solution (9)/(10) or the exponential solution (11)/(12).

The third case of a rotating frame in subsection 2, e.g. rotating about  $x_1$ , cannot be modelled at all by one-point models. Classical linear two-equation models are insensitive to rotation. However, even fully non-linear Reynolds-stress transport models (non-linear in the Reynolds-stresses) are insensitive to rotation about  $x_1$  for the present flow, elucidating a serious shortcoming of these models. There appears to be only one model which may account for system rotation in the present pure diffusion case. It is the model by Sjögren & Johansson (2000) which is non-linear in the mean-velocity gradient.

## 4. Summary

Turbulence generated at a vibrating grid is reconsidered. Analyzing the multi-point equation using Lie-group (symmetry) methods it is shown that three different invariant solutions (scaling laws) exist: classical diffusion solution (heat equation like), decelerating diffusion-wave solution and finite domain diffusion induced by rotation. Reynolds averaged models only capture either the diffusion-like solution or the decelerating diffusion-wave solution depending on the model constants. Finite domain diffusion is not admitted by any of the classical models.

## Acknowledgments

We would wish to thank A. V. Johansson for fruitful discussions on the flow and pointing towards the model of Sjögren & Johansson (2000).

## References

- Bluman, G. W. & Kumei S.: *Symmetries and Differential Equations*. Applied mathematical sciences, vol. 81, Springer. (1989).
- Durbin P. A., Pettersson Reif B. A.: *Statistical Theory and Modeling for Turbulent Flows*. Wiley. (2001).
- Launder B. E., Reece G. C., Rodi W.: Progress in the Development of a Reynolds-Stress Turbulence Closure, *J. Fluid Mech.*, **68**, (1975), 537-566.
- Lele S. K.: A Consistency Condition for Reynolds Stress Closures, *Phys. Fluids*, **28**(1), (1985), 64-68.
- Oberlack M.: On Symmetries and Invariant Solutions of Laminar and Turbulent Wall-Bounded Flows, *ZAMM*, **80**(11–12), (2000), 791-800.
- Oberlack M.: A Unified Approach for Symmetries in Plane Parallel Turbulent Shear Flows, *J. Fluid Mech.*, **427**, (2001), 299-328.
- Rotta, J. C.: *Turbulente Strömungen*. Teubner, Stuttgart. (1972).
- Sjögren T., Johansson A.V.: Development and calibration of algebraic nonlinear models for terms in the Reynolds stress transport equation, *Phys. Fluids*, **12**(6), (2000), 1554-1572.

# THE NON SELF SIMILAR SCALING OF VORTICITY IN A SHEAR LAYER

Scott C. Morris

*University of Notre Dame  
Notre Dame, IN, 46556*

John Foss

*Michigan State University  
East Lansing, Mi, 48824*

**Abstract:** Time series measurements of the spanwise vorticity fluctuations in a large single stream shear layer have been acquired. The magnitude of the fluctuations, as measured by the standard deviation, was normalized using dissipation variables and compared at two streamwise locations. These data indicate that the vorticity fluctuations do not follow a self similar form. Rather, it was found that the values increase in magnitude with downstream distance. An explanation of this phenomenon is provided.

**Keywords:** self similar, vorticity, shear layer.

## 1 INTRODUCTION AND EXPERIMENT

The principal of self similarity as a representation of moving equilibrium was introduced by Townsend (1956). Free shear layers provide an excellent example of this equilibrium, and they form one class of the canonical turbulent flow fields. A dimensionless variable that is written as a function of a dimensionless transverse coordinate is called self similar if the function does not change with downstream position. Recent vorticity measurements acquired in a large single stream shear layer will be used to support the following hypothesis. *The vorticity fluctuations in a shear layer do not scale in a self similar manner. Instead, these values increase with the logarithm of the streamwise location when scaled using the dissipation time scales.*

In previous research efforts, vorticity fluctuations in shear layers have been scaled with either the integral time scale ( $\theta/U_0$ ), or the dissipation time scale  $\sqrt{v/\epsilon}$ . Ballint and Wallace (1988), and Haw et al. (1989) used the inte-

gral time scales, and found that the normalized vorticity fluctuations increased dramatically with downstream distance. Since  $|\vec{\omega}|^2 = \varepsilon/v$  in homogeneous turbulence, the dissipation time scales are often chosen to represent the vorticity fluctuations, see, e.g., Rogers and Moser (1994), and Loucks (1998). These studies have found that the vorticity roughly scales in a self similar manner.

The present experiments have shown that scaling vorticity with dissipation scales yields values which increase slowly with downstream distance (note that the dimensional values decrease with  $x$ ). This increase has not previously been documented because of the relatively large streamwise development length required to observe an increase above the experimental uncertainty. A large scale single stream shear layer facility has been constructed at the Turbulent Shear Flows Laboratory at Michigan State University, see Figure 1. The Reynolds number of the boundary layer at separation is  $Re_\theta = 4650$ , based on the momentum thickness  $\theta(x=0) = \theta_0 = 9.6\text{mm}$ , and the constant free stream velocity  $U_0 = 7.1\text{m/s}$ . The shear layer test section is 9.7m in length from the separation point to the tunnel exit.

Spanwise vorticity measurements have been acquired using the compact four sensor hot-wire probe (Fig. 2) developed by Foss and coworkers, see, e.g., Haw et al. (1989). The two parallel wires record the magnitude of velocity with a small ( $\delta y \sim 1.4\text{mm}$ ) spatial separation. The sensors configured as an X-array are used to recover the  $v$  component of velocity. From these three signals, a micro circulation domain is constructed with the flow direction calculated using a convected distance from the local (in time) velocity magnitude (Fig. 2). The vorticity probe was traversed across the shear layer at two streamwise locations:  $x/\theta_0 = 384$  and 675. Time series data were acquired at 40kHz for 25 seconds.

## 2 RESULTS AND CONCLUSIONS

It is useful to consider the budget and scaling of the turbulent kinetic energy (TKE). The experiment described above provides information to calculate each of the terms except the pressure-velocity correlation terms, which were determined from the balance of the measured terms of the TKE equation

(see, e.g., Wygnanski and Fiedler (1970) or Morris(2002)). These data are shown in Figure 3 scaled by  $\theta/U_0^3$ . The dissipation term was calculated from the isotropic relation:  $\varepsilon \approx 30\sqrt{vu'^2}/\lambda_u^2$ . The transverse coordinate of the shear layer is represented by  $\eta=y/\theta$ , where  $\theta(x)$  is the local momentum thickness of the shear layer. The collapse of the data indicates that all of the terms scale in a self similar manner as expected. The argument can then be made that the dissipation time scale can be related to the integral quantities of the shear layer by  $\sqrt{\nu/\varepsilon} \sim \sqrt{\nu\theta/U_0^3}$ .

The profiles of the standard deviation of the vorticity time series data are shown in Figure 4. An increase in the peak vorticity of 15% can be observed between the two streamwise locations. It is argued that this increase is a general characteristic of free shear layer flows. Note that the vorticity probe resolution ( $\delta y/\eta_K$ ) at the up and downstream locations was found to be 7.8 and 7.0, respectively, where  $\eta_K$  represents the Kolmogorov length scale.

The physical mechanism by which the vorticity fluctuations increase can be considered in terms of the auto spectral density of the vorticity time series. These data are shown in Figure 5 for the spatial locations corresponding to the peak vorticity (roughly  $\eta=0$ ). The spectra are normalized by the dissipation scales. Also included in Figure 5 is the vorticity spectra calculated by fitting the one dimensional velocity spectra  $E_{11}(k_1)$ , and using isotropic relationships to arrive at  $\phi_\omega(k_1)$ .

Several distinctive features can be observed from the vorticity spectra. First, it is noted that the distributions at the two spatial locations agree well at the dissipation length scales, which indicates that the probe resolution is adequate to resolve the small scale vorticity motions. Second, a region can be observed [ $2 \times 10^{-3} < k_1 \eta_K < 0.1$ ] where the vorticity spectra follows a  $k^{-1}$  power distribution. This is in contrast to isotropic turbulence where there is no log-linear region in the one dimensional spectra.

An additional feature that can be observed in Figure 5 is the larger spectral values in the low wave number range at the downstream location. Observations made in the low wave number region (i.e., large scale motions) are often more instructive when viewing the inverse Fourier transform of the spectra, that is, the auto correlation function:  $R_{\omega\omega}$ . These data are shown in Figure 6 where time is normalized by the integral time scale ( $\theta/U_0$ ). These data show

that the vorticity correlation magnitudes at different streamwise locations are identical at large time delay when time is scaled by  $(\theta/U_0)$ . Specifically the first zero of the autocorrelation is found at a dimensionless time of  $t\theta/U_0 \approx 2.5$ , which was also found by Bruns et al. (1991).

The data have shown that the vorticity spectra at  $x/\theta(0)=384$  and 675, scaled by dissipation variables, correspond at the high wave numbers and deviate at the low wave numbers (Figure 5). The latter observation is quantitatively supported by the correspondence of the vorticity autocorrelation functions when scales with  $U_0/\theta$  (Figure 6). The increase in the vorticity fluctuations with downstream distance can now be explained by representing the variance of the vorticity fluctuations as the integral of the spectral density function:

$$(\tilde{\omega}_z^*)^2 = \int_{\log(k_1\theta)}^{\log(k_1\eta_K)} [k_1\eta_K \cdot \phi^* \omega_z(k_1)] d(\log(k_1\eta_K)) \quad (1)$$

where the superscript \* represents a quantity made dimensionless by dissipation scales. The limits of integration are justified given that the vorticity spectra does not contain significant values for wave numbers smaller than the integral scales or larger than the Kolmogorov scales. If it were assumed that the integrand (in square brackets) is roughly equal to a constant (see Figure 5) over this range of integration, then equation (1) implies that the vorticity variance will increase as the difference between the large scale ( $\theta$ ) and small scale ( $\eta_K$ ) motions increases. In a single stream shear layer this ratio increases with streamwise position (at a rate of  $\theta/\eta_K \sim x^{3/4}$ ).

## References

- Balint, J.L., Wallace, J.M., 1988 "Statistical properties of the vorticity field of a two-stream turbulent mixing layer," *Advances in Turbulence 2*, Springer-Verlag, NY.
- J.M. Bruns, R.C. Haw, and J.F. Foss, 1991, "The Velocity and Transverse Vorticity Fields in a Single Stream Shear Layer," proc. Eighth Turbulent Shear Flows Conference, T.U. Munich, 9-11, pp. 3-1-1 to 3-1-6.
- Haw, R.C., Foss, J.K., Foss., J.F., 1989, "Vorticity based intermittency measurements in a single stream shear layer," in *Advances in Turbulence 2*, eds. Fernholz, H., and Fiedler, H., Springer-Verlag, Berlin.
- Morris,S.C., 2002, Ph.D Thesis, Dept. of Mechanical Engineering, Mich. State University.

Rogers, M.M., Moser, R.D., 1994, "Direct simulation of a self-similar turbulent mixing layer," *Phys. Fluids*, Vol. 6, No. 2.

Townsend, 1956, The Structure of Turbulent Shear Flow, Cambridge University Press.

Wyganski, I., Fiedler, H.E., 1970, "The two-dimensional mixing region," *J. Fluid Mech.* Vol. 41, pp.327-361.

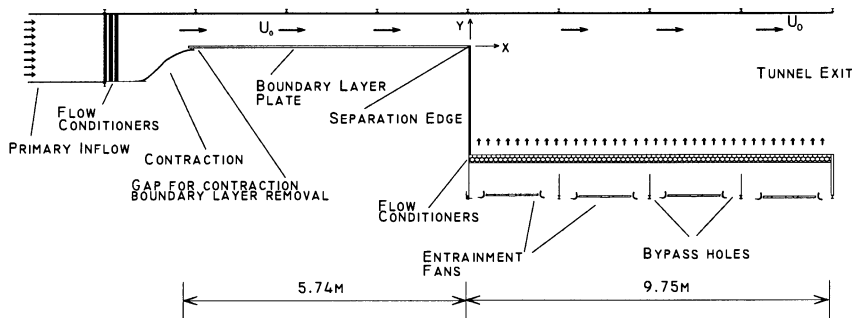


Figure 1.Schematic of the Single Stream Shear Layer Facility

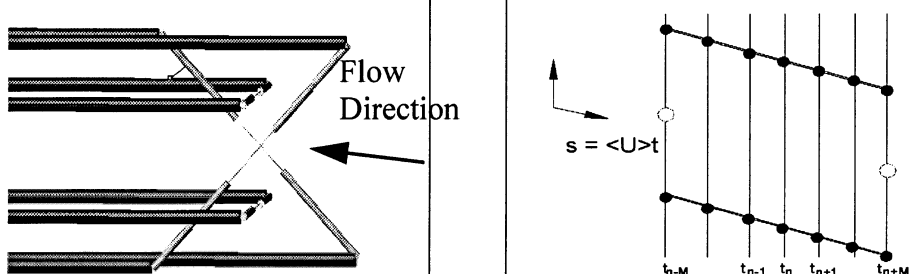


Figure 2.Schematic of vorticity probe and micro circulation domain

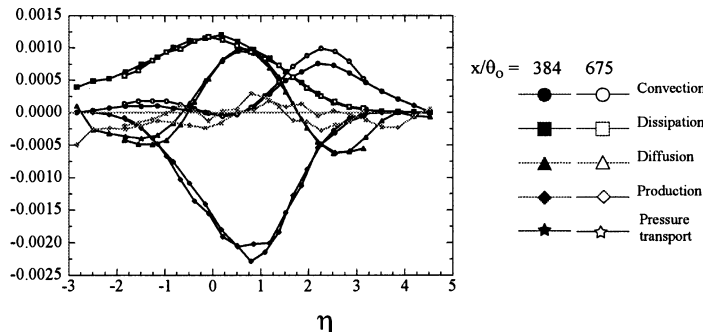


Figure 3.Measured terms of the turbulent kinetic energy budget

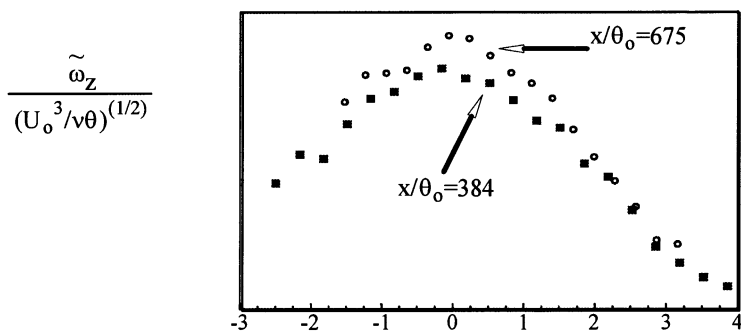


Figure 4. Profiles of the dimensionless vorticity fluctuations

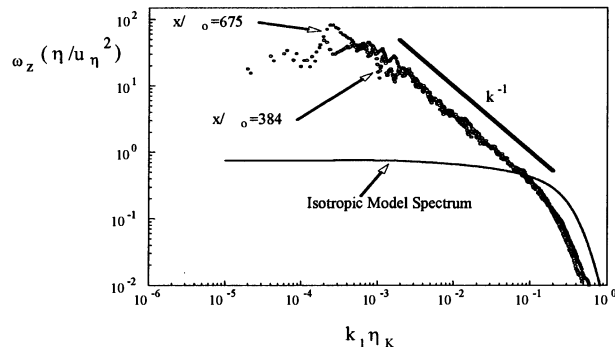


Figure 5. Autospectral density of the vorticity at the locations of peak fluctuation level normalized by dissipation scales. Note that  $\eta_K$  represents the Kolmogorov length scale.

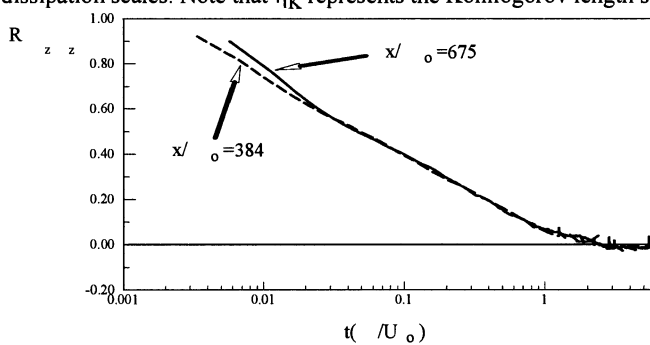


Figure 6. Autocorrelation function of the vorticity

# REYNOLDS AND FROUDE NUMBER SCALING IN STABLY-STRATIFIED FLOWS

Stephen M. de Bruyn Kops

*University of Massachusetts  
Amherst, MA 01003*

James J. Riley

*University of Washington  
Seattle, WA 98195*

Kraig B. Winters

*Scripps Institution of Oceanography, UCSD  
La Jolla, CA 92037*

**Abstract** High resolution direct numerical simulations and analytical scaling arguments are used to understand the dynamics of turbulence strongly affected by stable stratification, and to estimate the Reynolds number above which laboratory and numerical experiments of these flows must be conducted in order for the results to scale up to geophysical cases. For low Froude number  $F_h$  and high enough Reynolds number  $R_h$ , where  $F_h$  and  $R_h$  are based upon the horizontal integral scale of the motion, it is found that the simulated flows become quasi-horizontal with high vertical shearing of the horizontal velocity; this in turn leads to locally low Richardson numbers and susceptibility to shear instabilities. This occurs even though the nominal Richardson number is greater than order one. Kelvin-Helmholtz instabilities were observed to be one pathway to turbulence in the simulated flows. It is estimated that instabilities and turbulence in these flows will occur if  $Re_h F_h^2 > \mathcal{O}(1)$ , suggesting that this criterion need be met for the laboratory and numerical experiments to be useful in modeling geophysical scale flows.

**Keywords:** turbulence, stable stratification, Reynolds number, Froude number

## Introduction

Stably-stratified flows occur in most of the ocean below the mixed layer, in the atmosphere above the tropopause, and in the nocturnal atmospheric boundary layer over land. Turbulence in these flows is of great interest because it affects, e.g., climate, weather, and contaminant dispersion; it often decays due to the lack of a continuous source of energy. Examples of this include turbulence due to the breakdown of a propagating internal wave, turbulence resulting from a local shear instability, and turbulence due to wakes of islands, mountains, or vehicles.

Laboratory experiments by, e.g., Spedding et al., 1996a, Spedding et al., 1996b, Chomaz et al., 1993, and Bonnier et al., 2000, show that, when the effects of the stratification become strong, i.e., when the Froude number is of order one or less, the dynamics of stratified flows change dramatically and quasi-horizontal vortices form. As the turbulence develops without energy input from the mean flow, both the Reynolds and Froude numbers decrease. There results a competition in which Reynolds number effects tend to cause turbulence and gravity tends to suppress it so that turbulence erupts in patches and then decays. In this regime, the dynamics of the turbulence are not well understood and predictive methods work poorly. This is an area of geophysical turbulence where predictive methods are the weakest.

In the laboratory experiments just cited, the Reynolds numbers become low by the time the stratification effects become strong. In geophysical flows, however, the Reynolds number is very high, which leads to several open questions: (1) do the laboratory experiments scale up to the geophysical case, (2) do quasi-horizontal vortices exist in the geophysical case, and (3) if they do exist, what are their dynamics. In this paper, we address questions 1 and 3.

## Numerical Simulations

To address the open questions just raised, we use high resolution direct numerical simulations (DNSs) in conjunction with scaling analysis. The two flows studied via DNS are Taylor-Green vortices and a “vortex street.” The Taylor-Green vortex simulations (Riley and de Bruyn Kops, 2003) are analogous to the grid experiments of Fincham et al., 1996. They were initialized with perturbed Taylor-Green vortices (Taylor and Green, 1937) and run with nominal Reynolds and Froude numbers in the range 200 to 6400 and 1.4 to 4, respectively. This resulted in simulated flows ranging from barely turbulent to highly turbulent, and local stratification effects ranging from extremely strong to moderate. The “vortex street” simulations are analogous to late wake experiments (Spedding et al., 1996a). As with the Taylor-Green simulations, they were run for

a range of Reynolds and Froude numbers. All the simulations were computed with  $512^3$  or  $512 \times 512 \times 256$  grid points using massively parallel pseudo-spectral codes.

Quantitative results from the Taylor-Green simulations are reported by Riley and de Bruyn Kops, 2003. In summary, the simulated flows behave as expected in that the horizontal length scales grow and the vertical scales decrease with time, resulting in a quasi-horizontal flow with strong vertical shearing of the horizontal velocity. To better understand how this shearing leads to unstable patches and turbulence, we analyze the flow qualitatively here beginning with Fig. 1, in which the vertical velocity is shown on a horizontal plane through the region of maximum shear. The white line in each panel of the figure connects two material points as they move in time. We see that the flow is fairly calm at scaled time  $t = 17.5$ , but that an instability occurs in the vicinity of the white line by  $t = 20$ . By  $t = 22.5$ , the area around the line is engulfed in turbulence.

By slicing the domain vertically through the white line, the dynamics of this particular instability can be studied. In Fig. 2, the total density is shown on a vertical plane through the white line at  $t = 21.5$ . The classic Kelvin-Helmholtz roll-ups visible in the image give evidence of that mechanism being a pathway to the turbulent bursts that occur in these simulations.

A similar analysis is made of the vortex street simulations. As in the Taylor-Green case, the simulated flow evolves as expected based on laboratory results and theoretical arguments. By slicing the flow with a vertical plane through an unstable region, the instability mechanism is again observed to be Kelvin-Helmholtz. This can be seen in Fig. 3.

## Scaling Analysis

From these simulation results, in conjunction with theoretical and experimental results by other researchers, there emerges an explanation for instabilities and turbulence in strongly stratified flows. When the Froude number based on the horizontal integral scale of motion,  $F_h$ , is of order one or less, growth of the horizontal scales and nonlinear interactions cause continual development of small vertical scales. This occurs even though the initial buoyancy Richardson number is much larger than unity. The resulting regions of high shear and low local Richardson number make the flow susceptible to Kelvin-Helmholtz instabilities. For these instabilities to occur, however, the Reynolds number must be sufficiently high.

To estimate the required Reynolds number, we begin with the condition that the local buoyancy Richardson number  $Ri = N^2/(u'_h)^2/L_z^2$  is of

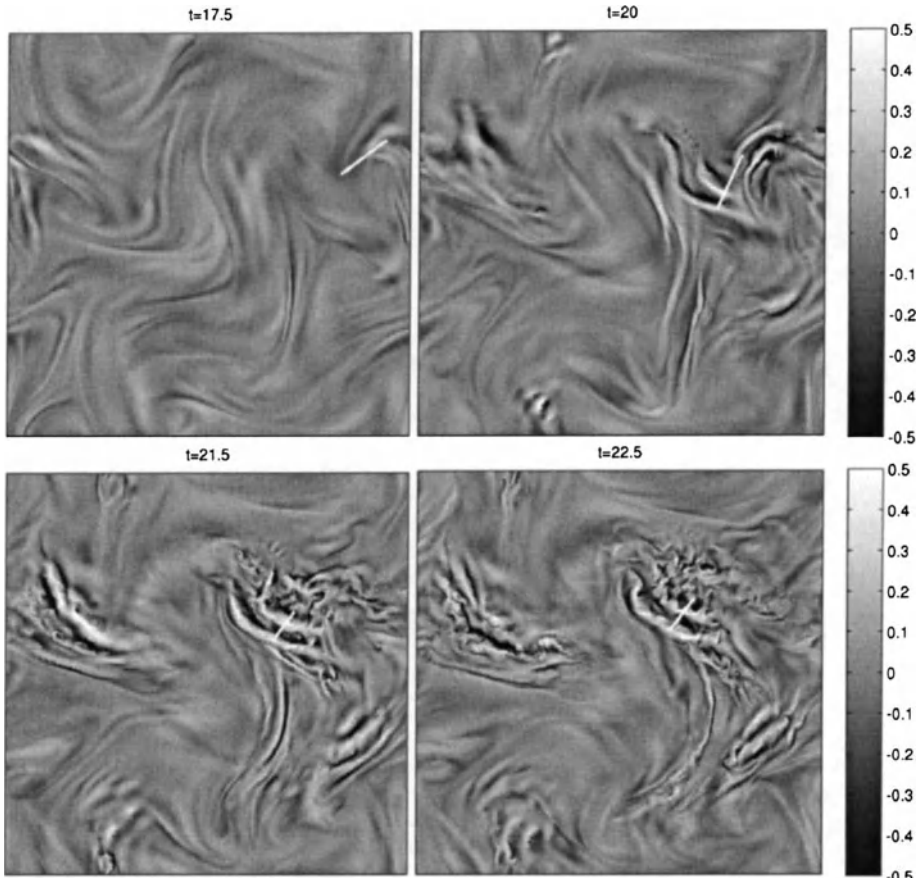


*Figure 1.* A horizontal slice through the vertical velocity field at the plane of maximum shear at four different times in a Taylor-Green simulation with Froude number 2 and Reynolds number 3200. The white bar connects two material points that move with time. The points start in a region of relative calm, experience an instability, and end up in a turbulent patch.



*Figure 2.* The total density on a vertical cut aligned with the white bar in Fig. 1,  $t = 21.5$ .

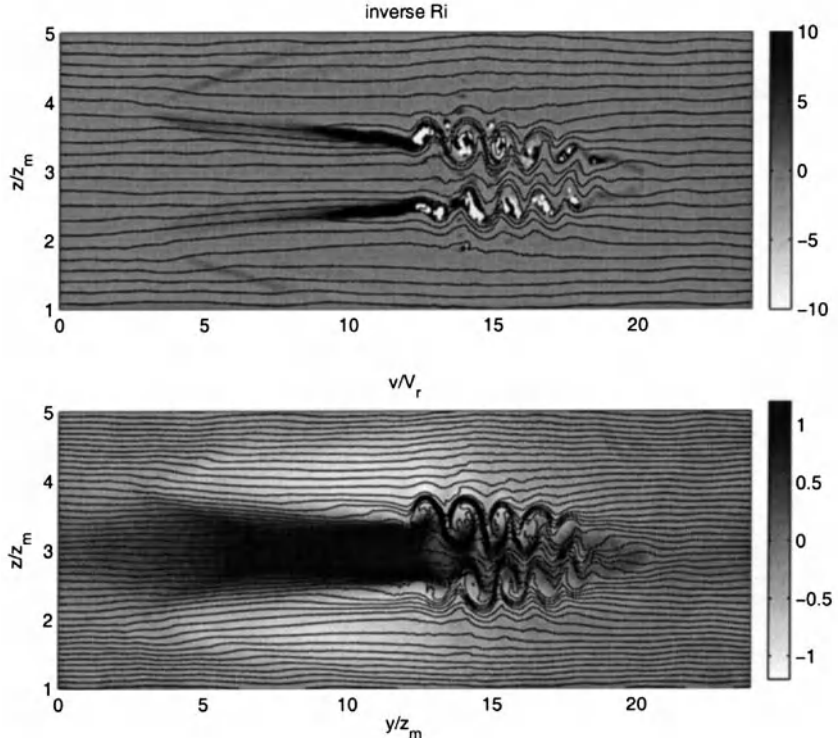


*Figure 3.* Upper panel: Inverse Richardson number in span-wise vertical plane from vortex street simulation. Values greater than 4 indicate potential for shear instability. Values less than zero indicate overturned density surfaces. Lower panel: spanwise velocity normalized by initial horizontal swirling velocity of vortices. Dark regions indicate flow to the right, light regions indicate flow to the left.

order one or less. Here,  $N$  is the buoyancy frequency,  $L_z$  is a length scale of the vertical shearing (Taylor scale), and  $u'_h$  is the mean square horizontal velocity. By assuming that the advection and viscous dissipation terms in the kinetic energy equation are of the same order of magnitude, we can estimate that the denominator is of order  $u'_h^3/\nu L_h$ , where  $L_h$  is the characteristic length of the horizontal motions. This leads to the Reynolds number criteria

$$Re_h = \frac{u'_h L_h}{\nu} > \mathcal{O}\left(\frac{1}{F_h^2}\right)$$

where  $F_h = u'/NL_h$ . A more detailed justification for this scaling is given by Riley and de Bruyn Kops, 2003.

It is important to note that while Kelvin-Helmholtz instabilities are observed in the simulated flows, there may be other pathways to turbu-

lence. The classic roll-ups shown in this paper are quite clear, but in simulations in the same series but with different nominal Reynolds and Froude numbers, turbulent patches appear with no obvious instability mechanism. Billant and Chomaz, 2000, have shown that, in model problems with strong stable stratification, the quasi-horizontal flows can also be subject to a “zig-zag” instability

## Conclusions

High resolution direct numerical simulations and analytical scaling arguments have been used to understand the dynamics of stably-stratified flows and to estimate the Reynolds number above which laboratory and numerical experiments of these flows must be conducted in order for the results to scale up to geophysical cases. Consistent with the results from other researchers, the simulated flows become quasi-horizontal with high vertical shearing of the horizontal velocity and low local Richardson numbers. Kelvin-Helmholtz instabilities were observed to be a pathway to turbulence in the simulated flows. Scaling arguments suggest that instabilities and turbulence can be expected in these flows provided that  $Re_h F_h^2 > \mathcal{O}(1)$ .

This research was funded by the U.S. Office of Naval Research, Grant No. N00014-00-1-0752, managed by Dr. L. Patrick Purtell; grants of high performance computer (HPC) time were provided by the Arctic Region Supercomputing Center and the Army HPC Research Center.

## References

- Billant, P. and Chomaz, J. M. (2000). Three-dimensional stability of a vertical columnar vortex pair in a stratified fluid. *J. Fluid Mech.*, 419:65–91.
- Bonnier, M., Eiff, O., and Bonneton, P. (2000). On the density structure of far-wake vortices in a stratified fluid. *Dyn. Atmos. Oceans*, 31:117–137.
- Chomaz, J.-M., Bonneton, P., Butet, A., and Hopfinger, E. J. (1993). Vertical diffusion of the far wake of a sphere moving in a stratified fluid. *Phys. Fluids A*, 5:2799.
- Fincham, A. M., Maxworthy, T., and Spedding, G. R. (1996). Energy dissipation and vortex structure in freely decaying, stratified grid turbulence. *Dyn. Atmos. Oceans*, 23:155–169.
- Riley, J. J. and de Bruyn Kops, S. M. (2003). Dynamics of turbulence strongly influenced by buoyancy. *Phys. Fluids*. (submitted).
- Spedding, G. R., Browand, F. K., and Fincham, A. M. (1996a). The long-time evolution of the initially-turbulent wake of a sphere in a stable stratification. *Dyn. Atmos. Ocean.*, 23:171.
- Spedding, G. R., Browand, F. K., and Fincham, A. M. (1996b). Turbulence, similarity scaling and vortex geometry in the wake of a towed sphere in a stably stratified fluid. *J. Fluid Mech.*, 314:53.
- Taylor, G. I. and Green, A. E. (1937). Mechanism of the production of small eddies from large ones. *Proc. Roy. Soc. A*, 158:499–521.

# THE NON-UNIVERSALITY OF THE LARGE WAVE NUMBER VORTICITY FIELD AT $R_\lambda=850$

John F. Foss and Scott. C. Morris

*Michigan State University, Mechanical Engineering Department, East Lansing, MI 48824  
University of Notre Dame, Department of Aerospace and Mechanical Engineering, Notre Dame, IN 46556*

**Abstract:** A fortuitous equality of the turbulence Reynolds number (850) in a large single-stream shear layer and an atmospheric boundary layer permits a direct comparison of their small scale properties. The velocity spectra:  $E_{11}$ ,  $E_{22}$  and  $H_{12}$  are in nominal agreement. The transverse vorticity spectra, however, exhibit strong differences.

**Key words:** vorticity

## 1. INTRODUCTION

It is rational to hypothesize that the small scale properties of quite large Reynolds number flows exhibit universal behavior. This viewpoint is advanced in numerous publications (see Pope (2000) for a representative discussion of this widely accepted approach to high Reynolds number flows) and it is supported by experimental evidence. Prominent among the latter are the measurements of Saddoughi and Veeravali (1994).

The present communication is to add to the high Reynolds number experimental evidence related to the small scale properties of the turbulent motion. It is based upon the data that are available to us from a large single stream shear layer (SSSL) (Morris (2002)) and from the atmospheric boundary layer (ABL) at the SLTEST facility – Dugway Proving Grounds, Utah (Klewicki, et al. (1995)).

Morris (2002) and Maher (2002) separately evaluated different measures of the estimated turbulence kinetic energy dissipation:  $\varepsilon$ . It was found that

$$\varepsilon = 15 \bar{v} \bar{v}'^2 / \lambda_v^2 \quad (1)$$

provided a self-consistent evaluation of  $\varepsilon$  and, for this reason, the following representation of the Reynolds number:  $R_\lambda = U_0 \lambda_v / v$  is used to provide a common basis for the SSSL and the ABL data sets. The transverse velocity Taylor microscale ( $\lambda_v$ ) can be evaluated as:

$$\overline{v'(x)v'(x + \delta x)} = 1 - \frac{\delta x^2}{\lambda_v^2} + \dots \quad (2)$$

for small  $\delta x$  values. Experimentally, the  $\delta x$  value is obtained from  $[-\bar{u}\delta t]$ .

The comparative measures are made possible by the use of the same experimental equipment in these two flows which have essentially the same  $R_{\lambda_v}$  values. Namely  $R_{\lambda_v} = 858$  for the SSSL and 850 for the ABL.

The relevant details regarding the two experiments are provided in Section 2. The small scale attributes of these two flows are presented in Section 3.

## 2.0 THE SEPARATE FLOW FIELDS

The large single stream shear layer (SSSL) is shown schematically in the companion paper (Morris and Foss) within this bound proceedings. Its maximum Reynolds number:  $R_\theta = U_0 \theta / v = 1.2 \times 10^5$  and shear layer momentum thickness:  $\theta = 0.2\text{m}$  were obtained at  $x/\theta(0) = 707$ .

The  $R_{\lambda_v}$  value quoted above was obtained in the central region of the shear layer ( $\bar{u} / U_0 \approx 0.5$ ).

The atmospheric boundary layer (ABL) was estimated to have an  $R_\theta$  value of  $3 \times 10^6$ . The estimated  $y^+$  location was 10,300 for the  $y=40\text{cm}$  distance above the desert floor.

The companion paper also gives a description of the four-wire transverse vorticity probe and its algorithm to recover  $(u, v, \omega_z)$  from the simultaneously sampled voltages. The probe scale is set by the separation distance:  $\delta y$ , between the two straight wires. The relative probe size as well as basic data from the SSSL and the ABL are presented in Table 1. Note, the symbol  $(\sim)$  shows the rms value of the corresponding time series values. The symbol:  $\eta_k$  is the Kolmogoroff microscale.

**TABLE 1: QUANTITATIVE VALUES FROM THE TWO EXPERIMENTS**

	ABL	SSSL
$\lambda_v$ (mm)	13	12.2
$\tilde{u}$ (m/sec)	1.02	1.17
$\tilde{\omega}_z$ (sec $^{-1}$ )	85	188
$\eta_k$ (mm)	0.34	0.2
$\delta y/\eta_k$	$\approx 5$	$\approx 7$

### 3.0 WAVE NUMBER SPECTRAL REPRESENTATIONS OF THE VELOCITY AND VORTICITY DATA

One-dimensional spectral data, where  $k_1 = 2\pi f / \bar{u}$ , are readily evaluated from the time series data of each experiment. The present focus, on the small scale properties of the velocity and the vorticity fields, is well served by these representations.

The spectral plots utilize a reference curve following that described by Pope (2000). Namely, if the x-component velocity power spectral density is fitted with the appropriate low-range, mid-range, high-range coefficients, then the isotropic relationships allow all other spectra to be computed. The latter then serve as reference curves for the y-component velocity spectra and the  $\omega_z$  spectra.

The Maher (2002) representation of the non-dimensional  $E_{11}$  spectra (see Fig. 1) will serve as a representation of the Pope (2000) technique for the ABL. The SSSL data were similarly fitted by this procedure and the

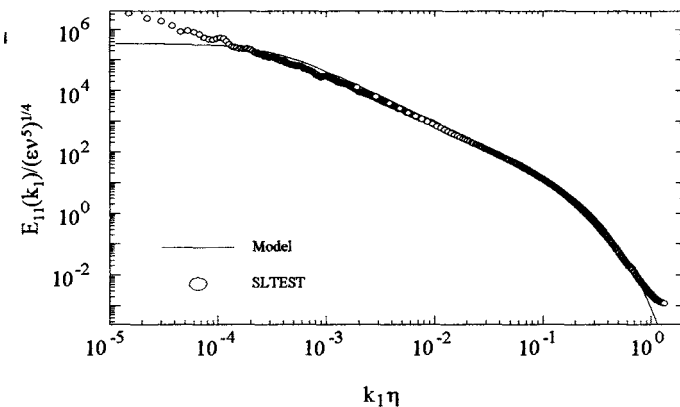


Fig. 1: Non-dimensional PSD for  $u'$ :ABL

agreement was quite good albeit with high frequency noise present for  $k_1 \eta_k \gtrsim 0.7$  Morris (2002). Fig. 2 presents the  $E_{22}$  spectral data and the reference curve for the ABL data. For reference, it is noted that the SSSL  $E_{22}$  data show a closer agreement with the isotropic reference condition. However, there are distinctly smaller amplitudes, e.g., 0.4 cf 0.65 at  $k_1 \eta_k = 0.01$ , in the measured SSSL values in comparison with those of the isotropic computation.

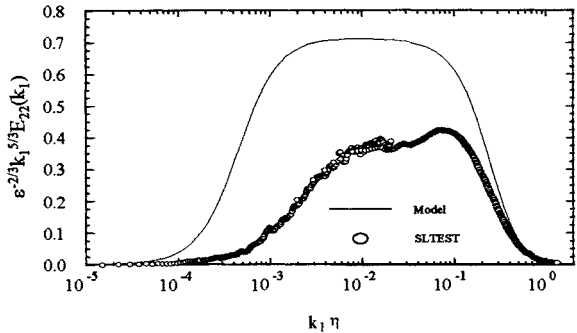


Fig. 2: Non-dimensional PSD for  $v'$ :ABL

Fig. 3 shows the coherence spectra for the ABL data. The SSSL  $H_{uv}$  values, for  $k_1 \eta_k \gtrsim 0.01$ , present an even stronger case for “local isotropy”; see Morris (2002). The companion paper: Morris and Foss (2003), shows the one-dimensional spectra for  $\omega_z$  in the SSSL. The ABL spectra for  $\omega_z$ , in contrast, agrees well with the isotropic condition at the largest  $k_1$  values; see Maher (2002).

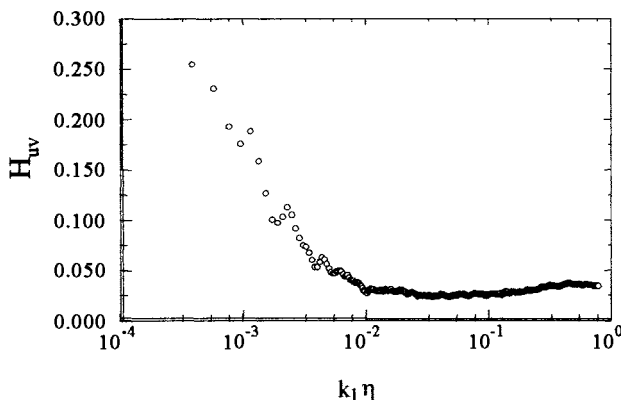


Fig. 3:  $H_{uv} = E_{12}^2 / E_{11}E_{22}$  for the ABL

The essential message of this contribution is shown in Figs. 5 and 6. Dramatically different pre-multiplied spectral distributions of vorticity are evidenced for these two flows. It must be inferred that the large scale attributes of the SSSL and the ABL are manifest in the high wave number vorticity field properties in contrast with the understanding that would have been inferred from the  $E_{22}$  and the  $H_{12}$  similarities for  $k_1\eta_k \gtrsim 0.01$  in these high  $R_\lambda$  flows.

#### **4.0 CONCLUSIONS**

The vorticity spectral data ( $E_{\omega_x\omega_z}$ ), provided for common  $R_{\lambda_v}$  values of 850, strongly contradict the anticipated universality for this relatively high Reynolds number. These data are provided for their guidance to those engaged in high Reynolds number modeling of turbulent flows.

#### **ACKNOWLEDGEMENTS**

The SLTEST measurements were made possible by a grant from the ONR to the University of Utah with MSU as a subcontractor (No. 2004093). This support, from the program of Dr. R. Joslin, is greatly appreciated. The PhD thesis work of Dr. Morris was supported by the Turbulent Shear Flows Laboratory at MSU.

#### **REFERENCES**

1. Klewicki, J.C., Metzer, M.M., Kelner, E., Thurlow, E.M., "Viscous Sublayer Flow Visualizations at  $R_\theta=1,500,000$ " *Physics of Fluids*, vol. 7, April 1995.
2. Maher, M.C., "velocity and Vorticity Measurements in the Atmospheric Boundary Layer", MS Thesis, 2002.
3. Morris, S.C., "The Velocity and Vorticity Fields of a Single Stream Shear Layer", PhD Dissertation, Michigan State University, May 2002.
4. Morris, S.C. and Foss, J.F., "The Non-Self Similar Scaling of Vorticity in a Shear Layer", IUTAM Symposium on Reynolds Number Scaling in Turbulent Flow, September 11-13, 2002 in Princeton, NJ.
5. Pope, S.B., *Turbulent Flows*, Cambridge Univ. Press, 2002.

6. Saddoughi, S.G. and Veeravalli, S.V., "Local isotropy in turbulent boundary layers at high Reynolds number", *J. Fluid Mech.*, **268**, pp. 333-372, 1994.

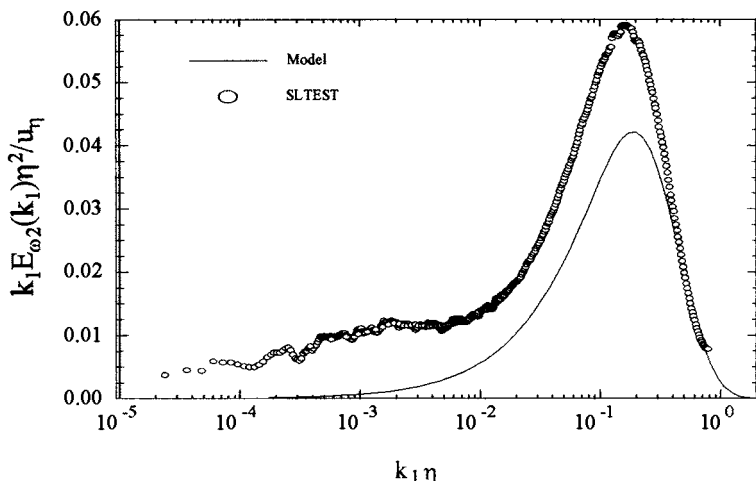


Fig. 4: Pre-multiplied, non-dimensional  $E_{\omega_z}$  PSD, ABL

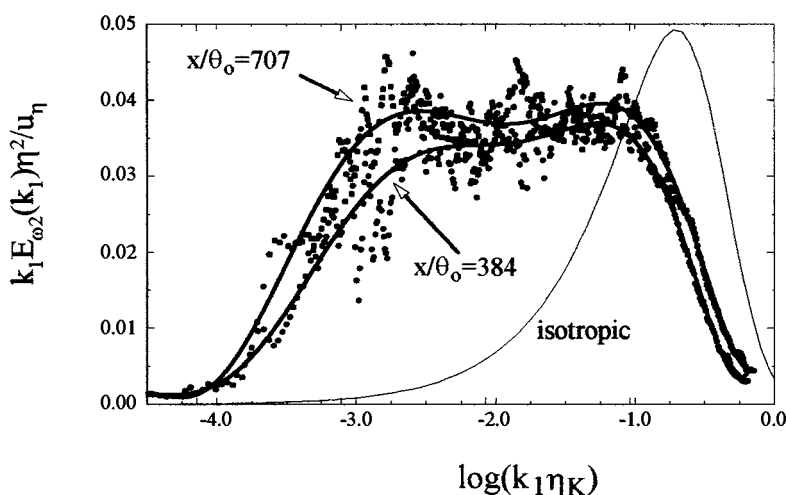


Fig. 5: Pre-multiplied, non-dimensional  $E_{\omega_z}$  PSD, SSSL

# REYNOLDS NUMBER DEPENDENCIES IN BOUNDARY LAYER AXIAL STRESS AND SCALAR VARIANCE TRANSPORT

M. Metzger\*, J. Klewicki, and P. Priyadarshana

*Physical Fluid Dynamics Laboratory*

*Department of Mechanical Engineering*

*University of Utah*

*Salt Lake City, Utah 84112*

## Abstract

Boundary layer axial stress,  $\langle u^2 \rangle$ , and scalar variance,  $\langle c^2 \rangle$ , transport were investigated using custom hot-wire/photoionization probes. The probes allow instantaneous measurement of all the terms in the evolution equations for  $\langle u^2 \rangle$  and  $\langle c^2 \rangle$ , excluding molecular diffusion and pressure-strain. Of particular interest are the dominant length scales participating in the transport. Turbulent transport in the wall normal direction was found to prevail over other terms in the evolution equations. Independent of Reynolds number, the peak in the spectra of the turbulent transport term was found to occur near  $\lambda_u$ , the Taylor microscale associated with  $u$ .

## 1. Introduction

Townsend, 1961 notes that “turbulent kinetic energy at a point may depend as much on transport processes from remote parts of the flow as on local production and dissipation”. Unfortunately, there has been little published work regarding the scales of motion responsible for the transport of momentum and turbulent kinetic energy in the boundary layer. Owing to a scarcity of data, Reynolds number dependencies of these scales remain essentially undocumented. The present study focuses on log-layer axial stress,  $\langle u^2 \rangle$ , which comprises the dominant wall region contribution to the turbulent kinetic energy. Instantaneous terms

---

\*corresponding author: metzger@eng.utah.edu

in the  $\langle u^2 \rangle$  transport equation are investigated and compared with the corresponding terms in the scalar variance,  $\langle c^2 \rangle$ , equation. In particular, well resolved spatiotemporal probe-based measurements allowed direct calculation of the spectra associated with the instantaneous terms in the two transport equations. Relevant scales of the turbulent transport, as derived from the spectra, are noted. Data were obtained at two Reynolds numbers based on momentum thickness,  $R_\theta = 2500$  in a wind tunnel and  $R_\theta \approx 2 \times 10^6$  in the atmospheric surface layer.

## 2. Axial Stress and Scalar Variance Transport

The evolution equation for  $\langle u^2 \rangle$  in the boundary layer may be written as

$$U \frac{\partial \langle u^2 \rangle}{\partial x} + W \frac{\partial \langle u^2 \rangle}{\partial z} = -2 \left( \langle u^2 \rangle \frac{\partial U}{\partial x} + \langle uw \rangle \frac{\partial U}{\partial z} \right) + 2 \left\langle \frac{p}{\rho} \frac{\partial u}{\partial x} \right\rangle - \left( \frac{\partial \langle u^3 \rangle}{\partial x} + \frac{\partial \langle wu^2 \rangle}{\partial z} \right) + \nu \nabla^2 \langle u^2 \rangle - 2\nu \left\langle \frac{\partial u}{\partial x_i} \frac{\partial u}{\partial x_i} \right\rangle, \quad (1)$$

where  $u$ ,  $w$  denote the velocity components in the axial,  $x$ , and wall normal,  $z$ , directions, respectively. Since the boundary layer is homogeneous, spanwise derivatives  $\partial/\partial y$  are assumed negligible. In the above, time averages are denoted by  $\langle \cdot \rangle$  or by a capital letter. The terms in Equation 1 represent, from left to right, advection by the mean flow, production due to mean gradients, pressure-strain correlation, turbulent transport, molecular diffusion, and turbulent kinetic energy dissipation.

In terms of identifying similarities in the physical processes dominating scalar and energy transport, it is instructive to compare Equation 1 with the evolution equation for the scalar variance,  $\langle c^2 \rangle$ ,

$$U \frac{\partial \langle c^2 \rangle}{\partial x} + W \frac{\partial \langle c^2 \rangle}{\partial z} = -2 \left( \langle uc \rangle \frac{\partial C}{\partial x} + \langle wc \rangle \frac{\partial C}{\partial z} \right) - \left( \frac{\partial \langle uc^2 \rangle}{\partial x} + \frac{\partial \langle wc^2 \rangle}{\partial z} \right) + D \nabla^2 \langle c^2 \rangle - 2D \left\langle \frac{\partial c}{\partial x_i} \frac{\partial c}{\partial x_i} \right\rangle, \quad (2)$$

where  $D$  denotes the molecular diffusion coefficient of the scalar. The only major difference between Equations 1 and 2 is the appearance of a pressure-strain term in the equation for  $\langle u^2 \rangle$ . Measurement of the budget of  $\langle u^2 \rangle$  as well as velocity triple correlations have been previously measured as a function of  $z$ , see for example Klewicki et al., 1994; Fernholz and Finley, 1996. Similarly, there have been some studies of the budget of  $\langle c^2 \rangle$ , see for example Krishnamoorthy and Antonia, 1987; Fackrell and Robins, 1982. However, the scales of motion associated with the dominant terms in Equations 1 and 2 have not been previously reported.

### 3. Experiment Description

Companion probe-based experiments were performed both in the atmospheric surface layer (ASL) that flows over the salt flats of Utah's western desert ( $R_\theta \approx 5 \times 10^6$ ) and in a large scale, low speed wind tunnel (WT) at the University of Utah ( $R_\theta = 2500$ ). Relevant boundary layer parameters for the two flows are presented in Table 1 where  $\lambda$  denotes the Taylor microscale,  $\delta$  is the boundary layer thickness, the superscript  $+$  indicates normalization using friction velocity  $u_\tau$  and kinematic viscosity  $\nu$ ,  $L$  represents the integral length scale, and  $\eta$  is the Kolmogorov length scale. As evident in the values of  $\delta^+$ , in particular, the present range of Reynolds numbers demonstrates the increase in scale disparity as the Reynolds number increases.

Table 1. Boundary layer parameters.

	$R_\theta$	$R_\lambda$	$\delta^+$	$L_u$ (m)	$\lambda_u$ (mm)	$\eta$ (mm)
ASL	$5 \times 10^6$	1000	$1.4 \times 10^6$	15	45	0.76
WT	2500	150	$1.0 \times 10^3$	0.23	17	0.65

Two different custom probes were used in the present study: (1) a six wire x-array and (2) a scalar transport probe, or STP. The six wire probe consists of a vertical stack of three hot-wire x-arrays spanning a distance of  $2\Delta z$ , where  $\Delta z = 2.65$  mm. The centers of all the x-arrays remain coplanar. The wire diameter is  $5 \mu\text{m}$  with an active length of 1 mm. This configuration allowed the measurement of  $u$  and  $w$ , in addition to the instantaneous  $\partial/\partial x$  and  $\partial/\partial z$  using Taylor's hypothesis and finite difference, respectively. The STP is a modular instrument comprised of two photo ionization detectors, each surrounded by a hot-wire x-array, with an overall sensor volume of  $4.8 \times 6 \times 4 \text{ mm}^3$ . The STP measures  $c$ ,  $u$ ,  $w$  and their respective axial and vertical derivatives, as well as scalar fluxes, e.g.  $wc$ , and flux gradients, see Metzger, 2002 for details. In the present study, the STP was positioned downstream of an elevated point source releasing a gaseous propylene. The sensor was located at the source height  $z = H$  in the near field,  $x/H < 20$ .

### 4. Length Scales

A comparison of length scale ratios between the ASL and WT flows is given in Table 2. In the ASL, the integral scales of  $w$  and  $c$  were approximately the same value and an order of magnitude less than  $L_u$ , the integral scale of  $u$ . The Taylor microscales of  $w$  and  $c$  were sim-

Table 2. Comparison of length scale ratios.

	$\lambda_c/\lambda_u$	$\lambda_w/\lambda_u$	$\lambda_c/L_c$	$\lambda_w/L_w$	$\lambda_u/L_u$
ASL	0.43	0.53	0.018	0.034	0.0038
WT	0.42	0.55	0.32	0.33	0.074

ilar and roughly half of  $\lambda_u$ . The same behavior was observed at low Reynolds number. At high Reynolds number,  $L_u/\lambda_u$  is of the order of  $10^3$ , while at low Reynolds number, the same ratio is only of the order of 10. This reflects the increase in scale disparity as the Reynolds number increases. Interestingly, the ratios  $\lambda_c/\lambda_u$  and  $\lambda_w/\lambda_u$  appear to be Reynolds number independent.

## 5. Variance Transport Equations

Figure 1 presents the relative magnitudes of the terms in Equations 1 and 2, excluding molecular diffusion and pressure-strain. These data were acquired in the log layer of the boundary layer using the STP, where  $x/H$  denotes the distance downstream from the point source. The magnitudes of the terms were normalized using the local rms, i.e.,

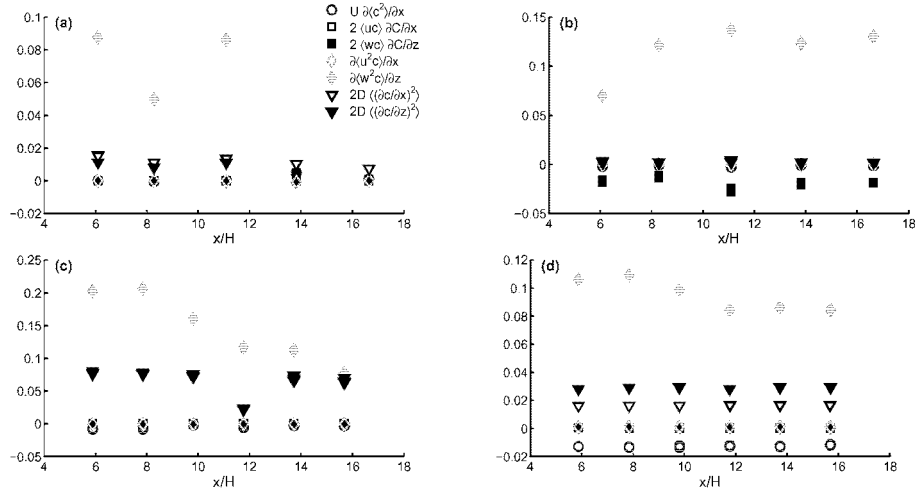


Figure 1. Magnitude of the terms in scalar variance and axial stress equations, normalized by local rms ( $u, c$ ) and Taylor microscale,  $\lambda_u$ . (a)  $\langle c^2 \rangle$ ,  $R_\theta = 5 \times 10^6$ , (b)  $\langle u^2 \rangle$ ,  $R_\theta = 5 \times 10^6$ , (c)  $\langle c^2 \rangle$ ,  $R_\theta = 2500$ , (d)  $\langle u^2 \rangle$ ,  $R_\theta = 2500$ . The symbols in (c) are the same as those in (a). The symbols in (b) and (d) are the same as those in (a) after replacing  $c$  with  $u$ .

$c'$  and/or  $u'$ , along with  $\lambda_u$ . At high Reynolds number, the vertical turbulent transport terms, i.e.,  $\partial\langle uw^2 \rangle / \partial z$  and  $\partial\langle wc^2 \rangle / \partial z$ , dominate both the  $\langle u^2 \rangle$  and  $\langle c^2 \rangle$  evolution equations. At low Reynolds number, the production term  $2\langle uw \rangle \partial U / \partial z$  in the  $\langle u^2 \rangle$  equation was of the same order of magnitude as  $\partial\langle uw^2 \rangle / \partial z$ . Interestingly, the normalized values of the dominant terms in the transport equations appear to be approximately 0.1 regardless of Reynolds number. This provides some support that  $\lambda_u$  may be the appropriate characteristic length scale in the transport process.

## 6. Spectra of the Instantaneous Transport

Figure 2 shows the weighted spectra of the turbulent transport terms at low and high Reynolds number. Spectra are derived using the instantaneous time series of  $\partial wu^2 / \partial z$  and  $\partial wc^2 / \partial z$ . Frequencies are normalized with  $\lambda_t$ , the Taylor time scale associated with  $u$ . In this case,  $\lambda_t$  was determined from an osculating parabola fit to the autocorrelation of  $u$  at zero time delay. Additionally, the spectra in Figure 2 are normalized such that the area under each curve is unity. The spectra associated with  $\partial wu^2 / \partial z$  and  $\partial wc^2 / \partial z$  exhibit many similarities. In particular, the peaks in the spectra occur near  $\lambda_t^{-1}$ . There also appears to be an increased contribution from low frequencies in the spectra of  $\partial wu^2 / \partial z$  at high  $R_\theta$ . The peaks in both the  $\partial wu^2 / \partial z$  and  $\partial wc^2 / \partial z$  spectra display a shift to higher frequencies at  $R_\theta = 5 \times 10^6$ . Figure 3, however, shows that this shift is due to a distance from the wall effect and not a true Reynolds number effect. The shift in the peak at high Reynolds number may be attributed to the fact that the Taylor time scale increases with

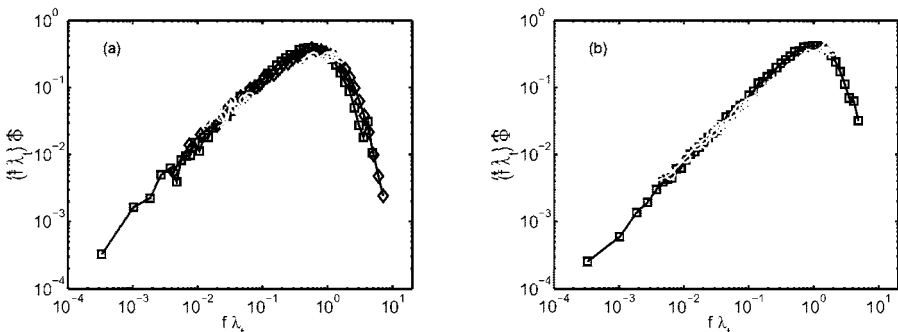


Figure 2. Weighted spectra of the instantaneous transport term normalized by the Taylor timescale, (a)  $\partial wu^2 / \partial z$  and (b)  $\partial wc^2 / \partial z$ . Symbols are  $\circ$ :  $R_\theta = 5 \times 10^6$  (STP),  $z^+ = 9000$ ;  $\square$ :  $R_\theta = 2500$  (STP),  $z^+ = 300$ ,  $\diamond$ :  $R_\theta = 2500$  (6wire),  $z^+ = 300$ .

distance from the wall. Figure 4 shows the same data in Figure 2 (a) but normalized by inner variables instead of the Taylor time scale. In this case, the peak at high Reynolds number shifts to lower frequencies relative to the lower Reynolds number wind tunnel data. This implies that the peak in the transport spectra scales at a rate intermediate to the rate of change of the Taylor and inner time scales.

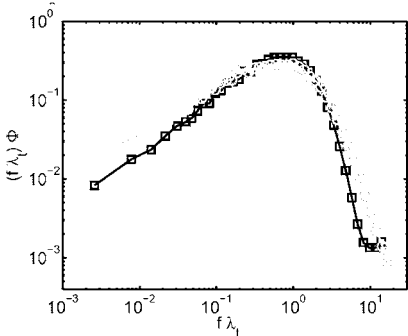


Figure 3. Weighted spectra of the instantaneous transport term normalized by Taylor timescale. Symbols are  $\circ$ :  $R_\theta = 5 \times 10^6$  (6wire),  $z^+ = 200$ ;  $\square$ :  $R_\theta = 2500$  (6wire),  $z^+ = 200$ .

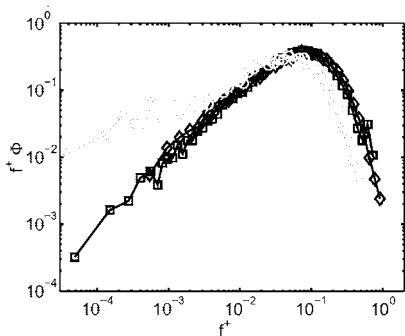


Figure 4. Weighted spectra of the instantaneous transport term normalized by inner variables. Symbols as in Figure 2.

## References

- Fackrell, J. E. and Robins, A. G. (1982). Concentration fluctuations and fluxes in plumes from point sources in a turbulent boundary layer. *Journal of Fluid Mechanics*, 117:1–26.
- Fernholz, H. and Finley, P. (1996). The incompressible zero-pressure-gradient turbulent boundary layer: An assessment of the data. *Progress in Aerospace Science*, 32:245–311.
- Klewicki, J., Murray, J., and Falco, R. (1994). Vortical motion contributions to stress transport in turbulent boundary layers. *Physics of Fluids*, 6:277–286.
- Krishnamoorthy, L. and Antonia, R. (1987). Temperature-dissipation measurements in a turbulent boundary layer. *Journal of Fluid Mechanics*, 176:265–281.
- Metzger, M. (2002). *Scalar dispersion in high Reynolds number turbulent boundary layers*. PhD thesis, University of Utah, Salt Lake City, Utah.
- Townsend, A. (1961). Equilibrium layers and wall turbulence. *Journal of Fluid Mechanics*, 11:97–120.

# Evidence of shear sheltering in atmospheric surface layer flow

Ann-Sofi Smedman<sup>1</sup>, Ulf Högström<sup>1</sup> and J.C.R. Hunt<sup>2,3</sup>

<sup>1</sup>*Uppsala University, Department of Earth Sciences, Meteorology, Villavägen 16, SE-752 36 Uppsala, Sweden;* <sup>2</sup>*Department of Space, Climate Physics and Geological Sciences, University College, Gower Street, London WC1, U.K.;* <sup>3</sup>*J.M.Burgers Centre, Delft Univ. of Technology, The Netherlands*

**Abstract:** Recent theoretical and computational developments show that a layer with strong shear may act as a barrier for eddies to penetrate through this layer, provided the horizontal velocity of the eddy is not far from that of the mean flow and the size of the eddy is appropriate. Analysis of atmospheric surface layer data from two marine sites indicates that this effect may explain observed reduction of spectral energy within a wide frequency range in situations when a low-level wind maximum is present.

**Key words:** shear sheltering, detached eddies, suppression of turbulence

## 1. INTRODUCTION AND THEORETICAL BACKGROUND

Hunt and Durbin (1999) have shown that a zone of strong shear may effectively prevent eddies present in the layer above this zone from penetrating into the layer below or vice versa. The physical mechanism behind this phenomenon can be understood in terms of vorticity induction in the shear zone by the eddy moving towards the shear zone. This manifests itself in the formation of alternating areas of horizontal convergence and divergence on the shear zone as the eddy passes by, this in turn leading to areas of upward motion, which tends to retard – or even completely stop – the further downward motion of the eddy. For this to happen, it is necessary that the horizontal motion of the eddy be close to that of the mean flow.

Calculations with Rapid Distortion Theory (RDT) have also shown that the effectiveness of this process is critically dependent on the size of the eddy and on details of the flow geometry.

## 2. THE MEASUREMENTS

Data are analyzed from two marine field experiments in the Baltic Sea. During spring and summer, the surface temperature of the Baltic Sea is usually appreciably lower than corresponding surface temperature over surrounding land, so warm air is being advected over cold water, resulting in a stable boundary layer and frequent occurrence of a low-level wind maximum. The two measuring sites are: (i) *Nässkär*, a small rock, situated in the outermost part of the Stockholm archipelago; (ii) *Östergarnsholm*, 4 km east of the big island Gotland. In this paper turbulence data obtained at about 10m above the water surface is analysed, together with data on wind and temperature profile up to about 30m. Additional radiosonde data give information on wind- and temperature structure of the entire boundary layer.

## 3. RESULTS

Figure 1 shows normalized standard deviation of the vertical velocity,  $\sigma_w / u_*$ , where  $u_*$  is friction velocity, plotted against the flux Richardson number  $R_f$  from Nässkär at 8m. Data have been divided into two groups (stars and dots) according to the value of the parameter  $C = U_{\max} / h^2$ , where  $U_{\max}$  is the maximum wind speed of the low-level jet and  $h$  the height to that maximum. The parameter  $C$  (units:  $m^{-1}s^{-1}$ ) can be considered as an approximation for the variation of vorticity across the layer. It is found that when  $C$  is small enough (the stars),  $\sigma_w / u_* = 1.2$ , which is a typical value in the atmospheric surface layer. In cases with much larger  $C$ ,  $\sigma_w / u_* = 1.0$ . A similar feature is observed for the non-dimensional standard deviation of the longitudinal and lateral components: for *small* values of  $C$ :  $\sigma_u / u_* \approx 2.2$  and  $\sigma_v / u_* \approx 1.9$ ; for *large* values of  $C$ :  $\sigma_u / u_* \approx 1.9$  and  $\sigma_v / u_* \approx 1.5$ . All values obtained for *small* values of  $C$  are typical atmospheric near-neutral values, whereas the values obtained for *large* values of  $C$  agree with values reported for the so-called ‘canonical’ laboratory boundary layer at moderate Reynolds number (e.g. Monin and Yaglom, 1971).

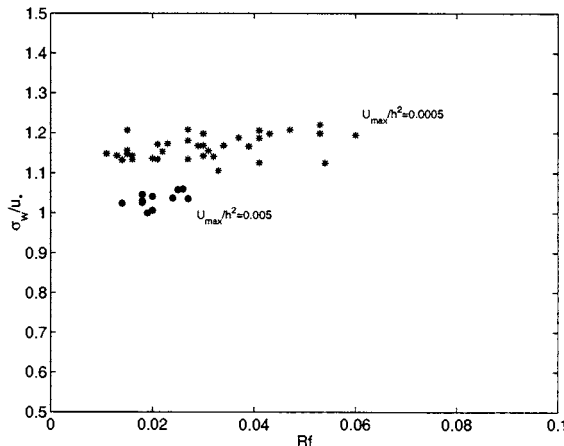
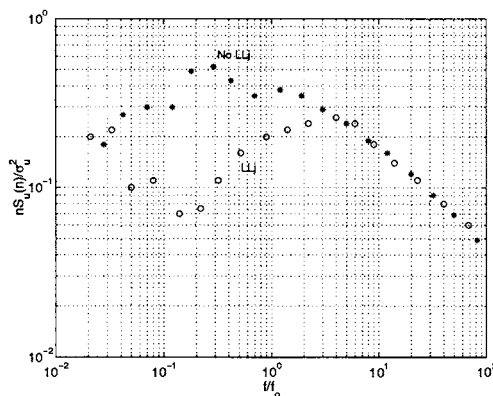


Figure 1. Normalized vertical velocity standard deviation for cases with slightly stable conditions plotted against the flux Richardson number  $R_f$ . The data are divided into two groups according to the value of a bulk profile curvature parameter

In another contribution to this volume, Högström et al., ibidem, it is reported that high Reynolds number atmospheric surface layer turbulence is dominated by large, detached eddies. It is pertinent to interpret the above result as shear sheltering preventing those relatively big eddies from penetrating down to the ground surface, leaving essentially a boundary-layer similar to that obtained in medium and low Reynolds number conditions, with eddies being created only by the surface instability process from below.

Then we would expect velocity spectra for cases with large  $C$  to show suppression of spectral energy for a certain frequency band. That this is indeed so, is clearly illustrated by Figure 2. It shows normalized mean longitudinal spectra plotted against  $f/f_0$ , where  $f_0$  is the frequency where the asymptote of the inertial subrange gives  $nS_u(n)/u_*^2 = 1$ . Kaimal et al. (1972) found that spectra from stable and neutral conditions collapsed in this representation. It is, however, known (Högström et al., 2002) that these authors high-pass filtered their spectra to some extent, and as actual spectra are found not collapse in the low-frequency range, the Kaimal et al. result is not likely to be applicable in this frequency range. The two mean spectra of Figure 2 do, however, represent the same height and similar stability conditions, so approximate spectral collapse would be expected (although the shape of the curve is expected to differ from the Kaimal, 1972 form). Nevertheless, the two mean spectra differ in a striking way: the spectrum denoted 'LLJ' has strongly suppressed energy in the spectral range  $3 \cdot 10^{-2} < f/f_0 < 3$  compared to that denoted 'NoLLJ'. The 'LLJ'-cases are characterised by the presence of a wind maximum in the height range  $300m > z > 40m$ .



*Figure 2.* Normalized mean longitudinal spectra from 8m plotted against normalized frequency. The data have been divided into two groups according to the presence of a wind maximum at low height, 'LLJ' (based on 118 spectra) or absence, 'NoLLJ' (based on 56 spectra)

## 4. CONCLUSIONS

It has been demonstrated that the presence of a low-level wind maximum in slightly stable atmospheric boundary layer flow strongly influences the turbulence structure near the surface: normalized velocity variances are found to be reduced to their 'canonical' values. This was shown to be related to strong reduction of spectral energy within a two decades wide spectral band. It is suggested that this reduction is due to the shear sheltering mechanism, which prevents detached eddies present near the top of the surface layer to penetrate down to the ground surface.

### References

- Högström, U., J.C.R. Hunt and A.Smedman: 2002, Theory and measurements for for turbulence spectra and variances in the atmospheric neutral surface layer. *Boundary-Layer Meteorol.*, **103**, 101-124.
- Högström, U., J.C.R. Hunt and A.Smedman: ibidem, A top-down theory for the neutral atmospheric surface layer. *In this volume*.
- Hunt, J.C.R. and P.A.Durbin:1999, Perturbed vortical layers and shear sheltering. *Fluid Dynamics Research*, **24**, 375-404.
- Kaimal, J.C., J.C.Wyngaard, Y. Izumi and O.R.Cote':1972, Spectral characteristics of surface-layer turbulence. *Quart.J. Roy.Met. Soc.*, **98**, 563-589.
- Monin, A.S. and A.M. Yaglom: 1971, Statistical Fluid Mechanics Vol. 1. The MIT Press. 769 pp.

# BACKGROUND ON SUPERFLUID TURBULENCE

Russell J. Donnelly

*Department of Physics University of Oregon, Eugene, OR 97403*

[russ@vortex.uoregon.edu](mailto:russ@vortex.uoregon.edu)

**Abstract** This symposium on superfluid turbulence is intended to introduce this subject to experts in classical turbulence, but who may not have much background in low temperature physics. This paper, in particular, is intended to give the necessary background on superfluidity to allow one to understand the papers following by Vinen and Barenghi.

**Keywords:** Helium II, superfluidity, quantized vortices, superfluid turbulence

## 1. Introduction

Liquid helium has a critical point of 5.2 K and a normal boiling point at 4.2 K. The phase diagram is shown in Figure 1. The thermal conductivity of helium I can be measured in an apparatus conceptually like that shown in Figure 2(a). The results of such measurements gives a thermal conductivity comparable to gases at room temperatures. This

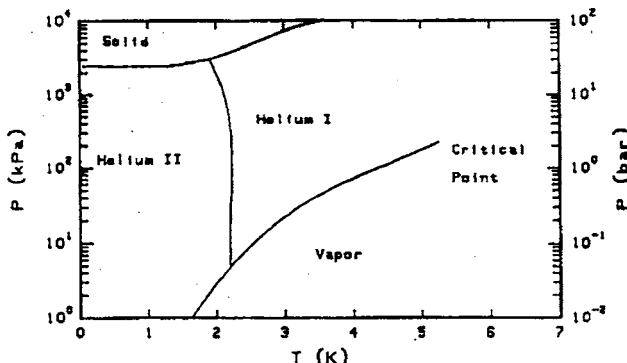
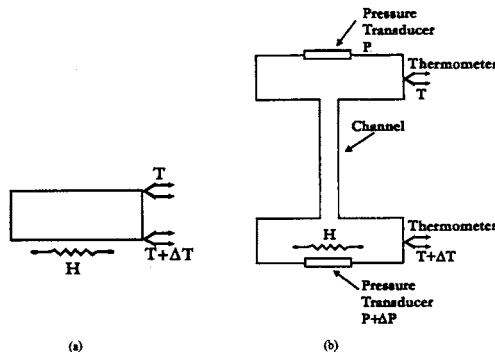


Figure 1. Phase diagram for liquid helium-4.



*Figure 2.* Apparatus for determining: (a) the thermal conductivity of helium I. Here  $H$  is an electrical heater. (b) The relationship between heat flux and temperature gradient in helium II. The orientation in this case is irrelevant, as gravity plays no observable role.

geometry is used today to study turbulent convection in helium I and critical helium gas by pushing the thermal gradient beyond the onset of convective instability in a gravitational field. (b) For helium II, however, the effective thermal conductivity is so high one must resort to fine channels to see anything at all. As we shall see below, the anomalously high thermal conduction is due to a counterflow between the normal and superfluid components of helium II: the superfluid flows to the heater, and normal fluid counterflows, in an arrangement which has no classical analogue.

## 2. The two-fluid model

Finding an explanation for the anomalously high thermal conductivity of helium II took time and further investigations. By the mid 1930's investigators had tried to measure the viscosity of helium II by means of oscillating pendulums of various kinds. The conclusion was that the damping corresponded to a finite viscosity of perhaps  $10^{-5}$  poise. However Allen and Misener [1] and Kapitza [2] in papers taken to represent the discovery (and naming) of superfluidity, showed that helium II could flow through very narrow slits without any pressure drop. It is known from experiments with superfluid gyroscopes that the superfluid has no viscosity at all and could actually flow forever, if kept cold. Another remarkable phenomenon discovered by Allen and Jones [3] is the fountain pressure. Consider two containers of helium II connected by a channel so fine that only the superfluid can flow between them. A temperature

difference  $\Delta T$  between them will produce a ‘fountain pressure’  $\Delta P$ , and these variables are related to the entropy per unit mass  $S$  by the relation

$$\Delta P/\Delta T = \rho S \quad (1)$$

where  $\rho$  is the density. Tisza[4] introduced the idea of a two fluid model to interpret these confusing experimental results. He considered two fluids, an Eulerian fluid, of density  $\rho_s$  which can flow easily through sub-micron channels and a Navier-Stokes type fluid called the ‘normal fluid’ of density  $\rho_n$  which damps the oscillating disc. These have a total density

$$\rho = \rho_n + \rho_s \quad (2)$$

To these equations must be added the fountain pressure:

$$\rho_s \frac{Dv_s}{Dt} = -\frac{\rho_s}{\rho} \nabla P + \rho_s S \nabla T \quad (3)$$

$$\rho_n \frac{Dv_n}{Dt} = -\frac{\rho_n}{\rho} \nabla P - \rho_s S \nabla T + \eta \nabla^2 v_n \quad (4)$$

and the expressions for conservation of mass and entropy,

$$\frac{\partial \rho}{\partial t} + \operatorname{div}(\rho_s v_s + \rho_n v_n) = 0 \quad (5)$$

$$\frac{\partial \rho S}{\partial t} + \operatorname{div}(\rho S v_n) = 0 \quad (6)$$

In the early days, the vorticity of the superfluid was taken to be exactly zero:

$$\omega \equiv \operatorname{curl}(v_s) = 0 \quad (7)$$

The quantitative measurement of  $\rho_n$  was first accomplished by Andronikashvili [5] who constructed a torsion pendulum consisting of a series of plates with spacing designed to trap the normal fluid. The extra mass of the trapped normal fluid changes the period of oscillation, and allows the normal fluid density  $\rho_n$  to be determined. Equation (1) then permits  $\rho_s$  to be calculated. The pendulum and currently accepted results are shown in Figure 3. These equations result in two velocities of sound:

$$u_1^2 \approx dp/d\rho, \quad u_2^2 \approx TS^2 \rho_s / C \rho_n \quad (8)$$

“First sound” is ordinary sound consisting of fluctuations in total density  $\rho$  and is continuous with the velocity of sound in helium I. “Second sound” consists of fluctuations in entropy and exists only in helium II. Modern counterflow channels span an enormous range of sizes and shapes. Their common design is hot and cold reservoirs connected by

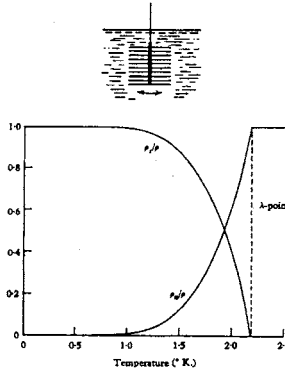


Figure 3. Andronikashvili pile of disks for determining the fraction of normal fluid and superfluid present as a function of temperature.

a channel of some kind. Channel sizes range over two orders of magnitude or more. The most elementary instrumentation is the placement of thermometers and pressure transducers at both ends of the channel, but variations can include second sound resonances (which we discuss below), chemical potential detectors, and other devices. Reviews are given by Tough [6] and by Donnelly [7].

### 3. Mutual friction

In the 1940's experiments on counterflow at Leiden showed that there is much more dissipation than could be accounted for by normal fluid viscosity alone. Gorter and Mellink [8] found, empirically, that adding a term  $F_{ns}$  which they named "mutual friction" of a certain form to the two fluid equations allowed one to describe the experimental results:

$$\rho_s \frac{D\mathbf{v}_s}{Dt} = -\frac{\rho_s}{\rho} \nabla P + \rho_s S \nabla T - F_{ns} \quad (9)$$

$$\rho_n \frac{D\mathbf{v}_n}{Dt} = -\frac{\rho_n}{\rho} \nabla P - \rho_s S \nabla T + F_{ns} + \eta \nabla^2 \mathbf{v}_n \quad (10)$$

$$F_{ns} = -\rho_s \rho_n A v_{ns}^2 \mathbf{v}_{ns} \quad (11)$$

where  $A$  is an experimentally determined constant, and

$$\mathbf{v}_{ns} = \mathbf{v}_n - \mathbf{v}_s, \quad (12)$$

The authors had no idea of the origin of this term, which was explained by Joe Vinen in his PhD thesis.

#### 4. Quantized vortex lines

Denying vorticity to the superfluid as in (7) demands that the superfluid cannot rotate. However experiments soon showed that the rotation of helium II was indistinguishable from that of helium I. Hall and Vinen [10] were able to show that in a bucket of rotating helium II, the normal fluid rotates uniformly with the bucket but the superfluid vorticity appears as a uniform array of discrete vortex lines parallel to the axis of rotation [9]. For most purposes, a quantized vortex line can be thought of as a classical vortex line with quantized circulation:

$$\oint \mathbf{v}_s \cdot d\mathbf{l} = \frac{h}{m} = \kappa = 9.97 \times 10^{-4} \text{ cm}^2 \text{ s}^{-1} \quad (13)$$

where the integration encircles the core (of radius the order of one Å),  $h$  is Planck's constant and  $m$  the mass of the helium atom. In a bucket rotating at angular velocity  $\Omega$  radians per second the areal density of vortex lines,  $n_v$ , is the same as the line density  $L$  measured as length of line per unit volume  $\text{cm}/\text{cm}^3 = \text{cm}^{-2}$ , and is given by the ratio of the vorticity of solid body rotation to the quantum of circulation:

$$n_v = L = 2\Omega/\kappa \approx 2000\Omega \text{ lines/cm}^2 \quad (14)$$

Vortex lines appear in more general flows as well, such as the counterflow experiment described above. In the latter the vortex lines appear only after some critical heat flux, and seem to be nearly randomly oriented with respect to the flow. The vortices are sometimes described as a 'tangled mass', and densities of the order of  $10^6 \text{ cm}^{-2}$  are easily generated. In the case of rotating helium II, Hall and Vinen [10] proposed that mutual friction is a consequence of forces acting on quantized vortex lines and were able to propose equations of motion with a different form of mutual friction:

$$F_{ns} = - (B\rho_n\rho_s/\rho) \hat{\Omega} \times (\Omega \times \mathbf{q}) - B'(\rho_n\rho_s/\rho) (\Omega \times \mathbf{q}) \quad (15)$$

where  $q = (v_s - v_n)$  and  $\hat{\Omega} = \Omega/|\Omega|$ . The component of mutual friction, then, in the direction of  $\mathbf{q}$  is simply  $F_{sn} = B(\rho_s\rho_n/\rho)\Omega q$ , where  $\Omega$  is one-half the mean vorticity  $\kappa L$  in the superfluid. Using these ideas, these equations can be generalized to work for homogeneous tangles of vortex line. The coefficients  $B$  and  $B'$  are called the mutual friction coefficients. Second sound absorption is a very sensitive tool which measures the  $B$  coefficient in the equation above, and of more interest for superfluid turbulence, the length  $L$  of quantized vortex line per unit volume, also referred to as a line density. The root mean square superfluid vorticity,  $\omega_s$ , is defined by  $\omega_s = \kappa L$ . The lower level of sensitivity is dramatic:

our least count in sensitivity is  $L = 10\text{cm}^{-2}$  leading to  $\omega_s = 10^{-2}\text{sec}^{-1}$ . On the higher end we have recorded values of  $\omega_s$  to  $50,000\text{sec}^{-1}$  (i.e. $L \sim 5 \times 10^7 \text{cm}^{-2}$ ) in turbulence produced by a towed grid (see Figure 5). The line density is deduced from the resonant amplitude of second sound:

$$L = \frac{4\pi\Delta_o}{\kappa B} \left( \frac{A_o}{A} - 1 \right) \quad (16)$$

where  $\Delta_0$  and  $A_0$  are the resonant half-width and amplitude in the absence of vortex lines, owing to absorption of second sound by the walls. The peak is also broadened since the product  $A\Delta$  is known to be constant, at least for modest reductions in  $A$ . Nevertheless the range of five orders of magnitude of vorticity measurement is an impressive achievement.

## 5. Dynamics of the vortex tangle in counterflow turbulence

A model for the dynamics of the tangle of quantized vortex lines, developed from the ideas of mutual friction, was introduced by Vinen in a classic series of papers [12]. This theory considers a spatially homogeneous distribution of vortex lines whose time rate of change is determined by competing growth and decay processes. Vinen derived the growth term by dimensional analysis and modeled the decay process after the decay of classical turbulence in the Kolmogorov cascade. He obtained

$$\frac{dL}{dt} = \chi_1 \frac{B \rho_n}{2 \rho} v_{ns} L^{\frac{3}{2}} - \frac{\chi_2 \kappa}{2\pi} L^2 \quad (17)$$

where  $\chi_1$  and  $\chi_2$  were undetermined parameters at the time. In steady state  $dL/dt = 0$  and the equilibrium line density is

$$L_0 = \gamma^2 v_{ns}^2 \quad (18)$$

where  $\gamma = \pi B \rho_n / \kappa \rho \chi_2$ . The  $v_{ns}^2$  dependence of predicted by Vinen's model is roughly correct above the critical heat flux.  $\gamma$ , which contains the temperature dependence, had to be determined experimentally since  $\chi_1$  and  $\chi_2$  were not well-known at the time.

## 6. Simulations of a vortex tangle

Schwarz [11] was the first to attempt to do direct numerical experiments on a vortex tangle in counterflow turbulence. He realized that the core of a vortex is so small compared with other scales, such as the inter-vortex spacing, that it could be characterized by a space curve. Schwarz's

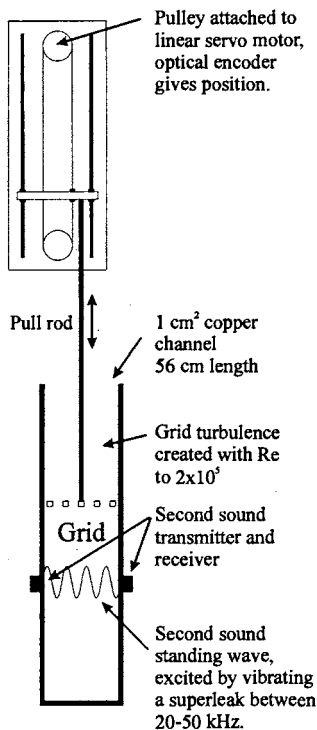


*Figure 4.* Towed grid apparatus. The flow is initiated by towing the grid upwards starting from the bottom of the channel, and analyzed by attenuation of second sound.

work is summarized in chapter 7 of Donnelly's book on vortices [9]. Much detail of observed counterflow turbulence is explained this way, including results on the coefficients  $\chi_1$  and  $\chi_2$  mentioned above. Recent work on simulations in turbulent superfluid flow will be discussed by Barenghi in this symposium.

## 7. Towed grid turbulence

The decay of homogeneous and isotropic turbulence is regarded as one of the fundamental problems of fluid dynamics. Experiments are usually performed in wind tunnels that study grid-generated turbulence as it decays downstream. A novel technique where turbulence is created by towing a grid through a stationary sample of helium II was first reported in Smith et al [13]. This technique has been improved in several ways in the past few years, allowing measurement of the rms. superfluid vorticity over the range of  $10^5$  Hz to 1 Hz. The apparatus is illustrated in Figure

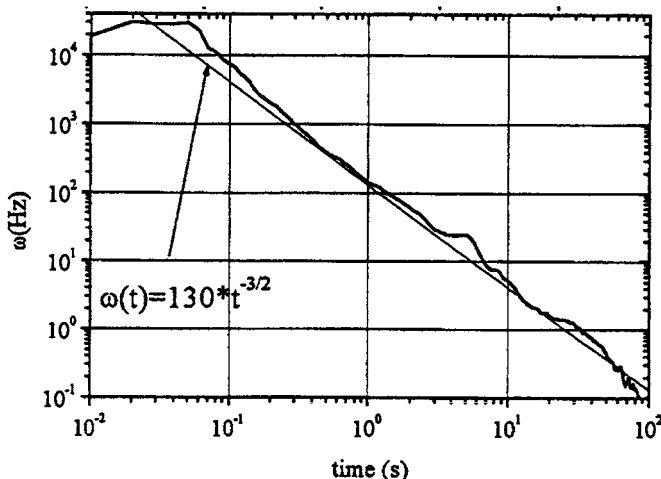


Figure 5. Decay of superfluid turbulence after towing the grid at 250 cm/s at 1.5 K.

4, and some typical results in Figure 5. Vinen will discuss the physics of this decay in his chapter of this symposium.

## References

- [1] J. F. Allen and A. D. Misener Nature **141**, 75 (1938).
- [2] P. L. Kapitza, Nature **141**, 74 (1938).
- [3] J. F. Allen and H. Jones Nature **141**, 243 (1938).
- [4] L. Tisza, Nature **141**, 913 (1938).
- [5] E. L. Andronikashvili J. Exp. Theor. Phys. USSR **18**, 429 (1946).
- [6] J. T. Tough in "Progress in Low Temp. Phys. VIII", 133 (1982).
- [7] R. J. Donnelly, J. Phys: Condens. Matter **11**, 7783 (1999).
- [8] C. J. Gorter and J. H. Mellink, Physica **15**, 285 (1949).
- [9] R. J. Donnelly "Quantized Vortices in Helium II" Cambridge (1991).
- [10] H. E. Hall and W. F. Vinen Proc. Roy. Soc. **A238**, 204, 215 (1956).
- [11] K. W. Schwarz, Phys. Rev. **B38**, 2398 (1988)
- [12] W. F. Vinen Proc. Roy. Soc. **A240**, 114, 128 (1957), **A242**, 493, **A243**, 400 (1958).
- [13] M. R. Smith, R. J. Donnelly, N. Goldenfeld and W. F. Vinen, Phys. Rev. Lett. **71**, 2583 (1993).

# SUPERFLUID TURBULENCE: EXPERIMENTS, PHYSICAL PRINCIPLES, AND OUTSTANDING PROBLEMS

W. F. Vinen

*School of Physics and Astronomy,  
University of Birmingham, Birmingham B15 2TT, UK*  
W.F.Vinen@bham.ac.uk.

**Abstract** The paper provides an introduction to turbulence in a superfluid (quantum turbulence), with special reference to cases where there is a simple classical analogue. The important experiments are described briefly, together with the most plausible interpretations. The quantum and classical cases are compared, similarities and differences in the underlying physical principles being emphasized. Outstanding problems are summarized. A more detailed discussion of the issues raised can be found in a recent review: W F Vinen and J J Niemela, *J. Low Temp. Phys.* **128**, 167 (2002).

**Keywords:** Superfluid turbulence; quantized vortex lines; vortex reconnections; classical turbulence; very low temperatures.

## 1. Introduction

Superfluid helium, formed from the common isotope  $^4\text{He}$ , differs in its fluid dynamical behaviour from a classical fluid in the following respects. At a finite temperature there is two fluid behaviour, a normal fluid component co-existing with a superfluid component, the two fluids able to flow with different velocity fields. The normal fluid is formed from microscopic thermally excited motion and behaves largely like a classical viscous fluid, although its viscosity is rather low (typically about  $10\mu\text{poise}$ ). The proportion of normal fluid falls with decreasing temperature, tending to zero at the absolute zero of temperature. The superfluid component can exhibit frictionless flow, and rotational motion of this component must take the form of quantized vortex lines, each with a core of microscopic size and a circulation  $\kappa = h/m_4$ , where  $h$  is Planck's constant and  $m_4$  is the mass of a helium atom. Turbulence is possible in both fluids, but that in the superfluid component must

take the form of some more or less irregular configuration of quantized vortex lines (a “vortex tangle”). To a large extent the vortex lines move according to classical laws: in the absence of any force on it, the vortex core moves with the local fluid velocity. Any motion of the core relative to the normal fluid leads to a frictional drag on the core proportional to the relative velocity (the drag is usually called “mutual friction”), and the resulting motion of the vortex is then in accord with the classical Magnus effect. Computer simulations have been carried out on the basis of these ideas (the vortex filament model), as explained in the chapter by Barenghi in this volume. Vortex reconnections can take place and must be included in a phenomenological manner in the vortex filament model, but an understanding of them requires a quantum mechanical description of the vortex core; a realistic description for liquid helium has not been developed, but what is probably a good qualitative description is provided by the non-linear Schrodinger equation (NLSE), which describes the behaviour of a dilute superfluid gas, and which is discussed in Barenghi’s chapter. We note for future reference that a two-fluid system can support two types of longitudinal wave: *first sound* in which the two fluids move in phase and give rise to a density fluctuation; and *second sound* in which they move in antiphase, giving rise to a lightly-damped temperature wave if the normal fluid has a small viscosity. In the presence of vortex lines second sound is attenuated by the mutual friction, and a measurement of this attenuation provides a sensitive tool for a study of the density of vortex lines.

Turbulence in superfluid  $^4\text{He}$  was discovered in the 1950s, but for many years the only type studied in detail was that associated with counterflow of the two fluids induced in a heat current. This type has no classical analogue, since it is maintained by the mutual friction accompanying the forced relative motion of the two fluids. In this chapter we are concerned with types of superfluid turbulence where there could be a classical analogue, and we focus on analogues of fully-developed, homogeneous turbulence, without boundary layers. Such analogues might exist in two cases: if the two fluids are not constrained to move with different velocities; or if the temperature is so low ( $\ll 1\text{K}$ ) that the normal fluid is effectively absent. We discuss both cases, describing first the relevant experiments, then the physical principles involved as far as they are understood, with finally an attempt to focus on the crucial outstanding problems. As we shall see, there are interesting, and perhaps surprising, similarities between the quantum and classical cases, although there are also important differences.

We refer the reader to the chapter by Donnelly for a review of the physics underlying superfluidity and to a recent review article [1] for a

more detailed discussion of superfluid turbulence (or “quantum turbulence”) and of the experiments and ideas underlying it. For convenience, we do not include in this chapter all the original references, which can, however, be found in the review article.

## 2. Coupled turbulence above 1K

Two important experiments relate to the first case. The simpler is that due to Maurer and Tabeling [2], who studied swirling flow generated by two counter-rotating blades in the helium. They observed the frequency spectrum of pressure fluctuations at a particular point in the flow in such a way that it is directly related to the turbulent energy spectrum. The result was remarkable, in that there was no observable difference between behaviour in the normal phase and that in the superfluid phase, the energy spectrum in both cases being of the Kolmogorov form for a single fluid. The pressure transducer had a size that was significantly larger than the Kolmogorov dissipation scale in either the normal phase or the normal fluid. Other experimental evidence suggests that the blades generate a high density of vortex line, the line spacing ( $\ell$ ) being similar in magnitude to the (very small) dissipation scale in the normal fluid (remember that the viscosity of the normal fluid is very small). The observed energy spectrum must therefore relate to large length scales for which a conventional fluid would exhibit an inertial range and which are large compared with the vortex-line spacing. The only reasonable interpretation is that the superfluid phase exhibits *quasi-classical behaviour* on length scales large compared with both the line spacing and the dissipation scale in the normal fluid; by this we mean that the two fluids have the same velocity field, so that dissipation due to mutual friction is absent, and that this common velocity field evolves in the same way as that in a classical fluid at high Reynolds number. The large scale motion must arise from a partial polarization of the vortex tangle. Since the Maurer-Tabeling experiment relates only to the inertial range, it tells us nothing about dissipative processes at high wavenumbers. In a classical fluid there are deviations from Kolmogorov scaling in the inertial range, associated, for example, with intermittency; Maurer and Tabeling show that these deviations persist into the superfluid phase, thus confirming quasi-classical behaviour on scales large compared with  $\ell$ .

The second important experiment relating to the first case is the Oregon towed grid experiment [3]. A grid is pulled through the superfluid helium, and an observation of the attenuation of second sound as a function of time is made in a small region in the wake of the grid. Such a grid would generate in a classical fluid something approximating to ho-

mogeneous isotropic turbulence. The grid generates a high density ( $L$ ) of vortex line, as do the blades in the Maurer-Tabeling experiment, but now the second sound provides a measurement of the way in which the line density decays in time. This decay depends on the dissipative processes. The interpretation is quite complicated, but, in summary, the experimental results are consistent in detail with the following picture. The two fluids have a common quasi-classical velocity field on length scales larger than the line spacing,  $\ell$ . On these length scales there is an inertial range with a single Kolmogorov spectrum, as in the classical case. The dissipation per unit total mass, occurring on a length scale of order the vortex line spacing, is given by

$$\epsilon = \nu' (\kappa L)^2. \quad (1)$$

The quantity  $(\kappa L)^2$  can be interpreted loosely as a mean square vorticity in the superfluid component, so that  $\nu'$  is an effective kinematic viscosity, values of which are obtained from the experiments [4]. This effective kinematic viscosity is similar in magnitude to that of the normal fluid, but it has a different temperature-dependence [4].

In the Oregon towed grid experiment the grid Reynolds number, based on the kinematic viscosity  $\nu'$ , is typically  $10^5$ . It should be added that the second-sound technique is extremely sensitive, so that decay of the effective vorticity can be followed over four or five decades. Quasi-classical features can therefore be studied that are hard to see with classical fluids [5].

These experimental results pose two problems. Why is there quasi-classical behaviour in an inertial range on length scales greater than the line spacing? And why is the dissipation given by Eq. (1)? There seem to be two possible answers to the first of these questions. Either the dynamics of the superfluid component on a large scale is inherently classical, mutual friction serving only to keep the two velocity fields accurately locked together. Or the superfluid dynamics is not inherently classical but is forced into classical behaviour by mutual friction with the normal fluid. The fact that both the Maurer-Tabeling experiment and the towed grid experiment show the same behaviour for normal fluid fractions ranging from unity to as small as 0.05 suggests that the former answer is the more likely to be correct, but no formal theoretical proof seems yet to exist [1]. Turning to the dissipation, we note that, although Eq. (1) has the classical form arising from viscous dissipation, the mechanism here cannot be purely classical. On a length scale of order the vortex line spacing the two velocity fields are very unlikely to match (one is dominated by the quantization of circulation), so that some of the dissipation must be due to mutual friction. Indeed this is the

only mechanism by which turbulence in the superfluid component decays at the temperatures concerned. Calculations that take account of both mutual friction and normal-fluid viscosity have recently been published. They are based on the approximation that the velocity of the normal fluid and that of the vortex lines become uncorrelated on length scales of order  $\ell$ ; they confirm the form of Eq. (1) and yield values of  $\nu'$  in fairly good agreement with experiment [1].

### 3. Superfluid turbulence at very low temperatures

This is interesting for two reasons. Since the normal fluid is effectively absent, experiments at these temperatures would settle arguments about the normal fluid forcing quasi-classical behaviour on the superfluid component on large length scales ( $\geq \ell$ ). And we are led to ask what dissipative mechanisms can operate when there is no normal fluid to provide either viscous dissipation or mutual friction. There are as yet hardly any experimental results, although it has been shown that a moving grid *can* generate turbulence at very low temperatures, and that the turbulence *does* decay, at a rate that is not very much less than that at higher temperatures. Experiments are actually rather difficult, because second sound, which is so powerful a tool, does not propagate at low temperatures. Present plans include the measurement of vortex line densities by ion-trapping, the observation of pressure fluctuations, and the monitoring of the rise in the temperature of the helium as the turbulence decays.

In the absence of experimental results we can only speculate about the behaviour that will be observed. Computer simulations, based on both the vortex filament model [6] and the NLSE [7], give some support for the view that quasi-classical behaviour can occur on length scales greater than  $\ell$ , although, given the inevitable limitations on available computer power, the range of wavevectors over which such behaviour can be explored is limited. The need for experiments is all the more urgent.

It is especially interesting to ask what dissipative mechanisms can operate on the turbulence. We discuss three possibilities, two of which are based on the decay of the turbulence into sound. Sound-wave quanta, or phonons, are the principal thermal excitations in the helium at low temperatures.

We know that classical turbulence can generate sound. In the context of quantum turbulence we note that a vortex line can radiate sound if it undergoes some type of oscillatory motion [8]. For a vortex tangle,

involving smooth vortex lines with characteristic curvatures of order  $\ell^{-1}$  (characteristic frequencies of order  $\kappa/\ell^2$ ), the rate of radiation of energy is much too small to account for a rate of loss of turbulent energy that is comparable with that obtaining at higher temperatures. We need vortex structures having much higher characteristic frequencies, which must involve regions of high curvature. Such regions can be generated by vortex reconnections. It is known from simulations that reconnections occur frequently in a vortex tangle at all temperatures (see [1] and references therein); the rate is of order  $\kappa\ell^{-5}$  per unit volume, which is typically  $10^{12} \text{ cm}^{-3}\text{s}^{-1}$ . They play an important role in the dynamical evolution of the tangle at all temperatures. Each reconnection leaves two sharp kinks on the vortex lines. At high temperatures such kinks are rapidly smoothed out by mutual friction, so that the lines maintain a rather smooth appearance. But at low temperatures they persist and can radiate sound. Each kink can be regarded as a superposition of Kelvin waves, covering a wide range of wavenumbers,  $\tilde{q}$ . One possibility [1] is that repeated reconnections lead to an increasing amplitude of these waves, leading in turn to strong non-linear coupling between waves with different  $\tilde{q}$ . The Kelvin-wave energy then spreads to higher and higher  $\tilde{q}$ , until the Kelvin-wave frequency ( $\sim \kappa\tilde{q}^2$ ) is large enough ( $\sim 1 \text{ GHz}$ ;  $\tilde{q} \sim 2 \times 10^8 \text{ cm}^{-1}$ ) for rapid sound radiation. Thus there may be something like a Kelvin-wave cascade, for  $\tilde{q} > \ell^{-1}$ , terminated by dissipation into sound. A classical cascade, existing for wavenumbers less than  $\ell^{-1}$ , can be expected to join smoothly to this cascade at wavenumbers of order  $\ell^{-1}$ .

A second source of energy dissipation is the reconnection process itself. Simulations based on the NLSE, which confirm from a simple model that reconnections do occur, show also that they are accompanied by the emission of sound (see the chapter by Barenghi in this volume). The energy loss per reconnection depends on the size of the vortex core. A small core probably means that this mechanism for dissipation is relatively unimportant in the case of liquid  ${}^4\text{He}$  [1].

If the turbulence is confined to a region of finite extent another loss mechanism can operate. Reconnections lead occasionally to the generation of small vortex rings, and a small ring, formed near the boundary of the turbulence, can escape, carrying energy with it, as shown explicitly in recent simulations [9]. Such a process would be seen as a size dependence of the decay rate.

It is possible to use what are essentially scaling arguments to estimate the rate of loss of energy from a Kelvin-wave cascade [1]. The result can be expressed in the form (1), with an effective kinematic viscosity given

by

$$\nu' = D\kappa, \quad (2)$$

where  $D \sim 1$  is a slowly varying (logarithmic) function of the vortex line density. The dissipation appears again to be quasi-classical in form (or at least approximately so), although the mechanism is totally different from the viscous dissipation in a classical fluid. A numerical accident means that  $\kappa$  is of order the kinematic viscosity of the normal fluid at high temperatures, so that we may expect that at very low temperatures superfluid turbulence will decay at a rate not very different from that at temperatures above 1K, as seems to be observed.

We emphasize that these considerations remain speculative, and that the results of experiments are awaited.

#### 4. Conclusions

Tentatively we conclude that free, fully developed, superfluid (quantum) turbulence may well be quite similar to its classical counterpart in its overall structure. In superfluid  $^4\text{He}$  there can be a quasi-classical inertial range, with a cascade feeding energy into dissipative processes taking place on small length scales. However, it is only in the inertial range that quasi-classical behaviour obtains. Although dissipation is described by formulae that appear to be classical in form, with effective kinematic viscosities, the detailed mechanisms are quite different from the viscous processes in a classical fluid, and they can involve processes that are novel to fluid dynamics.

Turbulence can also be generated in superfluid  $^3\text{He}$ . However, in this case the normal fluid is very viscous, and quasi-classical turbulence cannot be expected to occur in the presence of a significant fraction of normal fluid. Quasi-classical turbulence might be seen at very low temperatures, but the dissipative mechanisms are likely to be different because the vortex core in superfluid  $^3\text{He}$  is much larger than in superfluid  $^4\text{He}$  [1] and has different characteristics.

We emphasize that much of this account is speculation. There is an urgent need for new experiments, especially at very low temperatures, and for better theory.

#### References

- [1] W. F. Vinen, J. Low Temp. Physics, **128**, 167 (2002).
- [2] J. Maurer and P. Tabeling, Europhys. Letters, **43**, 29 (1998).
- [3] S. R. Stalp, L. Skrbek and R. J. Donnelly, Phys. Rev. Letters, **82**, 4831 (1999).
- [4] S. R. Stalp, J. J. Niemela, W. F. Vinen and R. J. Donnelly, Phys. Fluids, **14**, 1377 (2002).

- [5] L. Skrbek, J. J. Niemela and R. J. Donnelly, Phys. Rev. Letters, **85**, 2973 (2000).
- [6] T. Araki, M. Tsubota and S. K. Nemirovskii, Phys. Rev. Letters, **89**, 145301 (2002).
- [7] C. Nore, M. Abid and M. E. Brachet, Phys. Rev. Letters, **78**, 3896 (1997); Phys. Fluids, **9**, 2644 (1997).
- [8] W. F. Vinen, Phys. Rev., **B64**, 134520 (2001).
- [9] M. Tsubota, T. Araki and W. F. Vinen, Proceedings of the 23rd International Conference on Low Temperature Physics, Hiroshima, 2002. To be published.

# NUMERICAL SIMULATIONS OF VORTEX RECONNECTIONS IN SUPERFLUID TURBULENCE

Carlo F. Barenghi

*School of Mathematics, University of Newcastle*

*Newcastle upon Tyne, NE1 7RU, UK*

*C.F.Barenghi@ncl.ac.uk*

**Abstract** The results of numerical simulations of superfluid turbulence are presented which highlight the key role played by vortex reconnections.

**Keywords:** superfluid turbulence, vortex reconnection, energy spectrum.

## 1. Introduction

The quantum phase of liquid helium (helium II) is the intimate mixture of two fluid components, the normal fluid and the superfluid (Donnelly 1991). The former consists of thermal excitations and is modelled as a viscous fluid of density  $\rho_n$  and velocity  $\mathbf{v}_n$ . The latter is related to the quantum ground state and is a fluid of zero viscosity, density  $\rho_s$  and velocity  $\mathbf{v}_s$ . The total density  $\rho = \rho_n + \rho_s$  does not change much with the temperature  $T$ , but the relative proportions of  $\rho_n$  and  $\rho_s$  depend strongly on  $T$ . At absolute zero  $\rho_s/\rho = 1$  and  $\rho_n/\rho = 0$ , whereas at the phase transition ( $T = 2.17\text{ K}$ )  $\rho_s/\rho = 0$  and  $\rho_n/\rho = 1$ . The normal fluid is effectively negligible for  $T < 1\text{ K}$ .

Quantum mechanics imposes two constraints on the rotational motion of the superfluid (Barenghi, Donnelly & Vinen 2001). The first is that the circulation  $\Gamma$  around a superfluid vortex is constant ( $\Gamma = h/m \approx 10^{-3}\text{ cm}^2/\text{sec}$  where  $h$  is Plank's constant and  $m$  is the mass of the helium atom). The second is that the radius of the superfluid vortex core has the microscopic value  $a_0 \approx 10^{-8}\text{ cm}$ . Because of these constraints superfluid turbulence consists of a disordered tangle of thin vortex filaments (see figure 1), whereas turbulence in the normal component

consists of eddies of various size and strength like ordinary turbulence. Finally, the normal fluid and the superfluid vortex lines are coupled by a mutual friction force (Barenghi & al 1983).

The turbulent flow of helium II has been the subject of recent experiments. In particular, two problems have attracted much attention. The first is the observed classical behaviour of turbulent helium II in terms of decay rate (Smith & al 1993, Stalp & al 1999), pressure drops (Walstrom & al 1998), drag crisis (Smith & al 1999) and Kolmogorov's energy spectrum (Maurer & Tabeling 1998). This is surprising, due to well known non-classical aspects of two-fluid hydrodynamics (eg as second sound, fountain effect, thermal counterflow). It is clear that the normal fluid alone cannot be held responsible for the apparent classical behaviour, which is observed at temperatures as low as 1.4 K (at which  $\rho_n/\rho = 0.07$  only).

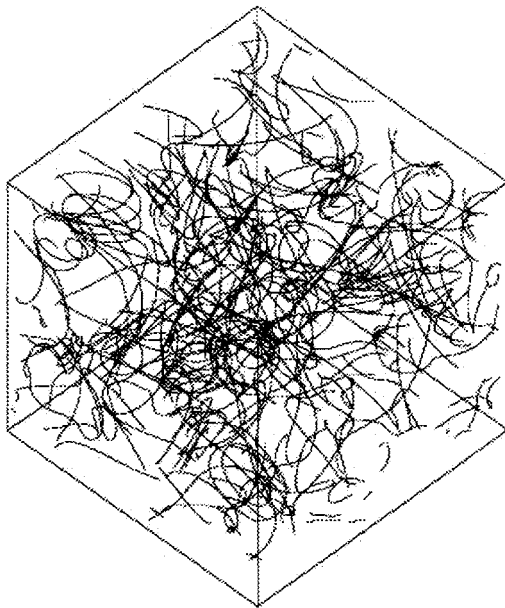


*Figure 1.* Tangle of superfluid vortex filaments (computation performed in a period box).

The second problem refers to the observation that, even at temperatures as low as 20 mK (Davies & al 2000), superfluid turbulence (typically generated by a vibrating grid) rapidly decays. This result raises the important question of what should be the mechanism to destroy kinetic

energy in the absence, at these very low temperatures, of the normal fluid, hence without any known dissipative process such as viscosity and friction.

The aim of this paper is to show that numerical simulations of superfluid turbulence can shed light into these problems. Before proceeding, it is instructive to describe the two models upon which these numerical simulations are based.

## 2. Schwarz's model

Since the radius of the superfluid vortex core is many orders of magnitude smaller than the average separation between vortices or any other scale of interest in the flow, it is convenient to think of a superfluid vortex filament as a space curve  $\mathbf{s} = \mathbf{s}(\xi, t)$  of infinitesimal thickness, where  $\xi$  is arc-length and  $t$  is time. Schwarz (1988) showed that the curve moves with velocity approximately given by

$$\frac{d\mathbf{s}}{dt} = \mathbf{v}_{si} + \alpha \mathbf{s}' \times (\mathbf{v}_n - \mathbf{v}_{si}), \quad (1)$$

where  $\alpha$  is a known temperature - dependent mutual friction coefficient,  $\mathbf{v}_n$  is the prescribed normal fluid velocity,  $\mathbf{s}' = d\mathbf{s}/d\xi$  and the self induced velocity  $\mathbf{v}_{si}$  is given by the classical Biot-Savart integral

$$\mathbf{v}_{si} = \frac{\Gamma}{4\pi} \int \frac{(\mathbf{r} - \mathbf{s}) \times d\mathbf{r}}{|\mathbf{r} - \mathbf{s}|^3}. \quad (2)$$

Schwarz's model is applied by discretizing an initial vortex configuration into a large number of points, which are then moved in time according to equations (1) and (2). In order to model superfluid turbulence Schwarz realized that the equations must be supplemented with the extra assumption that two vortices reconnect when they come sufficiently close to each other (Samuels 2001), something which was proved only years later using the NLSE model (Koplik & Levine 1993). The results obtained using Schwarz's model which we shall describe in the next sections refer to the limit of absolute zero ( $\alpha = 0$ ).

## 3. The NLSE model

The NLSE model describes superfluid helium at zero temperature. The theory of a weakly interacting Bose - Einstein condensate yields the following nonlinear Schrödinger equation (NLSE) for the complex wave function  $\psi$ :

$$i\hbar \frac{\partial \psi}{\partial t} = -\frac{\hbar^2}{2m} \nabla^2 \psi + V_0 \psi |\psi|^2 - E \psi, \quad (3)$$

where  $E$  is the chemical potential of a boson and  $V_0$  is the strength of the repulsive interaction between bosons. By substituting  $\psi = A \exp(iS)$  into eq. (3) one finds the classical continuity equation

$$\frac{\partial \rho_s}{\partial t} + \nabla \cdot (\rho_s \mathbf{v}_s) = 0, \quad (4)$$

and a modified Euler equation which, in tensor notation, is given by

$$\rho_s \left( \frac{\partial v_{sj}}{\partial t} + v_{sk} \frac{\partial v_{sj}}{\partial x_k} \right) = - \frac{\partial P}{\partial x_j} + \frac{\partial \Sigma_{jk}}{\partial x_k}, \quad (5)$$

where  $\rho_s = mA^2$  is the density,  $\mathbf{v}_s = (\hbar/m)\nabla S$  the velocity,  $P = V_0 \rho_s^2 / (2m^2)$  the pressure and  $\Sigma_{jk} = (\hbar^2/4m^2)\rho_s \partial^2 \ln(\rho_s) / \partial x_j \partial x_k$  the quantum stresses. Using cylindrical coordinates  $(r, \theta, z)$  and letting  $S = \theta$  one recovers the classical vortex of azimuthal velocity  $v_{s\theta} = \Gamma/2\pi r$ . The centre of the vortex is hollow ( $\rho_s \rightarrow 0$  as  $r \rightarrow 0$ ) and the vortex core radius  $a_0$  is the characteristic distance over which  $\rho_s$  drops from its bulk value to zero at the axis.

#### 4. Comparison between the two models

Schwarz's model and the NLSE model are complementary. The former is valid at any temperature and is incompressible; the latter is valid only at  $T = 0$  and allows sound waves. In Schwarz's model the vortex core has no structure and vortex reconnections are performed *ad hoc* by the numerical algorithm. The NLSE describes the structure of the vortex core, hence it is used to study phenomena such as vortex reconnections and vortex nucleation. The quantum stresses are negligible everywhere but in the region near a vortex core, so the NLSE can be interpreted as a regularization of the classical Euler equation.

#### 5. Vortex reconnections and sound pulses

Numerical simulations of vortex reconnections performed using the NLSE model revealed that, at the moment of reconnection, a sound wave in the form of an intense rarefaction pulse is generated (Leadbeater & al 2001). A reconnection event, therefore, transforms a fraction of the kinetic energy of the vortices into sound energy. Figure 2 shows a collision between two vortex rings. The core regions are visualized by plotting isosurfaces of the density, and the sound pulse which results

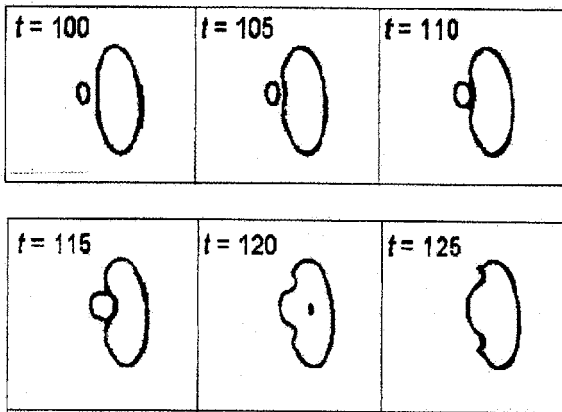


*Figure 2.* Vortex reconnection induced by the collision of two vortex rings (Leadbeater & al 2001). Note the sound pulse in the middle of the vortex loop at  $t = 120$ .

from the reconnection is the small dot at  $t = 120$ . The size of the pulse is of the order of  $a_0$  and its initial amplitude corresponds to a drop of the density from the bulk value to zero, as evident in figure 3. The pulse spreads and decreases in amplitude as it travels away.

## 6. Vortex reconnections and Kelvin waves

If a straight vortex line is deformed into a helix, the deformation propagates as a Kelvin wave of wavenumber  $k$  and angular velocity  $\omega \sim k^2$ . The power radiated by a Kelvin wave is negligible unless  $k$  is very large (Vinen 2000, 2001). The question is which physical mechanism can generate the high wavenumbers required to explain the decay of turbulence by radiation of sound. Using Schwarz's model, Kivotides & al 2001 showed that high values of  $k$  can be produced by vortex reconnections. The time sequence in figure 4 shows the evolution of four vortex rings initially launched against each other. It is apparent that the cusps left by vortex reconnections relax into large amplitude Kelvin waves, and the nonlinear interaction between these waves creates waves of higher and higher wavenumbers.

## 7. Energy spectrum

The results described above show that generation of sound, either directly in the form of bursts or indirectly via Kelvin waves, represents the "sink" of kinetic energy. The two processes take place together, as shown on the left of figure 5, and their relative importance depends on

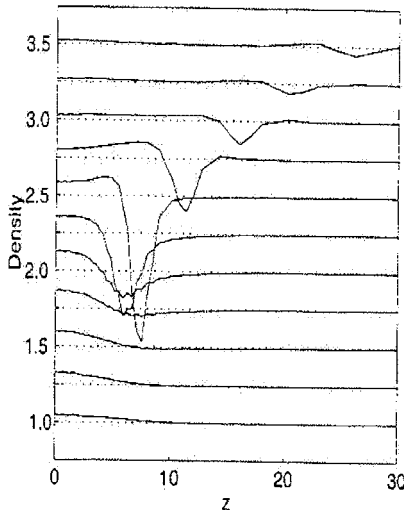


**Figure 3.** Density profiles along the  $z$  axis for a collision of two vortex rings initially set on the  $x, y$  plane. The curves, which correspond to profiles at 11 different times, are offset by 0.25 from each other for clarity. The density is normalized to the bulk value. Initially  $\rho_s \approx 1$ . As the rings approach there is a slight increase. The reconnection is followed by a sudden rarefaction pulse which moves along the  $z$  axes (Leadbeater & al 2001).

the vortex line density  $L$  (the length of vortex line per unit volume) which determines the reconnection rate.

The same argument which leads to the classical Kolmogorov  $k^{-5/3}$  energy spectrum then applies to superfluid turbulence. Preliminary evidence that this is indeed the case was found by Nore & al 1997 using the NLSE model but lacked convincing numerical resolution. Recently Araki & el 2002 confirmed Nore's result using Schwarz's model - see the right hand side of figure 5. Although there is no sound in Schwarz's model, the finite discretization (which effectively removes Kelvin waves of high  $k$ ) and the artificial removal of small loops were sufficient to provide an energy sink.

## 8. Discussion

The current theory of helium II turbulence (Vinen & Niemela 2002 ) is based on the recent finding that both normal fluid and superfluid obey Kolmogorov's law. Using Schwarz's model, Barenghi & et 2002 have

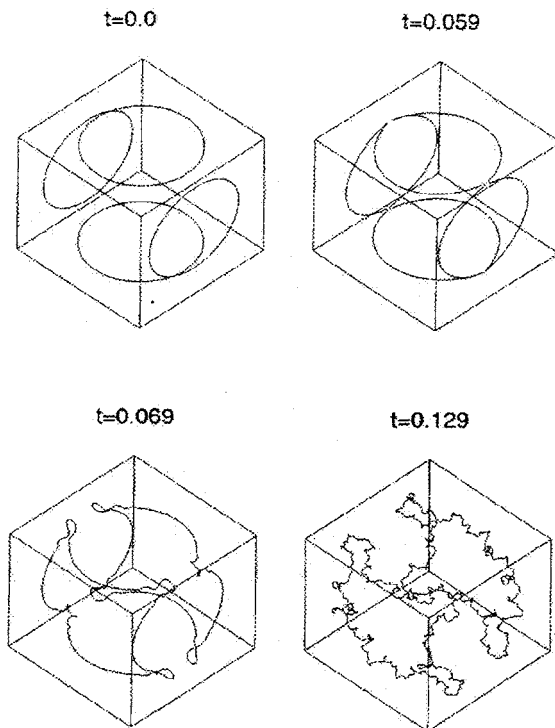


*Figure 4.* Collision of four vortex rings and generation of Kelvin waves of high wavenumber (Kivotides & al 2001).

recently shown that normal fluid eddies cause partial polarization of an initially random superfluid tangle over the lifetime of these eddies. This result suggests that the role of mutual friction is to keep the two fluids locked together over length scales larger than the average separation of vortices.

Schwarz's model is based on a prescribed normal fluid velocity  $\mathbf{v}_n$  rather than on a self-consistent solution of the normal fluid's Navier-Stokes equation. Further progress will require better understanding of the dynamics of coupled normal fluid and superfluid vortices, which until now has been studied only for very simple configurations (Kivotides & al 2000).

## References

- T. Araki, M. Tsubota & S.K. Nemirovskii, Phys. Rev. Letters **89**, 145301 (2002).
- C.F. Barenghi, S. Hulton and D.C. Samuels, submitted (2002).
- C.F. Barenghi, R.J. Donnelly and W.F. Vinen, J. Low Temp. Phys. **52** 189, (1983).

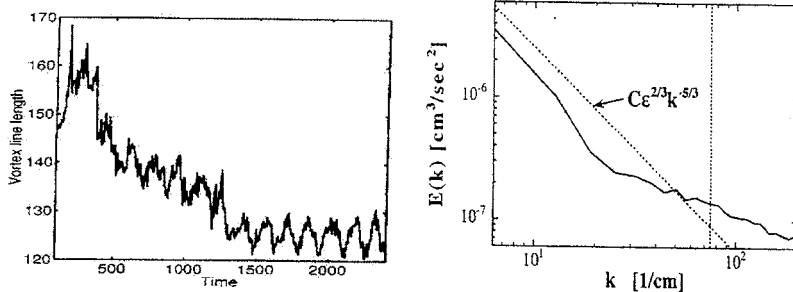


**Figure 5.** Left: Energy loss (represented by length of vortex line lost) vs time calculated using the NLSe model (from Leadbeater & al 2002): the sudden drops are caused by sound bursts, and the slow oscillatory decay is due to Kelvin wave radiation. Right: Energy spectrum of a superfluid vortex tangle at  $T = 0$  (from Araki & el 2002) calculated using Schwarz's model. The vertical dashed line shows the wavenumber  $k_\delta$  corresponding to the average vortex spacing  $\delta \approx L^{-1/2}$ .

- C.F. Barenghi, R.J. Donnelly & W.F. Vinen, *Quantized Vortex Dynamics And Superfluid Turbulence*, Springer, Heidelberg (2001)
- S.I. Davis, P.C. Hendry and P.V.E. McClintock, *Physica B* **280** 43 (2000).
- R.J. Donnelly, *Quantized Vortices In Helium II*, Cambridge University Press (1991).
- D. Kivotides, C.F. Barenghi and D.C. Samuels, *Science*, **290**, 777 (2000).
- D. Kivotides, J.C. Vassilicos, D.C. Samuels and C.F. Barenghi, *Phys. Rev. Letters*, **86**, 3080 (2001).
- J. Koplik, J. and H. Levine, *Phys. Rev. Letters* **71**, 1375-1378 (1993).
- M. Leadbeater, T. Winiecki, D.C. Samuels, C.F. Barenghi and C.S. Adams, *Phys. Rev. Letters* **86** 1410 (2001).
- M. Leadbeater, D.C. Samuels, C.F. Barenghi and C.S. Adams, to appear in *Phys. Rev. A* (2002).
- J. Maurer and P. Tabeling, *Europhys. Letters* **43**, 29 (1998).
- C. Nore, M. Abid and M.E. Brachet, *Phys. Rev. Letters* **78** 3896 (1997).
- D.C. Samuels, in *Quantized Vortex Dynamics And Superfluid Turbulence*, ed. by C.F. Barenghi, R.J. Donnelly & W.F. Vinen, Springer, Heidelberg (2001).
- K.W. Schwarz, *Phys. Rev. B* **38**, 2398 (1988).
- M.R. Smith, R.J. Donnelly, N. Goldenfeld and W.F. Vinen, *Phys. Rev. Lett.* **71**, 2583 (1993)
- M.R. Smith, D.K. Hilton and S.V. VanSciver, *Phys. Fluids* **11**, 751 (1999).
- S.R. Stalp, L. Skrbek, L. and R.J. Donnelly, *Phys. Rev. Letters* **82**, 4831 (1999).
- F. Vinen, *Phys. Rev. B* **61**, 1410 (2000); *Phys. Rev. B* **64** (13), 134520 (2001).
- W.F. Vinen & J.J. Niemela, to appear in *J. Low Temp. Physics* (2002).
- P.L. Walstrom, J.G. Weisend, J.R. Maddocks and S.W. VanSciver, *Cryogenics* **28**, 101 (1998).

# REYNOLDS NUMBER SCALING OF WALL LAYER VELOCITY-VORTICITY PRODUCTS

P. A. Priyadarshana and J. C. Klewicki

*Physical Fluid Dynamics Laboratory*

*Department of Mechanical Engineering*

*University of Utah*

*Salt Lake City, Utah 84112*

*priyadar@eng.utah.edu*

*klewicki@eng.utah.edu*

## Abstract

The wall normal gradients of Reynolds stress and turbulent kinetic energy are important in analyzing momentum transport in the turbulent boundary layer. These gradients can be expressed in terms of velocity-vorticity correlations. In this paper, properties of velocity-vorticity products over a three decade variation in Reynolds number are analyzed. Data were acquired in the near neutral atmospheric surface layer in the western desert of Utah and in a laboratory boundary layer. A custom made six-wire hot wire probe was employed to measure axial and wall normal velocities as well as spanwise vorticity. It is observed that the co-spectra of velocity and vorticity generally follows the vorticity spectrum at both high and low Reynolds number. Thus, it is concluded that the vortical motions dictate the scales over which the net correlation occurs. Normalization of vorticity spectra using the Taylor time scale appears to effectively remove Reynolds number variations.

**Keywords:** velocity, vorticity, Taylor microscale, viscous scale, stress transport

## Introduction

Descriptions of the physical mechanisms for momentum transport in high Reynolds number boundary layer turbulence remain incomplete. This situation exists in large part owing to the experimental challenges (i.e., the spatial and temporal resolution requirements) associated with probing the turbulence in such flows. As is shown explicitly herein, descriptions of the mechanisms for stress gradient generation require reso-

lution of the fluctuating vorticity field. The present research overcomes a number of the experimental challenges associated with high Reynolds number by probing the atmospheric surface layer.

According to Hinze, 1975, for an incompressible flow the following tensor identity holds.

$$\frac{\partial \overline{u_j u_i}}{\partial x_j} = -\epsilon_{ijk} \overline{u_j \omega_k} + \frac{1}{2} \frac{\partial \overline{u_j u_j}}{\partial x_i}. \quad (1)$$

This identity indicates that for a 2-D flat plate boundary layer ( $x$  in the flow direction,  $y$  normal to the wall), setting  $i = 1$ ,

$$\frac{\partial \overline{uv}}{\partial y} = \overline{w\omega_y} - \overline{v\omega_z} + \frac{1}{2} \frac{\partial (\overline{v^2} + \overline{w^2} - \overline{u^2})}{\partial x}, \quad (2)$$

and  $i = 2$ ,

$$\frac{\partial q}{\partial y} = 2\overline{v \frac{\partial v}{\partial y}} - \overline{u\omega_z} + \overline{w\omega_x}, \quad (3)$$

provides descriptions of the flow field interactions underlying the generation of the wall normal Reynolds stress and turbulent kinetic energy gradients respectively.

An issue particularly relevant to understanding the behavior of the indicated velocity-vorticity products is the widening disparity between the scales of motions contributing to the kinetic energy and enstrophy with increasing Reynolds number. As the Reynolds number is increased, the disparity between the large and small scales increases. The effect of scale disparity on velocity-vorticity products is analyzed and discussed in this paper.

## Experimental Facilities

The high Reynolds number data presented were acquired at the Surface Layer Turbulence and Environmental Science Test (SLTEST) facility (Metzger and Klewicki, 2001). All the measurements were made around sunset, under near neutrally stable atmospheric conditions. During each test run, the deviation of mean wind direction was less than  $\pm 5.0^\circ$ . The low Reynolds number data were acquired in an open circuit wind tunnel at the University of Utah.

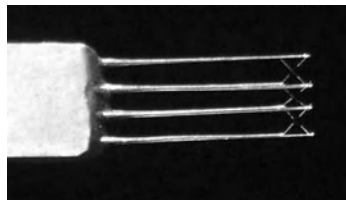


Figure 1. The six-wire probe

A custom made six wire probe (Figure 1) composed of three x-arrays was used to acquire instantaneous streamwise and wall normal velocities at several different wall normal positions. In both the laboratory and field experiments, the distance from the wall to the bottom of the x-array was measured with a cathetometer having a precision of  $\pm 0.0127\text{mm}$ . Constant temperature hot-wire anemometers (AA Lab-Systems AN-1003) were employed. A 16 bit simultaneous sample and hold A/D was used to acquire the hot-wire signals. A sampling frequency of 5kHz was used in all of the high Reynolds number experiments, while the low Reynolds number data were acquired at either 2kHz or 5kHz depending on the Reynolds number. The hot-wire sensor employed  $5\mu\text{m}$  diameter tungsten wires. These wires had a sensor length of 1mm, which is 4.72 and 10.8 wall units at Reynolds numbers 2668 and  $5 \times 10^6$  respectively. All the wires were calibrated immediately before and after each experiment.

## Results and Discussion

The present data show that both wall-normal velocity,  $v$ , and spanwise vorticity,  $\omega_z$ , consist of scales with peak spectral intensity near the Taylor frequency (inverse Taylor time scale) at all Reynolds numbers. Figure 2 shows inner normalized power spectra of  $v$  and  $\omega_z$ , and the co-spectra of  $v$  and  $\omega_z$  at both high and low Reynolds number. For all of these experiments, the dominant peak in the  $vw_z$  co-spectra occurs very close to the  $\omega_z$  spectral peak irrespective of the Reynolds number and distance from the wall. Figure 3 shows the power spectra of  $vw_z$  for the above velocity-vorticity time series. These show the frequency contribution to the  $vw_z$  variance is maximized near the Taylor frequency.

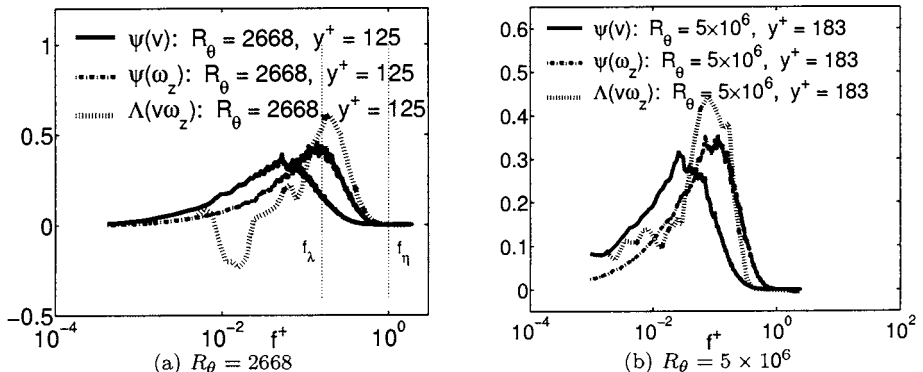


Figure 2. Inner normalized premultiplied co-spectrum of  $v$  and  $\omega_z$  and power spectra of  $v$  and  $\omega_z$

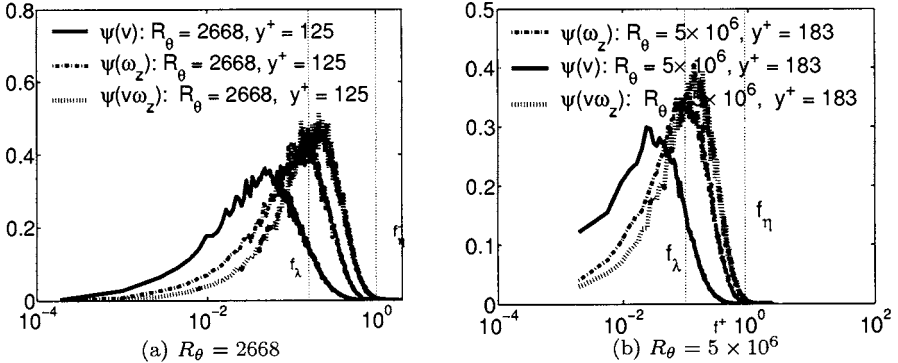


Figure 3. Inner normalized premultiplied power spectra of  $v, \omega_z$  and  $v\omega_z$

The inner normalized premultiplied co-spectra of streamwise velocity and spanwise vorticity at the Reynolds numbers 2668 and  $5 \times 10^6$  are shown in Figure 4. The premultiplied  $u\omega_z$  co-spectrum follows the  $\omega_z$  premultiplied power spectrum closely for all Reynolds numbers. An increase in spectral intensity in the streamwise velocity power spectra at low frequency at  $R_\theta = 5 \times 10^6$  is the major difference in between the two flow fields. However, there is no major difference in the premultiplied vorticity power spectra. Under all conditions, the premultiplied co-spectrum of  $u$  and  $\omega_z$  is peaked near where the peak in the premultiplied  $\omega_z$  power spectrum occurs. The premultiplied power spectra of  $u\omega_z$  is shown in Figures 5 (a) and (b). Here, the  $u\omega_z$  power spectra follow the  $\omega_z$  power spectra almost exactly.

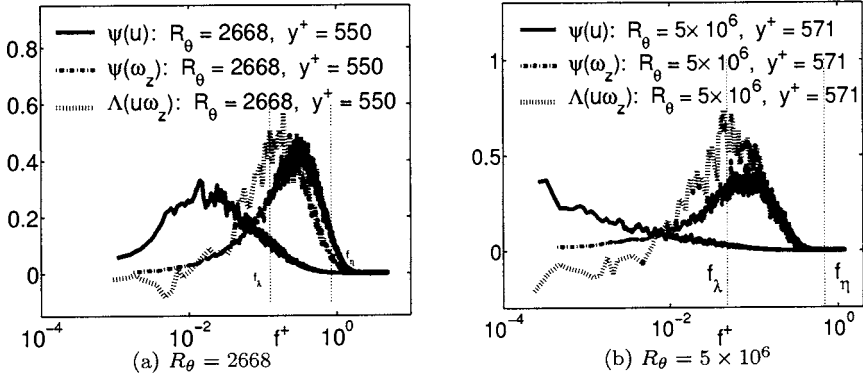


Figure 4. Inner normalized premultiplied co-spectrum and power spectra of  $u$  and  $\omega_z$

The above analysis, indicates that both in the low and high Reynolds number turbulent boundary layer, the velocity-vorticity co-spectra and

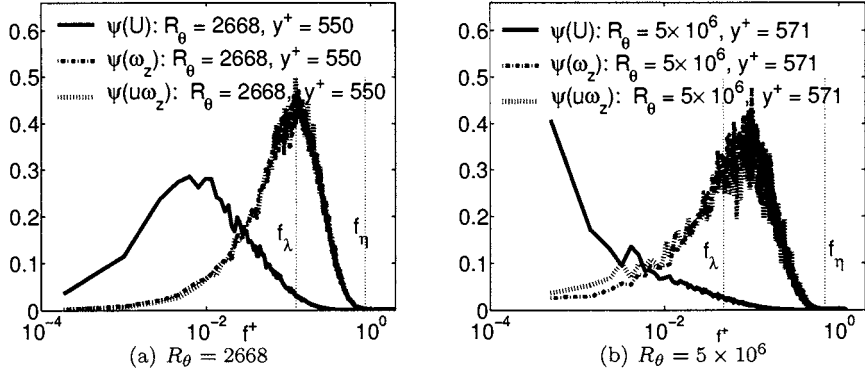


Figure 5. Inner normalized premultiplied co-spectrum and power spectra of  $u$  and  $\omega_z$

power spectra in large part tracks the premultiplied  $\omega_z$  power spectrum. The present interpretation therefore indicates that, independent of Reynolds number, the scales over which the velocity and vorticity correlate are dictated by the motions underlying the associated vorticity component. Understanding the behavior of vorticity is therefore seen as important in correctly understanding these velocity-vorticity correlations.

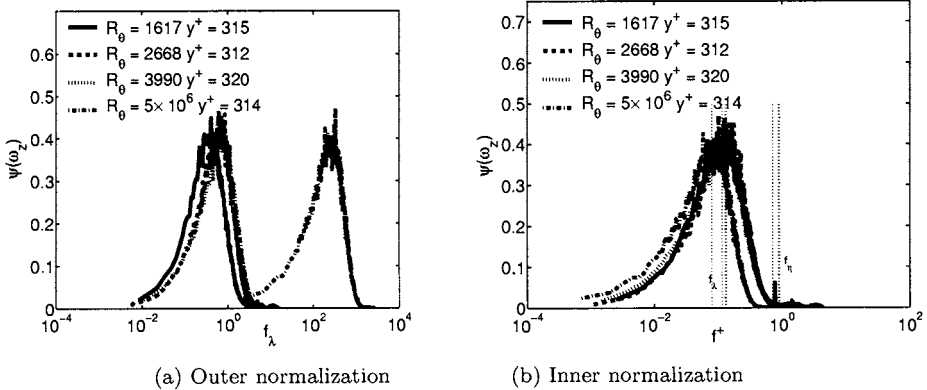


Figure 6. Outer and inner normalized premultiplied  $\omega_z$  power spectrum

To this end, the outer and inner normalizations of premultiplied  $\omega_z$  power spectra are presented in the Figures 6 (a) and 6 (b) respectively. Outer scaling appears to produce an overlap in the low Reynolds number data. In particular, the peaks in the outer normalized spectra at low Reynolds number all occur near  $f\theta/U_\infty = 1$ . From this, a rational interpretation would be that the vortical motions reside at the large scales.

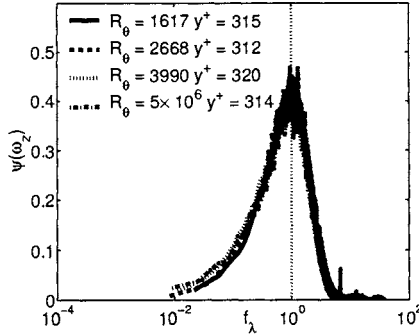


Figure 7. Taylor normalized premultiplied spanwise vorticity power spectra.

Examination of the  $R_\theta = 5 \times 10^6$  spectra, however, indicates that this interpretation breaks down as  $R_\theta$  becomes large. Clearly, the interpretation derived from the low  $R_\theta$  data is misinformed owing to the lack of scale separation. Inner normalization creates a much better merging of the premultiplied  $\omega_z$  spectra over the entire range of Reynolds number. However, the peak still exhibits a shift to lower frequency with increasing Reynolds number. It is clear from Figures 6(b), 2 and 4 that the peak in the premultiplied  $\omega_z$  power spectra is almost at the appropriate Taylor micro-scale. Thus, vorticity magnitudes as well as frequencies were normalized by the Taylor time-scale and are shown in Figure 7. Under this normalization, the premultiplied  $\omega_z$  power spectra merge over a broad range of frequencies starting near the Kolmogorov scale and extending up to an order of magnitude larger than the Taylor micro scale. There are small but apparent Reynolds number dependencies at higher and lower frequencies.

## Conclusion

The spectral intensity containing eddies of the velocity-vorticity products,  $v\omega_z$  and  $u\omega_z$  are relatively small in size. Furthermore, the premultiplied co-spectra of  $v$  and  $\omega_z$  and  $u$  and  $\omega_z$  as well as premultiplied power spectra of  $v\omega_z$  and  $u\omega_z$  closely follow the premultiplied  $\omega_z$  spectra. The premultiplied  $\omega_z$  power spectra has a peak near the Taylor time scale irrespective of the Reynolds number, and thus Taylor microscale normalization minimizes the Reynolds number effects in these spectra.

## References

- Hinze, J. O. (1975). *Turbulence*. McGraw-Hill.  
 Metzger, M. M. and Klewicki, J. C. (2001). A comparative study of near-wall turbulence in high and low reynolds number boundary layers. *Physics of Fluids*, 13(3):692–701.

# SCALING OF THE LARGE-SCALE MOTIONS IN FULLY DEVELOPED TURBULENT CHANNEL FLOW

Makoto Tsubokura and Tetsuro Tamura

*Department of Environmental Science and Technology*

*Tokyo Institute of Technology*

tsubo@depe.titech.ac.jp, tamura@depe.titech.ac.jp

**Abstract** Large-scale motions of fully developed turbulent channel flow were numerically investigated for the  $Re_\tau$  of up to 1180 using LES. They were found to be similar to the streak structures near the wall, but their streamwise and spanwise sizes reach about three times and twice as large as the channel-half width respectively independent of the  $Re_\tau$ .

**Keywords:** Large-scale motion, Large-eddy simulation, channel flow

## 1. Introduction and analysis method

It is known that there exist large-scale motions (LSM) at or above the logarithmic layer of wall-turbulence. Since the first prediction of Townsend [8], the sign of LSM has been found in the long tail of the time-delayed autocorrelation of the streamwise velocity, and the corresponding peak at the lower wavenumber of premultiplied power spectra [3, 4]. The difficulty of studying LSM lies in the fact that sufficiently large analysis region and high  $Re_\tau$  condition are required. Therefore their entire structures, relationship with a near-wall small organized structures, or effects on turbulence statistics has not yet been fully understood. In this study, we have adopted Large Eddy Simulation (LES) to meet the requirement mentioned above and investigated the scaling of LSM by observing the peak of the premultiplied power spectra.

Following isotropic eddy viscosity models are used for *subgrid*-scale (SGS),  $\tau_{ij} = \bar{u}_i u_j - \bar{u}_i \bar{u}_j$  and *subtest*-scale (STS) stresses,  $T_{ij} = \widetilde{\bar{u}_i u_j} - \widetilde{\bar{u}_i} \widetilde{\bar{u}_j}$ :

$$\tau_{ij} - \frac{1}{3} \delta_{ij} \tau_{kk} = -2C \frac{k}{3|\bar{S}|} \bar{S}_{ij}, k = \overline{u_k u_k} - \bar{u}_k \bar{u}_k, \quad (1)$$

$$T_{ij} - \frac{1}{3}\delta_{ij}T_{kk} = -2C\frac{K}{3|\tilde{\bar{S}}|}\tilde{\bar{S}}_{ij}, K = \widetilde{\bar{u}_k\bar{u}_k} - \tilde{\bar{u}_k}\tilde{\bar{u}_k}, \quad (2)$$

where  $S_{ij}$  is the strain rate tensor and  $S$  is its magnitude given as  $S = \sqrt{2S_{ij}S_{ij}}$ . The  $k$  and  $K$  are the SGS and STS turbulence energy. The model parameter included in these models is determined by the dynamic procedure [2] and *overtilde* denotes the *test* filtering operation. These models are developed for the dynamic procedure using Finite Difference Method (FDM). The most notable feature of these models is its insensitivity to the discrete *test* filtering operation by FDM [9].

The analysis model is a fully developed turbulent channel flow, where periodic boundary is considered for streamwise and spanwise directions, while no-slip condition is imposed on the wall. The uniform pressure gradient force acting for the streamwise direction drives the flow field to obtain the fully developed turbulence state. Hereafter streamwise, normal-wall and spanwise directions are given as  $x$ ,  $y$  and  $z$  respectively.

The fully conservative FDM scheme of Morinishi [6] on the staggered grid was adopted for discretization. The 4th order accuracy is considered for spatial derivatives except for the SGS term. This accuracy was determined from the compromise between the higher order requirement of SGS stress not to be dominated by numerical errors and the lower order requirement of non-linear term not to be contaminated by the aliasing error. For the detail of the numerical method, please refer to [9].

## 2. Results

### 2.1 Grid resolution and analysis region

Firstly, we investigate the grid resolution required for LSM. We have tested various grid resolutions for streamwise and spanwise directions, which are named as (I), (II), (III) and (IV) in table 1. To compare the results with existing DNS data, the  $Re_\tau$  and analysis region is restricted to 590 and  $2\pi\delta \times 2\delta \times \pi\delta$  respectively, which is consistent with DNS [7].

Figs. 1 and 2 indicate the two-point autocorrelation for the streamwise velocity for streamwise and spanwise separation respectively. Because the analysis region is not sufficient for LSM, correlation does not become zero at both streamwise and spanwise separations equivalent to the half of the analysis region ( $\Delta x/\delta = \pi$ ,  $\Delta z/\delta = \pi/2$ ). It is obvious that case (I) of the coarsest resolution severely underestimate the correlation compared with DNS results, while such underestimation is mitigated by using finer mesh. Among the cases tested here, (IV) shows good agreement with DNS results.

Table 1. Simulation parameters for LES.

Test cases	$Re_\tau = u_\tau \delta / \nu$	Region size $L_x \times L_y \times L_z$	Grid number $N_x \times N_y \times N_z$	Resolution $l_x^+ l_z^+$
DNS [7]	590	$2\pi\delta \times 2\delta \times \pi\delta$	$384 \times 257 \times 384$	9.7 4.8
(I)	590	$2\pi\delta \times 2\delta \times \pi\delta$	$64 \times 65 \times 64$	57.9 29.0
(II)	590	$2\pi\delta \times 2\delta \times \pi\delta$	$96 \times 65 \times 64$	38.6 29.0
(III)	590	$2\pi\delta \times 2\delta \times \pi\delta$	$128 \times 65 \times 64$	29.0 29.0
(IV)	590	$2\pi\delta \times 2\delta \times \pi\delta$	$128 \times 65 \times 96$	29.0 19.3
(V)	590	$8\pi\delta \times 2\delta \times 4\pi\delta$	$512 \times 65 \times 384$	29.0 19.3
(VI)	1180	$8\pi\delta \times 2\delta \times 2.25\pi\delta$	$1024 \times 97 \times 432$	29.0 19.3

Accordingly we would like to decide  $l_x^+ = 29.0$  and  $l_z^+ = 19.3$  as the required grid resolution for LSM in this study. It is worth noting that these resolutions for streamwise and spanwise directions are sufficient to reproduce the small-scale structures such as streaks near the wall. This fact clearly indicates that there will be strong relationship between the near-wall structures and the LSM at least for the  $Re_\tau = 590$  tested here, which will support the hierarchical structures of hairpin packets [1].

Taking this results into consideration, we have expanded the analysis region ((V) and (VI) in Table 1) to make two point correlation asymptotically become zero at a certain separation within the analysis region (Figures not shown).

## 2.2 Scaling

we examine the entire scale of the LSM here by using large analysis region shown as (V) and (VI) in Table. 1. The LSM can be visualized by drawing the instantaneous streamwise velocity fluctuation on the  $x$ - $z$  plane, which is given in Fig. 3. We can see the typical streak structures at the near-wall region in both  $Re_\tau$  (see top two figs. at  $y^+ \sim 10$ ). The LSM can be clearly observed above  $y^+ \sim 200$  (bottom-left and center and bottom-right figs.), which look like near-wall streaks but their size is an order of magnitude larger than them.

Figure 4 indicates the pre-multiplied power spectrum of a streamwise velocity fluctuation for the spanwise (*left two figs.*) and streamwise (*right two figs.*) directions respectively. The spectral peak moves from a higher wave number to a lower one as we go away from the wall in both cases.

In case of spanwise directions, the peak near the wall ( $y^+ \sim 10$ ) can be observed at different wavenumbers of  $k_z^* = 2\pi\delta/\lambda_z \sim 40$  and 80 for  $Re_\tau = 590$  and 1180 respectively, but which are equivalent to about  $\lambda_z^+ \sim 100$  in inner-layer scaling. Contrarily to the near-wall peaks, we

can see the peak at the wave number of  $k_z^* \sim 3.5$  in the region away from the wall for both  $Re_\tau$ . This peak at the lower wave number is more clearly distinguishable at the higher  $Re_\tau$  and its trace can be observed even in the vicinity of the wall (*arrow B*) in addition to the strong peak (*arrow A*) of the small scale streaks in second left of Fig. 4. In fact we can see the large low-speed structures in near-wall region more clearly at the higher  $Re_\tau$  (*on the right top of Fig. 3*) which corresponds to the LSM observed in the logarithmic layer ( $y^+ = 199, 398$  *right center and bottom*) This effect of LSM on the near-wall structure might explain the Reynolds number dependence on near-wall statistics. In the streamwise case, we can observe the similar tendency to the spanwise case.

The spanwise wavelength of the peak of the premultiplied power spectrum is shown in Fig. 5. Data for both  $Re_\tau$  collapse well near the wall ( $y^+ \leq 100$ ) in the inner-layer scaling and decaying asymptotically to  $\lambda_z^+ \sim 100$  (*left*). While in the region away from the wall ( $y/\delta \geq 0.25$ ), the largest wavelength reaches approximately  $\lambda_z \sim 1.7\delta$  (*center and right*) independent of the  $Re_\tau$ . The streamwise peak in Fig. 6 also shows the similar tendency, in which near-wall peak collapse well in the inner-layer scaling and decaying asymptotically to  $\lambda_x^+ \sim 1000$  while it reaches to  $\lambda_x \sim 3.2\delta$  independent of the  $Re_\tau$ . But contrarily to the spanwise peak, two or three peaks at lower wavenumber are simultaneously observed at or above the logarithmic layer for the  $Re_\tau = 1180$  case.

We understand that these LSM correspond to the ones having observed experimentally in the spatially developing turbulent boundary layer [5], which is called large uniform zones of lower momentum in their paper, and is supposed to be the universal feature of wall-turbulence.

## References

- [1] Adrian, R. J., Meinhart, C. D. and Tomkins, C. D. (2000), *J. Fluid Mech.* **422**, 1
- [2] Germano, M., Piomelli, U., Moin, P. and Cabot, W. H. (1991), *Phys. Fluids* **A3**, 1760
- [3] Jiménes, J. (1998), *Ann. Research Briefs, Center for Turbulence Research*, 137
- [4] Kim K. C. and Adrian, R. J. (1999), *Phys Fluids* **11**, 417
- [5] Meinhart, C. D. and Adrian, R. J. (1995), *Phys. Fluids* **7**, 694
- [6] Morinishi, Y., Lund, T. S., Vasilyev, O. V. and Moin, P. (1998), *J. Comput. Phys.* **143**, 90
- [7] Moser, R. D., Kim, J., and Mansour, N. (1999), *Phys. of Fluids* **11**, 943
- [8] Townsend, A. A. (1976), *The structure of turbulent shear flow* (2nd ed.)
- [9] Tsubokura, M. (2001), *Phys. Fluids* **13**, 500

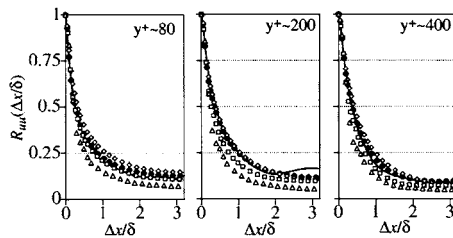


Figure 1. The two-point autocorrelation coefficient for the streamwise velocity for streamwise separation at  $y^+ \sim 80, 200, 400$ . (Symbols:  $\triangle$ , I( $64 \times 64$ );  $\square$ , II( $96 \times 64$ );  $\diamond$ , III( $128 \times 64$ );  $\bullet$ , IV( $128 \times 96$ ); —, DNS(Moser et al.)

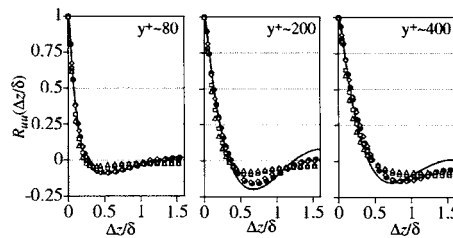


Figure 2. The  $u$ -autocorrelation for spanwise separation. (captions, see Fig. 1)

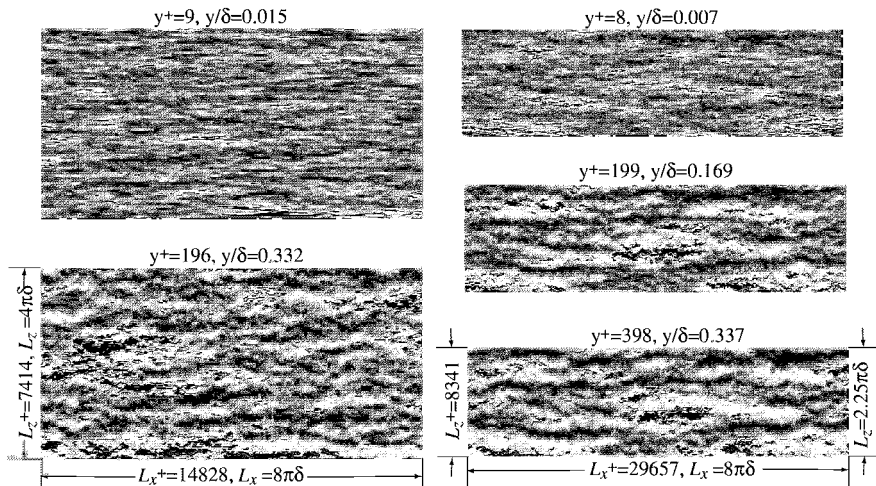


Figure 3. Instantaneous streamwise velocity fluctuation ( $u'/u_\tau$ ) on  $x-z$  plane. (left:  $Re_\tau = 590$ , case (V); right:  $Re_\tau = 1180$ , case (VI))

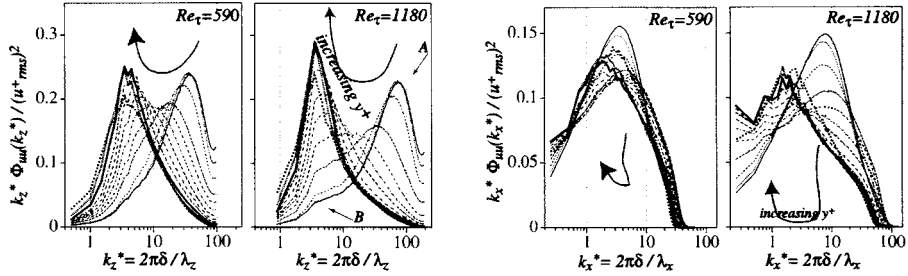


Figure 4. Pre-multiplied power spectrum of streamwise velocity fluctuation at  $y^+ \sim 4, 9, 20, 43, 61, 84, 113, 150, 196, 285, 395, 523$  ( $Re_\tau = 590$ ) and  $4, 8, 20, 49, 91, 144, 199, 299, 398, 477, 667, 957$  ( $Re_\tau = 1180$ ). (left, for spanwise; right, for streamwise directions)

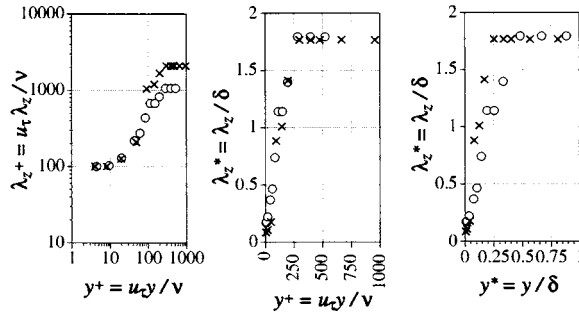


Figure 5. Spanwise wavelength of the peak of the pre-multiplied power spectrum. (a), inner( $y$ )-inner( $\lambda$ ); (b), inner-outer; (c), outer-outer scaling. (o,  $Re_\tau = 590$ ; x,  $Re_\tau = 1180$ )

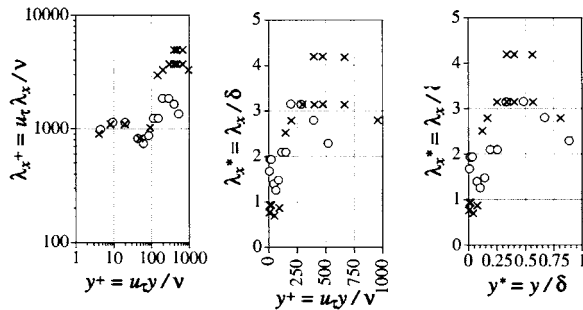


Figure 6. Streamwise wavelength of the peak of the pre-multiplied power spectrum. (captions, see Fig.5)

# THE MEAN VELOCITY PROFILE OF TWO-DIMENSIONAL FULLY DEVELOPED TURBULENT PLANE-CHANNEL FLOWS

F. Durst

*Professor of Fluid Mechanics (LSTM), D-91058 Erlangen, Germany*

*Durst@lstm.uni-erlangen.de*

E. S. Zanoun

*Ph.D. Student (LSTM), D-91058 Erlangen, Germany*

*Zanoun@lstm.uni-erlangen.de*

H. Nagib

*Rettaliata Professor of Mechanical and Aerospace Engineering (IIT), Chicago, IL 60616, USA*

*Nagib@iit.edu*

**Abstract** This work is concerned with the reliable determination of the value of the von Kármán constant for the logarithmic law of the wall. For this purpose, direct measurements of the mean velocity distribution in two-dimensional fully developed turbulent plane-channel flows were carried out. The results obtained were also employed to explain the wide scatter and the discrepancies in the von Kármán constant found in the literature. In addition, the entire set of the current data provides a good basis for assessing questions regarding the scaling of the mean velocity profiles in turbulent channel flows and also to make contributions to answer the question of whether a logarithmic or a power law exists in the overlap region. Data obtained in channel flow, over a wide range of Reynolds numbers, unequivocally support a Reynolds number-independent logarithmic law to describe the overlap region with  $\kappa = 0.37$  which is very close to  $\kappa = 1/e = 0.368$  and  $B = 3.7$  for  $Re_\tau \geq 2 \times 10^3$ .

**Keywords:** Turbulent, Channel Flow, von Kármán

## 1. Introduction

Substantial research work has been reported over a numbers of decades for cases of wall-bounded flows and interesting results have become available that provide useful information on time-averaged and turbulent flow properties in the wall region. Channel flow has proven to be of vital importance in practical engineering applications and also for understanding wall-bounded turbulent flows. In spite of this, many open questions remain and suggest further research relating to important issues of the law of the wall.

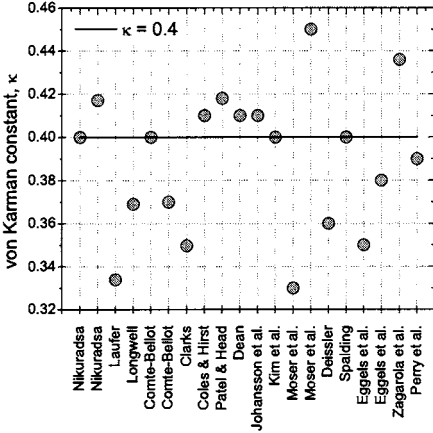


Figure 1. Values of the von Kármán constant obtained from various investigations.

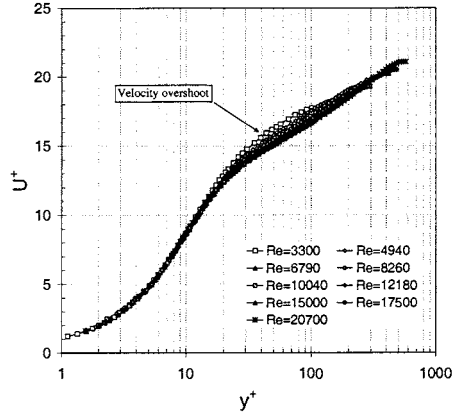


Figure 2. Mean velocity distribution for low Reynolds number range, Fisher [1999].

For this reason, the present paper is concerned with the mean velocity distribution of two-dimensional fully developed turbulent plane-channel flows.

The research summarized in this paper was triggered by recent publications containing suggestions for the normalized mean velocity distribution,  $U^+ = f(y^+)$ , in the so-called overlapping region of the flow, being either a logarithmic or a power law, e.g. see Barenblatt et al. [1993a, b], Zagarola & Smits [1998], Österlund et al. [1999, 2000], and Wosnik et al. [2000]. The existence of one or other of these laws was derived by methods already employed earlier for turbulent wall-bounded shear flows, e.g. see von Kármán [1930], Prandtl [1925, 1932], Taylor [1932] and Millikan [1938]. A wide scatter of the value of the von Kármán constant of the logarithmic law of the wall was found in the literature (Fig. 1). This scatter could be attributed either to inconsistencies in the general trends of the available experimental data which might be related to the measurement of the wall friction velocity,  $u_\tau$ , or to low Reynolds number effects as shown in Fig. 2 for  $Re_\tau \leq 570$  (see the overshoot for  $y^+ \leq 150$ ). Furthermore, theoretical postulations of flow behavior can yield wrong  $\kappa$ -values.

The authors' current work, therefore, aimed at direct measurements of the time-averaged velocity and from that the velocity gradient,  $dU^+/dy^+$ , was intended to give somewhat direct measurements of the small term in the corresponding momentum equation. From the natural logarithm of the mean velocity gradient,  $\ln(dU^+/dy^+) = f(\ln y^+)$  the value of the von Kármán constant,  $\kappa$ , of the logarithmic-law was derived. With this consistent approach, the authors aimed at obtaining reliable information regarding the mean velocity distribution without any hypothesis on the structure of the turbulence in two-dimensional fully developed turbulent plane-channel flow.

## 2. Experimental apparatus

**Test setup.** The experiments were carried out at LSTM. The test facility utilized has been described in a recent publication by Zanoun et al. [2002] to carefully carry out measurements for various Reynolds numbers in an air driven channel flow.

**Wall shear stress measurements.** Accurate and preferably independent measurement of the wall-shear stress is of primary importance for determining the exact values of the constants of the law of the wall. Therefore, two different independent techniques (pressure gradient and oil film interferometry) were applied to obtain the wall friction data,  $\tau_w$ , for each investigated Reynolds-number of the flow.

**Hot-wire anemometry.** A DANTEC 55M10 constant-temperature anemometer was used with a boundary layer probe (DANTEC, Type 55P15), equipped with a  $5\mu\text{m}$  diameter wire and an active wire length of 1.25 mm, providing an aspect ratio,  $l/d$ , of 250. All calibrations and measurements were performed with an 80% overheat ratio. Before each set of measurements, the hot-wire probe was calibrated against velocity measured with a Pitot tube at the channel entrance where a uniform and well-defined flow field existed.

**Wall distance.** Great care was taken to ensure a precise location of the hot wire at a reference distance from the wall. A calibration positioning procedure given with more detail in Durst et al. [2001] was applied in the present study. The absolute error in the wire positioning was estimated to be  $\Delta y \leq \pm 5\mu\text{m}$ .

## 3. Results and Analysis

The mean motion of a two-dimensional fully developed turbulent plane-channel flow is well described by the streamwise mean momentum equation as follows:

$$\frac{dU^+}{dy^+} = \left[ 1 - \frac{y^+}{Re_\tau} \right] + (\overline{u'_1 u'_2})^+, \quad (1)$$

where the normalization of all these terms in the equation is carried out with the corresponding characteristic velocity, length and time scales  $u_c = u_\tau = \sqrt{\tau_w/\rho}$ ,  $l_c = \nu/u_\tau$ ,  $t_c = \nu/u_\tau^2$ , and  $Re_\tau$  is defined as  $Re_\tau = u_\tau h/\nu$ ,  $h$  being half of the channel height.

Early attempts to study wall-bounded turbulent flows concentrated on the derivation of the turbulent momentum transport term  $-(\overline{u'_1 u'_2})^+$ , e.g. see Prandtl [1925, 1932], von Kármán [1930], Taylor [1932], Reichhardt [1951] and Deissler [1955]. To analyze flows described by equation (1), the data to be measured should be either  $(dU^+/dy^+)$  or  $-(\overline{u'_1 u'_2})^+$ . If one of these quantities is known, the other can be deduced using the above mean momentum equation. However, to treat  $-(\overline{u'_1 u'_2})^+$  "theoretically" and then to deduce from equation (1) a relationship for  $U^+ = f(y^+)$ , which is often presented in the literature, is far from being optimum. This is readily seen from Fig. 3, which shows the four terms in equation (1) indicating that, over a large and the most important part of the flow, at least for this study,  $dU^+/dy^+$  is the smallest term of the four and therefore is most sensitive to "modelling inaccuracies" introduced in the early research work. Experiments were performed in

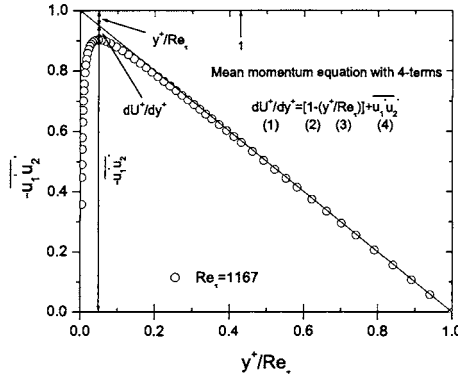


Figure 3. Magnitude of the four terms in the mean momentum equation of 2-D plane channel flow.

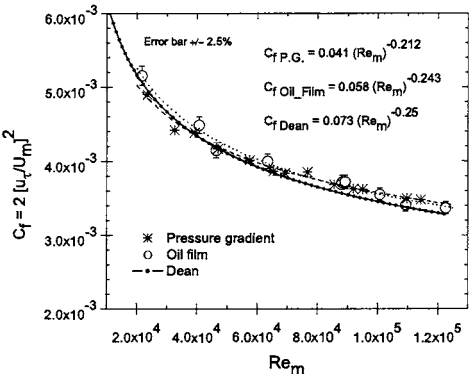


Figure 4. Measured skin friction coefficient from the pressure gradient and the oil film compared with Dean's formula ( $C_f = 0.073 Re_m^{0.25}$ ).

the Reynolds number range  $10^3 \leq Re_\tau \geq 5 \times 10^3$ . The wall shear stress, in wall-bounded turbulent flows, is conventionally expressed in terms of the local skin friction coefficient, i.e. in dimensionless form, as

$$C_f = 2 \left[ \frac{u_\tau}{U} \right]^2. \quad (2)$$

The resultant data for the wall skin friction coefficient obtained from both the pressure gradient and the oil film measurements are presented in Fig. 4. Good agreement of the wall skin friction data was found supporting the two-dimensionality of a channel of 1:12 aspect ratio. The data in Fig. 4 also compared well with the Dean's [1978] formula,  $C_f = 0.073 Re^{-0.25}$ , within  $\pm 2.5\%$  of the mean values.

Utilizing the wall friction data, the present mean velocity distributions were normalized using the corresponding wall shear velocity,  $u_\tau$ , to yield the dimensionless mean velocity,  $U^+ = F(y^+)$ , distribution. The resultant velocity profiles were then analyzed with respect to the question of whether the profile in the inertial sub-layer behaves in a logarithmic manner, as proposed by Prandtl [1925, 1932], von Kármán [1930], and Millikan [1938]:

$$U^+ = \frac{1}{\kappa} \ln y^+ + B, \quad (3)$$

where  $\kappa$  is the von Kármán constant and  $B$  is an additive constant, or whether it obeys a power law as proposed in the earlier investigations of Millikan [1938] and recently suggested by Barenblatt et al. [1993a, b] and Wosnik et al. [2000], i.e. in the form

$$U^+ = C y^{+\gamma}, \quad (4)$$

where  $C$  and  $\gamma$  are empirical constants, but are often Reynolds number dependent.

The following diagnostic functions were introduced, recently suggested by Österlund et al. [1999, 2000] and Wosnik et al. [2000], to see more clear the effect of the Reynolds number on the mean velocity profile:

$$\Xi = y^+ \frac{dU^+}{dy^+}, \quad \Gamma = \frac{y^+}{U^+} \left[ \frac{dU^+}{dy^+} \right]. \quad (5)$$

They represent the normalized slopes of the mean velocity distribution in either the logarithmic or the power region, respectively, and the behavior of both functions is shown in Fig. 5.

A constant behavior of  $\Xi$  for high enough Reynolds numbers leads to the existence of a logarithmic layer supporting Millikan's [1938] argument that a logarithmic law is expected in a high Reynolds number turbulent channel flow with a constant value of the von Kármán constant. In the inertial sublayer, all  $\Xi$  profiles in Fig. 5 showed a constant slope at  $y^+ \geq 150$ , which means that the logarithmic law is a good representation of the mean velocity measured in the overlap region. In addition, a constant behavior of the power-law diagnostic function,  $\Gamma$ , indicates that the mean velocity profile should behave in a power form. However, the general trend of the power-law diagnostic function is a monotonic decrease when plotted versus wall distance, as shown in Fig. 5. Therefore, the power law is far from useful to describe the mean velocity profile in the overlap region, see e.g. Clauser [1956], who came to the conclusion that no universal values can be assigned to  $C$  and  $\gamma$ .

Figure 6 shows the limits of each individual case where the best fit of the logarithmic law to the current data applies. The logarithmic interval was found to increase with increasing Reynolds number and extends almost up to the center of the channel for the highest Reynolds number case, see e.g. Kim et al. [1987], Wei and Willmarth [1989] and Gad-el-Hak and Bandyopadhyay [1993]. For the purpose of the current analysis, the authors adopted a new approach, which mainly depends on the natural logarithm of the mean velocity gradient, rather than that followed by Österlund et al. [1999, 2000]. All the data shown in Fig. 5 were re-plotted within the different ranges corresponding to the individual Reynolds number (see Fig. 6) and are shown in Fig. 7. With a common lower limit of  $y^+ = 150$ , all the higher Reynolds numbers results showed the same pattern where the logarithmic law fits the data within the experimental error. As a result, the data in Fig. 7 suggest that there exists a functional relationship for the far distant region of the normalized mean velocity distribution, given by

$$\ln \left[ \frac{dU^+}{dy^+} \right] = -\ln y^+ + B_1, \quad (6)$$

or rewritten as

$$\ln \left[ y^+ \frac{dU^+}{dy^+} \right] = B_1 \Rightarrow \left[ y^+ \frac{dU^+}{dy^+} \right] = e^{B_1}. \quad (7)$$

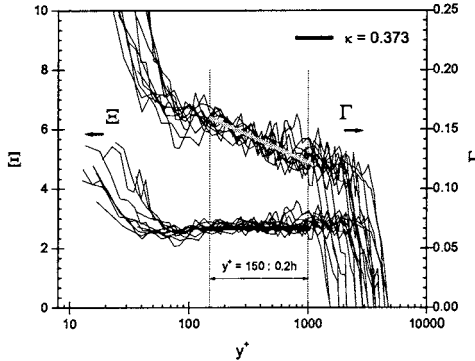


Figure 5. Diagnostic functions for the law of the wall.

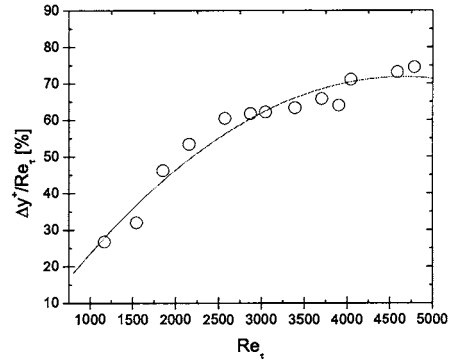


Figure 6. Maximum extent of logarithmic law region represented using inner scale.

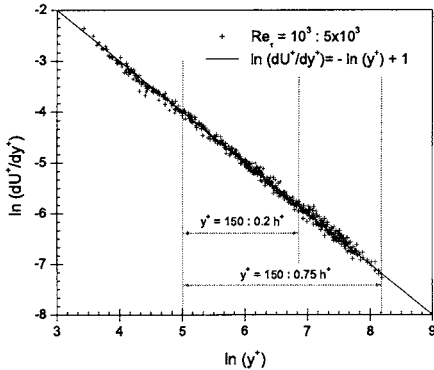


Figure 7. A ln-ln representation of the mean velocity gradient for different Reynolds numbers.

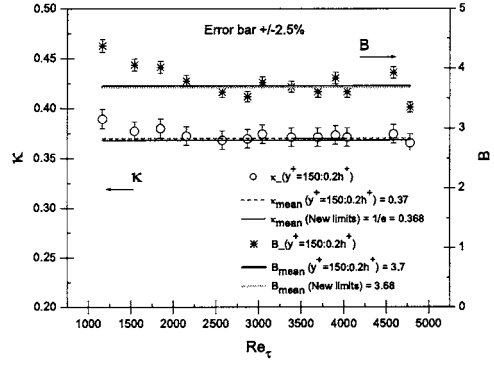


Figure 8. A summary of the von Kármán constant and the additive constant versus  $Re_\tau$  number.

This readily suggests a logarithmic representation for the far field of the normalized mean velocity profile with a von Kármán constant ( $\kappa$ ) of

$$\kappa = \left[ y^+ \frac{dU^+}{dy^+} \right]^{-1} = \frac{1}{e^{B_1}}. \quad (8)$$

A least-squares fit of the experimental data resulted in a value of  $1 \pm 2.5\%$  for the intercept  $B_1$ . The mean value of the additive constant  $B$  of the logarithmic law of the wall was then obtained from the mean velocity profile as

$$\Psi = U^+ - \frac{1}{\kappa} \ln y^+. \quad (9)$$

A constant behavior of  $\Psi$  in the region where the logarithmic law is valid was considered for an average calculation over all Reynolds numbers, i.e.  $10^3 \leq Re_\tau \leq 5 \times 10^3$ , giving  $B=3.74$  for  $\kappa = 0.373$ .

A summary of the results is presented in Fig. 8 for all the cases under study over the limits  $y^+ = 150$  and  $y/h = 0.2$ . It was found that following the traditional technique for data processing proposed by Österlund et al. [1999, 2000] for  $Re_\tau \geq 2 \times 10^3$  resulted in a von Kármán constant of 0.37 which is very close to the value found in this work,  $\kappa = 1/e = 0.368$ , assuming that  $B_1 = 1$  (within an accuracy of measurements of  $\pm 2.5\%$ ) and an additive constant  $B$  of 3.7.

#### 4. Conclusions

A careful analysis of the mean velocity distribution in the core region of a fully developed turbulent plane-channel flow revealed the following:

1. A logarithmic velocity distribution was found, giving a reasonably good approximation of the velocity profile in a fairly large part of the core region, almost up to the center of the channel.
2. A real logarithmic behavior in the overlap region exists for  $Re_\tau \geq 2 \times 10^3$  and the logarithmic interval increases with increasing Reynolds number.
3. With the new approach to data analysis, an interesting value of the von Kármán constant,  $\kappa = 1/e = 0.368$ , independent on the Reynold number, was obtained (cf. Goldstik & Stern [1977]).
4. The traditional technique for data processing proposed by Österlund et al. [1999, 2000] over the limits  $150 \leq y^+ \leq 0.2h^+$  resulted in Reynolds number independence of the von Kármán constant with a mean value of 0.37 for  $Re_\tau \geq 2 \times 10^3$ , which is in very close agreement with the value  $\kappa = 1/e = 0.368$  and with that obtained by Österlund et al. [1999, 2000] ( $\kappa = 0.38$ ), but, significantly different from that reported by Zagarola & Smits [1998] ( $\kappa = 0.436$ ).

#### References

- Barenblatt, G. I. (1993a). "Scaling laws for fully developed shear flows. Part 1. Basic hypotheses and analysis," *J. Fluid Mech.* 248, 513-520.  
 Barenblatt, G. I. and Chori, A. J. (1993b). "Scaling laws for fully developed shear flows. Part 2. Processing of experimental data," *J. Fluid Mech.* 248, 521-529.  
 Clark, J. A. (1968). "A study of incompressible turbulent boundary layers in channel flow," *ASME Journal of Basic Engineering* 90, pp. 455-467.  
 Clauser, F. H. (1956). "The turbulent boundary layer," *Adv. Appl. Mech.* 4, 1-51.  
 Comte-Bellot, G. (1963). "Turbulent flow between two parallel walls," PhD thesis (in French) University of Grenoble, (In English as ARC 31609), FM 4102.  
 Dean, R. B. (1978). "Reynolds number dependence of skin friction and other bulk flow variables in two-dimensional rectangular duct flow," *ASME J. Fluid Eng.* 100, 215-223.  
 Deissler, R. G. (1955). "Analysis of turbulent heat transfer, mass transfer and friction in smooth tubes at high Prandtl and Schmidt numbers," NACA Tech. Rep. 1210 (supersedes NACA Tech. Note 3145, 1954).  
 Durst, F., Zanoun, E. S., Pashtrapanska, M. (2001). "In situ calibration of hot wires close to highly heat-conducting walls," *Exp. Fluids* 31, 103-110.

- Eggels, J. G. M., Unger, F., Weiss, M. H., Westerweel, J., Adrian, R. J., Friedrich, R., Nieuwstadt, F. T. M. (1994). "Fully developed turbulent pipe flow: A comparison between direct numerical simulation and experiment," *J. Fluid Mech.* 268, 175-209.
- Fischer, M. (1999). "Turbulente wandgebundene Strömungen bei kleinen Reynoldszahlen" Dissertation, Universität Erlangen Nürnberg.
- Gad-el-Hak, M. and Bandyopadhyay, P. R. (1993). "Reynolds number effect on wall-bounded flows," *Appl. Mech. Rev.* 47, 307-365.
- Goldstik, M. A. and Stern, V. N (1977). "Hydrodynamic laws and turbulence," Academy of Science of the Soviet Union, Siberian Dep., Institute for Thermal Physics, Novosibirsk, 326-329 (in Russian).
- Huffman, G. D. and Bradshaw, P. (1972). "A note on von Kármán constant in low Reynolds number turbulent flows," *J. Fluid Mech.* 53, 45-60.
- Johansson, A. V. and Alfredsson, P. H. (1982) "On the structure of turbulent channel flow," *J. Fluid Mech.* 122, 295-314.
- Kim, J., Moin, P., Moser, R. (1987). "Turbulence statistics in fully developed channel flow at low Reynolds number," *J. Fluid Mech.* 177, 133-166.
- Laufer, J. (1954). "Investigation of turbulent flow in a two-dimensional channel," Report 1053-National Advisory Committee for Aeronautics, 1247-1266.
- Loehrke, K. I. and Nagib, H. M. (1972). "Experiments on Management of free-stream turbulence," AGARD Report No.598, IIT, Chicago, IL.
- Longwell, P. A. (1966). "Mechanics of Fluid Flow," McGraw-Hill, New York.
- Millikan, C. M. (1938). "A critical discussion of turbulent flows in channels and circular tubes," In Proc. 5th Intl Congress of Appl. Mech., 386-392.
- Moser, R. T., Kim, J., Mansour, N. N. (1999). "Direct numerical simulation of turbulent channel flow up to  $Re_\tau=590$ ," *Phys. Fluids* 11, 943-945.
- Nikuradse, J. (1932). "Gesetzmässigkeit der turbulenten Strömung in glatten Rohren," *Forschg. Arb. Ing.-Wes.* No. 356.
- Österlund, J. M., Johansson, A. V., Nagib, H. M., Hites, M. H. (1999). "Wall shear stress measurements in high Reynolds number boundary layers from two facilities," 30th AIAA Paper 99-3814, Fluid Dynamics Conference, Norflok, Virginia.
- Österlund, J. M., Johansson, A. V., Nagib, H. M., and Hites, M. H. (2000). "A note on the overlap region in turbulent boundary layers," *Phys. Fluids* 12, 1-4.
- Patel, V. C. and Head, M. R. (1969). "Some observations on skin friction and velocity profiles in fully developed pipe and channel flows," *J. Fluid Mech.* 38, 181-201.
- Perry, A. E., Hafez, S., Chong, M.S. (2001). "A possible reinterpretation of the Princeton superpipe data," *J. Fluid Mech.* 49, 395-401.
- Prandtl, L (1925). "Über die ausgebildete Turbulenz," *Z. angew. Math. Mech.*, 5, 136.
- Prandtl, L. (1932). "Zur turbulenten Strömung in Rohren und längs Platten," *Ergeb. Aerodyn. Versuch. Göttingen IV. Lieferung*, p.18.
- Reichardt, H. (1951). "Vollständige Darstellung der turbulenten Geschwindigkeitsverteilungen in glatten Leitungen," *Z. Angew. Math. Mech.* 31, 208-219.
- Spalding, D. B. (1961). "A single formula for the law of the wall," *ASME Journal of Applied Mechanics*, 455-458.
- Taylor, G. I. (1932). "The transport of vorticity and heat through fluid in turbulent motion," *Proc. Roy. Soc. London*, 135, 685-706.
- von Kármán, Th. (1930). "Mechanische Ähnlichkeit und Turbulenz," *Nachr. Ges. wiss. Goettingen*, p. 68.
- Wei, T. and Willmarth, W. W., (1989). "Reynolds number effects on the structures of a turbulent channel flow," *J. Fluid Mech.* 204, 57-95.
- Wosnik, M., Castillo, L., George, W. (2000). "A theory for turbulent pipe and channel flows," *J. Fluid Mech.* 421, 115-145.
- Zagarola, M. V., Smits, A. J. (1998). "Mean-flow scaling of turbulent flow," *J. Fluid Mech.* 373, 33-79.
- Zanoun, E. S., Nagib, H., Durst F., Monkewitz, P. (2002). "Higher Reynolds number channel data and their comparison to recent asymptotic theory," 40<sup>th</sup> AIAA-1102, Aerospace Sciences Meeting, Reno.

# NON-EXTENSIVE MODEL FOR TURBULENT FLOW IN A RAPIDLY ROTATING ANNULUS

\*

Sunghwan Jung, Brian D. Storey, Julien Aubert, and Harry L. Swinney  
`sunnyjsh@chaos.utexas.edu`

*Center for Nonlinear Dynamics, The University of Texas at Austin, Austin, Texas 78712 USA.*

## Abstract

We have conducted experiments on turbulence in a rapidly rotating annular tank. The flow is driven by pumping fluid into the tank through a semi-circle of holes; the fluid flows out through a semi-circle of holes on the opposite side of the annulus. We model the system using statistical mechanics with a non-extensive entropy. Assuming conservation of potential enstrophy and energy, we deduce a mean vorticity profile that agrees with the observations. Further, we find that the probability distribution for the vorticity is better fit by nonextensive than extensive theory.

Equilibrium statistical mechanics has long been used to model two-dimensional (2D) turbulence, but 2D turbulent flows can at best only be approximated in real systems [1]. Thin electrolytic layers and soap films [2] are used as approximately 2D systems but are limited by 3D dissipation and low Reynolds number. We use rapid rotation to achieve quasi-2D flow (Rossby number =  $5.3 \times 10^{-2}$ ), and strong pumping of fluid produces small-scale vortices that drive a turbulent flow (Reynolds number = 7000). Further, the annulus is tall so that the Ekman dissipation in the top and bottom boundary layers is small (Ekman number =  $5 \times 10^{-4}$ ); that is, vortex turnover time is short compared to the Ekman time. Measurements of the vorticity field in this system were reported in [3].

Here we examine the applicability of nonextensive statistical mechanics to our turbulent flow. The flow contains coherent vortices with sizes

\*This work is supported by O.N.R.

ranging up to the size of the system. The presence of large coherent structures indicates long range correlations, which suggests that a nonextensive theory would be more appropriate than the usual Boltzmann-Gibbs extensive statistical theory. Our analysis uses the Tsallis nonextensive generalization of entropy in statistical mechanics [4]. This approach has proved to be useful in describing the statistics of turbulence [5].<sup>1</sup> We propose a new model by following the statistical approach of Miller[1], who obtained relationships for the measurable (“dressed”) vorticity in turbulent 2D flow from consideration of the “microscopic vorticity” [6].

Our experiments were conducted on flow in an annular tank described in [3].<sup>2</sup> Particle Image Velocimetry (PIV) is used to obtain the full 2D velocity field.

We have found that maximizing either the extensive or the nonextensive entropy[6] leads to the same expression relating the streamfunction and the vorticity,  $\omega = -\nabla^2\psi$ :

$$\nabla^2\psi - (\beta_{\text{Ross}}r + \frac{\beta}{2\gamma}\psi) = 0, \quad (1)$$

which shows a linear relationship between  $\psi$  and  $\omega$ . The Rossby parameter  $\beta_{\text{Ross}}$  is determined by the geometry of the system, and the parameter  $\frac{\beta}{2\gamma}$  is obtained by fitting Eq. 1 to the streamfunction  $\psi$  from the experiment, using appropriate boundary conditions.<sup>3</sup>

We have derived expressions for Miller’s dressed vorticity[1] using the conservation of energy and potential enstrophy in both the extensive and nonextensive statistical approaches,

$$p^{\text{ext}}(\omega) \propto \int d\vec{r} \frac{1}{\phi(\vec{r})} e^{-\gamma\phi(\vec{r})^2} \sinh(2\gamma\alpha\phi(\vec{r})) \quad (2)$$

$$p^{\text{nonext}}(\omega) \propto \int d\vec{r} \frac{f(\omega)}{\phi(\vec{r})} \left[ 1 - \frac{(1-q)\gamma}{f(\omega)} \phi(\vec{r})^2 \right]^{\frac{q}{1-q}} \left\{ \left[ 1 + 2 \frac{(1-q)\gamma\alpha}{f(\omega) - (1-q)\gamma\phi(\vec{r})^2} \phi \right]^{\frac{1}{1-q}} \right. \\ \left. - \left[ 1 - 2 \frac{(1-q)\gamma\alpha}{f(\omega) - (1-q)\gamma\phi^2} \phi(\vec{r}) \right]^{\frac{1}{1-q}} \right\} \quad (3)$$

where, as shown in [6],  $\phi(\vec{r}) := \omega + \beta_{\text{Ross}}r + \frac{\beta}{2\gamma}\psi(\vec{r})$ ,  $\alpha$  is the fluctuation limit of the microscopic vorticity and  $\gamma$  is the Lagrange multiplier in front of the potential enstrophy.

The experimental result for the vorticity, averaged in the azimuthal direction, is compared in Fig. 1 with the prediction that we have obtained from nonextensive statistical mechanics. The two curves have the same qualitative features, the difference arising in part from the assumption of an inviscid fluid in the model. The inviscid model cannot

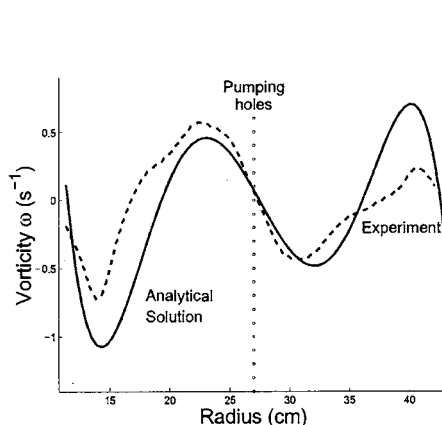


*Figure 1.* A comparison of the predicted radial dependence of azimuthally averaged vorticity (solid line, Eq. 1 with  $\frac{\beta}{2\gamma} = -0.158$ ) with measurements for a 2.5 Hz rotation rate and  $= 150 \text{ cm}^3/\text{s}$  pumping rate.

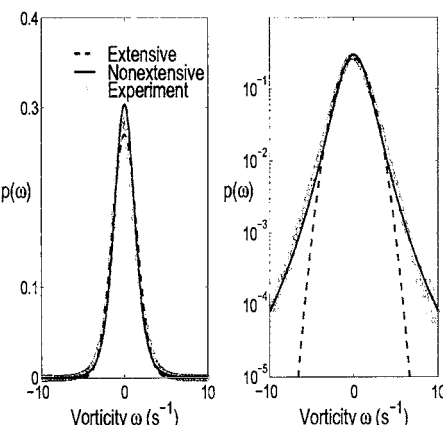


*Figure 2.* A comparison of the predicted PDF for the vorticity given by extensive theory (Eq. 1, dashed curves) and nonextensive theory (Eq. 2, solid curves) with the experimental data (2.5 Hz rotation rate and  $= 150 \text{ cm}^3/\text{s}$  pumping rate). A linear plot of the PDF is shown on the left to emphasize the fit near the peak, and a log plot is shown on the right to emphasize the fit in the tails.

capture a prominent feature of the data, the production of vortices at the inner and outer walls; these vortices certainly must affect the vorticity distribution in the interior of the annulus.

The PDF for the vorticity predicted by our extensive and nonextensive analyses is compared with our measurements in Fig. 2. The parameter values obtained in a least-squares fit to the nonextensive model are  $q = 1.9 \pm 0.2$ ,  $\gamma = 0.146 \pm 0.006$  and  $\alpha = 0.7 \pm 0.2$ ; for the extensive model,  $\gamma = 0.25 \pm 0.03$  and  $\alpha = 0.7 \pm 0.2$ . The nonextensive model fits the data well over the entire range including both the peaks and the tails of the PDF. The broad tails of the distribution arise because of the large vortices that form when small vortices of like sign merge.

In summary, we have found that the assumptions of energy and potential enstrophy conservation in a rapidly rotating inviscid flow lead in nonextensive statistical theory to predictions for the vorticity PDF and the radial dependence of the vorticity that agree well with our measurements on turbulent flow in a rapidly rotating annular tank. The

nonextensive theory yields broad tails of the PDF, which are not explained by extensive theory.

## Notes

1. For 3D turbulence, the assumption that an effective energy is conserved leads to a probability distribution functions (PDF) for velocity differences that fit data over a wide range of length scales. However, the assumption of conserved effective energy is not valid in a rotating fluid system.

2. The tank has an inner radius ( $r_i = 10.8$  cm), outer radius ( $r_o = 43.2$  cm), a sloping bottom and is covered by a solid transparent lid. The tank is spun with rotation frequencies  $\Omega/2\pi$  up to 2.5 Hz. The bottom depth varies from 17.1 cm at the inner radius to 20.3 cm at the outer radius. Water is continuously pumped through the tank in closed circuit via a ring of 120 circular holes located at the bottom of the tank. The overall pumping rate is between 150 and 350 cm<sup>3</sup>/s. The forcing holes are located at the mean radius of the annulus,  $r_f = 27$  cm. In order that zonal flow is not directly forced, the forcing is arranged in two semi-circles: one semi-circle of the forcing ring contains sources and the opposite semi-circle contains sinks.

3. The condition  $\int \omega|_{r=r_f} d\theta = 0$  holds since the forcing holes act as sources in one semi-circle and sinks in the opposite semi-circle on a ring at  $r = r_f$ . The second boundary condition is the conservation of the total circulation,  $\oint \vec{u} \cdot d\vec{l} = 0 = \int d\vec{r} \omega$ .

## References

- [1] D. Lyden-Bell, M. Not. R. Astron. Soc., **136**, 101, (1967), R.H. Kraichnan, Phys. Fluids **10**, 1417, (1967), J. Miller, Phys. Rev. Lett. **65**, 2137, (1990)
- [2] P. Tabeling, Phys. Rep., **362**, 1, (2002)
- [3] J. Aubert, S. Jung and H.L. Swinney, Geophys. Res. Lett. 015422, (2002)
- [4] C. Tsallis, J. Stat. Phys. **52**, 479, (1988), C. Tsallis, Braz. J. Phys. **29**, 1, (1999)
- [5] C. Beck, G.S. Lewis, and H.L. Swinney Phys. Rev. E **63**, 035303, (2001)
- [6] S. Jung, B.D. Storey, J. Aubert, and H.L. Swinney, in preparation.
- [7] C.N. Baroud, B.B. Plapp, Z.S. She and H.L. Swinney, Phys. Rev. Lett. **88**, 114501 (2002)
- [8] G. Holloway, Ann. Rev. Fluid Mech., **18**, 91, (1986)

# A UNIFIED THEORY FOR THE ORIGIN OF TURBULENCE AND ITS SUBSEQUENT EVOLUTION

S. C. Ling and H. P. Pao

*The Catholic University of America  
School of Engineering  
Washington, D.C. 20064*

**Abstract:** Through both experimental and analytical studies of the structure of fluid turbulence, it was found that turbulence possesses unique structures throughout its life cycle. That is, in the form of interacting line vortices. Although fluid is a continuum of particles, its basic dynamics is noted to be analogous to the particle mechanics of atom, planet and galaxy. That is, they all tend to follow the same *least-action* law of universe.

**Key words:** turbulence, line vortices, production, and evolution.

## INTRODUCTION

Up to the present twenty-first century, the subject of turbulence is still being looked upon as something that is totally random after its orderly birth. So far, this point of view and assumption has not led to a conclusive understanding of the subject. From my past measurements of a decaying turbulent-flow field, I found that turbulence has a very long distance correlation (Ling and Saad 1977). During a subsequent water-tunnel study of the inception of cavitation, I found that turbulence is formed initially by interacting line vortices, which are subsequently intensified through the straining action of the mean shearing-flow field (Ling et al. 1983). Based on these past studies, I have finally realized that all turbulence should maintain a very stable, interacting, vortex-line structure throughout its entire life cycle; but why?

## STRUCTURE OF A VORTEX LINE AT INCEPTION

When a realistic fluid is subjected to any differential motions that create shear stresses of sufficient spatial extent and intensity, it should, by the variation principle, transform into a lesser stress state of line vortices. If this is true, then a turbulent flow field should consist mainly of interacting line-vortices throughout its life cycle. Because the basic structure of turbulence consists mainly of interacting line vortices, it is of particular interest, to find out more about the velocity field of a vortex line at the moment of its birth. Based on the vortex model of Tan and Ling (1963) that has a minimum of

generation time, the universal structure of an isolated newborn line-vortex can be expressed as

$$V = \frac{4.88}{R} \left[ \exp \frac{-R^2}{(2.94 + \tau)} - \exp \frac{-R^2}{(1.47 + \tau)} \right], \quad (1)$$

where  $\tau = 4\upsilon t/r_o^2$  is the normalized decay-time  $t$ , and  $\upsilon$  kinematic viscosity.  $V = \upsilon/\upsilon_o$  is the normalized circulating-velocity  $\upsilon$ , and  $R = r/r_o$  the normalized radius  $r$ . Subscript  $o$  indicates the value at maximum  $\upsilon$  for  $t = 0$ . See Fig.1.

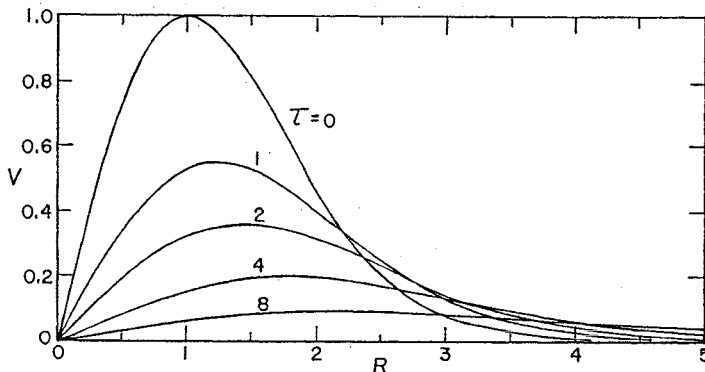


Figure 1. Universal diffusion and decay of an isolated line-vortex.

It is important to note from Eq.1 that the energy of a vortex will decay to 70% at a normalized decay-time of  $\tau = 0.4$ . Hence, for a large vortex with  $r_o = 1$  m the corresponding decay-time is  $t = 28$  hrs in water, or 7 hrs in air. That is why the wingtip vortex from a jumbo jet is so destructive to encounter in flight, while a small vortex with  $r_o = 0.5$  cm will decay to the same condition within 2.5 s and 0.63 s, respectively.

## PRODUCTION OF FLUID TURBULENCE

In the preceding sections we have identified line vortices as the preferred shearing-flow structure for a continuum, in which the volumetric stress is the least. This is, in part, analogous to the micro mechanics of an atomic particle, in which the electrons spin around a nuclear is based on the quantum principle of *least action*. The same may be extended to the celestial mechanics of planets and galaxies. That is, in these basic motions of nature, the centrifugal force of motion balances the electromagnetic or gravitational force. For a vortex-line element, its centrifugal force of motion is balanced by the pressure force; thus satisfying the same principle of least action. This is why a line vortex is a unique flow-structure that can be subjected to all forms of interaction; such as with a larger scale mean-motion, another vortex line, a flow boundary, and also self-interaction.

The basic phenomenon of turbulence was first experimentally observed through the study of the inception of cavitation (Ling et al., 1983). At the inception of cavitation for a turbulent boundary-layer flow, one observes micro-gas-cavity lines that appear like fine hairs originating from the flow boundary and streaming in the flow direction with an altitude angle of approximately  $45^\circ$  from the wall. By knowing the water-tunnel pressure and speed at various stages of cavitations, the strength of the cavitating line vortices can be determined. Therefore, knowing the quantitative developing sequences for these line vortices, one can simulate the production of hairpin vortices through a numerical-integration process.

To perform a simplified numerical analysis for the observed dynamic-process (Ahmad, Pao and Ling, 1995), one first assumes that there is a universal mean turbulent-flow field consisting of a steady laminar-sublayer and a logarithmic turbulent-flow layer. See Fig. 2. The mean velocity field is normalized as  $U^+ = U/U^*$ . The shear velocity  $U^*$  is defined as  $(\sigma_0/\rho)^{0.5}$ , where  $\sigma_0$  is the mean wall-shear-stress, and  $\rho$  the density of fluid. Since the development time for the formation of hairpin vortices is extremely short, the effect of fluid viscosity can be neglected; i.e., the rate of energy gained by the hairpin vortices is much greater than the rate of energy dissipated during this period. Therefore, the analytical model can be based upon the Boit-Savart line-integral equation where the vortex filaments are discretized in time steps with nodal points along the filaments. Subsequent motion and position of the node points are computed as the filaments develops in time and space. The following is a good representative analytical-simulation for the process. One first assumes that the pair of interacting line-vortices has both their axes, at the normalized time  $t^+ = tU^{*2}/\nu = 0$ , lain in a normalized horizontal plane of  $H^+ = HU^*/\nu = 70$ , and spaced  $W^+ = 150$  apart. The two line vortices are given the same maximum normalized circulation-strength of  $\Gamma_0^+ = \Gamma_0/\nu = 1000$ . The leading vortex-line is assumed to be straight, and is depicted as the solid line, while the trailing vortex-line is wavy and is shown as the dashed line. As the action evolves in time, there is the production of stronger hairpin-vortices; where the initial normalized peak-circulation velocity  $v_0^+ = v_0/U^*$  is increased from 3 to 11. See Fig. 2. This action provides a peak-turbulence intensity ratio of approximately  $(v_0^+ \cos 41^\circ + U_0^+)/U_0^+ = (7.8 + 22)/22 = 1.4$ , which is commonly detected at the intermediate layer of a turbulent boundary-layer flow. Following the rapid inception of turbulence, the line vortices are generally left to decay slowly in the wake field. From the previous cited references concerning the decay of turbulent-flow fields, it was found that turbulence generated by nearly all types of mechanisms, energies and scales, possesses a universal long-distance velocity correlation-function, which is close to a Cauchy distribution-function for both low and high Reynolds numbers (Ling and

Saad 1977). This clearly indicates that a decaying turbulence maintains a unique interacting line-vortex structure throughout its life span.

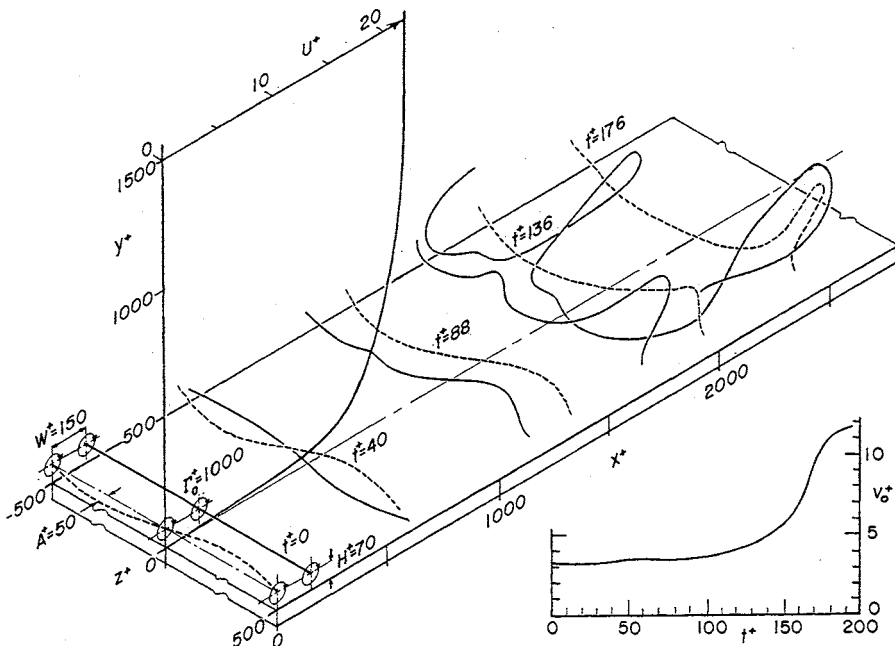


Figure 2. Isometric view of the development of hairpin vortices over a flow boundary.

## CONCLUSIONS

This paper provides a unified treatment for the origin of turbulence and its subsequent evolution that is based on *the principle of least action and stress*. As a logical extension, one might consider that the present state of universe to be the remnant of a *turbulent Big-Bang* process.

## REFERENCES

- Ahamad, H. D., Pao, H. P. and Ling, S. C. (1995), "Numerical simulation of the generation of micro-hairpin vortices," Turbulent Flows, FED Vol. 208, ASME, p. 43-47.
- Ling, S. C. and Saad, A. (1977), "Experimental study of the structure of isotropic turbulence with intermediate range of Reynolds number," Phys. of Fluids, Vol. 20, No. 11, p. 1796-1799.
- Ling, S. C., Gowing, S. and Shen, Y. T. (1983), "The role of micro-bubbles on cavitation inception on head forms," Fourteenth Symposium Naval Hydrodynamics, National Academy Press, p. 547-575.
- Tan, H. S. and Ling, S. C. (1963), "Final-stage decay of a single line vortex," J. of AIAA, Vol. 1, No. 5, p. 1193-1194.

# A REYNOLDS NUMBER INDEPENDENT MODEL FOR TURBULENCE IN COUETTE FLOW

Kumar Bobba, John Doyle and Mory Gharib

*Division of Engineering and Applied Science  
California Institute of Technology, Pasadena, CA  
bobba@galcit.caltech.edu*

**Abstract** In this paper we study theoretically and computationally the dynamics of linearized stream-wise constant Navier-Stokes equations, under external time varying deterministic disturbances.

**Keywords:** Turbulence, vortices, input-output measures.

## 1. Introduction

Hydrodynamic stability based on eigen values has been the main theoretical tool in understanding the dynamics of transition to turbulence in various fluid flows [4]. Though the roots of hydrodynamic stability have been established more than 100 years ago, we are yet far away from a complete theory of stability of fluids. In this paper we consider the effect of more general disturbances on fluid. We study the dynamics of 2D/3C Navier-Stokes equations linearized about Couette flow, under external time varying deterministic disturbances. We characterize the system behaviour using induced norms ( $L_1 \rightarrow L_2$ ,  $L_2 \rightarrow L_\infty$ )<sup>1</sup> and analytically compute these norms. The norms are then solved computationally. The results indicate that these induced norms peak at approximately the span wise wavenumber of stream-wise vortices observed in the boundary layer.

## 2. Globally stable 2D/3C equations

The model we study in this paper is stream-wise constant incompressible Navier-Stokes equations. Since this model depends on two space dimensions ( $y, z$ ) and has three velocities ( $u, v, w$ ) we call this 2D/3C model [2]. In the velocity-stream function formulation 2D/3C model

can be written as

$$v := \psi_z := \frac{\partial \psi}{\partial z}, \quad w := -\psi_y := -\frac{\partial \psi}{\partial y} \quad (1)$$

$$u_t = -\psi_z u_y + \psi_y u_z + \frac{1}{R} \Delta u \quad (2)$$

$$(\Delta \psi)_t = -\psi_z (\Delta \psi)_y + \psi_y (\Delta \psi)_z + \frac{1}{R} \Delta^2 \psi \quad (3)$$

$$u(\pm 1, z, t) = \pm 1, \quad \psi_z(\pm 1, z, t) = \psi_y(\pm 1, z, t) = 0 \quad (4)$$

This 2D/3C model has some very interesting features. In our previous work [1] we showed theoretically that this 2D/3C model is globally nonlinearly stable for all Reynolds number  $R$  about Couette flow, total energy scales like  $R^3$  and time scales like  $R$ . We have also shown that  $R$  can be eliminated from the equations by a transformation. The transformation leaves the boundary conditions invariant. Even though the only attractor for the above equations is laminar flow, we will show in the next section that these equations have interesting dynamics if looked at the right measures.

### 3. Analysis of 2D/3C equations

In this section we study the effect of time varying  $L_1$  and  $L_2$  disturbances on the linearized 2D/3C equations about Couette flow [5]. We model the disturbance as an additive forcing to the discretized linearized 2D/3C equations. The discretized linearized 2D/3C equations can be represented in following operator form

$$\dot{x}(t) = Ax(t) + Bw(t), \quad y(t) = Cx(t), \quad x(0) = x_0 \quad (5)$$

Here  $C$  is the output operator, i.e. it gives information about the variables we are interested in tracking. The operator  $B$  captures the structure of the disturbance and  $w(t)$  is the disturbance. In this paper  $B$  is chosen to be identity matrix, and  $C$  is chosen such that  $\|y(t)\|_2^2$  is the kinetic energy of the fluid.  $\|\cdot\|$  with subscript denotes appropriate norm.

#### 3.1 Impulse to energy induced norm

One can construct the solution to (5) from its Greens function  $g(t) = e^{At} BH(t)$ . Where  $H(t)$  is the Heaviside function. The solution is given by

$$y(t) = \int_{-\infty}^{\infty} g(t - \tau) w(\tau) d\tau \equiv (C_g w)(t) \quad (6)$$

$C_g$  is the convolution operator associated with  $g(t)$  and defined as above. One can think of convolution operator as a map  $C_g : w(t) \mapsto y(t) =$

$C_g w(t)$ . In this section we calculate the  $L_1 \rightarrow L_2$  induced norm of this map. Using (6)

$$\|y(t)\|_{L_2} = \left\| \int_{-\infty}^{\infty} g(t-\tau)w(\tau)d\tau \right\|_{L_2} \quad (7)$$

Applying the Minkowski inequality we get

$$\|y(t)\|_{L_2} \leq \int_{-\infty}^{\infty} \|g(t-\tau)w(\tau)\|_{L_2} d\tau \quad (8)$$

From the definition of  $L_2$  norm it follows that

$$\|y(t)\|_{L_2} \leq \int_{-\infty}^{\infty} \left[ \int_{-\infty}^{\infty} w^*(\tau)g^*(t-\tau)g(t-\tau)w(\tau)dt \right]^{\frac{1}{2}} d\tau \quad (9)$$

Here  $*$  is conjugate transpose. Making a change of variable and substituting the Greens function

$$\begin{aligned} \int_{-\infty}^{\infty} w^*(\tau)g^*(t-\tau)g(t-\tau)w(\tau)dt &= w^*(\tau) \left[ \int_{-\infty}^{\infty} g^*(u)g(u)du \right] w(\tau) \\ &= w^*(\tau) \left[ \int_0^{\infty} B^* e^{A^* u} C^* C e^{Au} B du \right] w(\tau) \end{aligned} \quad (10)$$

Defining  $X_o = \int_0^{\infty} e^{A^* u} C^* C e^{Au} du$  and substituting this we get

$$\|y(t)\|_{L_2} \leq \int_{-\infty}^{\infty} [w^*(\tau)(B^* X_o B)w(\tau)]^{\frac{1}{2}} d\tau \leq \|B^* X_o B\|_{\infty} \int_{-\infty}^{\infty} \|w(\tau)\|_2 d\tau \quad (11)$$

Therefore

$$\|C_g\|_{L_1 \rightarrow L_2} = \frac{\|y(t)\|_{L_2}}{\|w(t)\|_{L_1}} \leq \|B^* X_o B\|_{\infty} \quad (12)$$

In the appendix it is shown that the above bound can be achieved. We call this impulse to energy induced norm, since the worst case disturbance is an Delta function, and the total energy is given by the  $L_2$  norm of  $y(t)$ .

### 3.2 Energy to peak induced norm

In this section we compute analytically the  $L_2$  to  $L_{\infty}$  induced norm of the above map. Though there are other ways of computing this norm, we compute this here using the duality pairing argument based on previous case as it is very concise. First we note that the dual of  $L_1$  is  $L_{\infty}$  and the dual of  $L_2$  is  $L_2$ . We shall denote the dual by superscript  $\dagger$ . From the definition of dual [6] we have the following relations

$$C_g : L_1 \rightarrow L_2, \quad w \mapsto C_g w; \quad C_g^{\dagger} : L_2^{\dagger} = L_2 \rightarrow L_1^{\dagger} = L_{\infty}, \quad z \mapsto C_g^{\dagger} z \quad (13)$$

$$\langle z, C_g w \rangle = \langle C_g^{\dagger} z, w \rangle, \quad \|C_g\|_{L_1 \rightarrow L_2} = \|C_g^{\dagger}\|_{L_2 \rightarrow L_{\infty}} \quad (14)$$

Where  $\langle \cdot, \cdot \rangle$  denote duality pairing in the appropriate space. Using the above equalities and (6)

$$\langle z, C_g w \rangle = \int_{-\infty}^{\infty} z^*(t) C_g w(t) dt = \int_{-\infty}^{\infty} z^*(t) \left[ \int_{-\infty}^{\infty} g(t-\tau) w(\tau) d\tau \right] dt \quad (15)$$

One can exchange the first and second integrals by Fubinis theorem giving

$$\langle z, C_g w \rangle = \int_{-\infty}^{\infty} \left[ \int_{-\infty}^{\infty} g^*(t-\tau) z(t) dt \right]^* w(\tau) d\tau = \langle C_g^\dagger z, w \rangle \quad (16)$$

Therefore

$$(C_g^\dagger z)(t) = \int_{-\infty}^{\infty} g^*(-(t-\tau)) z(\tau) d\tau \quad (17)$$

It follows that  $C_g^\dagger = C_{g^*}$ , where  $C_{g^*}$  is the convolution operator associated with  $g^*(-t)$ . Hence, given a map  $C_g : L_2 \rightarrow L_\infty$ ,  $w \mapsto C_g w$ , it follows that this is dual map of  $C_{g^*} : L_1 \rightarrow L_2$ ,  $w \mapsto C_{g^*} w$ . Defining  $X_c = \int_0^\infty e^{Au} BB^* e^{A^* u} du$  it follows from (10,12,14) that

$$\|C_{g^*}\|_{L_1 \rightarrow L_2} = \|CX_c C^*\|_\infty = \|C_g\|_{L_2 \rightarrow L_\infty} = \frac{\|y(t)\|_{L_\infty}}{\|w(t)\|_{L_2}} \quad (18)$$

## 4. Results

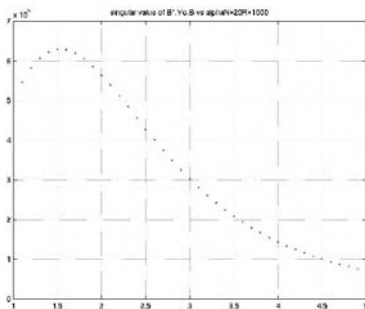
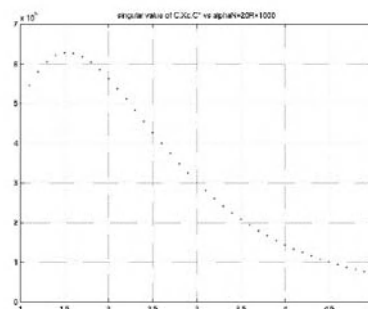
Computations done with spectral methods are discussed briefly below. For details see [3]. The results presented here are at  $R = 1000$ . In Figure(1) and Figure(2) are plotted the impulse to energy norm vs spanwise wave number  $\alpha$  and energy to peak induced norm vs  $\alpha$  respectively. From the plots we observe that both the norms peak at  $\alpha = 1.5$ . This peak corresponds to the near wall stream-wise vortices in the channel flows. By doing a search over the parameter space, it was also found that this wave number at which peak occurs is independent of  $R$  for approximately  $R > 50$ .

## 5. Conclusions

In this paper we studied theoretically and computationally the dynamics of linearized stream-wise constant Navier-Stokes equations, under external time varying deterministic disturbances. The results indicate that induced norms peak at approximately the span wise wavenumber of stream-wise vortices observed in the transiting boundary layer.

## Appendix: Tightness of bound

Let  $w_o$  be the normalized singular vector corresponding to the maximum singular value of  $B^* X_o B$  i.e.  $B^* X_o B w_o = \sigma_1 w_o$ . Now defining a sequence of func-

Figure 1.  $\|B^* X_0 B\|_\infty$  vs  $\alpha$ Figure 2.  $\|C X_c C^*\|_\infty$  vs  $\alpha$ 

tions parameterized by  $\epsilon$  such that  $w^\epsilon(t) = w_o \delta^\epsilon(t)$ ,  $\|w(t)\|_{L_1} = 1$  and  $\delta^\epsilon(t) \rightarrow \delta(t)$  as  $\epsilon \rightarrow 0$ . Taking the limit carefully, we have  $y^\epsilon(t) \rightarrow y(t) = g(t)w_o$ . Therefore  $\|C_g\|_{L_1 \rightarrow L_2} = \|B^* X_0 B\|_\infty$

## Notes

1.

$$\|w(t)\|_{L_1} = \int_{-\infty}^{\infty} \|w(t)\|_2 dt, \quad \|w(t)\|_{L_2} = [\int_{-\infty}^{\infty} \|w(t)\|_2^2 dt]^{\frac{1}{2}}, \quad \|w(t)\|_{L_\infty} = \sup_{-\infty \leq t \leq \infty} \|w(t)\|_2$$

## References

- [1] Bobba, K. M., Bamieh, B., and Doyle, J. C. (2002). Robustness and Navier-Stokes Equations, *IEEE 2002 Conference on Decision and Control*, Dec 10-13, Las Vegas, Nevada, USA.
- [2] Bobba, K. M., Bamieh, B., and Doyle, J. C. Highly Optimized Transitions to Turbulence, *submitted to Phys. Rev. Lett.*
- [3] Bobba, K. M. and Doyle, J. C. Uncertainty Analysis of Transition to Turbulence in 2D/3C Couette Flow, *to be submitted to Phys. Fluids*.
- [4] Drazin, P. G., and Reid, W. H. (1981). *Hydrodynamic Stability*, Cambridge University Press.
- [5] Wilson, D. A. (1989). Convolution and Hankel Operator Norms for Linear Systems, *IEEE Transactions on Automatic Control*, 34:1:94-97.
- [6] Yoshida, Y. (1980). *Functional Analysis*, Springer-Verlag, pages 193-195.

# SCALING OF THE NEAR-WALL LAYER BENEATH REATTACHING SEPARATED FLOW

Philip E. Hancock

*Fluids Research Centre*

*School of Engineering, University of Surrey, UK*

[p.hancock@surrey.ac.uk](mailto:p.hancock@surrey.ac.uk)

**Abstract** The fluctuating velocity in the near-wall layer is shown to scale on the fluctuating wall shear stress such that it has the form  $u'/u'_\tau = f(u'_\tau y/\nu)$ , where  $u'_\tau$  is a velocity based on the r.m.s of the wall shear stress fluctuation and  $u'$  is the r.m.s velocity. The observed dependency on  $u'_\tau y/\nu$ , which is independent of mean velocity and mean wall shear stress, exhibits a logarithmic region which extends to about 0.1 of the bubble height, and the viscous sublayer is quadratic in behaviour.

**Keywords:** Separated flow, near-wall layer

## 1. Introduction

It is clearly the case that a velocity scale based on the mean wall shear stress,  $\tau$ , cannot be appropriate for the near-wall turbulence in the vicinity of separation or attachment. This paper examines the use of the shear stress fluctuation as a basis for such a scale, in terms of the r.m.s of the (kinematic) shear stress fluctuation ( $\tau''/\rho$ ), namely the velocity scale,  $u'_\tau = \sqrt{\tau'/\rho}$ , where  $\tau' = \sqrt{\tau''^2}$ . Measurements show  $\tau'$  to remain large where  $\tau$  changes sign (fig. 2), as is to be expected.

Motions near a wall arise from scales of the order of the distance from the wall and larger. The motions in the outer part of a separated flow, where the intensities are large, are much larger in scale ( $L$ ) than the thickness of the near-wall layer and generate sweeping, inactive-type motions [e.g. [1]]. The simplest possible description for the tangential (r.m.s) velocity near the surface would be that it scales on  $y$ ,  $u'_\tau$  and  $\nu$ , where  $y/L$  is small enough for it to be of secondary importance. Therefore, we have that  $u'/u'_\tau = f(u'_\tau y/\nu)$ .

This is a direct counterpart to the classical argument for the inner layer of a boundary layer. There, the idea of inactive motion is needed to account for the (empirical) robustness of the inner layer scaling of the mean flow even though the tangential velocity fluctuations do not scale on  $u_\tau (= \sqrt{\tau/\rho})$ , as for instance in an adverse pressure gradient. This arises because a mean-flow scale is used for the near-wall turbulence. Here, we are using a scale derived from the turbulent fluctuations, and so the idea of inactive motion is not needed. Furthermore, if there is a region in which viscosity is insignificant, but where there is a gradient of  $u'$ , then we might anticipate  $\partial u'/\partial y \sim u'_\tau/y$ , leading to the familiar logarithmic form  $u'/u'_\tau = A + B \ln(u'_\tau y/\nu)$ , where  $A$  and  $B$  are constants, and where consistency with the viscous form has been imposed, providing a length scale for  $y$ . (Dimensionally, this is not unique as  $\partial u'^n/\partial y \sim u'^n_\tau/y$ , but for the present  $n$  is taken as unity.) For scaling of the mean flow see e.g. [2].

## 2. Experimental Set-up

Measurements were made using Pulsed-Wire-Anemometry (PWA) for velocity and wall shear stress in the near-wall layer beneath reattachment. PWA is designed to measure highly turbulent flows as arise in turbulent separated flows. The flow was generated by means of a normal flat plate mounted on the front of a horizontal splitter plate, as illustrated in figure 1, supported in the centre of the wind tunnel, of height 500mm. The fence height,  $h_f$ , of the normal plate above the splitter plate was 10.0mm.  $U_r$  was 5.9m/s and the Reynolds number,  $U_r h_f / \nu$ , was 3900. The distance to attachment,  $X_A$ , was 216mm, and the flow width was about  $7X_A$  implying the flow near the measurement plane would have been closely two-dimensional [3].

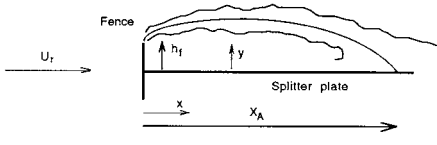


Figure 1. Flow rig.  
(Not to scale.)

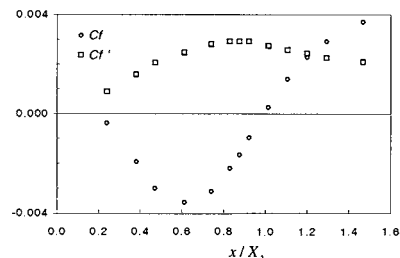


Figure 2. Coefficients of mean and fluctuating wall shear stress.

A special probe was built to measure the tangential velocity fluctuations close to the surface. Some correction in the very near-wall region is

needed because of a diffusion error that arises in regions of high velocity shear [4, 5], significant only inside  $u'_\tau y/\nu \sim 10$  or less. The pulsed-wire wall shear stress probe is one of the few methods of measuring the fluctuating wall shear stress in reversing flow. Once calibrated (in a standard turbulent boundary layer against a Preston tube) it provides a direct measure of shear stress in high intensity flows.

### 3. Results

Figure 2 shows coefficients of mean wall shear stress and the r.m.s. wall shear stress fluctuation,  $C_f$  and  $C'_f$ , respectively. As stated earlier,  $\tau'$  remains finite and 'large' through reattachment. Figure 3 shows the streamwise mean velocity profiles  $U(y)$  in the near-wall region, normalised by the free-stream reference speed,  $U_r$ , and figure 4 shows the streamwise Reynolds stress,  $\overline{u^2}$ .

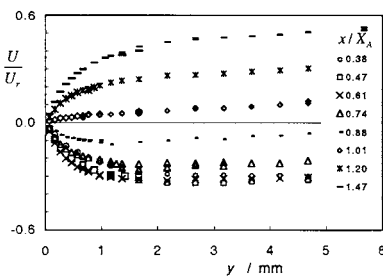


Figure 3. Mean velocity profiles.

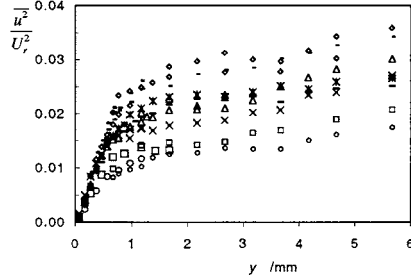


Figure 4. Mean square of fluctuating velocity. Symbols as in fig. 3.

Figure 5 shows the measurements of figure 4 but now in terms of  $u' = \sqrt{\overline{u^2}}$  normalised by the friction velocity based on the r.m.s of the local fluctuating wall shear stress,  $u'_\tau$ .  $y$  is normalised by  $\nu/u'_\tau$ . Clearly, i) to within the accuracy of the measurements, the measurements fall close to a single curve and, reminiscent of the mean velocity profile in the classical boundary layer, ii) there is a viscous sub-layer, as is to be expected, and iii) an approximately logarithmic region. The logarithmic region extends between about  $u'_\tau y/\nu = 15$  and 70. This outer edge is about 0.1 bubble heights - the edge of the bubble was at  $u'_\tau y/\nu$  of roughly 800. If this fraction of 0.1 is independent of Reynolds number then the extent of the logarithmic region in terms of  $u'_\tau y/\nu$  will increase with Reynolds number.

The line in figure 5 is from [6] and is for a sinusoidally oscillating viscous sub-layer. A consequence of this is that the viscous sub-layer is

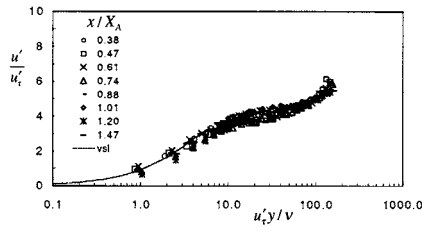


Figure 5.  $u'/u'_r$  as a function of  $u'_r y / v$

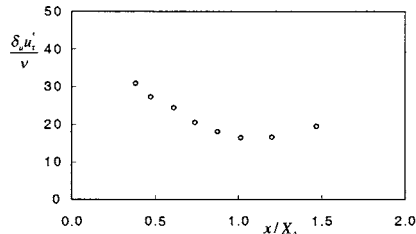


Figure 6. Extent of viscous effects,  $\delta_v$ .

linear only in the limit as  $y$  tends to zero; it is initially quadratic (as can be seen from various DNS data for wall flows).

Figure 6 shows the thickness,  $\delta_v$ , of the viscous-dominated part of the mean velocity profiles of figure 3, normalised by  $\nu/u'_r$ , as a function of  $x/X_A$ .  $\delta_v$  has been obtained from the profiles of  $U(y)$  as the point at which there is an incipient change in gradient, and is therefore only approximate. Nevertheless, figure 6 shows that viscous effects do not reach beyond a  $u'_r y / \nu$  of 30 for the profiles of figure 5. In the apparently logarithmic region the mean velocity gradients  $\partial U / \partial y$  and  $\partial U / \partial x$  are very much less, by about three orders, than the largest magnitude of  $\partial U / \partial y$  at  $y = 0$ . This is consistent with the lack of dependency on  $x$  of the profiles in figure 5.

## References

- [1] Fernholz, H. H. Near-wall phenomena in turbulent separated flows. *Acta Mechanica*, [Suppl] 4, 57-67, 1994.
- [2] Hardman, J. R. and Hancock, P. E. The near-wall layer beneath a moderately converging three-dimensional turbulent separated and reattaching flow. *Eur. J. Mech. B-Fluids*, 19:653-672, 2000.
- [3] Hancock, P. E. Low Reynolds number two-dimensional separated and reattaching flow. *J. Fluid Mech.*, 410, 101-122, 2000.
- [4] Schober, M., Hancock, P. E. and Siller, H. Pulsed-wire anemometry near walls. *Expts in Fluids*, 25, 151-159, 1998.
- [5] Hancock, P. E. Pulsed-wire measurements in the near-wall layer beneath reattachment. To be submitted.
- [6] Devenport, W. J. and Sutton, E. P. Near-wall behaviour of separated and reattaching flows. *AIAA J.*, 29, 25-31, 1991.

# HIGH-RESOLUTION DIRECT NUMERICAL SIMULATION OF TURBULENCE

– *Spectra of Fourth-Order Velocity Moments* –

Yukio Kaneda, Takashi Ishihara

*Department of Computational Science and Engineering,  
Graduate School of Engineering, Nagoya University, Chikusa-ku Nagoya 464-8603, Japan  
kaneda@cse.nagoya-u.ac.jp*

Mitsuo Yokokawa,\* Ken’ichi Itakura and Atsuya Uno  
*Earth Simulator Center, Japan Marine Science and Technology Center,  
Kanazawa-ku, Yokohama 236-0001, Japan*

**Abstract** High-resolution direct numerical simulations (DNSs) of incompressible turbulence based on an alias-free spectral method were performed on the Earth Simulator. Statistics of turbulence are studied by a DNS on  $1024^3$  grid points with a special emphasis on the spectra of moments fourth order in velocity. A brief review is given on some results of the preliminary analysis of the data of DNSs with up to  $2048^3$  grid points.

**Keywords:** Spectrum, Velocity quadratics, High-resolution DNS, Turbulence

## 1. Introduction

Owing to recent rapid and sustained development in hardware and computational algorithm, computational approaches are increasing their importance in the study of turbulence, as in many other fields in science and technology. Among the approaches is the method of direct numerical simulation (DNS) of turbulence, which provides us with detailed data on turbulence without experimental uncertainties, under well controlled conditions. There is in fact a long history of DNS of turbulence, especially that of canonical turbulence problems under simple geometri-

\* Present address: Grid Technology Research Center, Tsukuba Central 2, Tsukuba, 305-8568, Japan

cal boundary conditions (BCs), such as periodic BCs, which have been preferred from the view point of saving machine time and memory. However, even under such simple BCs, the degree of freedom or the resolution in the DNS is still severely limited by available computer memory and speed. In the pioneering study by Orszag(1969), the number of grid points ( $N^3$ ) was only  $32^3$ . Since then the number has increased rapidly. The increase has been almost exponential in time, (see, e.g., the review in Ishihara and Kaneda(2002)), and it has recently become possible to perform DNSs of incompressible turbulence with  $N = 1024$  or so. Such DNSs are expected to provide indispensable data for the study of turbulence in various aspects.

We performed high-resolution DNSs of incompressible turbulence in a periodic box on the basis of an alias-free spectral method on the Earth Simulator (ES). In Section 2, results of a DNS with  $N = 1024$  are presented with special emphasis on the spectra of the squares of velocity quadratics, which are fourth order in the velocity. In Section 3, a brief review is given on some results of the preliminary analysis of the data of DNSs on the ES with  $N$  up to 2048.

## 2. Spectra of fourth-order moments

Turbulence is a strongly nonlinear phenomenon. For example, consider the motion of an incompressible fluid of unit density, obeying the Navier-Stokes (NS) equations,

$$\frac{\partial}{\partial t} \mathbf{u} + (\mathbf{u} \cdot \nabla) \mathbf{u} = -\nabla p + \nu \nabla^2 \mathbf{u} + \mathbf{F}, \quad (1)$$

$$\nabla \cdot \mathbf{u} = 0, \quad (2)$$

where  $\mathbf{u}$ ,  $p$ ,  $\nu$ , and  $\mathbf{F}$  denote velocity, pressure, kinematic viscosity, and external force satisfying  $\nabla \cdot \mathbf{F} = 0$ , respectively. The term  $(\mathbf{u} \cdot \nabla) \mathbf{u}$  that represents one of the essence of turbulence, i.e., the effect associated with fluid motion is nonlinear in the velocity  $\mathbf{u}$ , and the nonlinearity is second order. The pressure is also second order in  $\mathbf{u}$ , because (1) and (2) give

$$\nabla^2 p = \left(\frac{1}{2}\omega^2 - e^2\right),$$

where  $e^2 \equiv e_{ij}e_{ij}$ ,  $e_{ij}$  ( $\equiv (\partial u_i / \partial x_j + \partial u_j / \partial x_i)/2$ ) is the rate of strain tensor,  $\omega = \text{rot } \mathbf{u}$  is the vorticity, and summation convention is used for repeated indices. Note also that the energy dissipation rate  $\epsilon = 2\nu e^2$  per unit mass, which is one of the key ingredients of many turbulence theories including Kolmogorov's theories, is also second order in  $\mathbf{u}$ . Thus

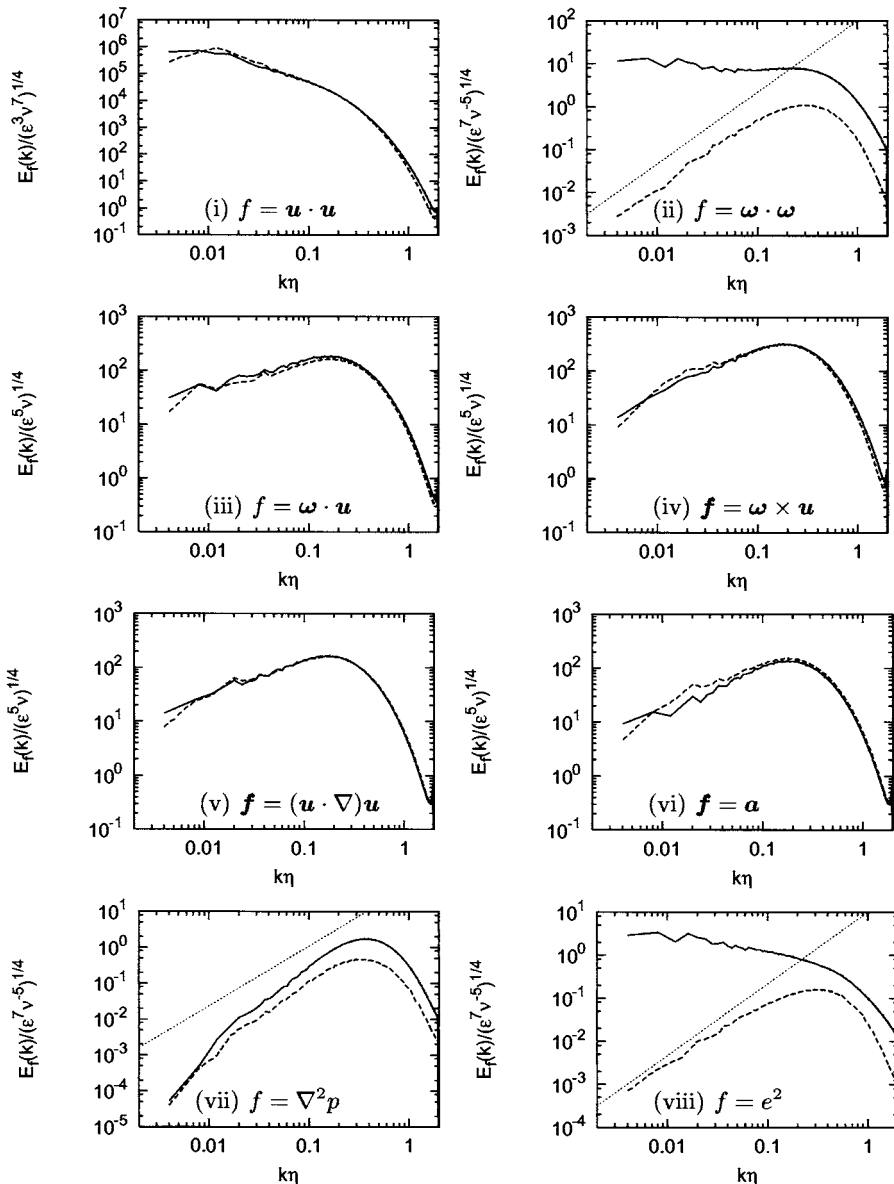


Figure 1. Spectra  $E_f(k)$  non-dimensionalized by  $\langle \epsilon \rangle$  and  $\nu$ , for  $f$ 's shown in the figures. In (vi),  $\boldsymbol{a} \equiv -(\mathbf{u} \cdot \nabla) \mathbf{u} - \nabla p$ . Solid and dotted lines are DNS and Gaussian values, respectively. Straight dotted lines show the slope  $\propto k^{5/3}$ .

the study of the statistics of velocity quadratics is expected to shed some light on our understanding of turbulence (see, e.g., Chen *et al.*(1989)).

Let  $f(\mathbf{x})$  be any of velocity quadratics, and  $\hat{f}(\mathbf{k})$  be its Fourier transform. Then, one of the most fundamental measures characterizing the statistics of  $f$  may be given by the spectrum  $E_f(k)$  defined as

$$E_f(k) = \sum_k \langle \hat{f}(\mathbf{q}) \hat{f}(-\mathbf{q}) \rangle,$$

where  $\sum_k$  denotes the sum over  $\mathbf{q}$  on the spherical shell satisfying  $k - \Delta k/2 < q \leq k + \Delta k/2$  (we put  $\Delta k = 1$  below), the brackets  $\langle \cdot \rangle$  denote the ensemble average, and we assume here  $E_f(k)$  to be well approximated by the sum  $\sum_k [\hat{f}(\mathbf{q}) \hat{f}(-\mathbf{q})]$  in one realization. When  $f$  is a vector, say  $\mathbf{f}$ ,  $\langle \hat{f}(\mathbf{q}) \hat{f}(-\mathbf{q}) \rangle$  is to be understood as  $\langle \hat{\mathbf{f}}(\mathbf{q}) \cdot \hat{\mathbf{f}}(-\mathbf{q}) \rangle$ .

Figure 1 shows the spectra  $E_f$ 's for various  $f$ 's by our recent DNS of forced turbulence obeying (1) and (2) in a periodic box with  $1024^3$  grid points. The method of the DNS is basically similar to those in our previous studies, and some of its details and run conditions may be found in Yamazaki *et al.*(2002) and Ishihara and Kaneda (2002). In the DNS, the minimum wavenumber is 1, and the maximum wavenumber  $k_{\max}$  and the kinematic viscosity were so chosen that  $k_{\max}\eta \sim 2$ , where  $\eta$  is the Kolmogorov length scale defined by  $\eta = (\nu^3/\langle \epsilon \rangle)^{1/4}$ . The Taylor micro-scale Reynolds number  $R_\lambda$  at a quasi-stationary state is 268, and the energy spectrum exhibits an inertial subrange (near  $k\eta = 0.02$ ) proportional to  $k^{-5/3}$ .

Figure 1 also shows the spectra obtained under the assumption that the joint probability distribution function of the velocity field is Gaussian. The spectra were obtained by first generating a fictitious Gaussian random field having exactly the same energy spectrum as the DNS field, and then measuring the spectra. The departure of the DNS values from the Gaussian values provides a simple and basic measure of the non-Gaussianity.

The comparison of the DNS and Gaussian values in Fig. 1 shows the followings:

- (1) The DNS spectra  $E_f(k)$  for  $f$ 's given by (i)  $\mathbf{u} \cdot \mathbf{u}$ , (iii)  $\boldsymbol{\omega} \cdot \mathbf{u}$ , (iv)  $\boldsymbol{\omega} \times \mathbf{u}$ , (v)  $(\mathbf{u} \cdot \nabla)\mathbf{u}$ , and (vi)  $\mathbf{a} \equiv -(\mathbf{u} \cdot \nabla)\mathbf{u} - \nabla p$  are close to those of the Gaussian field in the entire wavenumber range.
- (2) The DNS spectra  $E_f(k)$  for (ii)  $f = \boldsymbol{\omega} \cdot \boldsymbol{\omega} (\equiv \Omega)$  and (viii)  $f = e^2 (= \epsilon/(2\nu))$  are very different from those of the Gaussian field. The spectra of the Gaussian field scale like  $k^{5/3}$  in the inertial subrange, while the DNS spectra in the range scale like  $k^\alpha$  with  $\alpha < 0$ .
- (3) The scaling of the DNS spectrum of the square of (vii)  $\nabla^2 p$  is neither very different nor very close to that of the Gaussian field.

These results (1)–(3) are consistent with a DNS with  $k_{\max}\eta \sim 1$ , results of which are presented in Ishihara *et al.*(2002).

### 3. Higher-resolution DNS on the ES

The Earth Simulator (ES) is a parallel computer system of distributed-memory type. It consists of 640 processor nodes, each of which is a system with a shared memory consisting of 8 vector-type arithmetic processors (APs) with main memory unit of 16 GB and peak performance of 8 Gflops. Thus, the ES as a whole consists of 5120 APs with main memory of 10 TB and peak performance of 40 Tflops.

The ES provides us with a unique opportunity to perform DNSs of turbulence with resolution much higher than any other DNSs so far made. We recently performed DNSs of incompressible turbulence by an alias-free spectral method on  $2048^3$  grid points with double precision arithmetic on the ES, where the sustained performance of 16.4 Tflops was achieved. We also performed a DNS on  $4096^3$  grid points with double but partially single precision arithmetic. A report of the DNSs with an emphasis on the parallel computing aspect on the ES was presented in Yokokawa *et al.* (2002).

The DNSs give us valuable data on turbulence study. The analysis of the data is now under way, and some details of the results are presented in Kaneda *et al.*(2002) on the energy dissipation rate and energy spectrum, and in Ishihara *et al.*(2002) on the spectra of the squares of the velocity quadratics.

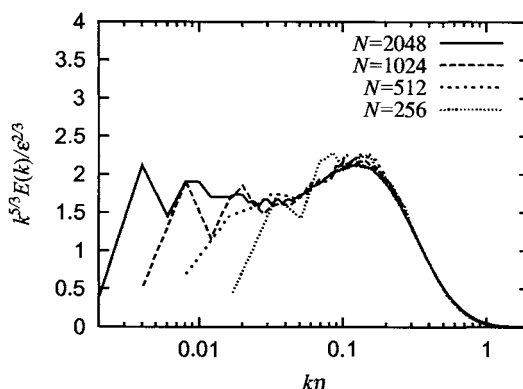
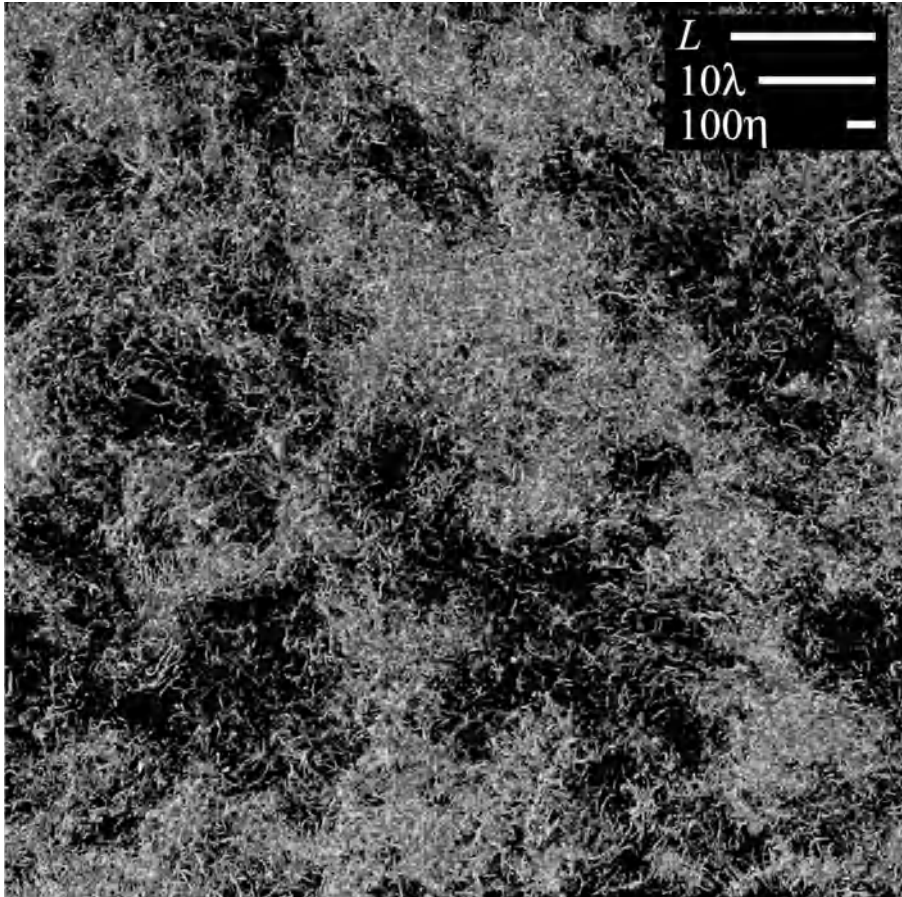


Figure 2. Compensated energy spectra from DNSs with  $256^3$ ,  $512^3$ ,  $1024^3$ , and  $2048^3$  grid points, for which  $R_\lambda = 94$ , 173, 268, and 429, respectively.



*Figure 3.* Intense-vorticity isosurfaces showing the region where  $|\omega| > \bar{\omega} + 4\sigma$ ;  $\omega$  is the vorticity, and  $\bar{\omega}$  and  $\sigma$  are the mean and standard deviation of  $|\omega|$ , respectively. The size of the display domain is  $(3141^2 \times 785)\eta$ , periodic in the vertical and horizontal directions.  $R_\lambda = 429$ . Three white-segments at the upper right show the integral length scale  $L = \pi/(2u'^2) \int [E(k)/k] dk$ ,  $10\lambda$ , and  $100\eta$ , respectively, where  $u'^2 \equiv \langle \mathbf{u} \cdot \mathbf{u} \rangle / 3$  and  $\lambda$  is the Taylor micro-scale.

Here we present an example of the results by the DNS with  $N = 2048$  and  $k_{\max}\eta = 2$ , for which  $R_\lambda \approx 429$  at a quasi-stationary state. Figure 2 shows the compensated energy spectrum  $k^{5/3}E(k)/\langle \epsilon \rangle^{2/3}$  for four different values of  $N$ , where  $E(k)$  is the energy spectrum. According to Kolmogorov's hypotheses, the compensated spectra in Fig. 2 must

be flat in the inertial subrange. A close inspection of the spectra for  $N = 2048$  in Fig. 2 suggests that the compensated spectrum be almost flat but a little tilted, say in  $0.01 < k\eta < 0.03$ . This implies that the energy spectrum scales like  $E(k) \propto k^{-\gamma}$  with  $\gamma$  being close to but a little different from Kolmogorov's value  $5/3$ . The similar is also the case in DNSs with  $k_{\max}\eta = 1$  (Yokokawa *et al.*, 2002; Kaneda *et al.*, 2002). As mentioned there, the detection of such a deviation, if there is any, is possible only by DNS with high enough resolution.

The data size generated by DNSs on such an advanced computer system as the ES is generally huge. In order to get intuitive understanding on turbulence field from such huge data, visualization of the flow field is very helpful. Figure 3 is an example of the visualization of the simulated turbulence field. It shows a snap shot of the vorticity field by the DNS with  $N = 2048$  and  $k_{\max}\eta = 2$ . In Fig. 3, we can see cluster-like structure at large scale, which suggests that the inertial subrange structure is quite different from the structure of individual small eddies.

## 4. A Theoretical Challenge

All of the Fourier transforms of  $\omega \cdot \omega (\equiv \Omega)$ ,  $e^2$  and  $\nabla^2 p$  may be written in the form

$$\hat{f}(\mathbf{k}) = C_{ijmn} \sum_{\mathbf{k}=\mathbf{p}+\mathbf{q}}^{\Delta} p_i q_j \hat{u}_m(\mathbf{p}) \hat{u}_n(\mathbf{q}),$$

where  $\sum_{\mathbf{k}=\mathbf{p}+\mathbf{q}}^{\Delta}$  denotes the sum over  $\mathbf{p}$  and  $\mathbf{q}$  satisfying  $\mathbf{k} = \mathbf{p} + \mathbf{q}$ ,  $C_{ijmn}$  is an appropriate nondimensional constant tensor, and we are assuming here the fluid density  $\rho$  to be unity and ignore the dimensionality of  $\rho$ . The difference between them comes only from that of the nondimensional coefficients  $C_{ijmn}$ 's. In spite of their dimensional similarity, Fig. 1 shows that  $E_{\Omega}(k)$  and  $E_{e^2}(k)$  are very different from  $E_{\nabla^2 p}(k)$ , and exhibit strong non-Gaussian scalings in the similarity range. It is unlikely that such a difference can be explained by any simple dimensional argument or model ignoring the  $i, j, m, n$ -dependence of the nondimensional coefficient  $C_{ijmn}$ . A theoretical challenge to explain the difference on the basis of the Navier-Stokes equations seems to be waited for.

In this respect, it is tempting to try a renormalized perturbation (RPT) approach. Regarding the energy spectrum, some Lagrangian two-point closure approximations that can be derived by RPT and are free from any ad-hoc tuning parameter are known to be in good agreement with experiments and DNSs. On the other hand, it seems widely accepted that the RPT approaches are incapable of explaining the non-Gaussian scalings such as in  $E_{e^2}(k)$ , as discussed by Chen *et al.*(1989).

Recently we revisited this problem from the Lagrangian viewpoint, and our preliminary analysis based on the Lagrangian renormalized approximation (Kaneda,1981) suggests that (i) the incompressibility condition play a key role in determining the scaling, and (ii) moments that are dimensionally exactly the same to each other may have different scalings, although much remains to be examined on the analysis.

## Acknowledgments

The authors are grateful to Dr. T. Sato, director-general of the Earth Simulator Center, for his encouragement and support for this work. The DNSs in this work were performed on the Earth Simulator. The data analyses were made on the ES and on a Fujitsu VPP5000/56 system at the Information Technology Center of Nagoya University. This work was supported by the “Research for the Future” program of the Japan Society for the Promotion of Science (JSPS) under the project JSPS-RFTF97P01101, a grant-in-aid for Scientific Research (B) 14340033 from JSPS, and grants-in-aid for Exploratory Research 14654073 and for Young Scientists (B) 13750059 from the Ministry of Education, Culture, Sports, Science, and Technology, of Japan.

## References

- Chen, H., Herring, J.R., Kerr, R.M., and Kraichnan, R.H. 1989 Non-Gaussian statistics in isotropic turbulence. *Phys. Fluids A* **1**(11), 1844-1854.
- Ishihara, T. and Kaneda, Y. 2002 High resolution DNS of incompressible homogeneous forced turbulence -Time dependence of the statistics-. *Proceedings of the International Workshop on Statistical Theories and Computational Approaches to Turbulence*, edited by Kaneda and Gotoh, Springer, 177-188.
- Ishihara, T., Kaneda, Y., Yokokawa, M., Itakura, K., and Uno, A. 2002 Spectra of the squares of velocity quadratics in high resolution direct numerical simulations of turbulence in a periodic box. to be submitted.
- Kaneda, Y. 1981 Renormalized expansions in the theory of turbulence with the use of the Lagrangian position function. *J. Fluid Mech.* **107**, 131-145 .
- Kaneda, Y., Ishihara, T., Yokokawa, M., Itakura, K. and Uno, A. 2002 Energy dissipation rate and energy spectrum in high resolution direct numerical simulations of turbulence in a periodic box. to be submitted.
- Orszag, S.A. 1969 Numerical methods for the simulation of turbulence. *Phys. Fluids*, **12** II-250-II-257.
- Yamazaki, Y., Ishihara, T., and Kaneda, Y. 2002 Effects of wavenumber truncation on high-resolution direct numerical simulation of turbulence. *J. Phys. Soc. Jpn.* **71**, 777-781.
- Yokokawa, M., Itakura, K., Uno, A., Ishihara, T. and Kaneda, Y. 2002 16.4-Tflops direct numerical simulation of turbulence by a Fourier spectral method on the Earth Simulator. *Proceedings of SC2002 High Performance Networking and Computing*, <http://www.sc-2002.org/paperpdfs/pap.pap273.pdf>.

# SCALING OF MULTI-PARTICLE LAGRANGIAN STATISTICS IN DIRECT NUMERICAL SIMULATIONS

P.K. YEUNG<sup>1</sup>, SHUYI XU<sup>1</sup>, M.S. BORGAS<sup>2</sup> and B.L. SAWFORD<sup>2</sup>

<sup>1</sup>*School of Aerospace Engineering, Georgia Institute of Technology, Atlanta, GA 30332, USA:*

<sup>2</sup>*CSIRO Atmospheric Research, PMB1 Aspendale, VIC 3195, Australia*

**Abstract** Basic results on the evolution of shape and size of three- and four-particle Lagrangian clusters are reported from direct numerical simulations at Taylor-scale Reynolds numbers between 90 and 400 in isotropic turbulence. At early times shape distortion by viscous effects is such that both the area and volume increase less rapidly than the two-particle separation. Later-time behavior is characterized by power-law increases and a self-similar shape distribution. Reynolds number effects are more prominent in measures of size than in shape parameters.

**Keywords:** Lagrangian statistics, direct numerical simulation

## 1. INTRODUCTION

The Lagrangian viewpoint of fluid mechanics is fundamental in statistical descriptions of turbulent dispersion. For a “cloud” of contaminant particles it is well known that the displacement of the center of mass, increase in linear size, surface area, and volume can be studied by considering the motion of fluid particles in groups of up to four. The behavior of these multi-particle Lagrangian statistics is of considerable interest in the calculations of higher-order moments of concentration fields in pollutant dispersion problems (e.g. Sawford *et al.* 2002), as well as in studies of Eulerian flow structure (e.g. Chertkov *et al.* 1999).

Direct numerical simulation (DNS) is a primary source of detailed Lagrangian data required for developments in stochastic modeling. However, because the range of time scales increases with Reynolds number less rapidly than the range of length scales, Reynolds number requirements for Kolmogorov similarity in Lagrangian statistics are (see Yeung

2002) usually stricter than for Eulerian quantities. Accurate parameterization of Reynolds number dependence is thus very important.

In this article, we provide a basic characterization of three- and four-particle Lagrangian statistics from DNS of isotropic turbulence at different Reynolds numbers. Important questions include whether measures of growth in size obey asymptotic power laws in time, and whether various shape parameters approach self-similarity regardless of size.

## 2. NUMERICAL SIMULATIONS

Stationary homogeneous isotropic turbulence has been simulated at grid resolutions from  $128^3$  to  $1024^3$  and Taylor-scale Reynolds numbers ( $R_\lambda$ ) nominally at 90, 140, 240 and 400, with the last three of these being sufficiently high for limited inertial range behavior in the Eulerian energy spectrum. Initially the particles are arranged as a collection of randomly-located right tetrahedra with equal separation distances ( $l_0$ ) between the base vertex and each of the other three vertices. This initial configuration was motivated by studies of two-particle dispersion, for which recent results on Reynolds number dependence are reported by Yeung & Borgas (2002). Each tetrahedron yields three right-angled isosceles and one equilateral triangle. The initial linear size  $l_0$  ranges from 1/4 of a Kolmogorov length scale to larger than one integral length scale. We limit our discussion here to detailed results from a long simulation at  $R_\lambda$  90 which captures the long-time asymptote unambiguously, and to the basic differences between results at  $R_\lambda$  90 and 400.

## 3. RESULTS

### 3.1 Three-particle statistics

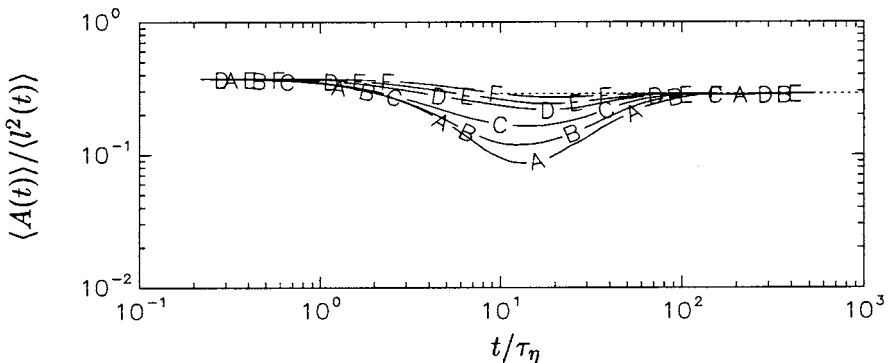


Figure 1. Evolution of normalized area at  $R_\lambda$  90, for  $l_0/\eta = 1/4, 1, 4, 16, 32, 64$  (lines A to F). Dashed line marks the value  $\sqrt{3}/6$ .

Figure 1 shows data at  $R_\lambda = 90$  for the mean area of initially isosceles triangles, normalized by the mean-square of the length of each side as the triangles evolve. At intermediate times (around 10 Kolmogorov time scales,  $\tau_\eta$ ) a substantial reduction for this normalized area indicates distortion by turbulent flow. This distortion is primarily a viscous-subrange effect, being strongest for small  $l_0$  where the relative motion of the particles involved would be influenced by turbulence at the small scales. The large-time limit is characterized by particles being far apart and moving independently, with (since the velocity fluctuations are approximately Gaussian) Gaussian-distributed displacements. The data are consistent with the limiting value of  $\sqrt{3}/6 \approx 0.289$  derived by Borgas (1998).

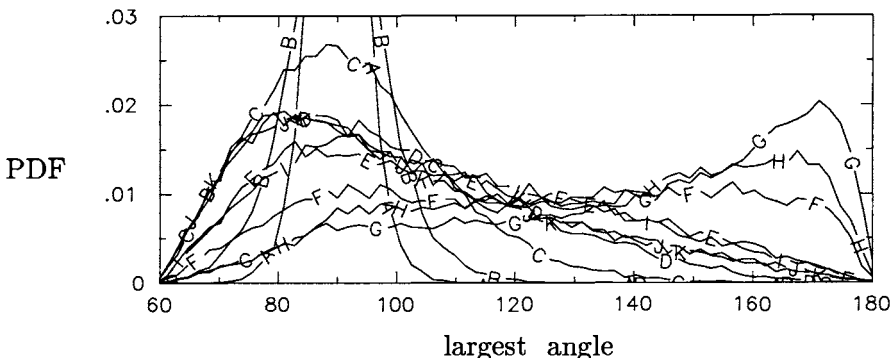


Figure 2. PDF of largest angle in triangle, for  $l_0/\eta = 1/4$  at  $R_\lambda = 90$ . Lines A-K are for logarithmically spaced time intervals ( $t/\tau_\eta \approx 1/4, 1/2, 1, 2, 4, 8, 16, 32, 64, 128, 256$ ). The high peaks at early times are truncated.

A more direct measure of shape is given in figure 2, as the probability density function (PDF) of the largest angle in the triangle at different times. Initially this PDF is a delta-function at 90 degrees. At intermediate times (lines G and H) it can be seen that obtuse triangles are favored, with the peak of the PDF occurring at nearly 170 degrees. In other words, the triangles have a tendency of almost closing up, corresponding to small area given the length of each side as inferred from figure 2. Ultimately, however, there is an asymptotic trend towards a similarity state, with the PDF attaining a peak at about 85 degrees. It should be noted that long-time *shape* statistics are essentially independent of both the initial shape distribution and the Reynolds number.

Because of faster dispersion, one can expect the rate of growth of the area of the triangles (as the particles move apart) to increase with Reynolds number. In figure 3 we show the area as a function of time, scaled by the Kolmogorov variables for data at  $l_0$  about 1/4 of a Kolmogorov length scale ( $\eta$ ) and at the lowest and highest Reynolds num-

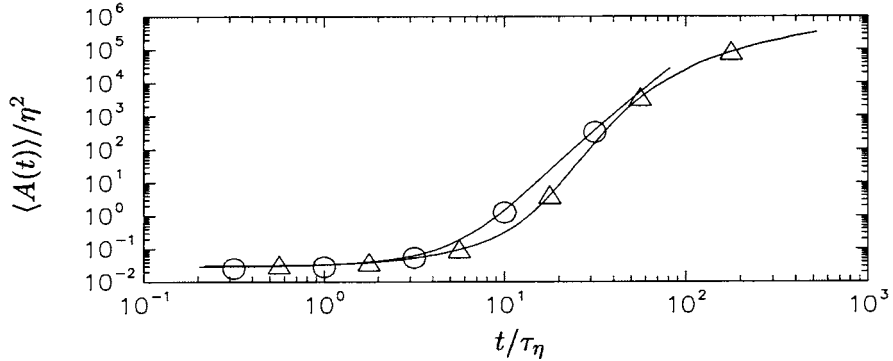


Figure 3. Kolmogorov-scaled area for  $l_0/\eta = 1/4$ , at  $R_\lambda$  90 ( $\Delta$ ) and 400 ( $\circ$ ).

bers ( $R_\lambda$  90 and 400) in the simulations. The data at  $R_\lambda$  400 is currently available only up to about  $80 \tau_\eta$ , and the curves nearly coincide at small times because of the normalization. Nevertheless, it can be seen that at higher Reynolds numbers these curves do rise more rapidly in time.

### 3.2 Four-particle statistics

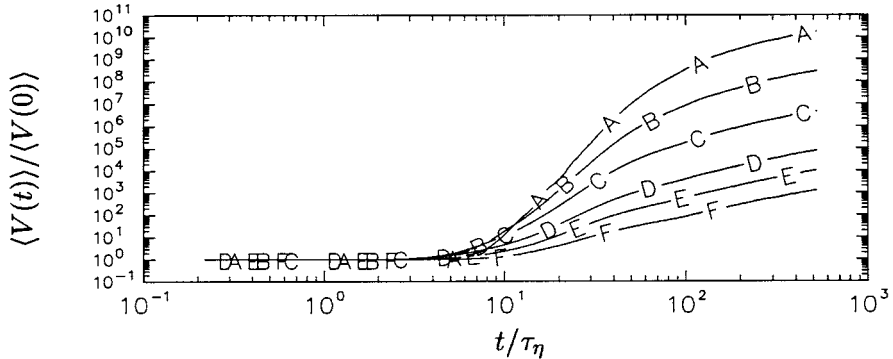


Figure 4.  $\langle V(t) \rangle / \langle V(0) \rangle$  for same conditions as figure 1.

For four-particle statistics we study the volume of the evolving tetrahedron, defined as  $1/6$  of the vector triple product of the position vectors of each of three particles relative to a fourth. Figure 4 shows the volume expansion ratio for different initial sizes. At small times and for small  $l_0$ 's, the volume is conserved by incompressibility since the relative velocities of the particles are proportional to velocity gradients which have a zero dilatation rate. Subsequently the area does grow rapidly with time, with  $t^{3/2}$  growth at large times which is consistent with the shape distribution again (as seen for the area in figure 1) approaching an asymptotic

state. The inertial-range regime deduced from classical arguments is one of  $t^{9/2}$  growth; however an unambiguous inference on this issue cannot be made at the Reynolds numbers currently accessible in the simulations.

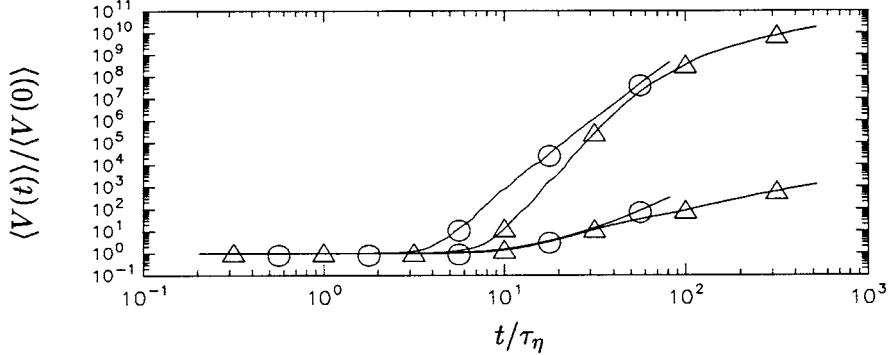


Figure 5.  $\langle V(t) \rangle / \langle V(0) \rangle$  for  $l_0/\eta = 1/4$  (upper curves), 64 (lower curves);  $R_\lambda$  90 ( $\Delta$ ) and 400 ( $\circ$ ).

Figure 5 shows the effects of Reynolds number on the volume expansion ratio, for two choices of  $l_0$ . As for the area in figure 3, for small  $l_0$  at higher  $R_\lambda$  we can observe a more rapid increase in size, which also begins earlier in Kolmogorov-scaled time units. For larger  $l_0$  the Reynolds number effect (in the chosen normalizations) is less pronounced at small times. Nevertheless, a higher  $R_\lambda$  does give a steeper slope of the curve at later times, reflecting a wider range of length scales in the flow.

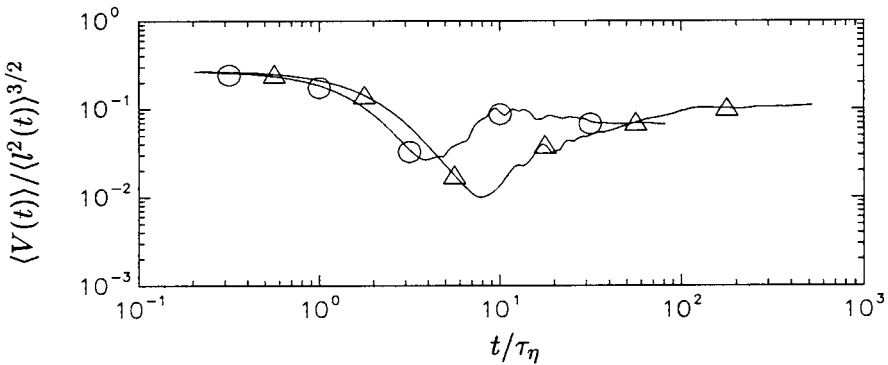


Figure 6.  $\langle V(t) \rangle / \langle l^2(t) \rangle^{3/2}$  for  $l_0/\eta = 1/4$ ;  $R_\lambda$  90 ( $\Delta$ ) and 400 ( $\circ$ ).

Finally, in figure 6 we consider the effects of Reynolds number on one of several possible shape parameters (e.g., see Pumir *et al.* 2000) for the four-particle clusters. We relate the volume to measures of length via the non-dimensional ratio  $\langle V(t) \rangle / \langle l^2(t) \rangle^{3/2}$ . At early and intermediate times

this ratio decreases, which implies that growth of volume begins more slowly than the growth of two-particle separation distance. At large times a well-defined asymptotic value is attained, in a manner similar to that seen for the normalized area in figure 1.

## 4. CONCLUSIONS

We have provided basic results on the evolution of shape and size of three- and four-particle Lagrangian clusters in isotropic turbulence. Generally, as a result of small-scale effects, at early times area and volume statistics increase more slowly than two-particle separation distances. Intermediate-time behavior is characterized by indicators of faster dispersion at high Reynolds numbers as well as shape distortion due to dissipation range effects. The results show a clear trend towards well-defined asymptotic limits at large times. The present numerical simulation database reaches up to Taylor-scale Reynolds number about 400, in a  $1024^3$  simulation which is being extended towards longer times. The present data are, as in the two-particle case (Borgas & Yeung 2002), expected to be useful for the more general problem of  $N$ -particle modeling (Sawford *et al.* 2002).

This work was supported in part by NSF, via Grant CTS-0121030.

## REFERENCES

- BORGAS, M.S. (1998) Meandering plume models in turbulent flows. *Proceedings of 13th Australasian Fluid Mechanics Conference*, (Monash University, Melbourne, Australia), pp. 139-142.
- BORGAS, M.S. & YEUNG, P.K. (2002) Relative dispersion in isotropic turbulence: Part 2. A new stochastic model with Reynolds number dependence. Submitted to *J. Fluid Mech.*
- CHERTKOV, M., PUMIR, A. & SHRAIMAN, B.I. (1999) Lagrangian tetrad dynamics and the phenomenology of turbulence. *Phys. Fluids* **11**, 2394-2410.
- PUMIR, A., SHRAIMAN, B.I. & CHERTKOV, M. (2000) Geometry of Lagrangian dispersion in turbulence. *Phys. Rev. Lett.* **85**, 5324-5327.
- SAWFORD, B.L., BORGAS, M.S. & YEUNG, P.K. (2002) Lagrangian modeling of turbulent diffusion in the atmosphere — recent developments. *Proceedings of IUTAM Symposium on Reynolds Number Scaling in Turbulent Flow*, Kluwer, Dordrecht (this volume).
- YEUNG, P.K. (2002) Lagrangian investigations of turbulence. *Ann. Rev. Fluid Mech.* **34**, 115-142.
- YEUNG, P.K. & BORGAS, M.S. (2002) Relative dispersion in isotropic turbulence: Part 1. Direct numerical simulations and Reynolds number dependence. Submitted to *J. Fluid Mech.*

# DEVELOPMENT OF HIGH REYNOLDS NUMBER OPTIMAL LES MODELS

R. D. Moser and P. Zandonade

*University of Illinois at Urbana-Champaign Champaign, IL 61801, USA*

[r-moser@uiuc.edu](mailto:r-moser@uiuc.edu)

## 1. Introduction

The well-known goal of large-eddy simulation (LES) is to simulate high-Reynolds number turbulent flows, without resolving the dissipative scales. This requires a model for the unresolved scales, and the primary challenge of LES is the development of such models. A wide variety of LES models have been used in a range of flows, with varying success (Meneveau and Katz, 2000; Lesieur and Métais, 1996). Recently, a new approach to the development of such models was proposed, called optimal LES. It is based on formal approximations to a well defined ideal LES evolution (Langford and Moser, 1999). The ideal LES has provably good properties, such as correct single-time statistics and minimum variance from the evolution of filtered turbulence, but unfortunately, the ideal LES model is impractical to determine.

An optimal LES model is determined in terms of small-separation (of order the filter scale) multi-point correlations, so the problem of optimal LES modeling reduces to modeling these correlations. To explore the properties of the modeling approach, these correlations have been computed from direct numerical simulations of moderate Reynolds number isotropic turbulence and turbulent channel flow. LES performed using the resulting models produce very good agreement with the statistics of the filtered DNS. An example from the isotropic turbulence and channel flow are shown in figures 1 and 2 respectively. This has given us encouragement to proceed to apply this modeling approach to high-Reynolds number turbulence, where it would actually be useful. This requires models (or data) for the multi-point correlations at high Reynolds number. The development of such models, and their application to the LES of high Reynolds number flows is the subject of this paper.

## 2. Optimal LES Formulations

In large eddy simulation, the large scales to be simulated are defined through the use of a filter. More precisely, we take the view that there is a mapping from the infinite dimensional space of possible solutions of the Navier-Stokes equations to a finite-dimensional representation that can be used in a simulation.

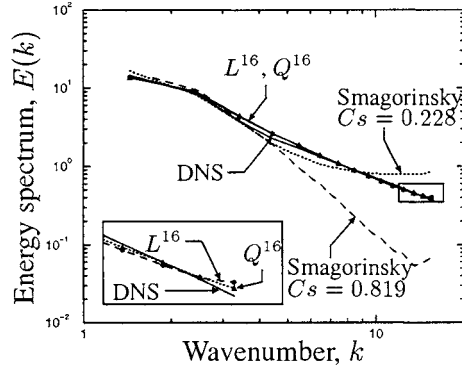


Figure 1. The three dimensional energy spectrum,  $E(k)$ , for filtered DNS and  $32^3$  LES with an optimal linear model ( $L^{16}$ ), an optimal quadratic model ( $Q^{16}$ ), and two cases of a Smagorinsky model.

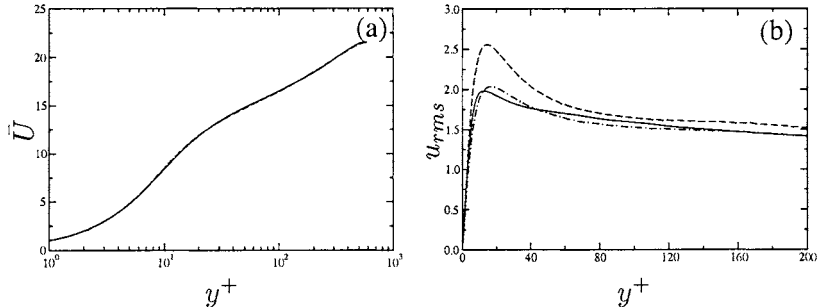


Figure 2. Mean and rms velocity profiles in wall coordinates from optimal LES (—), DNS (---) filtered DNS (···). Shown are (a) mean velocity, (b) rms streamwise velocity  $u_{rms}$ .

This mapping may include the numerical discretization used in the simulation. Let the velocity field be  $\mathbf{u}(\mathbf{x})$ , which is mapped to a finite set of LES state variables  $\mathbf{w}$  by a mapping signified by  $\tilde{\cdot}$ . An evolution equation for  $\mathbf{w}$  is commonly developed by filtering and manipulating the Navier-Stokes equations. In all cases, there is an unclosed term that must be modeled. Let this model term be  $\mathbf{M}$ . In optimal LES,  $\mathbf{M}$  is modeled using stochastic estimation (Langford and Moser, 1999; Adrian, 1990). In stochastic estimation, a restricted functional dependence is selected (e.g. linear or quadratic), and the coefficients in the resulting representation are determined to provide the closest possible approximation to the ideal model (Langford and Moser, 1999; Adrian et al., 1989). We call this approximation an optimal model.

## 2.1 Finite Volume LES

To be more specific, the optimal LES formulation is here applied to the particular mapping (filter) defined by a finite volume representation of the LES

field. In this case, the LES state variables are given by:

$$\mathbf{w}_j = \int_{\Delta_j} \mathbf{u}(\mathbf{x}) d\mathbf{x}, \quad (1)$$

where  $\Delta_j$  is the  $j^{\text{th}}$  finite volume in a finite volume mesh, and the evolution equation for  $\mathbf{w}$  is:

$$\dot{\mathbf{w}}_j = \sum_i (\mathbf{M}_{ji}^{\text{NL}} + \mathbf{M}_{ji}^P + \mathbf{M}_{ji}^V). \quad (2)$$

Here the  $M$ 's are (in order) the nonlinear flux, pressure force and viscous flux through the  $i^{\text{th}}$  face of the volume  $\Delta_j$ . In what follows, we will consider only the nonlinear flux, since the viscous flux will be negligible at high Reynolds number and the pressure force has been treated elsewhere (Langford and Moser, 2001). The nonlinear flux is

$$\mathbf{M}_{ji}^{\text{NL}} = \int_{\partial\Delta_{ji}} \mathbf{u}(\mathbf{x}) \mathbf{u}(\mathbf{x}) \cdot \hat{\mathbf{n}}(\mathbf{x}) d\mathbf{x}. \quad (3)$$

An optimal model for  $M^{\text{NL}}$  will need to be at least quadratic in  $\mathbf{w}$ , since the term is quadratically nonlinear. An appropriate optimal model is thus:

$$M_{ij}^{\text{NL}} = \sum_{\alpha} L_{ijk}^{\alpha} w_k^{\alpha} + \sum_{\alpha, \beta} Q_{ijkl}^{\alpha\beta} w_k^{\alpha} w_l^{\beta} \quad (4)$$

where the estimation coefficients  $L$  and  $Q$  are found by solving the following coupled equations:

$$\langle w_m^{\gamma} M_{ij}^{\text{NL}} \rangle = \sum_{\alpha} L_{ijk}^{\alpha} \langle w_k^{\alpha} w_m^{\gamma} \rangle + \sum_{\alpha, \beta} Q_{ijkl}^{\alpha\beta} \langle w_k^{\alpha} w_l^{\beta} w_m^{\gamma} \rangle \quad (5)$$

$$\langle w_m^{\gamma} w_n^{\delta} M_{ij}^{\text{NL}} \rangle = \sum_{\alpha} L_{ijk}^{\alpha} \langle w_k^{\alpha} w_m^{\gamma} w_m^{\delta} \rangle + \sum_{\alpha, \beta} Q_{ijkl}^{\alpha\beta} \langle w_k^{\alpha} w_l^{\beta} w_m^{\gamma} w_m^{\delta} \rangle \quad (6)$$

Note that the model coefficients are found in terms of the correlations of the LES state variables with themselves, and the correlation of the LES state variables with the model fluxes.

### 3. Determining the Needed Correlations

In the results reported in section 1, the correlations required for the optimal formulation were computed from direct numerical simulations. However, for an LES to be useful, a DNS cannot be necessary. A theoretical basis for determining the correlations is sought.

First, observe that the correlations appearing on the right hand sides of (5) and (6) are correlations between LES state variables. Thus, these correlations can be computed from an LES simulation. A dynamic procedure to determine these correlations is proposed, so it should not be necessary to determine them theoretically. This leaves only the two correlations on the left hand side of the

equations to be determined. These can be written in terms of mixed surface and volume integrals of the multi-point correlations  $T_{ijk}$  and  $F_{ijkl}$ , where

$$T_{ijk}(\mathbf{r}) = \langle u_i(\mathbf{x})u_j(\mathbf{x})u_k(\mathbf{x} + \mathbf{r}) \rangle \quad (7)$$

$$F_{ijkl}(\mathbf{r}, \mathbf{r}') = \langle u_i(\mathbf{x})u_j(\mathbf{x})u_k(\mathbf{x} + \mathbf{r})u_l(\mathbf{x} + \mathbf{r}') \rangle \quad (8)$$

To compute the needed correlations, it suffices to know  $T$  and  $F$  for separations smaller than the stencil size of the estimate.

### 3.1 Isotropic Correlations

When the turbulence is homogeneous and isotropic, simple theoretical approximations are sufficient to determine the required small-separation correlations. In this case, provided the Reynolds number is sufficiently high and the filter width is in the inertial range, Kolmogorov inertial range theory can be used. In particular, the Kolmogorov expressions for the second and third order structure functions are given by:

$$S_2(r) = C_1 \epsilon^{2/3} r^{2/3} \quad (9)$$

$$S_3(r) = \frac{4}{5} \epsilon r. \quad (10)$$

Isotropy then requires that the second and third order two-point correlation tensors be

$$R_{ij}(\mathbf{r}) = u^2 \delta_{ij} + \frac{C_1}{6} \epsilon^{2/3} r^{-4/3} (r_i r_j - 4r^2 \delta_{ij}) \quad (11)$$

$$T_{ijk}(\mathbf{r}) = \frac{\epsilon}{15} \left( \delta_{ij} r_k - \frac{3}{2} (\delta_{ik} r_j + \delta_{jk} r_i) \right). \quad (12)$$

Finally, if we also make the quasi-normal approximation, the 3-point quartic correlation can be expressed:

$$F_{ijkl}(\mathbf{r}, \mathbf{r}') = R_{ij}(0)R_{kl}(\mathbf{r}' - \mathbf{r}) + R_{ik}(\mathbf{r})R_{jl}(\mathbf{r}') + R_{il}(\mathbf{r}')R_{jk}(\mathbf{r}') \quad (13)$$

These expressions for  $R$ ,  $T$  and  $F$  can be integrated to obtain the correlations required to complete the optimal model formulation.

A preliminary implementation of optimal LES based on these models for the correlations has been completed for forced isotropic turbulence. The resulting spectrum for a nominally infinite Reynolds number LES on a  $32^3$  mesh is shown in figure 3. Also shown are comparable spectra from an LES based on DNS correlation data at  $Re_\lambda = 164$  and the filtered DNS data. The theoretically derived LES and DNS derived LES produce different results, but both provide reasonable and similar accuracy. In this preliminary calculation, the LES were performed with stencils of minimum extent (2-point stencils), whereas experience with DNS derived finite volume optimal LES shows that much better accuracy is obtained with 6-point stencils. A similar improvement in performance is expected with larger stencil theory-derived models.

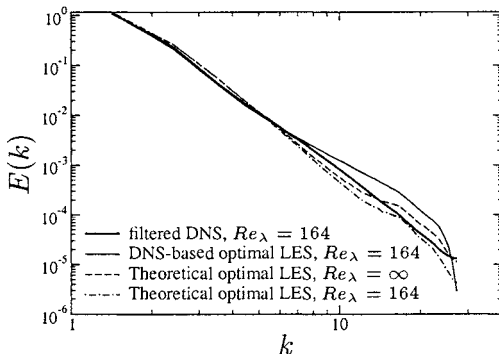


Figure 3. Spectra from theoretical and DNS-based optimal LES as compared to filtered DNS.

To complete the theoretical formulation of the model, the dissipation rate  $\epsilon$  must be determined. In the forced isotropic turbulence case described above, this was known *a priori*, because it was set by the definition of the forcing. However, in general it will need to be determined. Dissipation rate can be considered a free parameter in the model. It can be set through a dynamic procedure, similar to the setting of the Smagorinsky constant in the Smagorinsky dynamic model (Germano et al., 1991).

While the above analysis has been developed under the assumption that the turbulence is homogeneous and isotropic, it is expected that the resulting models will be valid as long as the small-scale (subgrid) turbulence is approximately homogeneous and isotropic. Thus, provided the cell sizes (filter widths) are sufficiently small, it is expected that models of this sort will be applicable to a wide variety of flows away from boundaries and other strong inhomogeneities.

### 3.2 Near-Wall Correlations

Developing models for the correlations in a strongly inhomogeneous flow is more challenging, but some of the same theoretical tools applied in the isotropic case can still be applied here. First, the correlations among LES state variables can still be determined from a running LES in a dynamic procedure. Inhomogeneity, however, does complicate this process because the most straightforward approach involves averaging in homogeneous spatial directions. The primary issue, though, is determining the correlations on the left-hand side of (5) and (6).

The ingredients used to model these correlations in the isotropic case are the Kolmogorov 2/3 and 4/5 laws and the quasi-normal approximation. Of these the 2/3 and 4/5 laws are not expected to be valid near the wall. However, the quasi-normal approximation can remain valid. The validity of the quasi-normal approximation is being tested in turbulent channel flow using the DNS data of (Moser et al., 1999), and preliminary results suggest that it remains a good

approximation. If this is the case,  $F_{ijkl}$  is known in terms of  $R_{ij}$ , leaving only  $R_{ij}$  and  $T_{ijk}$  to be determined.

One approach to modeling  $T_{ijk}$  near a wall that we are pursuing is to express it in terms of the quadratic correlation  $R_{ij}$ . This reduces the modeling problem to just that for the two-point correlation, for which significant scaling and empirical information is available. The two-point correlation equation defines a relationship between  $T_{ijk}$  and  $R_{ij}$ , which constrains this formulation, but more information is still required. Further, a model for  $R_{ij}$  is needed. The high-Reynolds number scaling research described in this volume is a promising source for the required information, and several possibilities are being pursued.

## 4. Conclusions

Optimal Large Eddy Simulation based on DNS statistical data has yielded excellent simulations results. In this paper, a technique for formulating such models based on theoretical considerations and dynamic “boot-strapping” has been outlined. This has yielded functioning models in isotropic turbulence, but in wall-bounded turbulence, further information is still required. In developing these theoretical near-wall optimal LES models, we are consumers of the high Reynolds number scaling research that is the subject of this volume. A number of promising approaches are being pursued based on work described in these pages.

## Acknowledgments

The research reported here has been supported by NSF and AFOSR through grant CTS-9616219, NSF grant CTS-001435 and AFOSR grant F49620-01-0181, and by the Center for Simulation of Advanced Rockets, which is funded by the Department of Energy through University of California grant B341494. This support is gratefully acknowledged.

## References

- Adrian, R. (1990). Stochastic estimation of sub-grid scale motions. *Appl. Mech. Rev.*, 43(5):214–218.
- Adrian, R., Jones, B., Chung, M., Hassan, Y., Nithianandan, C., and Tung, A. (1989). Approximation of turbulent conditional averages by stochastic estimation. *Phys. of Fluids*, 1(6):992–998.
- Germano, M., Piomelli, U., Moin, P., and Cabot, W. (1991). A dynamic subgrid-scale eddy viscosity model. *Phys. of Fluids*, 3:1760–1765.
- Langford, J. A. and Moser, R. D. (1999). Optimal LES formulations for isotropic turbulence. *J. Fluid Mech.*, 398:321–346.
- Langford, J. A. and Moser, R. D. (2001). Breakdown of continuity in large-eddy simulation. *Phys. of Fluids*, 11:943–945.
- Lesieur, M. and Métais, O. (1996). New trends in large-eddy simulations of turbulence. *Annu. Rev. of Fluid Mech.*, 28:45–82.
- Meneveau, C. and Katz, J. (2000). Scale-invariance and turbulence models for large-eddy simulation. *Annu. Rev. of Fluid Mech.*, 32:1–32.
- Moser, R., Kim, J., and Mansour, N. (1999). Direct numerical simulation of turbulent channel flow up to  $Re_\tau = 590$ . *Phys. Fluids*, 11(4):943–945.

# SIMILARITY SCALING AND STATISTICS OF PRESSURE FLUCTUATION IN TURBULENCE

Yoshiyuki Tsuji

*Department of Energy Engineering and Science, Nagoya University,  
Nagoya, AICHI, 464-8603, JAPAN*

**Abstract:** Pressure fluctuation was measured by using condenser microphone and piezoresistive transducer. Small scale statistics are studied from the point of Kolmogorov universal scaling. Power-law exponent of normalized pressure spectra and its probability shape are discussed. Clear power-law with scaling exponent  $-7/3$  is confirmed in the range of  $600 \leq R_\lambda$ , which is much larger value than the case of velocity fluctuation.

**Key words:** pressure fluctuation, universal scaling, Kolmogorov scaling

## 1. INTRODUCTION

Static pressure fluctuation is a basic flow variable in turbulence, but it is perhaps least understood quantity[1][2]. This is due to the difficulty inherent in measuring this term and, consequently, it is because of the lack of published experimental results[3-6]. Kolmogorov presented the hypotheses of small-scale statistics based on the idea of local isotropy, which is restated by the relation, for the case of pressure fluctuation,

$$E_{pp}(k_1) = \rho^2 \langle \varepsilon \rangle^{3/4} \nu^{7/4} \phi(k_1 \eta) \quad (1)$$

where  $\nu$  is kinetic viscosity,  $\langle \varepsilon \rangle$  is energy dissipation rate per unit mass on average, and  $\eta$  is Kolmogorov length scale. The function  $\phi$  has been believed to be universal so far. When the Reynolds number becomes large, the spectrum becomes a simpler form,

$$E_{pp}(k_1) = K_p \rho^2 \langle \varepsilon \rangle^{4/3} k_1^{-7/3} \quad (2)$$

This relation is investigated recently by direct numerical simulations [7-10]. On the other hand, there seems to be a few experimental support for Eq. (2) [4,5]. In this study we report on the statistics of pressure fluctuation measured in a free jet in the range of Reynolds number;  $300 \leq R_x \leq 1200$ .

## 2. EXPERIMENTAL CONDITION

The data were measured on the centerline in free jet. A small wind tunnel with nozzle size  $40 \times 40\text{mm}^2$  and a large wind tunnel which has  $400 \times 700\text{mm}^2$  nozzle was operated in the range of velocity  $5 \leq U_j \leq 15$ , where  $U_j, \text{m/s}$  is an average velocity at nozzle exit. On the centerline downstream,  $15 \leq x/D \leq 25$  ( $D = 40,400\text{mm}$ ,  $D$  is nozzle width), velocity and pressure fluctuation were measured during 15 minutes at a frequency of  $10\text{kHz}$ .

The measurement of pressure fluctuation in the flow field was accomplished with small piezoresistive transducer (Model XCS062, TEAC/KULITE) and standard quarter-inch condenser microphone (Model 7017, ACO. CO. LTD.). Transducer has a frequency response from D.C up to  $150\text{kHz}$  and its dynamic range is  $3.5 \times 10^3 \text{Pa}$ . The maximum errors contained in linearity and hysteresis are 0.25%. Microphone is available for measuring the frequency of  $20 \sim 70 \times 10^3 \text{Hz}$ . The lower frequency is restricted due to its mechanical system. Dynamic range is  $2 \times 10^{-2} \sim 3.2 \times 10^3 \text{Pa}$ , so very small amplitude can be measured. The probe is a standard Pitot-static tube, that is  $1.0\text{mm}$  outside diameter and  $0.1\text{mm}$  in thickness as indicated in Fig. 1. Four static-pressure holes ( $0.4\text{mm}$  in diameter) are spaced  $90^\circ$  apart and are located at a distance of 22 tube diameters from the tip of the probe to minimize sensitivity to cross-flow error. The leeward end is terminated by microphone or transducer. The schematic view is shown in Fig. 1. The sensor diameters are  $d_T = 1.6\text{mm}$  and  $d_M = 7.0\text{mm}$  for transducer and microphone, respectively. In this study, two different types of sensors are used.

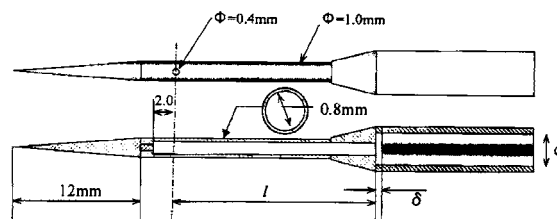


Figure 1. Schematic view of pressure probe.

The sensors were fitted with a tubing as a pressure duct and were inserted into the flow domain in such a way that the axis of the microphone (or the transducer) body was aligned with the mean stream. The frequency response of the system is limited by the Helmholtz-resonator response of the tube and sensor cavity[3][5]. This frequency is calculated by

$$f_r = (2\pi/U_s) \cdot \sqrt{S/\ell V} \quad (3)$$

where  $V$  is a cavity volume,  $\ell$  is a length of tube,  $U_s$  is sound velocity and  $S$  is cross section (also see Fig. 1). Here,  $V = \pi d^2 \delta / 4m^3$  and  $S = \pi(0.8 \times 10^{-3})^2 / 4m^2$ . The resonant frequency was computed to be  $2.1kHz$  and  $12.0kHz$  for microphone and transducer, respectively. We have to take care of the standing wave generated inside static tube, which locates between static hole and microphone head. This frequency is given by  $f_1 = U_s/\lambda$  where  $\lambda/4 = \ell$ . Standing wave causes a small disturbance in pressure fluctuation.  $f_1$  is about  $2.4kHz$  for microphone and  $4.6kHz$  for transducer, respectively. The spatial resolution is assumed to be a few times tube diameter then the corresponding frequency,  $f_s = U_c/(n \times d)$  is taken into account in the measurements. Here,  $U_c$  is the convection velocity or local mean velocity, and  $d$  is probe diameter.  $n$  is to be from 5 to 10[5].  $f_s$  is, for instance, about  $1.0kHz$  at  $U_c = 5.0m/s$ . Because  $f_s$  is smaller than  $f_1$  and  $f_r$ , we set the low-pass filter at  $f_s$  with checking the frequency spectra.

About the angle of pressure probe in the flow, we have preliminarily checked the effect of attack angle on the pressure data. The ratio of static pressure and kinetic pressure  $C_p = (\Delta p)/(\rho u'^2 / 2)$ ,  $\Delta p = p(\theta) - p(0)$ , is plotted against the angle between flow direction and probe angle  $\theta$ . Three different hole sizes were examined and the 8 static-hole probe was tested. The error is less than 2.5% for  $-15 \leq \theta \leq +15$ . Also the PDF shape does not change so much.

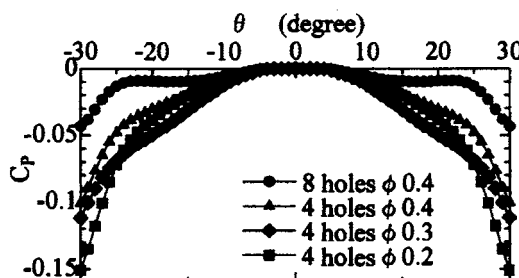


Figure 2. The effect of angle between the pressure probe and the flow direction is checked.

### 3. Result and Discussion

We have to qualify first the measured pressure for revelation of pressure statistics. Because there is an inevitable anxious that the phenomenon being measured might not be entirely a pressure fluctuation but it is intrinsic to the device. Taking the divergence of Navier-Stokes equation, Poisson equation is derived as

$$\nabla^2(p/\rho) = -\partial u_i / \partial x_j \cdot \partial u_j / \partial x_i \quad (4)$$

and it allows two-point pressure correlations to be expressed in terms of fourth-order structure functions of velocity. In homogeneous isotropic flow, the longitudinal velocity correlation  $g(r)$  is adopted for evaluating the right-hand side of Eq. (4) subject to quasi-normal assumption, which allows fourth-order velocity structure functions in turn to be factored into products of second-order quantities. In the case of  $g(r) \approx \exp(-r^2)$ , root mean square of pressure,  $p'$ , is scaled by the square of rms of velocity and fluid density,  $p' / (\rho u'^2) = C_1$  and then  $C_1$  becomes unity [1]. Batchelor evaluated  $C_1 = 0.58$  by using the value of  $g(r)$  measured in high Reynolds number flow. On the other hand, recent DNS data suggest  $C_1 \approx 1.0$  for  $R_\lambda < 300$  but a weak trend of decrease with Reynolds number is confirmed [7-10]. In the course of this study,  $C_1$  is found to be slightly depending on  $R_\lambda$ . It is about 0.7 for low Reynolds numbers,  $R_\lambda < 300$ , but increases gradually up to 1.0 until  $R_\lambda$  reaches 700. In larger Reynolds numbers,  $700 \leq R_\lambda \leq 1200$ , the ratio is almost constant;  $C_1 \approx 1.0$  [12].

Recent studies based on direct numerical simulation have shown that the PDF of pressure fluctuation is negatively skewed. Experimental data are compared with DNS at almost the same Reynolds number[12]. There is small qualitative difference around the core region, but on the negative side, PDF departs from Gaussian considerably. It is now a common consensus that low pressure region indicates the pileup of small coherent vortices which are surrounded with high energy dissipation regions. The right hand side of Eq. (4) is re-expressed as

$$-\partial u_i / \partial x_j \cdot \partial u_j / \partial x_i = \Omega/2 - S_{ij}S_{ij} \quad (5)$$

where  $S_{ij} = (\partial u_i / \partial x_j + \partial u_j / \partial x_i) / 2$ ,  $\Omega = |\omega|^2$  and the energy dissipation is given by  $\varepsilon = 2\nu S_{ij}S_{ij}$ . So large negative pressure region indicates large vorticity or small dissipation region. The small coherent vortices are well captured because the negative side of PDF matches sufficiently with DNS [12]. The negative tail of PDF can be approximated by a stretched exponential shape, in the form

$$P(p) \propto \exp[-a \cdot (p/p')^b] \quad (6)$$

where  $a$  and  $b$  are non dimensional parameters [10]. So the considerable interest is in whether the PDF, or the coefficients  $a$  and  $b$ , may depend on Reynolds number or not. Instead of  $a$  and  $b$ , because it is difficult to find out a reasonable fitting region, 3rd and 4th order moments are computed. The skewness (3rd order moment) is about  $-1.0$  and the flatness (4th order moment) is close to  $6.0$ , respectively, when the Reynolds number is large.

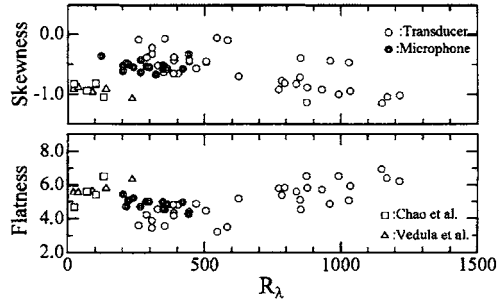


Figure 3. Skewness and flatness factor of pressure fluctuation.

Inertial scaling for pressure fluctuations is considered in terms of one-dimensional spectrum  $E_{pp}(k_1)$  in wave number space. Here  $k_1 \equiv 2\pi f/U$ ,  $f$  is a time frequency, and  $U$  is a local mean velocity. The classical results are given by Eqs. (1) and (2). But it is not yet proven that these scaling laws are valid. When the Kolmogorov's similarity hypothesis is extended to pressure, it is to assume an analogy between the mechanisms that cause pressure differences across spatial difference  $r$  in the inertial subrange and that causes the velocity differences  $\Delta u_r$ . Such an analogy is useful to explain some of the pressure differences [11] that part owing to local effect, but it might fail to capture the nonlocal contributions to the local pressure field, because Eq. (4) needs the boundary condition when it is solved. Some experiment has shown that  $E_{pp}(k_1) \propto k_1^{-7/3}$  [5] and some has reported that another scaling exponent was observed [6].

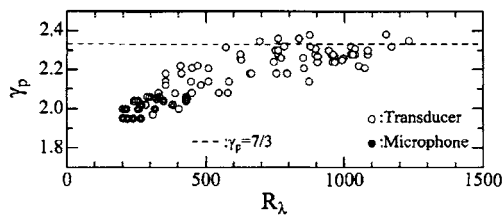


Figure 4. Spectral exponent defined by Eq. (7)

On the other hand, recent DNS have found that  $E_{pp}(k_1)$  is approximately proportional to  $k_1^{-5/3}$ , unlike Eq. (2), in the wave number range where the energy spectrum scales close to  $E_{uu}(k_1) \propto k_1^{-5/3}$ . There seems to be little agreement about the scaling of pressure spectrum when compared to the case of velocity fluctuation.

An appropriate power-law exponent is obtained when the pressure spectrum is approximated by the relation,

$$E_{pp}(k_1) = K_p \cdot \rho^2 \langle \varepsilon \rangle^{(3+\gamma_p)/4} \nu^{(7-3\gamma_p)/4} k_1^{-\gamma_p} \quad (7)$$

and the normalized spectrum  $E_{pp}(k_1)/k_1^{-\gamma_p}$  shows the most broad flat region. In Fig. 4, the exponents are plotted as a function of  $R_\lambda$ . They indeed depart from  $-7/3$  in small Reynolds numbers. This trend is similar to DNS, but little power-law region was confirmed in the range of  $R_\lambda < 300$ . So the  $-5/3$  scaling reported by recent DNS was not identified in this experiment.  $\gamma_p$  approaches  $7/3$  when  $R_\lambda$  is larger than 600. This is significantly higher Reynolds number than those needed for inertial scaling in velocity statistics. As the spectra are compared with velocity ones[12], it is noticed that pressure spectrum has a narrower scaling region than velocity. This is consistent with the result that we need the higher Reynolds numbers to realize clear  $-7/3$  power-law scaling.

## Acknowledgments

The author is grateful to Profs. T.Gotoh and K.R. Sreenivasan for their valuable comments and advice on this study. This work is supported by a Grant-in-Aid for Science Research (C2-13650175) by The Ministry of Education, Science and Culture of Japan.

## References

1. A.S.Monin and A.M.Yaglom, Statistical Fluid Mechanics (MIT, Cambridge, MA, 1975), Vol. 2.
2. M.Nelkin, Advances in Physics, **43**, 143 (1994).
3. Y.Kobashi, J. Physical Soc. Japan, **12**, 533 (1957).
4. B.G.Jones, R.J.Adrian, C.K.Nithianandan, H.P.Planchon Jr., AIAA Journal, **17**, 449 (1979).
5. W.K.George, P.D.Beuther, and R.E.A.Arndt, J. Fluid Mech., **148**, 155 (1984).
6. J.D.Albertson, G.G.Katul, M.B.Parlange, and W.E.Eichinger, Phys. of Fluids, **10**, 1725 (1998).
7. T.Gotoh and R.S.Rogallo, J.Fluid Mech., **396**, 257 (1999).
8. T.Gotoh and D.Fukayama, Physical Rev. Letter, **86** 3775 (2001).
9. P.Vedula and P.K.Yeung, Physics of Fluids, **11**, 1208 (1999).
10. N.Cao, S.Chen, and G.D.Doolen, Physics of Fluids, **11**, 2235 (1999).
11. R.J.Hill and J.M.Wilczak, J. Fluid Mech., **296**, 247 (1995).
12. Y.Tsuji and T.Ishihara, submitting (2002).

# CONVECTION, PRESSURE AND DISSIPATION IN THREE-DIMENSIONAL TURBULENCE

Tohru Nakano

*Department of Physics, Chuo University,  
Tokyo 112-8551, Japan*  
nakano@phys.chuo-u.ac.jp

Toshiyuki Gotoh

*Department of Systems Engineering, Nagoya Institute of Technology,  
Nagoya 466-8555, Japan*  
gotoh@system.nitech.ac.jp

**Abstract** The roles of the convection, pressure and dissipation are investigated in the equation for longitudinal velocity increment over the inertial range of stationary incompressible turbulence. The convection is the motor of the turbulence, while the pressure screens the convection increasing with the intensity of increment. The combined effect of the convection and the pressure is balanced by the dissipation for structure functions of order not less than five. At fourth order the dissipative term is irrelevant.

**Keywords:** Convection, pressure, dissipation, longitudinal increment.

## 1. Introduction

Convection, pressure and dissipation are the trinity in three-dimensional turbulence. The convection is the motor of the turbulence, while the pressure screens the convection partly. The combined effect of the convection and the pressure is balanced by the dissipation.

In the present paper we are concerned with the behavior of those three elements for the longitudinal velocity increment in the inertial region of incompressible fluid. The precise understanding of their roles will be helpful for modeling turbulence. Our strategy is to evaluate the contributions of the three elements with the aid of analysis of simulations

of high resolution[1]; the theoretical models to interpret the obtained results are given elsewhere[2].

## 2. Fundamental equations

Let us introduce the velocity difference  $w_i(\mathbf{x}_1, \mathbf{x}_2) = u_i(\mathbf{x}_2) - u_i(\mathbf{x}_1)$  at two points  $\mathbf{x}_1$  and  $\mathbf{x}_2$ . When  $\mathbf{x}_1$  and  $\mathbf{x}_2$  are denoted as  $\mathbf{x}_1 = \mathbf{X} - \mathbf{r}/2$  and  $\mathbf{x}_2 = \mathbf{X} + \mathbf{r}/2$ , the equation for the  $n$ th order moment of the longitudinal component  $w_1$  along  $\mathbf{r}$  becomes in the inertial region

$$n \left\langle w_1^{n-1} \left( w_j \frac{\partial}{\partial r_j} w_1 + \frac{\partial}{\partial X_1} \delta p \right) \right\rangle = -2n(n-1) \left\langle w_1^{n-2} \varepsilon_1(\mathbf{X}, \mathbf{r}) \right\rangle, \quad (1)$$

where

$$\varepsilon_1(\mathbf{X}, \mathbf{r}) = \frac{\nu}{2} (|\nabla u_1(\mathbf{x}_2)|^2 + |\nabla u_1(\mathbf{x}_1)|^2)$$

is the average of longitudinal dissipation rate at two points  $\mathbf{x}_1$  and  $\mathbf{x}_2$ . The derivation of (1) is given in Ref.[3]. In (1) we assumed the stationarity of turbulence, which is driven by the external forces. The Kolomogorov's 4/5 law is readily derived from (1) by equating  $n = 2$ [3].

## 3. Inertial terms; convection and pressure

Equation (1) is the most fundamental in describing the inertial range property of turbulence. The first term on the lhs of (1) is contribution from the convective term, and the second term is from the pressure term. One way of assessing those contributions is to compute the moments appearing on the lhs of (1) by varying  $n$  and  $r$ . Another way, which we employ here, is to evaluate the convection and pressure terms with the aid of the conditional average method with value of  $w_1$  fixed. Namely we compute

$$A(w_1) = \left\langle w_j \frac{\partial}{\partial r_j} w_1 \Big| w_1 \right\rangle, \quad B(w_1) = - \left\langle \frac{\partial}{\partial X_1} \delta p \Big| w_1 \right\rangle, \quad (2)$$

where  $\langle f|w_1 \rangle$  signifies the average of  $f$  with  $w_1$  fixed.

We computed  $A(w_1)$  and  $B(w_1)$  based on the large scale simulation with  $1024^3$  meshes[1], where the stationary turbulence with  $R_\lambda = 381$  was realized. The inertial region was found between  $80 \leq r/\eta \leq 200$ . The data were sampled over 138 shots during 6.6 eddy turnover times. In Fig.1 we depicted  $A(w_1)$  against  $w_1 / \sqrt{\langle w_1^2 \rangle}$ , whose feature is an asymmetric parabola with weight on the negative side of  $w_1$ ; it is negative near the origin. Figure 2 is the plot of  $B(w_1)$ , which is more like a symmetric parabola, and negative near the origin. The curvature of

the curves in both figures becomes smaller as the separation increases. Theoretical interpretation of  $A$  and  $B$  is possible, but not given here[2].

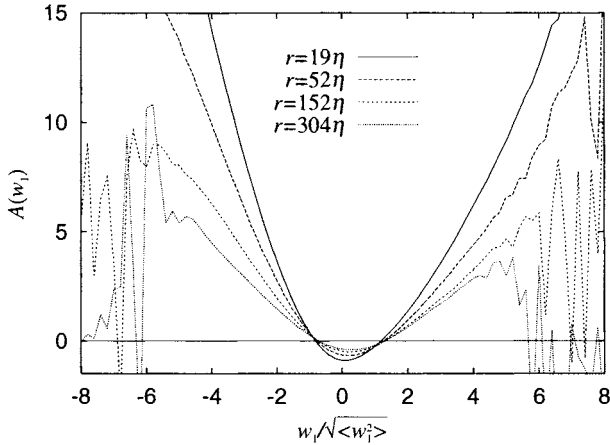


Figure 1. Plot of  $A(w_1)$  against  $w_1/\sqrt{\langle w_1^2 \rangle}$ .

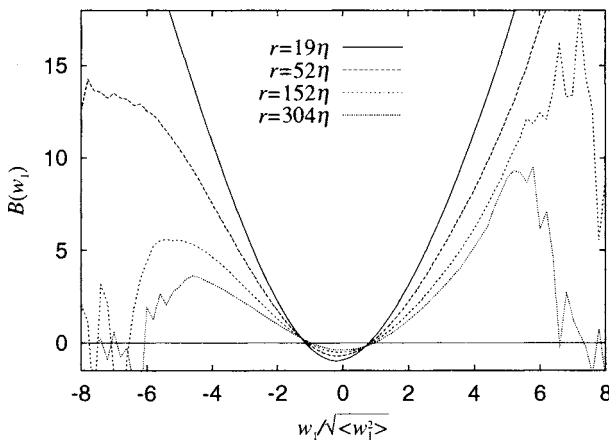


Figure 2. Plot of  $B(w_1)$  against  $w_1/\sqrt{\langle w_1^2 \rangle}$ .

It is necessary to know the relative magnitude of  $A$  and  $B$ . To this end we investigate the behavior of  $H(w_1) = A(w_1) - B(w_1)$ . Although  $H(w_1)$  is not depicted for sake of saving space, it monotonically decreases with  $w_1$  such that  $H(w_1) > 0$  for  $w_1 < 0$ , and  $H(w_1) < 0$  for  $w_1 > 0$ , although a close inspection indicates that  $H$  is slightly positive at  $w_1 = 0$ . This

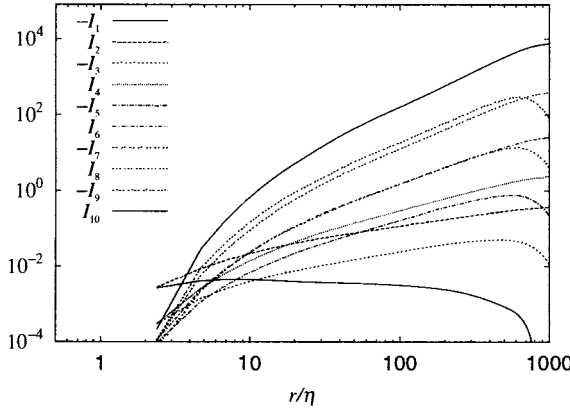


Figure 3. Plot of  $I_n$  against  $r/\eta$ . The curves at  $r/\eta = 200$  are  $I_1, I_3, I_2, I_5, I_4, I_6, I_7, I_8, I_9$  and  $I_{10}$  upward from bottom

means that  $A$  is predominant over  $B$  on the negative side of  $w_1$ , and the situation is opposite on the positive side. Since the conditional averaged energy cascade rate is given by  $w_1 H(w_1)$  according to the lhs of (3), it is negative irrespective of the sign of  $w_1$ , implying that energy cascade toward small scales occurs for any value of  $w_1$ . On the other hand, the direction of each energy cascade rate arising from the convective and pressure terms, i.e.  $w_1 A(w_1)$  and  $w_1 B(w_1)$ , is not so.

#### 4. Dissipation

In this section we focus on the right hand side of (1). First, we show how  $\varepsilon_1(\mathbf{x}_1, \mathbf{x}_2)$  is correlated to  $[w_1(\mathbf{X}, \mathbf{r})]^n$  by computing  $I_n \equiv \langle w_1^n \varepsilon_1 \rangle$ . Figure 3 is a plot of  $I_n$  against  $r/\eta$  for  $n$  from 1 to 10 based on the DNS. The inertial range is located in between  $r/\eta = 80$  and 200. The results are summarized as follows. (i) For  $n \geq 2$   $I_n$  scales with  $r$  in a power law in the inertial region, although the slope is less than the K41 value  $n/3$ , reflecting the intermittency effects. It is well balanced with the left hand side of (1) as shown later. (ii) Perplexing is the case  $n = 1$ .  $I_1$  decreases with  $r$ , on the contrary to the expectation  $I_1 \sim r^{1/3}$ . This tendency is confirmed for many simulations with Reynolds numbers less than 380, although those results are not shown here. (iii) In Fig.3 we notice that the slope of  $I_6$  is very close to that of  $I_7$ . A similar tendency holds between  $I_8$  and  $I_9$ .

This property combined with (1) suggests that  $\langle w_1^{2m} \rangle$  is closer to  $\langle w_1^{2m-1} \rangle$  than to  $\langle w_1^{2m+1} \rangle$ , in accordance with the observation by Stolovitzky, Sreenivasan and Juneja [4].

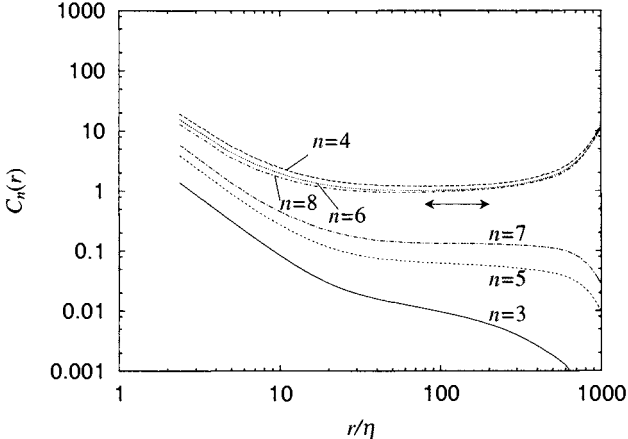


Figure 4. Plot of  $C_n(r)$  against  $r/\eta$  for various values of  $n$ . The line between arrows signifies the inertial region.

Next go to the estimation of the dissipative term in (1) in comparison with the inertial term, i.e. the left hand side of (1). For that purpose we compute from the DNS data

$$C_n(r) = -\frac{2n(n-1)\langle \varepsilon_1(\mathbf{X}, \mathbf{r}) w_1^{n-2} \rangle}{\langle w_1^{n+1} \rangle / r}. \quad (3)$$

We show the plot of  $C_n(r)$  against  $r/\eta$  for various values of  $n$  using the data of DNS in Fig.4, where the inserted solid line with arrows at both ends  $r/\eta = 80$  and  $200$  stands for the inertial region. We summarize the essential points drawn from Fig.4: (i) For  $n \geq 4$   $C_n(r)$  takes constant value  $C_n^*$  independent of  $r$  in the inertial region. It is remarkable that  $C_3(r)$  is not constant in the inertial region. This suggests that the rhs of (1) dose not balance with the lhs of (1) at  $n = 3$ . (ii) For even integers of  $n$ ,  $C_n^*$  seem to approach a constant value  $k$  from above like  $C_4^* > C_6^* > C_8^*$  as  $n$  increases. (iii) For odd  $n$ ,  $C_n^*$  increases with  $n$ . At the level of present resolution we could compute only up to  $C_7$ . At this moment it is not confirmed that  $C_n^*$  approaches the same constant  $k$  asymptotically for odd  $n$ .

We assume that  $C_n(r)$  approach constant values depending on parity of  $n$ . Comparing this observation with eq.(1) we are able to draw the

following conclusions. (i) For large  $n$  the pressure screens the convection term, so that the combined contribution from the convection and pressure is smaller by a factor  $1/n$  than that from the convective term only. (ii) For  $n = 3$  the dissipation term is negligible in the inertial region.

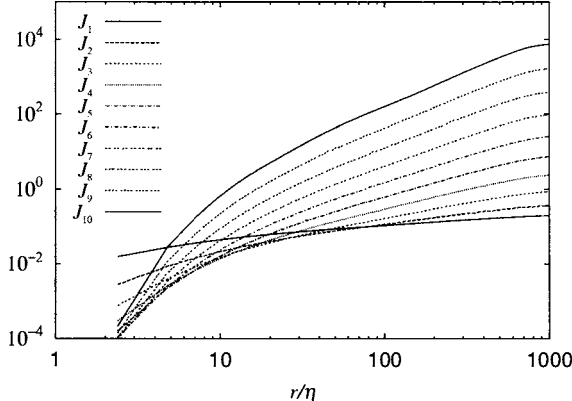


Figure 5. Plot of  $J_n$  against  $r/\eta$ .

It is common to employ the moments of the absolute value of  $w_1$  in the analysis of structure functions. In Fig.5 we depicted  $J_n(r) = \langle \varepsilon_1 |w_1|^n \rangle$  against  $r/\eta$ ;  $J_n(r)$  scales regularly in contrast to  $I_n(r)$ . When we compute

$$\tilde{C}_n(r) = -\frac{2n(n-1)\langle \varepsilon_1(\mathbf{X}, \mathbf{r})|w_1|^{n-2} \rangle}{\langle |w_1|^{n+1} \rangle / r}, \quad (4)$$

$\tilde{C}_n(r)$  was found to approach a constant value irrespective of a parity of  $n$  as  $n$  increases. This means that the structure functions of absolute increment, i.e.  $\langle |w_1|^n \rangle$ , also scale regularly with  $n$  as encountered in the usual analysis of  $\langle |w_1|^n \rangle$ .

## References

- [1] T. Gotoh, D. Fukayama and T. Nakano, Phys. Fluids **14** (2002) 1065 .
- [2] T. Nakano, T. Gotoh and D. Fukayama, submitted to Phys. Rev. E (2002).
- [3] D. Fukayama, T. Oyamada, T. Nakano, T. Gotoh and K. Yamamoto, J. Phys. Soc. Japan, **69** (2000) 701.
- [4] G. Stolovitzky, K.R. Sreenivasan and A. Juneja, Phys. Rev. E**48** (1993) R3217.

# DEPENDENCE OF LEVY STATISTICS WITH REYNOLDS NUMBER

*Application to turbulence intermittency and spray modeling*

Nicolas Rimbert and Olivier Séro-Guillaume

LEMTA, INPL-UHP-CNRS, 2 av. de la Forêt de Haye,  
F-54504 Vandoeuvre cedex

KAP

**Abstract:** In this poster, we show that Kida's log-stable law for the intermittency of turbulence can be extended over a wide range of Taylor scale Reynolds number  $Re_\lambda$ . This yields a simple relation between the scale parameter of the law and  $Re_\lambda$ . Since log-normal laws were firstly introduced by Kolmogorov for the size of particles under pulverization, log-stable laws are applied to the experimental drop size p.d.f. in an annular gas-liquid flow. Though the fitting is quite good there does not seem to be any clear relationship between the parameters of the law and the external parameters of the experiment. This may be related to a breaking of the homogeneity hypothesis.

**Key words:** Turbulence intermittency modeling, Turbulent spray modeling, Log Stable laws, Reynolds scaling of the parameters.

## 1. INTRODUCTION

Log-stable distributions have already been used to model turbulence intermittency by Schertzer *et al.* [1] and Kida [2]. Both Kida's studies led to a common value of the stability index  $\alpha = 1.65$ . Log-stable laws are a generalization of the log-normal laws first introduced in 1941 by Kolmogorov to describe a spray drop number p.d.f.[3]. This result was later used by Oboukov to describe turbulence intermittencies [4] and then back in turbulence by Kolmogorov in his 1962 "refined similarity hypothesis" paper [5]. We show in this poster that log-stable laws can be used both in turbulence intermittency modeling and for spray drop p.d.f. In turbulence, Kida's results is extended over of wide range of Taylor scale Reynolds number  $Re_\lambda$ . It is then shown that a simple scaling relation can be obtained between the parameters of the stable law and  $Re_\lambda$ . As for spray modeling, experimental data of Simmons and Hanratty [6] are fitted with a log-stable p.d.f. Though the fittings are good there does not seems to be any clear relation between the parameters of the law and the external parameters of the experiments. This may be related to a breaking of the homogeneity hypothesis.

## 2. LOG STABLE PDF IN TURBULENCE INTERMITTENCY MODELING

A random variable  $X$  [7] is said to have a stable distribution  $L_\alpha(x; \beta, \sigma, \delta)$  if there are parameters  $0 < \alpha \leq 2$ ,  $0 < \sigma$ ,  $-1 \leq \beta \leq 1$  and  $\delta$  real such that its characteristic function has the following form:

$$\hat{p}_\alpha(k; \beta, \sigma, \delta) = \exp\left(ik\delta - \sigma^\alpha |k|^\alpha [1 + i(sign(k))\beta\omega(|k|, \alpha)]\right) \quad (1)$$

where

$$\omega(|k|, \alpha) = \begin{cases} \tan(\alpha\pi/2) & \text{if } \alpha \neq 1 \\ -(2/\pi)\log|k| & \text{if } \alpha = 1 \end{cases}$$

$\alpha$  is the stability index governing the decrease of the tail of the probability,  $\sigma$  is the scale parameter, analogous to the standard deviation of the normal law, and  $\delta$  is the shift parameter governing, but not to be confounded with, the mean of the distribution.  $\beta$  is a skewness parameter, different from the traditional skewness:  $\beta = 0$  indicates a symmetric distribution and  $\beta < 0$ , for instance, a distribution skewed to the left

Let us define  $\varepsilon_r$  as the turbulence dissipation averaged over a ball of radius  $r$ . If the logarithm of  $\varepsilon_r$  is a stable law with skewness parameter  $\beta = -1$  then the following moments read [7]:

$$\langle \varepsilon_r^q \rangle = \exp \left[ q\delta - \frac{\sigma^\alpha}{\cos\left(\frac{\pi\alpha}{2}\right)} q^\alpha \right], q > 0$$

### 3. REYNOLDS DEPENDENCY OF THE SCALE PARAMETER

The following hyper-flatness factor  $H_p$  are defined as

$$H_p(r) = \frac{G_p(r)}{(G_2(r))^{p/2}} = \frac{\langle |u(x+r) - u(x)|^p \rangle}{\langle |u(x+r) - u(x)|^2 \rangle^{p/2}} \quad (3) \text{ where } G_p(r) = \langle |u(x+r) - u(x)|^p \rangle \quad (4)$$

and  $u$  is the turbulent velocity. Measurement of these hyper-flatness factors have been obtained by Kerr [8] from a DNS of homogeneous isotropic turbulence and have been experimentally measured by Belin *et al.*, up to a Taylor scale Reynolds number of 750 with accuracy [9].

Using the following hypothesis of Kolmogorov [5], who assumed that at high Reynolds number

$$|u(x+r) - u(x)| \sim \varepsilon_r^{1/3} r^{1/3}, \quad (5)$$

we can write coefficients  $H_p$  as

$$H_p = \frac{\langle \varepsilon_r^{p/3} \rangle}{\langle \varepsilon_r^{2/3} \rangle^{p/2}} = \exp(\xi_p) \quad (6) \text{ where } \xi_p = -\frac{\sigma^\alpha}{\cos\left(\frac{\pi\alpha}{2}\right)} \left\{ \left( \frac{p}{3} \right)^\alpha - \frac{p}{2} \left( \frac{2}{3} \right)^\alpha \right\} \quad (7) \text{ if equation (2) is used}$$

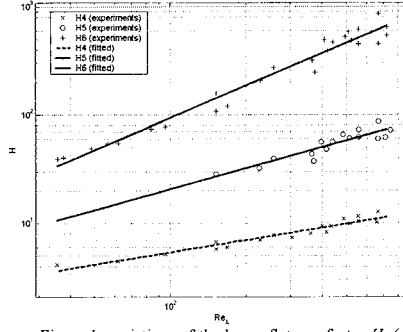


Figure 1: variations of the hyper-flatness factor  $H_4$  (+: experiments, solid line: fitting of a power-law),  $H_5$  (o: experiments, solid line: fitting of a power-law) and  $H_6$  (x: experiments, dashed line: fitting of a power-law) with Taylor scale Reynolds number  $Re_\lambda$

Figure 1 shows the evolutions of the hyper-flatness factor with  $Re_\lambda$ . As previously explained, for  $35 < Re_\lambda < 200$ , experimental points are obtained by the numerical simulations of Kerr and for  $200 < Re_\lambda < 750$ , they come from the experimental work of Belin *et al.* Lines are the results of the correlations (8), (9) and (10) which are of the form  $H_i = k_i \cdot Re_\lambda^{\alpha_i}$ . They were obtained for  $Re_\lambda$  ranging from 35 to 750.

$$H_4 = (0.95 \pm 0.31) Re_\lambda^{(0.376 \pm 0.05)} \quad (8)$$

$$H_5 = (1.07 \pm 0.68) Re_\lambda^{(0.642 \pm 0.15)} \quad (9)$$

$$H_6 = (0.99 \pm 0.51) Re_\lambda^{(0.989 \pm 0.08)} \quad (10)$$

Applying definition (6) one gets:

$$\xi_4 = 0.376 \ln(Re_\lambda) - 0.045 \quad (11)$$

$$\xi_5 = 0.642 \ln(Re_\lambda) + 0.069 \quad (12)$$

$$\xi_6 = 0.989 \ln(Re_\lambda) - 0.0126 \quad (13)$$

By assuming that the value of Kida  $\alpha = 1.65$  is correct and independent of the Reynolds number, by making use of (7) and by dividing the three relations (10), (11) and (12) by

$$\frac{1}{\cos(\pi\alpha/2)} \left[ \left( \frac{p}{3} \right)^\alpha - \frac{p}{2} \left( \frac{2}{3} \right)^\alpha \right], p=4, 5, 6 \quad (14)$$

one gets:

$$\sigma^\alpha = (0.53 \pm 0.04) \ln(Re_\lambda) + 0.00 \pm 0.20. \quad (15)$$

The three relations (10-11-12) merge in a single relation. It can be noted that if  $\alpha$  is a function of the Reynolds number, the possibility of having (15) is rather unlikely.

#### 4. LOG STABLE PDF IN SPRAY DROP PDF

Here, data are experimental data collected by Simmons *et al.* in a horizontal annular gas-liquid flow [6]. They are given through a normalized volume distribution function  $f_V$  which is defined as:

$$\frac{dV}{dD} = f_V(D), \quad \int_0^\infty f_V(D) dD = 1 \quad (16)$$

where  $D$  is the drop diameter. Important parameters of the experiments are  $V_{SL}$  the velocity of the liquid relatively to the solid cylinder, ranging from 2.2 to 13.5 cm/s and  $V_{SG}$  the velocity of the gas relatively to the solid, ranging from 30 to 50 m/s.

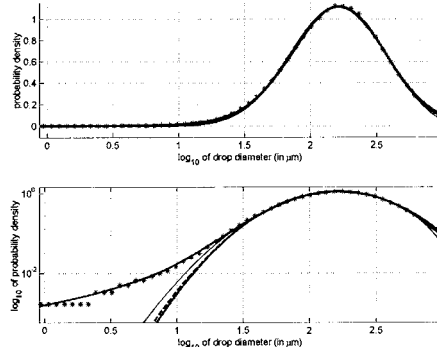


Figure 2: fitting of the drop spray p.d.f.  $V_{SL} = 0.041$  m/s  $V_{SG} = 35$  m/s.  
From left to right the p.d.f. are log-stable p.d.f., Upper-limit Evans  
p.d.f., log-normal p.d.f. and log-Weibull p.d.f.

The p.d.f. is calculated by the inverse Fourier transform of (1). All the four parameters  $\alpha, \beta, \sigma, \delta$  were free in order to give the best fit to the experimental data. Nevertheless the value  $\beta = -1$  has been found in almost all experimental case and can no longer be considered as an independent parameter. The logarithmic experimental p.d.f. is calculated from the bin distribution of the volume: the cumulated volume of drops in the bin  $[\log(d_i), \log(d_{i+1})]$  is taken to be the probability  $p_i$  that the logarithm of the drop diameter is located within this interval. The corresponding density  $y_i$  is then  $p_i$  divided by the width of the interval. This density is then affected to the midst of the interval. The p.d.f. is then fitted by minimizing the error function:

$$Err_2 = \sqrt{\frac{(y_i - \bar{y}_i)^2}{y_i^2}} \quad (17)$$

where  $y_i$  are the measurements and  $y_i$  the results of the fitting as shown in Figure 1.  $Err_2$  for the log-stable p.d.f. vary from 1 to 5 percent. In figure 2, comparison is made between log-stable and traditional p.d.f used in atomization study: Upper-limit Evans, log-Weibull and log-normal p.d.f. On the lower diagram the p.d.f. has been represented on a logarithmic scale putting an emphasis on the tail of the distribution. It is clear that log-stable laws tackle better with the left tail of these p.d.f..

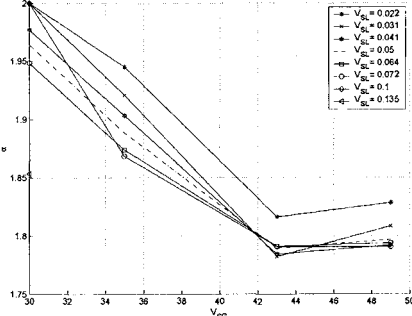


Figure 3: stability index  $\alpha$  found for different values of  $V_{SG}$  and  $V_{SL}$ .

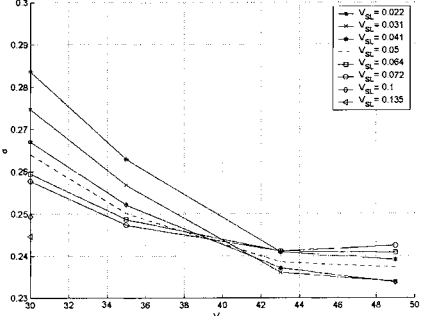


Figure 4: scale parameter  $\sigma$  found for different values of  $V_{SG}$  and  $V_{SL}$ .

Figure 3 and figure 4 shows the evolution of the stability index  $\alpha$  and scale parameter  $\sigma$  with two external parameters  $V_{SG}$  and  $V_{SL}$ . However, there does not seem to be any clear relation between these parameters.

## 5. CONCLUSION

Log-stable laws offer a good alternative to standard model both in turbulence intermittency modeling and in spray drop p.d.f modeling. Nevertheless, there seems to be important differences between the two presented cases. In homogeneous isotropic turbulence modeling, the stability index seems to be independent of the Reynolds number and the scale parameter simply related to it by relation (15). In spray modeling, there does not seem to be, in the case of an horizontal annular gas-liquid flow, any clear similarity law linking  $\alpha$  and  $\sigma$  to  $V_{SG}$  and  $V_{SL}$ . By comparison with turbulence experiments, we cannot make here any homogeneity hypothesis since larger drops and smaller drops are eventually separated by sedimentation (though the effect is not dominant since the Froude number is high). This sedimentation effect has been reported by Simmons and Hanratty [6] and eventually leads to the breaking of the homogeneity of the flow. Actually, when the gas flow speed is increased the stratification of the droplets is somewhat modified.

## REFERENCES

- [1] Schertzer D. and Lovejoy S. *Scaling and multifractal processes* Nonlinear variability in geophysics Institut d'etudes scientifiques de Cargese 1993
- [2] Kida S. *Log-Stable Distribution and Intermittency of Turbulence* J. Phys. Soc. Jap. **60**, 1, 5-8, 1991 and Kida S. *Log-stable distribution in turbulence* Fluid Dyn. Res. **8**, 135-138, 1991
- [3] Kolmogorov, A.N. *On the logarithmically normal law of distribution of the size of particles under pulverization*, Dokl. Akad. Nauk SSSR **31**, 99-101, 1941
- [4] Oboukhov A.M. *Some specific features of atmospheric turbulence*, J. Fluid Mech. **13**, 77-81, 1961
- [5] Kolmogorov, A.N. *A refinement of previous hypotheses concerning the local structure of turbulence in a viscous incompressible fluid at high Reynolds number*, J. Fluid Mech. **13**, 82-85, 1962
- [6] M.J.H. Simmons and T.J. Hanratty (2001) *Droplet size measurements in horizontal annular gas-liquid flow* Int. J. Multiphase Flow, **27**, 861
- [7] Samorodnitsky G. et Taqqu M.S. *Stable non-Gaussian random processes*. Chapman & Hall, 1994
- [8] Kerr R. M. *Higher-order derivative correlations and the alignment of small-scale structure in isotropic numerical turbulence* J. Fluid. Mech. **153**, 31-58, 1985
- [9] Belin F., Maurer J., Tabeling P., and Willaime H. *Velocity gradient distributions in fully developed turbulence : an experimental study* Phys. Fluids **9** (12), 3843-3850 1997 and Tabeling P. and Willaime H. *Transition at dissipative scales in large-Reynolds-number turbulence* Phys. Rev. E, **65**, 066301, 2002

# THE ASYMPTOTIC PROFILES IN FORCED CONVECTION TURBULENT BOUNDARY LAYERS

Luciano Castillo and Xia Wang

*Department of Mechanical, Aerospace and Nuclear Engineering*

*Rensselaer Polytechnic Institute, USA*

*castil2@rpi.edu*

**Abstract** Two new inner and outer temperature scalings are derived by means of similarity analysis of the equations of motion in forced convection turbulent boundary layers. Using the new scalings, the temperature profiles collapse into a single curve regardless of the strength of pressure gradient (PG) and changes in upstream conditions. Thus, the true asymptotic solution exists for temperature field even at a finite Peclet number.

**Keywords:** similarity analysis; forced convection; turbulent boundary layers; upstream conditions; pressure gradient; scaling laws; asymptotic solutions.

## 1. INTRODUCTION

Similarity analysis will be applied to seek the inner and outer temperature scalings which are proved to yield the asymptotic temperature profiles. In the limit as  $Re \rightarrow \infty$ , the boundary layer equations become independent of  $Re$ ; therefore, any scaling or function representing the boundary layer solutions must also be independent of the local  $Re$ . This is the “so-called” Asymptotic Invariance Principle: AIP (George & Castillo 1997). Hence, in this limit, the inner and outer scalings of turbulent boundary layers can be determined. In this investigation, attention will be given to the temperature profiles in a 2-D, incompressible, steady turbulent boundary layer with forced heat transfer between the wall and the free stream.

The inner and the outer energy equations describing the problem discussed here are given as

$$-\frac{q_w}{\rho c_p} = a \frac{\partial T}{\partial y} - \langle tv \rangle, \quad (1.1)$$

$$U \frac{\partial T}{\partial x} + V \frac{\partial T}{\partial y} = \frac{\partial}{\partial y} [- \langle tv \rangle]. \quad (1.2)$$

The related boundary layer conditions are as  $y \rightarrow 0$ ,  $T \rightarrow T_w$ ,  $\langle tv \rangle \rightarrow 0$ ,  $a \frac{\partial T}{\partial y}|_{y=0} = -\frac{q_w}{\rho c_p}$ ; and as  $y \rightarrow \infty$ ,  $T \rightarrow T_\infty$ ,  $\langle tv \rangle \rightarrow 0$ . The above equations can describe the energy transport in the turbulent boundary layer exactly in the limit as  $Pe \rightarrow \infty$ .

## 2. COMPARISONS OF VARIOUS SCALINGS

Using the AIP and assuming a different inner length scale from the Reynolds analogy, a new inner temperature scaling is obtained by similarity analysis. Combining the definition of the thermal displacement thickness with the similarity analysis, a new outer temperature scaling is obtained, which yields the asymptotic temperature profiles. Table 1.1 shows the comparison of scalings from the Reynolds analogy, GWC (George et al. 1997), and the present analysis. Clearly, the new temperature scalings are different from the other two for both the inner and the outer region, respectively. Notice that for the Reynolds analogy, only one single temperature scaling exists. In this table,  $St$  represents the Stanton Number;  $P_r$  the Prandtl Number;  $\delta_T$  the thermal boundary layer thickness; and  $\delta_T^*$  the thermal displacement thickness.

Table 1.1. Inner and outer temperature scalings.

	<i>Reynolds analogy</i>	<i>GWC</i>	<i>Present analysis</i>
Inner	$y_T^+ = \frac{yu_\tau}{\nu}$	$y_T^+ = \frac{yU_\infty}{\nu} St$	$y_T^+ = \frac{yU_\infty}{\nu} \sqrt{St}$
	$T_{si} = \frac{q_w}{\rho C_p u_\tau}$	$T_{si} = T_w - T_\infty$	$T_{si} = P_r (T_w - T_\infty) \sqrt{St}$
Outer	$\bar{y}_T = \frac{y}{\delta_T}$	$\bar{y}_T = \frac{y}{\delta_T}$	$\bar{y}_T = \frac{y}{\delta_T}$
	$T_{so} = \frac{q_w}{\rho C_p u_\tau}$	$T_{so} = (T_w - T_\infty) \frac{St}{C_f/2}$	$T_{so} = (T_w - T_\infty) \frac{\delta_T^*}{\delta_T}$

The experimental data studied here include the zero pressure gradient (ZPG) data (Blackwell 1972), the adverse pressure gradient (APG) data (Blackwell 1972; Orlando et al. 1974) and the favorable pressure gradient (FPG) data (Thielbahr et al. 1969). The PG data considered here have the different strength of PG and different upstream conditions (wind tunnel speed in this case). Figure 1.1(a), 1.1(c) and 1.1(e) show the inner temperature profiles in semi-log scale for all the above

measurements using three scalings in table 1.1. The data show the obvious dependence on PG and upstream conditions using the classical scaling or the GWC scaling. However, using the new scaling, all the data nearly collapse into one single curve, regardless of the strength of PG and upstream conditions. Figure 1.1(b), 1.1(d), and 1.1(f) show the same experimental data, but plotted in outer variables. Evidently, using the new scaling, all APG profiles collapse to a single curve although a small difference among APG, FPG and ZPG profiles exists. Clearly, the new scaling can remove effects of the upstream conditions and the strength of PG in the boundary layer, contrary to the classical scaling. This result is also consistent with the recent findings (Castillo et al. 2001) which show that there are only three velocity profiles in turbulent boundary layers: each for ZPG, FPG and APG flow respectively.

### 3. CONCLUSION

In summary, the similarity analysis shown here enables us to find the true asymptotic solutions in forced convection turbulent boundary layers, and it provides new insight into the effects of upstream conditions and the external PG in both the inner and the outer flow.

### REFERENCES

- Blackwell, B. F., Kays, W. M. and Moffat, R. J. (1972). The turbulent boundary layer on a porous plate: an experimental study of the heat transfer behavior with adverse pressure gradients. *Report No. HMT-16*, Thermosciences Division, Stanford University.
- Castillo, L. and George, W. K. (2001). Similarity analysis for turbulent boundary layer with pressure gradient: outer flow, *AIAA Journal*, 39(1): 41-47.
- George, W. K. and Castillo, L. (1997). Zero-pressure-gradient turbulent boundary layer. *Applied Mechanics Reviews*, 50: 689-729.
- George, W. K., Wosnik, M. and Castillo, L. (1997). Similarity Theory for forced convection thermal boundary layer. *Transp. Phenomena in Thermal Science and Process Engineering*, 1: 239-244.
- Orlando, A. F., Kays, W. M. and Moffat, R. J. (1974). Turbulent transport of heat and momentum in a boundary layer subject to deceleration, Suction, and Variable Wall Temperature. *Report No. HMT-17* Thermosciences Division, Stanford University.
- Thielbahr, W. H., Kays, W. M. and Moffat, R. J. (1969). The turbulent boundary layer: experimental heat transfer with blowing, suction, and favorable pressure gradient. *Report No. HMT-5*, Thermosciences Division, Stanford University.

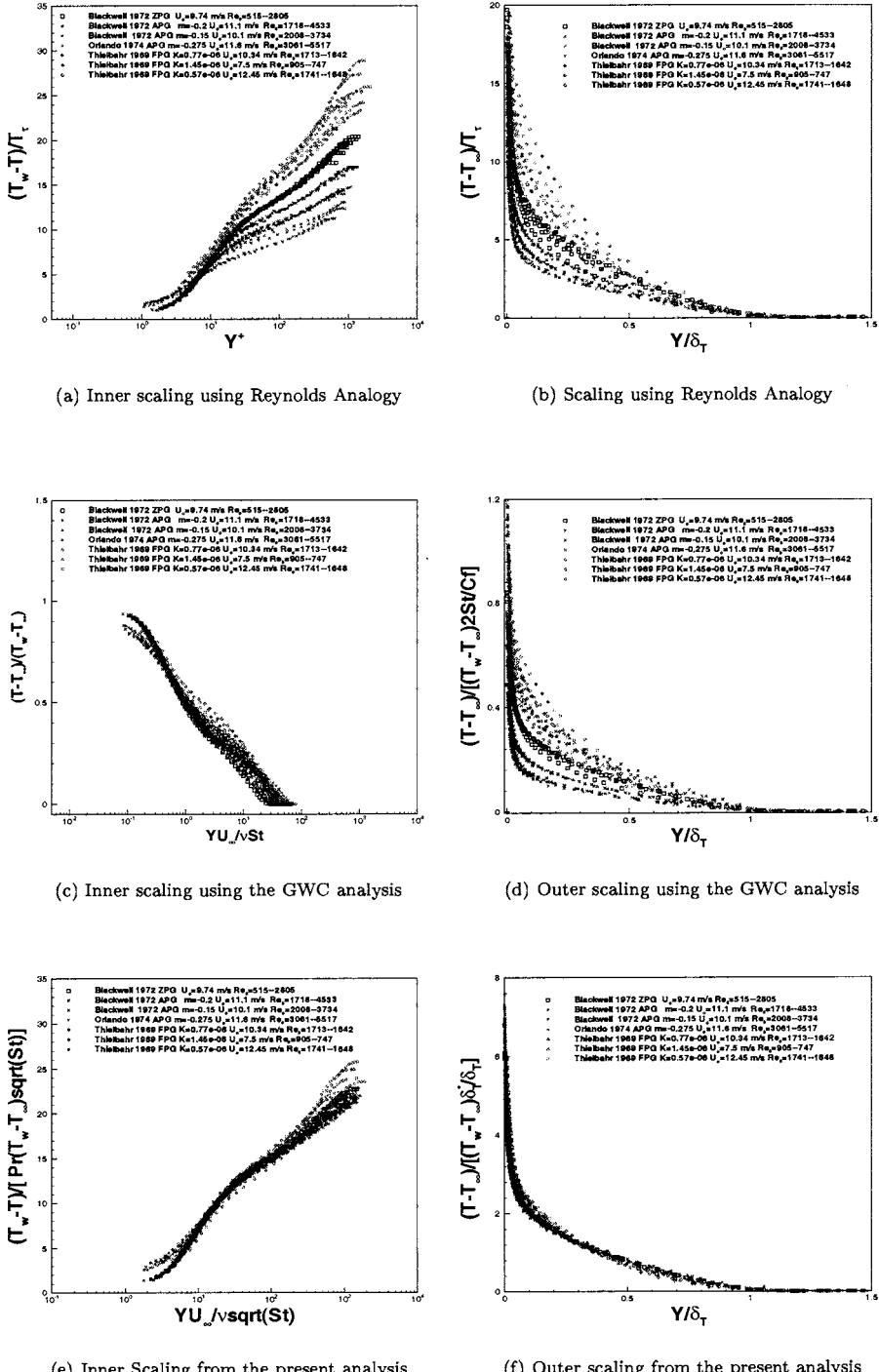


Figure 1.1. Comparisons of different temperature scalings for the ZPG, APG and FPG flow.

# SCALING TURBULENT BOUNDARY LAYER WITH SUCTION OR BLOWING

Raul Bayoan Cal and Luciano Castillo

*Department of Mechanical, Aerospace and Nuclear Engineering*

*Rensselaer Polytechnic Institute*

*castil2@rpi.edu*

**Abstract** The problem of transpired turbulent boundary layers subject to external pressure gradients has been analyzed using the similarity analysis of the equations of motion. Two main results were found. Firstly, the mean deficit profiles in zero pressure gradient (ZPG) or adverse pressure gradient (APG) boundary layer collapse with the free stream velocity, but to different curves depending on the blowing parameter and external pressure gradient. Secondly, the dependence on the blowing parameter and pressure gradient is completely removed from the outer flow when the mean deficit profiles are normalized by the Zagarola and Smits scaling.

**Keywords:** similarity analysis; transpiration; turbulent boundary layers; upstream conditions; pressure gradients; scaling laws; suction; blowing.

## 1. INTRODUCTION

Transpired boundary layers have been a well-known studied problem in engineering because of their direct industrial applications. It has been proven that suction delays separation by increasing the viscous drag. Suction also enhances stability in the boundary layer and decreases its thickness. Andersen, Kays and Moffat (Andersen et. al. 1972) carried out a series of measurements in which the main objective was to understand and analyze the influence of suction and blowing on the downstream flow.

The main objective of this investigation is to compare various scalings for the mean deficit profiles with the classical scaling (Clauser 1954).

Particularly, the scaling proposed by Thomas and Hasani (Thomas and Hasani 1992) using the suction parameter, the scaling from Castillo and George (George and Castillo 2001) using similarity analysis and the empirical scaling proposed by Zagarola and Smits (Zagarola and Smits 1998) will be used. Furthermore, the experimental data of Andersen et. al. with and without pressure gradient will be used to study the effects of suction and blowing in the outer flow of turbulent boundary layers.

## 2. RESULTS

The mean deficit profiles in the classical theory are normalized by the friction velocity, such that the outer flow is independent of the local Reynolds number. Table 1.1 summarizes the normalized velocity using the scaling proposed by the classical approach (top row), Thomas and Hasani (second row), Castillo and George (third row), and Zagarola and Smits (last row). The first column represents the investigator or theory, the second denotes the outer scaling for  $U_{so}$ , and the third column explains the main points and comments for each given scaling.

Table 1.1. The Outer Mean Velocity Deficit Scalings

Investigator	Velocity Scaling	Deficit	Observations
Classical Scaling $\frac{U_\infty - U}{U_\infty}$	$U_{so} = u_*$		Profiles do not collapse and the effects of the transpiration cannot be recognized. Figures 1.1.(a) and 1.2.(a)
Thomas/Hasani $\frac{U - U_\infty}{U_\infty}$	$U_{so} = u_*(1 + \beta + B_M)^{1/2}; \beta = \frac{\delta_1}{\tau_o} \frac{dP}{dx}; B_M = \frac{\rho v_o U_\infty}{\tau_o}$		Profiles collapse to a single curve, but the scaling fails when $\beta + B_M = -1$ or at separation. Figures 1.1.(b) and 1.2.(b)
Castillo/George $\frac{U_\infty - U}{U_\infty}$	$U_{so} = U_\infty$		Profiles collapse, but to different curves. The shape of the profiles are affected by the blowing parameter as well as the external pressure gradient. Figures 1.1.(c) and 1.2.(c)
Zaragola/Smits $\frac{U_\infty - U}{U_\infty}$	$U_{so} = U_\infty(\delta_*/\delta)$		Profiles collapse to a single curve. The effects of both transpiration and pressure gradient are completely removed from the outer flow. Figures 1.1.(d) and 1.2.(d)

Using the similarity analysis of the equations of motion in turbulent boundary layers with transpiration, the parameters for suction/blowing and pressure gradient are given as:

$$V_o^+ = \frac{V_o}{U_\infty d\delta/dx}, \quad (1.1)$$

$$\Lambda_\beta \equiv \frac{\delta}{\rho U_\infty V_o} \frac{dP_\infty}{dx} = \text{constant}, \quad (1.2)$$

$$\Lambda \equiv \frac{\delta}{\rho U_\infty^2 d\delta/dx} \frac{dP_\infty}{dx} = \text{constant}. \quad (1.3)$$

Notice that a power law relation,  $\delta \sim U_\infty^{-1/\Lambda}$ , exists if an equilibrium boundary layer exists at all. Therefore, the logarithm of  $\delta$  and  $U_\infty$  must show a linear relationship with a constant slope,  $-1/\Lambda$ , if the flow is in equilibrium. Using the present data, it will be shown that an equilibrium flow exists even when suction or blowing is present in the flow.

A comparison of various scalings for the mean velocity deficit profiles is shown in this section using the experimental data from Andersen and collaborators. Figure (1.1) shows the mean deficit velocity profiles for the APG flow subject to suction at the wall. The profiles for ZPG and APG flows with blowing at the wall are shown in figure (1.2) for various scaling laws. The observations of each particular scaling are given in the third column of table 1.1.

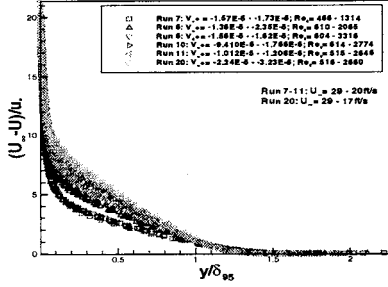
### 3. CONCLUSION

It was shown that mean deficit profiles subject to suction or blowing in ZPG and APG boundary layer collapse with the free stream velocity,  $U_\infty$ , but to different curves depending on the blowing parameter and the external pressure gradient. This is true as long as the upstream conditions are kept fixed. More importantly, the dependence on the initial conditions, the blowing parameter, and the strength of pressure gradient are completely removed from the outer flow once the mean deficit profiles are normalized by the Zagarola and Smits scaling,  $U_\infty \delta_*/\delta$ .

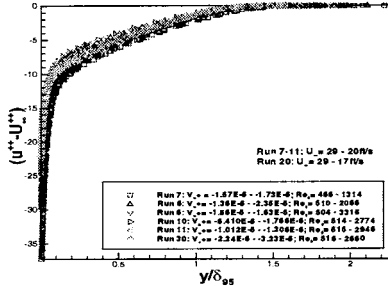
### REFERENCES

- Castillo, L. and George, W.K. "Similarity Analysis for Turbulent Boundary Layer with Pressure Gradient: Outer Flow," *AIAA Journal*, 39, 1, 41-47, (2001).
- Andersen, P.S., Kays, W.M. and Moffat, R.J. "The Turbulent Boundary Layer on a Porous Plate: An Experimental Study of the Fluid Mechanics for Adverse Free-Stream Pressure Gradients," *Report HMT-15*, Dept. of Mech. Eng., Stanford University, Stanford, CA (1972).
- Thomas, L.C. and Hasani, S.M. "Equilibrium Boundary Layers A New Wall / Outer Variable Perspective," *Transactions of ASME*, 114, 152-154 (1992).
- Zagarola, M.V. and Smits, A.J. "Mean-Flow Scaling of Turbulent Pipe Flow," *J. Fluid Mech.* 373, 33-79, (1998).

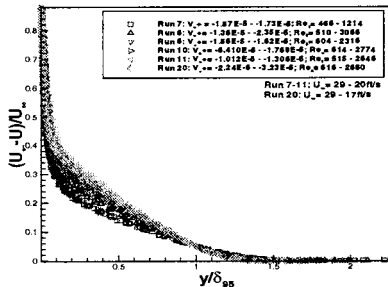
Clauser, F.H. "Turbulent Boundary Layer", *Adv. Applied Mech.*, IV, 1-51  
(1954).



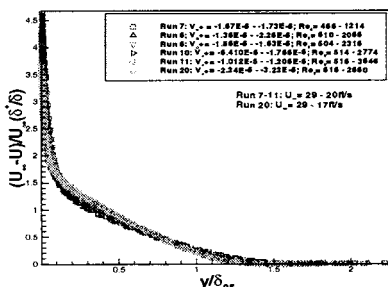
(a) Classical Scaling



(b) Thomas/Hasani Scaling

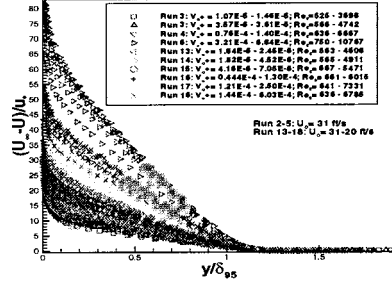


(c) Castillo/George Scaling

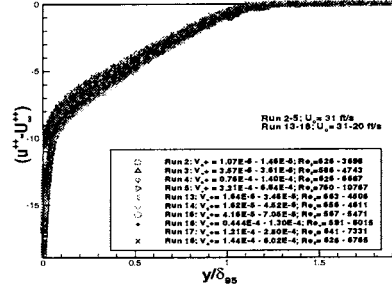


(d) Zagrarola/Smits Scaling

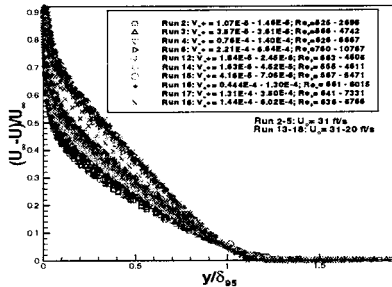
Figure 1.1. Mean velocity deficit profiles in APG with suction at the wall.



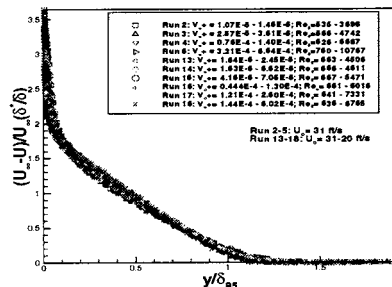
(a) Classical Scaling



(b) Thomas/Hasani Scaling



(c) Castillo/George Scaling



(d) Zagrarola/Smits Scaling

Figure 1.2. Mean velocity deficit profiles for ZPG and APG with blowing at the wall.

# HOMOGENEOUS ANISOTROPIC TURBULENCE

L. Biferale

*Dipartimento di Fisica, Università di Tor Vergata, Roma, Italy  
INFM, Unità di Tor Vergata, I-00133, Roma, Italy.*

I. Daumont

*Dipartimento di Fisica, Università di Tor Vergata, Roma, Italy*

A. Lanotte\*

*CNR-ISAC, I-73100, Lecce, Italy  
INFM, Unità di Tor Vergata, I-00133, Roma, Italy.  
lanotte@roma2.infn.it*

F. Toschi

*CNR-IAC, I-00161, Roma, Italy  
INFM, Unità di Tor Vergata, I-00133, Roma, Italy.*

**Abstract** We present a numerical study of *anisotropic* statistical fluctuations in stationary *homogeneous* turbulent flows. By means of a new argument, we are able to predict the dimensional scaling exponents,  $\zeta_d^l(p) = (p + l)/3$ , for the projections of the  $p$ -th order structure function in the  $l$ -th sector of the rotational group. Using these as a reference for normal behaviour, we show that the measured exponents are anomalous, i.e., they exhibit a clear deviation from the dimensional prediction. Some preliminary results about decaying anisotropic turbulence are also given.

The validity of the ideas of restoration of universality and isotropy at small scales in turbulent flows as posed by the classical theory is still under debate in modern fluid dynamics(Frisch, 1996). Literature

---

\*Corresponding author

is rich of experimental, theoretical, and numerical works on the subject (Kurien and Sreenivasan, 2000; Shen and Warhaft, 2002; Arad et al., 1999; Biferale and Toschi, 2001). We have now some indications about the tendency towards isotropisation in various turbulent systems, but still we are not able to assess in a clean and quantitative way if, for example, the exponent characterising isotropic fluctuations is universal or not.

From an experimental point of view, it is not an easy task to build up experiments with different large-scale energy injection mechanisms, willing to probe universality; even more difficult is to build an experimental set-up allowing to probe anisotropic fluctuations (Kurien and Sreenivasan, 2000).

The main theoretical difficulties stem obviously from the nonlinearity of the problem: indeed, this has led various authors to tackle the linearised problem in many different ways. This is the case for example of (Yoshida and Kaneda, 2000; Arad and Procaccia, 2001; Grossmann et al., 2001). In (Yoshida and Kaneda, 2000), authors derive a linearisation of the Navier-Stokes equation with respect to the perturbation of a basic state and they assume the basic state to be a Kraichnan like velocity field (Kraichnan, 1994) (i.e., homogeneous, isotropic, with Gaussian statistics and  $\delta$ -correlated in time). From this starting point, they derive the steady-state equation for second-order moments and calculate the scaling exponents  $\zeta^l(2)$  for the isotropic part ( $l = 0$ ) and the first anisotropic fluctuation ( $l = 2$ ). Among the admissible  $\zeta^l(2)$ , those which dominate the scaling behaviour at small scales are associated to the so-called zero modes, that is the homogeneous solutions of the equation under exam. In (Arad and Procaccia, 2001), authors consider a “linear-pressure - model”: it is the transport equation for a passive vector with pressure, where again the driven field is a Kraichnan like velocity field. But at difference with the previous work, the present model equation does not contain a stretching term. Arad *et al.* solve the equation of the second order moments for any  $l$ , showing in particular that the spectrum of anisotropic scaling exponents can increase with  $l$  without bounds. This means that contributions in the scaling behaviour from higher anisotropic sectors  $\sim r^{\zeta^l(2)}$  decay faster as the scale becomes  $r$  smaller and smaller.

Grossman and collaborators also solve the steady-state equation for second order moment for any anisotropic fluctuation of order  $l$ , but within a variable-scale mean field theory of the Navier-Stokes equation and at changing the analytical properties of the forcing term. In their model, the mean field approximation implies that large scales feel the small ones as some sort of eddy viscosity.

Few comments are in order: in the first two cases, the dominant scaling

solutions are the zero-modes - thus containing also intermittency effects - but of a linear equation. So in general, we do not expect them to be equal to those associated to the full non-linear dynamics. In the third case, mean-field theory calculation excludes any intermittency effects: so the prediction is for the dimensional or normal scaling exponents  $\zeta^l(2)$ . But here the tensorial nature of the second order moments is not taken into account and this weakens their argument.

Numerical simulations certainly represent a good tool to investigate the issue: the main drawback is in the low values of the accessible Reynolds number, but at difference with experiments the whole velocity field is measurable and so the complete angular information about the flow is at disposal. In particular, the  $3D$  rotational group ( $SO(3)$ ) decomposition can be fully exploited to quantify different degrees of anisotropy. For these reasons, we decided to look at the problem by means of numerical simulations of a perfectly homogeneous and non isotropic flow: homogeneity, as will be clear in the sequel, is a fundamental assumption for the  $SO(3)$  decomposition to be meaningful.

We simulated a “Random Kolmogorov Flow”, i.e. a flow where only one component of the velocity is forced,  $v_z$ , at two wavenumbers (say  $k_1 = (1, 0, 0)$  and  $k_2 = (2, 0, 0)$ ). The forcing has fixed (in time) amplitudes and random phases. The large scale forcing is hence obviously non isotropic, but because of the random phases (whose values are  $\delta$  correlated in time) homogeneity is ensured. Energy is dissipated by an hyper-viscosity term at small scales. The integration is performed by a standard pseudo-spectral code on a periodic cubic domain of 256x256x256 grid points.

In order to quantify the anisotropies we have measured longitudinal structure functions along generic directions:

$$S_p(\mathbf{r}) = \langle [(\mathbf{v}(\mathbf{x}) - \mathbf{v}(\mathbf{x} + \mathbf{r})) \cdot \hat{\mathbf{r}}]^p \rangle, \quad (1)$$

and then decomposed them onto irreducible representation of the rotational group. This is particularly simple for scalar quantities, involving only the spherical harmonics  $Y_{lm}$ :

$$S_p^{lm}(|\mathbf{r}|) = \int S_p(\mathbf{r}) Y_{lm}(\hat{\mathbf{r}}) d\Omega. \quad (2)$$

In the inertial range of scales we expect that each fluctuation contributes to the raw structure function  $S_p(\mathbf{r})$  behaviour, with a power law term of the form:  $S_p^{lm}(r) \sim a_{lm}^p r^{\zeta(p)}$ . To give an assessment of the normal or anomalous behaviour of anisotropic fluctuations, we first need an estimate for the dimensional values of the exponents  $\zeta^l(p)$  for all orders  $p$  and in all sectors  $l$ . Our argument is presented in some detail in (Biferale

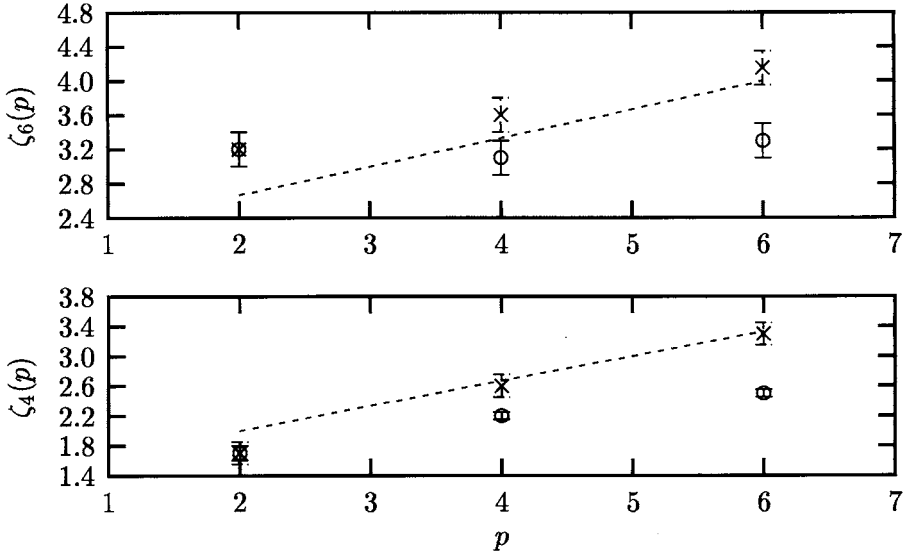


*Figure 1.* Comparison between the dimensional estimate,  $\zeta_d^j(p) = (p+j)/3$ , (straight lines), the measured exponents,  $\zeta^j(p)$  ( $\circ$ ) and the exponents,  $\zeta_r^j(p)$ , obtained after random dephasing ( $\times$ ), for  $p = 2, 4, 6$ . Top: sector  $j = 6$ , bottom: sector  $j = 4$ . Error bars are estimated by looking both at fluctuations in the local slopes and by performing the same analysis on different sub-samples.

et al., ): it is based on the idea that large-scale energy forcing and/or the boundary conditions are such as to enforce a large-scale anisotropic driving velocity field  $\mathbf{U}$ . A prediction for intermediate (small) scales anisotropic fluctuations may then be obtained by studying the influence on the inertial range of the large-scale  $\mathbf{U}$ : its major effect will be an instantaneous shear  $S_{ik} = \partial_k U_i$  acting as an anisotropic forcing term on small scales.

For our interest now, we just recall that our argument leads to the following expression for the scaling exponents  $\zeta_d^l(p) = (p+l)/3$  (“d” stands for dimensional). This last coincides with K41 dimensional prediction for the exponents of the isotropic fluctuation and with Lumley’s prediction  $\zeta^{l=2}(2) = 4/3$  for the first anisotropic exponent  $l = 2$  of the second order structure function. The analysis of the data from the numerical simulation showed high intermittency as a function of the order of the velocity correlation within each fixed anisotropic sector: the measured exponents  $\zeta^l(p)$  are well below the dimensional values  $\zeta_d^l(p)$  (see Fig. 1). In addition, it has been highlighted that the dimensional behaviour plays an important role, fixing the sub-leading background scaling. Indeed, it is easy to

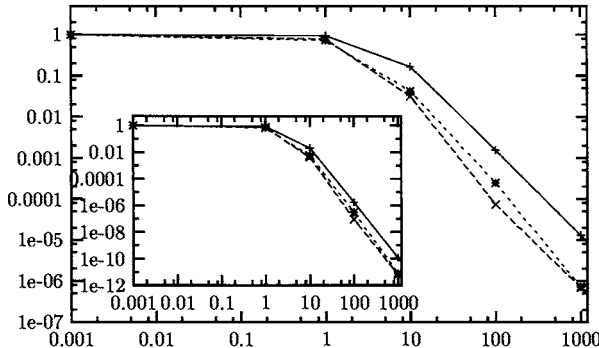


*Figure 2.* Fixed scale, long time decaying of the second order projections  $S_2^{lm}$  ( $r = 40, t$ ) on the isotropic sector ( $j = 0, m = 0$ ) (top curve) and the two most intense anisotropic sectors, ( $j = 2, m = 2$ ) and ( $j = 4, m = 0$ ) (bottom curves) up to  $t \sim 10^3 \tau_0$ , being  $\tau_0$  the reference large scale eddy turn over time.

see that when we break the spatial organisation of the field by randomly re-shuffling all velocity phases,  $\hat{u}_i(\mathbf{k}) \rightarrow P_{il}(\mathbf{k}) \hat{u}_l(\mathbf{k}) \exp(i\theta_l(\mathbf{k}))$ , where  $P_{il}(\mathbf{k})$  is the incompressibility projector, we obtain a dimensional scaling for the projections  $S_p^{lm}(r)$ .// Finally a hierarchical organization of scaling exponents at fixed order of the velocity correlation at changing the anisotropic sector is found. This is in agreement with classical K41 theory and shed some light on what is commonly called “persistence of anisotropies”: indeed, the numerical results tell us that isotropy is restored at small scales and the observed persistence of anisotropies is a combined effect of intermittency and anisotropy (Biferale and Vergassola, 2001). Another way to look at the question of restoration of isotropy at small scales in turbulent flows is by considering the decay process. Starting from independent configurations of the stationary anisotropic run of the Random Kolmogorov Flow, we also studied the temporal evolution of the decay process. We measured the full observable (2) and single point quantities (like  $\langle v_i(t)v_j(t) \rangle$  and  $\langle \omega_i(t)\omega_j(t) \rangle$ ) as a function of time, at various different times (equispaced on logarithmic scale). As expected, energy and enstrophy decay as  $t^{-2}$  and  $t^{-2.5}$  respectively.

We just present some preliminary results concerning the study of the decay of the isotropic  $S_p^{l=0}(r, t)$  and anisotropic parts  $S_p^l(r, t)$ . In Fig. 2, there is a plot of the long-times decaying properties of the second order projections  $S_2^l(|\mathbf{r}|)$  on the isotropic and anisotropic setors at a fixed

scales in the inertial range, say  $r = 40$ . The anisotropic sectors show the tendency to decay faster than the isotropic one, i.e. at fixed scale there is a tendency toward a recovery of isotropy for times long enough. This is a first, but clear, indication that restoration of isotropy at small scale is a robust feature of turbulent flows.

## References

- Frisch, U. (1996). *Turbulence: The Legacy of A. N. Kolmogorov* Cambridge University Press, Cambridge, UK.
- Kurien, S. and Sreenivasan, K. (2000). Anisotropic scaling contributions to high-order structure functions in high-Reynolds-number turbulence. *Phys. Rev. E*, 62:2206–2212.
- Shen, X. and Warhaft, Z. (2002). Longitudinal and transverse structure functions in sheared and unsheared wind-tunnel turbulence. *Phys. Fluids*, 14:370–381.
- Arad, I., L'vov, V. S. and Procaccia, I. (1999). Correlation functions in isotropic and anisotropic turbulence: The role of the symmetry group. *Phys. Rev. E*, 59:6753–6765.
- Biferale, L. and Toschi, F. (2001). Anisotropic homogeneous turbulence: hierarchy and intermittency of scaling exponents in the anisotropic sectors. *Phys. Rev. Lett.*, 86:4831–4834.
- Yoshida, K. and Kaneda, Y. (2000). Anomalous scaling of anisotropy of second order moments in a model of a randomly advected solenoidal vector field. *Phys. Rev. E*, 63:016308-1–016308-8.
- Arad, I. and Procaccia, I. (2001). Spectrum of anisotropic exponents in hydrodynamic systems with pressure. *Phys. Rev. E*, 63:056302-1–056302-19.
- Grossmann, S., Von der Heydt, A. and Lohse, D. (2001). Scaling exponents in weakly anisotropic turbulence from the Navier-Stokes equation. *J. Fluid Mech.*, 440:381–390.
- Kraichnan, R. H. (1994). Anomalous scaling of a randomly advected passive scalar. *Phys. Rev. Lett.*, 72:1016–1019.
- Biferale, L., Daumont, I., Lanotte, A. and Toschi, F. (2002). Anomalous and dimensional scaling in anisotropic turbulence. *Phys. Rev. E*, to appear.
- Biferale, L. and Vergassola, M. (2001). Isotropy vs anisotropy in small-scale turbulence. *Phys. Fluids*, 13:2139–2141.

# FOUR-DIMENSIONAL MEASUREMENTS OF THE STRUCTURE OF DISSIPATIVE SCALES IN AN AQUEOUS NEAR-ISOTROPIC TURBULENCE

L. J. Jiang, S. S. Shy\*, T. S. Yang, and J. H. Lee

*Department of Mechanical Engineering, National Central University, Chung-Li 32054, TAIWAN*

**Abstract:** This note reports a particle image velocimetry technique for obtaining fully resolved measurements of the velocity field  $\mathbf{u}(x,y,z,t)$  throughout a four-dimensional spatiotemporal region on the inner scale in a near-isotropic stationary turbulence generated by a pair of vibrating grids in a water tank. The method uses a high-speed successive sweeping laser sheet and two synchronous high-speed stereo CCD cameras combined with a fast image processing system, so that the underlying full spatial velocity field and the corresponding kinetic energy dissipation rate field can be determined. Measurements confirm that the distribution of the dissipation rate field is a highly intermittent phenomenon, in which high kinetic energy dissipation rates occur infrequently and are correlated with regions of high principal strain rate, in consistent with the results found by Sreenivasan & Antonia. The fine structures of the kinetic energy dissipation rate field in the present turbulence are complex, containing line-like, blob-like, and sheet-like structures with the diameter, size, and thickness ranging in scale from 1 to 6 Kolmogorov scale ( $\eta$ ) with a mean of about  $3\eta$ . These data are useful for investigating topological features of fine structure turbulence.

**Key words:** 4D PIV, kinetic energy dissipation rate, fine structures, vibrating grids turbulence, near-isotropic turbulence

## 1. INTRODUCTION

Mixing occurs at the finest scales of turbulence, an important issue for enormous practical applications, which has been thoroughly investigated by many theories, simulations, and experiments [e.g., 1-5]. There are, however,

\* Corresponding author: [sshy@cc.ncu.edu.tw](mailto:sshy@cc.ncu.edu.tw); Fax: 886-3-425-4501

some issues which are not well understood, in particular, the topological features of fine scale turbulence.

Ever since Burgers [1] and Townsend [2], three canonical structures of the dissipative scales for the vorticity field in turbulence were recognized as the line-like, sheet-like, and blob-like elements, respectively. The line-like structure has one major dimension much greater than the other two, whereas the sheet-like structure has one major dimension much smaller than the other two. Kuo & Corrsin [6] found experimentally that finest scales were more to be line-like than sheet-like in a fully turbulent flow. Furthermore, She et al. [3] concluded that the highest values of the vorticity were concentrated in line-like structures using direct numerical simulations. However, Buch & Dahm [5] reported that the sheet-like structure is the only underlying canonical element of the scalar field fine structure for turbulent flows, based on a co-flow axisymmetric turbulent jet with high-speed, full spatial laser-induced fluorescence (LIF) measurements. Using similar LIF technique, Shy et al. [7] also measured scalar dissipation rate fields in a near-isotropic turbulence that was generated by a pair of vertically vibrating grids in a water tank. They found that fine scale mixing occurs in both strained laminar diffusion sheet-like layers and line-like tubes (roughly circular interactions are observed). Note that the scalar gradient is most closely aligned with the largest compressive principal strain axis (normal to the vorticity) [8]. More recently, Tsurikov & Clemens [9] measured simultaneously the scalar and the kinetic energy dissipation structures of the co-flow axisymmetric turbulent gas-phase jet using 2-D LIF and 2-D PIV techniques, respectively. They reported that the scalar dissipative structures are sheet-like, while the structures of the KE dissipation rate field are more topologically complex. However, the jet flow is a free shear turbulence, unlike the vibrating-grids turbulence (VGT) which has zero-mean-shear characteristics or numerical isotropic turbulence which is commonly assumed to be statistically time-invariant in periodic domains. Hence, different types of turbulence may be one of the reasons for the aforementioned discrepancy on fine structures of turbulence. In addition, the true dissipation rate must be obtained from all three-dimensional velocity data fields, because 2-D measurements can only yield 4~5 of 9 components of the strain rate tensor. Therefore, there is a need to further study the true dissipative structures, in particular, the full spatial KE dissipation rate field in statistically stationary isotropic turbulence, such as the one presented here using a high-speed 4D particle image velocity (PIV) in the VGT flow.

The transport equation for the kinetic energy in turbulence [10] can be written as

$$\frac{\partial q}{\partial t} + \vec{u} \cdot \nabla q + \nu \nabla^2 q = -\vec{u} \cdot \nabla p + \nu (\nabla \vec{u} \cdot \nabla \vec{u}^T) - \varepsilon \quad (1)$$

where  $\bar{u}$  is the velocity vector,  $q = 1/2 \bar{u} \cdot \bar{u}$  the KE per unit mass,  $p$  the pressure,  $\nu$  the kinematic viscosity of the fluid, and  $\varepsilon$  the KE dissipation rate, respectively. Note that  $\varepsilon$  can be represented as

$$\varepsilon = 2\nu s : s \quad (2)$$

where  $s = 1/2(\partial u_i / \partial x_j + \partial u_j / \partial x_i)$  is the strain rate tensor in index notation. In order to measure  $\varepsilon$  directly, the resolution of measurements must be high enough to resolve the finest length and time scales of turbulence and the measurements must be in all three spatial dimensions such that direct differentiation of the velocity gradients can be performed. Thus, the corresponding full spatial vorticity, strain rate, and KE dissipation rate fields can be extracted and then used to the identification of the aforementioned canonical elements of the fine scale structures of KE dissipation rate fields in near-isotropic stationary turbulence.

## 2. EXPERIMENTAL

Figure 1 shows schematic diagrams of the experimental setup, including the VGT apparatus and the associated 4-D PIV arrangements. The reader is directed to Ref. [11] for a detailed treatment of the VGT apparatus. However, vertically oscillating a pair of horizontally-oriented, specially-designed grids in a water tank of  $15 \text{ cm} \times 15 \text{ cm} \times 30 \text{ cm}$  can generate near-isotropic stationary turbulence in the core region between the two grids. In this study, the distance between the two grids is fixed to be  $10.56 \pm 2 \text{ cm}$ , where the grid stroke is  $S = 2 \text{ cm}$ , the grid mesh size is  $M = 3 \text{ cm}$ , and the grid oscillation frequency is  $f = 6 \text{ Hz}$ , yielding a grid turbulent Reynolds number  $Re_g = fSM/\nu = 3,600$ .

The full spatial velocity field measurements are obtained via a very low inertia, galvanometric mirror scanner to sweep synchronously a 5-W Argon-ion laser sheet through the desired spatial volume of  $1.4 \text{ cm} \times 1.2 \text{ cm} \times 0.50 \text{ cm}$  in the centre of the tank between the two grids (Fig. 1). These images are recorded by two synchronized high-speed CCD cameras (up to 8,000 frames/s) with PCI data acquisition cards and computers. In this study, the two CCD cameras are operated at 250 frames/s, each data image having  $480 \times 420$  pixels. Thus, the temporal separation between successive data planes is 4 ms and the spatial resolution is about  $29 \mu\text{m}$ , which are respectively much smaller than the estimated Kolmogorov time (42 ms) and length (0.21 mm) scales. The seeding particles for the present PIV measurements in water are polyethylene with a mean diameter of  $15 \mu\text{m}$  and a density of  $1.03 \text{ g/cm}^3$ .

Following the work of Adrian and his co-workers [12] and Hu et al. [13], a 3-D calibration procedure was used in the present study, as schematically shown in Fig. 2. The distorted images of a uniform Cartesian grid (see Fig. 2) was first calibrated at several locations across the thickness of each laser

sheet (0.3 cm) along the scanning z-direction (see Fig.1) using the mapping function between 3D object fields ( $x,y,z$ ) and 2D camera image planes ( $X^{(c)}, Y^{(c)}$ ) at which  $X^{(c)} = F^{(c)}(x,y,z)$ , where  $c = L,R$  for left and right cameras. Then the displacement of a particle image on camera c is  $\Delta X_i^{(c)} = F^{(c)}(x_j + \Delta x_j) - F^{(c)}(x_j)$ , where  $i = 1,2$  and  $j = 1,2,3$ . Following that the first-order relationship between an image plane displacement on each of both cameras and an object plane displacement is  $\Delta X_i^{(c)} \approx \nabla F_{ij}^{(c)} \Delta x_j$  by applying Taylor series expansion and volume averaging over the interrogation cell, where  $\nabla F_{ij}^{(c)} = \partial F_i^{(c)} / \partial x_j$ . Hence, the wanted 3-D displacements can be determined using a least-squares approach [12]. Note that the present mapping function was a multidimensional polynomial, fourth order in x- and y-directions paralleling the laser sheet and second order in z-direction normal to the laser sheet plane, same as that used by Hu et al. [13] with 31 coefficients to be determined by the least-squares method. Using a Matlab-based cross-correlation PIV software together with the adaptive windows offset developed by Hart [14] for greater accuracy, the 3-D velocity fields can be thus obtained.

### 3. RESULTS

Figure 3 displays three typical 3D velocity maps at three different  $z$  positions obtained from the present 4D PIV imaging. The three axes are normalized by the local strain-limited viscous diffusion scale  $\lambda_v$ , which is approximately 5.9 times the Kolmogorov scale  $\eta$  [5]. The different colors denote the local velocity component in the  $z$ -direction at each data point, see the color bar for magnitude and orientation. Also plotted is the reference arrow of 1.44 cm/s, which is the energy-weighted r.m.s. turbulent intensity for the VGT flow at  $f=6$  Hz obtained by LDV measurements [11]. The true KE dissipation rate field can be thus determined by differentiation of these data planes in all three directions.

A typical spatial data volume of the logarithm of the 3-D KE dissipation rate field  $\log_{10}\epsilon/\langle\epsilon\rangle$  is shown on Fig. 4a, where  $\langle\epsilon\rangle$  is the measured local mean KE dissipation rate averaged over the data volume. Each data plane in the data volume is obtained by direct differentiation of the velocity data in the three adjacent data planes as the typical example shown in Fig. 3 using linear central differences. The 256 different colors represent the logarithm of the local instantaneous KE dissipation rate in the VGT flow. As shown in Fig. 4a, the fully resolved 3-D  $\log_{10}\epsilon/\langle\epsilon\rangle$  field confirm that the distribution of the KE dissipation rate field is a highly intermittent phenomenon, in which high KE dissipation rates occur very infrequently (only about 2 % volume fraction in any given data volume fraction of the present flow), in consistent with the results found by Sreenivasan & Antonia [4].

In order to display the fine structures of the KE dissipation rate field in a more clear way, we plot only high values of KE dissipation rate data for  $\log_{10}\varepsilon/\langle\varepsilon\rangle \geq 0.66$  and their corresponding iso-surface distributions (less than 2 % volume fraction) are shown in Fig. 4b. The fine structures of the KE dissipation rate field in the present turbulence are complex, containing mainly line-like and blob-like structures as well as some sheet-like structure at which all dissipations are concentrated. We estimate the average sizes of these KE dissipative structures, as schematically shown in Fig. 5. It is found that the thickness ranges in scale from  $1 \sim 6 \eta$  with a mean slightly less than  $3 \eta$ . Due to the space limit, other statistical and scaling properties will be discussed elsewhere.

#### 4. REFERENCES

- [1] Burgers, J. M., A Mathematical model illustrating the theory of turbulence. *Adv. Appl. Mech.*, Vol. 1, pp. 171-199 (1948).
- [2] Townsend, A. A., On the fine-scale structure of turbulence. *Proc. R. Soc. Lond. A.*, Vol. **208**, pp. 534-542 (1951).
- [3] She, Z. S., Jackson, E., and Orszag, S. A., Intermittent vortex structures in homogeneous isotropic turbulence, *Nature*, Vol. **344**, pp. 226-228 (1990).
- [4] Sreenivasan, K. R., and Antonia, R. A., The phenomenology of small-scale turbulence. *Ann. Rev. Fluid Mech.*, Vol. **29**, pp. 435-472 (1997).
- [5] Buch, K. A., and Dahm, W. J. A., Experimental study of the fine scale structure of conserved scalar mixing in turbulent shear flows. I.  $Sc \gg 1$ . *J. Fluid Mech.*, Vol. **317**, pp. 21-71 (1996).
- [6] Kuo, A. Y., and Corrsin, S., Experiments on the geometry of the fine-structure regions in fully turbulent fluid. *J. Fluid Mech.*, Vol. **56**, pp. 447-479 (1972).
- [7] Shy, S. S., Gee, K. L., and Lee, E. I., Three-dimensional measurements of scalar dissipation rates in a zero-mean-shear turbulence. *J. Flow Visual. Image Process.*, Vol. **6**, pp. 177-187 (1999).
- [8] Kerr, R. M., Higher-order derivative correlations and the alignment of small scale structures in isotropic numerical turbulence. *J. Fluid Mech.*, Vol. **153**, pp. 31-58 (1985).
- [9] Tsurikov, M. S., and Clemens, N. T., The structure of dissipative scales in axisymmetric turbulent gas-phase jets. *AIAA Paper 2002-0164* (2002).
- [10] Hinze, J. O., *Turbulence*, McGraw-Hill, New York (1975).
- [11] Shy, S. S., Tang, C. Y., and Fann, S. Y., A nearly isotropic turbulence generated by a pair of vibrating grids. *Exp. Thermal and Fluid Sci.*, Vol. **14**, pp. 251-262 (1997).
- [12] Soloff, S. M., Adrian, R. J., and Liu, Z-C., "Distortion compensation for generalized stereoscopic particle image velocimetry," *Meas. Sci. and Technol.*, Vol. **8**, pp. 1441-1454 (1997).
- [13] Hu, H., Saga, T., Kobayashi, T., Taniguchi, N., and Yasuki, M., Dual-plane stereoscopic particle image velocimetry : system set-up and its application on a lobed jet mixing flow. *Exp. Fluids*, Vol. **31**, pp. 277-293 (2001).
- [14] Hart, D. P., "Super-resolution PIV by recursive local-correlation", *J. of Visual.*, Vol. **10**, pp. 1-10 (1999).

This research was supported by the National Science Council, Taiwan (NSC 91-2212-E-008-030) and INER (912001 INER 012).

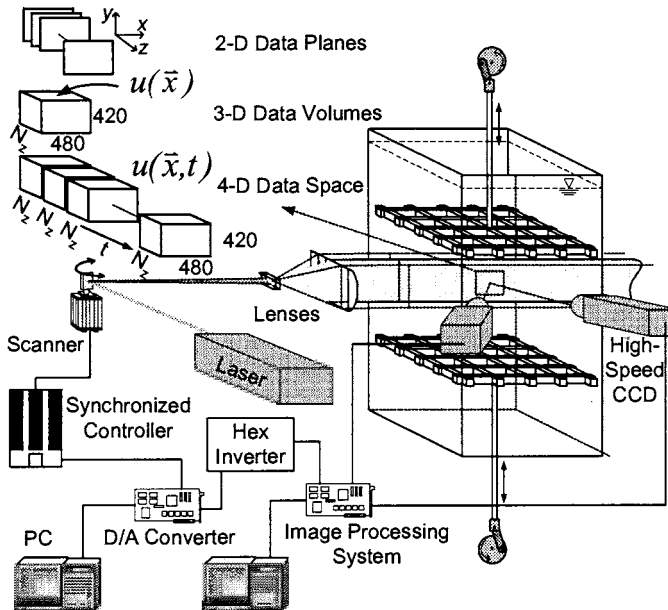


Fig.1. Schematic of the experimental setup, including the vibrating-grids turbulence generator and the associated 4-D PIV arrangements, each image data plane having a field of view of  $1.4 \text{ cm} \times 1.2 \text{ cm}$ .

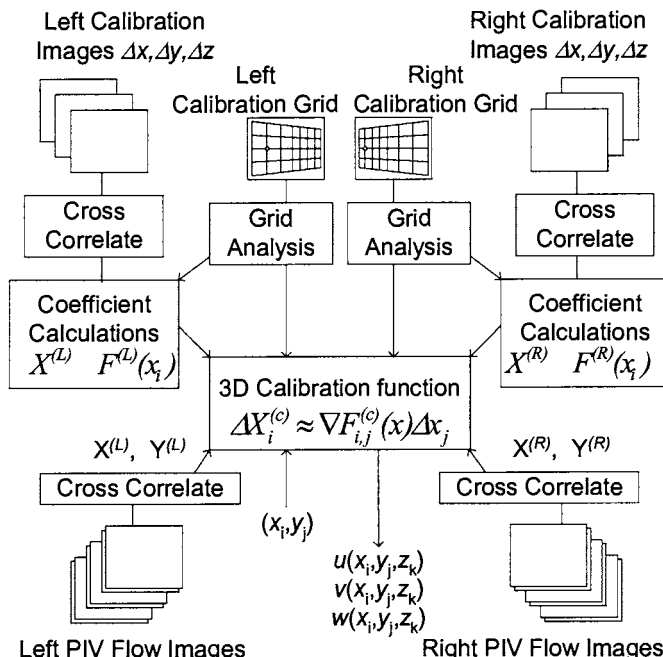


Fig.2. Flow chart for procedures of 3-D calibration and PIV acquisition and interrogation to compute displacements in the image data plane.

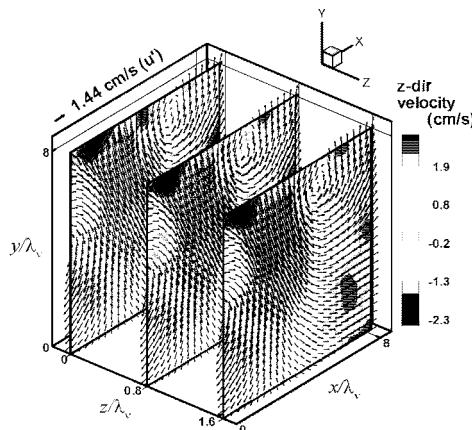


Fig. 3. The 3-D velocity maps at three different  $z$  positions, where  $\lambda_v$  is the local strain-limited viscous diffusion scale and  $\lambda_v \approx 5.9\eta$ . The color bar indicates the velocity component in the  $z$ -direction. The reference velocity arrow of 1.44 cm/s is the energy-weighted r.m.s. turbulent intensity at  $f = 6$ Hz measurements by LDV [11].

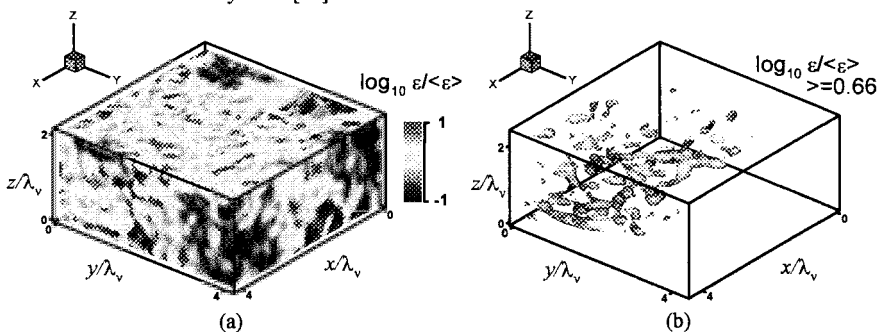


Fig. 4. (a) The 3-D kinetic energy dissipation rate field in the VGT flow where  $f = 6$ Hz and  $\langle \varepsilon \rangle$  is the mean kinetic energy dissipation rate averaged from the corresponding data volume. (b) Only the iso-surface distributions of fine-scale structures for  $\log_{10} \varepsilon / \langle \varepsilon \rangle \geq 0.66$  are plotted.

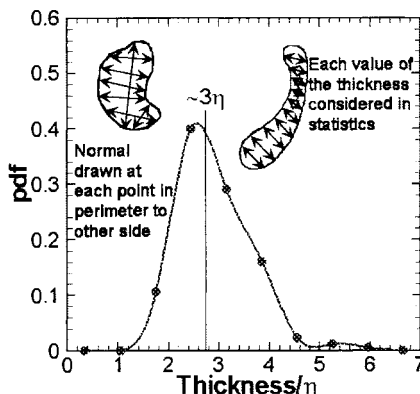


Fig. 5. The probability density function of the thickness of kinetic energy dissipation structures based on Fig. 4(b).

# MIXING

*Randomness, Space dimension, Reynolds number*

Emmanuel Villermaux

*Université de Provence & Institut Universitaire de France*

*IRPHE, 13384 Marseille Cedex 13, France*

villerma@irphe.univ-mrs.fr

**Abstract** Experiments including confined mixtures in two and three dimensions and Reynolds numbers  $Re$  ranging from 0.1 to  $10^4$  show that the evolution mechanism of a scalar mixture relaxing towards uniformity is a random aggregation process essentially independent of the Reynolds number. The rate of the process is related to the topology of the stirring motions which differs depending on the dimensionality of space.

**Keywords:** Mixing, stirring, diffusion, aggregation, turbulence

## Introduction

A mixture is a transient state between the initial segregation of the constituents, and their ultimate homogeneity. The overall mixing process of a drop of dyed fluid in a stirred medium involves two phenomena : a process of dispersion of the drop in the diluting medium by which the phases interpenetrate, and a process of interaction between the dispersed elements from which homogeneity arises. It is shown here that the mixture's evolution is directed by a random aggregation process essentially independent of the detailed stirring mechanism. The elementary bricks are stretched sheets whose rates of diffusive smoothing and coalescence built up the overall mixture concentration distribution, which pertains to a family of distributions stable by self-convolution.

### 1. Three dimensional, high Reynolds number mixing

Let a turbulent jet of water plus dye discharge in a square, transparent, long duct. The jet and the duct are immersed in a large tank filled with transparent water at rest. The jet exit velocity  $u$  is such that

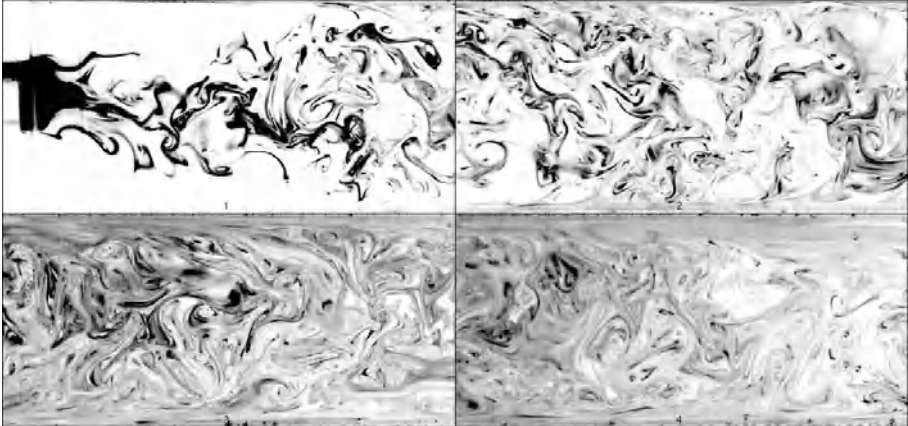


*Figure 1.* Mixing of a dye discharging from a jet of diameter  $d = 8$  mm in a square ( $L \times L$  with  $L = 3$  cm) duct. From 1 to 4, successive instantaneous planar cuts of the scalar field at increasing downstream locations in the duct showing the progressive uniformization of the dye concentration.

$Re = ud/\nu \simeq 10^4$ . As can be seen on Fig. 1, the dye rapidly invades the whole duct cross section and its concentration differences are progressively erased as it travels downstream to relax towards a more or less uniform mixture. The process conserves the average concentration  $\langle C \rangle$  of the dye.

The distribution  $P(C)$  presents a skewed, bell shape which gets narrower around  $\langle C \rangle$  very well described by a family of one parameter distributions, namely Gamma distributions

$$P(X = C/\langle C \rangle) = \frac{n^n}{\Gamma(n)} X^{n-1} e^{-nX}. \quad (1)$$

It is seen on Fig. 2 that the fairness of the fit holds for the whole concentration range, down to quite low probability levels, and accounts for the downstream deformation of  $P(C)$  through the single parameter  $n$ , whose dependence on the downstream location is quite strong: Fig. 2 suggests a power-law dependence with an exponent close to  $5/2$ . The dependence of  $n$  on the jet Reynolds number is, although noticeable, very weak.

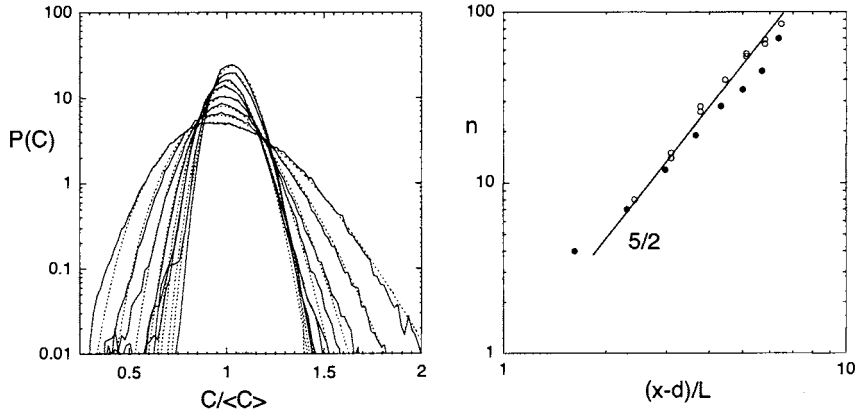


*Figure 2.* Left: Downstream evolution of the concentration distribution  $P(C)$  as the dye progresses along the duct as shown on Fig. 1. The concentration distribution of the evolving mixture gets narrower around the average concentration  $\langle C \rangle = 0.3$ . solid line: experimental distributions, dashed line: distributions given by Eq. (1). Right: Fitting parameter  $n$  of the distributions (1) as a function of the downstream distance  $(x - d)/L$ .  $\square$ :  $Re = 10^4$ ,  $\bullet$ :  $Re = 5 \times 10^3$ .

## 2. Two dimensional, low Reynolds number mixing

Consider now the experiment consisting in stirring a blob of dye with a rod in a thin layer of very viscous fluid, by a two-dimensional, quasi-periodic protocol consisting in slicing the medium in the plane of the fluid layer with a small rod (Fig. 3). A number of parallel cuts is made in one direction, and then the same number at right angle, this operation defining one cycle. This very much looks like the motion of a straw in a milk shake.

At low Reynolds number (the typical Reynolds number of the motion of the rod is  $10^{-1}$ ), the fluid is deformed by the passage of the rod on a scale which is given by its own size. The maximal rate of stretch is obtained for fluid particles close to the rod trajectory, while the protocol leaves nearly unstretched fluid parcels which therefore keep a concentration close to the initial concentration as the number of cycles is increased. Concomitantly, fluid particles are brought together in the wake of the rod, and coalesce. The amplitude of the slicing movements is constant through the cycles, so that the average concentration of the dye is conserved; these ingredients are very similar to those described above. The dye concentration distributions  $P(C)$  displayed on Fig. 4 are actually found to be reasonably well described by the Gamma functions family of

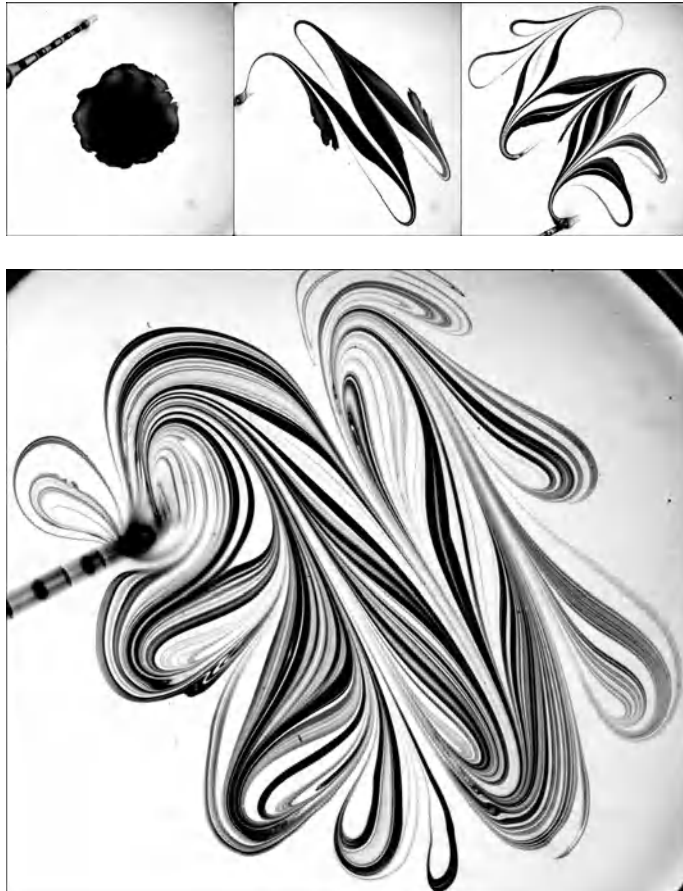


*Figure 3.* Top: The stirring protocol of a drop of ink deposited at the surface of pure Glycerol using a small rod. The sequence displays the initial state, half, and a completed stirring cycle. Bottom: The mixture's state after  $2\frac{1}{2}$  completed stirring cycles.

Eq. (1). The index  $n$  varies as the  $3/2$  power of the number of stirring cycles.

### 3. Stretching enhanced diffusion

The stirring motions progressively convert a compact blob in a set of sheets of increasing surface and decreasing thickness (Girimaji and Pope 1990, Duplat and Villermaux 2000). The intersects of these sheets with the visualization plane are visible on Fig. 1 in the form of ligaments. Let  $s(t)$  be the distance between two material particles in the direction  $z$  perpendicular to a sheet, and  $\sigma(t) = \partial \ln s(t) / \partial t$  its rate of

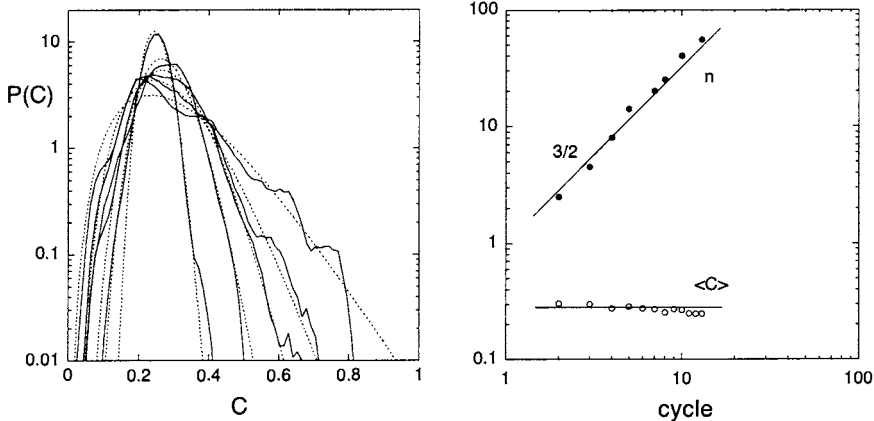


Figure 4. Left: Evolution of the dye concentration distribution  $P(C)$  after 3, 4, 5, 6 and 13 stirring cycles. The concentration distribution of the evolving mixture gets narrower around the average concentration  $\langle C \rangle$ . solid line: experimental distributions, dashed line: distributions given by Eq. (1). Right: Fitting parameter  $n$  and average concentration of the distributions (1) as a function of the number of cycles.

compression. If  $c(z, t)$  is the scalar concentration profile across the sheet, the convection-diffusion transport equation reduces to a one dimensional problem provided the radius of curvature of the sheet is large compared to its thickness (Dimotakis and Catrakis 1999). In that case the direction  $z$  aligns with the direction of maximal compression and for a species with diffusion coefficient  $D$

$$\frac{\partial c(z, t)}{\partial t} + \sigma(t)z \frac{\partial c(z, t)}{\partial z} = D \frac{\partial^2 c(z, t)}{\partial z^2}. \quad (2)$$

By the change of variables  $\tau = D \int_0^t dt'/s(t')^2$  and  $\xi = z/s(t)$ , Eq. (2) reduces (Ranz 1979, Marble 1988, Ottino 1989) to a simple diffusion equation  $\partial c(\xi, \tau)/\partial \tau = \partial^2 c(\xi, \tau)/\partial \xi^2$ . The topology of the stirring motions select particular forms for  $s(t)$ . Starting with a sheet of initial uniform concentration and thickness  $s_0$ , the maximal concentration in  $z = 0$  writes

$$c(0, t) = \text{erf}(1/4\sqrt{\tau}). \quad (3)$$

We describe several generic examples: in incompressible flows in two dimensions where the length of material lines grow like  $\gamma t$  (Meunier and Villermaux 2003), the mean transverse thickness of the scalar fila-

ments decrease as  $s(t) = \frac{s_0}{\sqrt{1+(\gamma t)^2}}$  and thus  $\tau = \frac{Dt}{s_0^2} (1 + \frac{(\gamma t)^2}{3})$ , providing  $c(0, t) \sim (t/t_s)^{-3/2}$  for  $t > t_s$ , with  $t_s \sim \frac{1}{\gamma} Pe^{1/3}$ , where  $Pe = \gamma s_0^2/D$  is a Péclet number. If material surfaces in three dimensions grow like  $(\gamma t)^2$ , then (Villermaux and Rehab 2000),  $s(t) = s_0/(1 + (\gamma t)^2)$  and  $\tau = \frac{Dt}{s_0^2} (1 + \frac{2}{3}(\gamma t)^2 + \frac{1}{5}(\gamma t)^4)$ , providing  $c(0, t) \sim (t/t_s)^{-5/2}$  for  $t > t_s$ , with  $t_s \sim \frac{1}{\gamma} Pe^{1/5}$ . For flows in which the length of material lines increases exponentially in time like  $e^{\gamma t}$  as realized by a succession of stretching and folding motions in random flows (Batchelor 1952),  $s(t) = s_0 e^{-\gamma t}$  and  $\tau = \frac{Dt}{s_0^2} (e^{2\gamma t} - 1)$  providing  $c(0, t) \sim e^{-\gamma t}$  for  $t > t_s$  with  $t_s \sim \frac{1}{2\gamma} \ln Pe$ .

These timescales are the relevant mixing times as soon as the inverse of the elongation rate  $\gamma^{-1}$  is smaller than the diffusive time of the sheet constructed on its initial size  $s_0^2/D$ , that is for  $Pe \gg 1$ . In this limit,  $t_s$  is essentially given by the time needed to deform the sheet  $\gamma^{-1}$  and pure diffusion (for which  $c(0, t) \sim (Dt/s_0^2)^{-1/2}$ ) is enhanced by the substrate motion.

#### 4. Mixture composition and kinetics

However, the sheets interact as they move in the flow so that their diffusive boundaries interpenetrate to give rise to new sheets whose concentration profile is the *addition* of the original ones. This elementary interaction rule is a consequence of the linearity of the diffusion Eq. (1) and this coalescence process explains why, although the concentration of each individual element  $c \equiv c(0, t)$  decreases in time according to Eq. (3), the average concentration  $\langle C \rangle$  is conserved. Because of the irregular stirring motions, the addition of the concentration levels is made at random among those available in the population  $P(C)$  at time  $t$  which therefore evolves by self-convolution as

$$\frac{\partial P}{\partial t} = -\frac{\partial}{\partial C} \left( \left\langle \frac{dc}{dt} \right\rangle P \right) + \frac{dn}{dt} \left( -P + P^{\otimes(1+1/n)} \right). \quad (4)$$

The first Liouville transport term in Eq. (4) accounts for the decrease of the individual concentration levels given by Eq. (3), and the second is the convolution interaction term. The asymptotic solution of Eq. (4) is, irrespective of the initial condition for  $P(C)$ , a Gamma distribution of order  $n$ .

The average concentration of the mixture is a result of the relative weight of these two terms and is not, in general, constant. The piling-up of the concentration levels by coalescence contributes, through the second term of Eq. 4, to the increase of the average concentration by

a factor given by  $\exp\{\int dn/n\} = n$ . The average concentration is thus conserved if the damping factor of Eq. (3) balances exactly the coalescence rate that is when

$$n = \frac{1}{c(0, t)}. \quad (5)$$

The only difference between the two previous experiments in three, and two dimensions, respectively, lies in the kinetics of the decrease of the elementary sheet concentration levels given by Eq. 3. Stretching motions in 3D form sheets whose maximal concentration  $c(0, t)$  decays like  $t^{-5/2}$  whereas 2D motions form filaments whose maximal concentration decays like  $t^{-3/2}$ .

The coalescence mechanism giving rise to Eq. (1), will therefore make the average concentration  $\langle C \rangle$  constant if

$$n \sim t^{-3/2} \quad \text{in 2D, and} \quad n \sim t^{-5/2} \quad \text{in 3D,} \quad (6)$$

as expected from Fig. 2 and 4. Note that the apparent power law in the channel flow is a transient effect reflecting the fact that the temporal window of the mixture's evolution covers, at most, a few large scale turnover time  $\gamma^{-1} \sim L/u'$ . Indeed, material lines increase like  $L/L_0 = \exp(\gamma t) = \exp(u't/L) = \exp(u'/u \times x/L)$  where  $x = ut$  is the distance from the injection point of the scalar blob in the medium advected at a velocity  $u$ . In the channel flow, the turbulence intensity is such that  $u'/u \approx 0.08$  (Schlichting 1987) and the downstream distances of observation in the present experiments are such that  $x/L < 10$  so that  $L/L_0 \approx 1 + u'/u \times x/L = 1 + \gamma t$ , realizing in practice an elongation linear in time, inducing, in this three dimensional flow,  $n \sim t^{5/2}$ . This behavior has thus to be understood as the birth of the ultimate exponential regime, but this slight difference, if any, has strictly no consequence on the mechanism building-up the concentration distribution  $P(C)$  which solely relies on *random additions* of concentration levels, independently of the *rate* at which these additions are made.

## Conclusion

It is instructive to see that an experiment performed at a very low Reynolds number produces composition fields very similar to those obtained at much larger Reynolds number (Fig. 2 and 4). The reason is that the evolution mechanism is the same. The motion of the rod in the two-dimensional viscous fluid plays the role of the small-scale stirring motions present in high Reynolds number flows. Their role is to ensure

the independence –in the statistical sense of Eq. (4)– of the concentration levels additions giving rise to the self-convolutive construction of the mixture composition; a particularly simple paradigm for the impact of turbulence on mixing.

## References

- Batchelor, G.K. 1952 The effect of homogeneous turnulence on material lines and surfaces. *Proc. Roy. Soc. A* **213**, 349–366.
- Dimotakis, P. E. and Catrakis, H. J. Turbulence, fractals and mixing. in *Mixing: Chaos and Turbulence*, CHATÉ, H., VILLERMAUX, E. AND CHOMAZ, J. M. (Eds.), Kluwer Academic/Plenum Publishers, New York, 1999.
- Duplat, J. and Villermaux, E. 2000 Persistency of material element deformation in isotropic flows and growth rate of lines and surfaces. *Eur. Phys. J. B* **18**, 353–361.
- Girimaji, S. S. and Pope, S. B. 1990 Material-element deformation in isotropic turbulence. *J. Fluid Mech.* **220**, 427–458.
- Marble, F. E. 1988 Mixing, diffusion and chemical reaction of liquids in a vortex field *Chemical reactivity in liquids: fundamental aspects*, Moreau, M. and Turq, P. Editors, Plenum Press.
- Meunier, P. and Villermaux, E. 2003 How vortices mix *J. Fluid Mech.* **476**, 213–222.
- Ottino, J. M. 1989 *The kinematics of mixing: stretching, chaos, and transport*. Cambridge University Press.
- Ranz, W. E. 1979 Application of a stretch model to mixing, diffusion and reaction in laminar and turbulent flows. *AICHE Journal* **25**, (1), 41–47.
- Schlichting, H. 1987 *Boundary layer theory*, McGraw-Hill, Inc., New York.
- Villermaux, E. and Rehab, H. 2000 Mixing in coaxial jets. *J. Fluid Mech.* **425**, 161–185.

# THE SPECTRAL TRANSFER IN ISOTROPIC TURBULENCE

William K. George  
Chalmers University of Technology  
SE 412 96 Gothenburg, Sweden  
and  
Honglu Wang  
EASi Engineering  
Madison Heights, MI 48071, USA

**Abstract** The spectral energy transfer in isotropic decaying turbulence is examined using DNS and experiments. The universal equilibrium range idea of Kolmogorov (1941) does not apply at the highest Reynolds numbers available. By contrast, the equilibrium similarity hypothesis of George (1992) is in excellent agreement with all the data.

**Keywords:** spectra, turbulence, non-linear, energy transfer, equilibrium

## 1. Introduction

There are few topics in turbulence that have been the subject of more theories and speculation than the spectral energy transfer. Almost all of these begin with the some variation of the assumptions of Kolmogorov (1941). Monin and Yaglom (1975) provide a comprehensive review of the literature prior to publication, while Frisch (1995) contains much of the more recent material. This paper considers only isotropic decaying turbulence, although the results clearly have implications well beyond this special case.

## 2. Basic equations

For isotropic decaying turbulence, the spectral energy equation is given by:

$$\frac{\partial E}{\partial t} = T - 2\nu k^2 E \quad (1)$$

where  $E(k)$  is the three-dimensional energy spectrum function and  $T(k, t)$  is the non-linear spectral transfer, both averaged over spherical shells of radius  $k$  (v. Batchlor 1953).

The turbulence kinetic energy,  $3u^2/2$ , is obtained by integrating  $E(k, t)$  over all wavenumbers. The dissipation,  $\epsilon$ , can be obtained by similarly integrating the last term of equation 1. The integral of  $T(k, t)$  over all wavenumbers must be identically zero, since there can be no net gain from the non-linear transfer. Note that many authors have preferred to work with the spectral flux,  $\epsilon_k$ , defined from  $T(k, t) \equiv -\partial \epsilon_k / \partial k$ .

### 3. Is there a universal equilibrium range?

**Classical idea 1:** Kolmogorov (1941) argued that it was plausible to assume that at very high Reynolds numbers the high wavenumbers could be assumed to be in statistical equilibrium with respect to the energy-containing ones. In other words, for sufficiently high wavenumbers,

$$\frac{\partial E}{\partial t} \approx 0 \quad (2)$$

so that:

$$T(k, t) \approx 2\nu k^2 E(k, t) \quad (3)$$

Batchelor (1953) refers to this range as the *universal equilibrium range*, and its presumed existence is at the root of most turbulence theories.

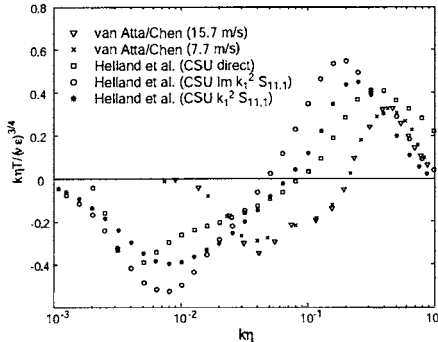
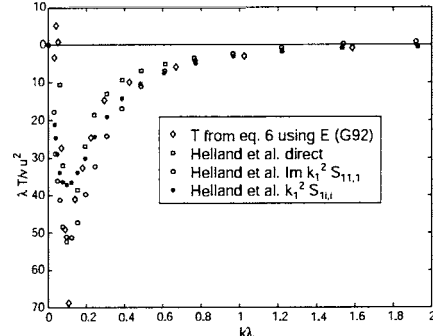
**Classical idea 2:** Kolmogorov (1941) further argued that if the separation between dissipative and energy containing scales was sufficiently large, then there should exist an intermediate range of wavenumbers, the *inertial subrange*, for which the spectral flux was nearly constant, or alternatively,  $T(k, t) \approx 0$ . Integration of equation 3 from infinity implies immediately that:

$$\epsilon_k(k, t) \approx \epsilon; \quad L^{-1} \ll k \ll 1/\eta \quad (4)$$

where  $L$  is the integral scale and  $\eta$  is the Kolmogorov microscale. If  $\epsilon_k$  and  $k$  are the only parameters governing this inertial subrange, it follows on dimensional grounds alone that  $E \propto \epsilon^{2/3} k^{-5/3}$ , one of the best-known results in turbulence.

It has been generally believed that both these classical ideas have been proven beyond reasonable doubt to be correct, largely based on energy spectrum measurements alone. In fact, there are no experiments or DNS results which confirm these ideas directly in the only types of flows for which they can be tested, namely *statistically non-stationary* flows.

Figure 1 shows three attempts by van Atta and co-workers to directly measure  $T(k, t)$  using the flow downstream of grids in two different windtunnels. The first is at the modest grid Reynolds numbers typical of most grid turbulence experiments,  $R_M = 25,000$  ( $R_\lambda \approx 50$ ); while the second is in a very large wind tunnel for which  $R_M = 410,000$  ( $R_\lambda = 237$ ). None of the data show even a trend toward a region for which  $T \approx 0$ , but instead all cut rather sharply through zero — at about  $k\eta \approx 0.2$  for the lower Reynolds number experiments

Fig 1.  $T/(\nu\epsilon)^{3/4}$  vs  $k\eta$ , HvAS77, vAC68.Fig 2.  $\lambda T/\nu u^2$  vs  $k\lambda$ , HvAS77 with eq. 6.

of van Atta and Chen (1969) and at  $k\eta \approx 0.065$  for the much higher Reynolds number CSU experiment of Helland et al. (1977). Interestingly, especially in light of the alternative theory discussed below, *all* experiments show this zero crossing at  $k\lambda \approx 2$ , which is well into the dissipative range at about the peak in the dissipation spectrum. Finally, as noted by the experimenters, there is no region in even the high Reynolds number experiment for which  $\epsilon_k$  is approximately constant.

Thus while it might still be true that Kolmogorov's arguments for a universal equilibrium range apply at much higher Reynolds numbers than  $R_\lambda = 237$ , there are no observable trends in these data to support this view. Nor are there any other *non-stationary* experiments at higher Reynolds number (to the best of our knowledge).

#### 4. An alternative idea: equilibrium similarity

An alternative hypothesis was put forth in George (1992). This has since been referred to as the *equilibrium similarity* hypothesis (c.f. George et al. 2001). The basic hypothesis is that all the relevant terms in the governing equations achieve an equilibrium, and maintain that equilibrium as the flow evolves in time or space. It can be contrasted with the Kolmogorov idea where statistical equilibrium is achieved as the wavenumber is increased. In equilibrium similarity, all scales achieve dynamical equilibrium together. If the equations and boundary conditions admit to such similarity solutions, they appear to always be observed in nature.

Following George (1992), solutions to equation 1 are sought (and found) of the form:

$$E(k, t) = E_s(t)f(kl(t)) \quad \text{and} \quad T(k, t) = T_s(t)g(kl(t)) \quad (5)$$

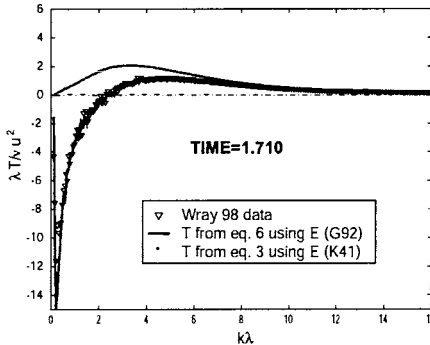


Fig 3. Wray DNS and eq. 6.

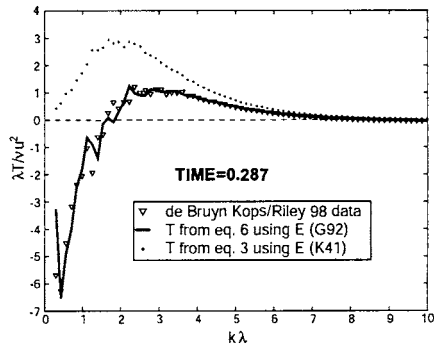


Fig 4. DeBruyn-Kops/Riley DNS and eq. 6.

where none of the scaling functions can be specified arbitrarily, but must be determined by application of the equilibrium similarity hypothesis. It is straightforward to show that equilibrium similarity solutions are possible *for fixed initial conditions* if  $l(t) = \lambda$ , the Taylor microscale, together with  $E_s/(u^2\lambda) = \text{constant}$  and  $\lambda T/(\nu u^2) = \text{constant}$ . It can be shown that equilibrium similarity implies a power law decay of the energy in time ( $u^2 \sim t^n$ ), but with an exponent,  $n = -(p + 1)/2$ , uniquely determined by the energy spectrum near zero wavenumber (i.e.,  $E(k, t) = C_p k^p$  near  $k = 0$ ). Wang et al. (2000), George et al. (2001), and Wang and George (2002) discuss various implications and inferences from this, and use the results to show the limitations due to box size of several recent DNS of decaying turbulence. Here only the spectral transfer will be considered.

Substitution into equation 1 yields directly the following transformed equation which relates the non-dimensional non-linear transfer,  $g(\bar{k})$ , to the non-dimensional energy spectrum,  $f(\bar{k})$ , by:

$$g = \left\{ - \left[ \frac{5}{n} \right] (\bar{k} f' + f) - 10f \right\} + 2\bar{k}^2 f \quad (6)$$

where  $\bar{k} = k\lambda$  and the prime denotes differentiation with respect to  $\bar{k}$ . Thus the dimensionless energy and spectral transfer depend only on the wavenumber normalized by the Taylor microscale,  $\bar{k}$ , and the constant decay exponent,  $n$ , which in turn depends only on the initial spectrum near  $k = 0$  as noted above. Most importantly,  $f$  and  $g$  are completely independent of the local Reynolds number during decay, even though the  $R_\lambda$  is continuously decreasing. Note the term in curly brackets is the transformed version of  $\partial E/\partial t$ , and is the term assumed to be negligible in the Kolmogorov theory.

Figure 2 shows the application of equation 6 to high Reynolds number data of Helland et al. shown in Figure 1 using  $n = -1$ . The results are remarkably

good. The high wavenumbers have not been shown to make the low wavenumber agreement more obvious, but these were affected by probe roll-off above  $k\lambda \approx 4$  anyway. The agreement is no real surprise, since the “approximate similarity hypothesis” these authors used to account for the dominant contribution of  $\partial E/\partial t$  to their data (equation 4.2 in their paper), can be derived directly from equation 6 if it is assumed that  $n = 1$  (which for the high Reynolds number experiment it was). The agreement between data and theory (not shown) for the low Reynolds number experiments of van Atta and Chen (1968) is even better and at all wavenumbers to  $k\eta \approx 1$ , the highest measured.

Figures 3 and 4 show the spectral transfer for two recent  $512^3$  DNS of decaying isotropic turbulence by Wray (1998) and deBruyn Kops and Riley (1998). The normalized spectral energy transfer,  $g(\bar{k}) = \lambda T/(\nu u^2)$  is calculated using only the decay rate parameter,  $n$ , and the DNS energy spectra normalized with  $u^2$  and  $\lambda$  to obtain  $f(\bar{k}) = E/(u^2\lambda)$ . The values of  $n$  were  $-1.5$  and  $-1.17$  respectively, and were obtained from plots of  $d\lambda^2/(\nu dt) = -10/n$  to avoid the confusion of a virtual origin. The procedures to obtain these values and plots of the normalized spectral data are described in detail in Wang and George (2002). The Kolmogorov microscale and integral scale can be located on these plots using  $\lambda/\eta = 13.5$  and  $L/\lambda = 4.5$  for the Wray data and  $\lambda/\eta = 11.2$  and  $L/\lambda = 3.4$  for the deBruyn Kops/Riley data at the times shown. These correspond to  $R_\lambda = 50$  and  $30$  respectively. Also shown on the plots for reference is the dissipation spectrum which would equal the non-linear transfer spectrum of equation 3 if Kolmogorov’s ideas applied. Clearly they do not.

Only a single time has been shown for each data set. But the DNS data can be examined at all times. Once the similarity regime identified by Wang and George (2002) is entered, the collapse at all wavenumbers *for fixed initial conditions* is excellent. There is, however, evidence of a slight overestimate of the spectral values above the Kolmogorov microscale for early times due to the limited numerical resolution. Most importantly, there is no evidence that the zero-crossings, maxima or minima vary from one time to another when plotted in these Taylor variables, even though the ratio of  $\lambda/\eta$  is changing slowly with time.

## 5. Conclusions

Two hypotheses for the spectral energy decay of isotropic turbulence have been explored, and compared to the experimental and DNS data. The evidence does not support Kolmogorov’s universal equilibrium range assumption. By contrast, the equilibrium similarity hypothesis of George 1992 is in excellent agreement with all the data, including the high Reynolds number wind tunnel experiment. There are no adjustable parameters in Equation 6. Nonetheless, the agreement between theory and the directly computed (or measured) non-linear

spectral transfer is excellent. The zero-crossings are captured almost exactly, as are both the location and values of the maximum and minimum values.

In spite of the above, it is not impossible that Kolmogorov's ideas may apply at much higher Reynolds numbers, since even the high Reynolds number wind tunnel experiment only marginally satisfies the requirement that the local turbulence time scale in the inertial subrange be much less than that of the energy containing eddies,  $3u^2/2\epsilon$ . Unfortunately it probably will not be possible to settle this question until computers become much, much larger and faster, or until experiments can be carried out in special low turbulence wind tunnels with very long test sections (e.g., the proposal of Karlsson et al. 2001). Since almost all turbulence models and theories have been built on these Kolmogorov ideas, the answers to the questions raised herein will affect virtually every aspect of our understanding of turbulence.

## 6. Acknowledgements

The authors are especially grateful to T. Gunnar Johansson and Christian Wollblad of Chalmers for many helpful discussions.

## References

- Batchelor, G.K. (1953) *Homogeneous Turbulence*. CUP, Cambridge, UK
- de Bruyn Kops, S.M. and Riley, J.J. (1998) Direct numerical simulation of laboratory experiments in isotropic turbulence. *Phys. Fluids A*, **10**, 9, 2125 – 2127.
- Frisch, U. (1995) *Turbulence: the legacy on AN Kolmogorov*, CUP, Cambridge, UK.
- George, W.K. (1992) The Decay of Homogeneous Isotropic Turbulence. *Physics of Fluids A*, **4**, 7, 1492 – 1509.
- George, W.K., Wang, H., Wollblad, C. and Johansson, T.G. (2001) 'Homogeneous Turbulence' and Its Relation to Realizable Flows. *Proc. 14th Australasian Fluid Mechanics Conf.*, Dec 10 – 14, 2001, Adelaide U., Adelaide, Australia.
- Holland, K. N., van Atta, C.W., and Stegun, G.R. (1972) Spectral energy transfer in high Reynolds number turbulence, *J. Fluid Mech.*, **79**, 337 – 359.
- Karlsson, R.I., George, W.K., Johansson, T.G., and Wosnik, M. (2001) The 'Nordic Wind Tunnel' — a proposal to build a very large turbulence research facility. *ERCOFTAC Bull.*, **51**, 17.
- Kolmogorov, A. (1941) The local structure of turbulence in incompressible viscous fluid for very high Reynolds numbers. *C. R. Akad. Sci. SSSR*, **30**, 301.
- Monin and Yaglom (1975) *Statistical Fluid Mech., vol II*, MIT Press., Cambridge, MA, USA.
- Van Atta, C. W. and Chen, W. Y. (1968) Measurements of spectral energy transfer in grid turbulence. *J. Fluid Mech.*, **38**, 743 – 763.
- Wang, H., Gamard, S., Sonnenmeier, J.R. and George, W.K. (2000) Evaluating DNS of isotropic turbulence using similarity theory, *Proc. of ICTAM 2000, Chicago, Ill*, Aug. 27 - Sep. 1, 2000 (Extended version available as a TRL Rept from <http://www.tfd.chalmers.se/trl/>)
- Wang, H. and George, W.K. (2002) The integral scale in isotropic turbulence. *J. Fluid Mech.*, **459**, 429 – 443.
- Wray, A. (1998) Decaying isotropic turbulence. In AGARD Advisory Rept 345, 63–64.

# **$R_\lambda$ DEPENDENCE OF THE KOLMOGOROV CONSTANT AND SCALING**

B. R. Pearson<sup>1</sup>, P. -Å. Krogstad<sup>2</sup> and G. R. Johnson<sup>1</sup>

<sup>1</sup>School of Mechanical, Materials, Manufacturing Engineering & Management. University of Nottingham, Nottingham NG7 2RD, UK

<sup>2</sup>Dept. of Appl. Mech., Thermo. & Fluid Dynamics, Norwegian University of Science & Technology, N-7491 Trondheim, Norway

**Abstract** We attempt to answer one of the outstanding issues in turbulence – does asymptotic inertial range scaling exist and if so, does it exist in a complete or incomplete similarity form? Although we cannot form a firm conclusion our results suggest we are tantalizingly close.

## **1. Introduction**

Asymptotic scaling hypotheses[1, 2, 3] make definite predictions for the behavior of the inertial range (IR) structure. Our view is that none of these hypotheses have been verified irrefutably by either experiment or computation. Results, such as those shown in Refs. [4, 5], usually deal with the Taylor micro-scale Reynolds number ( $R_\lambda$ ) dependence of IR parameters such as the scaling exponent and pre-factor for the 1-dimensional turbulent kinetic-energy spectrum  $\phi_u$  and its Fourier pair, the second-order longitudinal structure function  $\langle(\delta u)^2\rangle$ . For example, assuming the simplest incomplete similarity[2] forms for both  $\phi_u$  and  $\langle(\delta u)^2\rangle$  gives,

$$\phi_u^* = K k_1^{*-p} (L^*)^{5/3-p} \quad , \quad (1)$$

$$\langle(\delta u^*)^2\rangle = C_\kappa r^{*\zeta} (L^*)^{2/3-\zeta} \quad . \quad (2)$$

Here, the pre-factors  $K$  and  $C_\kappa$  are the Kolmogorov constants,  $p$  and  $\zeta$  are IR scaling exponents and  $L$  is a characteristic length-scale of the macro-scale motion at which turbulent kinetic energy is injected into the flow. In both Eqs. (1) and (2) the \* signifies K41[1] normalization by the dissipative length scale  $\eta \equiv \nu^{3/4}\langle\varepsilon\rangle^{-1/4}$  ( $\nu$  is the kinematic viscosity and

$\langle \varepsilon \rangle$  is the mean turbulent kinetic energy dissipation rate) and velocity scale  $u_\kappa \equiv \nu^{1/4} \langle \varepsilon \rangle^{1/4}$ .

Verification of complete similarity[1] – which is also known as “fully developed turbulence” – in the IR consists of determining whether or not  $p = 5/3$  and  $\zeta = 2/3$ . Additionally,  $K$  and  $C_\kappa$  must be  $R_\lambda$  independent. Incomplete similarity hypotheses, e.g. Ref. [2], usually predict a slight  $R_\lambda$  independent correction to  $p$  and  $\zeta$  – attributed to the “intermittent” nature of  $\varepsilon$ . Also, for isotropic turbulence,  $L^* = 15^{-3/4} C_\varepsilon R_\lambda^{3/2}$  ( $C_\varepsilon \equiv \langle \varepsilon \rangle L / \langle u^2 \rangle^{3/2}$  is the dimensionless dissipation rate[8]), hence the  $R_\lambda$  dependence for  $K$  and  $C_\kappa$  [Eqs. (1) and (2)] follows. Recently, an alternative hypothesis for incomplete similarity – called “asymptotic covariance”[3] – was proposed and this hypothesis predicts inverse  $\ln(R_\lambda)$  dependencies for both (pairs of) the Kolmogorov constant and the scaling exponent with the possibility that “fully developed” turbulence may never exist as a limiting state.

For high  $R_\lambda$  turbulence with a large scaling range a number of simple relationships exist[4]:

$$p - \zeta - 1 = 0 \quad , \quad (3)$$

$$C_\kappa/K - \pi / [\Gamma(p) \sin\{\pi(p-1)/3\}] = 0 \quad , \quad (4)$$

$$C_\kappa/K - \pi / [\Gamma(1+\zeta) \sin(\pi\zeta/3)] = 0 \quad . \quad (5)$$

Equation (3) is true for any Fourier pair with “large enough” power-law ranges. Strictly, Eqs. (4) and (5) are one and the same if, and only if, Eq. (3) is true. Note that complete similarity[1] i.e.  $p = 5/3$  and  $\zeta = 2/3$  gives the well-known result  $C_\kappa/K \approx 4.02$ . However, Eq. (3) can also be true for the simpler of the proposed incomplete similarity solutions e.g. Ref.[2], and  $C_\kappa/K$  can asymptote to a value other than  $\approx 4.02$ . Alternatively, asymptotic covariance disregards Eqs. (4) and (5) altogether.

Equations (3)–(5) can be considered as “diagnostic” tools for investigating the  $R_\lambda$  dependence for IR quantities. One aspect which potentially makes the present study rigorous is that Eqs. (3)–(5) invite a complementary investigation in both wavenumber and physical space. It is the aim of the present work to assess the  $R_\lambda$  dependence, if any, for Eqs. (3)–(5). If we observe that Eq. (3) is not immediately true, which is likely for insufficient  $R_\lambda$ , it is still of interest to determine whether or not Eqs. (4) and (5) are converging as  $R_\lambda$  increases. Moreover, if Eq. (3) appears to be tending to zero, is  $p$  tending to  $5/3$ ? is  $\zeta$  tending to  $2/3$ ? and is the ratio  $C_\kappa/K$  tending to  $4.02$ ? Alternatively, if none of Eqs. (3)–(5) are obeyed, does this suggest that asymptotic covariance is a plausible hypothesis? Finally, can we estimate what minimum value of

$R_\lambda$  is needed to confidently form a conclusion? We will present results in the range  $150 \lesssim R_\lambda \lesssim 1200$  for the same geometry. To our knowledge, a  $R_\lambda$  dependence study in both  $k_1$ -space and  $r$ -space in the same geometry has yet to be attempted.

## 2. Experimental Details

The data are acquired in a turbulent wake which decays downstream of a perforated plate superimposed over a bi-plane grid of square rods. Further details of this geometry, which we call a *NORMAN* grid, and of the experimental procedure are given in Ref. [8]. In order to span a large  $R_\lambda$  range, two wind-tunnels are used. The first grid is located in a blow-down wind-tunnel of test section dimensions  $35 \times 35 \text{ cm}^2$  and 2 m length. For this grid,  $150 \lesssim R_\lambda \lesssim 500$ . The second grid is located in the *NTNU* recirculating wind-tunnel which has a test section of  $2.7 \times 1.8 \text{ m}^2$  cross section and 11 m length and for this grid,  $390 \lesssim R_\lambda \lesssim 1200$ . The *NTNU* grid is shown in Figure 1(a). Signals of the streamwise turbu-

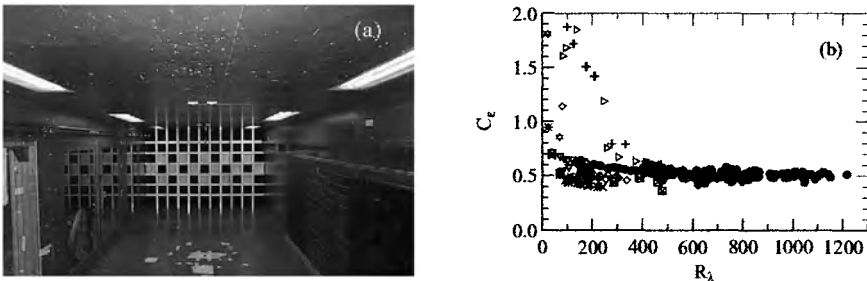


Figure 1. (a) The *NORMAN* grid located in the *NTNU* wind-tunnel. (b) The dimensionless dissipation rate  $C_e$ , ●, *NORMAN* grid data  $150 \lesssim R_\lambda \lesssim 1200$ . All of the other symbols are explained in Ref. [8].

lent velocity  $u$  are acquired on the mean velocity centreline forty mesh lengths downstream of the grid using the constant temperature anemometry (CTA) hot-wire technique. At this location  $\langle u^2 \rangle^{1/2}/U \approx 16\%$  and  $R_\lambda$  independent. A single-wire probe made of  $1.27 \mu\text{m}$  diameter Wollaston (Pt-10% Rh) wire is used. For the *NTNU* data, the wire sensing length  $l^*$  is  $0.5 \lesssim l^* \lesssim 2$  and for the smaller tunnel, the worst wire resolution is  $\approx 4\eta$ . Long time series,  $\approx 10^5$  integral time scales, are acquired for the majority of the data sets. Time differences  $\tau$  and frequencies  $f$  are converted to streamwise distance ( $x \equiv \tau U$ ) and 1-dimensional longitudinal wavenumber ( $k_1 \equiv 2\pi f/U$ ) respectively using Taylor's hypothesis. We have no concerns using Taylor's hypothesis here since it has already been demonstrated, in decaying 2-dimensional grid turbu-

lence at a downstream location where  $\langle u^2 \rangle^{1/2}/U \approx 14\%$ , that moments of longitudinal velocity differences are equal whether measured with or without invoking the hypothesis[6].

### 3. Results

Kolmogorov[1] relied on the notion of  $C_\epsilon$  being independent of  $R_\lambda$  in formulating his complete similarity hypothesis for the IR structure. Figure 1(b) shows that  $C_\epsilon$  in the current flow is indeed independent of  $R_\lambda$  when  $R_\lambda \gtrsim 400$ . However, it has been recently conjectured that  $C_\epsilon$  independent of  $R_\lambda$  is also consistent with K62-type incomplete similarity[7]. It is worth noting that asymptotic covariance[3] predicts a  $R_\lambda$  dependence for  $C_\epsilon$ .

Data for  $C_\epsilon$  alone cannot answer the question of how the IR structure scales. We need to test Eqs. (1) and (2) more directly. Before we can do this, we must decide on where to look for the IR, or overlap, scaling region. Briefly, we consider the correct overlap region to be the region that is “approximately” independent of  $R_\lambda$  irrespective of whether scaled by the macro-velocity and length scales,  $\langle u^2 \rangle^{1/2}$  and  $L$ , or the

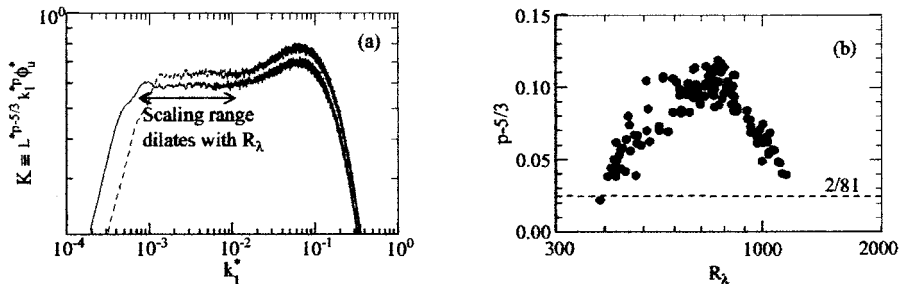


Figure 2. (a) Examples of  $K$ , Eq. (1). —,  $R_\lambda \approx 915$ ; —,  $R_\lambda \approx 1100$ . (b)  $\bullet, p - 5/3$ , the deviation of the measured spectral scaling exponent Eq. (1) in the NORMAN grid,  $150 \lesssim R_\lambda \lesssim 1200$ . —, a K62[2] correction assuming an “intermittency” exponent  $\mu = 2/9$ .

dissipative velocity and length scales,  $u_\kappa$  and  $\eta$ . By “approximately” we are allowing for the possibility of incomplete similarity in the IR. More detailed justification for our choice of the scaling region can be found in Refs. [9, 10].

We have shown[9, 10] that the data have no scaling either in  $k_1$ -space or  $r$ -space when  $R_\lambda \lesssim 400$  which is, perhaps coincidentally, also when  $C_\epsilon$  begins to be  $R_\lambda$  independent for this flow [Figure 1(b)]. Figure 2(a) shows two examples of energy spectra weighted by estimated values of  $p$ . The plateaus are considered to be evidence for self-similar scaling

regions. The upper  $k_1^*$  limit for the scaling region is  $k_1^* \approx 10^{-2}$  and is approximately  $R_\lambda$  independent. Beyond this value of  $k_1^*$  are the prominent “pre-dissipative bumps.” We are not concerned by the apparently low value of  $k_1^*$  for the upper scaling range limit – we believe it can be explained by a simple “order of magnitude” argument: the average  $k_1^*$  for viscous dissipation is  $\log_{10} k_1^* \approx 0$  and the average  $k_1^*$  for the most active dissipative events has been shown to be  $\log_{10} k_1^* \approx -1$ , it is plausible that an upper  $k_1^*$  limit for an IR free from the influence of strong dissipative events could not be expected until  $\log_{10} k_1^* \approx -2$ .

Figure 2(b) shows the  $R_\lambda$  dependence for the deviation of the IR spectral scaling exponent  $p$  [Eq. (1)] from the complete similarity value of  $5/3$  and from a K62[2] “anomalous scaling” correction. A non-monotonic behavior is evident and it is most probable that the behavior is not universal. We believe it to be the signature of what we have previously [9, 10] called “scaling anomaly factors” (SAF) e.g. the “finite scale” effect due to insufficient  $R_\lambda$ , the “lingering” influence of non-universal large-scale anisotropy, inhomogeneity and mean shear.

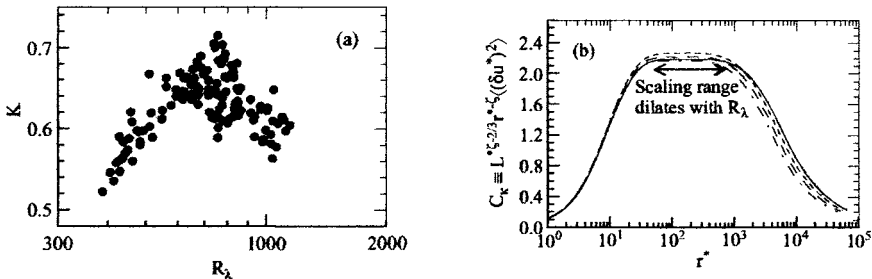


Figure 3. (a)  $\bullet$ ,  $K$ , the spectral Kolmogorov constant [Eq. (1)] measured in the NORMAN grid  $150 \lesssim R_\lambda \lesssim 1200$ . (b) Examples of the structure function constant  $C_\kappa$ , Eq. (2). —,  $R_\lambda \approx 675$ ; - - -,  $R_\lambda \approx 750$ ; - · -,  $R_\lambda \approx 830$ ; —,  $R_\lambda \approx 915$ .

A possible explanation for the  $R_\lambda$  dependent behavior of  $p$  could be the following: when the scaling range is initially established (and it must eventually be established at some value of  $R_\lambda$  that has ensured sufficient separation between the wavenumbers representative of the dissipative and energetic scales e.g.  $R_\lambda \approx 400$  for the current case) it has approximately zero length, and is therefore free from the effects of the SAF; at this  $R_\lambda$ ,  $p$  has, perhaps paradoxically, an initial value equal to its asymptote. As  $R_\lambda$  increases and the IR grows in size the scaling range is more and more influenced by the SAF until a  $R_\lambda$  of maximum influence is reached (which appears to be  $R_\lambda \approx 700$ ), after which, as  $R_\lambda$  continues to increase, the influence of the SAF decreases (which must inevitably happen). We are not certain of the asymptotic value of  $p$ , i.e. whether

it is a value indicative of complete or incomplete similarity in the IR. If the current trend for  $p$  when  $R_\lambda \gtrsim 700$  continues we are confident we can answer this question when  $R_\lambda \approx 2000$  in this flow. Also, it may be worthwhile to extensively and accurately investigate the flow in the range when scaling is thought to be established ( $300 \lesssim R_\lambda \lesssim 400$ ) to determine if the above conjecture that the initial value of  $p$  is equal to its asymptote is true.

Having established a spectrum of  $p$ , we can estimate the values of the spectral Kolmogorov constant,  $K$  [Eq. (1)] for each data set. Figure 3(a) shows that  $K$  appears to have a  $R_\lambda$  dependence very similar to that of  $p$  and this is not too surprising considering the influence of  $p$  in Eq. (1). The initial magnitude of  $K \approx 0.52$  at  $R_\lambda \approx 390$  agrees with the consensus value[4, 5] of  $K \approx 0.53 \pm 0.05$ . However,  $K$  then increases with  $R_\lambda$  to a maximum value of  $\approx 0.7$  at  $R_\lambda \approx 700$  and then decreases while  $R_\lambda$  continues to increase. The above discussion for  $p$  probably equally applies to  $K$ . For  $\langle (\delta u^*)^2 \rangle$  we use the same technique

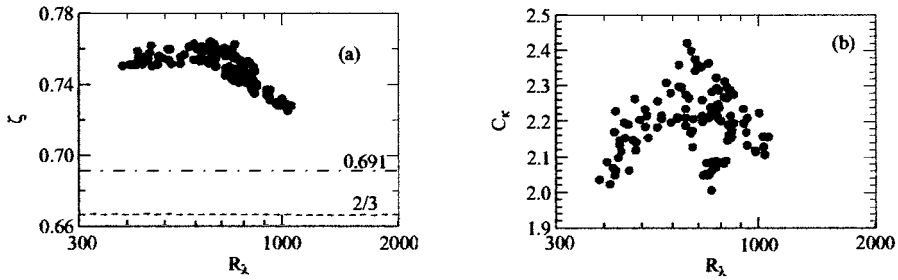


Figure 4. (a)  $\bullet$ ,  $\zeta$ , the measured structure function scaling exponent Eq. (2);  $--$ ,  $\zeta = 2/3$ , K41[1];  $- - -$ ,  $\zeta \approx 0.691$ , K62 log-normal model[2] with  $\mu = 2/9$ . (b)  $\bullet$ ,  $C_\kappa$ , the structure function Kolmogorov constant [Eq. (2)] measured in the *NORMAN* grid  $150 \lesssim R_\lambda \lesssim 1200$ .

as that for  $\phi_u^*$  to find the overlap region. Figure 3(b) shows a number of examples of  $\langle (\delta u^*)^2 \rangle$  weighted by the estimated value of  $\zeta$ . The obvious plateaus are considered to be convincing proof of the correct choice for the overlap region and  $\zeta$ . The  $R_\lambda$  dependence of  $\zeta$  is shown in Figure 4(a). The  $R_\lambda$  dependence is quite different to that of  $p$  for  $R_\lambda$  up until the “knee-point” which occurs at  $R_\lambda \approx 700$ . We attribute this difference in scaling to the sensitivity of the Fourier transform between  $\phi_u^*$  to  $\langle (\delta u^*)^2 \rangle$  on the macro-scale limit of the integrand. Also, it is well-known that spectra show evidence of scaling at lower  $R_\lambda$  than the corresponding structure function. It is interesting that the magnitude of  $R_\lambda$  at the knee-point corresponds to the maximum in  $p$  shown in Figure 2(b). Also, the decrease in  $\zeta$  from  $R_\lambda \gtrsim 700$  onwards is similar in behavior to that

of  $p$ . Figure 4(b) shows the  $R_\lambda$  dependence for  $C_\kappa$  and the dependence is very similar to that of  $K$  shown in Figure 2(b). The magnitude of  $C_\kappa \approx 2.02$  at the establishment of a scaling range is within the consensus range of  $C_\kappa \approx 2.0 - 2.2$ [4, 5]. In a similar manner to  $K$ ,  $C_\kappa$  then increases with  $R_\lambda$  to a maximum value of  $\approx 2.3 \pm 0.05$  at  $R_\lambda \approx 700$  and then decreases as  $R_\lambda$  continues to increase. The scatter in  $C_\kappa$  is considerably more than that for  $K$ , but this fact is not surprising considering the greater ambiguity in measuring  $\zeta$  compared to measuring  $p$ . Figure 5(a)

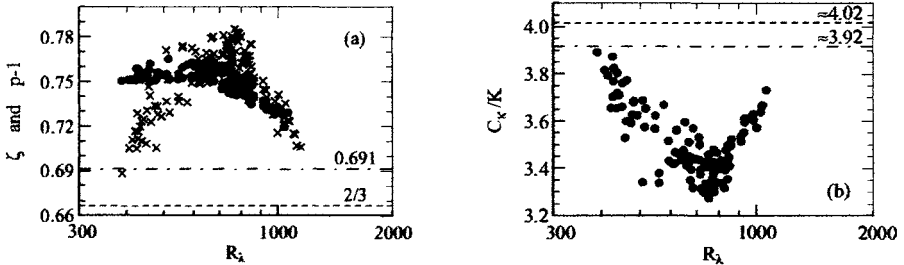


Figure 5. (a)  $\times$ ,  $p - 1$ , measured spectral scaling exponent Eq. (1);  $\bullet$ ,  $\zeta$ , measured structure function scaling exponent Eq. (2); —,  $p - 1$  and  $\zeta = 2/3$ , K41[19]; —,  $p - 1$  and  $\zeta \approx 0.691$ , K62 log-normal model[24] with  $\mu = 2/9$ . (b)  $\bullet$ ,  $C_\kappa/K$  measured in the NORMAN grid  $425 \lesssim R_\lambda \lesssim 1060$ ; —,  $\approx 4.02$  when  $p = 5/3$  and  $\zeta = 2/3$ , K41[1]; —,  $\approx 3.92$  when  $p - 1$  and  $\zeta \approx 0.691$ , K62 log-normal model[2] with  $\mu = 2/9$

shows the  $R_\lambda$  dependence of  $\zeta$  and  $p - 1$ . There appears to be agreement when  $R_\lambda \gtrsim 1000$  which indicates that Eq. (3), the Fourier pairing of the scaling exponents, is beginning to be obeyed. This suggests that the IR has dilated to a sufficient length to be less and less influenced by the effects of the anisotropic/inhomogeneous large scales as it grows with  $R_\lambda$ . To our knowledge, this is the first time this observation has been documented. Finally, Figure 5(b) shows the  $R_\lambda$  dependent behavior of  $C_\kappa/K$ . We cannot be certain of the final magnitude for  $C_\kappa/K$  but, again, if the trend for  $R_\lambda \gtrsim 700$  is maintained we believe we will know when  $R_\lambda \approx 2000$ . Space precludes the display of Eqs. (3)–(5). It follows from Figure 5(a) that Eq. (3) is approximately zero from  $R_\lambda \gtrsim 1000$ . We can also report that Eqs. (4) and (5) are also approaching zero, in keeping with Figures 5(a) and (b), for  $R_\lambda \gtrsim 1000$ .

#### 4. Final Remarks

We believe we are tantalizingly close to answering an outstanding issue in turbulence – does asymptotic IR scaling exist and if so, does it exist in a complete or incomplete similarity form? To answer this confidently, we

need to double  $R_\lambda$  in the current geometry. However, much work needs to be done on developing sub-miniature hot-wire probes and increasing the CTA signal-to-noise ratio required for these high  $R_\lambda$ .

## Acknowledgments

BRP is grateful to the University of Nottingham for an *Overseas Conference Fund* award.

## References

- [1] Kolmogorov, A. N., 1941, The Local Structure of Turbulence in an Incompressible Fluid for Very Large Reynolds Numbers, *Dokl. Akad. Nauk. SSSR* **30**, 299–303.
- [2] Kolmogorov, A. N., 1962, A Refinement of Previous Hypotheses Concerning the Local Structure of Turbulence in a Viscous Incompressible Fluid at High Reynolds Number, *J. Fluid Mech.* **13**, 82–85.
- [3] Barenblatt, G. I. & Goldenfield, N., 1995, Does Fully Developed Turbulence Exist? Reynolds Number Independence versus Asymptotic Covariance, *Phys. Fluids* **7**, 3078–3082.
- [4] Monin A. S. & Yaglom, A. M., 1975, *Statistics of Turbulence*, Vol. 2, MIT Press.
- [5] Praskovsky, A. & Oncley, S., 1994, Measurements of Kolmogorov Constant and Intermittency Exponent at High Reynolds Number, *Phys. Fluids* **6**, 2886–2888; Sreenivasan, K. R. 1995, On the Universality of the Kolmogorov Constant, *Phys. Fluids* **7**, 2778–2784; Mydlarski, L. & Warhaft, Z., 1996, On the Onset of High-Reynolds Number Grid-Generated Wind Tunnel Turbulence, *J. Fluid Mech.* **320**, 331–368.
- [6] Belmonte, A., Martin, B. & Goldburg, W. I., 2000, Experimental Study of Taylor's Hypothesis in a Turbulent Soap Film, *Phys. Fluids* **12**, 835–845.
- [7] Stolovitzky, G. & Sreenivasan, K. R., 1995, Intermittency, the Second-Order Structure Function, and the Turbulent Energy-Dissipation Rate, *Phys. Rev. E* **52**, 3242–3244.
- [8] Pearson, B. R., Krogstad, P. -Å. & van de Water, W., 2002, Measurements of the Turbulent Energy Dissipation Rate, *Phys. Fluids* **14**, 1288–1290.
- [9] Pearson, B. R., Krogstad, P. -Å. & Carper, M. A., 2001, Re Dependence of the Energy Dissipation Rate and Spectrum in Shear Flows, In *Proceedings of the 14th Australasian Fluid Mechanics Conference*, (Ed. B. B. Dally), Adelaide, 167–170.
- [10] Pearson, B. R., Johnson, G. R. & Krogstad, P. -Å., 2002, The Kolmogorov Constant, Intermittency and Scaling, in *Advances in Turbulence IX*, (Eds. I. P. Castro, P. E. Hancock & T. G. Thomas), CIMNE, Barcelona, 49–52.

# SUPPRESSION OF VORTICAL MOTIONS IN COMPRESSIBLE ISOTROPIC TURBULENCE

Hideaki Miura

*Theory and Computer Simulation Center,  
National Institute for Fusion Science,  
322-6 Oroshi, Toki, Gifu 509-5292, Japan*  
miura@toki.theory.nifs.ac.jp

**Abstract** Evolution of vortex structures in compressible decaying isotropic turbulence is investigated by means of direct numerical simulation. It is shown that strength of swirling motions is suppressed by compressibility. The suppression is attributed to the reduction of vortex stretching on central axes of vortices. In order to find the origin of the vortex stretching reduction, dynamical evolution of individual vortex axis is observed. Excitations and propagations of acoustic and Kelvin waves along vortex axes are observed. The growth of the two waves is strongly related with the suppression of the vortex stretching.

**Keywords:** Vortex stretching, compressibility, isotropic turbulence

## Introduction

Over the past two decades, a considerable number of studies have been made on compressibility effects on turbulence. It has been shown that compressibility reduces activity of turbulence. (See a review by Lele 1994). Clarifying mechanism of the suppression has been one of the most important subjects of compressible turbulence research. In this article, we aim to clarify compressibility effects on vortex structures in turbulence. We conduct direct numerical simulation (DNS) of decaying isotropic turbulence of compressible and incompressible fluids and compare their vortex structures.

## 1. DNS of decaying isotropic turbulence

We solve the Navier-Stokes equations for compressible and incompressible fluids by the pseudo-spectral method and Runge-Kutta-Gill

scheme under the  $(2\pi)^3$  triply-periodic boundary condition. The Reynolds number is  $Re_0 = 1000$  and the Prandtl number is  $Pr_0 = 0.7$ . Compressible DNS with the Mach number  $M_0^2 = 2.0, 0.5$  and  $0.1$  are conducted and referred to as C1, C2 and C3, respectively. An incompressible run with  $Re_0 = 1000$  is referred as I. All runs are performed on a  $N^3 = 256^3$  grid. The Taylor's micro-scale Reynolds numbers of the four runs start from  $Re_\lambda \simeq 140$  and decay to 30. Turbulent Mach numbers  $M_t$  of compressible runs are small (typically  $M_t = 0.4$  for C1), so that shocklets are not observed.

In the previous work (Miura 2002), it has been shown that the root mean square fluctuations of the pressure and the enstrophy density are sensitive to compressibility. It has also been shown that the total volume of compressible vortices is about 35% smaller than incompressible vortices. Based on the preliminary work, we study compressibility effects on vortex structures.

## 2. Vortex structures in turbulence

Properties of tubular vortices in turbulence are investigated by the use of our vortex identification scheme(Miura and Kida 1997, Kida and Miura1998a), by which we extract central axes of vortices (vortex axes) and swirling regions of them (vortex cores) out of DNS data.

In order to see compressibility effects on vortex structures, it is important to study strength of swirling motions of vortices. The swirling strength is well represented by the longitudinal vorticity  $\omega_{\parallel}$  on vortex axes. The symbol  $\parallel$  represents that the quantity is for the component parallel to the vortex axes. In Fig.1, the time evolution of  $\langle \omega_{\parallel}^2 \rangle_A$  is shown. The brackets  $\langle \rangle_A$  represent the average over all vortex axes. The longitudinal vorticity becomes smaller as compressibility becomes stronger from I to C3, C2 and C1, showing that compressibility reduces the strength of swirling motions of vortices. Since the longitudinal vorticity  $\omega_{\parallel}$  is generated by the vortex stretching  $\sigma = \partial u_{\parallel} / \partial x_{\parallel}$ , it is relevant to see how compressibility changes  $\sigma$  on vortex axes. In Fig.2, the time evolution of  $\langle \sigma^2 \rangle_A$  is shown for the four runs. The mean squared vortex stretching  $\langle \sigma^2 \rangle_A$  decreases as compressibility becomes stronger. Thus the suppression of the longitudinal vorticity, or the strength of swirling motions of vortices, are attributed to the reduction of the vortex stretching.

In order to clarify how the vortex stretching is reduced, the time evolution of individual vortices are tracked. In Fig.3, vortex axes and some typical vortex cores of run C1 in a region on a  $96^3$  grid are shown. We observe bulge structures on the surfaces of vortex cores inside the ellipses.

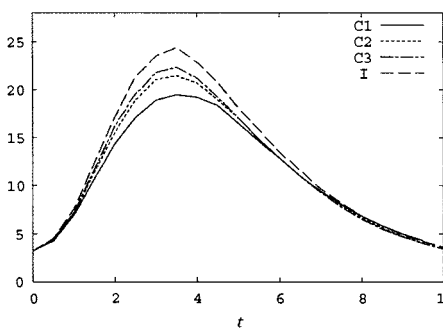


Figure 1. Time evolution of  $\langle \omega_{\parallel}^2 \rangle_A$ .

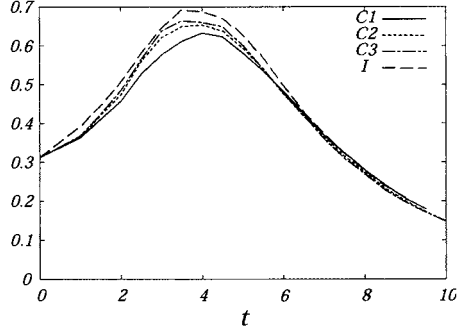


Figure 2. Time evolution of the mean stretching squared,  $\langle \sigma^2 \rangle$ .

The bulges look axi-symmetric about vortex axes. From observations of time-sequences of the vortex cores, the bulges are considered to travel along vortex axes.

In Fig.4, a snapshot of  $\sigma$  on vortex axes of the four runs, which share the same ancestor vortex at the initial time, are shown. The abscissa is a distance measured along the axis from one end of the axis toward the other end. We observe rapid oscillations of vortex stretching associated with the bulges in Fig.3. Note that the amplitudes of the oscillations become larger as compressibility becomes stronger, and simultaneously, the mean level of  $\sigma$  becomes lower. These bulge structures are not observed on the incompressible vortex axes and considered to be intrinsic to compressible vortices. Close observations show that the short-wavelength oscillations consist of two kinds of waves. One kind of waves is identified as a sort of sound waves because the wavelengths and propagation speeds of them are related each other with the dispersion relation of the sound waves. The other kind of waves is associated with the vorticity waves, which are often called as the Kelvin waves. We observe that the mean levels of vortex stretching on vortex axes become weaker as the amplitudes of the two waves become larger. It suggests that the growth of the waves is strongly related with the vortex stretching reduction.

### 3. Summary

Compressibility effects on turbulent vortices is investigated numerically. Compressibility suppresses swirling motions of vortices through suppression of the vortex stretching. In the course of dynamical evolution of individual vortices, acoustic and Kelvin waves are excited on



*Figure 3.* Bulge structures along compressible vortex cores.

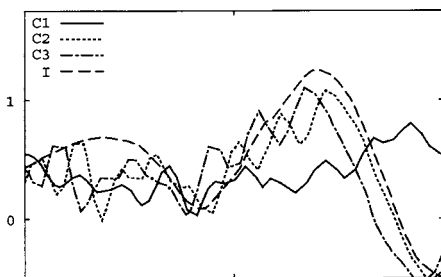


*Figure 4.* A comparison of  $\sigma$  on vortex axes among four runs C1, C2, C3 and I.

vortex axes. It is worth noting that similar phenomena have been observed in superfluid turbulence (Kivotides et al. 2001). The detailed mechanism of the vortex stretching suppression is left to be examined. Investigations on these issues should be reported soon.

This work was partially supported by the Grant-in-Aid for Scientific Research for Encouragement of Young Scientists (B)(No.13750155) from Japan Society for the Promotion of Science, and the Grant-in-Aid for Scientific Research on Priority Area B (No.12125203) from the Ministry of Education, Culture, Sports, Science and Technology of Japan. Numerical computations were carried out on the SX-4 system in the Theory and Computer Simulation Center, NIFS.

## References

- Lord Kelvin, "Vibrations of a columnar vortex", *Phil. Mag.* **10** (1880) 155.
- D. Kivotides, J.C. Vassilicos, D. C. Samuels and C. F. Barenghi, "Kelvin Waves Cascade in Superfluid Turbulence", *Phys. Rev. Lett.* **86** (2001) 3080.
- S. Kida and H. Miura, "Swirl Condition on a Low-Pressure Vortices", *J. Phys. Soc. Japan* **67** (1998) 2166.
- S. K. Lele, "Compressibility effects on turbulence", *Ann. Rev Fluid Mech.* **26** (1994) 211.
- H. Miura, "Analysis of vortex structures in compressible isotropic turbulence", *Comp. Phys. Comm.* **147** (2002) 552.
- H. Miura, and S. Kida, "Identification of Tubular Vortices in Turbulence", *J. Phys. Soc. Japan*, **66** (1997) 1331.

# ON THE REGULARITY OF SOLUTIONS TO THE NAVIER-STOKES EQUATIONS

Jacques Lewalle

*Syracuse University*

[jlewalle@syr.edu](mailto:jlewalle@syr.edu)

**Abstract** A directional modulus of continuity is used to evaluate the scaling of each term in the incompressible Euler and Navier-Stokes equations. This is done by expressing the equations in terms of continuous Hermitian wavelets (derivatives of Gaussians), for which the exact scaling is easily derived. In the case of 3-D Euler with equal  $h$ 's in all directions, runaway singularities are found for  $h < 1/3$ . In 2- and 3-D, it is found that the viscous term dominates for positive  $h$ 's.

**Keywords:** Regularity, Navier-Stokes, Euler, wavelets, scaling

## 1. Background.

The finite-time regularity of solutions of the Navier-Stokes and Euler equations remains a theoretical as well as practical problem. For non-differentiable (weak) solutions, the possibility of inviscid dissipation [9, 2, 4, 5] could affect our understanding of the dissipation rate  $\epsilon$  in common models. The relation between regularity and vorticity is well established [1, 8].

Relevant concepts include velocity differences (modulus of continuity), filtering (mollifying), vorticity, scaling, and exact dynamics. Section 2 introduces wavelet tools that combine all these elements. It is known that continuous wavelets can be used for the characterization of Besov spaces [10]. In particular, Hermitian wavelets yield a tractable form of the Navier-Stokes (NS) equations [7], which makes possible the evaluation of each term. A multidimensional variant of the modulus of continuity and the corresponding scaling is applied to the the NS equations.

## 2. Formulation

We start from the incompressible NS equations

$$\partial_t u_i - \nu \partial_{jj}^2 u_i = -\partial_i \left( \frac{p}{\rho} \right) - \partial_j (u_i u_j). \quad (1)$$

Some of the most productive options result from the elimination of pressure as a dependent variable. Here we follow earlier work [7] and introduce flexion as the Laplacian of velocity  $\alpha_i = \partial_{kk}^2 u_i$ . Taking the Laplacian of Eq.(1) and eliminating pressure yields

$$\partial_t \alpha_i - \nu \partial_{jj}^2 \alpha_i = \partial_{ijk}^3 (u_j u_k) - \partial_{jkk}^3 (u_i u_j), \quad (2)$$

in support of which the (3-D) Biot-Savart equation takes the form

$$u_i = \frac{1}{4\pi} \int \frac{\alpha'_i}{|x - x'|} dx'. \quad (3)$$

It can be seen that the Fourier transform of Eq.(2) is identical (within a factor  $k^2$ ) to the familiar Fourier-velocity formulation.

Scale resolution is introduced through the  $N$ -dimensional Gaussian filter  $F_s(x) = (4\pi s)^{-N/2} \exp(-\frac{x^2}{4s})$  (note that the scale  $s$  has dimensions  $L^2$ ). The filtered flexion is

$$\alpha_i^> = F_s(x) * \alpha_i = \int \alpha_i(x') F_s(x - x') dx'. \quad (4)$$

Noting that  $\partial_{kk}^2 \alpha_i^> = \partial_s \alpha_i^>$ , the general form of the filtered Eq.(2) is

$$(\partial_t - \nu \partial_s) \alpha_i^> = \partial_{ijk}^3 (u_j u_k)^> - \partial_{jkk}^3 (u_i u_j)^>. \quad (5)$$

The wavelet formalism[3, 6] provides another interpretation of filtered flexion, and another formula for the reconstruction of the velocity field. Indeed the isotropic Mexican-hat wavelet  $\psi(x, s)$  is given by

$$\psi(x, s) = \partial_{kk}^2 F_s(x) = \partial_s F_s(x). \quad (6)$$

Therefore,

$$\alpha_i^> = \psi(x, s) * u_i = \tilde{u}_i(x, s), \quad (7)$$

and Eq.(5) governs the evolution of the velocity wavelet coefficients. Furthermore, the inverse wavelet transform can be written [7]

$$u_i = \int \frac{ds}{s} s \alpha_i^>, \quad (8)$$

which is equivalent to Eq.(3).

These tools mesh very well with the modulus of continuity:

$$\delta u = u(x) - u(x-y) \sim |y|^h, \quad (9)$$

which has emerged as a useful diagnostic of regularity. Kolmogorov scaling (K41) predicts an average  $h = 1/3$ . For differentiable fields, Taylor series correspond to positive integer  $h$ 's. Any value  $h < 1$  is an indicator of singularity. Then, it is easy to show [3, 10]

$$\int F_s(y) \delta u \, dy = u - u^> = u^< \sim s^{\frac{h}{2}} \quad (10)$$

It can also be proved that derivatives of order  $n$  follow the scaling  $\partial_x^n u^> \sim s^{\frac{h-n}{2}}$  and in particular

$$\tilde{u} \sim s^{\frac{h}{2}-1} \quad (11)$$

Directional variability of the modulus of continuity is defined by the relation

$$\delta_j u_i = u_i(x_j) - u_i(x_j - y_j) \sim y_j^{h_{ij}} \quad (12)$$

Then, proceeding as above, it follows that

$$\tilde{u}_i \sim s^{\frac{\sum_j h_{ij} - 2}{2}}. \quad (13)$$

Similarly, each derivative of the wavelet coefficients will lower the exponent by  $1/2$ .

With these tools, we can determine the scaling of the various terms in the wavelet-based Navier-Stokes equations (5). The evaluation of the nonlinear terms relies on the Constantin-E-Titi (CET) relation [2], and yields

$$(u_i u_j)^> \sim s^{\sum_m \frac{h_{im} + h_{jm}}{2}}. \quad (14)$$

### 3. Results and discussion

Accordingly, the small-scale dominant exponents (i.e. the smallest exponents) for the various terms in the equations are shown in Table 1. The central column in the table gives the general expressions as derived above; the right column lists the scaling exponents under the simplifying assumption that all  $h_{im}$ 's are equal to a single value  $h$ . A dominance of nonlinear terms would lead to runaway singularities, since any scaling of the evolution term would be instantly overwhelmed by the nonlinearities.

The case of all  $h$ 's equal allows the simplest conclusions, and some cautions to be discussed below. If we ignore the viscous term (Euler dynamics), and seek the smallest of  $\frac{Nh}{2} - 1$  and  $Nh - \frac{3}{2}$ , we see that the

term	general	all $h$ 's equal
evolution	$\frac{\sum_m h_{im} - 2}{2}$	$\frac{Nh}{2} - 1$
pressure	$\min_{jk} \frac{\sum_m (h_{jm} + h_{km}) - 3}{2}$	$Nh - \frac{3}{2}$
convective	$\min_j \frac{\sum_m (h_{im} + h_{jm}) - 3}{2}$	$Nh - \frac{3}{2}$
viscous	$\frac{\sum_m h_{im} - 4}{2}$	$\frac{Nh}{2} - 2$

Table 1. Dominant exponents for evolution, pressure, convective and viscous terms in N-dimensional Euler and Navier-Stokes dynamics.

nonlinearities dominate if  $h < \frac{1}{N}$ . Thus, in the case of 3-D turbulence, we recover the K41 exponent as the threshold of runaway singularities and the Onsager threshold of possible inviscid dissipation, which is encouraging. However, for  $N = 2$ , a threshold of  $h = \frac{1}{2}$  contradicts recent results [4]. Two explanations are possible for this anomaly, and are currently under study. First, it is possible that all  $h$ 's cannot be equal for some kinematic reason; second, it is conceivable that some combination of terms disappear under summation so that their exponent would become irrelevant. Either or both of these reasons would make the above estimates upper bounds for any runaway singular behavior. Furthermore, it is easy to see that the viscous term dominates for any  $h > -\frac{1}{N}$ , so that we conclude that positive  $h$ 's correspond to Navier-Stokes regularity.

A preliminary study of the case of directional  $h_{im}$ 's was carried out by generating random numbers in some interval  $(X, 1)$ , and tabulating results. A gradual increase of occurrence of singularities was observed as  $X$  is lowered, but no sharp threshold was noticed among hundreds of samples. No viscous singularities were noted for  $X > 0$ .

## References

- [1] Beale, Kato & Majda, Commun. Math. Phys. **94**, 61-66 (1984).
- [2] Constantin, E & Titi, Commun. Math. Phys. **165**, 207-209 (1994).
- [3] Daubechies, *Ten Lectures on Wavelets*, S.I.A.M. (1992).
- [4] Duchon & Robert, Nonlinearity **13**, 249-255 (2000).
- [5] Eyink, Nonlinearity **14**, 787-802 (2001).
- [6] Farge, Ann. Rev. Fluid Mech. **24**, 395-457 (1992).
- [7] Lewalle, J. Turbulence **1**, 004, 1-15 (2000).
- [8] Majda, Commun. Pure Appl. Math. **39**, S186-S220 (1986).
- [9] Onsager, Nuovo Cimento **6**, 279-287 (1949).
- [10] Perrier & Basdevant, Math. Models Meth. Appl. Sci. **6**, 649-664 (1996).

# NEWS ABOUT THE INTERMITTENCY EXPONENT

J. Cleve<sup>1</sup>, M. Greiner<sup>2</sup>

<sup>1</sup>*Institute for Physical Science and Technology, University of Maryland, College Park, MD 20742, USA*

<sup>2</sup>*Corporate Technology, Information & Communications, Siemens AG, D-81730 München, Germany*

**Abstract** The quality of scaling in different observables is discussed.

For the characterization and understanding of fully developed turbulence noticeable attention is paid to scaling behavior. We will discuss and compare some scaling observables.

The most frequent used quantities to illustrate scaling in fully developed turbulence are the structure functions  $S_n \equiv \langle (\vec{e}_r \cdot (\vec{v}(\vec{x} + \vec{r}) - \vec{v}(\vec{x})))^n \rangle \propto r^{\xi_n}$ . But even for very high Reynolds number turbulent flows the scaling range for structure functions is very short and additional manipulation of the data like extended self similarity or SO(3) decomposition have been applied to extend the scaling range. This leads us to the question if not other observables or other fields are better suited to investigate scaling. We will illustrate the scaling behavior of different observables for two different sets of data, an atmospheric boundary layer recorded under nominally steady condition and a cryogenic helium jet.

The atmospheric boundary layer was recorded on top of a meteorological tower at about 35m above ground. The Reynolds number for this data set based on the Taylor microscale  $\lambda = \sqrt{\langle u^2 \rangle / \langle (\partial u / \partial x)^2 \rangle}$  is  $R_\lambda \equiv \sqrt{\langle u^2 \rangle} \lambda / \nu = 17000$ , where  $\nu$  is the kinematic viscosity. To calculate  $\lambda$  we used the method described in [1]. The integral length, defined via the velocity autocorrelation function, is about  $77 \times 10^3 \eta$ , where  $\eta = (\nu^3 / \langle \epsilon \rangle)^{1/4}$  is the Kolmogorov dissipation scale. See [2] for more details about the experimental setup.

The second data set is a longitudinal velocity-component record from the centerline of a gaseous helium jet at 4.3 K and has a moderate Reynolds number of  $R_\lambda = 465$ . The ratio between integral length and

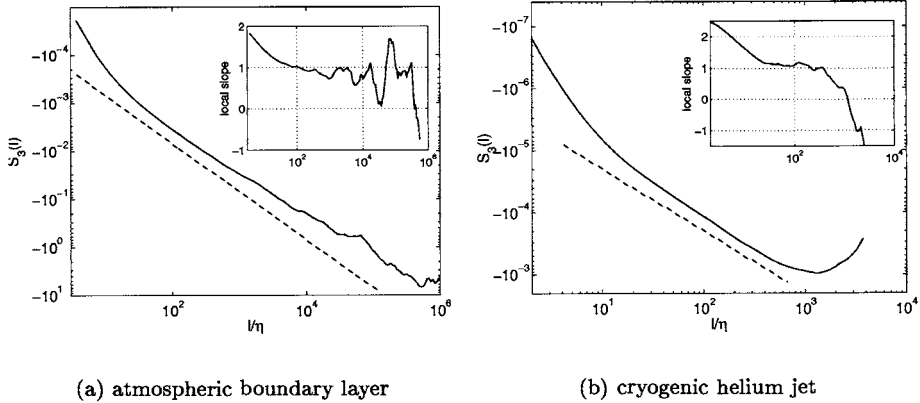


**Figure 1.** Third-order velocity structure functions  $S_3(r)$  for two data sets. Dashed line corresponds to the expected scaling with exponent 1. The inset shows the local slope.

dissipation scale is  $L/\eta = 720$ . The resolution of the data is  $\Delta x/\eta = 1.4$ . The spectral density of the cryogenic helium jet shows some noise towards smaller scales due to instrument noise. We removed this noise by means of a Wiener filter to ensure a correct calculation of derivatives. Further details and a description of the experimental setup can be found in [3].

In Figure 1 the third order structure function is shown. As one can see in the local slope in the inset the scaling range is very short and an extraction of the scaling exponent would be ambiguous. Is this poor scaling unavoidable in turbulence or is it only apparent in structure functions?

Figure 2 illustrates the two point correlation  $\langle \varepsilon(x+d)\varepsilon(x) \rangle / \langle \varepsilon(x) \rangle^2$  of the energy dissipation. The scaling range covers most of the inertial range and the local slope in the inset exhibits a flat plateau up to about the integral length  $L$ . The size of the scaling range is much larger than for the case of structure functions. However, the deviation from perfect scaling towards smaller scales look rather puzzling because the correlation increases beyond the power law behavior. One would expect that dissipation - because it smoothes out fine structures - works against the increase of two point correlations. But this behavior does not reflect a physical process. It is a consequence of the experimental limitations of the measurement. To calculate the energy dissipation one would need the three-dimensional velocity field to access all derivatives involved in the construction of  $\varepsilon$ . Since usually only one component is available,

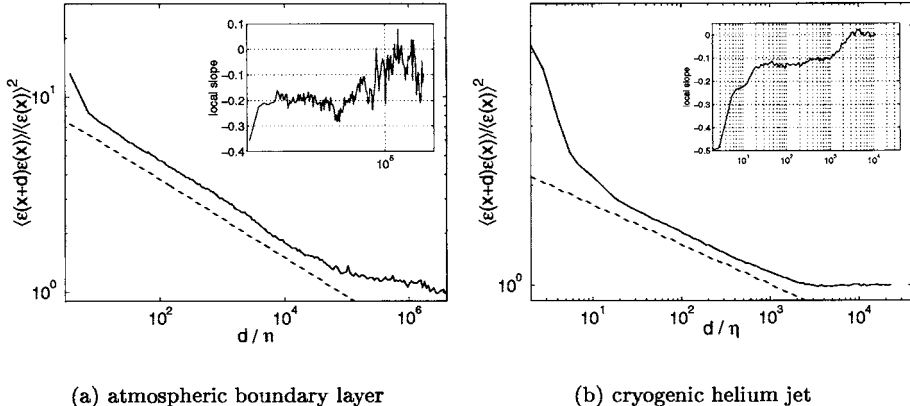


Figure 2. Normalized two-point correlation of the surrogate energy dissipation with local slope  $d \ln \langle \varepsilon_i^2 \rangle / d \ln l$  in the inset

one-dimensional surrogates  $\varepsilon \equiv 15\nu(\frac{\partial u}{\partial x})^2$  are used. For homogeneous isotropic turbulence the mean of this definition is equal to the mean of the true dissipation field. As explained in [4] the surrogacy leads to deviations in the two point correlation for small distances but results in the same correlation for all larger distances.

This behavior of the two point correlator has further implications. A close relative, the so called integral moment  $\langle \epsilon_l^n \rangle$  with  $\epsilon_l = l^{-1} \int_l \epsilon_{\text{surr}}(x) dx$ , is a frequently studied observable. In second order this quantity is simply an integral over the two point correlation (see [5])

$$\langle \varepsilon_l^2 \rangle = \frac{1}{l^2} \int_l dx_1 \int_l dx_2 \langle \varepsilon_{\text{surr}}(x_1) \varepsilon_{\text{surr}}(x_2) \rangle . \quad (1)$$

To see when the integral moment shows the same scaling exponent as the two-point correlator, and in what range of scales, we assume the simple functional form for the latter:

$$\langle \varepsilon_{\text{surr}}(x+d) \varepsilon_{\text{surr}}(x) \rangle = \begin{cases} c & (d < \eta') \\ a(\eta'/d)^\mu & (\eta' \leq d \leq L') \\ 1 & (d \geq L') \end{cases} \quad (2)$$

For the sake of simplicity  $\langle \varepsilon \rangle = 1$ , and  $a(\eta'/L')^\mu = 1$  ensures continuity at the decorrelation length  $L'$ . Inserting this equation into (1) yields

$$\left\langle \varepsilon_l^2 \right\rangle = \frac{2a}{(1-\mu)(2-\mu)} \left( \frac{\eta'}{l} \right)^{\mu} + 2 \left( c - \frac{a}{1-\mu} \right) \left( \frac{\eta'}{l} \right) + \left( \frac{a}{1-\mu/2} - c \right) \left( \frac{\eta'}{l} \right)^2 \quad (3)$$

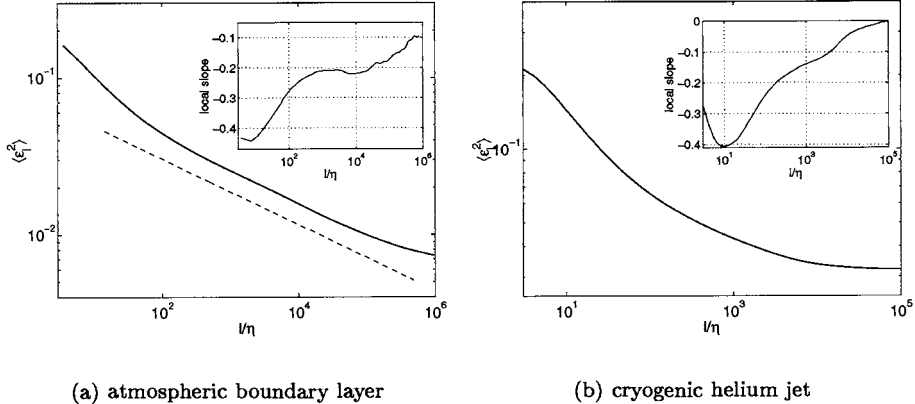


Figure 3. Second-order integral moment; inset: local slope.

for  $\eta' \leq l \leq L'$ . The integral moment comes with a dominant “true” scaling term, but the small scale behavior of the two point correlation introduces two correction terms, which disturb the perfect scaling at small scales. A closer look at Figure 2 suggests that  $c > a/(1 - \mu)$ , which explains why the integral moment shows poorer scaling than the two point correlation and even destroys the scaling for the moderate Reynolds number case as shown in Figure 3.

Work is in progress to understand why the intermittency exponents for the two data sets are different, i.e.  $\mu = 0.2$  and  $0.12$  for the atmospheric boundary layer and the cryogenic helium jet, respectively. It could mean that there is a dependence on Reynolds number and/or flow geometry.

## References

- [1] D. Aronson and L. Löfdahl, Phys. Fluids A5, 1433 (1993).
- [2] B. Dhruva, *An Experimental Study of High Reynolds Number Turbulence in the Atmosphere*, PhD thesis, Yale University (2000); see also Sreenivasan K.R. and Dhruva B. Prog. Theor. Phys. Suppl. 130, 103 (1998).
- [3] O. Chanal, B. Chebaud, B. Castaing and B. Hébral, Eur. Phys. J B17, 309 (2000).
- [4] J. Cleve, M. Greiner and K. R. Sreenivasan, accepted for publication in Eur. Phys. Letter (2003).
- [5] A.S. Monin and A.M. Yaglom, *Statistical Fluid Mechanics*, Vol. 2, (MIT Press, Cambridge, 1971).

# A GAS-PHASE NEAR-ISOTROPIC TURBULENCE AND ITS WAVELET ANALYSIS FOR STUDYING FINE-SCALE INTERMITTENCY

T. S. Yang and S. S. Shy\*

*Department of Mechanical Engineering, National Central University, Chung-Li 32054, TAIWAN*

**Abstract:** The correlations between spatial and temporal behaviours of both fine-scale intermittency and the scaling of  $n^{\text{th}}$ -order velocity structure function in a near-isotropic turbulence are studied experimentally, without adopting Taylor's hypothesis, using a high-speed digital particle image velocimetry together with the wavelet transform analysis. In the dissipation range, the spatial and the temporal intermittency of intense vorticity structures occur around  $5 \sim 10 \eta$  and  $\tau_k$ , respectively, where  $\eta$  and  $\tau_k$  are the Kolmogorov length and time scale of turbulence. In the inertial range the anomalous scalings of both spatial and temporal velocity structure functions are identical and values of scaling exponents are found to be within the range between the  $\beta$ -model and the She-Leveque model.

**Key words:** fine-scale intermittency, velocity structure function, wavelet transform, digital particle image velocimetry, near-isotropic turbulence

## 1. INTRODUCTION AND EXPERIMENTAL METHODS

Most previous experimental studies on isotropic turbulence were conducted in the wind tunnel where a mean flow was passed through a grid and point measurements were commonly used to obtain turbulence characteristics. Thus, the spatial correlation of turbulence can be only extracted from the available temporal correlation data by adopting the well-known Taylor's hypothesis [1,2]. In this note, we use a high-speed digital particle image velocimetry (DPIV) to obtain the evolution of velocity fields of a near-isotropic turbulence generated by a pair of counter-rotating fans and perforated plates in a cruciform apparatus (see Fig. 1). Thus, without the adopting Taylor's hypothesis the correlations between spatial and temporal

\* Corresponding author: [sshy@cc.ncu.edu.tw](mailto:sshy@cc.ncu.edu.tw); Fax: 886-3-425-4501

behaviours of both fine-scale intermittency and the scaling of the  $n^{\text{th}}$ -order velocity structure function in near-isotropic turbulence with zero-mean-shear are investigated for the first time.

In this study, we set the fan frequency  $f = 7$  Hz for which the Reynolds number based on the Taylor microscale ( $Re_\lambda$ ) is 120. For a detail treatment of the cruciform apparatus, the reader is directed to Refs. [3,4]. The  $n^{\text{th}}$ -order velocity structure function is  $\langle \Delta V(r)^n \rangle = \langle |V(t+r) - V(t)|^n \rangle \sim r^{\zeta(n)}$ , where  $\langle \Delta V(t) \rangle = V(t+r) - V(t)$  is the velocity increment between two points at a separation  $r$  and  $\zeta(n)$  is the scaling exponent. Camussi et al. [1] have analyzed the scaling properties of the longitudinal and transverse velocity functions, respectively  $\zeta_L(n)$  and  $\zeta_T(n)$ , in wind-tunnel turbulence for  $Re_\lambda=37$  and found  $\zeta_L(n) \approx \zeta_T(n)$ , not significantly influenced by the mean flow [1]. However, Zhou & Antonia [2] found  $\zeta_T(n) < \zeta_L(n)$  in the presence of a mean shear for  $Re_\lambda=27\text{-}100$ . This discrepancy and the need for evaluation of Taylor's hypothesis motivate the present study.

A continuous 1-D complex-valued ‘Morlet’ wavelet is applied to transform the velocity signals obtained from DPIV measurements. From Farge [5], the wavelet transform coefficient  $W(a,b)$  of a real-valued time signal, such as the time evolution of the velocity signal  $V(t)$ , is defined as the inner product between  $V(t)$  and an analyzing wavelet,  $W(a,b) = \int_{-\infty}^{\infty} V(t) \phi_{a,b}^*(t) dt$ , where  $\phi_{a,b}(t) = (1/\sqrt{a}) \phi((t-b)/a)$ ,  $a$  and  $b$  are dilatation and translation parameters, the asterisk of  $\phi$  represents the complex conjugate, and the complex-valued ‘Morlet’ wavelet  $\phi(t) = (e^{i\omega_0 t}) e^{-t^2/2}$ . We set  $\omega_0=2\pi$  in this study. In addition, the flatness factor,  $FF$ , of the wavelet coefficient is calculated to identify the level of intermittency, in which  $FF = \left\langle |W(a,b)|^4 \right\rangle_t / \left\langle |W(a,b)|^2 \right\rangle_t^2$ . The subscript  $t$  represents the analysis in the time domain and the same relations hold for analyses in the spatial domain when  $t$  is replaced by the longitudinal and transverse variables,  $x$  and  $y$ , respectively. The velocity structure function,  $F(r) = \langle |\Delta V(r)| \rangle$ , is also investigated to determine the trend in intermittency in the inertial range of turbulence. As pointed out by Farge et al. [6], the velocity increment is equivalent to a wavelet transform with the Haar wavelet  $\phi(t) = \delta(t+1) - \delta(t)$ . Therefore, the scaling exponents,  $\zeta(n)$ , in the inertial range can be estimated using the extend self-similarity (ESS) method [7] as  $F_n(r) = \left\langle |W(r,t)|^n \right\rangle_t \sim \left\langle |W(r,t)|^3 \right\rangle_t^{\zeta(n)}$ .

## 2. RESULTS AND DISCUSSION

Figure 2a displays instantaneous flow velocity and vorticity maps of fan-stirred near-isotropic turbulence, showing intense vortical structures possessing significant intermittent distribution; Fig. 2b is the  $FF$  of wavelet

coefficients as a function of the length scale obtained from both the longitudinal ( $u$ ) and transverse ( $v$ ) velocity components along the  $x$ -axis at three different  $y$  positions. Maximum values of  $FF$ , an indication of the average scales of intense vortical structure, are around 0.2-0.4 cm, which are five to ten times larger than the Kolmogorov length scale, in consistent with DNS result [8]. On the other hand, Fig. 3 shows the fluctuation of  $FF$  as a function of characteristic frequency scale that represents small-scale temporal intermittent phenomena. Peak values of  $FF$  for both  $u$  and  $v$  components occur around 160 Hz, on the same order of the Kolmogorov time of turbulence,  $\tau_k=0.01$  s. Hence, the use of the Taylor's hypothesis in the dissipation range is incorrect.

We estimate the velocity structure functions without adopting the Taylor's hypothesis. The result shows that the spatial and temporal scaling exponents are identical,  $\zeta_L(n) \approx \zeta_T(n)$ , suggesting the present turbulence has a very high degree of isotropy. In Fig. 4, only scaling exponents in the temporal domain of the present results are shown for brevity; also shown are scaling exponents obtained from several models of K41 [9],  $\beta$  [10], She-Leveque (SL) [11] and lognormal (LN) [12] with  $\mu=0.2$ , previous experimental data [2], and the numerical result [13] for comparison. As can be seen, the anomalous scaling of the velocity structure function away from K41 is significant and the present data are fallen within the range between the  $\beta$ -model and the SL model.

## REFERENCES

- [1] Camussi, R., Barbegal, D., Guj, G., and Stella, F., Transverse and longitudinal scaling laws in non-homogeneous low Re turbulence, *Phys. Fluids* **9**(12), pp. 1181-1191 (1996).
- [2] Zhou, T., and Antonia, R. A., Reynolds number dependence of the small-scale structure of grid turbulence, *J. Fluid Mech.* **406**, pp. 81-107 (2000).
- [3] Shy, S. S., Lin, W. J., and Wei, J. C., An experimental correlation of turbulent burning velocities for premixed turbulent methane-air combustion, *Proc. R. Soc. Lond. A* **456**, pp. 1997-2019 (2000).
- [4] Shy, S. S., I, W. K. and Lin, M. L., A new cruciform burner and its turbulence measurements for premixed turbulent combustion study, *Exp. Thermal Fluid Sci.* **20**, pp. 105-114 (2000).
- [5] Farge, M., Wavelets transforms and their application to turbulence, *Ann. Rev. Fluid Mech.* **24**, pp. 395-457 (1992).
- [6] Farge, M., Kevlahan, N., Perrier, V., and Schneider, K., Turbulence analysis, modeling and computing using wavelets, *Wavelets in Physics*, ed. J. C. van der Berg, Cambridge University Press, Cambridge, pp. 117-200, (1999).
- [7] Benzi, R., Ciliberto, S., Tripiccione, R., Baudet, C., Massaioli, F., and Succi, S., Extended self-similarity in turbulent flows, *Phys. Rev. E* **48**, pp. R29-R32 (1993).
- [8] Jiménez, J., Wary, A., Saffman, P. G., and Rogallo, R. S., The structure of intense vorticity in isotropic turbulence, *J. Fluid Mech.* **255**, pp. 65-90 (1993).
- [9] Kolmogorov, A. N., The local structure of turbulence in incompressible viscous fluid for very large Reynolds numbers, *C. R. Acad. Sci. USSR* **30**, pp. 299-303 (1941).
- [10] Frisch, U., Sulem, P. L., and Nelkin, M., A simple dynamical model of intermittent fully developed turbulence, *J. Fluid Mech.* **87**, pp. 719-736 (1978).
- [11] She, S. Z., and Leveque, E., Universal scaling laws in fully developed turbulence, *Phys. Rev. Lett.* **72**, pp. 336-339 (1994).
- [12] Kolmogorov, A. N., A refinement of previous hypothesis concerning the local structure of turbulence in a viscous incompressible fluid at high Reynolds number, *J. Fluid Mech.* **13**, pp. 82-85 (1962).
- [13] Vincent, A., and Meneguzzi, M., The spatial structure and statistical properties of homogeneous turbulence, *J. Fluid Mech.* **225**, pp. 1-20 (1991).

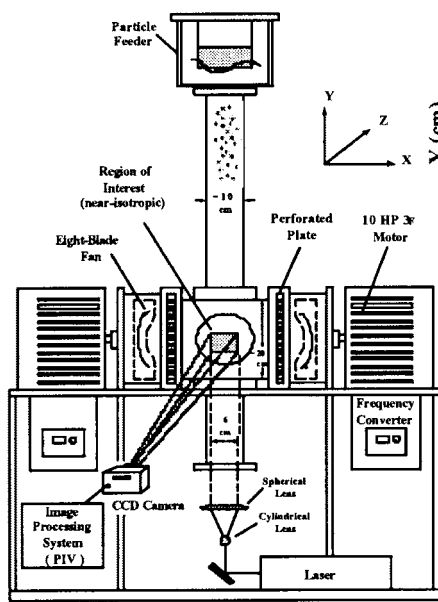


FIG. 1. Schematic diagrams of the cruciform apparatus with the associated image acquisition system.

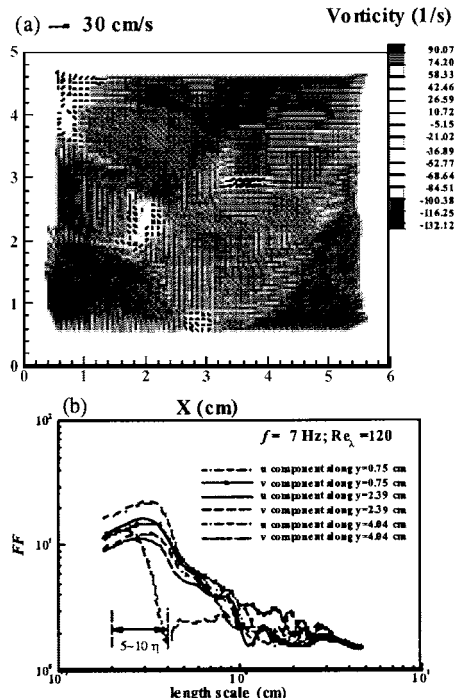


FIG. 2. (a) The instantaneous fluid velocity and vorticity maps obtained by DPIV in the region of interest where the fan frequency  $f = 7$  Hz and  $Re_\lambda = 120$ ; (b) the flatness factor as a function of the length scale, where both horizontal and vertical velocity components along the xaxis at three different  $y$  positions are shown.

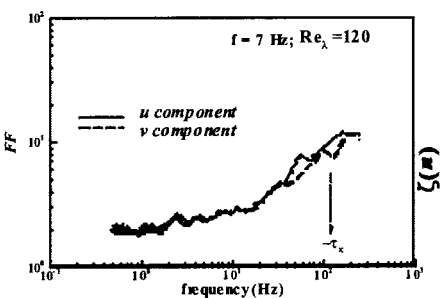


Fig. 3. The flatness factor plotted against the frequency for both horizontal and vertical velocity components. These data are averaged from nine points, equally spaced in the field of view (see Fig. 2a), over a time period of 2 s.

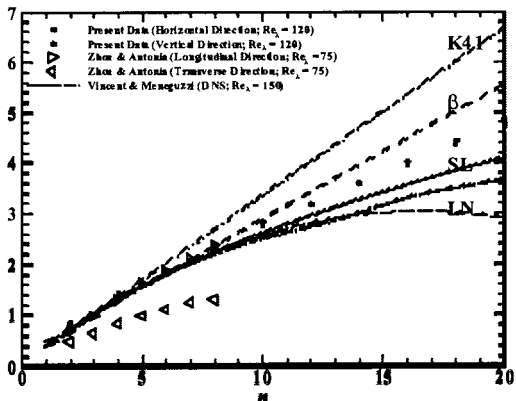


FIG. 4. The scaling exponent as a function the order of velocity structure function. Solid symbols: present data; also shown are previous theoretical, experimental, and numerical results for comparison.

# ASYMMETRIC TIME CORRELATIONS IN TURBULENT SHEAR FLOWS

Bruno Eckhardt, Arne Jachens and Jörg Schumacher

*Fachbereich Physik, Philipps Universität Marburg, D-35032 Marburg, Germany*

**Abstract** Cross correlations between normal and downstream velocity fluctuations in a turbulent shear flow are shown to carry information about the non-normal amplification process. The creation of spanwise modulated streaks by downstream vortices implies an asymmetry in temporal correlation functions. We verify this in numerical simulations in shear flows with  $Re_\lambda \approx 100$ .

**Keywords:** Coherent structures, time correlations, liftup process

Coherent structures are an ubiquitous feature of turbulent shear flows (Townsend 1976, Holmes et al 1996). Various kinds of vortices, streaks or waves have been identified and considerable efforts have gone into identifying their dynamical origins and evolution. In boundary layers the non-normal amplification or lift-up effect (Landahl 1980, Boberg and Brosa 1988, Trefethen et al 1992, Grossmann 2000) is often an important source for coherent structures. Waleffe (1995, 1997) and Hamilton et al (1995) have discussed how lift-up and instabilities form a complete regeneration cycle that can explain sustained large scale fluctuations. The aim of our analysis is to find evidence for this process in statistical measures, in particular in temporal cross-correlation functions.

Following Waleffe (1995, 1997) and Hamilton et al (1995) the recycling process has three steps: i) downstream vortices mix fluid in the normal direction and drive modulations in the downstream velocity, forming so-called streaks. ii) streaks undergo an instability to the formation of vortices pointing in the normal direction. iii) the mean shear profile now turns these vortices again in downstream direction, thus closing the loop. Of these processes the ones in step iii) and ii) are reasonably fast, whereas the one in i) is fairly slow, since it is connected with the lift-up and thus only linear in time. Evidence for this regeneration mechanism was found in various flows (Hamilton et al 1995, Waleffe 1995, 1997, Grossmann 2000). Within a dynamical system picture the regeneration

process can be connected to a periodic orbit, as in the case of Kawahara and Kida (2001). The complete application of this picture to turbulence is complicated not only by the presence of many more periodic orbits (as found by Schmiegel (unpublished) for a low-dimensional model), but also by the possibility of other spatial variabilities than just a periodic variation in spanwise and downstream directions. Therefore, in order to identify this process in fully developed turbulent flows other indicators have to be found.

The indicator for non-normal amplification that we focus on here is a temporal cross-correlation function (Eckhardt and Pandit 2002). Since the vortex drives the streak a cross-correlation between the vortex and the streak should be asymmetric in time: if the streak is probed after the vortex then there might be a correlation, if it is probed before then there should not be a correlation.

The origin of such correlations can be made clear in the context of a linear analysis around a laminar profile (Eckhardt and Pandit, 2002). let  $\mathbf{u}_0 = S y \mathbf{e}_x$  be the shear flow profile, let  $\omega(t)$  the amplitude of a vortex and  $s(t)$  be the amplitude of the streak, and assume that the non-linear fluctuations can be modelled by white noise. The resulting linear stochastic model can be solved analytically and the cross-correlation between vortex and streak,

$$C_{\omega,s}(t) = \langle \omega(t') s(t' + t) \rangle_{t'}, \quad (1)$$

becomes

$$C_{\omega,s}(t) = \begin{cases} -Se^{\lambda t} & t < 0 \\ -S(1 + \lambda t)e^{-\lambda t} & t > 0 \end{cases}. \quad (2)$$

As expected it is asymmetric. The sign of the correlation function follows from the sign of the velocity gradient: if the downstream velocity increases with  $y$  (positive  $S$ ), then a positive velocity component will bring up slower fluid, hence make a negative change in the streak. Similarly, if it brings faster fluid down, it will make a positive contribution in downstream velocity, but with a negative vertical direction. So in both cases the cross correlation is negative. In addition, the correlation function is proportional to the shear rate  $S$ . The asymmetry follows from an additional term for positive times, so that the ratio

$$Q(t) = C(t)/C(-t) = 1 + \lambda t \quad (3)$$

is simply linear.

Clearly, this form of the correlation function is obtained under a series of assumptions, some of which are discussed in (Eckhardt and Pandit 2002), and further verification is required. In boundary layers the

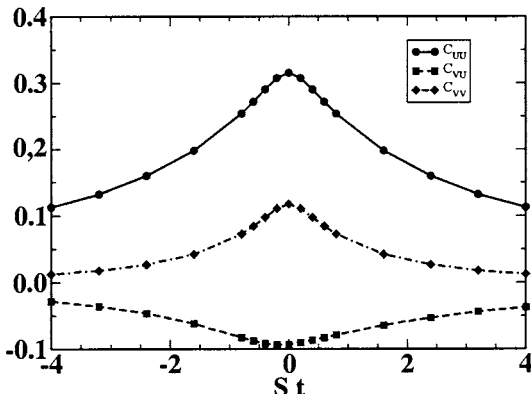


Figure 1. Temporal correlation functions in a turbulent shear flow. The downstream component is  $U$ , the normal component is  $V$ . Times are in dimensionless shear times, the Taylor Reynolds number is  $Re_\lambda = 100$ . The auto-correlation functions are symmetric, the cross-correlation function is negative and slightly asymmetric.

mean flow and Taylors frozen flow hypothesis are usually combined to translate temporal correlations into spatial correlations (e.g. Townsend 1976). This problem is avoided in a Lagrangian frame of reference or in a comoving frame without mean flow. Evidence for the asymmetry in a Lagrangian correlation function can be found in Fig. 1 of (Pope 2002), in a discussion of stochastic Lagrangian models. For Eulerian correlation functions we turn to our numerical simulations of a shear flow (Schumacher and Eckhardt 2000, Schumacher 2001).

The flow is bounded by parallel free-slip surfaces and driven by a steady volume force that maintains a linear shear profile (Schumacher and Eckhardt 2000). The statistical properties of the flow are in good agreement with other approximations to homogeneous shear flows (Schumacher 2001). What is important for our analysis is the fact that the mean downstream velocity vanishes: we can thus calculate correlation functions in a situation without mean flow (in the center) or with a slow mean flow (off-center, up to about half the distance to the surfaces).

The results from a simulation with  $Re_\lambda \approx 100$  are shown in Fig. 1. The auto-correlation functions of the downstream ( $U$ ) and normal ( $V$ ) velocity components are symmetric in time. The cross-correlation function is negative and slightly asymmetric. In order to analyze the asymmetry further we show in Fig. 2 both a magnification of the central region and the ratio (3). The agreement with the linear prediction is satisfactory, considering the many non-linear processes in this fairly turbulent flow.

In summary, we have identified an asymmetry in temporal cross-correlation functions between downstream and normal velocity components in turbulent shear flows. The linearity of the asymmetry supports the connection to the liftup effect. For the analysis of experimental data the effects of a mean flow, of rigid boundaries and also of spatial

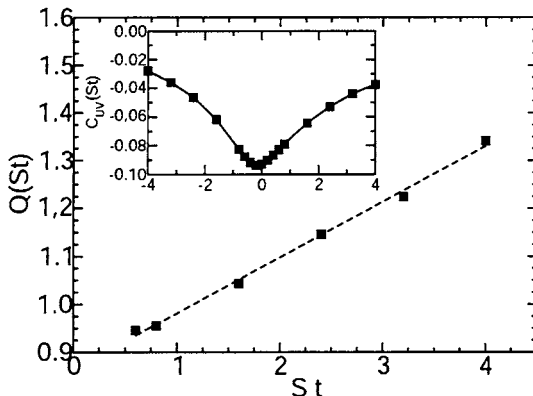


Figure 2. Asymmetry in the cross-correlation function for short times. The large frame shows the ratio of the cross-correlation function for positive and negative times,  $Q(t) = C(t)/C(-t)$ , where a linear behaviour is detected. The inset shows a magnification of the cross-correlation function of Fig. 1 near the center.

inhomogeneities have to be investigated. We have evidence that the effect is strongest near the boundary and decreases as one moves into the turbulent volume. This would be consistent with the decrease of the mean shear gradient and would indicate that non-normal amplification becomes less important further away from the boundaries.

### Acknowledgements

We thank the Deutsche Forschungsgemeinschaft for support and the Neumann Center for Computing at the Forschungszentrum Jülich für computing time and support on their Cray T90.

### References

- Boberg, L. and Brosa, U. (1988), Z. Naturforsch. A, **43**, 697
- Eckhardt, B. and Pandit, R. (2002) *Noise-correlations in turbulent shear flows*, Eur. J. Phys. B, submitted
- Grossmann, S. (2000), Rev. Mod. Phys. **72**, 603
- Hamilton, J.M., Kim, J. and Waleffe, F. (1995), J. Fluid Mech. **287**, 317
- Holmes, P., Lumley, J.L. and Berkooz, G. (1996), *Turbulence, coherent structures, dynamical systems and symmetry*, (Cambridge University Press, Cambridge)
- Kawahara, G. and Kida, S. (2001), J. Fluid Mech. **449**, 291
- Landahl, M., (1980), J. Fluid Mech. **98**, 243
- Pope, S.B. (2002), Phys. Fluids **14**, 1070
- Schumacher, J. (2001), J. Fluid Mech. **441**, 109
- Schumacher, J. and Eckhardt, B. (2000), Europhys. Lett. **52**, 627
- Townsend, A.A. (1976), *The structure of turbulent shear flows*, 2nd ed. (Cambridge University Press, Cambridge)
- Trefethen, N.L., Trefethen, A., Reddy, S.C. and Driscoll, T.A. (1992) Science **261**, 578
- Waleffe, F. (1995), Phys. Fluids **7**, 3060
- Waleffe, F. (1997), Phys. Fluids **9**, 883

# EXPERIMENTAL TESTS OF MEAN VELOCITY DISTRIBUTION LAWS DERIVED BY LIE GROUP SYMMETRY METHODS IN TURBULENT BOUNDARY LAYERS

Arne V. Johansson & Björn Lindgren

*Dept. of Mechanics, KTH*

*SE-100 44 Stockholm, Sweden*

*viktor@mech.kth.se, oso@mech.kth.se*

Jens M. Österlund

*Swedish Defence Research Agency, Aeronautics FFA*

*SE-172 90 Stockholm, Sweden*

*obj@foi.se*

**Abstract** New scaling laws for turbulent boundary layers recently derived (see Oberlack, 2001) using Lie group symmetry methods have been tested against experimental data from the KTH data-base for zero-pressure-gradient turbulent boundary layers. The most significant new law gives an exponential variation of the mean velocity defect in the outer (wake) region. It was shown to fit very well the experimental data over a large part of the boundary layer, from the outer part of the overlap region to about half the boundary layer thickness ( $\delta_{99}$ ). A small modification of the innermost part of the log-layer is predicted by the same method, in the form of an additive constant within the log-function, and was confirmed by the experimental data.

**Keywords:** Scaling laws, Lie group methods, ZPG turbulent boundary layers, experiments

## Introduction and theoretical considerations

The idea of using continuous transformation group (Lie group) symmetries to identify scaling laws in different regions of zero pressure-gradient turbulent boundary layer flow is evaluated using data from experiments. The scaling laws tested here have been obtained by Oberlack, 2001.

In recent years there has been a large number of papers published on the issue of the functional form of the mean velocity distribution in the overlap region between the inner (near-wall) and outer regions. Alternatives to the traditional log-law have been proposed by e.g. Barenblatt, 1993, George et al., 1997 and others. Österlund et al., 2000b; Österlund et al., 2000a tested these competing theories using highly accurate measurements in high Reynolds number turbulent boundary layer flow with zero pressure-gradient and found that the classical theory still seemed to give the most accurate description of the data.

A short description of the Lie group symmetry method is given below, that essentially follows that of Oberlack, 2001. We consider mean flows (without system rotation) that depend only on one independent coordinate, the wall-normal distance  $x_2$ . The inviscid dynamics are studied by considering the equation for the steady two-point correlation tensor,

$$R_{ij}(\mathbf{x}, \mathbf{r}) = \overline{u'_i(\mathbf{x}, t) u'_j(\mathbf{x} + \mathbf{r}, t)}, \quad (1)$$

for positions,  $\mathbf{x}$ , where influence from viscous stresses etc is negligible, and for separations,  $\mathbf{r}$ , associated with length scales that are negligibly influenced by viscosity. The evolution equation for  $R_{ij}$  inherits the symmetries from the Euler equations, which yields an interesting possibility for new insights into turbulence dynamics through the transferred Lie group symmetries.

The basic idea of symmetry methods for differential equations is to construct methods of finding transformations of the differential equation that does not change its functional form with the change of variables.

$$\mathbf{F}(\mathbf{x}, \mathbf{y}, \mathbf{y}_i) = 0 \Leftrightarrow \mathbf{F}(\mathbf{x}^*, \mathbf{y}^*, \mathbf{y}_i^*) = 0 \quad (2)$$

where  $\mathbf{x}$  is the vector of independent variables,  $\mathbf{y}$  is the vector of dependent variables, index  $i$  denotes all derivatives of order  $i$  on  $\mathbf{y}$  and  $*$  denotes the transformed variables. Concentrating our efforts on Lie group symmetries we have analytic transformations that depend on a continuous parameter,  $\epsilon$ ,

$$S_\epsilon : \mathbf{x}^* = \phi(\mathbf{x}, \mathbf{y}; \epsilon) \quad \text{and} \quad \mathbf{y}^* = \psi(\mathbf{x}, \mathbf{y}; \epsilon). \quad (3)$$

From a Taylor expansion with respect to  $\epsilon$  we can derive the transformation groups in infinitesimal form,

$$S_\epsilon : \mathbf{x}^* = \mathbf{x} + \epsilon \xi(\mathbf{x}, \mathbf{y}) + O(\epsilon^2) \quad (4)$$

and  $\mathbf{y}^* = \mathbf{y} + \epsilon \eta(\mathbf{x}, \mathbf{y}) + O(\epsilon^2)$

where  $\xi = \frac{\partial \phi}{\partial \epsilon} \Big|_{\epsilon=0}$  and  $\eta = \frac{\partial \psi}{\partial \epsilon} \Big|_{\epsilon=0}$  are the so called infinitesimals.

The striking feature about the Lie group method is that the transformation in infinitesimal form (only terms of order  $\epsilon$  kept) is fully equivalent to the transformation in global form (as given by 3). The continuous form can hence be determined from the infinitesimals by integrating the first order system

$$\frac{d\mathbf{x}^*}{d\epsilon} = \xi(\mathbf{x}^*, \mathbf{y}^*), \quad \frac{d\mathbf{y}^*}{d\epsilon} = \eta(\mathbf{x}^*, \mathbf{y}^*) \quad (5)$$

with initial conditions  $\mathbf{x}^* = \mathbf{x}$ ,  $\mathbf{y}^* = \mathbf{y}$  at  $\epsilon = 0$ .

Furthermore, an important property of the Lie groups is that all linear combinations of distinct symmetry groups,  $S_\epsilon^{(i)}$  also are symmetry groups. This property is also inherited by the infinitesimal form. The infinitesimals satisfy the characteristic equation (see Oberlack, 2001)

$$\frac{dx_1}{\xi_1(\mathbf{x}, \mathbf{y})} = \dots = \frac{dx_m}{\xi_m(\mathbf{x}, \mathbf{y})} = \frac{dy_1}{\eta_1(\mathbf{x}, \mathbf{y})} = \dots = \frac{dy_m}{\eta_m(\mathbf{x}, \mathbf{y})}. \quad (6)$$

Under the assumption of parallel flow where the mean velocity can be described by  $\bar{u}_i = \bar{u}_1(x_2)\delta_{ij}$ , the admitted symmetries of the  $R_{ij}$ -equation are described by an equation of characteristics of the following form

$$\frac{dx_2}{k_{s_1}x_2 + k_{x_2}} = \frac{dr_{[k]}}{k_{s_1}r_{[k]}} = \frac{d\bar{u}_1}{(k_{s_1} - k_{s_2})\bar{u}_1 + k_{\bar{u}_1}} = \frac{dR_{[ij]}}{2(k_{s_1} - k_{s_2})R_{[ij]}}, \quad (7)$$

where brackets mean that summation over repeated indices should not be made. It can also be seen as a four parameter symmetry group, where the four parameters are  $k_{s_1}, k_{x_2}, k_{s_2}, k_{\bar{u}_1}$ . The symmetry can be seen as a scaling and translation transformation of the wall distance and the mean velocity, and a resulting scaling symmetry of the Reynolds stress.

By specification of the values of the two scaling symmetry constants,  $k_{s_1}$  and  $k_{s_2}$ , scaling laws for different planar shear-flows can be obtained.

## The overlap region in plane wall-bounded shear-flows

Sufficiently close to the solid boundary in wall-bounded flows such as a zero pressure-gradient boundary layer or channel flow, we have a region of constant total shear stress, *i.e.*

$$u_\tau^2 = \nu \frac{\partial \bar{u}_1}{\partial x_2} - \overline{u'_1 u'_2}. \quad (8)$$

We note that in such regions the friction velocity,  $u_\tau$ , can be seen as an external parameter or boundary condition which inhibits the scaling of the streamwise velocity,  $\bar{u}_1$ . Let us now consider a region where equation 8 is valid, but restrict our attention to the part sufficiently far from the wall such that the viscous influence is negligible. Since no scaling of the streamwise velocity is admitted, we see from equation 7 that  $k_{s_1} - k_{s_2}$  must be equal to zero, *i.e.*  $k_{s_1} = k_{s_2}$ . Inserting this into equation 7 and integrating we find the following expression for the streamwise velocity,

$$\bar{u}_1 = \frac{k_{\bar{u}_1}}{k_{s_1}} \ln \left( x_2 + \frac{k_{x_2}}{k_{s_1}} \right) + B. \quad (9)$$

In this form, that was derived by Oberlack (see *e.g.* Oberlack, 2001) we recognize the classical log-law but with an extra constant  $A = k_{x_2}/k_{s_1}$  inside the logarithm. We also recognize the Kármán constant  $\kappa = k_{s_1}/k_{\bar{u}_1}$ .

Afzal and Yajnik, 1973, have proposed similar forms of the log-law using a series expansion. Also, Buschmann and Gad-el Hak, 2002 have investigated this form. Wosnik et al., 2000 investigated this form for the pipe flow case.

When free scaling of the mean velocity,  $\bar{u}_1$ , is inhibited we readily see from the characteristic equation 7, that the solution,  $\tilde{r}_k$ , for the separation becomes  $\tilde{r}_k = r_k/x_2$ , and that (see also Oberlack, 2001)

$$R_{ij} = \tilde{R}_{ij}(\mathbf{r}/x_2) \quad (10)$$

## The outer region

In the outer region of the flow we consider wall-distances of the order of the outer lengthscale, *i.e.* a scale that is of the order of the boundary layer

thickness. In this region the flow is, hence, influenced by the outer geometrical restriction. This acts as a boundary condition and is thereby a symmetry breaking condition that prohibits a free scaling of the wall-normal coordinate. In the symmetry group described by equation 7 we must, hence, put  $k_{s_1} = 0$ , which implies that

$$\frac{d\bar{u}_1}{dx_2} = -\frac{k_{s_2}}{k_{x_2}}\bar{u}_1 + \frac{k_{\bar{u}_1}}{k_{x_2}} \quad (11)$$

Integration gives that

$$\bar{u}_1 = C_{exp} \exp\left(-\frac{k_{s_2}}{k_{x_2}}x_2\right) + \frac{k_{\bar{u}_1}}{k_{s_2}}. \quad (12)$$

This velocity law derived by Oberlack, 2001 is the first one that has been obtained from first principles for (parts of) the outer region.

The free stream boundary condition implies that  $k_{\bar{u}_1}/k_{s_2} = U_\infty$ . To enable similarity type of descriptions the scaling of the wall-normal coordinate in the outer region must be done with a lengthscale that is characteristic for the boundary layer thickness. Here we will choose to use the Clauser-Rotta length scale ( $\Delta = \delta_* U_\infty / u_\tau$ , where  $\delta_*$  is the displacement thickness). We can now rewrite equation 12 as

$$\frac{\bar{u}_\infty - \bar{u}_1}{u_\tau} = F(\eta) = C_1 \exp\left(-C_2 \frac{x_2}{\Delta}\right) \quad (13)$$

where  $C_1$  and  $C_2$  are constants. The validity of the exponential velocity law in the outer region will here be tested against experimental data, and the constants  $C_1$  and  $C_2$  will be determined from the KTH database for zero pressure-gradient turbulent boundary layers (Österlund, 1999).

Solving the characteristic equation 7 for  $R_{ij}$  in the outer region gives an exponential behaviour of the correlation functions with twice the exponent as compared to that for the velocity defect (equation 13) *i.e.*

$$R_{ij} = \tilde{R}_{ij}(\mathbf{r}) \exp\left(-2C_2 \frac{x_2}{\Delta}\right). \quad (14)$$

**The Reynolds shear-stress in the wake region** The Reynolds shear-stress profile in the region where the velocity defect exhibits an exponential variation, can be derived from the mean streamwise momentum equation neglecting the influence of viscosity, along with the continuity equation. Assuming that the normalized turbulent shear-stress is a function of  $\eta = x_2/\Delta$ ,

$$-\frac{\overline{u'_1 u'_2}}{u_\tau^2} = g(\eta) \quad (15)$$

we get the following momentum equation to zeroth order in  $\gamma = u_\tau/U_\infty$ ,

$$g'(\eta) = H_{12}\eta F'(\eta), \quad (16)$$

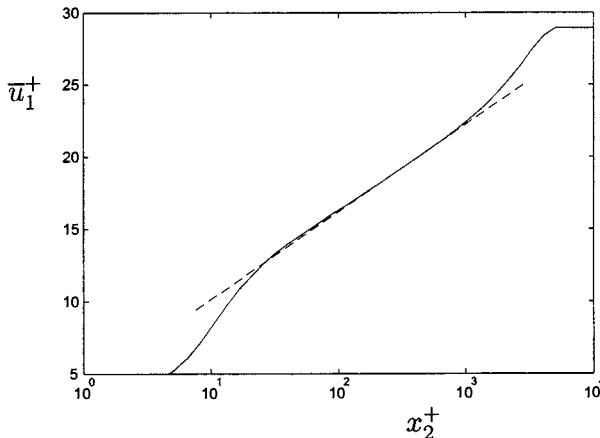


Figure 1. Mean velocity profile in inner scaling from Österlund, 1999. Note the "hump" in the inner part of the log region. (Dashed line: log-law with  $\nu = 0.38$ ,  $B = 4.1$ )  $Re_\theta = 14300$

where prime denotes differentiation with respect to  $\eta$  and  $H_{12} = \delta_*/\theta$  is the shape factor. The zeroth order (in  $\gamma$ ) solution  $g_0(\eta)$  is found by inserting the exponential velocity defect law into equation 16, and reads

$$g_0(\eta) - g_0(\eta_0) = H_{12} \frac{C_1}{C_2} [(C_2\eta + 1) \exp(-C_2\eta) - (C_2\eta_0 + 1) \exp(-C_2\eta_0)]. \quad (17)$$

## Results for ZPG turbulent boundary layers: The overlap region

The form of the velocity distribution in the region inside the overlap region but sufficiently far from the wall for the viscous stress to be negligible, is predicted to take the form

$$\bar{u}_1^+ = \frac{1}{\nu} \ln(x_2^+ + A^+) + B \quad (18)$$

With a positive value of  $A^+$ , such a form should give a small overshoot (relative to the standard log-law) in the innermost part of (or just below) the overlap region. Such a behaviour has been observed in many experimentally obtained mean velocity profiles for turbulent boundary layers. A sample profile from the KTH data-base is shown in figure 1.

A small overshoot around (or just below)  $x_2^+ = 100$  is clearly seen. Similar results can be found in other experiments and simulations. We should note that the modified log-law cannot be part of the actual overlap region since it has a form that cannot be matched with the formulation in outer scaling. This is consistent with the finding that it only influences the mean profile below the inside limit of the universal overlap region defined to be  $x_2^+ \approx 200$  by Österlund et al., 2000b.

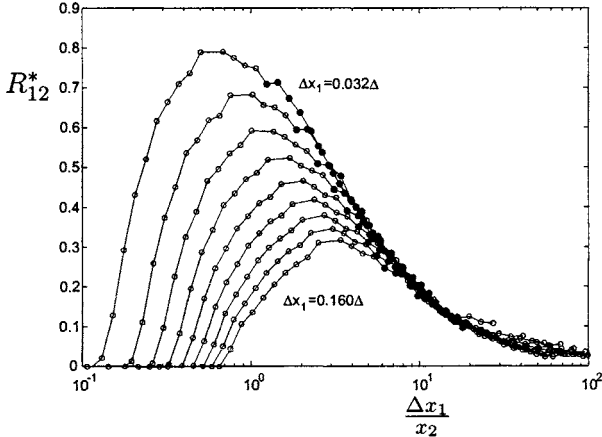


Figure 2. The  $R_{12}^*$  correlation plotted against separation scaled with wall distance. Filled symbols (circles) represent points within the log-layer ( $x_2^+ > 200$  &  $x_2/\delta_{95} < 0.15$ ). Separations ( $\Delta x_1/\Delta = 0.032, 0.048, 0.064, 0.080, 0.096, 0.112, 0.128, 0.144$  &  $0.160$ ) are estimated by use of Taylor's hypothesis.  $Re_\theta = 17600$ .

The streamwise-wall-normal component of the two-point correlation function normalized with the friction velocity squared, *i.e.*

$$R_{12}^*(\mathbf{x}, \mathbf{r}) = \frac{\overline{u'_1(\mathbf{x}, t) u'_2(\mathbf{x} + \mathbf{r}, t)}}{u_\tau^2}, \quad (19)$$

where  $*$  denotes normalization with  $u_\tau^2$ , was calculated for a number of separations in the streamwise direction using Taylor's hypothesis ( $\Delta x_1 = \bar{u}_1 \Delta t$ ).

From the characteristic equation 7, we saw in the previous section that the two-point correlation should depend on the variable,  $r_k/x_2$ , alone. When plotting  $R_{12}^*$  against  $\Delta x_1/x_2$ , as suggested by Lie group symmetry scaling, the data collapse for the points from the logarithmic overlap region (figure 2). The good agreement between the theory and the experimental data strongly supports the validity of the parallel flow assumption is valid in the logarithmic overlap region.

## The wake region

The mean streamwise velocity profiles from the KTH data-base (Österlund, 1999) used here cover a wide range of Reynolds numbers. In figure 3, 70 of these profiles, with Reynolds number based on the momentum-loss thickness ranging from 2500 to 27000, are plotted in outer scaling, *i.e.* as the velocity defect against the wall-distance normalized by the Clauser-Rotta boundary layer thickness. Despite the large number of profiles we can observe a very good collapse of the data. In the log-lin plot we can observe a substantial range ( $0.025 \leq x_2/\Delta \leq 0.11$ ) where the data fall onto a straight line, *i.e.* where the velocity defect exhibits an exponential variation with wall-distance, with the

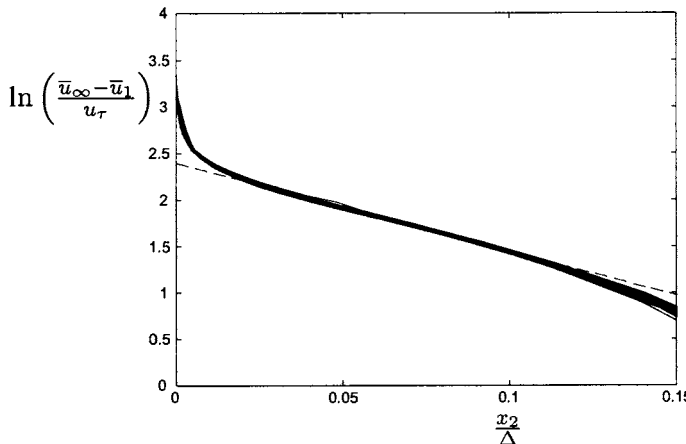


Figure 3. 70 mean velocity profiles from Österlund, 1999 with  $2530 < Re_\theta < 27300$  and the exponential wake law (dashed line)

constants determined as

$$C_1 = 10.5 \quad C_2 = 9.5. \quad (20)$$

The close fit covers a range of about  $0.11 \leq x_2/\delta_{99} \leq 0.50$  and is thereby substantially larger than the region with a logarithmic velocity law.

The innermost part with an exponential velocity-defect variation corresponds approximately to the end of the overlap region (at  $x_2/\Delta \approx 0.025$ ), where the velocity defect has a logarithmic variation. The transition between the two forms is smooth, although some adjustment region must exist to match higher order derivatives between the two forms.

In the outermost part of the wake region the velocity defect decreases more rapidly than what is predicted by the exponential law. Neither intermittency nor viscous effects seem to be the major factor to explain the rapid decrease of the velocity defect. The conclusion is therefore that the reason for the exponential defect law to fail outside  $x_2/\Delta = 0.12$  has to be found elsewhere, and most probably, in effects of non-parallel flow. This is further evidenced by the behaviour of the two-point correlations  $R_{12}$  and  $R_{22}$  for large separations  $\Delta x_1$ . The observed behaviour was indeed far from the exponential form (14) derived under the assumption of parallel flow.

The Reynolds shear-stress profile corresponding to the exponential form of the velocity defect law was derived and the solution to zeroth order in  $\gamma$  for the normalized shear-stress  $(-\bar{u}'_1 \bar{u}'_2 / u_\tau^2)$ , given by equation 17, is shown for  $Re_\theta = 22530$  in figure 4. We see that this solution has the correct functional behaviour in the region with exponential velocity defect but that the error in magnitude is of order  $\gamma$ .

The solution for  $g(\eta)$  that is accurate to first order in  $\gamma$  is of similar form to  $g_0(\eta)$ . As seen in figure 4, it represents the Reynolds shear-stress accurately in the region where an exponential behaviour of the velocity defect can be observed.

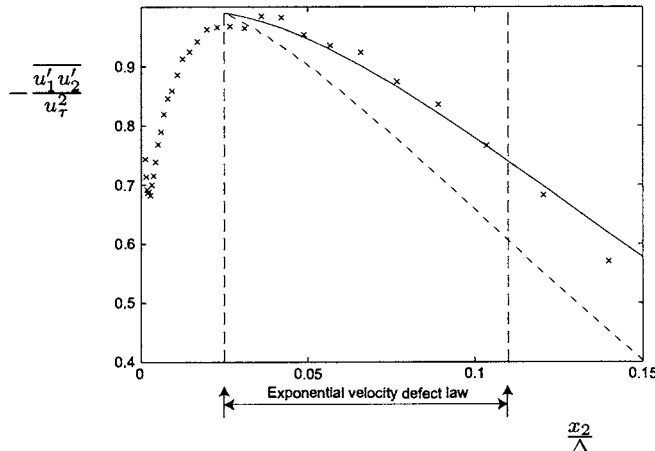


Figure 4. Normalized Reynolds shear-stress at  $Re_\theta = 22530$ . Solid and dashed curves represent solutions accurate to first and zeroth order in  $\gamma$ , respectively.  $g_0(\eta_0) = 0.99$  and  $g_1(\eta_0) = 0$  have been chosen to give the best fit to the experimental data.  $\eta_0 = 0.025$ .

## References

- Afzal, N. and Yajnik, J. (1973). Analysis of turbulent pipe and channel flows at moderately large reynolds number. *J. Fluid Mech.*, 61:23–31.
- Barenblatt, G. I. (1993). Scaling laws for fully developed turbulent shear flows. part 1. basic hypotheses and analysis. *J. Fluid Mech.*, 248:513–520.
- Buschmann, M. H. and Gad-el Hak, M. (2002). Reynolds-number-dependent scaling law for turbulent boundary layers. In *IUTAM symposium on Reynolds number scaling in turbulent flow*. Princeton University, NJ, USA.
- George, W. K., Castillo, L., and Wosnik, M. (1997). Zero-pressure-gradient turbulent boundary layer. *Applied Mech. Reviews*, 50:689–729.
- Oberlack, M. (2001). A unified approach for symmetries in plane parallel turbulent shear flows. *J. Fluid Mech.*, 427:299–328.
- Österlund, J. M. (1999). *Experimental Studies of Zero Pressure-Gradient Turbulent Boundary-Layer Flow*. PhD thesis, Department of Mechanics, Royal Institute of Technology, Stockholm.
- Österlund, J.M., Johansson, A.V., and Nagib, H.M. (2000a). Comment on ‘a note on the intermediate region in turbulent boundary layers’ [Phys. Fluids 12, 2159]. *Phys. Fluids*, 12:2360–2363.
- Österlund, J.M., Johansson, A.V., Nagib, H.M., and Hites, M.H. (2000b). A note on the overlap region in turbulent boundary layers. *Phys. Fluids*, 12(1):1–4.
- Wosnik, M., Castillo, L., and George, W. K. (2000). A theory for pipe and channel flows. *J. Fluid Mech.*, 421:115–145.

# REVISED LOG-LAW CONSTANTS FOR FULLY-DEVELOPED TURBULENT PIPE FLOW

B. J. McKeon, \*\*\*J. F. Morrison, \*\*W. Jiang, \*J. Li & A. J. Smits

Department of Mechanical and Aerospace Engineering, Princeton University,  
Princeton, New Jersey 08544-0710, U.S.A.

*Permanent address:* \*Victoria University of Technology, Melbourne, Australia

\*\*CARDC, P. O. Box 211 Mianyang, Sichuan 621000, P. R. China

\*\*\*Department of Aeronautics, Imperial College, London SW7 2BY, England

## Abstract

The mean velocity profiles of fully-developed turbulent pipe flow obtained by Zagarola & Smits (1998) and McKeon *et al.* (2002) were corrected for the static pressure measurement error and the velocity gradient Pitot displacement error reported recently by McKeon & Smits (2002) and McKeon *et al.* (2002). This analysis leads to new and more accurate values of von Kármán and additive constants in the logarithmic region in pipe flow. An interesting comparison with lower Reynolds number boundary layer studies is also made.

## 1. Introduction

The existence of a logarithmic overlap region in the mean velocity profile in wall-bounded turbulent shear flows, the related coefficients and their constancy (or otherwise) has long been a contentious issue. Traditionally accepted values for the von Kármán constant  $\kappa$  and additive constants  $B$  (inner scaling) and  $B^*$  (outer scaling) are approximately 0.41, 5.0 and 0.8, respectively, and it has been generally believed that the log law holds for approximately  $100 < y^+ < 0.2R^+$ , where  $y^+ = yu_\tau/\nu$ ,  $y$  is the distance from the wall,  $u_\tau = \sqrt{\tau_w/\rho}$ ,  $\nu$  is the kinematic viscosity,  $\tau_w$  is the shear stress at the wall,  $\rho$  is the fluid density and  $R^+ = Ru_\tau/\nu$ , where  $R$  is the radius of the pipe.

In contrast, the mean velocity study of Zagarola & Smits (1998) in the Princeton Superpipe facility (referred to from now on as ZS) suggested

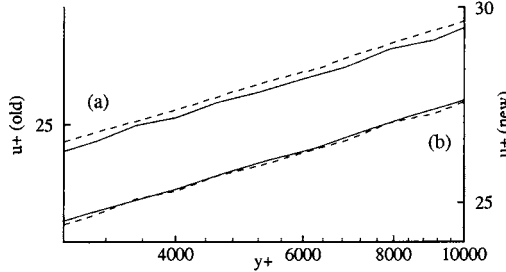


Figure 1. Velocity profiles for the ZS data at  $Re_D = 3 \times 10^6$  (solid lines) and  $10 \times 10^6$  (dashed lines): (a) static pressure corrections due to Shaw (1960); (b) corrections due to McKeon & Smits (2002).

a power law for  $60 < y^+ < 500$  and, if the Reynolds number was high enough ( $Re_D > 400 \times 10^3$ ), a log law for  $600 < y^+ < 0.07R^+$  given by

$$U^+ = \frac{1}{0.436} \ln y^+ + 6.15. \quad (1)$$

These log-law limits and constants are significantly different from those found in the past, and indicate that viscosity continues to exert an influence much further from the wall than previously recognized. A more recent mean velocity study in the same facility using a Pitot tube of diameter  $d = 0.3$  mm (as compared with 0.9 mm in the ZS case) was reported by McKeon *et al.* (2002). They found an interesting trend in the original ZS velocity data: at a given  $y^+$ ,  $U^+$  decreased as the Reynolds number increased (see figure 1(a)), the trend growing with increasing Reynolds number. One explanation for this effect could be the increasing effect of the surface roughness. Alternatively, since the corrections made to the data were based on studies at low Reynolds number, the corrections may have been in error.

The most important corrections applied by ZS were (1) the correction for deflection of the streamlines due to the presence of the Pitot probe in a region of shear (“Pitot correction”), and (2) the correction for the effect of the finite size of a pressure tap on static pressure measurement (“static correction”). Note that for all except the lowest Reynolds numbers, the point closest to the wall is much further out than the inner peak in turbulence intensity located at  $y^+ \approx 15$  (Morrison *et al.*) and thus the effect of the correction for turbulence is small.

With respect to the Pitot correction, ZS applied the correction proposed by Chue (1975). Pitot corrections were re-evaluated by McKeon *et al.* (2002) who found that, over the entire Reynolds number range of

the Superpipe and for  $y \geq 2d$ , MacMillan's and Chue's methods gave identical results.

With respect to the static correction, ZS used the one proposed by Shaw (1960). However, Shaw's results were obtained for  $d_t^+ = \bar{U}d_t/\nu \leq 800$ , compared with values of 6500 found in the Superpipe. McKeon & Smits (2002), however, found that an additional parameter, the ratio of tapping diameter to pipe diameter,  $d_t/D$ , was important to the problem. Different values of the pressure error are obtained if a large value of  $d_t^+$  is achieved by using a large tapping, or by using a small viscous length scale ( $\nu/u_\tau$ ). In addition, the maximum error was found to grow with Reynolds number for small enough tappings, well beyond the asymptotic limit of approximately  $3.0\tau_w$  for  $d_t^+ \geq 1000$  suggested by Shaw. When these new static pressure corrections are applied to the mean velocity data of ZS, the deviations shown in figure 1 are removed.

## 2. New Results

The results reported here make use of the static correction due to McKeon & Smits (2002), and only used data points for  $y \geq 2d$ , that is, where the results are independent of the Pitot correction. However, to allow a direct comparison with the ZS data, the Chue Pitot correction was used throughout. In all other respects, the analysis follows that of ZS.

The value of  $\kappa$  was found from a least squares fit of the friction factor formulation obtained by integrating the log-law to the centerline:

$$\frac{1}{\lambda^{0.5}} = \frac{\bar{U}}{\sqrt{8}u_\tau} = C_1 \log(Re \lambda^{0.5}) + C_2 \quad (2)$$

where  $\lambda$  is the friction factor,  $Re = \rho\bar{U}D/\mu$  and  $C_1$  and  $C_2$  are constants that may or may not be functions of Reynolds number. This procedure for finding  $\kappa$  assumes the existence of a logarithmic region and is valid if the surface is not transitionally rough. The effect of roughness would cause the apparent value of  $\kappa$  to increase, and the value of  $B$  to decrease.

The curve fit was performed over different Reynolds numbers ranges until a range was found where  $\kappa$  did not change when the range was made smaller. Finding a constant value of  $\kappa$  indicates simultaneously that roughness effects are not significant, that outer similarity is observed, and that the error in deriving equation (1) caused by ignoring the deviation of the velocity profile from the log law close to the wall is negligible.

The data from both mean velocity studies (ZS data using  $d = 0.9$  mm, and the new data using  $d = 0.3$  mm) yield  $\kappa = 0.421 \pm 0.002$  for  $310 \times 10^3 \leq Re_D \leq 13 \times 10^6$ . The values of  $\lambda$  for  $Re_D > 18 \times 10^6$  for the

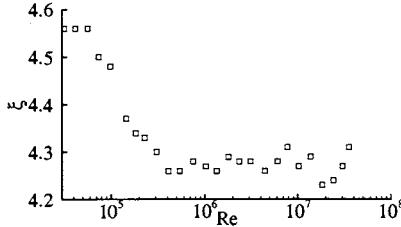


Figure 2. The variation of  $\xi = (U_{CL} - \bar{U})/u_\tau$  with Reynolds number.

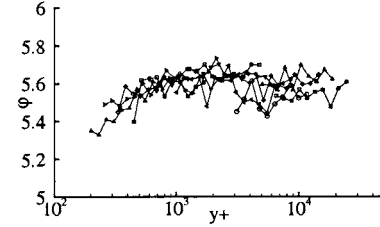


Figure 3. Variation of  $\Psi$  with  $y^+$  for  $y/R < 0.12$ .

0.9 mm probe and for  $Re_D > 13 \times 10^6$  for the 0.3 mm probe are too large to lie satisfactorily on the curve-fit. In contrast, ZS found  $\kappa = 0.436$  for  $Re_D > 400 \times 10^3$ .

It is an important point that no other range that included lower values of Reynolds numbers led to a constant value of  $\kappa$ . Consider the following Reynolds number ranges and the corresponding values of  $\kappa$ :

$$\begin{aligned}\kappa &= 0.423 && \text{for } 31 \times 10^3 \leq Re_D \leq 35 \times 10^6 \\ &= 0.421 && \text{for } 540 \times 10^3 \leq Re_D \leq 18 \times 10^6 \\ &= 0.410 && \text{for } 31 \times 10^3 \leq Re_D \leq 540 \times 10^3\end{aligned}$$

(taken from McKeon *et al.* (2002)). If any of these ranges is reduced, the value of  $\kappa$  will change, indicating that the original range did not define a region of constant  $\kappa$ . The value of 0.421 was also obtained (over the range  $310 \times 10^3 \leq Re_D \leq 13 \times 10^6$ ) from a curve-fit of the non-dimensional centerline velocity  $U_{CL}^+$ . This provides a rigorous test since the analysis of the log law in outer scaling must give the same result as the analysis of the one in inner scaling. In addition, the ratio  $\xi = (U_{CL} - \bar{U})/u_\tau$  must also be constant. Figure 2 shows that  $\xi = 4.28$  for  $Re_D \geq 310 \times 10^3$ , which agrees well with the friction factor results.

The values of the additive constants were established by estimating the deviation of the data from a log law with  $\kappa = 0.421$ . That is, the function  $\psi$  was plotted, where

$$\psi = U^+ - \frac{1}{\kappa} \ln y^+ \quad (3)$$

and  $\psi$  should equal  $B$ , a constant, in the logarithmic region. Figure 3 shows that  $B$  is constant and equal to  $5.60 \pm 0.08$  for  $y^+ > 600$ . The outer limit is found in a similar manner and is given by  $y^+ < 0.12R^+$ . These limits correspond to a logarithmic law only existing for Reynolds numbers greater than  $230 \times 10^3$ . In addition,  $B^*$  was found to have a

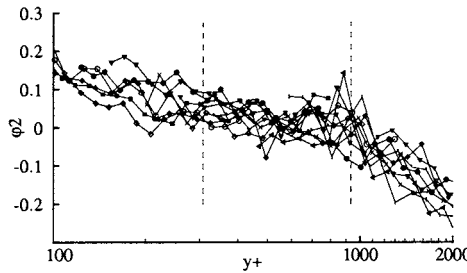


Figure 4. Variation of  $\Psi_2$  with  $y^+$ , as given in equation 4.

constant value of  $1.20 \pm 0.1$  in the range above the minimum Reynolds number for the presence of a log-law with constant  $\kappa$ .

This new analysis thus leads to a coherent picture of the log law: friction factor, inner scaling, outer scaling and  $(U_{CL} - \bar{U})/u_\tau$  results all lead to the same constants and limits of applicability.

It can also be shown, similar to ZS, that a power law is a good fit for the region  $50 < y^+ < 300$  or  $0.12R^+$ , where the constants were found using a least-squares determination to be given by  $C = 8.49$  and  $\Lambda = 0.142$ .

Further examination of the region closer to the wall reveals an interesting comparison with recent boundary layer observations (for example, Österlund *et al.* (2000)). They found a log law with  $\kappa = 0.38$  and  $B = 4.1$  in the range  $200/R^+ < y/R < 0.15$  for  $6000 < Re_\theta < 27,000$  in a zero-pressure-gradient boundary layer. Even the maximum value corresponds to a relatively low pipe flow Reynolds number (approximately equivalent to  $Re_D < 300 \times 10^3$ ). Figure 4 compares the present data to a similar log-law, given by equation 4 with constants slightly altered to give the best fit to our data:

$$\psi_2 = U^+ - \frac{1}{0.385} \ln y^+ - 4.15. \quad (4)$$

It can be seen that equation 4 fits our data reasonably well, but only for a very short region in  $y^+$  which lies below the point where the pipe flow data suggest the log law begins. Therefore even if this region scales logarithmically, this is not the overlap region of complete similarity, since the Reynolds number appears to be too low. While it has not been conclusively shown that boundary layers and pipe flows will have the same form in the inner region, it can be seen that a similar phenomenon to that found in the boundary layer is also reproduced in the Superpipe. It should be noted that the additional checks used here to confirm the

log-law cannot be used to analyze boundary layer data (nor does the accuracy of the shear stress measurement, in general, permit such precise analysis). The friction factor relationship, for example, is not simple. In addition, few studies have covered Reynolds number ranges that are equivalent to that available in the Superpipe. It is worth repeating that the maximum Reynolds number in the Österlund *et al.* (2000) study barely exceeds the equivalent pipe Reynolds number for which the log-law detailed in this paper is shown to exist.

### 3. Conclusions

Our findings confirm the conclusions of ZS that for the majority of the Reynolds number ranges obtained in laboratory settings the overlap log law does not yet appear, and that viscosity has an effect further from the wall than traditionally believed. The static pressure correction of McKeon & Smits (2002) has been shown to have a significant effect on the constants obtained for the log law in fully developed pipe flow. New values of the von Kármán and additive constants that are consistent with all aspects of the data are proposed ( $\kappa = 0.421 \pm 0.002$  and  $B = 5.60 \pm 0.08$ ) for a logarithmic overlap law in the region  $600 < y^+ < 0.07R^+$  for  $Re_D > 230 \times 10^3$  ( $R^+ > 9 \times 10^3$ ).

ONR Grant No. N00014-99-1-0340 is gratefully acknowledged.

### References

- CHUE, S. H. 1975 Pressure probes for fluid measurement. *Prog Aerospace Sci.* **16** (2).
- MACMILLAN, F. A. 1956 Experiments on Pitot-tubes in shear flow. *Ministry of Supply, Aero. Res. Counc. R & M 3028*.
- MCKEON, B. J., LI, J., JIANG, W., MORRISON, J. F. & SMITS, A. J. 2002 Additional measurements and analysis of high Reynolds number fully-developed pipe flow *Advances in Turbulence IX: Eds. I.C. Castro, P.E. Hancock & T.G. Thomas (CIMNE)*
- MCKEON, B. J., LI, J., JIANG, W., MORRISON, J. F. & SMITS, A. J. Pitot probe corrections in fully-developed turbulent pipe flow. *In preparation.*
- MCKEON, B. J. & SMITS, A. J. 2002 Static pressure correction in high Reynolds number fully-developed turbulent pipe flow. *Meas. Sci. Tech.* **13**.
- MORRISON, J. F., MCKEON, B. J., JIANG, W., & SMITS, A. J. Scaling of the streamwise velocity component in turbulent pipe flow. *Sub. J. Fluid Mech.*
- ÖSTERLUND, J. M., JOHANSSON, A. V., NAGIB, H. M. & HITES, M. H. 2000 A note on the overlap region in turbulent boundary layers. *Phys. Fluids* **12**.
- SHAW, R. 1960 The influence of hole dimensions on static pressure measurements *J. Fluid Mech.* **7**(4).
- ZAGAROLA, M. V. & SMITS, A. J. 1998 Mean flow scaling in turbulent pipe flow. *J. Fluid Mech.* **373**.

# SCALING OF THE TURBULENT BOUNDARY LAYER AT HIGH REYNOLDS NUMBERS

M. B. Jones, N. Nishizawa, M. S. Chong

*Department of Mechanical and Manufacturing Engineering  
The University of Melbourne, Parkville, Victoria, AUSTRALIA  
mbjones@mame.mu.oz.au*

I. Marusic

*Department of Aerospace Engineering and Mechanics  
University of Minnesota, Minneapolis, Minnesota 55455*

**Abstract** Experimental results are presented for high Reynolds number turbulent boundary layers. A flat plate zero pressure gradient layer has been studied in a new high Reynolds number boundary layer tunnel. Measurements were made of the mean flow in the Reynolds number range of  $3.6 \times 10^3 < R_\theta < 6.0 \times 10^4$  based on momentum thickness. The data supports the existence of a logarithmic law of the wall in the overlap region and constants  $\kappa = 0.41$  and  $A = 5.0$  are found to best fit the data.

**Keywords:**

## 1. Introduction

The classical approach to mean flow scaling is to seek similarity laws in two regions of the flow, a region adjacent to the wall and region adjacent to the edge of the boundary layer. These regions are often referred to as the *inner flow* region and the *outer flow* region. Applying dimensional analysis arguments in these regions leads to the classical laws

$$U/U_\tau = f(zU_\tau/\nu) \quad (1)$$

$$(U_1 - U)/U_\tau = g(z/\delta_c) \quad (2)$$

where  $U$  is the mean streamwise velocity,  $U_\tau$  is the wall shear velocity,  $z$  is the wall normal coordinate,  $\nu$  is the kinematic viscosity,  $U_1$  is the local freestream velocity, and  $\delta_c$  is the boundary layer thickness. Equation (1) (first derived by Prandtl, 1925) represents a similarity law for the inner flow and is known as *the law of the wall*, and (2) (first derived by von

Kármán, 1930) represents a similarity law for the outer flow and is known as the velocity defect law.

Using the Millikan, 1938 argument that there exists a region of overlap between (1) and (2) gives the classical results

$$\frac{U}{U_\tau} = \frac{1}{\kappa} \ln(z^+) + A \quad \text{and} \quad (3)$$

$$\frac{U_1 - U}{U_\tau} = -\frac{1}{\kappa} \ln(\eta) + B \quad (4)$$

where  $z^+ = zU_\tau/\nu$ ,  $\eta = z/\delta_c$ ,  $\kappa$  is the Karman constant,  $A$  is the universal smooth wall constant and  $B$  depends on the large scale flow geometry. The overlap region will be referred to as the fully turbulent wall region (TWR) and it is often assumed to begin at  $z^+ = 100$  and extend to  $z/\delta_c = 0.15$ . The Millikan, 1938 argument is one of several arguments that can be used to derive the logarithmic law of the wall. However all rely on the basic assumption that in the TWR the velocity gradient is independent of viscosity. Notable alternatives to the above theory have been proposed by George and Castillo, 1997 and Barenblatt et al., 2000.

## 2. Experimental Method

Experiments were performed in an open return blower wind tunnel. The important feature of the tunnel is the working section length of 27 m. This allows high Reynolds numbers to be obtained through the long development length, thus avoiding many of the experimental difficulties associated with using the alternative methods of achieving high Reynolds numbers, such as the use of compressed air or high velocities. The tunnel was run at three reference Reynolds numbers corresponding to nominal reference freestream velocities of  $U_\infty = 10$  m/s, 20 m/s and 30 m/s.

In order to maintain a zero pressure gradient the ceiling incorporates adjustable spanwise slots which allow for the bleeding of air. In addition, the height of the ceiling can be varied. Through these mechanisms it was possible to maintain the  $C_p$  distribution to within  $\pm 0.0050$  for the 20 m/s and 30 m/s flow cases, where  $C_p = 1 - (U_1/U_\infty)^2$ . However for the 10 m/s flow case the the  $C_p$  distribution fell within  $\pm 0.0065$ .

Mean velocity profiles were measured with both a Pitot-static probe and a normal hot-wire. The Pitot tube readings were corrected for the effect of shear using the MacMillan, 1956 correction.

For the three reference Reynolds numbers measurements were made at different streamwise stations, varying from  $x = 1$  m to  $x = 25$  m. This gave a Reynolds number range of  $960 < K_\tau < 22400$ , where  $K_\tau = \delta_c U_\tau / \nu$ . Transition to turbulence was initiated by a trip wire of diameter

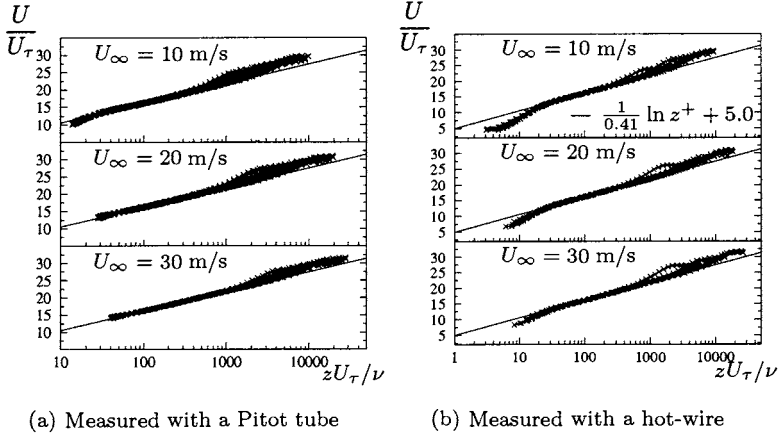


Figure 1. Mean velocity profiles for the complete range of streamwise stations.

0.4 mm placed at  $x = 0$ . The boundary layer studied developed on the smooth aluminium floor of the working section. The freestream turbulence level was found to be less than 0.05%.

For the results presented here the Clauser chart was used to determine the values of  $U_\tau$ . It must be noted that for the Clauser chart to return correct values of  $U_\tau$  (3) must be valid and constants  $A$  and  $\kappa$  specified. Hence care must be taken in interpreting the mean flow results since an a-priori assumption about the appropriate mean flow scaling has been made. However if the Clauser chart method is collapsing the data in the TWR, across the complete Reynolds number range of the experiments then at least a velocity scale has been found that is equal to  $U_\tau$  to within a constant of proportionality and the only a-priori assumption is the that (1) is correct. The approach taken here is to analyse the data using the Clauser chart with different combinations of constants. If the data shows poor collapse onto (3) the constants can be discounted as being the correct ones. Three cases were considered: traditional constants of  $\kappa = 0.41$  and  $A = 5.0$ ; the Osterlund, 1999 constants of  $\kappa = 0.38$  and  $A = 4.1$ ; and the Zagarola and Smits, 1998 constants of  $\kappa = 0.436$  and  $A = 6.15$ . To make any further comment on the validity of the constants in (3) requires an independent method of determining  $U_\tau$ .

### 3. Inner-flow scaling

Mean velocity profiles measured with a Pitot are shown in figure 1(a) and measured with a normal hot-wire in figure 1(b). Here the data is normalised assuming  $\kappa = 0.41$ ,  $A = 5.0$  and it can be seen good collapse in the TWR is achieved across the full Reynolds number range. The

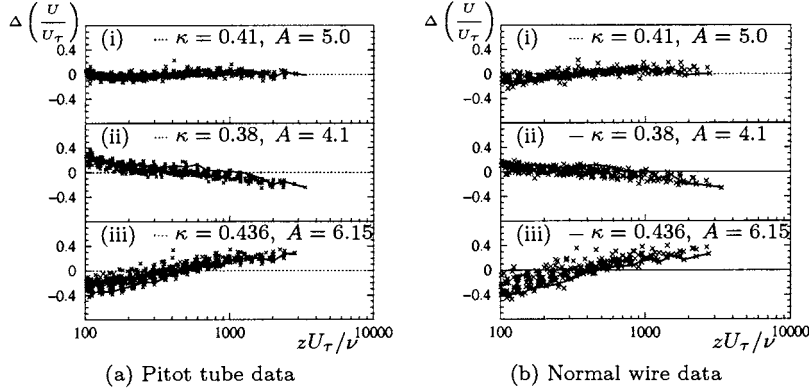


Figure 2. Deviation of data from log-law (3) when data is normalised to best fit; (i)  $\kappa = 0.41$ ,  $A = 5.0$ , (ii)  $\kappa = 0.38$ ,  $A = 4.1$  and (iii)  $\kappa = 0.436$ ,  $A = 6.15$ . Only data in the TWR ( $100 < z^+ < 0.15K_\tau$ ) is shown.

quality of the collapse in the TWR is shown in figure 2 where (3) has been subtracted from the data (ie.  $\Delta(U/U_\tau)$  is plotted). Also shown in figure 2 are the results of normalising the data assuming a priori that the correct constants are  $\kappa = 0.38$ ,  $A = 4.1$  and  $\kappa = 0.436$ ,  $A = 6.15$ . It can be seen that the traditional constants (ie.  $\kappa = 0.41$ ,  $A = 5.0$ ) best collapse the data onto (3) with specified constants. When the other constants are used the data shows more scatter and this is most pronounced in the case of the Zagarola and Smits, 1998 constants. This scatter is a consequence of fitting the wrong log-law over a large Reynolds number range. Further, for the Osterlund, 1999 and Zagarola and Smits, 1998 constants the data does not appear to fit the required gradient  $1/\kappa$  as a consequence the values of  $U_\tau$  obtained from best fit (ie. Clauser chart) will be more sensitive to the limits defining the TWR.

The suitability of a logarithmic law in the overlap region can be investigated by plotting the non-dimensional velocity gradient pre-multiplied by  $z^+$ , ie.

$$D_1 = z^+ \frac{dU^+}{dz^+}, \quad (5)$$

where  $U^+ = U/U_\tau$ . If a log-law exists, equation (5) should equal a constant. Further, if the profiles have been scaled with the correct values of  $U_\tau$  the constant should equal  $1/\kappa$ . Figure 3 shows the result of plotting equation (5) for all data in the range  $100 < z^+ < 0.15K_\tau$ . There is no smoothing or averaging of data, so figure 3 contains a degree of scatter. Nevertheless, the data does show agreement with the logarithmic law. The agreement is more clearly seen by considering the individual profile shown in figure 3, which corresponds to the highest  $R_\theta$  profile. It should

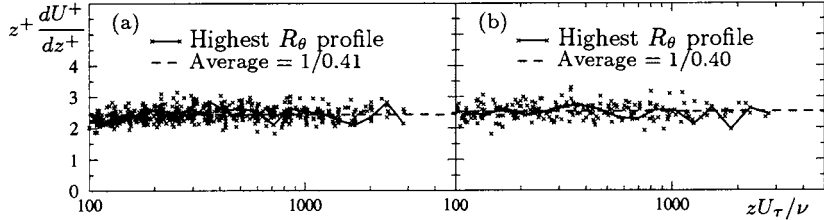


Figure 3. Logarithmic law diagnostic function (5) for all profiles, data from TWR, for (a) Pitot tube and (b) normal wire.

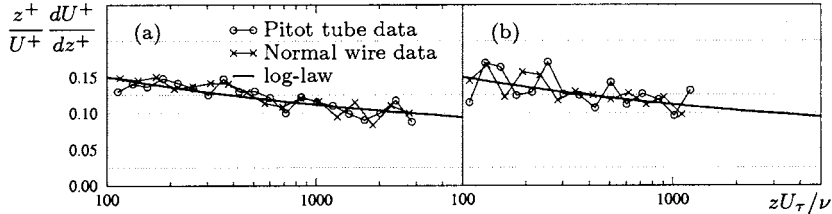


Figure 4. Power law diagnostic function (6) in TWR, for (a)  $R_\theta = 62000$  profile and (b) for  $R_\theta = 24000$  profile. Both Pitot and hot-wire results are shown.

be noted that the choice of  $U_\tau$  serves to simply scale the values of  $D_1$  for a given profile and the Clauser chart method does not force  $D_1$  to a constant for a given profile.

Figure 4 shows the function

$$D_2 = \frac{z^+}{U^+} \frac{dU^+}{dz^+} \quad (6)$$

plotted in the range  $100 < z^+ < 0.15K_\tau$ , for the highest Reynolds number profile and a lower Reynolds number profile. If a power law is the correct form equation (6) should plot as a constant value equal to the power appearing in the power law. However the results indicate that  $D_2$  has a preferred slope (consistent with a log law) which suggests the power law is not the correct functional form. A similar trend is observed for the other profiles at other Reynolds numbers.

#### 4. Outer-flow scaling

Figure 5 shows the defect velocity obtained from Pitot measurements normalised using different velocity scales. Based on an analysis at infinite Reynolds number, George and Castillo, 1997 claims the correct choice for the velocity scale in (2) is  $U_1$  and that the choice of  $U_\tau$  is incompatible with similarity of the momentum equation in the outer region of the flow. However as can be seen from figure 5 the quality of the collapse is much better when  $U_\tau$  is used as the scaling velocity. The quality of the

collapse is further improved if we use  $U_1\delta^*/\delta_c$  as the outer velocity scale where  $\delta^*$  is the displacement thickness. Incorporating the integral scale  $\delta^*$  in the definition of the velocity scale effectively forces this collapse. The velocity scale  $U_1\delta^*/\delta_c$  is equivalent to the velocity scale  $U_{CL} - \bar{U}$  that Zagarola and Smits, 1998 propose for pipe flow, where  $U_{CL}$  is the centreline velocity and  $\bar{U}$  is the average pipe velocity. The question is whether the correct velocity scale is simply the velocity scale that best collapses the data. An alternative interpretation is given in Perry et al., 2002 where the zero pressure gradient layer is not assumed to necessarily be in a state of equilibrium (ie. defect self-similarity). In the analysis of Perry et al., 2002  $U_\tau$  is used as the velocity scale and the layer evolves from arbitrary initial conditions to a state very close to equilibrium. Hence as the layer is evolving defect self-similarity is not expected. Indeed if the stations upstream of  $x = 5$  m are removed from figure 5 the collapse when  $U_\tau$  is used as the velocity scale is greatly improved.

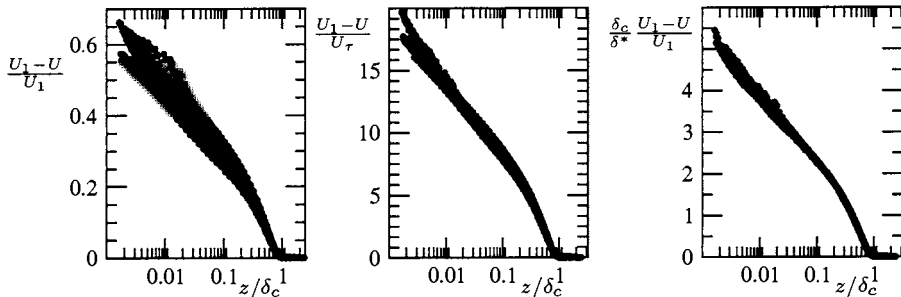


Figure 5. Velocity defect plots using different scaling velocities for all Pitot tube data ( $994 < K_r < 22407$ ).

## 5. Conclusions

The mean velocity profiles are found to be well described by a logarithmic law of the wall in the fully turbulent wall region. The traditional values of  $\kappa = 0.41$  and  $A = 5.0$  are found to best collapse the data. Using the outer velocity scale  $U_1\delta^*/\delta_c$  leads to the best collapse of the defect velocity. However using  $U_\tau$  as the outer velocity scale may be the correct choice since this is consistent with the recent calculations of Perry et al., 2002 where the layer is expected to evolve to a self-similar state.

## References

- Barenblatt, G. I., Chorin, A. J., and Prostokishin, V. M. (2000). Self-similar intermediate structures in turbulent boundary layers at large reynolds numbers. *J. Fluid Mech.*, 410:263–283.

- George, W. K. and Castillo, L. (1997). Zero-pressure-gradient turbulent boundary layer. *Applied Mechanics Reviews*, 50(12):689–729.
- MacMillan, F. (1956). Experiments on pitot-tubes in shear flow. R.& M. 3028, Aero. Res. Counc.
- Millikan, C. B. (1938). A critical discussion of turbulent flows in channels and circular tubes. In *Proc. 5th Int. Congress of Appl. Mech.*, pages 386–392, Cambridge, Mass.
- Osterlund, J. M. (1999). *Experimental studies of zero pressure gradient turbulent boundary layer*. PhD thesis, Stockholm Royal Institute of Technology, Department of Mechanics.
- Perry, A. E., Marusic, I., and Jones, M. B. (2002). On the streamwise evolution of turbulent boundary layers in arbitrary pressure gradients. *J. Fluid Mech.*, 461:61–91.
- Prandtl, L. (1925). Über die ausgebildete turbulenz. *ZAMM*, 5:136–139.
- von Kármán, T. (1930). Mechanische Ähnlichkeit und turbulenz. In *Math. Phys. Klasse*, page 58, Nachr. Ges. Wiss. Göttingen.
- Zagarola, M. V. and Smits, A. J. (1998). Mean flow scaling of turbulent pipe flow. *J. Fluid Mech.*, 373:33–79.

# HOT-WIRE MEASUREMENTS OF TWO-POINT CORRELATIONS IN THE FLAT PLATE BOUNDARY LAYER AT HIGH REYNOLDS NUMBERS

R. Abstiens, W. Schröder and W. Limberg

*RWTH Aachen, Aerodynamisches Institut, Wüllnerstr. zw. 5 u. 7, D-52062 Aachen, Germany  
Tel.: +49 241-809 4358, Fax.: +49 241-809 2257, e-mail: ronald@aia.rwth-aachen.de*

**Abstract:** Two-point correlations were measured in the  $8 \times 6 \text{ m}^2$  test section of the low-speed German-Dutch wind tunnel at Reynolds numbers up to  $\text{Re} = 50 \times 10^6$ . In the experiments a zero pressure gradient turbulent boundary layer along a flat plate with a length of 13.5 m was generated. The two-point correlations were measured at freestream velocities of 40 m/s and 60 m/s with two triple hot-wire probes, which could be moved independently above the surface of the flat plate. With this setup it was possible to collect data for the normal and shear stresses in the normal and in the spanwise direction for all levels. It is the objective of this investigation to obtain a database for turbulent boundary layers at large Reynolds numbers with exactly known boundary conditions that can be used, e.g., to validate subgrid scale models in large-eddy simulations and to experimentally verify the new exponential law in the outer region of the boundary layer [1]. Additionally, velocity profiles of the boundary layer and two-point correlations in the normal and spanwise direction were measured to study the variation of the integral length scale in the spanwise direction.

**Key words:** High Reynolds number, two-point correlations, hot-wire measurements, Particle-Image Velocimetry

## 1. INTRODUCTION

Today, it is completely out of reach to perform a direct numerical simulation for flows over slender bodies at Reynolds numbers in the range of  $10^7$ . Therefore, to gain more insight into the turbulent structure of such

boundary layer flows, some experiments were performed over the last years. Unfortunately, the number of those investigations is quite limited, since there is only a few facilities, which satisfy the condition to reach the high Reynolds number regime under top quality flow conditions. Besides the additional physical understanding such experiments are to deliver data to validate numerical solutions. In [2, 3] Fernholz et al. measured mean velocity and Reynolds-stress profiles in the incompressible turbulent boundary layer with zero pressure gradient on the aerodynamically smooth side wall of the German-Dutch wind tunnel. The measurements provided a complete set of data for the turbulent stresses for Reynolds numbers based on the momentum thickness  $\theta$  up to  $Re_\theta = 6 \times 10^4$ . Saddoughi and Veeravally investigated the boundary layer in the test section of the Full-Scale Aerodynamic Facility at NASA Ames Research center. Subsequent experimental investigations were performed later by Oesterlund and Johansson at the KTH in Stockholm at Reynolds numbers of  $Re_\theta = 27300$  to analyze the impact of the facility on the measured two-point correlations [4]. The turbulence generation in a turbulent boundary layer for  $Re_\theta = 9700$  was investigated on the basis of streamwise two-point-correlations and wall shear stresses by hot-film and hot-wire data [5].

Measurements in the high Reynolds number range were also carried out in the atmospheric boundary layer. However, due to thermal convection and different surface roughnesses the conditions for the development of the boundary layer are uncertain [6].

The motivation for this study was to deliver a database to investigate the impact of the wall normal distance on the integral length in the spanwise direction. First, we describe the test facility, setup and experimental techniques and then discuss the results.

## **2. TEST FACILITY AND TEST SETUP**

Measurements of two-point correlations were performed in the  $8 \times 6 \text{ m}^2$  test section of the low-speed German-Dutch wind tunnel (DNW) at Reynolds numbers up to  $Re = 50 \times 10^6$ . The freestream velocity was varied between 40 m/s and 60 m/s. The temperature in the test section was kept constant within  $0.5^\circ \text{ C}$  during the measuring period. Fluid mechanical characteristics of the tunnel are described by Meier et al. in [7].

In the experiments a zero pressure gradient turbulent boundary layer with a maximum thickness of 150 mm in the measurement cross section was generated. An elliptical profile at the leading edge guaranteed an attached flow at the nose. The distance from the leading edge to the measurement

position on the aerodynamically smooth surface of the plate was 13.5 m (Fig. 1). The two-point correlations were measured using two triple hot-wire probes, one of which could be shifted in the vertical direction and the other one could be moved in the normal, spanwise and streamwise direction such that theoretically a cubic zone of  $300 \times 300 \times 300$  mm<sup>3</sup> above the surface of the flat plate could be analyzed.

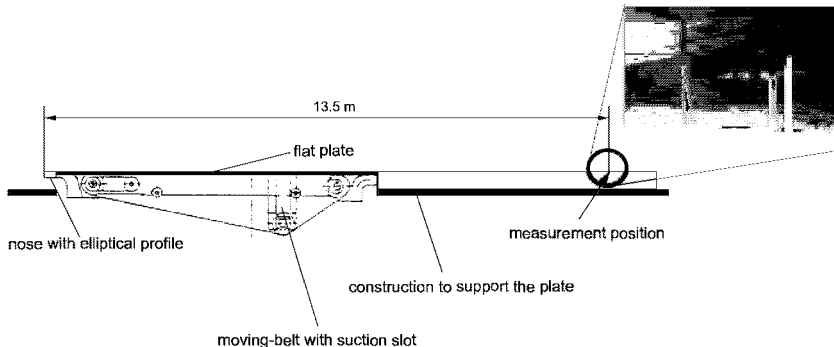


Figure 1. Test setup in the  $8 \times 6$  m<sup>2</sup> DNW-LLF test section with the flat plate. The zoom shows the two triple hot-wire probes.

### 3. EXPERIMENTAL TECHNIQUES

The three-sensor hot-wire measuring technique was developed at the Aerodynamisches Institut and was already applied in experiments in the DNW [1]. The probes were calibrated *in situ* on the basis of King's law with three calibration points. While one probe was in a fixed position, the second hot-wire probe was shifted resulting in 450 measuring points in six different planes. The plane nearest the wall was located  $y=3.5$  mm above the surface of the flat plate, one plane was positioned at  $y=300$  mm in the freestream flow field, while the others lay in the log and outer region at  $y=15, 30, 75$ , and 200 mm. The hot-wire instrumentation consisted of two TSI IFA 100 hot-wire bridges. Between 32,000 and 128,000 samples were taken at a frequency of 10 – 50 kHz in each point. Data was collected for the Reynolds normal and shear stresses  $u_i' u_j'$  mainly in the normal and in the spanwise direction for all planes. The measurements were used to determine mean velocity profiles in the normal direction and two-point correlations in the normal and spanwise directions to analyze the impact of the wall normal distance on the turbulent length scales in both directions.

## 4. RESULTS

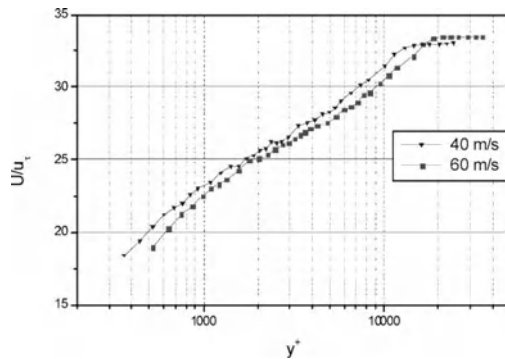


Figure 2. Boundary layer profiles in inner scaling at 40 m/s and 60 m/s,  $x = 13.5$  m ( $u_\tau$  is determined by a relation from [8]).

The velocity profiles for the two tunnel conditions are given in inner scaling in Fig. 2. The friction velocity  $u_\tau$  was calculated by the semi-empirical relation of Fernholz [8], which holds for a zero pressure gradient boundary layer. The shift between the distributions in Fig. 2 results from the  $u_\tau$  value. The higher the free-stream velocity, the larger the friction velocity,  $u_\tau(40 \text{ m/s}) = 1.23 \text{ m/s}$  and  $u_\tau(60 \text{ m/s}) = 1.78 \text{ m/s}$ , which is why on the one hand, the edge of the boundary layer is indicated at larger  $y^+$  values and on the other hand, the distribution of the smaller velocity lies slightly above the greater freestream velocity curve.

The two-point correlations from the hot-wire data for the streamwise, the normal, and the spanwise velocity component, which were measured at both freestream velocities are presented in Fig. 3 for two fixed probe positions  $y_f = 15 \text{ mm}$  and  $30 \text{ mm}$ . The wall distance is scaled with the boundary layer thickness, which is defined by the 99.5 % rule. The correlations of the streamwise velocity components have a much larger value than the v- and w-components. The latter show a sharp drop in the vicinity of the wall leading to a clearly smaller integral scale than that of the streamwise correlations. The scaling of the data with the boundary layer thickness allows the comparison of the scaling behavior for different origins of the correlations normal to the wall. The u- and v-components have positive values whereas the w-component is slightly negative in the outer part of the boundary layer. If the sign change in the distribution of the w-component indicates some kind of vortical structure the intersection point should be independent of the

sign of the two-point correlations. However, this is not satisfied in Fig. 3. We assume the intersection point to be defined by the distance between the fixed and the moving probe, in other words, it indicates a mutual perturbation of both probes. The comparison between the correlation coefficients  $R_{uu}$  in Fig. 4a for 40 m/s and 60 m/s at two different positions normal to the wall show almost a perfect correspondence between the distributions, which is in agreement with the log law. That is, the  $R_{uu}$ -based length scale is independent of the Reynolds number and is constant in the log law. The streamwise correlation coefficients in Fig. 4b indicate different values of the spanwise based integral length scale. This variation has to be taken into account when the spanwise extension of the computational domain in a direct numerical simulation is defined, since the validity of the periodicity condition is determined by the integral length scale.

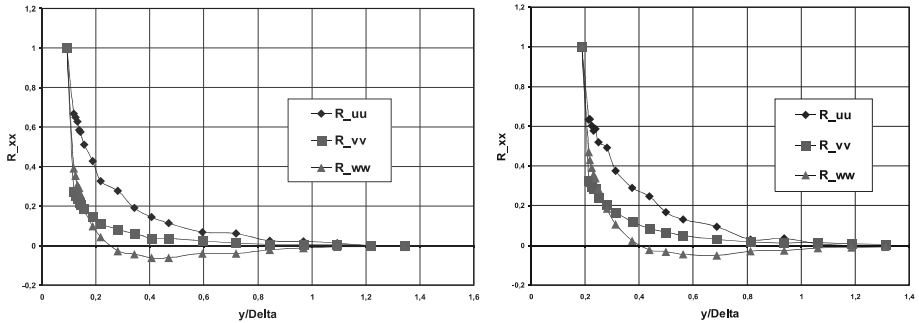


Figure 3. Coefficients for different two-point correlations for 40 m/s at 15 mm (left) and 30 mm (right).

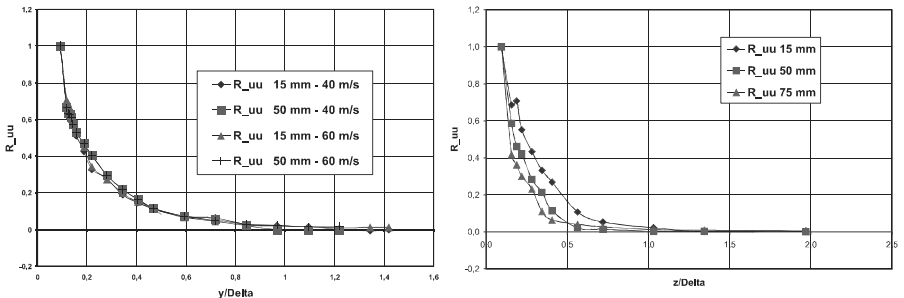


Figure 4. a) Two-point correlations coefficient  $R_{uu}$  for 40 m/s and 60 m/s at different positions (left). b) Preliminary results for the streamwise two-point correlations in the spanwise direction at 60 m/s (right).

The boundary layer on the flat plate was investigated experimentally in the  $8 \times 6 \text{ m}^2$  low-speed German-Dutch wind tunnel at Reynolds numbers up to  $\text{Re} = 50 \times 10^6$ . Two-point correlations were measured at freestream velocities of 40 m/s and 60 m/s with two triple hot-wire probes in a cubic zone above the surface of the flat plate. The results for the streamwise two-point correlations in the normal direction confirm a constant integral length scale in the log layer. However, in the spanwise direction a significant variation of the length scale was measured.

## ACKNOWLEDGEMENTS

The authors gratefully acknowledge the support by the Deutsche Forschungsgemeinschaft (DFG) and the Deutsches Zentrum für Luft- und Raumfahrt (DLR) and the German-Dutch wind tunnel (DNW).

## REFERENCES

- [1] M. Oberlack, "Symmetries in turbulent boundary-layer flows", *Center for Turbulence Research, Stanford University/NASA Ames, Annual Research Briefs*, 1996.
- [2] H. H. Fernholz, Krause, E., Nockemann, M., Schober, M., "Comparative measurements in the canonical boundary layer at  $\text{Re} < 6 \times 10^4$  on the wall of the German-Dutch wind tunnel", *Phy Fluids*, vol. 7(6), pp. 1275-1281, 1995.
- [3] D. G. Saddoughi, Veeravali, S. V., "Local isotropy in turbulent Boundary layers at high Reynolds number", *J. Fluids Mech.*, vol. 268, pp. 333-372, 1994.
- [4] J. M. Österlund, Johansson, A. V., Nahib, H. M., Hites, M. H., "Mean-flow characteristics of High Reynolds Number Turbulent Boundary Layers from two Facilities", presented at 30th Fluid Dynamics Conference (28 June - 1 July), Norfolk, Virginia, 1999.
- [5] J. M. Österlund, Johansson, A. V., "Measurements in a flat plate turbulent boundary layer", presented at Turbulence shear-flow phenomena 1. TSFP-1, Santa Barbara, California, USA, 2000.
- [6] M. M. Metzger, Klewicki, J. C., "A comparative study of near-wall turbulence in high and low Reynolds number boundary layers", *Physiks of Fluids*, vol. 13 No. 3, pp. 692-701, 2001.
- [7] H. U. Meier, Michel, U., Kreplin, H. P., "The influence of wind tunnel turbulence on the boundary layer transition", in *Perspectives in Turbulence Studies*, H. U. Meier, Bradshaw, P., Ed.: Springer Verlag, 1987, pp. 26-46.
- [8] H. H. Fernholz, "Ein halbempirisches Gesetz für die Wandreibung in kompressiblen turbulenten Grenzschichten bei isothermer und adiabater Wand", *ZAMM 51*, pp. 146-147, 1971.

# ON THE EXPERIMENTAL SORTING OF COMPETING THEORIES FOR WALL-BOUNDED TURBULENT FLOWS

Martin Wosnik and T. Gunnar Johansson

*Department of Thermo and Fluid Dynamics*

*Chalmers University of Technology*

*S-41296 Gothenburg*

**Abstract** Base-case wall-bounded turbulent flows have become of great interest once again, because of practical issues, e.g. apparent Reynolds-number and initial condition effects despite facilities of increasing quality and Reynolds-number range, and also because of some researchers pointing out shortcomings of the classical theory. Differences between two competing theories for the mean flow are reviewed and methods for experimentally sorting them are discussed.

## 1. Introduction

The *logarithmic law with constant coefficients* for the overlap layer of wall-bounded turbulent flows had been accepted as one of the (few) cornerstones of turbulence theory for many decades. In recent years, this topic once thought solved has become an active area of research again, on one hand because of practical issues, e.g. apparent Reynolds-number and initial condition effects despite experimental facilities of increasing quality and Reynolds-number range, and on the other hand because of some researchers' persistence in pointing out the inconsistencies in the classical theory, e.g. George and Castillo, 1997 (the cumulative review paper of an investigation that began with George, 1988).

Several competing theoretical approaches based on the (reduced) Reynolds-averaged Navier-Stokes (RANS) equations now exist for a variety of base-case wall-bounded turbulent flows. It is thereby important to distinguish between developing, non-parallel-in-the-mean flows such as turbulent boundary layers and wall jets and fully developed, parallel-in-the-mean flows such as turbulent pipe and channel flows.

This paper will deal only with the *zero pressure gradient turbulent boundary layer*, unless explicitly stated otherwise. Differences between

competing theories for the mean flow are reviewed, and different methods for experimentally sorting competing theories are examined.

## 2. Turbulent Boundary Layers: Review of Classical vs. More General Approach

We will begin by briefly comparing two theoretical approaches to zero pressure gradient turbulent boundary layers based on RANS equations. The reduced  $x$ -momentum equation for the *outer* part of the boundary layer (thin shear layer assumption,  $1/\delta \gg 1/L$ ) is

$$U \frac{\partial U}{\partial x} + V \frac{\partial U}{\partial y} = \frac{\partial}{\partial y} [- < uv >] \quad (1)$$

where  $U \rightarrow U_\infty$  as  $y \rightarrow \infty$ . Equation (1) cannot account for the near-wall or *inner* region, therefore the  $x$ -momentum equation is rescaled with a cross-stream length scale,  $\eta(x) \propto \nu/U_{S_i}$ , in order to retain the leading order viscous term and meet the no-slip condition,

$$0 = \frac{\partial}{\partial y} \left[ \nu \frac{\partial U}{\partial y} - < uv > \right] \quad \text{or} \quad \nu \frac{\partial U}{\partial y} - < uv > = \frac{\tau_w}{\rho} \equiv u_*^2 \quad (2)$$

if integrated with respect to  $y$  from the wall (B.C.:  $U = 0$  at  $y = 0$ ).

If equations (1) and (2) are the *governing equations* for this problem, then proper *scaling laws* must be similarity solutions to them. Therefore **assumption no.1** in any analysis attempting to find scaling laws is: *Similarity solutions to the governing equations exist.*

### 2.1 Classical Approach

The classical approach proceeds with **assumption no.2**: *The (single) velocity scale is the friction velocity  $u_*$ .* Solutions at infinite Reynolds number are sought of the form

$$\frac{U}{u_*} = f_{i\infty}(y^+) \quad \text{and} \quad \frac{U - U_\infty}{u_*} = F_{o\infty}(\bar{y}) \quad (3)$$

where  $y^+ = u_* y / \nu$  and  $\bar{y} = y / \delta$ . Clauser, 1954, following Millikan, 1938 matched inner and outer velocity profiles and derivatives at *infinite* Reynolds number (asymptotic analysis)

$$F_{o\infty}(\bar{y}) + \frac{U_\infty}{u_*} = f_{i\infty}(y^+) \quad \text{and} \quad \bar{y} \frac{dF_{o\infty}}{d\bar{y}} = y^+ \frac{df_{i\infty}}{dy^+} \quad (4)$$

to yield logarithmic velocity profiles

$$\frac{U}{u_*} = \frac{1}{\kappa} \ln y^+ + B_i \quad \text{and} \quad \frac{U - U_\infty}{u_*} = \frac{1}{\kappa} \ln \bar{y} + B_o \quad (5)$$

where  $\kappa$ ,  $B_i$  and  $B_o$  are constants.

## 2.2 More General Approach

George and Castillo, 1997 do not assume any scaling laws at the outset, but start with a general form of a solution, which reduces to similarity solutions in the limit of infinite Reynolds number,

$$\frac{U}{U_{Si}(x)} = f_i(y^+, \delta^+) \quad \text{and} \quad \frac{U - U_\infty}{U_{So}(x)} = f_o(\bar{y}, \delta^+) \quad (6)$$

where  $y^+ = y/\eta(x)$ ,  $\bar{y} = y/\delta(x)$  and  $\delta^+ \equiv u_*\delta/\nu$ . Velocity scales,  $U_{Si/o}(x)$  and inner and outer length scales,  $\eta(x)$  and  $\delta(x)$  remain to be determined. Note that scaling laws for other quantities, e.g. the Reynolds stress, can be written in a similar way. These scaling laws must lose their dependence on the Reynolds number asymptotically, just as the omitted terms in the governing equations (1) and (2) vanish asymptotically (*Asymptotic Invariance Principle*), i.e.,  $f_i(y^+, \delta^+) \rightarrow f_{i\infty}(y^+)$  and  $f_o(\bar{y}, \delta^+) \rightarrow f_{o\infty}(\bar{y})$ .

To answer “What scaling factors are consistent with the equations of motion?”, solutions to the governing equations are sought of the form

$$\frac{U - U_\infty}{U_{so}(x)} = f_{o\infty}(\bar{y}) \quad \text{and} \quad \frac{\langle -uv \rangle}{R_{so}(x)} = r_{o\infty}(\bar{y}) \quad (7)$$

for the outer region. Substituting (7) into (1) and clearing terms:

$$\begin{aligned} & \left[ \left( \frac{U_\infty}{U_{So}} \right) \frac{\delta}{U_{So}} \frac{dU_{So}}{dx} \right] f_{o\infty} + \left[ \frac{\delta}{U_{So}} \frac{dU_{So}}{dx} \right] f_{o\infty}' - \left[ \frac{U_\infty}{U_{So}} \frac{d\delta}{dx} \right] \bar{y} f_{o\infty}' \\ & - \left[ \frac{d\delta}{dx} + \frac{\delta}{U_{So}} \frac{dU_{So}}{dx} \right] f_{o\infty}' \int_0^{\bar{y}} f_{o\infty}(\xi) d\xi = \left[ \frac{R_{So}}{U_{So}^2} \right] r_{o\infty}' \end{aligned} \quad (8)$$

A similarity solution can only be possible if the bracketed terms have the same  $x$ -dependence, i.e., are proportional to each other (or be identically zero, the trivial solution).

$$\left( \frac{U_\infty}{U_{So}} \right) \frac{\delta}{U_{So}} \frac{dU_{So}}{dx} \sim \frac{\delta}{U_{So}} \frac{dU_{So}}{dx} \sim \left( \frac{U_\infty}{U_{So}} \right) \frac{d\delta}{dx} \sim \frac{d\delta}{dx} \sim \frac{R_{So}}{U_{So}^2} \quad (9)$$

Comparing terms it follows that the asymptotically proper scales are:  $U_{So} = U_\infty$  (to within a constant of proportionality) and  $R_{So} = U_\infty^2 d\delta/dx$ . The same methodology applied to the inner layer leads to the commonly used scales,  $U_{Si} = u_*$ ,  $R_{Si} = u_*^2$  and  $\eta = \nu/u_*$ .

Inner and outer velocity profiles and derivatives are then matched at large, but *finite* Reynolds number (*Near-Asymptotics*).

$$1 + f_o(\bar{y}, \delta^+) = \frac{u_*}{U_\infty} f_i(y^+, \delta^+) \quad \text{and} \quad \frac{\bar{y}}{1 + f_o} \frac{df_o}{d\bar{y}} = \frac{y^+}{f_i} \frac{df_i}{dy^+} \quad (10)$$

which, after some algebra, yields the first order solutions

$$\frac{U}{U_\infty} = C_o(\delta^+) \left( \frac{y+a}{\delta} \right)^{\gamma(\delta^+)} \quad \text{and} \quad \frac{U}{u_*} = C_i(\delta^+) \left( \frac{y+a}{\eta} \right)^{\gamma(\delta^+)} \quad (11)$$

The offset  $a$  is essential for proper invariance ( $y \rightarrow y + a$ ), since these equations must work for any choice of origin (Oberlack, 1997). Thus, the more general approach (one assumption less than classical theory) leads to velocity profiles in the overlap region.<sup>1</sup> <sup>2</sup> There are two velocity scales, the friction velocity  $u_*$  and the free-stream velocity  $U_\infty$ , so the overlap layer depends on both. (for details see George and Castillo, 1997).<sup>3</sup>

## 2.3 Closing the equations for practical/engineering purposes

Up to this point neither theory has addressed the closure problem inherent in the RANS approach. Experimental data is needed to find the actual values of the coefficients  $\kappa$ ,  $B_i$  and  $B_o$ , as well as  $\gamma(\delta^+)$ ,  $C_i(\delta^+)$  and  $C_o(\delta^+)$ . In other words, from here on, theoreticians are at the mercy of experimentalists. Therefore, theories cannot be discounted simply because new experimental results are in disagreement with empirical curves (coefficients) obtained by comparing to other, older data sets.

## 3. Sorting Theories

### 3.1 Velocity profile plots

The usual log-log and semi-log plotting of velocity data alone in inner variables is *not* very useful in distinguishing between theories, since the difference between theories is often smaller than the combined uncertainty in velocity and wall shear stress measurements. The wall shear stress (or friction velocity,  $u_* \equiv \sqrt{\tau_w/\rho}$ ) error is by far the larger one, typically  $\geq 3\%$ . For a discussion of accuracy of some direct and indirect measuring techniques, c.f. Johansson and Castillo, 2002.

### 3.2 Distinguishing Between Logarithmic and Power Law

A somewhat more helpful tool when used properly are velocity derivative plots. Often a “power law diagnostic function”  $\Gamma$  (c.f. Österlund et al., 2000, figure 6) is used, which in inner variables is defined as  $\Gamma \equiv y^+ / U^+ dU^+ / dy^+$ , where  $U^+ = U/u_*$ . If a region in the velocity profile is governed by a simple power law,  $U^+ = C (y^+)^p$ , then a horizontal tangent  $\Gamma = p$  should exist for all profiles. If the power law has a Reynolds number dependent coefficient and exponent,  $U^+ = C(\delta^+) (y^+)^{p(\delta^+)}$ ,

then  $\Gamma$  can *only* be applied to individual profiles (different profiles must not be averaged together). If, on the other hand, one wants to test

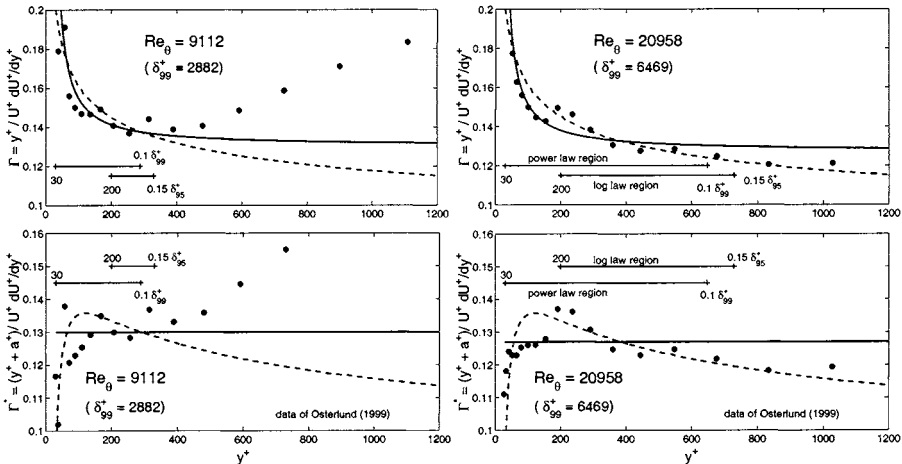


Figure 1. Experimental data, logarithmic and power law profiles plotted in the form of  $\Gamma$  (equation 12, top two plots) and  $\Gamma^*$  (equation 13, bottom two plots) for moderate ( $Re_\theta = 9,112$ , left two plots) and higher Reynolds number ( $Re_\theta = 20,959$ , right two plots). Filled circles: data of Österlund, 1999; dashed lines: log law (eqn. 5 substituted in eqns. 12 and 13),  $U^+ = 1/0.38 \ln y^+ + 4.2$ ; solid lines: power law (eqn. 11 substituted in eqns. 12 and 13),  $a^+ = -16$ ,  $\gamma = 0.130$  for  $Re_\theta = 9,112$  and  $\gamma = 0.127$  for  $Re_\theta = 20,959$ , respectively.

whether experimental data support a power law overlap profile of the form of equation (11),  $\Gamma$  will not produce a horizontal tangent, since

$$\Gamma = \frac{y^+}{U^+} \frac{dU^+}{dy^+} = \frac{y^+}{y^+ + a^+} \gamma \neq \text{const.} \quad (12)$$

A modified form of this “diagnostic function”,  $\Gamma^*$ , becomes useful for individual profiles if defined as follows

$$\Gamma^* = \frac{y^+ + a^+}{U^+} \frac{dU^+}{dy^+} = \gamma(\delta^+) \quad (\text{for eqn. 11}) \quad (13)$$

Figure 1 shows data and theories in the form of  $\Gamma$  (equation 12) and  $\Gamma^*$  (equation 13) for moderate and high Reynolds number, respectively. The narrow regions of applicability of each theory are also shown. From the two experimental data sets used here one could argue for *either* a logarithmic law with constant coefficients *or* a power law in  $(y + a)$ . It appears that presently available data alone cannot distinguish between the two proposals, at least not at these Reynolds numbers.

## 4. Concluding remarks

The differences between the classical theory and alternative approaches are small, and true sorting criteria may only be available for higher Reynolds numbers, as well as higher measurement accuracy. There are several clues that the classical log law may be too simplistic a formulation, e.g., the presence of the *mesolayer* – the classical log-law does not work well inside of  $y^+ < 300$  (George and Castillo, 1997; Österlund et al., 2000) – and the fact that empirically found mixed scalings appear to work – a manifestation of the Reynolds number dependence of the overlap layer (DeGraaf and Eaton, 2000).

## Notes

1. A logarithmic or power friction law can be obtained by subtracting outer from inner (eqns.5) or dividing outer by inner velocity profile (eqns.11)
2. In fully developed turbulent pipe and channel flows only a single velocity scale,  $u_*$ , is needed (Wosnik et al., 2000). This will, of course, lead to logarithmic profiles in the overlap layer, in contrast to boundary layers (non-parallel, developing flow)
3. The methodology of letting the scaling laws float and determining them from conditions for similarity arising from the governing equations has been termed Equilibrium Similarity by George and co-workers. It has been successfully applied to isotropic, decaying turbulence, near and far wake, axisymmetric and plane jet, as well as a variety of wall-bounded flows.

## References

- Clauser, F. H. (1954). The turbulent boundary layer. *Adv. Appl. Mech.*, IV:1–51.
- DeGraaf, J. D. and Eaton, J. K. (2000). Reynolds-number scaling of the flat-plate turbulent boundary layer. *Journal of Fluid Mechanics*, 422:319–346.
- George, W. K. (1988). Another look at the log (or is it a power law?) velocity profile for a zero-pressure gradient boundary layer. *Bulletin of the American Physical Society*, 33(10):2301.
- George, W. K. and Castillo, L. (1997). Zero-pressure-gradient turbulent boundary layer. *Applied Mech. Rev.*, 50(12):689–729.
- Johansson, T. G. and Castillo, L. (2002). Near-wall measurement in turbulent boundary layers using LDA. In *Proceedings of FEDSM 2002, ASME*, Montreal, Canada.
- Millikan, C. B. (1938). A critical discussion of turbulent flow in channels and circular tubes. In *Proceedings of the 5th Int. Congress on Applied Mechanics, Cambridge, MA*, pages 386–392. John Wiley and Sons, New York, NY.
- Oberlack, M. (1997). Unified theory for symmetries in plane parallel turbulent shear flows. manuscript 163, Center for Turbulence Research, NASA Ames/Stanford University (also submitted to jfm).
- Österlund, J. M. (1999). *Experimental studies of zero pressure-gradient turbulent boundary layer flow*. PhD thesis, Royal Institute of Technology, Sweden.
- Österlund, J. M., Johansson, A. V., Nagib, H. M., and Hites, M. H. (2000). A note on the overlap region in turbulent boundary layers. *Phys. Fluids*, 12(1):1–4.
- Wosnik, M., Castillo, L., and George, W. K. (2000). A theory for turbulent pipe and channel flows. *Journal of Fluid Mechanics*, 421:115–145.

# SCALING OF NEAR-WALL STRUCTURES IN TURBULENT BOUNDARY LAYERS SUBJECTED TO ADVERSE PRESSURE GRADIENT

Y. Nagano and T. Houra

*Department of Mechanical Engineering, Nagoya Institute of Technology*

*Gokiso-cho, Showa-ku, Nagoya 466-8555, JAPAN*

*nagano@heat.mech.nitech.ac.jp*

**Abstract** A scaling law of the near-wall structures in turbulent boundary layers subjected to a sustained adverse pressure gradient is experimentally investigated. The near-wall bursting phenomena in the boundary layer are remarkably elongated in time in comparison with those in zero-pressure-gradient flows, and thus time scales increase with an increasing pressure gradient parameter  $P^+$ . The increase in time scales is not in proportion to the corresponding increase in the conventional viscous time scale  $\nu/u_\tau^2$ . It is found that the Taylor time scale is the most appropriate to describe the essential characteristics of non-equilibrium adverse pressure gradient flows. This is also true for the zero-pressure-gradient flows in the Reynolds-number range studied. Even the wall-limiting behavior of streamwise velocity fluctuations for different  $P^+$  is well correlated in the coordinates based on the Taylor time scale.

**Keywords:** Turbulent Boundary Layer, Adverse Pressure Gradient, Bursting Period, Taylor Time Scale, Wall-Limiting Behavior

## 1. Introduction

In theory as well as in practice, it is of fundamental importance to investigate the effects of pressure gradients on the structure of turbulent boundary layers. From the viewpoint of engineering, the efficiency of fluid machinery, such as a diffuser and turbine blades, is often restricted by the occurrence of separation due to a pressure rise in the flow direction. Therefore, it is very important to elucidate the effects of an adverse pressure gradient (APG) and establish a flow control method to avoid flow separation. In addition, the study of turbulent boundary

layers subjected to a pressure gradient promises the further benefit of a deeper understanding of wall turbulence, which may not be obtained under an equilibrium zero-pressure-gradient (ZPG) condition. In the present study, we discuss the scaling-law of the near-wall structures in APG flows.

## 2. Experimental apparatus

The experimental apparatus used is the same as described in our previous studies (Nagano *et al.*, 1998; Houra *et al.*, 2000). The working fluid (air) flows successively through the settling chamber, two-dimensional contraction, test section, plenum chamber and blower. The test section is composed of a flat-plate on which an air-flow turbulent boundary layer develops, and a roof-plate to adjust pressure gradients. The aspect ratio at the inlet to the test section is 13.8 (50.7 mm high  $\times$  700 mm wide). Under the present measurement conditions, the free-stream turbulence level is below 0.10%. Velocity was measured with hot-wire probes, i.e., a handmade subminiature normal hot-wire (diameter: 3.1  $\mu\text{m}$ ; length: 0.6 mm), and a specially devised X-probe for measurement of two velocity components in the streamwise ( $x$ ) and wall-normal ( $y$ ) directions (diameter: 3.1  $\mu\text{m}$ ; length: 0.6 mm  $\simeq 9 \nu/u_\tau$ ; and spacing: 0.30 mm  $\simeq 4.6 \nu/u_\tau$ ). In the APG flow, the pressure gradient  $dC_p/dx$  [ $C_p = (\bar{P} - \bar{P}_0)/(\rho\bar{U}_0^2/2)$ , and  $\bar{P}$ ,  $\bar{P}_0$  and  $\bar{U}_0$  are the mean pressure, the reference inlet pressure, and the reference inlet velocity, respectively] keeps a nearly constant value of 0.6  $\text{m}^{-1}$  over the region  $65 \text{ mm} \leq x \leq 700 \text{ mm}$ , and then decreases slowly ( $x$  is the streamwise distance from a tripping point). On the other hand, the pressure gradient parameter normalized by inner variables  $P^+ [= \nu(d\bar{P}/dx)/\rho u_\tau^3]$  and the Clauser parameter  $\beta [= (\delta^*/\tau_w)d\bar{P}/dx]$  increase monotonously, thus yielding moderate to strong APG.

## 3. Results and discussion

We investigate the characteristic time scale pertaining to the bursting phenomena,  $\bar{T}_B$ , obtained from the short-time averaged autocorrelation function method (Kim *et al.*, 1971; Hishida and Nagano, 1979). We obtained the mean burst period  $\bar{T}_B$  as the ensemble-averaged value of the delay time when the autocorrelation coefficient takes the first maximum. When we adopt a short time range, say from 3 to 7  $\bar{T}_B$ , for the data processing time, the mean burst period is independent of the data processing time. Figure 1 shows the normalized bursting periods in ZPG ( $660 < R_\theta < 1800$ ) and APG flows ( $1290 < R_\theta < 3350$ ). As seen from this figure, in the low-Reynolds-number range, the inner scaling is

Table 1. Scaling parameters for bursting period

Year	Author(s)	Detection method(s)	Reynolds number range	Best candidates
1971	Kim <i>et al.</i>	Hydrogen-bubble, Short-time averaged autocorrelation	$R_\theta = 666, 1100$	Outer variables
1971	Rao <i>et al.</i>	Band-pass filtering	$620 < R_\theta < 9450$	Outer variables
1973	Lu & Willmarth	Quadrant splitting	$R_\theta = 4230, 38000$	Outer variables
1982	Bandyopadhyay	-	-	Non-existence
1983	Blackwelder & Haritonidis	VITA	$1000 < R_\theta < 10000$	Inner variables
1984	Alfredsson & Johansson	VITA	$13800 < Re_c <$ 123000	Mixed variables
1987	Luchik & Tie- derman	Quadrant splitting, VITA, $u$ -level	$8700 < Re_b < 17800$	Inner variables
1986	Shah & Antonia	VITA, $u$ -level	$651 < R_\theta < 13173$	Mixed variables

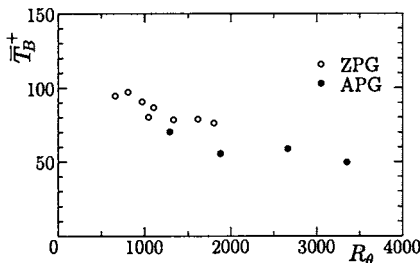
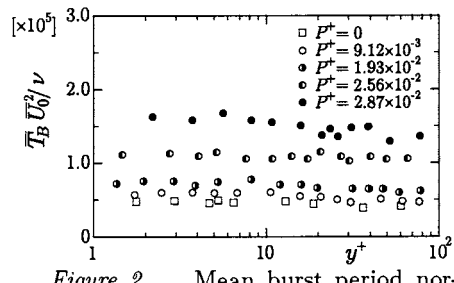


Figure 1. Scaling of the mean burst period with inner variables

Figure 2. Mean burst period normalized by  $\nu/\bar{U}_0^2$ 

appropriate for the mean bursting periods of ZPG flows (Blackwelder and Haritonidis, 1983; Kim and Spalart, 1987).

On the other hand, there are many arguments about the scaling of the mean burst period in APG flows (White and Tiederman, 1990; Tillman and Kistler, 1996; also see Table 1). Bandyopadhyay (1982) claimed that a universal value of the nondimensional period between bursts does not exist, though this might be an extreme view. It becomes obvious from Fig. 2 that the mean burst period  $\bar{T}_B$  changes significantly with  $P^+$ . This increase in the mean burst period cannot be correlated to the conventional viscous time scale  $\nu/u_\tau^2$ , as shown in Fig. 1. Moreover, if we scale the bursting period with the viscous time scale, the energy-producing events in the APG flow seem to occur at shorter intervals than those in the ZPG flow. Thus, one might think that the turbulent motions in the APG flow are still active (Tillman and Kistler, 1996). However, in the APG flow, near-wall turbulent motions are less active

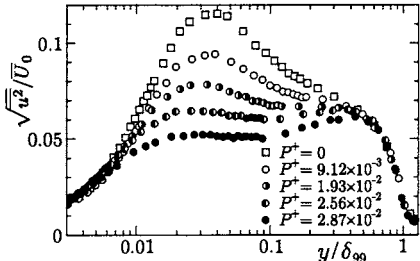


Figure 3. Turbulent intensities of streamwise velocity fluctuation  $u$

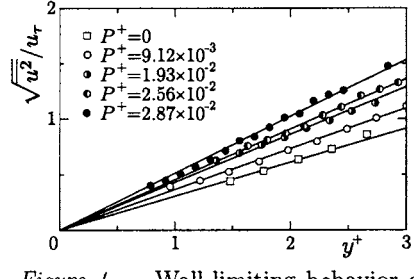
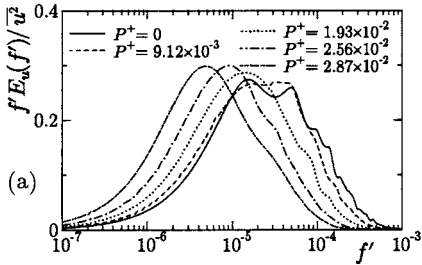
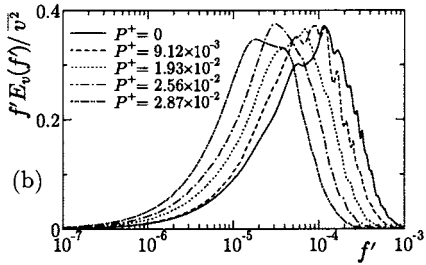


Figure 4. Wall-limiting behavior of streamwise intensity



(a)



(b)

Figure 5. Power spectra of velocity fluctuations in the log region ( $y^+ \approx 50$ ,  $y/\delta_{99} \approx 0.1$ ); (a) streamwise  $u$ , (b) wall-normal  $v$

because of the reduction in the turbulent energy production (Nagano *et al.*, 1998).

Figure 3 shows the intensity profiles of the streamwise velocity component  $u$ , normalized by the free-stream velocity  $\bar{U}_0$  at the inlet to the test section. The abscissa indicates the distance from the wall normalized with the boundary layer thickness  $\delta_{99}$ . With an increasing APG effect, the reduction in turbulence intensities can be seen in the wall region ( $y/\delta_{99} < 0.4$ ), whereas all the profiles in the outer layer are kept unchanged. These profiles cannot be correlated in conventional wall coordinates even in the near-wall region. As shown in Fig. 4, the distributions of  $\sqrt{\bar{u}^2}/u_\tau$  near the wall follow each  $P^+$ -dependent straight line which coincides with the origin. From these results, the conventional scaling law using the viscous scale ( $u_\tau, \nu$ ) cannot be applied to the scaling of the near-wall statistics for non-equilibrium APG flows.

Power spectra of  $u$  and  $v$  fluctuations in the log region ( $y^+ \approx 50$ ) are presented in Figs. 5(a) and 5(b), respectively, against the dimensionless frequency  $f'$  ( $= f\nu/\bar{U}_0^2$ ). As expected from the bursting periods in Fig. 2, the frequencies of energy-containing eddies in both spectra gradually shift toward the lower frequency with increasing  $P^+$ .

As described above, in the APG flows, the change in the time scale is apparent. Thus, to obtain the best scaling parameter, we have ex-

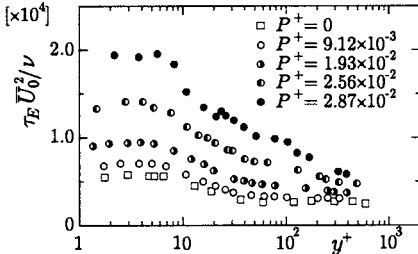


Figure 6. Distributions of Taylor time scale  $\tau_E$

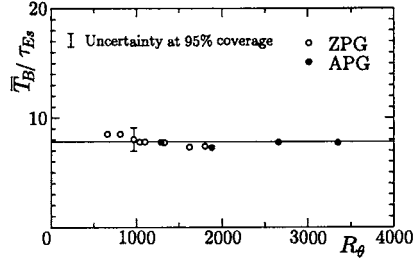


Figure 7. Mean burst period normalized by  $\tau_{E_s}$

amined the six characteristic time scales, i.e., the viscous time scale, the Kolmogorov time scale, the Taylor time scale, the time scale for energy-containing eddies, the integral time scale, and the time scale corresponding to mean shear rate. By using the above six time scales, we have analyzed the temporal turbulent structures of the APG flows. As a result, the Taylor time scale  $\tau_E$  is found to be the most appropriate for representing the temporal behavior of turbulence quantities and for universally scaling the turbulence statistics<sup>1</sup>. The distributions of the measured Taylor time scale  $\tau_E$  ( $= \sqrt{2 \bar{u}^2 / (\partial u / \partial t)^2}$ ) in the wall-normal direction are shown in Fig. 6. One may find that  $\tau_E$  increases with increasing pressure gradient parameters  $P^+$ . In proximity to the wall, however,  $\tau_E$  becomes almost constant for a given  $P^+$ . Thus, we define a near-wall Taylor time scale,  $\tau_{E_s}$ , by a value of  $\tau_E$  at the outer edge of the viscous sublayer, i.e.,  $y^+ \simeq 3$ . If we adopt  $\tau_{E_s}$ , as seen in Fig. 7, the normalized period  $\bar{T}_B / \tau_{E_s}$  tends to collapse at any pressure gradient level and any Reynolds number studied.

The sample result of the spectra arranged with a new dimensionless frequency,  $f''$  ( $= f \tau_E$ ), is presented in Fig. 8. Spectra of both the  $u$  and  $v$  fluctuations are found to be correlated well. As can be clearly seen from these figures, we conclude that the Taylor time scale is the best scaling parameter for both ZPG and APG flows.

Next, we present the scaling of the wall-limiting behavior of streamwise turbulence intensity in Fig. 9. If the conventional wall unit is used as a length scale, remarkable differences appear in the wall-limiting behavior between the ZPG and APG flows, with a systematic deviation from the ZPG case, as shown in Fig. 4. On the other hand, the use of the time scale  $\tau_{E_s}$  makes all the profiles collapse with the linear relation,

<sup>1</sup>Klewicki's group has proven that the Taylor time scale is most relevant to uniquely represent the power spectra at much higher Reynolds numbers, i.e.,  $R_\theta \simeq 10^6 - 10^7$  (IUTAM Symposium, Princeton, 2002).

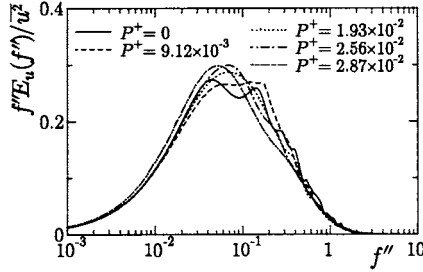


Figure 8. Power spectra of  $u$  arranged with  $f''$  in the log region ( $y^+ \simeq 50$ ,  $y/\delta_{99} \simeq 0.1$ )

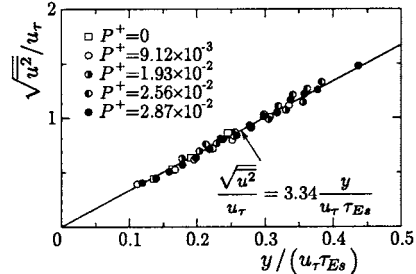


Figure 9. Wall-limiting behavior of streamwise intensity arranged with  $\tau_{Es}$

$$\sqrt{\bar{u}^2}/u_\tau = 3.34 y/(u_\tau \tau_{Es}) \quad \text{or} \quad \sqrt{\bar{u}^2} \cdot \tau_{Es}/y = 3.34, \quad (1)$$

irrespective of the values of  $P^+$  as shown in Fig. 9.

## 4. Conclusions

Experimental investigation has been made on the scaling of the near-wall structures in non-equilibrium turbulent boundary layers subjected to adverse pressure gradients. The main results are: The conventional scaling law using the wall units can not be applied to the scaling of the near-wall statistics of the non-equilibrium APG flows; and the Taylor time scale  $\tau_E$  is the most appropriate to describe the essential characteristics of the near-wall structure of non-equilibrium APG flows.

This work was supported by Japan Society for the Promotion of Science (JSPS) through Grant-in-Aid for Scientific Research (B) (No. 13450083).

## References

- Alfredsson, P.H. and Johansson, A.V., *Phys. Fluids*, **27** (1984), 1974.
- Bandyopadhyay, P.R., *Phys. Fluids*, **25** (1982), 1751.
- Blackwelder, R.F. and Haritonidis, J.H., *J. Fluid Mech.*, **132** (1983), 87.
- Hishida, M. and Nagano, Y., *Trans. ASME: J. Heat Transfer*, **101** (1979), 15.
- Houra, T., Tsuji, T., and Nagano, Y., *Int. J. Heat Fluid Flow*, **21** (2000), 304.
- Kim, H.T., Kline, S.J. and Reynolds, W.C., *J. Fluid. Mech.*, **50** (1971), 133.
- Kim, J. and Spalart, P.R., *Phys. Fluids*, **30** (1987), 3326.
- Lu, S.S. and Willmarth, W.W., *J. Fluid Mech.*, **60** (1973), 481.
- Luchik, T.S. and Tiederman, W.G., *J. Fluid Mech.*, **174** (1987), 529.
- Nagano, Y., Tsuji, T. and Houra, T., *Int. J. Heat Fluid Flow*, **19** (1998), 563.
- Rao, K., Narashimha, R. and Badri Narayanan, M.A., *J. Fluid Mech.*, **48** (1971), 339.
- Shah, D.A. and Antonia, R.A., *Phys. Fluids A*, **1** (1989), 318.
- Tillman T.G. and Kistler, A.L., *AIAA J.*, **34** (1996), 1070.
- White, J.B. and Tiederman, W.G., *ONR Rept.* (1990), PME-FM-90-2.

# **AN EXPERIMENTAL STUDY OF A SELF-PRESERVING BOUNDARY LAYER WITH A POWER-LAW VARIATION OF FREE-STREAM VELOCITY**

Shinsuke Mochizuki, Takatsugu Kameda and Hideo Osaka

*Yamaguchi University, 2-16-1 Tokiwadai, Ube 755-8611, Japan*

**Abstract:** A careful experimental investigation on the scaling law of the turbulent boundary layers was made at a self-preserving condition adjusting free-stream velocity in a power-law variation of  $x^n$ . The similarity of mean velocity profile was examined with the wall shear stress value determined by newly designed drag balance measurement device. The logarithmic velocity profile does hold universality with the Kármán constant 0.41 and additive constant C=5.0 under a mild adverse pressure gradient.

**Key words:** Self-preserving, Law of the wall, Drag balance measurement, Adverse pressure gradient

## **1. INTRODUCTION**

Turbulent boundary layers subjected by adverse pressure gradients are a major topic in fluid dynamics especially in engineering field such as diffuser or aircraft wing. Since experiment by Ludwig-Tillmann (1949), the mean velocity profile has been believed to hold same logarithmic form observed in a flat plate turbulent boundary layer. However, many corrections have been proposed for the similarity of the mean velocity profile in the wall layer and recently Nagano-Tagawa-Tsuji (1993) and Spalart-Watmuff (1993) have made the experimental verifications.

In an experimental investigation on the local similarity of the turbulent boundary layer that is continuously developing under the free-stream, we

must pay attention to the followings: 1.Measurement of the wall shear stress, 2.High level of two-dimensionality, 3.Well spatial resolution of sensors in high Reynolds number flows, and 4.Compatibility of local similarity to the equations of motion. The wall shear stress, the most important quantity for discussion of dynamics in the wall turbulence, should be determined by the method being free from any similarity assumptions. By employing quantitative measure such as balance in the momentum integral equation, two-dimensionality is carefully set up over streamwise extent. The momentum integral equation tends to imbalance under strong adverse pressure gradient (Coles-Hirst, 1968). The similarity laws in boundary layers are supposed to be secured as Reynolds number approaches infinity. Otherwise, spatial resolution must be sufficiently well to measure correctly mean velocity as well as Reynolds stresses. The accepted local similarity of the statistical quantities must have compatibility to the equations of motion, that is, the equations of motion can be reduced to an ordinal differential equation by transformation with relevant velocity and length scales.

The similarity of mean velocity profile was investigated in a self-preserving boundary layer with power-law variation of the free-stream velocity. Zero-displacement drag balance measurement device has been designed to measure the wall shear stress value under the adverse pressure gradient. The logarithmic mean velocity profile will be presented from the careful experimental study under a mild adverse pressure gradient.

## 2. EXPERIMENTAL SET-UP AND MEASUREMENT TECHNIQUE

The experimental investigation was made in a low turbulence wind tunnel which test section is 1m wide and 6m long (Fig.1). Adjusting roof of the test section is making the power-low variation of free-stream velocity with a constant  $m=-0.188$  seen in Fig.3. A new drag balance instrument was developed for the wall shear stress measurement seen in Fig.2. The floating element has 20mm circular friction surface, 0.1mm gap for surrounding surface and 0.2mm lip size. A feedback system with magnetic coil keeps zero-displacement of the floating element to prevent errors due to

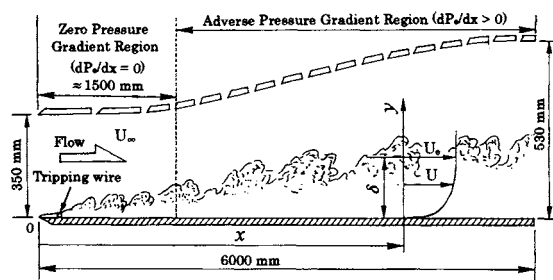


Figure1: Flow field, coordinate system and nomenclature.

non-uniform gap. The velocity measurement was carried out with a single and a crossed hot-wire probes connected to constant temperature anemometers. The sensors were made of a tungsten filament of 0.0031mm diameter and 0.62mm active length. Spatial separation of two wires of the crossed hot-wire probe is 0.25mm which corresponds to 5 times the viscous wall length over self-preserving flow.

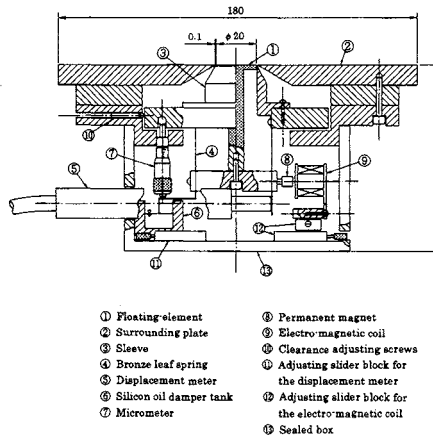


Figure 2: Zero-displacement drag balance.

### 3. EXPERIMENTAL RESULTS

#### 3.1 Self-preserving development

Compatibility of self-similar profiles to the equations of motion requires constant skin-friction coefficient and linear development of boundary layer thickness (Rotta, 1962). As confirmed in Fig.3, the boundary layer thickness grows linearly over  $x=3,750\text{-}4,700\text{mm}$ . The local skin-friction coefficient plotted as a function of momentum thickness Reynolds number takes smaller values compared with the semi-empirical equations for flat plate boundary layer (Fig.4). The Preston tube method utilizing 1.06mm dynamic pressure tube gives somewhat larger coefficient under the adverse pressure gradient.

Employing the momentum integral equation quantitatively checked two-dimensionality of the boundary layer:

$$2 \frac{d\theta}{dx} = - \frac{2\theta}{U_e} \frac{dU_e}{dx} (H + 2) - \frac{2}{U_e^2} \int_0^\delta \frac{\partial}{\partial x} (\bar{v}^2 - \bar{u}^2) dy - \frac{2}{U_e^2} \int_0^\delta \left( \int_0^y \frac{\partial^2 \bar{u}\bar{v}}{\partial x^2} dy - \delta \frac{\partial^2 \bar{u}\bar{v}}{\partial x^2} \right) dy + C_f, \quad (1)$$

must be balanced. Imbalance in the equation was evaluated with experimental data and typical value over  $x=3,750\text{-}4,500\text{mm}$  is 5% of the left hand side term. Specifics of some important parameters are given in Table 1.

Table 1. Characteristics of the boundary layer at measuring location ( $x=4,500\text{mm}$ )

$R_\theta \equiv \theta U_1 / \nu$	10,700	$\delta^+ \equiv \delta u_t / \nu$	2,580
$\beta = (\delta^+ / \tau_w) dP_e / dx$	1.302	$P^+ \equiv (v / \rho u_t^3) dP_e / dx$	0.0024
Wake parameter $\Pi$	1.590	Shape factor $G$	10.2

### 3.2 Logarithmic mean velocity profile

Logarithmic mean velocity is given in Fig.5 and compared with a standard log-law with Kármán constant of 0.41 and  $C=5.0$  (Coles-Hirst, 1968). The logarithmic mean velocity profile agrees well with the standard profile, if the wall shear stress value is determined by the reliable drag balance measurement.

## REFERENCES

- Ludwig,H. and Tillman,W.: "Investigations of the wall shearing stress in turbulent boundary layers", NACA TN 1285, 1949.
- Nagano,Y., TagawaM. and Tsuji,T.: "Effect of adverse pressure gradients on mean flows and turbulence statistics in a boundary layer", *Turbulent Shear Flows 8*, 7-21, Springer, 1993.
- Spalart,P.R. and Watmuff,J.H., "Experimental and numerical study of turbulent boundary layer with pressure gradient", *J. Fluid Mech.*, **249**, 337-371, 1993.
- Coles,D. and Hirst,E.A.: "The young persons guide to the data", *Proc. AFOSR-IFP-Stanford Conference*, 1968.
- Rotta,J.C.: "Turbulent boundary layers in incompressible flow", *Progress Aeronautical Science*, **2**, Pergamon press, 1962.

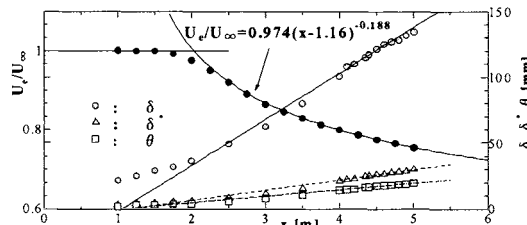


Figure 3: Streamwise variation of free-stream velocity and boundary layer thickness.

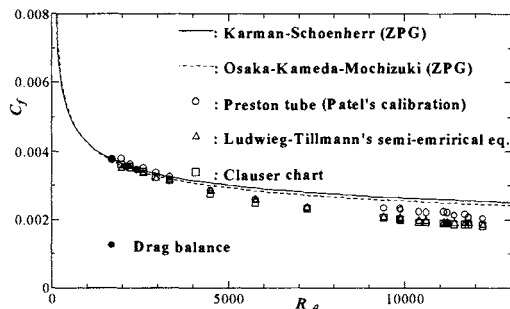


Figure 4: Local skin-friction coefficient.

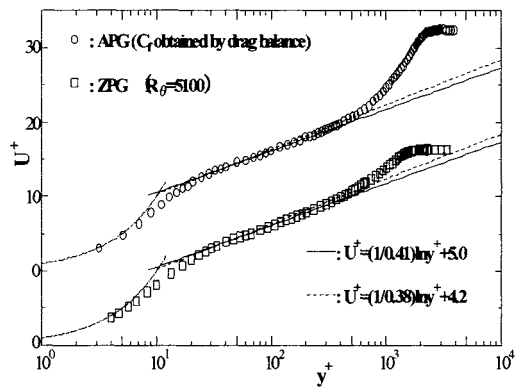


Figure 5: Logarithmic mean velocity profile.

# **ON THE USE OF THE REYNOLDS NUMBER TO SCALE THE EFFECTS OF OBSTACLES ON A DEPTH-LIMITED FLOW IN A GRAVEL-BED RIVER**

Thomas Buffin-Bélanger<sup>1</sup> and André G. Roy<sup>2</sup>

<sup>1</sup>*Geography Department, The University of Western Ontario, London (Ontario), N6A 5C2, Canada. (tbuffinb@uwo.ca)* <sup>2</sup>*Département de géographie, Université de Montréal, C.P. 6128 Succ. Centre-Ville, Montréal (Québec), H3C 3J7, Canada. (andre.roy@umontreal.ca)*

**Abstract:** Results from flume experiments looking at the effects of a pebble cluster on the turbulent flow field in flows at four high Reynolds numbers are presented. The Reynolds number did not control the flow dynamics in the vicinity of the cluster. However, significant effects of flow depth and velocity were observed.

**Key words:** roughness element, gravel-bed river, high Reynolds number

## **1. INTRODUCTION**

Turbulent flows in gravel-bed rivers are dominated by the effects of protruding roughness elements, such as large clasts and pebble clusters. The effects of these roughness elements and their spatial arrangement have critical implications on flow resistance, sediment transport dynamics, and micro-habitat characteristics. Although some effects are beginning to be well understood, the flow structure around pebble clusters has yet to be described for the wide range of flow depths and velocities occurring in rivers. These studies have to take into account that the turbulent boundary layer in rivers may not be fully developed, as the flow is depth-limited. The effects of a pebble cluster on the flow will take many forms in response to the complex assemblage of velocities and depths. This is usually assessed by describing the flow using a Reynolds number. Experimental studies of flows at low

Reynolds number have shown that flow regions and flow structures are dependent upon the Reynolds numbers. At high Reynolds number, this dependency seems to disappear. By combining velocity and depth, the Reynolds number may therefore hide the separate effects of these variables on the turbulent flow. We address this issue using laboratory experiments with a natural pebble cluster submitted to flows at a high Reynolds number.

## 2. METHODS AND DATA ANALYSIS

Experiments were carried out in a recirculating flume. A natural pebble cluster was positioned on water worked gravels. The three velocity components were measured using an Acoustic Doppler Velocimeter. Dense grids of one minute time series at 25 Hz were sampled in the streamwise-vertical plane along the cluster centerline. Two flow depths and two flow velocities were used in combination to produce four flows with Reynolds numbers ranging from 49 000 to 180 000. This arrangement permitted the individual and combined effects of velocity and depth to be investigated. Flow visualization was done by injecting a milky white fluid downstream from the obstacle.

Time series were validated for weak signal correlation and signal-to-noise ratio, submitted to a spike removal function, and passed through a Gaussian low-pass filter. We investigated the spatial variability of the normalized magnitude of the *UV* flow vector ( $M^*$ ) and of the turbulent kinetic energy ( $K^*$ ) defined as:

$$M^* = [(\langle U \rangle^2 + \langle V \rangle^2)^{0.5}] / u^* \quad (1)$$

$$K^* = [0.5 (\langle u^2 \rangle + \langle v^2 \rangle + \langle w^2 \rangle)] / (u^*)^2 \quad (2)$$

where  $U$  and  $V$  are instantaneous measurements in the streamwise and vertical velocity directions,  $u$ ,  $v$  and  $w$  are the velocity fluctuations of the streamwise, vertical and lateral velocity components respectively,  $\langle \cdot \rangle$  designates an average value,  $u^*$  is the shear velocity measured upstream from the pebble cluster.

## 3. THE TURBULENT FLOW FIELD

The spatial distributions of  $K^*$  for the four flows is shown in Figure 1. The effect of the cluster is clearly seen downstream as  $K^*$  values are four times higher than upstream. This occurs in a zone expanding from the top of the obstacle towards both the water surface and the bed. Although this was

observed at all flow conditions, there were some differences between flows. For example, the region of high  $K^*$  extends further downstream for the deep flows than for the shallow ones where it expands closer to the bed. Two mechanisms can explain these patterns. The first one relates to flow separation and shearing in the zone downstream from the crest of the cluster and probably to the development of shedding motions. These are low velocity fluid parcels that are ejected towards the surface from the recirculating flow region downstream from the obstacle (Figure 2). Once ejected, these parcels move obliquely towards the surface as fluid with higher velocities is separating them. The second mechanism comes from the fluctuation of the reattachment point. The location of this point fluctuates in time, and hence there are regions downstream from the cluster that are intermittently located in the recirculating flow region or in the upwelling flow region. This generates strong momentum exchange as flow motions shift from an upstream to a downstream orientation.

Figure 1. Spatial distribution of  $K^*$

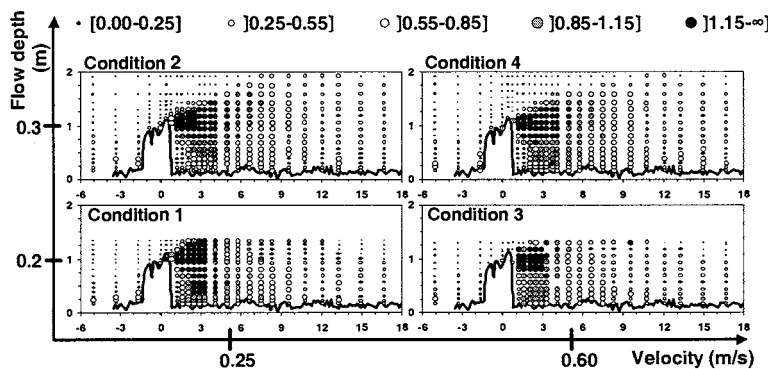
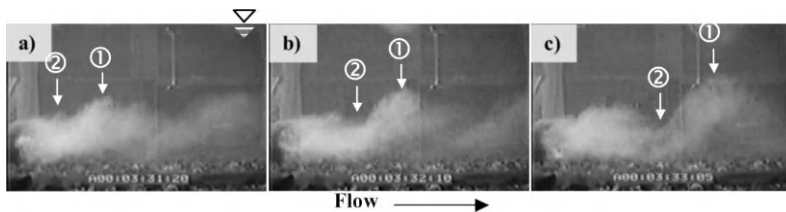


Figure 2. Interlaced (1) shedding and (2) high speed sweeping motions.

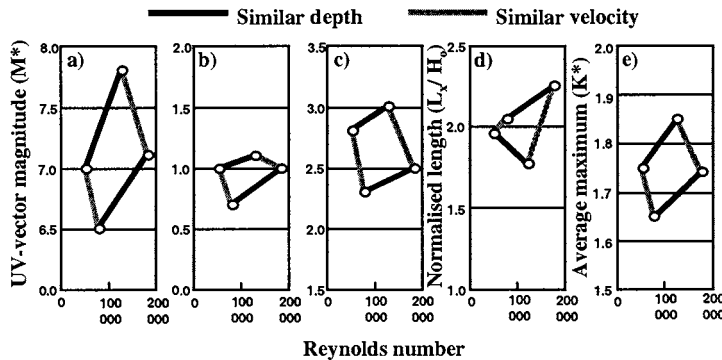


#### 4. SCALING RELATIONSHIPS

We have investigated the relationships between parameters from key flow regions in the vicinity of the cluster and the Reynolds number (Figure 3). Weak relationships emerged. However, when looking at the individual

effect of velocity or depth, clearer relationships appear. To highlight these, grey lines and dark lines were used to connect flow conditions with similar velocity and similar depth, respectively (Figure 3).  $M^*$  increases with increasing flow velocity and decreases with flow depth when depth and velocity are kept constant, respectively (Figure 3a, b and c). The length of the recirculating flow region is nearly twice as long as the height of the cluster (Figure 3d). Increasing the depth of flow for a similar velocity results in a longer recirculating flow region. Different slopes reveal that this effect is more pronounced for higher velocities than for lower velocities. However, there is no systematic variation in the length of the recirculating zone when velocity is increased for a similar depth. Finally, Figure 3e shows that, from low to high velocities for similar depths, the maximum  $K^*$  increases whereas from low to high water depths for similar velocities, the maximum  $K^*$  decreases.

Figure 3.  $M^*$  in a) the accelerating flow region, b) the recirculating flow region, and c) the upwelling flow region. d) the length of the recirculating flow region. e)  $K^*$  downstream from the obstacle.



## 5. CONCLUSIONS

The results show that the Reynolds number does not control the magnitude and direction of  $M^*$ , the length of the recirculating flow region, nor the maximum  $K^*$  downstream from the cluster. Thus, the flow dynamics surrounding the cluster seems independent of the Reynolds number. However, the Reynolds number can be obtained from several combinations of depths and velocities, this conclusion hides important individual effects from these two variables on the flow dynamics around a cluster.

The authors thank the Fonds FCAR and NSERC of Canada for their financial support. The first author thanks the Department of Geography at Lancaster University (UK). Dr. A. Kirkbride provided valuable assistance.

# REYNOLDS NUMBER SCALING OF LEAKAGE VORTEX FLOW

Wesley H. Brewer

*Computational Simulation and Design Center*

*Mississippi State University*

*Starkville, MS 39762*

[wbrewer@erc.msstate.edu](mailto:wbrewer@erc.msstate.edu)

Stuart D. Jessup

*Naval Surface Warfare Center*

*Carderock Division*

*9500 MacArthur Boulevard*

*West Bethesda, MD 20817*

[JessupSD@nswccd.navy.mil](mailto:JessupSD@nswccd.navy.mil)

Young T. Shen

*Naval Surface Warfare Center*

*Carderock Division*

*9500 MacArthur Boulevard*

*West Bethesda, MD 20817*

[ShenYT@nswccd.navy.mil](mailto:ShenYT@nswccd.navy.mil)

**Abstract** To study the Reynolds number scaling of cavitation inception, a ducted propulsor simulation is developed and extensively validated with experimental results. The simulation is used as a tool for investigating the minimum pressure, circulation, and axial/tangential velocities in the vortex core, thus providing a means of correlating these quantities to Reynolds number. The simulation reveals that the leakage vortex exhibits little dependence on Reynolds number, while the trailing edge vortex appears to exhibit classical trends. Moreover, the trailing edge, albeit the weaker vortex, appears to be causing inception.

**Keywords:** cavitation, inception, tip, leakage, flow, vortex, unstructured, computational fluid dynamics

## 1. Introduction

Tip-leakage vortex interaction is the primary cause of cavitation inception for ducted propulsors. Little has been published on the tip-leakage vortex interaction from an experimental approach. One notable exception is a paper by Farrell and Billet (Farrell and Billet, 1994), who develop a correlation to predict leakage vortex minimum pressure. There is even less work on computational simulation of tip-leakage flows. Another notable exception is a paper by Lee et al. (Lee et al., 1998), who numerically model the leakage vortex flow evident in ducted propulsors using a structured approach. In this work, an unstructured simulation is developed to study Reynolds number scaling of tip-leakage vortex cavitation inception, and is discussed in more detail in (Brewer, 2002). Simulations were performed at a variety of Reynolds numbers ranging from one million to one billion, representative of model to full scale Reynolds numbers.

## 2. Simulation methodology

Recently, Mississippi State University developed an unstructured, Reynolds-Averaged Navier-Stokes (RANS) solver, named *U<sup>2</sup>NCLE*. The unstructured approach allows for automated nodalization of complex geometries using the Advancing-Front/Local-Reconnection (AFLR) unstructured grid generator (Marcum, 1995). *U<sup>2</sup>NCLE* solves the finite-volume based discretization of the integral form of the RANS equations (Hyams, 2000):

$$\frac{\partial}{\partial t} \int_{\Omega} Q dV + \int_{\partial\Omega} \vec{F} \cdot \vec{n} dA = \frac{1}{Re} \int_{\partial\Omega} \vec{G} \cdot \vec{n} dA + \int_{\Omega} s dV \quad (1)$$

where  $Re$  is the Reynolds number,  $Q = [p, u, v, w]^T$ ,  $\vec{F}$  is the inviscid flux vector,  $\vec{G}$  is a viscous flux vector containing the shear stress terms, and  $s$  is a source term to account for relative motion of the propeller. Equation 1 is discretized over small vertex-centered control volumes  $\Omega$  created by the median dual of the surrounding vertices. This equation is solved interactively with a one-equation Spalart-Allmaras turbulence model. The system of equations are solved on a parallel computer using a discretized Newton relaxation (DNR) approach (Whitfield and Taylor, 1991).

The simulation is performed on a ducted propulsor which was also experimentally investigated in the 36-inch water tunnel at the NAVSEA Surface Warfare Center, Carderock Division. Figure 1 shows the resulting trailing vortex structure from both the experiment and the simulation.

A numerical post-processing analysis tool was developed to quantitatively investigate the resulting vortex structure. The method interrogates the simulated flowfield to extract such quantities as: (1) the average vortex diameter  $a$ ,

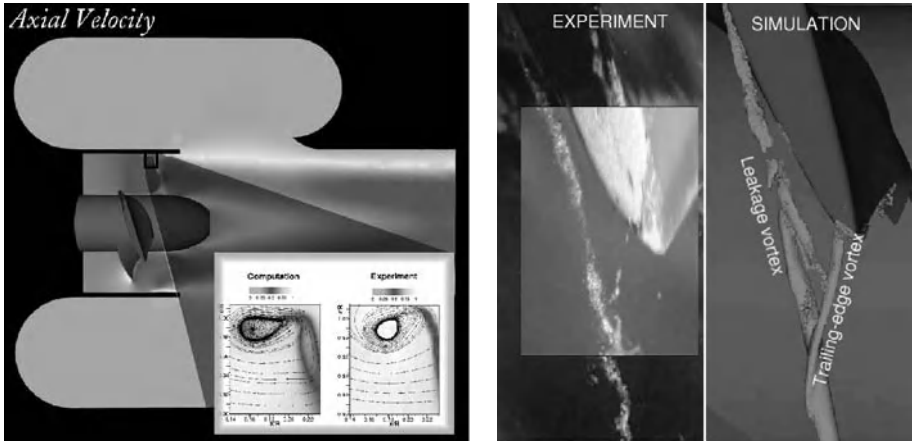


Figure 1. Simulation of ducted propulsor in 36-inch water tunnel test section. *Left:* axial and streamwise velocity distribution. *Right:* Cavitation comparisons with experiment.

Table 1. Reynolds dependence on  $-C_{P_{min}}$ ,  $\gamma$ ,  $v_t^{avg}$ , and  $v_s$ .

$Re$	$\gamma$	$-C_{P_{min}}$	$v_t^{avg}$	$v_s$
$1.0 \times 10^6$	0.0710	4.8110	1.2496	1.6619
$2.0 \times 10^6$	0.0813	5.0051	1.3231	1.6875
$1.2 \times 10^7$	—	5.3166	1.3644	1.7095
$1.0 \times 10^8$	—	5.8937	1.5021	1.7802
$1.0 \times 10^9$	—	6.0776	1.5181	1.8217

lated flowfield to extract such quantities as: (1) the average vortex diameter  $a$ , (2) circulation  $\gamma$ , (3) average  $v_t^{avg}$  and maximum  $v_t^{max}$  tangential velocities, (4) minimum pressure  $-C_{P_{min}}$ , and (5) the vortex core streamwise velocity  $v_s$ .

### 3. Scaling analysis

As shown in Figure 1, the leakage vortex is the predominant vortex, which is easier to compute and analyze. The simulation was interrogated along the leakage vortex core axis to find minimum core pressure, maximum average tangential velocity, and streamwise core velocity. The Reynolds dependence of these variables are given in Table 1. From these results, the following trends are observed for the leakage vortex:

$$-C_{P_{min}} \sim Re^{0.03} \quad v_t^{avg} \sim Re^{0.03} \quad v_s \sim Re^{0.01} \quad \gamma \sim Re^{0.02} \quad (2)$$

Thus, the leakage vortex is shown to exhibit a very low dependence on Reynolds number. A similar trend in Reynolds number dependence of the leakage vortex is shown in (Green, 1989). However, the trailing edge vortex exhibits more classical trends that are evidenced in corresponding experimental investigations (Shen, 2001).

The scaling exponent,  $n$ , is computed from the computational results in the following manner:

$$n = \log_b \left( \frac{C_{P_{min}}^s}{C_{P_{min}}^m} \right) \quad \text{where} \quad b = \frac{Re_s}{Re_m} \quad (3)$$

In this analysis,  $Re_m$  was taken constant at  $1.0 \times 10^6$ , while  $Re_s$  was allowed to vary through the Reynolds number range. Expressing this relationship in the form of a power law gives:

$$\frac{\sigma_s}{\sigma_m} = \frac{C_{P_{min}}^s}{C_{P_{min}}^m} = \left( \frac{Re_s}{Re_m} \right)^n \quad (4)$$

The following table shows the computed results of the comparison between the leakage vortex scaling exponent  $n_{LV}$  and the trailing-edge vortex exponent  $n_{TEV}$  for different model to full-scale scaling ratios  $Re_s/Re_m$ . Figure 2 reveals the relative independence of the Reynolds number on the Leakage vortex flow.

$Re_s/Re_m$	$n_{LV}$	$n_{TEV}$
2	0.057	0.350
12	0.051	0.323
100	0.044	0.306
1000	0.034	0.264

## 4. Summary

A Reynolds number scaling analysis using an unstructured RANS simulation revealed that the static minimum pressure is not sensitive to the Reynolds number. Cavitation inception measurements show strong Reynolds number dependency. Leakage vortex cavitation inception is not directly related to the static minimum pressure. Therefore, it is postulated that the trailing edge tip vortex, albeit a much weaker vortex, is the mechanism causing cavitation inception on ducted propulsors.

## Acknowledgments

Support for this research was provided by Dr. Patrick Purtell of ONR under grant number N-00014-01-1-0455-01050428 and was monitored by Dr. Kihah Kim. This support is greatly appreciated. *Soli Deo gloria.*

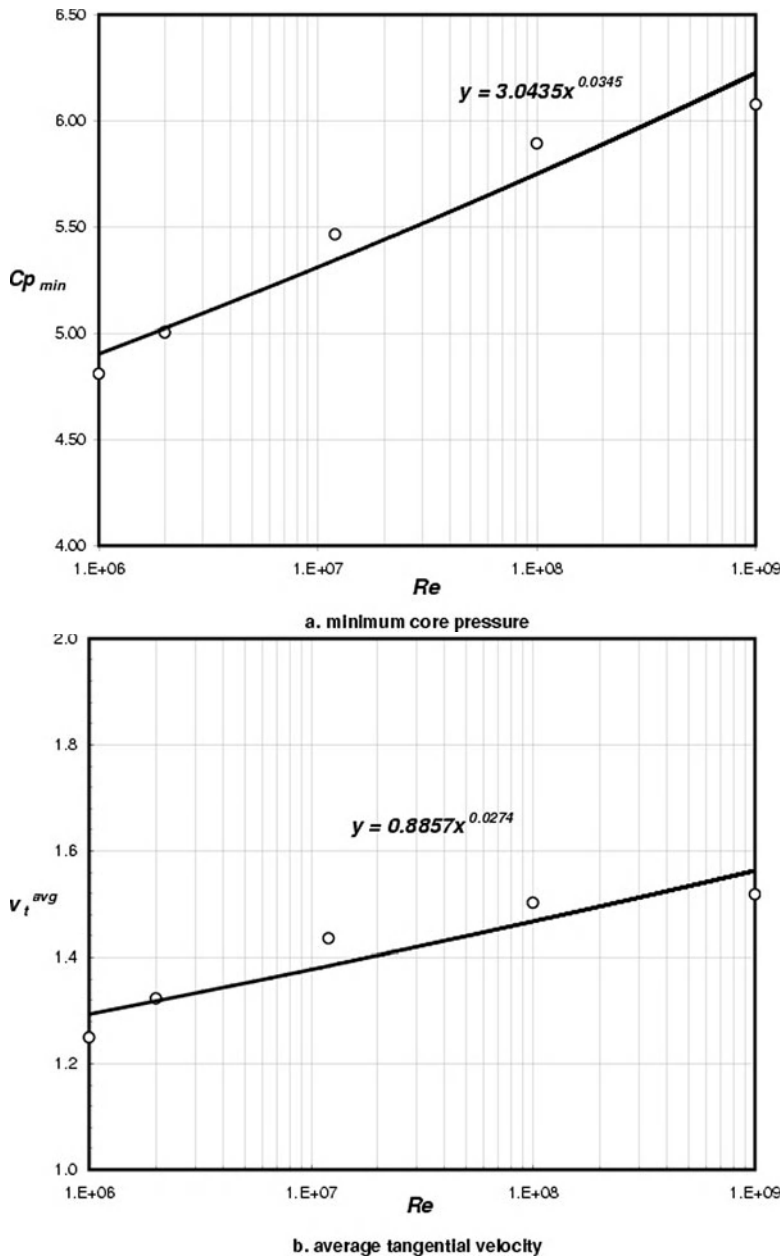


Figure 2. Reynolds number dependence on pressure and tangential velocity.

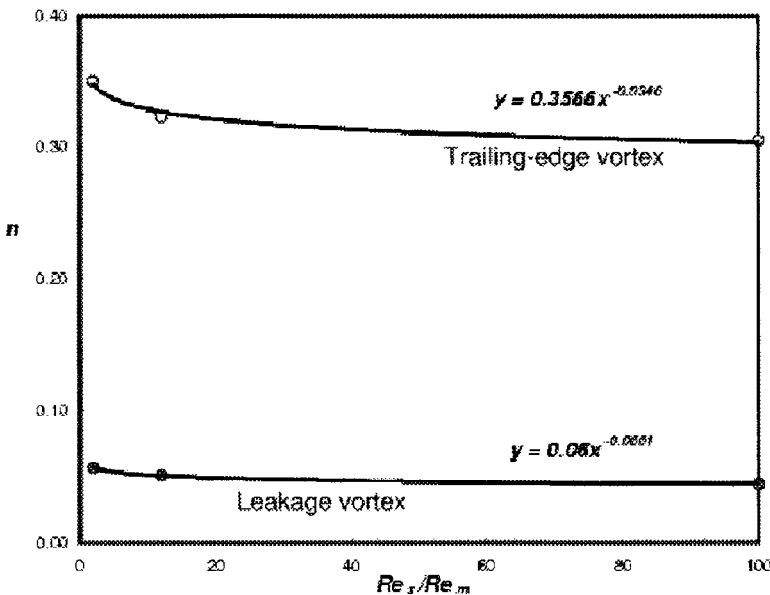


Figure 3. Reynolds number dependence on scaling exponent  $n$ .

## References

- Brewer, W. H. (2002). *On simulating tip-leakage vortex flow to study the nature of cavitation inception*. Ph.D. dissertation, Mississippi State University, May 2002.
- Farrell, K. J., and M. L. Billet (1994). "A Correlation of Leakage Vortex Cavitation in Axial-Flow Pumps," Journal of Fluids Engineering [September].
- Green, S. I. (1998). "Trailing Vortex Core Unsteadiness - an Exploratory Study of Reynolds Number Effects," AIAA Journal, 88-3623-CP.
- Hyams, Daniel (2000), "An Investigation of Parallel Implicit Solution Algorithms for Incompressible FLows on Unstructured Topologies," Ph.D. Dissertation, Mississippi State University [May].
- Lee, Y.-T., J. Feng, C. Merkle, and M. Tse (1998). "Effects of Tip-Clearance Flows," Proceedings of the Twenty-Second Symposium on Naval Hydrodynamics, pp. 959-972, Washington, D.C.,
- Marcum, D. L., and N. P. Weatherhill (1995). "Unstructured Grid Generation Using Iterative Point Insertion and Local Reconnection." AIAA, 33(9) [September], pp. 1619-1625.
- Shen, Y.T., Stuart D. Jessup, and Scott Gowing (2001). "Tip Vortex Cavitation Inception Logarithmic scaling." Naval Surface Warfare Center Technical Report, NSWCCD-50-TR-2001/060 [October].
- Whitfield, D. L. and L. K. Taylor (1991). "Discretized Newton-Relaxation Solution of High Resolution Flux-Difference Split Schemes," AIAA Paper No. 91-1539 [June].

# EVALUATION OF MIXING ENERGY IN LABORATORY FLASKS

Vikram J. Kaku

*Department of Mechanical Engg, Temple University, Philadelphia, PA*

Michel C. Boufadel

*Department of Civil and Environmental Engg, Temple University, Philadelphia, PA*

boufadel@temple.edu

Albert D. Venosa

*National Risk Management Lab, US Environmental Protection Agency, Cincinnati, OH*

**Abstract** Turbulence generated in the Swirling flask (SF) and the Baffled flask (BF) by an orbital shaker (at 150 RPM) were examined using hot-wire anemometer (HWA) data. Two-dimensional (i.e. radial and azimuthal) velocity measurements were used to determine dissipation rates, and Kolmogorov microscales within the flasks. The energy dissipation rate in the BF was about one order of magnitude larger than that in the SF. The size of the Kolmogorov microscale in the BF was smaller than that in the SF, thereby allowing for better mixing.

**Keywords:** Energy dissipation rate, Kolmogorov microscale, Oil spills, Hot-wire anemometer.

## 1. Introduction

The dispersion of oil during an oil spill in the sea is strongly dependent on the turbulence structure of waves. The evaluation of the effectiveness of a particular dispersant at sea has been hampered by large experimental uncertainties in the sea. Hence various governmental agencies have adopted laboratory experiments. A widely used experiment is the Swirling flask (SF) test (Fingas, et al., 1987). It consists of placing a mixture of seawater, oil and dispersants in the SF positioned on an orbital shaker. The EPA is considering to use Baffled flask (BF), whose baffles results in an over-and-under motion of water flow.

We have adopted the energy dissipation rate as a surrogate measure for the mixing occurring in each flask (Camp and Stein, 1943). These rates were computed based on velocity measurements (obtained using a hot-wire anemometer) in each flask.

## 2. Experimental Set-up

The glassware used in this work consisted of a 125 ml simple swirling flask (SF) and a 150 ml simple baffled flask (BF). The set-up included an orbital shaker, sliding position table with flask holder and a hot wire anemometer (HWA) integrated with a computer data acquisition module. Each flask contained 120 ml water as the working fluid, and was held in place by a flask holder. The hotwire was TSI model 1054B constant-temperature anemometer with 1210-20W single cylindrical quartz-coated platinum probe. The HWA was interfaced to a computer using data acquisition board, DAS 1401, by Keithley with a built-in analog-to-digital circuit. Labtech Notebook Pro, by Laboratory Technologies, was used to acquire data. Data (velocities) were collected from HWA for an orbital shaker speed of 150 RPM. The data sampling frequency was 1000 Hz. The velocities were measured in the center vertical plane at an interval of 2 mm in the radial direction. Seventy and eighty locations were sampled in the SF and the BF, respectively. The sampling duration was 10 sec.

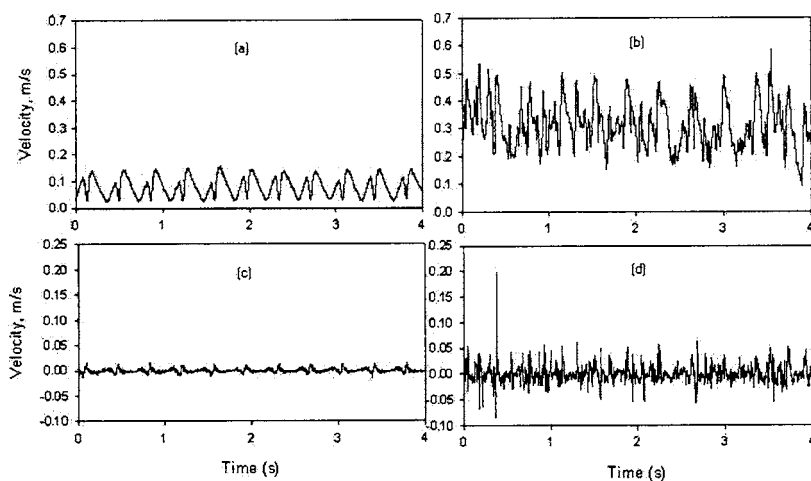


*Figure 1.* Representative time series in the SF and BF. (a and b) Velocity series; (c and d) Turbulent velocity series.

### 3. Data Analyses and Results

#### 3.1 Signal Characteristics

Fig. 1 shows time series of the radial velocity signal in the SF and the BF, 10 mm below the surface of the water. Time series of the SF (fig.1(a)) shows a 0.4 sec periodicity (roughly equivalent to 150 RPM i.e. orbital shaker speed). This was confirmed by autocorrelation analysis of the signal (refer fig.7 of Kaku, *et al.*, 2002). Weighted moving average method was used to obtain turbulent velocity, shown in fig.1(c and d). It can be seen that there are higher turbulent velocity fluctuations in the BF than that in the SF.

#### 3.2 Spectral Analyses

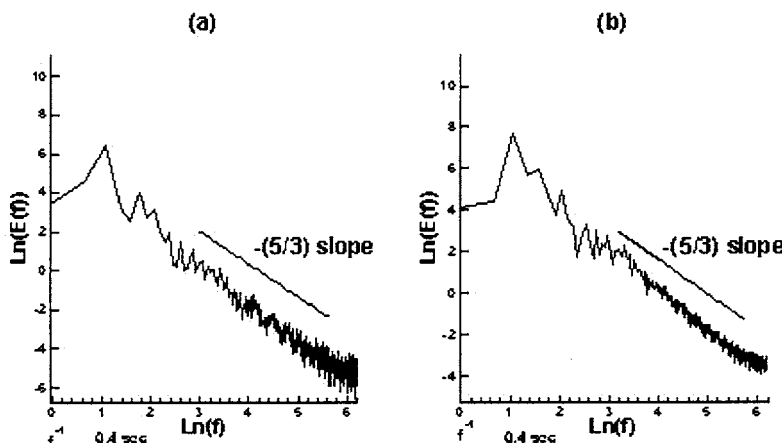


Figure 2. One-dimensional (radial) energy spectra (a)SF (b)BF

The one-dimensional energy spectrum  $E(f)$  as a function of frequency satisfies the following equality:

$$\overline{u'^2} = \int_0^{\infty} E(f) df \quad (1)$$

where  $u'$  is the turbulent velocity fluctuation, the overbar represents time average, and  $f$  is the radian frequency ( $2\pi/\text{time}$ ). The spectra (fig.2) show typical characteristics of the turbulence energy spectrum; at high frequency a  $-5/3$  slope emerges (see also the work of Kaku, *et al.*, 2002).

### 3.3 Energy Dissipation Rate

The dissipation rate can be calculated as follows:

$$\epsilon = A \frac{\overline{u'^2}}{\tau_E} \quad (2)$$

where A is a constant of order unity and  $\tau_E$  is Eulerian integral time scale.  $\tau_E$  is calculated by numerical integration of the filtered autocorrelation coefficient function up to the first zero crossing. The Kolmogorov microscale was estimated by:

$$\eta = \left( \frac{\nu^3}{\epsilon} \right)^{1/4} \quad (3)$$

where  $\nu$  is the kinematic viscosity of water. All the results are summarized in table 1.

*Table 1.* Summary of Turbulence parameters in the SF and BF

Flask	Mean Velocity $u_{avg}$ (cm/s)	Avg. Diss. rate $\bar{\epsilon}$ ( $m^2/s^3$ )	Integral time $\tau_E$ (sec)	Kolmogorov microscale $\eta(\mu m)$
SF	6.0	$1.29 \times 10^{-4}$	0.202	296.70
BF	27.0	$6.33 \times 10^{-3}$	0.0592	112.11

### Acknowledgments

This research was supported by the USEPA through contract no. PR-OH-01-00381.

### References

- Camp, T.R. & P.C. Stein. (1943). "Velocity gradient and internal work in fluid motion," *J. Boston Soc. of Civ. Engrs.*, 30(4), pp. 219-237.
- Fingas, M.F., M.A. Bobra, & R.K. Velicogna. (1987). "Laboratory studies of the chemical and natural dispersibility of oil," *Proc. Int. Oil Spill Conf.*, American Petroleum Institute, pp. 241-246.
- Kaku, V.J., M.C. Boufadel, & A.D. Venosa. (2002). "Evaluation of mixing energy in the swirling and baffled flasks," *Oil & Hydrocarbon Spills III*, WIT Press, pp. 211-218.

# DRAG REDUCTION IN TURBULENT FLOWS USING LORENTZ FORCE ACTUATION

Jinil Park, Charles Henoch and Kenneth Breuer

## 1. Introduction

Results from an experiment on the effects of Lorentz force actuation on turbulent channel flows are presented. This concept has been explored for turbulent flow control in a variety of different geometrical configurations by a number of researchers both numerically (Crawford and Karniadakis, 1997; Berger et al., 2000) and experimentally (Nosenschuck and Brown, 1993; Henoch and Stace, 1995). The experimental results have demonstrated limited success but have been troubled by many problems, including electrode corrosion and bubble formation due to electrolysis, and ambiguities in assessing the changes in the drag due to the control. The current experiment uses Lorentz forces to actuate the turbulent shear flow with a *cross-flow* velocity,  $w(y, z, t)$  (where  $z$  is the crossflow coordinate, and  $y$  is the wall-normal coordinate). This mode of forcing is similar to spanwise oscillation (Jung et al., 1992; Choi and Roach, 1997) but does not require physical motion of the wall.

## 2. Actuator Design and performance

A schematic of the actuator used in the present experiments is shown in figure 1. In this configuration, the actuator is designed to generate a Lorentz force in the cross-flow direction (out of the page as shown in figure 1). This is accomplished by interlacing a series of Neodymium-Boron-Iron magnets ( $B \approx 0.5T$ ) oriented  $N - S - N - S$ , etc., with a series of electrodes which are also energized in an alternating manner:  $-$ ,  $+$ ,  $-$ ,  $+$ , etc. In this manner, the electric and magnetic field lines are always crossing each other such that the Lorentz force acts out of the page. The direction and magnitude of the Lorentz force is controlled by varying the electric field strength and polarity. The electrodes are protected with a conductive polymer paint so that corrosion and bubble formation are completely eliminated.

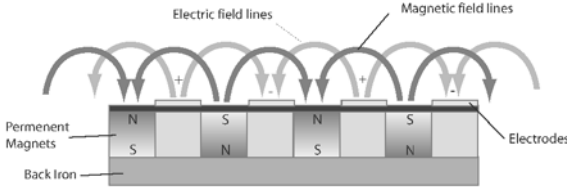


Figure 1. Schematic of the Lorentz Force Actuator. The flow is from left to right and the induced Lorentz force is out of the page. For the experiments described here, the spacing between magnets and electrodes is 3.1 mm

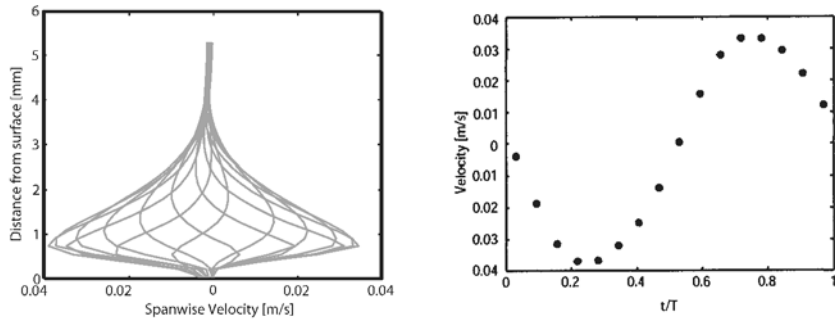


Figure 2. Left frame: velocity profiles due to oscillatory spanwise forcing using the Lorentz Force Actuator, Right frame: variation of spanwise velocity at a fixed height from the wall over a complete cycle.

Figure 2 shows a plot of the spanwise velocity profiles (averaged in the spanwise direction) induced by the Lorentz Force Actuator (or LFA) and operated with zero phase velocity (uniform spanwise oscillation). These profiles were measured in a “fishtank” - a tank with zero mean flow and measured using high-resolution PIV. Several profiles are plotted at different phases during the cycle. The velocity reaches a maximum at approximately 1 mm above the surface and dies out at a distance of about 4 mm. These length scales are solely determined by the streamwise spacing of the magnet-electrode pattern shown in fig 1. For the current experiments, this spacing was 3.1 mm (1/8 of an inch).

These profiles are in excellent agreement with the velocity profiles computed by (Berger et al., 2000). The maximum velocity, plotted as a function of time in figure 2b, shows a sinusoidal response of the flow suggesting a linear response to the input forcing voltage (also confirmed experimentally). The maximum induced velocity for this level of excitation (3 volts) is 4 cm/sec. More details of the actuators and their performance may be found in (Park et al., 2002).

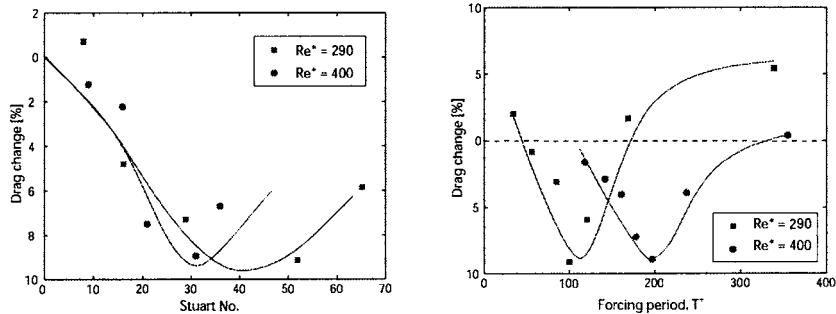


Figure 3. Left frame: Percent drag reduction versus Stuart number at two different Reynolds numbers. Right frame: Percent drag reduction versus non-dimensional forcing period,  $T^+$ .

### 3. Effects on Turbulent Drag

The effect of the spanwise oscillatory Lorentz force on the turbulent drag was measured in a low speed salt-water channel. The test section measures  $4.5 \times 91$  cm and is 3.6 meters long, ensuring fully developed turbulent flow. One wall of the last 150 cm of the test section is comprised of Lorentz force actuators, as described above. This entire surface is suspended on four wires so that a direct measurement of drag can be made over the actuated surface. The drag is measured by the force-rebalance of the plate using a servo-control system which holds the test surface at a fixed position, independently of the drag and the actuation forces. This arrangement reduces errors associated with the non-ideal stiffness of the hanging ribbons, electrical connections, etc.

Figure 3 shows the percentage change in the turbulent drag measured using the full-channel drag balance. The solid line is a smooth line through the data drawn by eye and does not represent any theoretical or formal curve-fit. However, it is clear that drag reduction is achieved for a variety of forcing conditions and that the result varies reasonably smoothly with forcing amplitude (as represented by the non-dimensional Stuart number,  $St$ ) and forcing frequency (as represented by the non-dimensional forcing period,  $T^+$ ). Although it is too early to draw definitive conclusions, one result is particularly curious - the forcing period for optimal performance appears to increase with Reynolds number (i.e. a lower non-dimensional frequency). This is in contrast to the numerical results of (Berger et al., 2000), and the issue needs to be resolved by taking more measurements over a wider range of Reynolds numbers. It is also worth noting that, as the Reynolds number changes, the physical dimensions of the actuator do not change, and thus the non-

dimensional size of the actuator and its corresponding Lorentz force *do* change (although not very much for the two Reynolds numbers presented here).

At these low velocities, the drag measurements are difficult and changes in drag are sometime subtle. For this reason, at each test condition, the consistency of the measurement was checked by measuring the drag on the plate before and after control was applied, and by measuring the “apparent drag” on the plate with zero flow, both with and without Lorentz force control. These measurements served to confirm that the measurements of drag changes were real and not experimental artifacts.

Although these are early results, we feel confident in concluding that the Lorentz Force actuation does result in net drag reduction, as predicted by the DNS simulations. However, the variation of the control performance as a function of the frequency, amplitude and most importantly, the Reynolds number, is still unclear and will be clarified in subsequent experiments.

## Acknowledgments

This work was supported by DARPA/TTO under the supervision of Dr. Richard Wlezien. The authors would like to acknowledge Jim Paduano, George Karniadakis, Vasilios Symonides, and Jin Xu for many valuable discussions. Francis Choi and Evan Chan helped with the measurements of the electrode performance and finally, the general technical support of Chet Klepadlo and Dan Thivierge has been invaluable.

## References

- Berger, T., Lee, C., Kim, J., and Lim, J. (2000). Turbulent boundary layer control utilizing the lorentz force. *Phys. Fluids*, 12:631.
- Choi, K.-S. and Roach, P. E. (1997). Turbulent boundary layer drag reduction using an oscillating wall. AIAA Paper 97-1870.
- Crawford, C. and Karniadakis, G. (1997). Reynolds stress analysis of EMHT-controlled turbulence. Part I: Streamwise forcing. *Phys. Fluids*, 9:788–806.
- Henoch, C. and Stace, J. (1995). Experimental investigation of a salt water turbulent boundary layer modified by an applied streamwise magnetohydrodynamic body force. *Phys. Fluids*, 7:1371.
- Jung, W., Mangiavacchi, N., and Akhavan, R. (1992). Suppression of turbulence in wall-bounded flows by high frequency oscillations. *Phys. Fluids*, 4:1605–1607.
- Nosenchuck, D. and Brown, G. (1993). Discrete spatial control of wall shear stress in a turbulent boundary layer. In So, R., Speziale, C., and Launder, B., editors, *Near-Wall Turbulent Flows*, pages 689–698, New York. Elsevier Science.
- Park, J., Henoch, C., and Breuer, K. (2002). Lorentz force actuators for wall-based flow control. *Expt. Fluids*. (Submitted).

## LIST OF PARTICIPANTS

Abstiens, Ronald Aerodynamisches Institut, Aachen <a href="mailto:ronald@aia.rwth-aachen.de">ronald@aia.rwth-aachen.de</a>	Castillo, Luciano Rensselaer Polytechnic Institute <a href="mailto:castil2@rpi.edu">castil2@rpi.edu</a>
Adrian, Ronald Uni. Illinois Urbana Champaign <a href="mailto:r-adrian@uiuc.edu">r-adrian@uiuc.edu</a>	Chong, Min S The University of Melbourne <a href="mailto:chong@mame.mu.oz.au">chong@mame.mu.oz.au</a>
Barenghi, Carlo F. Newcastle University <a href="mailto:c.f.barenghi@newcastle.ac.uk">c.f.barenghi@newcastle.ac.uk</a>	Cleve, Jochen MPI Dresden <a href="mailto:clev@theory.phy.tu-dresden.de">clev@theory.phy.tu-dresden.de</a>
Bobba, Kumar California Institute of Technology <a href="mailto:bobba@galcit.caltech.edu">bobba@galcit.caltech.edu</a>	Crook, Andrew NASA Ames Research Center <a href="mailto:acrook@ctr.stanford.edu">acrook@ctr.stanford.edu</a>
Brasseur, James The Pennsylvania State University <a href="mailto:brasseur@psu.edu">brasseur@psu.edu</a>	de Bruyn Kops, Stephen University of Massachusetts <a href="mailto:debk@ecs.umass.edu">debk@ecs.umass.edu</a>
Breuer, Kenneth Brown University <a href="mailto:kbreuer@brown.edu">kbreuer@brown.edu</a>	Donnelly, Russ University of Oregon <a href="mailto:russ@vortex.uoregon.edu">russ@vortex.uoregon.edu</a>
Brewer, Wesley H. Mississippi State <a href="mailto:wbrewer@erc.msstate.edu">wbrewer@erc.msstate.edu</a>	Durst, Franz University of Erlangen-Nuremberg <a href="mailto:durst@lstm.uni-erlangen.de">durst@lstm.uni-erlangen.de</a>
Buffin-Bélanger, Thomas Université du Québec à Rimouski <a href="mailto:thomas_buffin-belanger@uqar.ca">thomas_buffin-belanger@uqar.ca</a>	Eckhardt, Bruno Philipps Universitat Marburg <a href="mailto:bruno.eckhardt@physik.uni-marburg.de">bruno.eckhardt@physik.uni-marburg.de</a>
Buschmann, Matthias H. Technische Universitat Dresden <a href="mailto:hanno@ism.mw.tu-dresden.de">hanno@ism.mw.tu-dresden.de</a>	Eiff, Oliver <a href="mailto:eiff@imft.fr">eiff@imft.fr</a>

Fernholz, Hans  
 Technische Universitat Berlin  
[fernholz@pi.tu-berlin.de](mailto:fernholz@pi.tu-berlin.de)

Foss, John  
 Michigan State University  
[foss@egr.msu.edu](mailto:foss@egr.msu.edu)

George, William K.  
 Chalmers University of Technology  
[wkgeorge@tfd.chalmers.se](mailto:wkgeorge@tfd.chalmers.se)

Goto, Susumu  
 National Institute for Fusion Science  
[goto@toki.theory.nifs.ac.jp](mailto:goto@toki.theory.nifs.ac.jp)

Gotoh, Toshiyuki  
 Nagoya Institute of Technology  
[gotoh@system.nitech.ac.jp](mailto:gotoh@system.nitech.ac.jp)

Hancock, Philip  
 University of Surrey  
[p.hancock@surrey.ac.uk](mailto:p.hancock@surrey.ac.uk)

Hayakawa, Michio  
 Hokkaido University  
[haya@eng.hokudai.ac.jp](mailto:haya@eng.hokudai.ac.jp)

Hogstrom, Ulf  
 Uppsala University  
[ulf@big.met.uu.se](mailto:ulf@big.met.uu.se)

Iwamoto, Kaoru  
 The University of Tokyo  
[iwamoto@thtlab.t.u-tokyo.ac.jp](mailto:iwamoto@thtlab.t.u-tokyo.ac.jp)

Jiménez, Javier  
 E.T.S., Madrid  
[jimenez@torroja.dmt.upm.es](mailto:jimenez@torroja.dmt.upm.es)

Johansson, Arne  
 KTH, Stockholm  
[johansson@mech.kth.se](mailto:johansson@mech.kth.se)

Jones, Malcolm  
 The University of Melbourne  
[mbjones@mame.mu.oz.au](mailto:mbjones@mame.mu.oz.au)

Joslin, Ronald D.  
 Office of Naval Research  
[rjoslin@onr.navy.mil](mailto:rjoslin@onr.navy.mil)

Jung, Sunghwan  
 University of Texas at Austin  
[sunnyjsh@chaos.ph.utexas.edu](mailto:sunnyjsh@chaos.ph.utexas.edu)

Kameda, Takatsugu  
 Yamaguchi University  
[kameda@yamaguchi-u.ac.jp](mailto:kameda@yamaguchi-u.ac.jp)

Kaneda, Yukio  
 Nagoya University  
[kaneda@cse.nagoya-u.ac.jp](mailto:kaneda@cse.nagoya-u.ac.jp)

Kitoh, Osami  
 Nagoya Institute of Technology  
[kitoh@cfi.mech.nitech.ac.jp](mailto:kitoh@cfi.mech.nitech.ac.jp)

Klewicki, Joe  
 University of Utah  
[klewicki@eng.utah.edu](mailto:klewicki@eng.utah.edu)

Knobloch, Karsten  
 Technische Universitat Berlin  
[knobloch@pi.tu-berlin.de](mailto:knobloch@pi.tu-berlin.de)

Kunkel, Gary  
 University of Minnesota  
[marusic@umn.edu](mailto:marusic@umn.edu)

Lanotte, Alessandra  
 Polo Universitario  
[alessandra.lanotte@roma2.infn.it](mailto:alessandra.lanotte@roma2.infn.it)

Lewalle, Jacques  
 Syracuse University  
[jlewalle@syr.edu](mailto:jlewalle@syr.edu)

Lindgren, Bjorn  
 KTH, Stockholm  
[oso@mech.kth.se](mailto:oso@mech.kth.se)

Ling, S.C.  
 The Catholic University of America  
[buchler@cua.edu](mailto:buchler@cua.edu)

- Makihara, Takafumi  
National Institute for Fusion Science  
[makihara@toki.theory.nifs.ac.jp](mailto:makihara@toki.theory.nifs.ac.jp)
- Marusic, Ivan  
University of Minnesota  
[marusic@umn.edu](mailto:marusic@umn.edu)
- McKeon, Beverley  
Princeton University  
[bjmckeon@princeton.edu](mailto:bjmckeon@princeton.edu)
- Meneveau, Charles  
Johns Hopkins University  
[meneveau@jhu.edu](mailto:meneveau@jhu.edu)
- Metzger, Meredith  
University of Utah  
[metzger@eng.utah.edu](mailto:metzger@eng.utah.edu)
- Miura, Hideaki  
National Institute for Fusion Science  
[miura@toki.theory.nifs.ac.jp](mailto:miura@toki.theory.nifs.ac.jp)
- Miyauchi, Toshio  
Tokyo Institute of Technology  
[tmiyauch@es.titech.ac.jp](mailto:tmiyauch@es.titech.ac.jp)
- Mochizuki, Shinsuke  
Yamaguchi University  
[shinsuke@yamaguchi-u.ac.jp](mailto:shinsuke@yamaguchi-u.ac.jp)
- Morris, Scott C.  
University of Notre Dame  
[smorris1@nd.edu](mailto:smorris1@nd.edu)
- Morrison, Jonathan  
Imperial College  
[j.morrison@ic.ac.uk](mailto:j.morrison@ic.ac.uk)
- Moser, Robert  
Uni. Illinois Urbana Champaign  
[r-moser@uiuc.edu](mailto:r-moser@uiuc.edu)
- Nagano, Yasutaka  
Nagoya Institute of Technology  
[nagano@heat.mech.nitech.ac.jp](mailto:nagano@heat.mech.nitech.ac.jp)
- Nagib, Hassan H.  
Illinois Institute of Technology  
[nagib@iit.edu](mailto:nagib@iit.edu)
- Nakano, Tohru  
Chuo University  
[nakano@phys.chuo-u.ac.jp](mailto:nakano@phys.chuo-u.ac.jp)
- Nelkin, Mark  
[mark.nelkin@nyu.edu](mailto:mark.nelkin@nyu.edu)
- Nickels, Tim  
Cambridge University  
[tbn22@eng.cam.ac.uk](mailto:tbn22@eng.cam.ac.uk)
- Nieuwstadt, Frans  
Delft University of Technology  
[f.nieuwstadt@wbmt.tudelft.nl](mailto:f.nieuwstadt@wbmt.tudelft.nl)
- Oberlack, Martin  
Technische Universitat Darmstadt  
[oberlack@hyhy.tu-darmstadt.de](mailto:oberlack@hyhy.tu-darmstadt.de)
- Osterlund, Jens  
Swedish Defence Research Agency  
[odj@foi.se](mailto:odj@foi.se)
- Pao, Hsien P.  
The Catholic University of America  
[pao@cua.edu](mailto:pao@cua.edu)
- Pearson, Bruce R.  
University of Nottingham  
[bruce.pearson@nottingham.ac.uk](mailto:bruce.pearson@nottingham.ac.uk)
- Peng, Gaozhu  
Rutgers University  
[gaozhu@caip.rutgers.edu](mailto:gaozhu@caip.rutgers.edu)
- Priyadarshana, Paththage A.  
University of Utah  
[priyadar@eng.utah.edu](mailto:priyadar@eng.utah.edu)
- Procaccia, Itamar  
Weizmann Institute, Israel  
[itamar.procaccia@weizmann.ac.il](mailto:itamar.procaccia@weizmann.ac.il)

Quach, Dan  
 McMaster University  
quachd@mcmaster.ca

Tsubokura, Makoto  
tamura@depe.titech.ac.jp  
 The University of Electro-  
 Communications, Tokyo  
tsubo@mce.uec.ac.jp

Riley, James J.  
 University of Washington  
rileyj@u.washington.edu

Tsuji, Yoshiyuki  
 Nagoya University  
c42406a@nucc.cc.nagoya-u.ac.jp

Sawford, Brian  
 CSIRO, Australia  
brian.sawford@csiro.au

Villermaux, Emmanual  
 IRPHE, Marseille  
Emmanuel.Villermaux@irphe.univ-mrs.fr

Sreenivasan, Katepalli  
 ICTP, Trieste  
krs\_jfm@ictp.trieste.it

Vinen , Joe  
 Birmingham University  
w.f.vinen@bham.ac.uk

Shy, Shenqyang (Steven)  
 National Central University  
ssh@cc.ncu.edu.tw

Wosnik, Martin  
 Chalmers University of Technology  
wosnik@tfd.chalmers.se

Skote, Martin  
 KTH, Stockholm  
mskote@yahoo.se

Yakhot, Victor  
 Boston University  
vy@bu.edu

Smedman, Ann-Sofi  
 Uppsala University  
annsofi@big.met.uu.se

Yang, Tzu Sen  
 National Central University  
s3364013@cc.ncu.edu.tw

Smits, Alexander  
 Princeton University  
asmits@princeton.edu

Yeung, P.K.  
 Georgia Institute of Technology  
yeung@peach.ae.gatech.edu

Tamura, Tetsuro  
 Tokyo Institute of Technology

Zabusky, Norman J.  
 Rutgers University  
nzabusky@caip.rutgers.edu

Tatsumi, Tomomasa  
 IUTAM, Kyoto University  
tatsumi@skyblue.ocn.ne.jp

Zhang, Shuang  
 Rutgers University  
zhang@caip.rutgers.edu

## AUTHOR INDEX

R. Abstiens	279	A. Jachens	253
J. Aubert	137	L. J. Jiang	207
C. F. Beranghi	109	W. Jiang	265
L. Biferalle	201	A. V. Johansson	257
K. Bobba	145	T. G. Johansson	285
M. S. Borgas	37, 163	G. R. Johnson	229
M. C. Boufadel	311	M. B. Jones	271
K. S. Breuer	315	S. Jung	137
W. H. Brewer	305	V. J. Kaku	311
T. Buffin-Bélanger	301	T. Kameda	297
M. H. Buschmann	5	Y. Kaneda	155
R. B. Cal	191	N. Kasagi	23
L. Castillo	191, 195	O. Kitoh	29
M. S. Chong	271	J. C. Klewicki	45, 83, 117
J. Cleve	245	K. Knobloch	11
I. Daumont	201	P. Å. Krogstad	229
S. M. de Bruyn Kops	71	G. J. Kunkel	17
R. J. Donnelly	93	A. Lanotte	201
J. C. Doyle	145	J. H. Lee	207
F. Durst	129	J. Lewalle	241
B. Eckhardt	253	J. Li	265
H.-H. Fernholz	11	W. Limberg	279
J. F. Foss	65, 77	B. Lindgren	257
M. Gad-el-Hak	5	S. C. Ling	141
W. K. George	223	I. Marusic	17, 271
M. Gharib	145	B. J. McKeon	265
T. Gotoh	181	M. Metzger	45, 83
M. Greiner	245	H. Miura	237
S. Guenther	59	S. Mochizuki	297
P. Hancock	151	S. C. Morris	65, 77
M. Hayakawa	29	J. F. Morrison	265
C. Henoch	315	R. D. Moser	169
U. Höglström	53, 89	Y. Nagano	291
T. Houra	291	H. Nagib	129
J. C. R. Hunt	53, 89	K. Nakabayashi	33
T. Ishihara	155	T. Nakano	181
K. Itakura	155	N. Nishizawa	271
K. Iwamoto	23	M. Oberlack	59

H. Osaka	297	T. Tamura	123
J. M. Österlund	257	T. Tatsumi	1
H.P. Pao	141	F. Toschi	201
J. Park	315	M. Tsubokura	123
B. R. Pearson	229	Y. Tsuji	175
P. A. Priyadarshana	83, 117	A. Uno	155
J. J. Riley	71	A. D. Venosa	311
N. Rimbert	187	E. Villermaux	215
A. G. Roy	301	W. J. Vinen	101
B. L. Sawford	37, 163	H. Wang	223
W. Schröder	279	X. Wang	191
J. Schumacher	253	K. B. Winters	71
O. Séro-Guillaume	187	M. Wosnik	285
S. S. Shy	207, 249	S. Xu	163
A.-S. Smedman	53, 89	T. S. Yang	207, 249
A. J. Smits	265	P. K. Yeung	37, 163
B. D. Storey	137	M. Yokokawa	155
Y. Suzuki	23	P. Zandonade	169
H. L. Swinney	137	E. S. Zanoun	129

# Mechanics

---

## **FLUID MECHANICS AND ITS APPLICATIONS**

*Series Editor:* R. Moreau

### *Aims and Scope of the Series*

The purpose of this series is to focus on subjects in which fluid mechanics plays a fundamental role. As well as the more traditional applications of aeronautics, hydraulics, heat and mass transfer etc., books will be published dealing with topics which are currently in a state of rapid development, such as turbulence, suspensions and multiphase fluids, super and hypersonic flows and numerical modelling techniques. It is a widely held view that it is the interdisciplinary subjects that will receive intense scientific attention, bringing them to the forefront of technological advancement. Fluids have the ability to transport matter and its properties as well as transmit force, therefore fluid mechanics is a subject that is particularly open to cross fertilisation with other sciences and disciplines of engineering. The subject of fluid mechanics will be highly relevant in domains such as chemical, metallurgical, biological and ecological engineering. This series is particularly open to such new multidisciplinary domains.

1. M. Lesieur: *Turbulence in Fluids*. 2nd rev. ed., 1990 ISBN 0-7923-0645-7
2. O. Métais and M. Lesieur (eds.): *Turbulence and Coherent Structures*. 1991 ISBN 0-7923-0646-5
3. R. Moreau: *Magnetohydrodynamics*. 1990 ISBN 0-7923-0937-5
4. E. Coustols (ed.): *Turbulence Control by Passive Means*. 1990 ISBN 0-7923-1020-9
5. A.A. Borissov (ed.): *Dynamic Structure of Detonation in Gaseous and Dispersed Media*. 1991 ISBN 0-7923-1340-2
6. K.-S. Choi (ed.): *Recent Developments in Turbulence Management*. 1991 ISBN 0-7923-1477-8
7. E.P. Evans and B. Coulbeck (eds.): *Pipeline Systems*. 1992 ISBN 0-7923-1668-1
8. B. Nau (ed.): *Fluid Sealing*. 1992 ISBN 0-7923-1669-X
9. T.K.S. Murthy (ed.): *Computational Methods in Hypersonic Aerodynamics*. 1992 ISBN 0-7923-1673-8
10. R. King (ed.): *Fluid Mechanics of Mixing*. Modelling, Operations and Experimental Techniques. 1992 ISBN 0-7923-1720-3
11. Z. Han and X. Yin: *Shock Dynamics*. 1993 ISBN 0-7923-1746-7
12. L. Svarovsky and M.T. Thew (eds.): *Hydroclones*. Analysis and Applications. 1992 ISBN 0-7923-1876-5
13. A. Lichatarowicz (ed.): *Jet Cutting Technology*. 1992 ISBN 0-7923-1979-6
14. F.T.M. Nieuwstadt (ed.): *Flow Visualization and Image Analysis*. 1993 ISBN 0-7923-1994-X
15. A.J. Saul (ed.): *Floods and Flood Management*. 1992 ISBN 0-7923-2078-6
16. D.E. Ashpis, T.B. Gatski and R. Hirsh (eds.): *Instabilities and Turbulence in Engineering Flows*. 1993 ISBN 0-7923-2161-8
17. R.S. Azad: *The Atmospheric Boundary Layer for Engineers*. 1993 ISBN 0-7923-2187-1
18. F.T.M. Nieuwstadt (ed.): *Advances in Turbulence IV*. 1993 ISBN 0-7923-2282-7
19. K.K. Prasad (ed.): *Further Developments in Turbulence Management*. 1993 ISBN 0-7923-2291-6
20. Y.A. Tatarchenko: *Shaped Crystal Growth*. 1993 ISBN 0-7923-2419-6
21. J.P. Bonnet and M.N. Glauser (eds.): *Eddy Structure Identification in Free Turbulent Shear Flows*. 1993 ISBN 0-7923-2449-8
22. R.S. Srivastava: *Interaction of Shock Waves*. 1994 ISBN 0-7923-2920-1
23. J.R. Blake, J.M. Boulton-Stone and N.H. Thomas (eds.): *Bubble Dynamics and Interface Phenomena*. 1994 ISBN 0-7923-3008-0

# Mechanics

---

## FLUID MECHANICS AND ITS APPLICATIONS

*Series Editor:* R. Moreau

24. R. Benzi (ed.): *Advances in Turbulence V.* 1995 ISBN 0-7923-3032-3
25. B.I. Rabinovich, V.G. Lebedev and A.I. Mytarev: *Vortex Processes and Solid Body Dynamics.* The Dynamic Problems of Spacecrafts and Magnetic Levitation Systems. 1994 ISBN 0-7923-3092-7
26. P.R. Voke, L. Kleiser and J.-P. Chollet (eds.): *Direct and Large-Eddy Simulation I.* Selected papers from the First ERCOFTAC Workshop on Direct and Large-Eddy Simulation. 1994 ISBN 0-7923-3106-0
27. J.A. Sparenberg: *Hydrodynamic Propulsion and its Optimization. Analytic Theory.* 1995 ISBN 0-7923-3201-6
28. J.F. Dijksman and G.D.C. Kuiken (eds.): *IUTAM Symposium on Numerical Simulation of Non-Isothermal Flow of Viscoelastic Liquids.* Proceedings of an IUTAM Symposium held in Kerkrade, The Netherlands. 1995 ISBN 0-7923-3262-8
29. B.M. Boubnov and G.S. Golitsyn: *Convection in Rotating Fluids.* 1995 ISBN 0-7923-3371-3
30. S.I. Green (ed.): *Fluid Vortices.* 1995 ISBN 0-7923-3376-4
31. S. Morioka and L. van Wijngaarden (eds.): *IUTAM Symposium on Waves in Liquid/Gas and Liquid/Vapour Two-Phase Systems.* 1995 ISBN 0-7923-3424-8
32. A. Gyr and H.-W. Bewersdorff: *Drag Reduction of Turbulent Flows by Additives.* 1995 ISBN 0-7923-3485-X
33. Y.P. Golovachov: *Numerical Simulation of Viscous Shock Layer Flows.* 1995 ISBN 0-7923-3626-7
34. J. Grue, B. Gjevik and J.E. Weber (eds.): *Waves and Nonlinear Processes in Hydrodynamics.* 1996 ISBN 0-7923-4031-0
35. P.W. Duck and P. Hall (eds.): *IUTAM Symposium on Nonlinear Instability and Transition in Three-Dimensional Boundary Layers.* 1996 ISBN 0-7923-4079-5
36. S. Gavrilakis, L. Machiels and P.A. Monkewitz (eds.): *Advances in Turbulence VI.* Proceedings of the 6th European Turbulence Conference. 1996 ISBN 0-7923-4132-5
37. K. Gersten (ed.): *IUTAM Symposium on Asymptotic Methods for Turbulent Shear Flows at High Reynolds Numbers.* Proceedings of the IUTAM Symposium held in Bochum, Germany. 1996 ISBN 0-7923-4138-4
38. J. Verhás: *Thermodynamics and Rheology.* 1997 ISBN 0-7923-4251-8
39. M. Champion and B. Deshaies (eds.): *IUTAM Symposium on Combustion in Supersonic Flows.* Proceedings of the IUTAM Symposium held in Poitiers, France. 1997 ISBN 0-7923-4313-1
40. M. Lesieur: *Turbulence in Fluids.* Third Revised and Enlarged Edition. 1997 ISBN 0-7923-4415-4; Pb: 0-7923-4416-2
41. L. Fulachier, J.L. Lumley and F. Anselmet (eds.): *IUTAM Symposium on Variable Density Low-Speed Turbulent Flows.* Proceedings of the IUTAM Symposium held in Marseille, France. 1997 ISBN 0-7923-4602-5
42. B.K. Shivamoggi: *Nonlinear Dynamics and Chaotic Phenomena. An Introduction.* 1997 ISBN 0-7923-4772-2
43. H. Ramkissoon, *IUTAM Symposium on Lubricated Transport of Viscous Materials.* Proceedings of the IUTAM Symposium held in Tobago, West Indies. 1998 ISBN 0-7923-4897-4
44. E. Krause and K. Gersten, *IUTAM Symposium on Dynamics of Slender Vortices.* Proceedings of the IUTAM Symposium held in Aachen, Germany. 1998 ISBN 0-7923-5041-3
45. A. Biesheuvel and G.J.F. van Heyst (eds.): *In Fascination of Fluid Dynamics. A Symposium in honour of Leen van Wijngaarden.* 1998 ISBN 0-7923-5078-2

# Mechanics

---

## FLUID MECHANICS AND ITS APPLICATIONS

*Series Editor:* R. Moreau

46. U. Frisch (ed.): *Advances in Turbulence VII*. Proceedings of the Seventh European Turbulence Conference, held in Saint-Jean Cap Ferrat, 30 June–3 July 1998. 1998 ISBN 0-7923-5115-0
47. E.F. Toro and J.F. Clarke: *Numerical Methods for Wave Propagation*. Selected Contributions from the Workshop held in Manchester, UK. 1998 ISBN 0-7923-5125-8
48. A. Yoshizawa: *Hydrodynamic and Magnetohydrodynamic Turbulent Flows*. Modelling and Statistical Theory. 1998 ISBN 0-7923-5225-4
49. T.L. Geers (ed.): *IUTAM Symposium on Computational Methods for Unbounded Domains*. 1998 ISBN 0-7923-5266-1
50. Z. Zapryanov and S. Tabakova: *Dynamics of Bubbles, Drops and Rigid Particles*. 1999 ISBN 0-7923-5347-1
51. A. Alemany, Ph. Marty and J.P. Thibault (eds.): *Transfer Phenomena in Magnetohydrodynamic and Electroconducting Flows*. 1999 ISBN 0-7923-5532-6
52. J.N. Sørensen, E.J. Hopfinger and N. Aubry (eds.): *IUTAM Symposium on Simulation and Identification of Organized Structures in Flows*. 1999 ISBN 0-7923-5603-9
53. G.E.A. Meier and P.R. Viswanath (eds.): *IUTAM Symposium on Mechanics of Passive and Active Flow Control*. 1999 ISBN 0-7923-5928-3
54. D. Knight and L. Sakell (eds.): *Recent Advances in DNS and LES*. 1999 ISBN 0-7923-6004-4
55. P. Orlandi: *Fluid Flow Phenomena. A Numerical Toolkit*. 2000 ISBN 0-7923-6095-8
56. M. Stanislas, J. Kompenhans and J. Westerweel (eds.): *Particle Image Velocimetry. Progress towards Industrial Application*. 2000 ISBN 0-7923-6160-1
57. H.-C. Chang (ed.): *IUTAM Symposium on Nonlinear Waves in Multi-Phase Flow*. 2000 ISBN 0-7923-6454-6
58. R.M. Kerr and Y. Kimura (eds.): *IUTAM Symposium on Developments in Geophysical Turbulence* held at the National Center for Atmospheric Research, (Boulder, CO, June 16–19, 1998) 2000 ISBN 0-7923-6673-5
59. T. Kambe, T. Nakano and T. Miyauchi (eds.): *IUTAM Symposium on Geometry and Statistics of Turbulence*. Proceedings of the IUTAM Symposium held at the Shonan International Village Center, Hayama (Kanagawa-ken, Japan November 2–5, 1999). 2001 ISBN 0-7923-6711-1
60. V.V. Aristov: *Direct Methods for Solving the Boltzmann Equation and Study of Nonequilibrium Flows*. 2001 ISBN 0-7923-6831-2
61. P.F. Hodnett (ed.): *IUTAM Symposium on Advances in Mathematical Modelling of Atmosphere and Ocean Dynamics*. Proceedings of the IUTAM Symposium held in Limerick, Ireland, 2–7 July 2000. 2001 ISBN 0-7923-7075-9
62. A.C. King and Y.D. Shikhmurzaev (eds.): *IUTAM Symposium on Free Surface Flows*. Proceedings of the IUTAM Symposium held in Birmingham, United Kingdom, 10–14 July 2000. 2001 ISBN 0-7923-7085-6
63. A. Tsinober: *An Informal Introduction to Turbulence*. 2001 ISBN 1-4020-0110-X; Pb: 1-4020-0166-5
64. R.Kh. Zeytounian: *Asymptotic Modelling of Fluid Flow Phenomena*. 2002 ISBN 1-4020-0432-X
65. R. Friedrich and W. Rodi (eds.): *Advances in LES of Complex Flows*. Proceedings of the EUROMECH Colloquium 412, held in Munich, Germany, 4–6 October 2000. 2002 ISBN 1-4020-0486-9
66. D. Drikakis and B.J. Geurts (eds.): *Turbulent Flow Computation*. 2002 ISBN 1-4020-0523-7
67. B.O. Enflo and C.M. Hedberg: *Theory of Nonlinear Acoustics in Fluids*. 2002 ISBN 1-4020-0572-5

# Mechanics

---

## **FLUID MECHANICS AND ITS APPLICATIONS**

*Series Editor:* R. Moreau

68. I.D. Abrahams, P.A. Martin and M.J. Simon (eds.): *IUTAM Symposium on Diffraction and Scattering in Fluid Mechanics and Elasticity*. Proceedings of the IUTAM Symposium held in Manchester, (UK, 16-20 July 2000). 2002 ISBN 1-4020-0590-3
69. P. Chassaing, R.A. Antonia, F. Anselmet, L. Joly and S. Sarkar: *Variable Density Fluid Turbulence*. 2002 ISBN 1-4020-0671-3
70. A. Pollard and S. Candel (eds.): *IUTAM Symposium on Turbulent Mixing and Combustion*. Proceedings of the IUTAM Symposium held in Kingston, Ontario, Canada, June 3-6, 2001. 2002 ISBN 1-4020-0747-7
71. K. Bajer and H.K. Moffatt (eds.): *Tubes, Sheets and Singularities in Fluid Dynamics*. 2002 ISBN 1-4020-0980-1
72. P.W. Carpenter and T.J. Pedley (eds.): *Flow Past Highly Compliant Boundaries and in Collapsible Tubes*. IUTAM Symposium held at the University of Warwick, Coventry, United Kingdom, 26-30 March 2001. 2003 ISBN 1-4020-1161-X
73. H. Sobieczky (ed.): *IUTAM Symposium Transsonicum IV*. Proceedings of the IUTAM Symposium held in Göttingen, Germany, 2-6 September 2002. 2003 ISBN 1-4020-1608-5
74. A.J. Smits (ed.): *IUTAM Symposium on Reynolds Number Scaling in Turbulent Flow*. Proceedings of the IUTAM Symposium held in Princeton, NJ, U.S.A., September 11-13, 2002. 2003 ISBN 1-4020-1775-8
75. H. Benaroya and T. Wei (eds.): *IUTAM Symposium on Integrated Modeling of Fully Coupled Fluid Structure Interactions Using Analysis, Computations and Experiments*. Proceedings of the IUTAM Symposium held in New Jersey, U.S.A., 2-6 June 2003. 2003 ISBN 1-4020-1806-1